The Development of High-Speed PIV Techniques and Their Application to Jet Noise Measurement

By
Andrew Skeen

Submitted for the Degree of
Doctor of Philosophy in Engineering

University of Warwick
School of Engineering

December 2006

Abstract

This thesis describes the design, development and deployment of a high-speed jet flow measurement system. The apparatus was created in response to the need to collect a large quantity of statistically-converged aerodynamic data from a series of commercial turbofan engine models. This acquisition was performed in conjunction with acoustic measurements as part of the EU CoJeN project to investigate jet noise production, and associated noise reduction techniques.

Particle Image Velocimetry is a well established flow measurement technique, but its application outside of the laboratory can be limited by a relatively low sample rate and the need to operate in a hostile environment. This thesis presents a multiple camera technique – used as the basis for the jet measurement system – that is capable of acquiring both time-series PIV data at MHz rates, and continuous, statistically independent measurements at up to 14 Hz.

The resultant PIV measurement rig was therefore capable of acquiring time-averaged velocity and turbulence data from the whole of a $^{1}_{10}$ scale coaxial engine exhaust plume (down to 4m or 20D) in no more than 1 hour. The ~500°C Mach ≤ 0.9 jets were also scanned volumetrically in order to check the spatial alignment of the nozzle and flow streams, and all PIV measurements were synchronised to simultaneous LDA acquisition, thus enabling the data to be validated. Finally, the cameras were used to acquire novel 6-frame time-series data at $\leq$ 330 kHz, which was used to calculate time-space correlations within the exhaust.

By providing a highly automated and completely remote-controlled system, the exhaust measurements could be repeated over 3 operating conditions and 2 nozzle geometries, thereby providing a comprehensive description of the flow field. The data, having been systematically post-processed, has been shown to agree well with concurrent measurements, and it will now be used to validate CFD models of coaxial jet flow. By improving the quality of computational flow prediction in this way, the time taken to design and test quieter jet engines will be significantly reduced.

Contents

Abstract i

Contents ii
List of Figures viii
List of Tables xvi
Abbreviations and Acronyms xviii
Acknowledgements xix
Declaration xx

1. Introduction 1

1.1. Jet Noise Research 2
1.1.1. Motivation 2
1.1.2. Aircraft Noise Production & Reduction 4
1.2. Particle Image Velocimetry 6
1.2.1. The Capabilities of PIV 6
1.2.2. High-Speed PIV 7
1.3. The CoJeN Project 8
1.3.1. Aims & Objectives 8
1.3.2. Experimental Validation Work 8
1.3.3. Jet Exhaust PIV Measurements 9

2. Particle Image Velocimetry 11

2.1. Introduction 12
2.1.1. Principle of Operation 12
2.1.2. Multidimensional PIV 22
2.2. Seeding 35
2.2.1. Flow Depiction 35
2.2.2. Reflectivity and Brightness 45
2.2.3. Recorded Particle Image Size 51
2.2.4. Summary of Seeding Requirements 52
2.2.5. Recognised Seeding Materials 53
2.2.6. Seeding Generators 55
2.3. Illumination 59
2.3.1. Introduction 59
2.3.2. Lasers 61
2.3.3. Light Sheet Generation 66

2.4. Camera Sensors 68

2.4.1. Introduction 68

2.4.2. Principle of Operation 69

2.4.3. CCD Sensors 70

2.4.4. CMOS Sensors 76

2.4.5. Colour Sensing 78

2.4.6. Cameras for Cross-Correlation 80

2.4.7. Cameras for High-Speed Time-Series Acquisition 81

2.4.8. Image Quality 87

2.4.9. Imaging Lenses 90

2.5. Image Analysis 92

2.5.1. Introduction 92

2.5.2. Optical Correlation 93

2.5.3. Digital Cross-Correlation 95

2.5.4. Super-Resolution Techniques 97

2.5.5. Vector Validation 100

3. A Novel Method for the Acquisition of High Speed TR-PIV Data 103

3.1. Introduction 104

3.1.1. High-Speed Time-Series Acquisition 104

3.1.2. Proposed Technique 107

3.1.3. Camera Calibration 110

3.1.4. 'Nudged' Back-Projection 114

3.2. Experimental Application and Results 115

3.2.1. Experimental Apparatus 115

3.2.2. Calibration Image Analysis 117

3.2.3. Image Back-Projection 121

3.2.4. Image Subtraction 124

3.3. Conclusions 125

3.3.1. Light-Sheet Limitations 125

3.3.2. Single Exposure Acquisition 127

4. Coaxial Jet Noise Project: Introduction 128

4.1. Introduction 129

4.1.1. Aims & Objectives 129

4.1.2. Project Structure 131

4.2. Jet Noise 132

4.2.1. Background 132

4.2.2. Noise Reduction Techniques 133
4.2.3. Noise Prediction Techniques 135
4.3. CoJeN Experimental Work 137
4.3.1. Test Nozzles 137
4.3.2. Test Operating Conditions 138
4.3.3. Flow Measurements 139
4.3.4. Time-Space Correlation 141

5. Coaxial Jet Noise Project: Experiment Design 143
5.1. Requirements and Specification 144
5.1.1. Exhaust Measurement Volume 144
5.1.2. Measurement Parameters 145
5.1.3. Temporal Constraints 145
5.1.4. Physical Constraints 146
5.2. Imaging System 148
5.2.1. Requirements and Options 148
5.2.2. Variable Zoom Imaging System 149
5.2.3. PIV Image Quality 151
5.2.4. Spatial Resolution 153
5.2.5. Acquisition Speed 156
5.2.6. Camera Selection 157
5.2.7. Lens Selection 160
5.3. Illumination System 162
5.3.1. Laser Hardware 162
5.3.2. Light Sheet Formation and Combination 163
5.3.3. Light Sheet Alignment 166
5.4. Experimental Facility 168
5.4.1. The NTF at Qinetiq 168
5.4.2. Rig Support Structure 169
5.5. Mechanical Rig Design 171
5.5.1. Component Layout 171
5.5.2. Rig Construction 174
5.5.3. Motorised Traverses 176
5.5.4. Projection Optics Traverse 179
5.5.5. Laser Alignment Mirrors 180
5.5.6. Camera Traverse 181
5.5.7. Traverse Positioning Accuracy 183
5.6. Control System 185

5.6.1. Software Options 185
5.6.2. Custom Control Software 186
5.6.3. Frame-Grabbing Software 193
5.6.4. Triggering Electronics 194
5.7. Computer System 197
5.7.1. Acquisition and Storage Requirements 198
5.7.2. RAID Disk Array Machines 200
5.7.3. Archive Storage 204
5.7.4. Machine Networking 206
5.8. Ancillary Systems 207
5.8.1. 3-Component PIV System 207
5.8.2. Background-Oriented Schlieren 208
5.8.3. Observation Cameras 209
5.8.4. Automatic PC Starter 210
5.9. Seeding 211
5.9.1. Considerations and Requirements 211
5.9.2. Seeding Generation 213
5.9.3. Seeding Performance 217
5.10. Systems Overview 219
6. Coaxial Jet Noise Project: Processing, Results and Analysis 222
6.1. Datasets Collected 223
6.1.1. Phase 2: Volumetric Cross-Planes 223
6.1.2. Phase 3: Full Exhaust Mapping 225
6.1.3. Phase 4: Time-Resolved PIV 226
6.2. Issues Encountered 228
6.2.1. Camera Clock Performance 228
6.2.2. Left / Right Velocity Bias 231
6.2.3. LDA Interference Filter 237
6.2.4. PC Disk Access Failures 241
6.3. Generic Processing Workflow 243
6.3.1. File Renumbering 243
6.3.2. Image Back-Projection 245
6.3.3. Spatial Calibration 248
6.3.4. Cross-Correlation 251
6.3.5. Vector Filtering 253
6.4. Phase 2 Processing & Results 256
6.4.1. Cross-Plane Reconstruction 257

6.4.2. Circle Fitting 260
6.4.3. Discussion 263
6.5. Phase 3 Processing & Results 265
6.5.1. Additional Vector Filtering 265
6.5.2. Left / Right Velocity Correction 275
6.5.3. Exhaust Maps 287
6.5.4. Discussion 290
6.6. Phase 4 Processing & Results 298
6.6.1. High-Resolution Back-Projection 298
6.6.2. Time-Space Correlation 301
7. Conclusions and Further Work 306
7.1. Conclusions 307
7.2. Further Work 308
8. Bibliography 311
9. Appendix 328
9.1. Miscellany 329
9.1.1. Optical Calibration 329
9.1.2. Linear Camera Modelling 331
9.1.3. Innolas Multi-Pulse Laser System 336
9.1.4. The Hough Transform 338
9.1.5. Calibration Image Analysis Application 341
9.1.6. The CoJeN Project Partners 347
9.1.7. PIV Camera Database 348
9.1.8. Light Sheet Mirror Positioning 351
9.1.9. Light Sheet Alignment Software 355
9.1.10. YAPP Screenshots 358
9.1.11. Acute PkPG2116 Timing Synchroniser 361
9.1.12. Q-Switch Delay Accuracy 364
9.1.13. File Transfer Application Log File 366
9.1.14. Background-Oriented Schlieren System 367
9.1.15. Automatic PC Starter 370
9.2. CoJeN Experimental Results 371
9.2.1. Acquisition Parameters 371
9.2.2. Phase 2 Cross-Axial Planes 372
9.2.3. Phase 3 Exhaust Mappings 373
9.3. Engineering Drawings 377

9.3.1. NTF Chamber Gantry 377
9.3.2. CoJeN Rig Base 379
9.3.3. CoJeN Rig Laser Support Structure 380
9.3.4. CoJeN Projection Optics Traverse 382
9.3.5. CoJeN Light Sheet Projection Optics 388
9.3.6. CoJeN Camera Traverse System 390
9.4. Matlab Code 403
9.4.1. Image Cross-Correlation Code 403
9.4.2. Calibration Image Analysis Software 404
9.4.3. Light Sheet Projection Simulation 414
9.4.4. Variable Zoom Imaging System Simulation 417
9.4.5. Constant Zoom Imaging System Simulation 422
9.4.6. CoJeN Rig Mechanical Layout Optimisation 424
9.4.7. Background Oriented Schlieren 426
9.4.8. Innolas Pulse Intensity Jitter Tester 430
9.4.9. Time-stamp Recognition Script 433
9.4.10. Phase 2 Processing Script 436
9.4.11. Phase 3 Processing Script 446

List of Figures

Figure 1.1 – Number of US airports with noise control measures (Boeing noise website). 3

Figure 1.2 – Noise sources in a 1992-era aircraft (NASA, 1999). 5

Figure 2.1 – Pulsed light velocimetry techniques, adapted from (Adrian, 1991). 13

Figure 2.2 – A typical PIV experimental arrangement. 14

Figure 2.3 – Speckle, high and low density seeding images, as per LSV, PIV & PTV. 15

Figure 2.4 – Framing and pulse-coding options, adapted from (Adrian, 1991). 16

Figure 2.5 – Stereoscopic PIV by means of translated cameras. 24

Figure 2.6 – Obliquely viewed target with and without Scheimpflug mounts (Davis manual; LaVision). 25

Figure 2.7 – Angular stereoscopic PIV, using the Scheimpflug arrangement. 26

Figure 2.8 – Mapped stereoscopic images. 29

Figure 2.9a) 3D3C HPIV data, from (Zhang, et al., 1997); b) HPIV recording and reconstruction, adapted from (Hinsch, 2002). 32

Figure 2.10 – Intensity based particle filtering, from (McCluskey, 1992). 34

Figure 2.11 – The particle-laden jet profiles of (Levy and Lockwood, 1981). 37

Figure 2.12 – A particle's representation of fluid flow, from (Westerweel, 1997). 39

Figure 2.13 – Particulate flow following accuracy vs. particle size. 44

Figure 2.14 – Predominant scattering regimes, from (Wallace and Hobbs, 1977). 46

Figure 2.15 – Representative angular scattering profiles, from (Kidder and Haar, 1995). Note logarithmic scales. 47

Figure 2.16 – Mie scattering of TiO_2 particles in air (note logarithmic scale). 48

Figure 2.17 – 90° Mie scattering intensity of TiO_2 particles in air 48

Figure 2.18 – Mie scattering of transparent and opaque particles. 49

Figure 2.19 – Geometric reflectivity for selected seeding materials. 50

Figure 2.20 – Imaged particle diameter (in pixels) vs. actual particle diameter. 51

Figure 2.21 – Liquid particulate aerosol generators: a) Nebuliser; b) Laskin nozzle. 56

Figure 2.22 – Atomised particle size distributions, from (Kähler, 2003). 57

Figure 2.23 – Single, and dual-phase fluidised bed seeders, from (Melling, 1997). 58

Figure 2.24 – Q-switched flash-lamp pumped solid state laser cavity. 62

Figure 2.25 – Pockels cell Q-switching. 63

Figure 2.26 – Brewster's angle. 63

Figure 2.27 – 'Sliced' Nd:YAG laser pulses, from (Lempert, et al., 2002). 65

Figure 2.28 – Cylindrical lens sheet forming optics, from (Stanislas and Monnier, 1997) and (LaVision FlowMaster system manual). 66
Figure 2.29 – The FujiFilm Super-CCD family, along side a regular sensor. 70
Figure 2.30 a) Simple CCD structure; b) CCD pixel readout electronics. 71
Figure 2.31 – Types of CCD sensor readout, adapted from (Lai, et al., 1998). 72
Figure 2.32 – Front (left) and back (right) illuminated CCD sensors. 74
Figure 2.33 – An EM-CCD frame-transfer sensor. 75
Figure 2.34a) CMOS sensor architecture; b) Typical APS (CTIA) readout electronics, from (Bigas, et al., 2006). 76
Figure 2.35a) Trichroic prism separation; b) Mosaic filtering; c) Vertically integrated. 78
Figure 2.36 – The 'frame-straddling' technique. 80
Figure 2.37 – CCD interline sensor with 4 separate readout taps. 82
Figure 2.38 – The Shimadzu HPV-1 sensor layout, from (Etoh, et al., 2003). 85
Figure 2.39 – Image intensifier gated dual-sensor high-speed camera. 86
Figure 2.40 – Examples of radial distortion. 91
Figure 2.41 – Fourier transformation of an auto-correlation PIV image. 93
Figure 2.42 – Auto-correlation maps produced by 3 methods, from (Westergaard and Buchhave, 1993). 94
Figure 2.43 – Typical direct and FFT cross-correlation maps. 96
Figure 2.44 – The effect of interrogation window size. 96
Figure 2.45 – The first 2 stages of recursive multi-pass correlation. 98
Figure 2.46 – Deformed interrogation windows, from (Scarano, 2002). 99
Figure 2.47 – Spurious vectors, from (Nogueira, et al., 1997). 100
Figure 2.48 – Multiple peak correlation map (profiles). 101
Figure 2.49 – Local vector comparison and filtering. 102
Figure 3.1 – The mapping of separate cameras' views onto a common FOV. 107
Figure 3.2 – Single exposure multi-sensor acquisition. 107
Figure 3.3 – Multiple-exposure multi-sensor acquisition technique. 108
Figure 3.4 – Light sheet thickness and camera depth of field. 109
Figure 3.5 – The pin-hole camera model. 110
Figure 3.6 – 3D camera calibration using circular markers. 113
Figure 3.7 – Particle positioning error due to an unknown light sheet position. 114
Figure 3.8a) The Innolas 10-pulse laser system; b) Statistics from 100 10-pulse sequences. 116
Figure 3.9 – High-speed flow experiment. 116
Figure 3.10 – Multiply-exposed high-speed flow images. 117

Figure 3.11a) 3D calibration plate; b) Typical calibration plate image. 118
Figure 3.12 – Matlab calibration plate image analysis application. 119
Figure 3.13 – Graphical and CSV output of the calibration image analysis script. 120
Figure 3.14 – The vertical dot separation for each column of Figure 3.13. 120
Figure 3.15 – The BatchProcess software. 122
Figure 3.16 – The difference between back-projection calibration images. 122
Figure 3.17 – Horizontal and vertical components of a back-projection error map. 123
Figure 3.18 – The subtraction of multiply-exposed images. 124
Figure 3.19 – Particle image positioning error, caused by a thick light sheet. 125
Figure 3.20 – Particle diameter and maximum position error for various camera angles. 126
Figure 3.21 – 3 overlapped views of particles in a thick light sheet. 127
Figure 4.1 – A turbofan engine (Wikipedia website). 132
Figure 4.2 – Coaxial jet mixing regions. 133
Figure 4.3 – The effect of increasing bypass ratios on jet noise, from (Neise, 2004). 134
Figure 4.4a) Lobed forced mixer (NASA AT website); b) Serrated Rolls Royce Trent 800 engine (Qinetiq website); c) GE CFM56-5a5 engine with chevrons (Neise, 2004). 135
Figure 4.5 – Plain and serrated short cowl and coplanar nozzle geometries. 137
Figure 4.6 – PIV measurement planes. 140
Figure 4.7 – Time-space correlation using PIV vector maps. 142
Figure 5.1 – CoJeN measurement area of interest. 144
Figure 5.2 – RANS predictions for short cowl nozzle, OP.1.3: a) Temperature; b) Horizontal-component velocity. (Volvo Aero) 146
Figure 5.3 – Variable-zoom imaging system example. 149
Figure 5.4 – The 31 positions calculated as required for Phase 3 if Z_a = 9 px/mm. 154
Figure 5.5 – Simulated Phase 3 acquisition times. 155
Figure 5.6 – Interwoven PIV acquisition. 156
Figure 5.7 – PIV camera database webpage (insert: filtering parameters). 158
Figure 5.8 – Lens DOF requirements as a function of camera angle. 161
Figure 5.9 – NeoPIV head and power supply. (Litron; Oxford Lasers) 162
Figure 5.10 – Dual cylindrical lens sheet forming optics. 163
Figure 5.11 – 4-beam laser combination. 164
Figure 5.12a) Three laser light-sheet combination; b) Mirror gimbal mount. 165
Figure 5.13 – Possible methods of laser light sheet misalignment. 166
Figure 5.14 – The laser light sheet alignment application. 167

Figure 5.15 – The NTF at Qinetiq, Farnborough. (Qinetiq website) 168
Figure 5.16 – The bogeys and drive system. 169
Figure 5.17 – NTF, with support structure and CoJen rigs. 170
Figure 5.18a) World-orthogonal CoJeN rig arrangement; b) Angled arrangement. 171
Figure 5.19 – Downstream view of CoJeN rig components. 172
Figure 5.20 – CoJeN rig light sheet angle optimisation. 173
Figure 5.21 – Downstream view of CoJeN rig component layout, with $\theta = 30.7°$. 174
Figure 5.22 – The CoJeN rig steel framework. 175
Figure 5.23 – The CoJeN rig laser enclosure. 175
Figure 5.24 a) Milford Instruments motor driver; b) Quad motor driver unit. 177
Figure 5.25 – CoJeN traverse limit switches and junction box. 178
Figure 5.26 – The light sheet projection traverse (insert: with dust shield). 179
Figure 5.27 – Laser alignment mirrors (insert: ventilated dust cover). 180
Figure 5.28 – The CoJeN camera traverse. 181
Figure 5.29a) CoJeN cameras in situ; b) Variable and fixed angled camera mounts... 182
Figure 5.30 – LDA head and alignment ruler, mounted on the camera traverse. 183
Figure 5.31 – DC motor control electronics. 184
Figure 5.32 – YAPP control software interface. 187
Figure 5.33 – The YAPP *Hardware* window. 188
Figure 5.34 – The YAPP *Workflow* window. 189
Figure 5.35 – The YAPP *Variables* window. 190
Figure 5.36 – YAPP pulse train output action interface. 191
Figure 5.37 – YAPP hierarchical data processing. 192
Figure 5.38 – 16-bit image viewing and manipulation in YAPP 193
Figure 5.39 – Multiplexed laser triggering circuit. 195
Figure 5.40a,b) The Acute PkPG sequencer; c) Laser trigger demultiplexer. 195
Figure 5.41 – PkPG timing error distribution. 196
Figure 5.42 – CoJeN camera and RAID PC arrangement. 201
Figure 5.43 – RAID 5 data storage. 202
Figure 5.44 – CoJeN RAID array write speed. 203
Figure 5.45 – LaCie 250 Gb external hard drive: a) alone; b) in situ. 204
Figure 5.46 – Directory moving software. 205
Figure 5.47 – 3D PIV cameras mounted on the CoJeN rig. 207
Figure 5.48 – Instantaneous BOS vector map; part of a high-speed helium jet study by the author. 208

Figure 5.49 a) Camera system components; b) Traverse camera; c) Pan/tilt camera...209
Figure 5.50 – Software to view, select, and move the observation cameras 210
Figure 5.51 – The performance of TiO_2 seeding in air, based on equation (2.19). 212
Figure 5.52 – 0.3 μm Huntsman Tioxide TR38 particles. 212
Figure 5.53a) LaVision seeding generator; b) The TiO_2 drying facilities. 213
Figure 5.54 – The core and bypass seeding generators used for CoJeN tests. 214
Figure 5.55 – Vi-Count aerosol generator, as used for flightstream seeding. 216
Figure 5.56 – Good CoJeN seeding, as seen by the PIV cameras. 217
Figure 5.57 – Intermittent jet seeding. 218
Figure 5.58 – Agglomerated seeding around the instrumentation rake. 218
Figure 5.59 – The CoJeN rig in situ. 219
Figure 5.60 – CoJeN rig electronics. 220
Figure 5.61 – Control room computer systems. 221
Figure 6.1 – Phase 2 measurement positions. 224
Figure 6.2 – Phase 2 measurement timing. 224
Figure 6.3 – Phase 3 measurement positions. 225
Figure 6.4 – Phase 4 measurement timing. 226
Figure 6.5 – Camera 4 images, using 1 and 2 taps, with a 40 MHz clock. 229
Figure 6.6 – Dark noise histograms for cameras 1-5, for all operating modes. 230
Figure 6.7 – Instantaneous and (enhanced) time-averaged phase 3 images. 231
Figure 6.8 – Left/right difference, and average intensity for camera 1, frame A. 232
Figure 6.9 – Instantaneous and time-averaged vector maps (horizontal component). .233
Figure 6.10 – Typical phase 3 frame A & B intensity histograms. 234
Figure 6.11 – Camera sides, as arranged during the CoJeN tests. 236
Figure 6.12 – Average of 350 phase 3 PIV images, from cameras 2 and 5. 238
Figure 6.13 – Effect of Newton's rings on the vertical-component displacement. 240
Figure 6.14 – Internal interference filter reflections. 240
Figure 6.15 – Generic processing workflow for CoJeN data. 243
Figure 6.16 – An embedded timestamp in an image's top left corner. 244
Figure 6.17 – CoJeN image back-projection. 247
Figure 6.18a) Long-exposure image of LDA beams; b) Image of nozzle tip. 249
Figure 6.19 – Spatial filtering applied to a phase 2 vector map. 254
Figure 6.20 – Phase 2 processing script interface. 256
Figure 6.21 – Representative phase 2 axial dataset. 257
Figure 6.22 – All phase 2 data; non-interpolated. 258

Figure 6.23 – Cross-axial statistics (short cowl nozzle / OP 1.8, at 897 mm). 258
Figure 6.24 – Axial velocity cross-planes (short cowl nozzle / OP 1.8). 259
Figure 6.25 – Axial velocity cross-planes (coplanar nozzle / OP 1.3). 259
Figure 6.26 – Cross-axial circle fitting points. 260
Figure 6.27 – Cross-axial circular axial velocity contours (coplanar nozzle, OP 1.3). 261
Figure 6.28 – Jet position vs. axial distance. 262
Figure 6.29 – Non circular mean axial velocity contours (coplanar nozzle, OP 1.3)...263
Figure 6.30 – Central slice axial mean & RMS profiles for all phase 2 data. 264
Figure 6.31 – Spurious vectors, from a phase 3 CoJeN image. 265
Figure 6.32 – The spatial filtering of a phase 3 instantaneous axial-velocity map.....266
Figure 6.33 – Unsorted and sorted vector time-series (run 546a, camera 2). 266
Figure 6.34 – IFR filtering example (top-hat probability distributions). 268
Figure 6.35 – Inter-fractional range filtering of normally distributed data. 269
Figure 6.36 – Axial RMS data before and after IFR filtering (run 546a, camera 2). ...270
Figure 6.37 – Secondary axial IFR filtering. 271
Figure 6.38 – The effect of double axial IFR filtering.....272
Figure 6.39 – The effect of axial IFR filtering on filter thresholds (run 535a, camera 2). 273
Figure 6.40 – Combined effect of all phase 3 vector filtering (run 546a, camera 2)....274
Figure 6.41a) Vector map correction strips; b) Associated 'error map'. 276
Figure 6.42 – Application of the initial left / right correction. 276
Figure 6.43 – Axial mean and RMS velocity (run 501c, camera 1). 278
Figure 6.44 – Time-averaged axial-component velocity contours. 280
Figure 6.45 – Typical radial profile of axial-component velocity (and discontinuity). 281
Figure 6.46 – Comparison of left / right (axial) displacement differences. 281
Figure 6.47 – LRDD vs. measurement position (short cowl nozzle, OP 1.1). 282
Figure 6.48 – Left/right velocity difference vs. image intensity. 283
Figure 6.49 – Uncorrected mean axial velocity map (short cowl nozzle / OP 1.1). 283
Figure 6.50 – Raw and fitted axial velocity profiles (top row, short cowl, OP 1.1). 284
Figure 6.51 – Typical left/right correction factors; a) mean; b) standard deviation. 285
Figure 6.52a) Unsmoothed; b) Quadratically smoothed bias correction map. 286
Figure 6.53 – CoJeN phase 3 display script.....287
Figure 6.54 – Mean axial and radial, and axial RMS velocities (short cowl, OP 1.1). 288
Figure 6.55 – Mean axial and radial, and axial RMS velocities (coplanar; OP 1.2). ...289
Figure 6.56 – Radial profiles of mean axial velocity (short cowl; OP 1.1). 290

Figure 6.57 – Axial component turbulence levels for both nozzles under OP. 1.2. 291
Figure 6.58 – Radial profiles of turbulent kinetic energy (short cowl; OP. 1.2). 292
Figure 6.59 – Jet deviation (short cowl, OP1.2). 293
Figure 6.60 – Bullet wake position and jet centre vs. axial position. 293
Figure 6.61 – Phase 2 and 3 jet deviation measurements (coplanar; OP 1.2). 294
Figure 6.62 – Phase 3 and 4 LDA measurements. 295
Figure 6.63 – Comparison of PIV and LDA data. 296
Figure 6.64 – Phase 4 processing. 298
Figure 6.65 – Phase 4 camera projection corrections. 299
Figure 6.66 – Phase 4 'nudged' and back-projected calibration images. 300
Figure 6.67 – 67 kHz 'movie' of axial flow velocity (2m from short-cowl nozzle). ...300
Figure 6.68 – 21 kHz 'movie' of large-scale vorticity (2m from short-cowl nozzle). .300
Figure 6.69 – Space-time correlation maps for 15 τ values; $\mathbf{x} = (0, 6.3)D$. 301
Figure 6.70 – Typical time-space correlation profiles. 302
Figure 6.71 – Time-space correlation peak displacement and strength vs. τ. 303
Figure 6.72 – LDA and PIV convection speed measurements. 304
Figure 6.73 – Time-space 'decorrelation' rate vs. axial sample 222
Figure 7.1 – The modified jet measurement rig. 309
Figure 9.1 – Optical fringe analysis and correlation, adapted from (Grant, 1997). 329
Figure 9.2 – Linear camera model with coincident axes. 331
Figure 9.3 – Two-coordinate imaging system, from (Fu, et al., 1987). 332
Figure 9.4 – Innolas Pockels cell controller. 336
Figure 9.5 – Innolas 10-pulse control system schematic 337
Figure 9.6 – Photodiode measuring circuit 337
Figure 9.7 – Corresponding points and lines in both Cartesian and Hough space. 338
Figure 9.8 – An example of the Hough accumulator. 339
Figure 9.9 – Typical calibration grid image and associated Hough accumulator. 340
Figure 9.10 – Calibration plate image AOI selection. 341
Figure 9.11 – Sobel edge-detected (and filled) calibration plate image dots. 342
Figure 9.12 – Iterative image thresholding GUI. 343
Figure 9.13 – Typical (initial) Hough map. 344
Figure 9.14 – Typical secondary Hough map. 345
Figure 9.15 – Secondary Hough lines superimposed on first Hough map. 345
Figure 9.16 – The pco.2000 camera (PCO). 349
Figure 9.17 – Representative selection of high-speed cameras. 350

Figure 9.18 – Multiple mirror light sheet combination. 351
Figure 9.19 – Beam combination simulation. 354
Figure 9.20 – Laser light sheet alignment image and profile. 357
Figure 9.21 – YAPP 'workflow' interface, with dialogs. 358
Figure 9.22 – YAPP 'hardware' interface, with dialogs. 359
Figure 9.23 – YAPP 'variables' interface, with dialogs. 360
Figure 9.24 – Generic YAPP PGV file and structure. 363
Figure 9.25 – 1000 NeoPIV flash-lamp to Q-switch delay intervals. 364
Figure 9.26 – Distribution of the final 500 samples shown in Figure 9.25. 365
Figure 9.27 – Q-switch triggering delay line circuit. 365
Figure 9.28 – CoJeN BOS system in situ. 367
Figure 9.29a) Typical image recorded by BOS system; b) Trigger recording. 368
Figure 9.30 – BOS image dot centroid positions. 369
Figure 9.31a) Individual BOS marker dot; b) Instantaneous centroiding quality. 369
Figure 9.32 – Automatic PC starting circuit. 370
Figure 9.33 – Phase 3 run positions and Δt values. 371
Figure 9.34 – CoJeN rig dimensions. 379
Figure 9.35 – CoJeN projection optics traverse. 382
Figure 9.36 – The CoJeN camera traverse 'vertical' section. 390
Figure 9.37 – The CoJeN camera traverse 'horizontal' section. 399
Figure 9.38 – 'Vertical' camera traverse counterweight arrangement. 400

List of Tables

Table 2.1 – Seeding materials and typical physical characteristics. 54
Table 2.2 – Summary of liquid and solid seeding for gas flows. 55
Table 2.3 – Common PIV lasers with typical characteristics. 61
Table 2.4 – High-speed camera technologies and typical performance characteristics.81
Table 2.5 – The calculation of overall image sensor efficiency. 87
Table 2.6 – Sources of image noise. 88
Table 2.7 – Noise and sensitivity related characteristics for the pco.2000 camera. 89
Table 3.1 – Representative selection of high-speed time-series studies. 105
Table 4.1 – CoJeN project schedule. 131
Table 4.2 – CoJeN operating conditions. 138
Table 4.3 – The CoJeN measurement programme. 139
Table 5.1 – Variable-zoom imaging system simulations. 149
Table 5.2 – Commercially available motorised zoom lenses. 150
Table 5.3 – Acceptable seeding concentrations for CoJeN imaging system. 152
Table 5.4 – *C*-ratios for different imaging system parameters (0.53m FOV). 152
Table 5.5 – Short-list of CoJeN camera candidates. 159
Table 5.6 – Factors affecting the choice of lens *f*-number.....160
Table 5.7 – Object distance vs. FOV for a 55 mm lens. 161
Table 5.8 – Equipment placement during the CoJeN test. 170
Table 5.9 – Milford Instruments 5-595 motor driver specification. 177
Table 5.10 – Pulse generator varieties, as suitable for PIV experiment triggering. ...194
Table 5.11 – Predicted number of CoJeN measurements. 198
Table 5.12 – Distribution of measurements by each CoJeN camera. 200
Table 6.1 – Phase 2 data acquired during the CoJeN test. 225
Table 6.2 – Phase 3 data acquired during the CoJeN test. 226
Table 6.3 – Phase 4 data acquired during the CoJeN test. 227
Table 6.4 – pco.2000 camera environmental requirements. 229
Table 6.5 – Left / right intensity differences, from raw Phase 3 image data. 231
Table 6.6 – Left/right horizontal displacement difference in Phase 3 vector maps....234
Table 6.7 – An example of non-sequential image saving. 244
Table 6.8 – CoJeN image back-projection.....246
Table 6.9 – Calibration points from camera 1's perspective. 250
Table 6.10 – CoJeN cross-correlation processing parameters. 252

Table 6.11 – CoJeN vector filtering parameters. 253
Table 6.12 – Phase 2 vector coverage, before and after filtering. 255
Table 6.13 – Jet divergence results from phase 2 measurements. 262
Table 6.14 – The variables associated with left / right velocity correction. 277
Table 6.15 – Similar RMS values for non-similar data biasing. 279
Table 6.16 – Jet and bullet wake deviation, in the phase 3 measurement plane.....294
Table 6.17 – Phase 4 projection correction correlation settings. 299
Table 9.1 – CoJen project partners, and their work package involvement. 347
Table 9.2 – Camera database variables. 348
Table 9.3 – The pco.2000 camera specifications. (PCO) 349
Table 9.4 – Acute PkPG2116 electrical specification. 361
Table 9.5 – Acute PkPG2116 commands. 362
Table 9.6 – CoJeN rig description. 379
Table 9.7 – Summary of the (maximum) weight borne by the camera traverse.....400

Abbreviations and Acronyms

ADC	Analogue to Digital Converter.
AOD	Acousto-Optical Deflector.
AOI	Area Of Interest.
CW	Continuous Wave [laser].
DAQ	Data Acquisition [device].
DLL	Dynamically Linked Library.
FIFO	First-In First-Out [memory].
FOV	Field Of View.
KVM	Keyboard Video Mouse [switch].
LUT	Look-Up Table.
MDI	Multiple Document Interface.
MFC	Microsoft Foundation Classes.
Nd:YAG	Neodymium-doped Yttrium Aluminium Garnet.
Nd:YLF	Neodymium-doped Yttrium Lithium Fluoride.
NTF	[The QinetiQ] Noise Test Facility.
SEM	Scanning Electron Microscope.
SNR	Signal-to-Noise Ratio.
TIFF	Tagged Image File Format.
VNC	Virtual Network Computing.
XML	Extensible Markup Language.

Acknowledgements

I would like to express my thanks to all those whose support and assistance have made this thesis possible. I am particularly grateful to my supervisor, Prof. Bryanston-Cross, for the guidance provided throughout my PhD, not to mention the opportunity to work on so many varied and interesting projects.

Dr. Paul Dunkley cannot go unmentioned, his help having been invaluable on many an occasion. I am also indebted to the School of Engineering technicians, for their part in turning designs into reality, and my colleagues and friends in the Optical Engineering group, for providing a never ending source of camaraderie.

Declaration

This thesis contains the results of research undertaken by me between September 2003 and November 2006 in the School of Engineering at the University of Warwick. This thesis is entirely my own work and contains nothing done in collaboration with others except where explicit acknowledgement has been given.

This work has not been submitted in whole or in part for any other degree of diploma.

Andrew James Skeen

The University of Warwick,

November 2006

1. Introduction

1.1. Jet Noise Research

1.1.1. Motivation

Noise pollution from commercial aircraft is a good example of an aerodynamic effect that results in very real, worldwide problems. Despite the fact that jet aircraft have become significantly quieter every decade (on a thrust-equalised basis), 5% annual growth in the number of flights being operated, coupled with the ever-larger planes being used, means that noise pollution is one of the air transport industry's most challenging problems.

The effects of aircraft noise exposure range from sleep loss and irritation to cardiovascular and mental health problems, and the UK government estimates that over ½ million people in this country alone would be severely affected were restrictions not in place (Parliamentary Office of Science and Technology, 2003). Figures such as this are calculated by comparing the population density around an airport with those areas of land that experience an 'effective perceived noise level' in excess of 57 dB(A) L_{eq}. The units of the EPNL ensure that noise is normalised by both the frequency-dependent sensitivity of human hearing, and the number, duration and timing of flights throughout the day.

Restrictions on the amount of noise produced by any one plane are set by the International Civil Aviation Organisation, and in turn adopted as national legislation by the ICAO's member states. From 1977 to 1996, 'Chapter 3' legislation has imposed maximum values on the noise from aircraft (of different weights) during both take-off

and landing, with the current 'Chapter 4' legislation introducing a further 10 dB reduction in the limits. In practise however, most aircraft produce significantly less noise than is permitted under ICAO rules, and locally enforced, airport-specific legislation proves far harder to comply with (Rolls-Royce, 2005).

Airports use a range of techniques in order to reduce their noise footprint, starting with 'noise abatement procedures' such as orienting flight paths over the least densely populated areas, or instructing pilots to climb more steeply and apply the greatest thrust at different times during take-off. More drastically, an airport may impose absolute limits on the noise (and therefore size) of planes using its runways, or instead enforce curfews on larger flights during the night time. Heathrow, Stanstead and Gatwick airports have gone further by totalling an airline's noise emissions, and fining those that exceed a 'London noise quota'. As is clear from Figure 1.1 below, the increasing popularity of such measures has ensured that it remains in the airlines, airports and government's interests to persist in efforts to produce ever quieter aircraft.

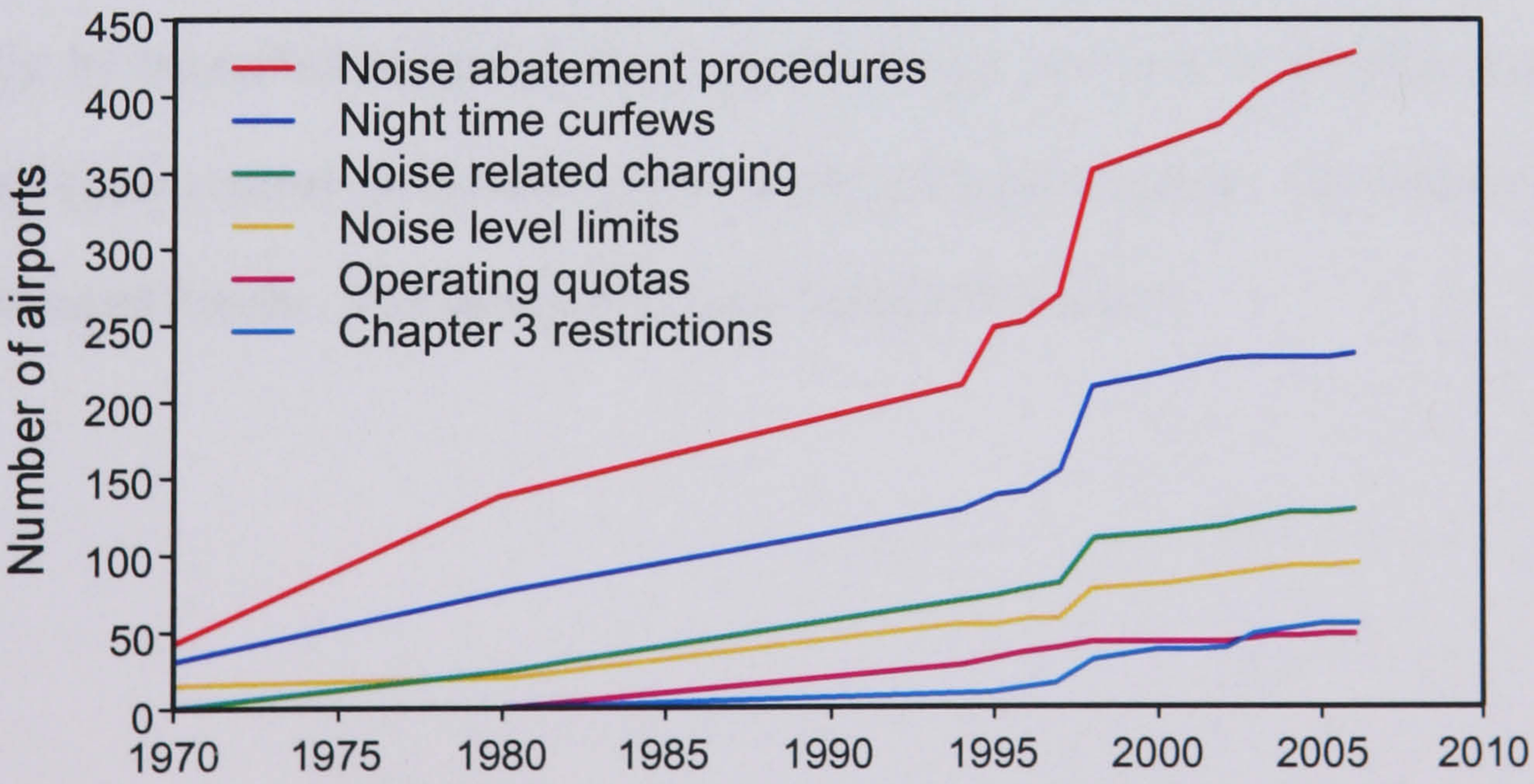

Figure 1.1 – Number of US airports with noise control measures (Boeing noise website).

1.1.2. Aircraft Noise Production & Reduction

Aircraft noise can be divided between that produced by the airframe, and that produced by the engines. Airframe noise is primarily generated at the boundary shear layers between the plane and the surrounding air, and convection of these layers beyond the tail and wings' trailing edges (Fink, 1976). Landing gear, flaps and ailerons also shed vortices, which in turn contribute significantly to the acoustic energy released. Due to the nature of these sources however, it is difficult to reduce airframe noise without adversely affecting the performance of the aircraft as a whole and, for this reason, airframe noise is more likely to be reduced using noise abatement procedures, such as using slower, steadier decent that minimises the use of wing control surfaces during the approach to landing (Clarke, 2000).

During take-off in particular, the engines form the more significant source of aircraft noise, and this can in turn be divided into internally generated noise, from the spinning fan and turbine blades (and associated flow-straightening stators), and that generated externally, by the turbulent mixing of the exhaust gases. As shown in the figure on page 5, internal noise sources tend to be dominant, but it is exhaust noise – the domain of the work discussed herein – that proves the most difficult to control.

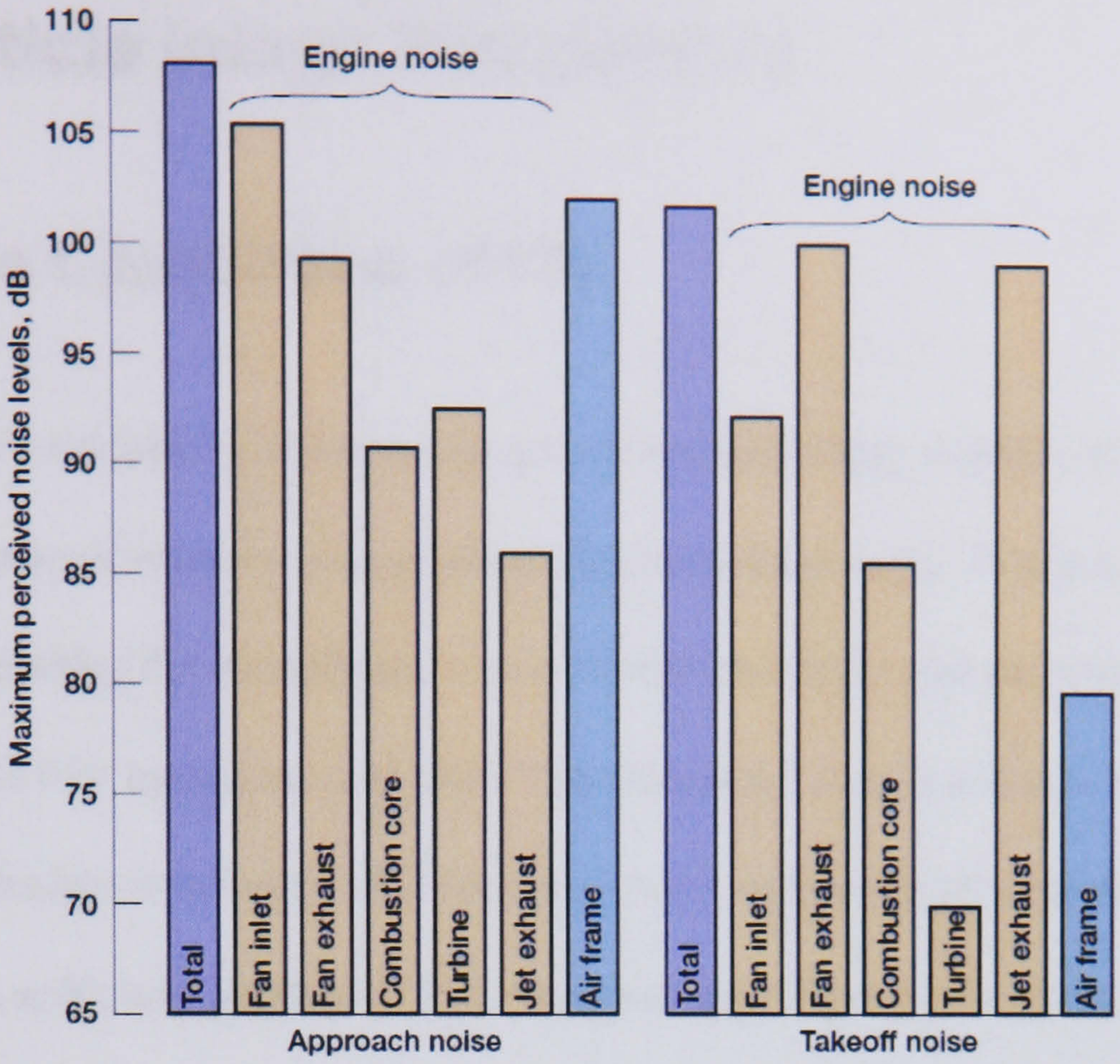

Figure 1.2 – Noise sources in a 1992-era aircraft (NASA, 1999).

Internally generated engine noise can be suppressed by wrapping the engine body and inlets with noise-deadening materials, but exhaust noise can only be reduced by designing an engine nozzle geometry (and set of operating conditions) that minimises the amount of turbulent mixing inside the exhaust plume. While the overall success of such efforts can be determined using a single microphone noise measurement, it is necessary to understand the *spatial* distribution of these noise-producing mixing regions if design iterations are to be based on anything more than intuition.

1.2. Particle Image Velocimetry

1.2.1. The Capabilities of PIV

Particle Image Velocimetry is a non-contact optical technique, capable of determining a fluid's instantaneous velocity at multiple points, simultaneously. While a single PIV measurement enables the identification of coherent structures and patterns within a flow, a series of PIV measurements allow time-averaged statistics (such as the mean and turbulence intensity) to be calculated for every point within the measurement volume. By acquiring a sufficient number of PIV measurements from a jet engine's exhaust plume, the relative strength *and* position of the turbulent mixing regions can be measured, thereby providing insight into how these areas may be reduced.

Chapter 2 of this thesis introduces the principles of PIV, and the myriad of variations on the basic technique. Particular attention is paid to the apparatus involved, as nearly all of the technique's current limitations are a direct result of an inability to procure equipment with the necessary characteristics. The increasing resolution of camera sensors may, for example, allow holographic PIV to enter the digital realm, while the continued development of semiconductor based laser light sources should remove one of the barriers to ultra high-speed measurements. In addition to reviewing such practical requirements for successful PIV, the chapter also discusses the image processing necessary in order to provide data of an accuracy and resolution that is equal, if not in excess, of comparable single-point measurement techniques.

1.2.2. High-Speed PIV

While PIV is relatively well established as a technique for collecting time-averaged statistics, it is difficult to study the *temporal* evolution of anything but the slowest flows on account of the low (typically ≤ 5 Hz) acquisition rates achieved using standard PIV equipment. This is primarily due to the bandwidth limitations of current digital camera technology, which is discussed in detail in Section 2.4. In the case of jet noise research, these constraints hinder researchers' ability to measure – for example – the dissipation rate of vortex structures within the exhaust, this being related to the efficiency with which kinetic energy is converted to acoustic energy. Quantitative noise prediction is particularly dependent on having derived a flow's time and length scales, but such parameters are almost invariably measured using complex two-point LDA or anemometry equipment.

Specialised high-speed PIV acquisition techniques and apparatus are discussed throughout Chapter 2, but Chapter 3 introduces a means of using cheaper, non-high-speed PIV cameras to acquire time-series image data at MHz rates. By exposing n cameras to multiple illumination pulses, it is shown that $2n$ images of single pulses can be theoretically reconstructed by means of very accurate geometric back-projection. A more practical variant of the technique (in which $n+1$ images are captured) is subsequently applied to a jet exhaust test, thereby demonstrating a high-speed time-series PIV measurement without the usual need for additional, specialised hardware.

1.3. The CoJeN Project

1.3.1. Aims & Objectives

The EU-funded Computation of Coaxial Jet Noise (CoJeN) project – which is detailed in Chapter 4 – aims to accelerate the development of computational tools capable of accurately predicting the noise generated by a prospective turbofan engine design. Not only would such accurate simulation reduce the cost of engine development (thereby making European manufacturers more competitive globally), but the time to market would also be reduced, in turn benefiting the individuals and groups that are adversely affected by aircraft noise.

Despite its apparent computational bias, a large part of the project centres on a series of experimental jet exhaust measurements, designed primarily to provide validation data for the prediction codes being developed. In addition to supplying a wealth of information for comparison with predictions, the comprehensive test campaign also served as an opportunity to develop advanced measurement techniques, and compare results obtained using different methods.

1.3.2. Experimental Validation Work

The experimental phase of CoJeN consisted of the aerodynamic and acoustic testing of 3 representative engine nozzle designs, using $^1/_{10}$ scale models installed in the Hampshire-based Noise Test Facility (NTF), operated by QinetiQ Ltd. Data was collected under a number of operating conditions, using the following techniques:

- Far-field microphone measurements, to give an indication of noise levels on the ground.
- Near-field microphone array measurements, to allow the approximate axial position of sound-producing regions to be identified.
- Pressure and temperature measurements, using a probe inserted inside the nozzle.
- LDA measurements, to provide high sample rate velocity data at single points.
- PIV measurements, to generate flow statistics over a large area.

The PIV measurements – which constituted the largest dataset collected during the test – were performed by both Universidad Carlos III de Madrid, and the University of Warwick. Collecting velocimetry data from the length of the jet exhaust plume, as the author was tasked with doing, was however dependent on the use of specially designed apparatus, capable of accurate, reliable and remote operation within the harsh, industrial environment of the NTF.

1.3.3. Jet Exhaust PIV Measurements

The design and construction of the Warwick PIV rig is described in Chapter 5, as is the *modus operandi* of the hardware, software and electronics. Significant features of the system include its large data storage capacity; a high level of automation (which allowed the measurement volume to be remotely adjusted mid-test), and – more significantly – a high data sampling rate.

With NTF operating costs proving the overriding constraint on the number of tests that could be run, it was of considerable benefit to offer a system capable of continuous

measurement at 12 Hz; achieved by means of bespoke RAID disk storage arrays, and the 'interleaving' of PIV measurements from multiple cameras (described in Sections 5.2 and 5.7). Not only did the use of multiple cameras reduce the time taken to acquire statistically-converged velocity and turbulence data; it also enabled the collection of time-series PIV measurements – as described in Chapter 3 – which were in turn used to calculate time-space correlations (a measure of energy dissipation efficiency) within the jet.

The analysis and results from the volumetric, planar mapping, and time-series data collected during CoJeN are presented in Chapter 6 of this thesis. In addition to the cross-correlation intrinsic to PIV, significant pre- and post-processing of the data was necessary in order to remove artefacts caused by the concurrent acquisition of PIV and LDA data, and NTF environmental effects on the cameras. The means by which these errors were corrected are presented, as is a representative sample of results, which will now be used to validate the CFD codes developed by CoJeN project partners.

2. Particle Image Velocimetry

2.1. Introduction

Particle image velocimetry, or PIV, is a popular and established technique for the simultaneous acquisition of multi-dimensional velocity data throughout the whole of a planar measurement volume. Although the principle of modern digital PIV (DPIV) was demonstrated by Leese et al. in 1971 it took over 10 years before the technique was christened as such, after two research teams independently suggested the name be used to reclassify low seeding density Laser Speckle Velocimetry (Adrian, 1984; Pickering and Halliwell, 1984).

This chapter discusses the principles of PIV, the experimental procedure and apparatus necessary to conduct such tests, and the methods of subsequent image analysis. The discussion centres on methods and equipment used for digital particle image velocimetry, which is fast becoming the *de facto* standard for planar flow measurement.

2.1.1. Principle of Operation

PIV is just one of several techniques capable of measuring instantaneous velocity fields (Meinhart, et al., 1998). Unlike Doppler global velocimetry (Samimy and Wernet, 2000) or scalar imaging velocimetry (Dahm, et al., 1991) however, pulsed light velocimetry techniques such as PIV estimate velocities by measuring the spatial displacement of markers within the flow, and dividing the associated time interval.

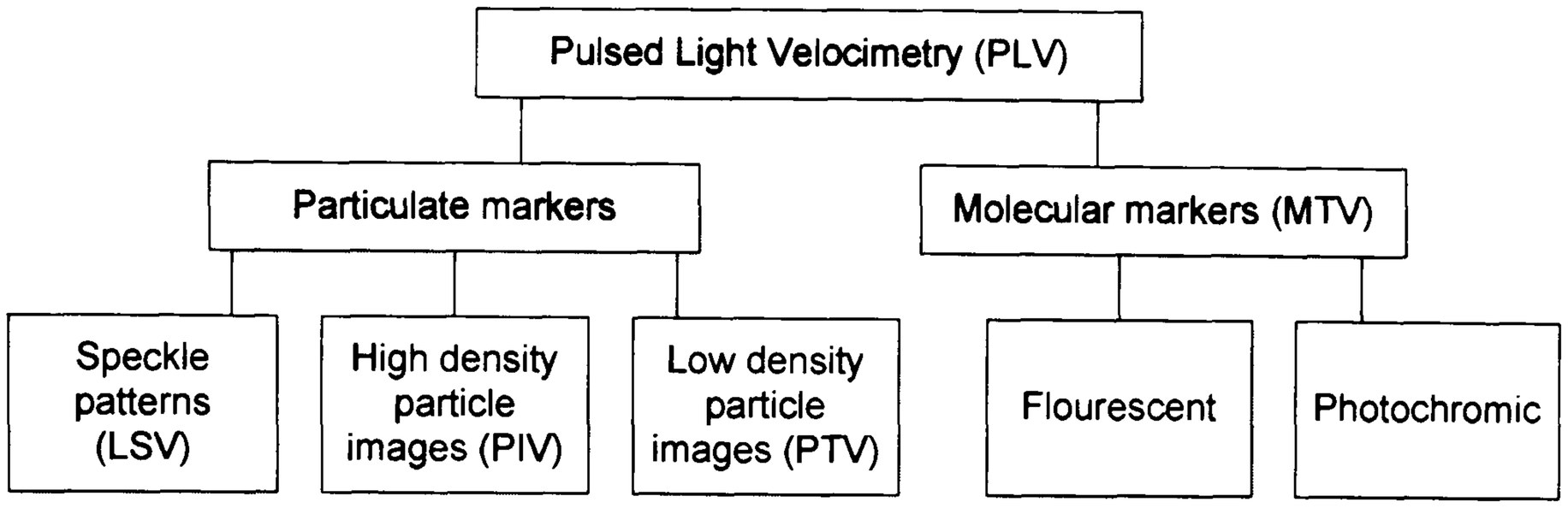

Figure 2.1 – Pulsed light velocimetry techniques, adapted from (Adrian, 1991).

With the exception of volumetric PTV, all PLV techniques define their measurement plane by means of a thin, 2-dimensional, light sheet projected into the flow. One (or more) cameras record two (or more) exposures of the flow markers, with timing interval Δt. While the images could be recorded by means of short camera exposures (Tsushima, et al., 2004), it is much more common for the light sheet to originate from a pulsed light source (with pulse duration δt).

Molecular tagging velocimetry (MTV) enables simultaneous velocity measurements to be made at multiple, user-specified points within a homogeneously seeded fluid by means of laser excitation to create fluorescing or opaque markers within the flow (Stier and Koochesfahani, 1999). Experimental studies typically project a 2-dimensional grid of pulsed ultra-violet light into the flow, thereby creating either fluorescent or opaque lines, the intersections of which can be tracked between two sequential camera exposures (Meinhart, et al., 1998; Park, et al., 1999).

Particulate marker PLV techniques, which instead seed the flow with externally introduced particles of a different material phase, are significantly easier to implement than MTV and – as a result – more commonly used. Unlike MTV however, care must

be taken to ensure the markers' movements are representative of the surrounding fluid flow. A typical particulate-PLV experimental arrangement is depicted below:

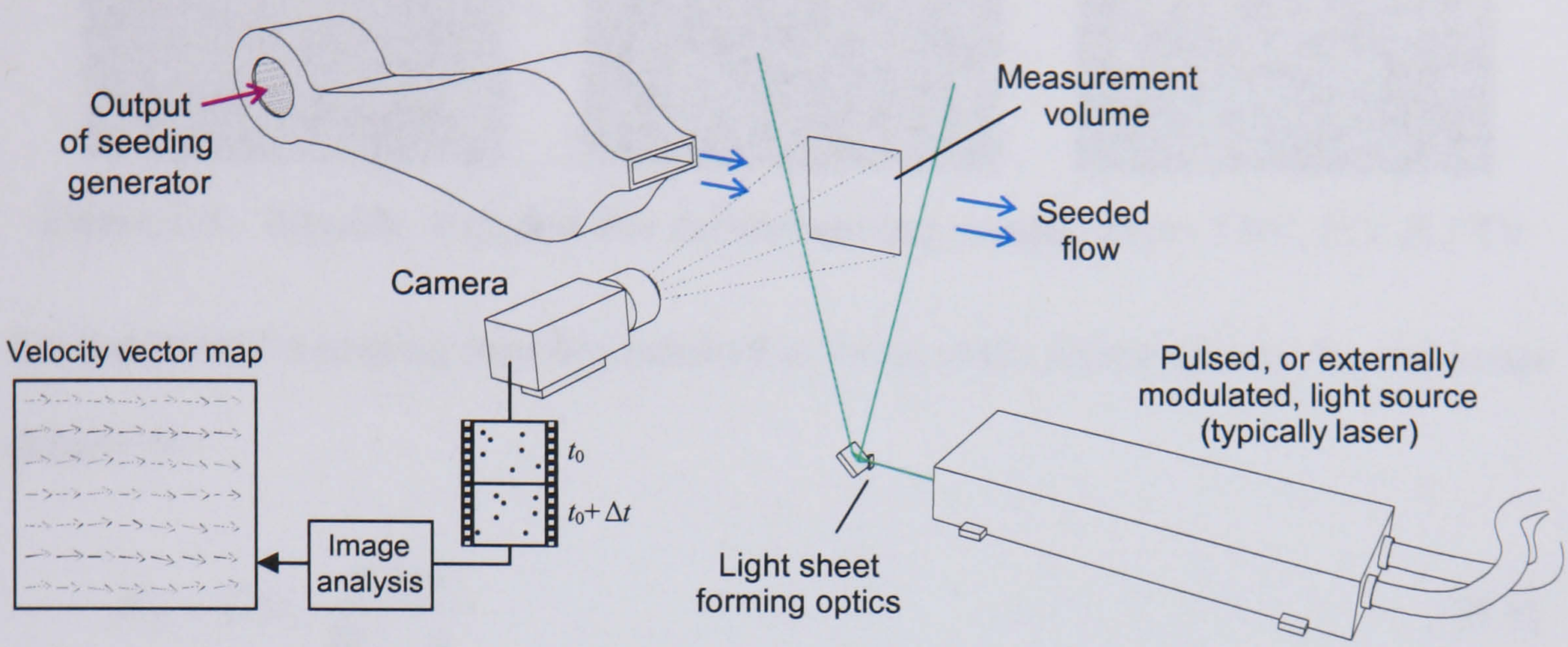

Figure 2.2 – A typical PIV experimental arrangement.

LSV, PIV, and PTV differ in the density of the flow seeding. Laser speckle velocimetry requires an extremely large concentration of seeding particulates in the measurement volume, such that the image formed by the camera becomes a speckle pattern, produced by the interference between light reflected from individual particles. Particle image velocimetry and particle tracking velocimetry instead use a lower seeding density, such that individual particles may be discerned in the recorded images.

In cases of very sparse seeding, or situations in which very dense vector maps are desired, PTV may be used to track the motion of individual particulates, a purpose for which many different algorithms exist. Both PIV and LSV images are instead analysed by means of image correlation, in which patterns (formed by either a group of particles or a region of speckle) are matched between exposures. This chapter will restrict itself to a discussion of PIV only, even though the analysis methods are equally applicable to LSV, as the experimental methods are to PTV.

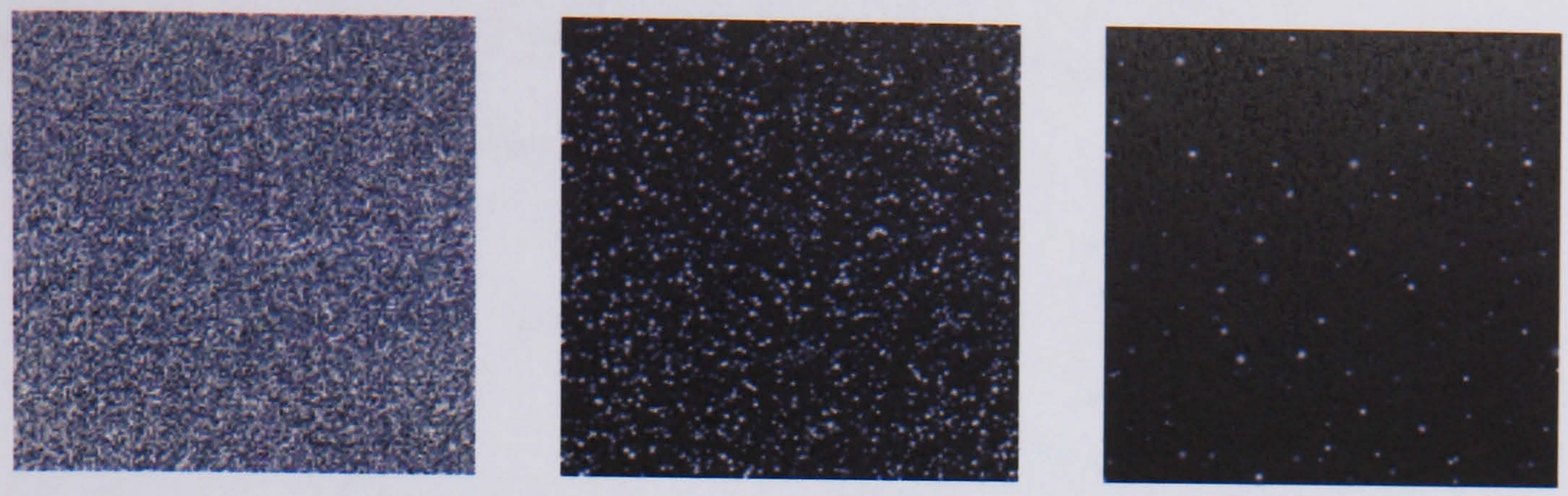

Figure 2.3 – Speckle, high and low density seeding images, as per LSV, PIV & PTV.

An experiment's seeding may be classified in terms of the source density N_S, and image density N_I:

$$N_S = C\Delta z_0 \frac{1}{M^2}\frac{\pi d_\tau^2}{4} \tag{2.1}$$

$$N_I = C\Delta z_0 \frac{1}{M^2} A_I \tag{2.2}$$

…where C is the number of seeding particulates per unit volume; Δz_0 the light sheet thickness; M the magnification factor between the measurement plane and the camera's image plane; d_τ the diameter of the image a single particle on the image plane; and A_I the area (within the image plane) studied in order to produce a single velocity vector (otherwise known as the interrogation window size).

The source density N_S is the average number of particles in an area of the light sheet equivalent to the size of a single particle's image. If $N_S > 1$ it is probable that the recorded image will contain multiple, overlapping, particle images; if $N_S < 1$, it is more probable that particles will appear distinct and spaced out.

The image density N_I is the average number of particles in the area searched during the calculation of a single velocity vector. Unlike PTV, both PIV and LSV rely on tracking regions of many particles, i.e. $N_I \gg 1$. Specifically (Keane and Adrian, 1990) state that

for successful PIV, N_I should exceed 15. We can therefore conclude that suitable seeding levels for the three forms of PLV are given by:

LSV: $N_S \gg 1$ PTV: $N_S \ll 1;\ N_I \approx 1$ PIV: $N_S \ll 1;\ N_I > 15$

2.1.1.1. Framing and Pulse-Coding

For a given camera and light source, there are a number of measurements possible, each a combination of the number of images recorded, and the number of illumination pulses per image. The available options are presented below, where a single particle's recorded image is shown:

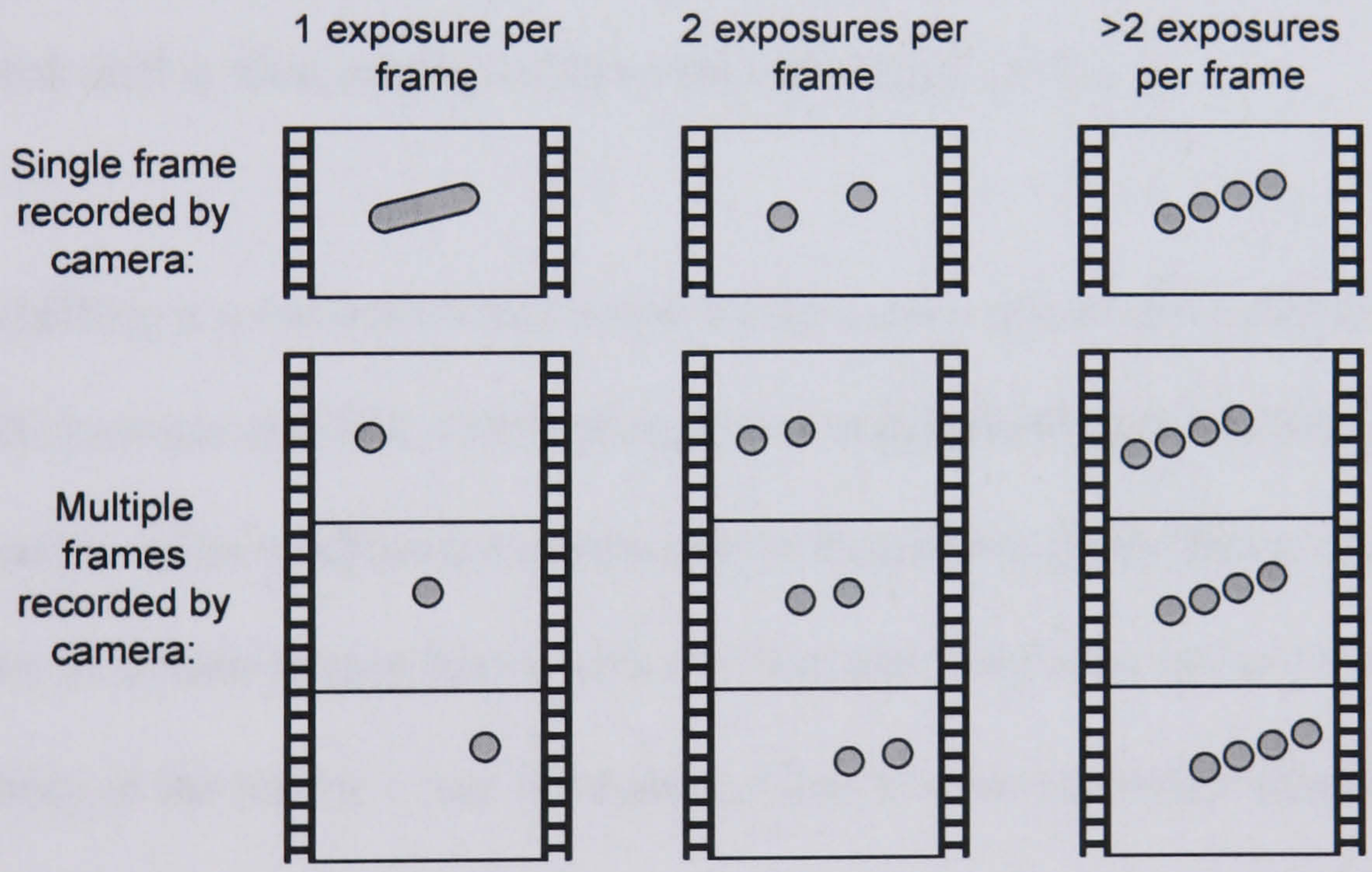

Figure 2.4 – Framing and pulse-coding options, adapted from (Adrian, 1991).

In all cases, it can be seen that the flow's velocity and bearing can be deduced from the recorded image(s), but the accuracy with which a velocity vector can be produced differs for each option. The image produced by a single long exposure is considered a particle streak velocimetry measurement which, like PTV, has been successfully applied in 3-dimensions (Sinha and Kuhlman, 1992). Streak velocimetry in a 2D plane is however limited to qualitative visualisation, as the streak length is reduced whenever

out-of-plane motion causes a particle to move outside the light sheet. The use of short, multiple, exposures in the other coding options eliminates this problem.

Single image frames containing multiple exposures can be solved by means of auto-correlation (discussed in Section 2.5), but there is an inherent directional ambiguity. In Figure 2.4, for example, it would not be clear whether the flow was moving from left to right or vice-versa. For simple flows prior knowledge negates this problem, but measurements from turbulent flows experiencing small scale flow reversals can prove problematic to interpret. (Adrian, 1986) introduced a solution to this problem in the form of image shifting, in which the 2nd of 2 exposures is moved within the recorded image by an amount greater than the maximum reversed flow displacement. This additional shift is then subtracted from the calculated vectors.

Image shifting is most commonly achieved by means of a rotating mirror (Landreth, et al., 1988; Lawson and Wu, 1999), though non-mechanical methods have also been developed in order to allow measurements to be made in faster flows; remove the difficulty of synchronising lasers with mirrors; and reduce the errors caused by uncertainty in the mirror's rate of rotation. Non-mechanical image shifting typically requires orthogonally polarised light, rotated 90° between pulses. (Landreth and Adrian, 1988) incorporated a birefringent uniaxial crystal (whose refractive index changes depending on incident light's polarisation angle) in their imaging system, resulting in the pulses' scatter being recorded in different positions. (Lourenco, 1993) used an alternative configuration comprising a polarising beam-splitter and slanted quarter-wave plates.

An alternative method for the removal of directional ambiguity is colour-coding, in which light of different wavelengths is used for each exposure (Gogineni, et al., 1998; Jaw, et al., 2003). By splitting the recorded colour images by hue, the result is analogous to a multiple frame acquisition approach. It is also possible to vary both δt and Δt between multiple exposures (Halloin and Jottrand, 1994), though methods of analysing such images automatically are not as well established.

The use of more than 2 exposures on a single frame (or more than 1 on multiple frames) typically leads to a higher quality of auto-correlation result, albeit at the possible expense of reduced instantaneousness of the measurement. This is because of the lower probability that a particle will be photographed 'by itself', because it was outside the light sheet during the other illumination(s). An increased number of pulses also increases the effective seeding density, thereby helping to ensure $N_I > 15$.

Multiple frame recording came of age in the 1990's, after Luiz Lourenco persuaded Kodak to manufacture digital camera sensors capable of recording two images a short time apart (Adrian, 2005). Until that time, multiple frame acquisition of anything but the slowest flows was only possible using cinematographic recording (which was limited by the difficulty of precise alignment of neighbouring frames), or video cameras which were limited in both frame rate and resolution.

The current availability of suitable cameras means that multiple-frame, single exposure acquisition, and analysis by means of cross-correlation, has now become *de rigueur* for PIV studies. Not only does the use of 1 pulse on each of 2 frames remove the problem of directional ambiguity, but the correlation results are also of a higher quality than if

both pulses were on a single frame, analysed by means of auto-correlation. On average, the dynamic range of such cross-correlated measurements is double that of auto-correlation results (Keane and Adrian, 1992).

The recording of more than 2 frames of PIV data allows the development of a flow over time to be investigated. Such time-resolved PIV (TR-PIV) studies are becoming increasingly popular, and have been used to track the evolution of turbulent structures within flames (Honoré, et al., 2000; Kawanabe, et al., 2000), jets (Wernet and Opalski, 2004), and to validate numerical simulations of bluff body flows (Williams, et al., 2003). The ease with which TR-PIV may be implemented depends however on the speed at which the flow structure of interest develops: once it becomes necessary to collect successive velocity maps at greater than 20 Hz or so, specialised lasers and cameras (as described in Section 2.4.7) must be used, at predictable expense.

2.1.1.2. Experimental Parameters

One of the most fundamental variables in a PIV experiment is the time between illumination pulses Δt. As with most elements of a PIV experiment however, there are contradictory requirements regarding its value:

- Δt should be long enough (with respect to the pulse duration) that the recorded particle images are sharp, and not mere blurs. It is recommended that $\Delta t / \delta t > 20$ (Gray, et al., 1991).
- Δt should be short enough that the measurement remains, to all intents and purpose, instantaneous. If Δt is too long, the measurement becomes a Lagrangian representation of Eulerian fluid forces, averaged over both space and time.

- Δt should be short enough that only a small number of particles move out of the light sheet in that time. It is suggested that $|\overline{w}|\Delta t < \frac{1}{4}\Delta z_0$ (Keane and Adrian, 1990).

- Δt should be long enough that the recorded particle displacement $ds = M\mathbf{v}\Delta t$ is significantly greater than the absolute error intrinsic to the analysis method employed (typically < 0.5 pixels), thereby ensuring an adequate signal-to-noise ratio.

- (Adrian, 1991) recommends that the intial analysis interrogation window size $A_I > 4M\Delta t\sqrt{u^2 + v^2}$, but as A_I increases so does the area over which the calculated velocity is spatially averaged. The pulse separation is therefore commonly determined by deciding the spatial resolution required, then adjusting Δt until $\mathrm{d}s \leq \frac{1}{4}A_I$, where $\mathrm{d}s$ is the perceived particulate displacement.

(Boillot and Prasad, 1996) formulated a detailed model for the calculation of optimum pulse separation values, based on most of these factors, concluding that:

$$\Delta t_{opt} = \sqrt{\frac{2cd_\tau}{M|\dot{\mathbf{u}}|}} \tag{2.3}$$

…where $\dot{\mathbf{u}}$ is the fluid's acceleration, and c a dimensionless quantity (typically between 0.05 and 0.10) that relates the effect of various experimental factors on the level of random noise in the image correlation process.

The width of the light sheet Δz_0 is also a matter for consideration. In the case of 2-component PIV, a thick light sheet will contribute to low velocity bias, by tolerating the measurement of particles with a high out-of-plane velocity. A particle moving directly towards the camera at high speed, for example, will be interpreted as a particle of zero

velocity. Conversely, an infinitesimally thin sheet will provide accurate measurements, but only if particles remain within the sheet for the duration Δt, which is unlikely.

Whenever possible therefore, the measurement volume should be placed at a position within the flow that minimises out-of-plane motion, thereby allowing a reasonable light sheet width. When – as in most cases – this is not possible, a compromise must be made, based on the maximum acceptable out-of-plane velocity w of a recorded particle:

$$w_{\max} = \frac{\Delta z_0}{\Delta t} \tag{2.4}$$

We may define the resulting low velocity bias as being up to:

$$bias_{\max} = \frac{\sqrt{(\bar{\mathbf{v}}\Delta t)^2 - \Delta z_0{}^2}}{\bar{\mathbf{v}}\Delta t} \tag{2.5}$$

For example, particles travelling at 10 m/s within a 4mm wide light sheet, where Δt = 1ms, could be interpreted as moving as slowly as 91.6% of their true speed, if they change their bearing with relation to the light sheet. (Prasad, 2000), who derived the potential 'perspective error' of a 2D measurement in terms of a particle's bearing, similarly found velocity errors of up to 10% based on a fluid with equal in- and out-of-plane velocities, and typical optical parameters.

Comparing these errors thus defined with Keane and Adrian's suggestion that $\Delta z_0 > 4|\bar{w}|\Delta t$ reveals the importance of prior knowledge of $\bar{w}$ and $w_{\max}$ when placing and selecting a light sheet thickness. In situations where this is not practical, 3-dimensional PIV may instead be implemented.

2.1.2. Multidimensional PIV

Thus far, the discussion has been limited to the use of a single camera, used to capture 2-component velocity data from a 2-dimensional measurement plane (2D2C). The same principles can however be extended to the acquisition of 3-component data from a 3-dimensional measurement volume (3D3C).

2.1.2.1. Volumetric Techniques

Perhaps the simplest way to acquire 3D3C data is by using volumetric particle tracking velocimetry (3D-PTV). By illuminating the whole of a measurement volume and viewing it with multiple cameras (each equipped with a lens of sufficient focal depth), the location of particles can be tracked in 3 dimensions, thereby producing volumetric streamlines.

3D-PTV experiments typically employ 3 (sometimes 4) cameras in order to reduce the ambiguity in matching corresponding particle images between cameras. Such frame sets are often analysed using the epipolar approach, in which previous spatial calibration of the cameras allows the construction of epipolar lines in camera views, based on the position of individual particles (Nilsen and Hådem, 1994). Only dots that lie on all applicable epipolar lines can be considered members of a particle image triplet, the real-world position of which is subsequently calculated.

A related technique is defocused digital PIV (DDPIV); a technique developed at Caltech which is now available as a commercial system called VioFlow. Three triangular pinholes are used to project triplet particle images onto one or three camera sensors.

Despite the name, low seeding densities are used, which allows the interrogation of individual particle image triangles (Willert and Gharib, 1992).

The 3-dimensional position of seeding particles is calculated by measurement of the position, and size, of recorded particle image triangles. (Pereira, et al., 2000) gives the in- and out-of-plane spatial resolution of one such system as 0.08 and 1.30 pixels respectively. As well as the ability to measure 3-dimensional flows using a single camera, DDPIV is also able to measure particle size, a fact used by (Gharib, et al., 2002) to track both the position and size of air bubbles passing through a spinning propeller.

2.1.2.2. 3-Component PIV

While 3D-PTV tracking of up to 900 particles per image has been demonstrated (Maas, 1990), volumetric techniques are invariably limited by their relatively sparse vector distribution, meaning that any estimation of vorticity in particular can contain large errors (Sinha and Kuhlman, 1992). It is for this reason that multi-dimensional PIV is often preferred to 3D-PTV, despite the latter's greater simplicity.

The extension of 2-dimensional planar PIV to 3-components is typically achieved by means of colour encoding or stereoscopy. Many alternative techniques have been demonstrated however, such as moving the light sheet at the same speed as the flow and using information from the image correlation function (Raffel, et al., 1995); simultaneous viewing through lenses of different focal lengths (Grant, et al., 1995); and tomographic reconstruction of the particle distribution (Elsinga, et al., 2005).

Colour-encoded 3-component PIV involves the positioning of 2 (or more) parallel light sheets, each of a different colour. By measuring the colour of particle images, their out-of-plane motion may be deduced. (Cenedese and Paglialunga, 1989) demonstrated the tracking of particles, and their colour, as they moved through a spatially calibrated 2-colour light sheet. Both (Stefanini, et al., 1993) and (Ruck, 2003) extended the technique to 3 colour planes, and (Dinkelacker, et al., 1992) took advantage of sheet intensity instead of hue. (Brücker, 1996a) used 2 light sheets but did not track the colour of individual particles, instead using the strength of correlations between successive images of each colour to deduce particle groups' out-of-plane motion.

The difficulty of accurately arranging parallel multi-coloured light sheets means that stereoscopic PIV has become the usual method for acquiring 3-component data. Two cameras, mounted some distance apart, are able to calculate the out-of-plane motion of a particle in a finite-thickness light sheet by comparing the differences in perceived motion (Gauthier and Riethmuller, 1988).

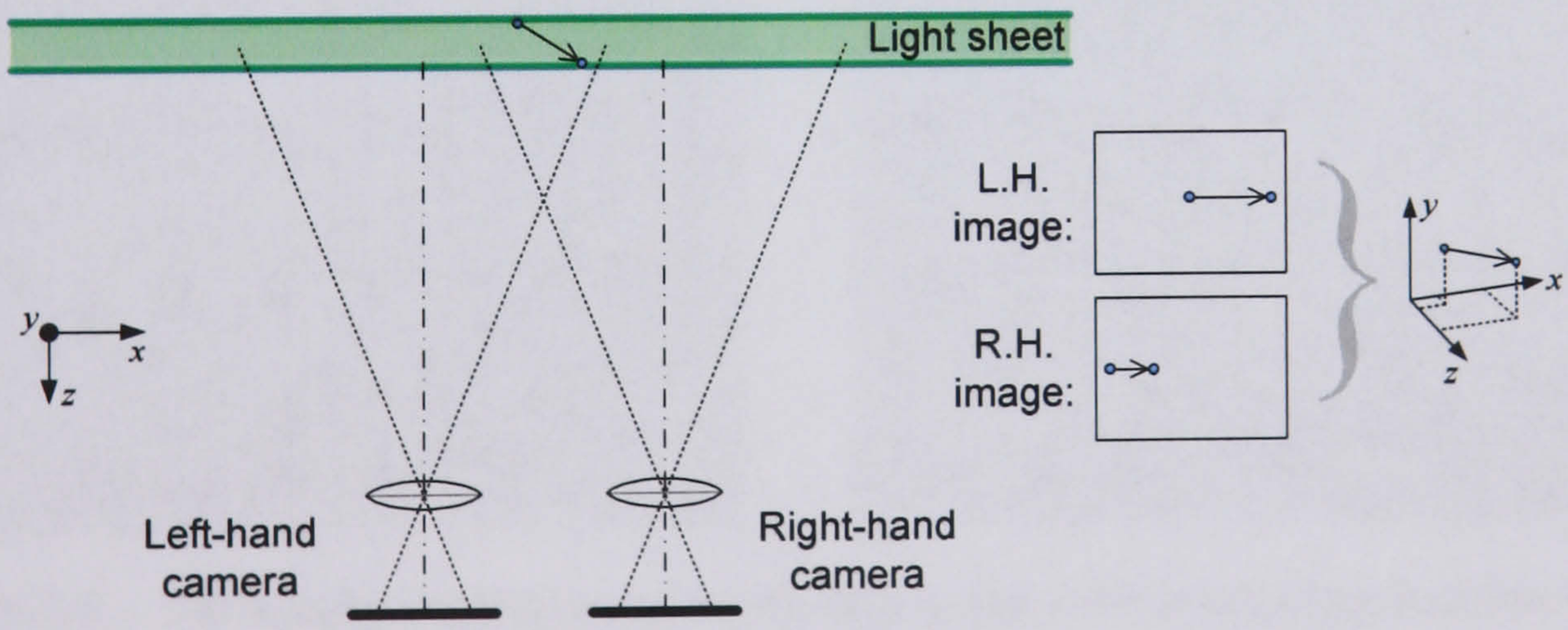

Figure 2.5 – Stereoscopic PIV by means of translated cameras.

Whilst the sensitivity to out-of-plane motion increases with camera separation, it is obvious from Figure 2.5 that normal cameras and lenses, translated orthogonally, are limited by the decreasing combined measurement volume. Practical systems, such as

those used by (Soloff, et al., 1997), therefore translate each camera's lens sideways, relative to the sensor. This results in an optical axis that is at an angle to the light sheet, thereby enabling greater separation of the cameras while maintaining overlapping fields of view. Although (Lecerf, et al., 1999) reports out-of-plane accuracy of 1% for such a translated lens system, the concept is generally limited by the degraded performance of camera lenses at oblique angles. For this reason, the use of angled cameras has become the norm.

Simply rotating two cameras, with normally seated lenses, about a common viewing point will only produce usable stereoscopic PIV images if the camera's depth of focus δz (defined on page 90) is greater than the light sheet thickness Δz_0. Given the angles involved in a typical stereoscopic camera arrangement, this is rarely the case and recorded images will resemble that on the left of Figure 2.6, i.e. out of focus towards the edges:

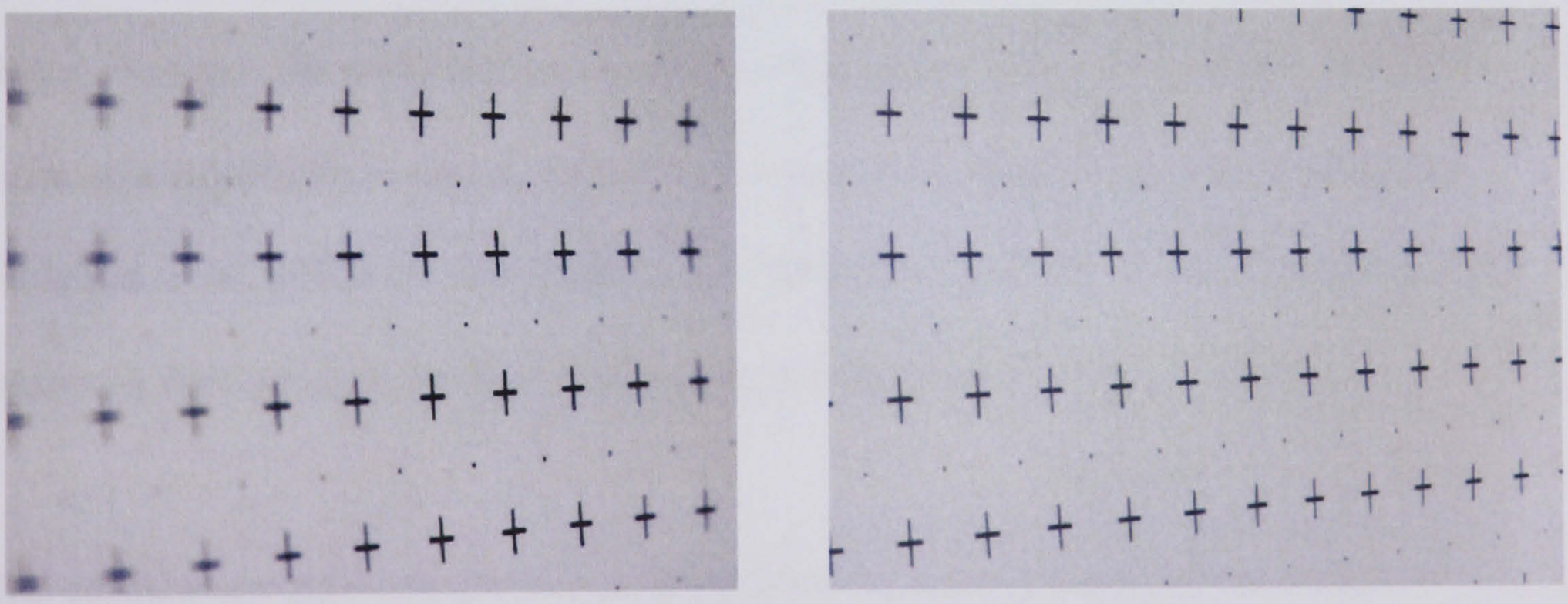

Figure 2.6 – Obliquely viewed target with and without Scheimpflug mounts (Davis manual; LaVision).

As illustrated above right, this problem can be solved by adopting the Scheimpflug principle, in which the image, object, and lens planes all intersect along a common line (the Scheimpflug line):

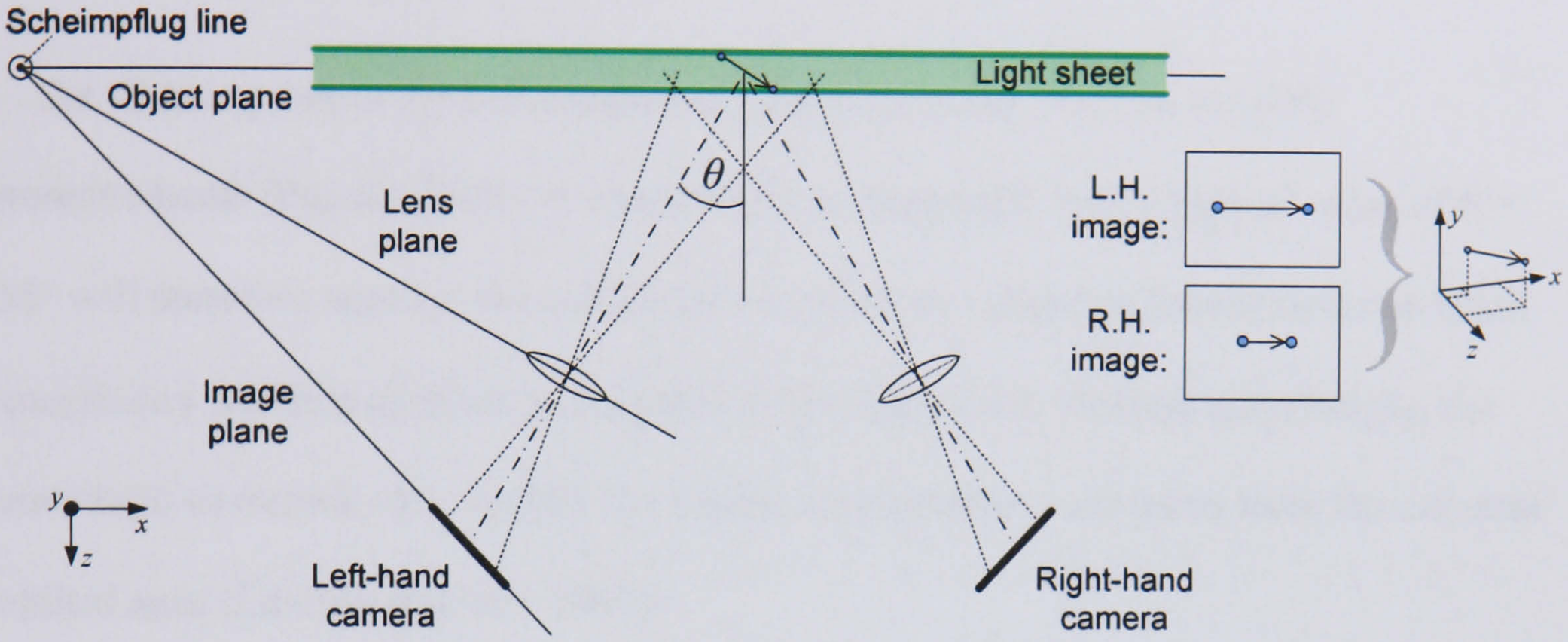

Figure 2.7 – Angular stereoscopic PIV, using the Scheimpflug arrangement.

While the Scheimpflug arrangement (realised through the use of special camera lens mounts) ensures that particle images are sharply focused, thereby increasing the accuracy of correlation results, it also intensifies the problem of a varying magnification factor M across the width of the camera's image plane (Zang and Prasad, 1997) . As the nominal magnification factor, image sensor size, and angle θ increase, so does the variation in M, which in turns leads to a reduced measurement volume, because each camera's field of view becomes increasingly trapezoidal (Prasad, 2000).

The camera separation angle θ should therefore be chosen on the basis of the measurement volume required, but more importantly, the relative accuracy of the in- and out-of-plane velocity component measurements. As the angular separation increases, in-plane particle motion is projected onto the camera sensor as an ever decreasing displacement, resulting in greater measurement uncertainty due to the

velocity-independent nature of image correlation errors. The relative uncertainty of velocities calculated from the centre of the measurement volume can be defined as:

$$\frac{\sigma_{out-of-plane}}{\sigma_{in-plane}} = \frac{\sqrt{2}}{\tan(\theta)} \tag{2.6}$$

…the $\sqrt{2}$ being due to the fact 2 cameras contribute to the in-plane velocity measurements (Prasad, 2000). A stereoscopic arrangement with a typical value of $\theta =$ 35° will therefore result in the calculated out-of-plane velocities having twice as much uncertainty attached as those in the plane of the light sheet. Perhaps surprisingly, the error ratio decreases very slightly the further measurements are taken from the cameras' optical axes (Lawson and Wu, 1997).

Stereoscopic cameras can be arranged in a variety of positions: left and right, above and below, or on opposite sides of the light sheet (which allows both cameras to be positioned in forward scatter with respect to the light source, thereby collecting significantly more scattered light). It is unusual however for the cameras to be angled relative to each other in more than one plane, i.e. with non-parallel Scheimpflug lines. (Walker, 2001) successfully demonstrated such a system using specially constructed motorised lens mounts, with camera optical axes raised ~30° from the light sheet normal, then rotated 30-40° from the vertical. While all velocity components were calculated with errors no greater than ~2%, the dual-axis arrangement is unpopular because of the difficulty of 3-dimensional focussing, and the further reduction in measurement volume size.

The analysis of stereoscopic images is dependent on knowing the relative position of the light sheet and cameras. If the appropriate distances and angles have been measured,

then the 3rd velocity component can be extracted from each cameras' perceived displacement entirely geometrically. (Prasad and Adrian, 1993) successfully applied such an approach to the study of a rotating disk in glycerine, including corrective terms for all the refractive index boundaries. The geometric approach is however complex, time consuming, and open to significant error caused by inaccurate measurement of the experimental arrangement.

Optical calibration involves the generation of a generalised function to describe the relationship between the camera image-plane and real-world coordinate system, thereby sidestepping the need for physical measurements. At least 6 pairs of associated world- and image-plane coordinates are captured, typically using either a flat calibration plate such as that shown in Figure 2.6, traversed through the measurement volume, or a stationary dual-level plate. The calibration process then iteratively calculates a calibration matrix that is able to translate between the two coordinate systems. Stereoscopic image pairs may be interpreted by the back-projection of either the image pixels or calculated displacement vectors, onto the real-world plane occupied by the light sheet. In the first case – known as mapping – the raw recorded images are projected (by means of the calibration matrix) onto the plane of the light sheet, whose position relative to the calibration plate will be known. The area common to both cameras' fields of view is found, and the appropriately cropped image pairs from both left and right cameras correlated as per usual. Trigonometry is then used to convert the resulting two 2-component vector maps into a single 3-component map.

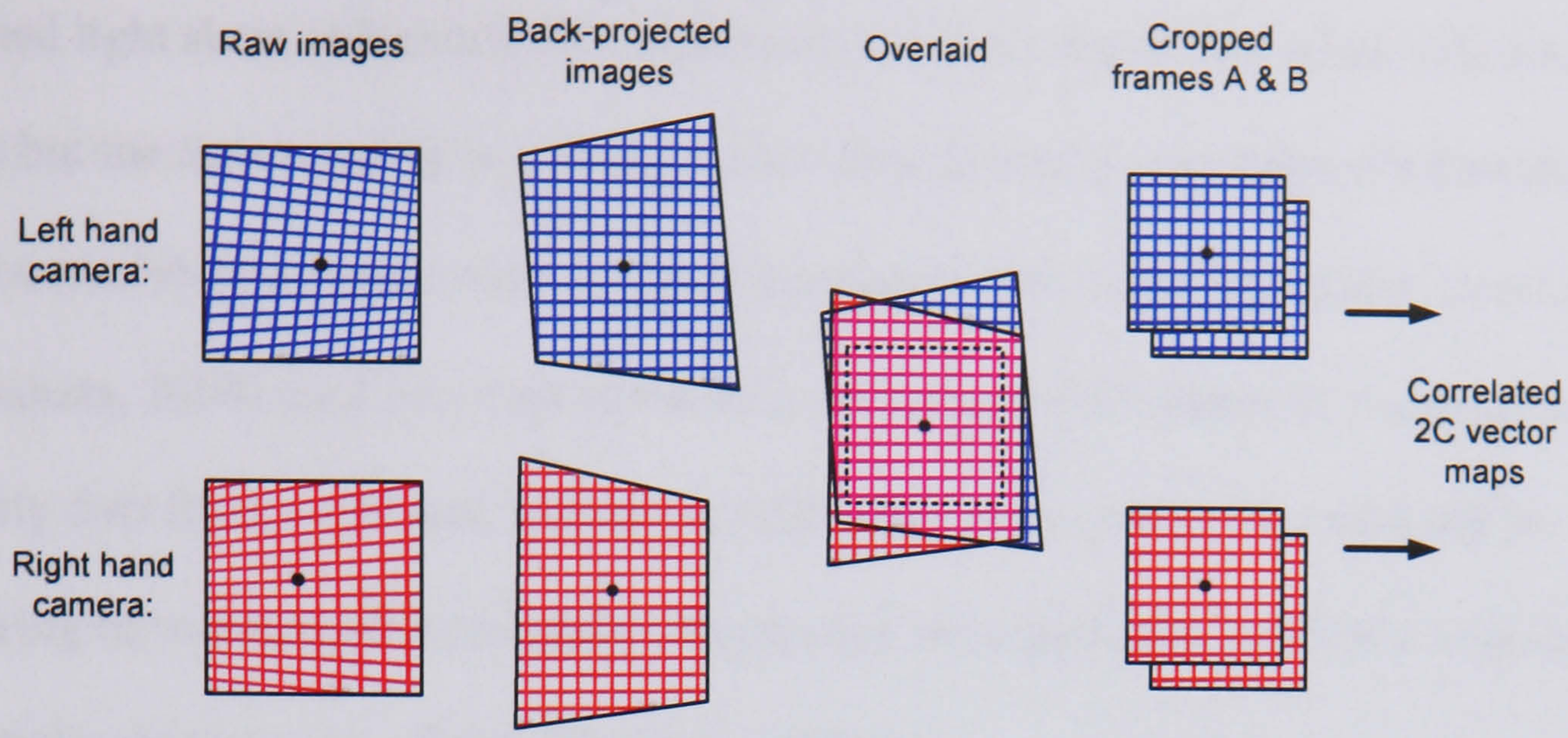

Figure 2.8 – Mapped stereoscopic images.

In the second case – known as warping – the cameras' image pairs are correlated against each other in their raw form. The two resulting 2-component vector maps then have to be back-projected in order to produce an analogous result to mapping (except with irregularly spaced vectors that have to be interpolated between to calculate the 3-component map). Regularly spaced warped vector maps can be created if the positions of the image sub-regions used to generate each intermediate vector are first calculated by forward-projection. Warping, despite being significantly faster than mapping, is however slightly less accurate, and correction of any misalignment between the calibration plate and light sheet is more difficult (Coudert and Schon, 2001).

2.1.2.3. 3-Dimensional PIV

The simplest way to acquire PIV data in 3 dimensions is to stack several parallel light sheets next to each other, and acquire either 2 or 3-component velocity data from each plane separately. The separation can be either temporal, by using the same camera(s) to record images from a scanned light sheet, or optical, in which multiple cameras record simultaneously from several coexisting parallel light sheets.

Scanned light sheet volumetric PIV requires a relatively simple apparatus (Prenel, et al., 1989) but the time required to capture a data set is limited by the camera's framing rate and the resolution of acquisition in the dimension normal to the light sheet. (Hori and Sakakibara, 2004) used two high speed cameras to record 50 planes of 3-component velocity data from a 100 mm^3 volume in 0.22 s, but most studies are restricted to capturing time-averaged statistically independent velocity fields, or slowly evolving – essentially steady-state – flows (Brücker, 1996b).

By replacing a single scanned light sheet with several stationary, parallel sheets, data can be acquired simultaneously throughout a volume, albeit with limited 3rd dimension resolution. (Liberzon, et al., 2004) used just 2 cameras with relatively short depths of focus, and 3 light sheets 12.5 mm apart to perform 3D3C PIV. The cameras' images were digitally reconstructed onto the 3 planes by examination of the level of blurring in every particle's image. The most common method of multi-plane acquisition is however the use of different polarisation states, or wavelengths, for each of the light sheets. All planes are then able to be viewed simultaneously by separate, suitably filtered cameras.

Dual-plane PIV experiments are often easiest to set up when using orthogonally polarised light sheets, due to the fact that most lasers already emit linearly polarised light. Introducing a half-wave plate in front of one laser rotates the angle of polarisation by 90°, thereby producing *s*- and *p*-polarised light sheets (c.f. Figure 2.26, page 63) which are in turn viewed by *s*- and *p*-filtered cameras (Kähler and Kompenhans, 2000; Marusic, et al., 2004; Wernet, et al., 2003).

The success of polarised dual-plane PIV is dependent on the light scattered by each seeding particle maintaining the incident illumination's polarisation state. This requires small (< 5 μm), non-absorbing spherical particles, viewed close to side-on (Landreth and Adrian, 1988; Lourenco, 1993), but it is also dependent on the purity of the illumination's original polarisation state. (Hu, et al., 2001) reported a contrast ratio of 100:1, indicating that cross-talk between such light sheet layers is typically negligible.

Colour has also been used to differentiate between parallel light sheets. (Mullin and Dahm, 2005) used an Nd:YAG laser and Nd:YAG pumped dye laser to create sheets of 532 nm and 635 nm light which were viewed by two pairs of stereoscopic cameras, each equipped with suitable filters. (Cenedese and Paglialunga, 1989) instead used a Bragg cell to split the output of an argon ion laser into blue and green beams, which were then recorded by a 3CCD colour camera. Unfortunately both techniques suffer difficulties in producing more than 2 colours with sufficient power, due to a lack of high conversion efficiency dyes in colours other than red, and the highly unequal relative powers of argon ion laser lines.

As an alternative to multiple lasers with 1 sensor per colour, (McGregor, et al., 2005) demonstrated that stimulated Raman scattering of a pulsed laser source in an optical fibre can generate up to 11 distinct colours, each with sufficient energy for PIV image capture. By distributing these colours through a volume, and capturing images with a Foveon™ colour image sensor (discussed on page 78), the z-axis particle location can be related directly to the recorded particulate hue. Similarly, (Ruck, 2003) used an acousto-optical cell to mix red, green and blue lines from a white-light laser, and a galvanometer to spatially distribute thus-produced multi-coloured light sheets.

2.1.2.4. Holographic PIV

Like 3D-PTV, holographic PIV (HPIV) is able to record particles' positions within a 3D space but at much higher particle densities, as is evident from the non-interpolated vectors shown in Figure 2.9a. As with standard holography, high resolution film is used to record the interference pattern formed between a coherent reference beam, and light scattered from the seeding particles. The use of laser pulses of rotated polarisation, and birefringent imaging elements, enables the recording of both cross- and auto-correlation images. Details of the many possible optical arrangements are given by (Royer, 1997).

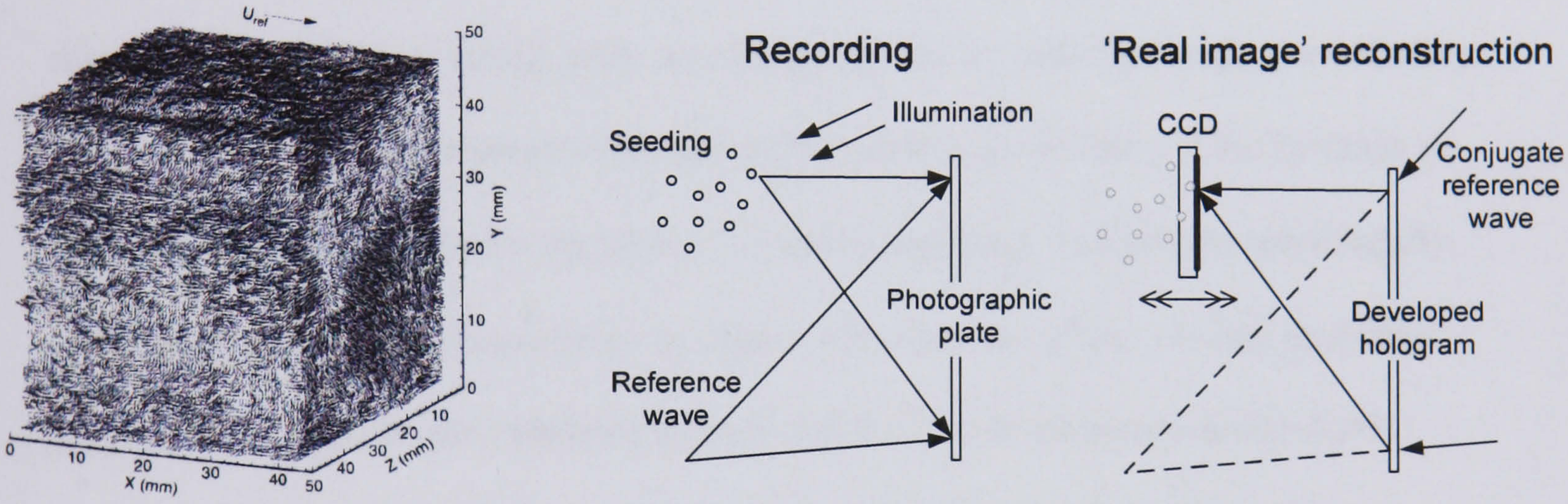

Figure 2.9a) 3D3C HPIV data, from (Zhang, et al., 1997); b) HPIV recording and reconstruction, adapted from (Hinsch, 2002).

By illuminating an HPIV hologram with the original reference beam, a virtual particle image can be formed, and light is emitted from the hologram as if it were being scattered from the particles. By reversing the reference wave (as shown in Figure 2.9b), images of the particles will be projected onto their original positions, allowing the tomographic digitization of the particle distribution by scanning a CCD sensor depth-wise through the image space (Hinsch, 2002).

While holography holds some clear advantages over standard PIV, the complexity of the necessary optical arrangement, its use of chemical plates, the time-consuming

reconstruction process, and the current lack of unified strategies for the correlation of the quantity of data collected means that HPIV remains a sporadically used technique. It is probable however that future advances in digital image sensor technology will enable much of the current research into digital holography to be realised in a form that is accessible to a much wider audience.

2.1.2.5. Multiphase Flows

Under certain circumstances, even 3D3C velocity data is insufficient to describe a fluid flow in the required detail. Multiphase flows consist of the simultaneous motion of more than one fluid (or solid), such as bubbles in beer or coffee grounds in a cafetière. A comprehensive measurement should therefore comprise as many velocity maps as there are phases (e.g. one for the beer, one for the bubbles). Multiphase (particularly two-phase) flows are of importance to many industries, for whom mixing processes (between fuel and air, for example) must be carefully monitored and understood.

Multiphase flows in which the different phases are moving at markedly different speeds may be analysed without any alteration to the standard PIV apparatus: such flows will produce distinct 'peaks' in the resultant correlation map (as explained in Section 2.5). Suitable interpretation of the map allows the generation of separate velocity vectors for each position in the measurement volume. Such an approach may however suffer from the limited dynamic range of PIV analysis: as has been shown, the choice of Δt must be made with careful consideration of the fluid velocity, meaning that any flow (be it multi- or single phase) that contains a large velocity gradient, ideally requires multiple values of Δt. (Pereira, et al., 2004) used a high speed camera to record several images

within a short time period, thereby providing a selection of Δt's depending on which images are correlated together. (De Ponte, et al., 2001) instead provided 3 differently coloured illumination pulses, timed such that the choice of coloured images to correlate gives 3 possible Δt values.

Given the nature of multiphase flow, it is often possible to introduce different seeding particles into each flow. Recorded particle images can then be categorized according to colour or intensity, size, or frequency response. (Khalitov and Longmire, 2002) used both size and brightness to distinguish the different seeding introduced into a turbulent channel flow. (Lindken and Merzkirch, 2002) superimposed shadowgraphy images of bubbles with PIV particulate images, and used histogram analysis to split the recorded images according to intensity. Similarly, (McCluskey, 1992) used particle intensity filtering, as shown below, to model the motion of pulverised coal particles in a power station's fuel transport system.

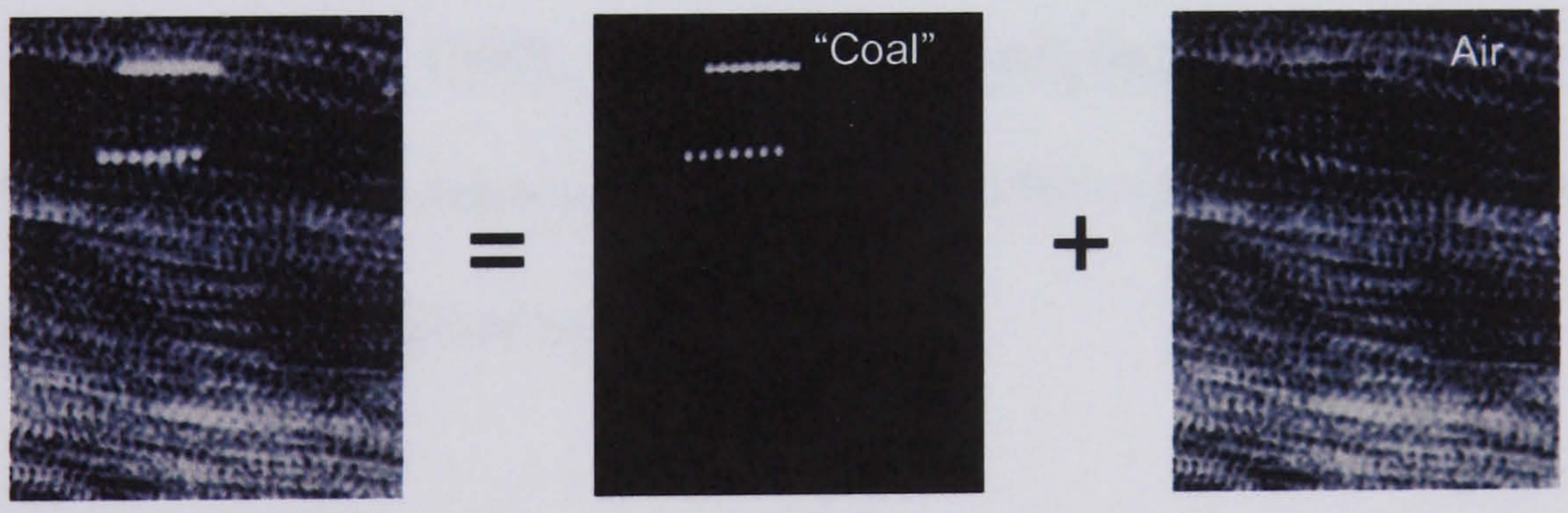

Figure 2.10 – Intensity based particle filtering, from (McCluskey, 1992).

(Towers, et al., 1999) instead used multi-colour lasers and filtered camera sensors with a mixture of normal and fluorescent seeding particles, to enable independent cross-correlation measurements from impinging jets. In this way, particles from each jet could be distinguished by the colour of their scattered light.

2.2. Seeding

The seeding particulates serve two, contradictory roles: to follow the surrounding fluid as faithfully as possible, while scattering a large amount of energy from the light sheet to the camera(s). The resulting compromise that therefore has to be made is dependent on not only the experimental equipment available, but also the type of flow being studied.

2.2.1. Flow Depiction

(Westerweel, 1997) defines 'ideal' seeding as:

- Particulates that do not interact with each other.
- Particulates that do not alter the flow, or properties, of the fluid.
- Particulates that follow the motion of the fluid exactly.

As pointed out by (Melling, 1997), 1 μm particles at a (quite typical) concentration of $10^9/m^3$ will have an average separation of 1000 diameters, meaning that we can assume the 1st requirement to be fulfilled by most flows.

2.2.1.1. Flow Alteration

The effect of seeding on the fluid under study can be quantified using non-PLV measurement techniques, such as hot-wire anemometry or LDA with amplitude-based filtering of reflections from the seeding under test (Chen, et al., 2000). Such experiments have shown that a flow's turbulence level can be altered significantly by the introduction of particulates. Furthermore, small particles have been found to reduce turbulence, while large particles can increase it (Fessler and Eaton, 1999).

Figure 2.11 reproduces the results of (Levy and Lockwood, 1981), who took LDA profiles 0.3 m downstream of a 15 mm diameter ~10 m/s turbulent jet. It can be seen that while very large amounts of 1 mm diameter sand increased the jet's turbulence and velocity (due to entrainment of the gas as the grains fell under gravity), copious quantities of 215 μm mean diameter sand both damped the turbulence and decreased the mean axial velocity.

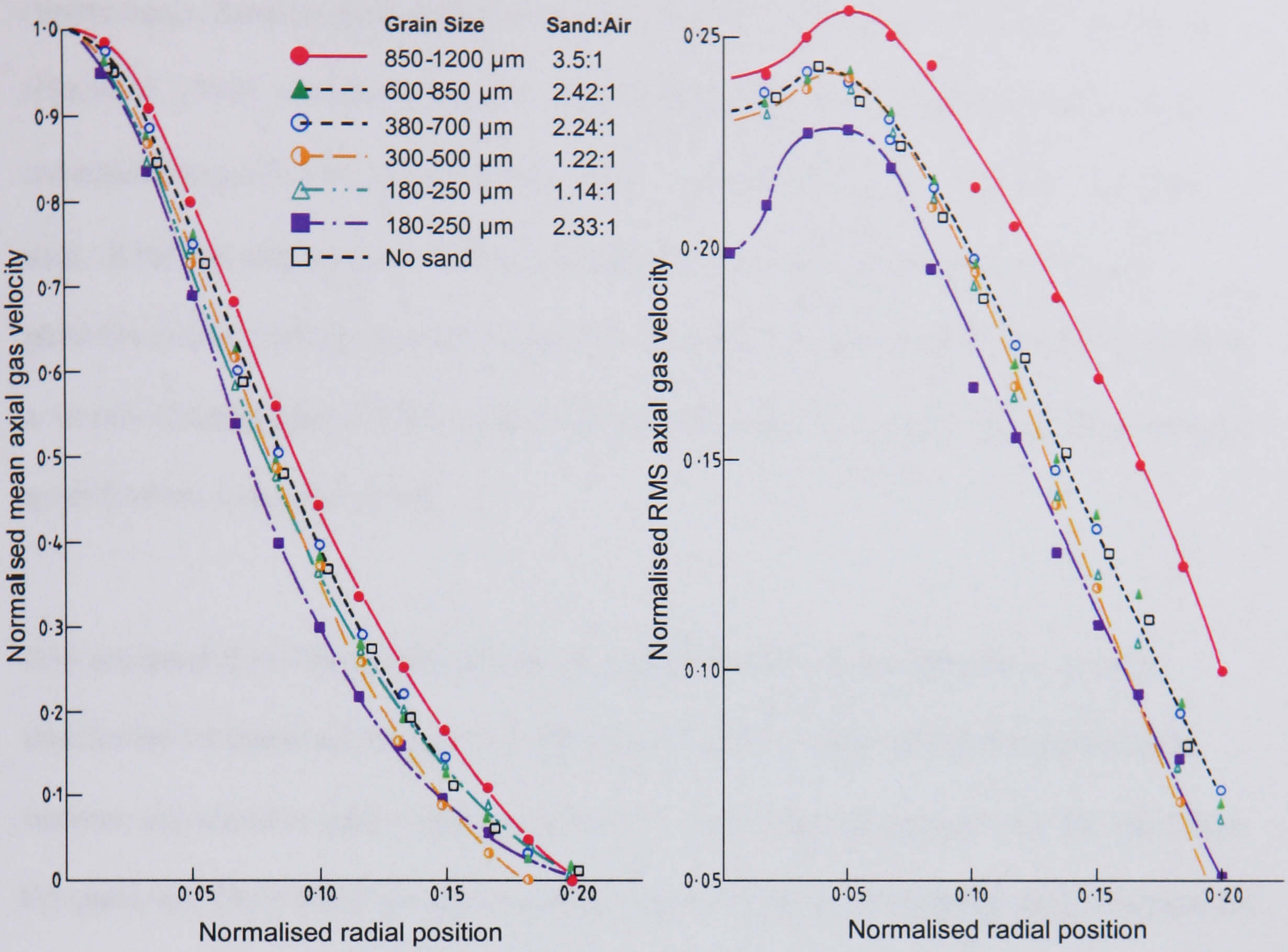

Figure 2.11 – The particle-laden jet profiles of (Levy and Lockwood, 1981).

The mechanisms by which such modifications occur are still under debate, with competing theories available for exactly what flow properties determine the magnitude and polarity of the change. (Hetsroni, 1989) concluded that particles with a Reynolds number above 400 tend to enhance turbulence, perhaps due to vortex shedding, whereas a smaller Re_p leads to a reduction in turbulence. (Gore and Crowe, 1991) showed that the turbulence was increased when the particle diameter exceeded $^1/_{10}$ of the characteristic eddy length (and vice versa). (Kulick, et al., 1994) instead related turbulence attenuation to an increasing Stokes number and mass loading.

As might be deduced from Figure 2.11, the quantity and size of particles typically required for turbulence *enhancement* is well above the range found in most PIV

experiments. Smaller particles however, such as 13 μm droplets in a 50-60 m/s air jet (Hetsroni, 1989), have been found to almost halve a flow's turbulent intensity, when introduced in sufficient quantities (air : seed volumetric flow rate $\approx 3\times10^5$: 1). That said, (Khalitov and Longmire, 2003) found that an equivalent number of 20 μm particles (mass loading ratio 0.7%) had no discernable effect on the turbulence levels in a 10 m/s channel flow. Clearly a method of predicting the potential for seeding-induced modification would be of use.

It is accepted that whereas the inertia of larger particles means that their travel is unaffected by turbulent structures within the flow, the ability of smaller particles to become entrained in eddies allows turbulent energy to be dissipated from the fluid into the particles. Only when the particles become so small that negligible energy is required to accelerate them to the same speed as the flow, does turbulence cease to be reduced. Following this rationale, there is general consensus that turbulence attenuation from small particles reduces with the number of particles and the particle Stokes number: a dimensionless quantity that describes the motion of particles in fluid flow, derived on page 43 (Fessler and Eaton, 1999).

Fortunately, seeding for PIV experiments should be chosen on the basis of a minimal Stokes number anyway, in order that the particles are capable of revealing the fluid's turbulence, and the next section discusses the means by which this can be achieved. It is however of note that inappropriately chosen seeding may not only prove incapable of following the fluid under study, but also modify the behaviour of that flow.

2.2.1.2. Flow Following

Unlike single point sensors such as hot-wire anemometers, PIV measures the Lagrangian velocity $\boldsymbol{v}$ of seeding particles, even though it is in fact the Eulerian velocity $\boldsymbol{u}$ of the surrounding fluid that is typically of more interest. In steady state flows, with zero acceleration, the time derivatives of the Lagrangian and Eulerian are both zero, but in non-laminar flows the difference between $\boldsymbol{u}$ and $\boldsymbol{v}$ is dependent on the velocity gradients, and therefore acceleration, within the fluid. Together with PIV's assumption that particulates experience zero acceleration between exposures t_1 and t_2, it can be seen that there are multiple physical sources of measurement error, as demonstrated below:

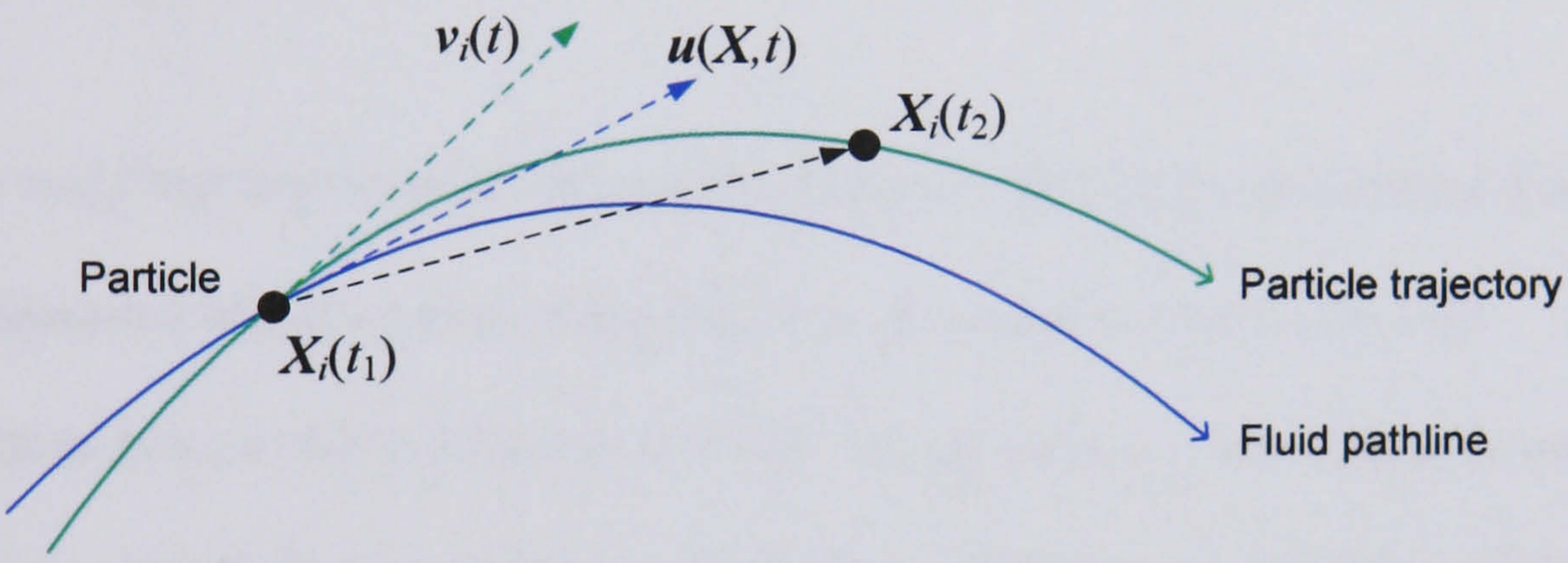

Figure 2.12 – A particle's representation of fluid flow, from (Westerweel, 1997).

As previously stated, $t_2 - t_1 = \Delta t$ should be sufficiently short that the difference between the perceived displacement of $\boldsymbol{X}$ and $\boldsymbol{v}.\Delta t$ is negligible, leaving only the relative motion between particle and fluid $|\mathbf{v} - \mathbf{u}|$ to be quantified. This velocity lag can be influenced by gravity or buoyancy forces, particle spin, Brownian motion and centrifugal forces, but these effects usually pale into insignificance compared to the effects of particle inertia.

Inertia, as considered by Newton in his first law of motion, can be considered as the resistance to acceleration. In the context of flows, fluid acceleration is accentuated by high frequency fluctuations such as those generated by small vortices. The resulting

velocity lag $|\mathbf{v}-\mathbf{u}|$ is therefore dependent on acceleration, and thus mass which can be considered in terms of the ratio between fluid and particle density. In the case of water, the density of fluid and particulate are often similar, meaning that seeding will follow the flow much better than in an air flow.

The motion of a particle in a fluid flow can be calculated by means of Stokes' law, if the particle Reynolds number is sufficiently small ($Re_p<1$). As can be seen in the definition below, this holds true for small particle sizes, and low relative velocities. For example, a 1 μm particle in air, travelling at 1 m/s less than the surrounding fluid, has $Re_p \approx 0.06$.

$$\mathrm{Re}_p = \frac{|\mathbf{v}-\mathbf{u}|d_p}{\nu_f} \tag{2.7}$$

Suffixes p and f represent particulate and fluid properties; d the diameter; ρ density; μ and ν the dynamic and kinematic viscosity. For non-spherical particles the aerodynamically equivalent diameter is used. The equation for the unsteady motion of a single spherical particle suspended in a fluid flow was determined by Basset in 1888 as:

$$\frac{\pi\rho_p d_p^3}{6}\dot{\mathbf{v}} + \frac{\pi\rho_f d_p^3}{12}(\dot{\mathbf{v}}-\dot{\mathbf{u}}) = 3\pi\mu_f d_p(\mathbf{v}-\mathbf{u}) + \frac{\pi\rho_f d_p^3}{6}\dot{\mathbf{u}} - \frac{3d_p^2\sqrt{\pi\mu_f\rho_f}}{2}\int_0^t \frac{d\xi}{\sqrt{t-\xi}}\frac{d(\mathbf{v}-\mathbf{u})}{d\xi} \tag{2.8}$$

The terms in equation (2.8) can be interpreted as: (Durst, et al., 1981)

1. Force required to accelerate the particle.
2. Force required to accelerate the increased 'virtual' mass added by fluid displacement.
3. Stoke's drag force.
4. Force due to the pressure gradient caused by the acceleration of the fluid.
5. The 'Basset history integral', which defines resistance caused by unsteadiness.

Both (Grant, 1997) and (Adrian, 1991) disregard the Basset term and effect of fluid density in order to present the simplified equation for motion:

$$\frac{\pi\rho_p d_p^3}{6}\dot{\mathbf{v}} = \frac{1}{2}C_D\frac{\pi\rho_f d_p^2}{4}|\mathbf{v}-\mathbf{u}|(\mathbf{v}-\mathbf{u}) \tag{2.9}$$

$$\rightarrow \quad |\mathbf{v}-\mathbf{u}| = \sqrt{\frac{4}{3}\frac{\rho_p}{\rho_f}\frac{d_p}{C_D}\dot{\mathbf{v}}} \tag{2.10}$$

…where C_D is the coefficient of drag between particle and fluid. It can be seen from equation (2.10) that for a constant C_D, the velocity slip is proportional to the square root of particulate size and fluid acceleration. (Adrian, 1991) (who omits the ½ term in equation (2.9)) has shown that calculations of the lag of a 1 μm particle (with $C_D = 0.1$) undergoing an acceleration of 10^6 m/s^2 up to 100 m/s, closely matches experimental LDA measurements (4 - 5% lag in both cases).

We can estimate the drag force on the particle using Stoke's drag law – given in equation (2.11) – and thus the drag coefficient using Rayleigh's drag equation (2.12):

$$\mathbf{F}_d = 3\pi\mu_f d_p(\mathbf{v}-\mathbf{u}) \tag{2.11}$$

$$\mathbf{F}_d = \frac{1}{2}\rho_f(\mathbf{v}-\mathbf{u})^2\frac{\pi d_p^2}{4}C_D \tag{2.12}$$

$$\rightarrow \quad C_D = \frac{3\pi\mu_f d_p(\mathbf{v}-\mathbf{u})}{\frac{1}{8}\rho_f(\mathbf{v}-\mathbf{u})^2\pi d_p^2} = \frac{24\mu_f}{\rho_f d_p(\mathbf{v}-\mathbf{u})} \tag{2.13}$$

$$\rightarrow \quad C_D = \frac{24\nu_f}{d_p(\mathbf{v}-\mathbf{u})} = \frac{24}{Re_p} \tag{2.14}$$

Substituting equations (2.13) in (2.9) gives:

$$|\mathbf{v}-\mathbf{u}| = \frac{\rho_p d_p^2\dot{\mathbf{v}}}{18\mu_f} = \frac{\rho_p d_p^2\dot{\mathbf{v}}}{18\rho_f\nu_f} \tag{2.15}$$

(Hetsroni, 1989) notes that the velocity lag divided by the acceleration gives the particle time constant τ_p otherwise known as the relaxation time, or time required to accelerate a particle to ~63% of the fluid velocity:

$$\tau_{p,Stokes} = \frac{|\mathbf{v}-\mathbf{u}|}{\dot{\mathbf{v}}} = \frac{\rho_p d_p^2}{18\rho_f\nu_f} \tag{2.16}$$

If $\mathrm{Re}_p > 1$, C_D will be greater than that given by equation (2.13), leading to reduced values for both the velocity lag and relaxation time. For Reynolds numbers up to 700, (Torobin and Gauvin, 1959) report the modification of the drag coefficient by a factor of $(1 + 0.15Re_p^{0.687})$ which in turn leads to a slightly more robust definition of the particle time constant (Fessler and Eaton, 1999):

$$\tau_p = \frac{\tau_{p,Stokes}}{1+0.15Re_p^{0.687}} \tag{2.17}$$

The ratio of the particle response time to a representative time scale in the flow is the Stokes number: a dimensionless measure of the responsiveness of particles in a fluid flow. It may be defined thus:

$$St = \frac{\tau_p}{\tau_f} \tag{2.18}$$

If $St \ll 1$, particles follow the flow perfectly, with $|\mathbf{v}-\mathbf{u}| \rightarrow 0$. For $St \gg 1$ however, a particle will continue along its own trajectory, irrespective of the motion of the fluid. The fluid's time constant τ_f is determined as a characteristic length (of, for example, the most energetic eddies) divided by the mean flow speed.

For highly turbulent flows, it is useful to consider the maximum frequency of fluid oscillation that can be followed accurately. By considering solutions to equation (2.8), (Melling, 1997) presents equations for the relative amplitude η and phase β of a particulate experiencing oscillation of frequency f_c:

$$\eta = \left(1 + \frac{\left(2\pi f_c \rho_p d_p^2\right)^2}{324\mu_f^{\,2}}\right)^{-0.5} \tag{2.19}$$

$$\tan\beta = \frac{-2\pi f_c \rho_p d_p^2}{18\mu_f} \tag{2.20}$$

Rearranging equation (2.19) allows calculation of the particle size required in order to follow a fluid's oscillation with a given relative amplitude:

$$d_p = \frac{\sqrt[4]{324\mu_f^2\left(\eta^{-2}-1\right)}}{\sqrt{2\pi f_c \rho_p}} \tag{2.21}$$

For example, in order for TiO_2 seeding in air ($\mu_f = 1.8\times10^{-5}$ kg.m^{-1}.s^{-1}, $\rho_p = 3500$ kg.m-^{3}) to follow turbulent oscillations of 10 kHz with 99% amplitude accuracy, it may be calculated that the particles should have a diameter no greater than 0.45 μm. Equation (2.20) gives an associated phase lag of 7.8° (or 2%), but this value is only important if the

PIV data is to be synchronized with LDA measurements, which may be more sensitive to the motion of smaller particles.

Substituting values for polystyrene in water ($\mu_f = 0.8\times10^{-3}$ kg.m^{-1}.s^{-1}; $\rho_p = 1050$ kg.m^{-3}) in equation (2.21) gives $d_p = 5.6$ μm, thereby reiterating the fact that typical particulates have better flow following ability in water than air (Rudoff and Bachalo, 1991). As demonstrated in Figure 2.13 however, it should be remembered that the relationship between d_p and η is highly non-linear at high values – a fact that highlights the potential for problems caused by particle agglomeration.

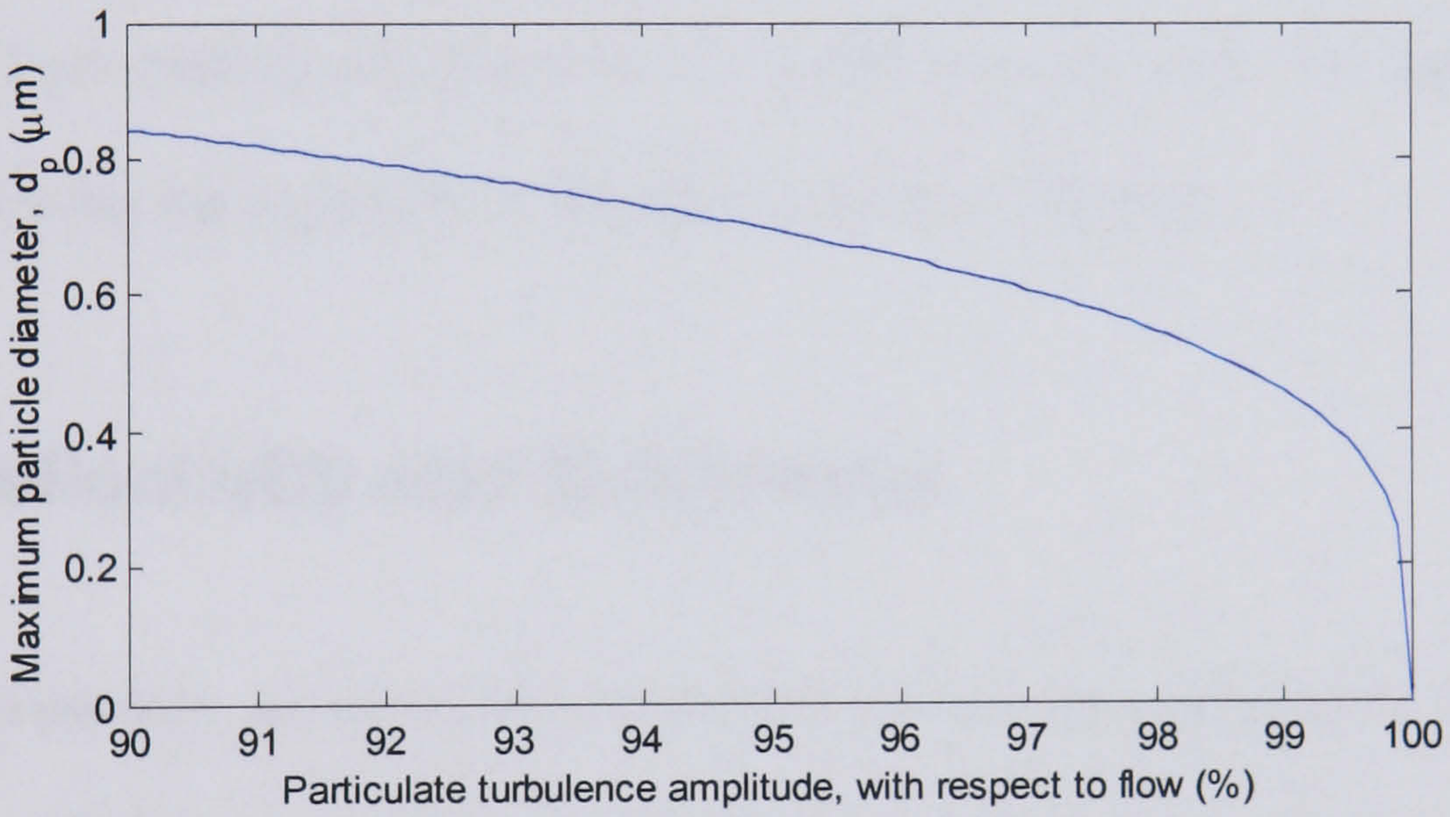

Figure 2.13 – Particulate flow following accuracy vs. particle size.

2.2.1.3. Vortex Seeding

In the case of swirling flows, the centrifugal force experienced by particles is no longer negligible, and vortices can empty of their seeding. (Leishman, 1996) demonstrates seeding density reductions of over 50% in the tip vortex of a helicopter rotor, for example. (Melling and Whitelaw, 1973) give the radial velocity of a particle, due to centrifugal force as:

$$v_r = \frac{\rho_p d_p^2 r \omega^2}{18 \mu_f} \tag{2.22}$$

…where ω is the angular velocity of the vortex, and r the distance between its centre and the particle. It is assumed that the fluid does not move radially, and that the fluid and particle have equal tangential velocity. This may be compared the with tangential particle velocity:

$$v_t = r\omega \tag{2.23}$$

The ratio of the two is proportional to d_p^2. For example, a 10 μm TiO_2 particle 1 mm from the centre of a 100 rps air vortex will move tangentially at 0.1 m/s, but radially at 0.013 m/s. A 1 μm particle would instead move 100 times slower in the radial direction, therefore following the trajectory of the fluid much more closely.

2.2.2. Reflectivity and Brightness

Upon hitting a particle, incident photons may be absorbed or scattered, by either diffraction or diffusion (comprising interference and reflection). It is also possible that photons will be emitted from the particle. The relevant contribution of these effects changes with the ratio of particle size to illumination wavelength, and as a result there are 3 different theories of light scattering: geometric, Mie, and Rayleigh scattering. The size parameter χ is a simple means of determining the predominate mechanism.

$$\chi = \frac{2\pi r}{\lambda} = \frac{\pi d_p}{\lambda} \tag{2.24}$$

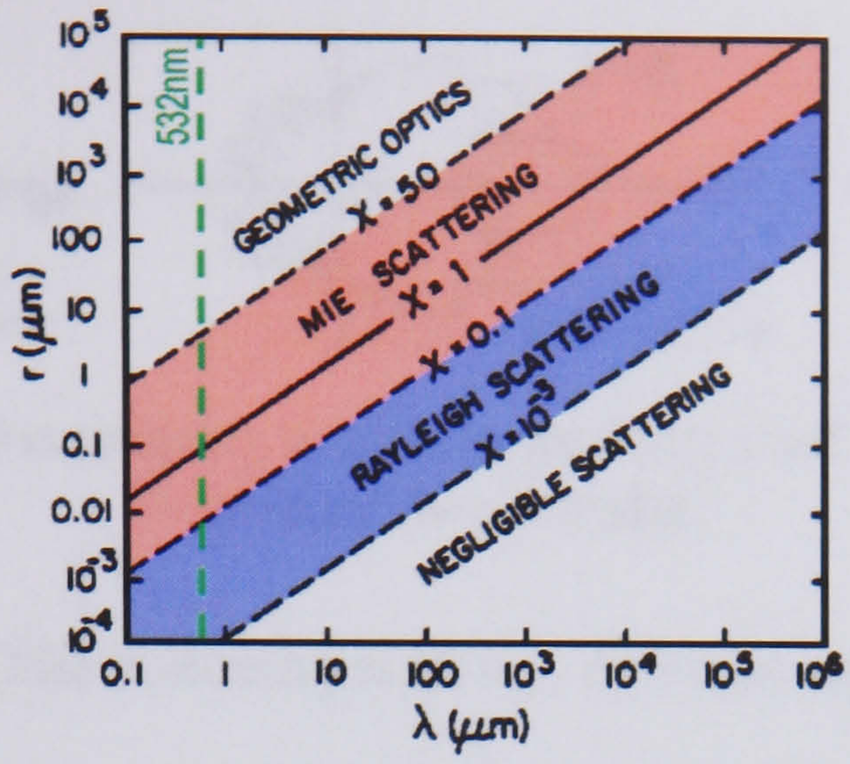

Figure 2.14 – Predominant scattering regimes, from (Wallace and Hobbs, 1977).

As indicated above, when $\chi \gg 50$ (i.e. $d_p \gg \lambda$), light scattering may be considered to occur by purely geometrical means, with the mean light energy ε collected by the receiving optics proportional, on average, to $(d_p/\lambda)^2$ (Adrian, 1991). Because the area of a large particle's recorded image increases in proportion to d_p^2, there is little advantage to using particles larger than 100 μm or so, unless the measurement area covered by one pixel or film grain is larger than the particle diameter.

For $\chi \ll 0.1$ (or $d_p \ll \lambda$) Rayleigh scattering, which is more applicable to molecules than solid particles, applies and the scattered energy is proportional to $(d_p/\lambda)^4$ (the heavy wavelength dependence being the reason the sky is blue). Most PIV particulates however belong in the realm of Mie scattering, in which the mean energy received is approximately proportional to $(d_p/\lambda)^3$, but due to intra-particle interference, it is also extremely dependent on viewing angle.

It is of note that the scattered energy is proportional to λ^{-n}, where n is dependent on the dominant scattering regime. For Mie scattering ($n \approx 3$), the transition from 633 nm red light to 532 nm green light will yield approximately 1.7 times more scattered light.

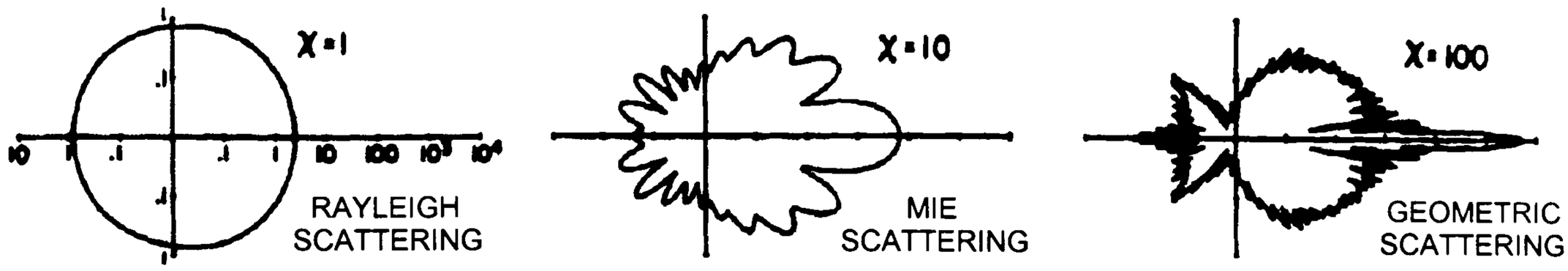

Figure 2.15 – Representative angular scattering profiles, from (Kidder and Haar, 1995). Note logarithmic scales.

The angular sensitivity of Mie scattering is clearly demonstrated in Figure 2.15 above. Whereas Rayleigh scattered light is equally bright in both forward- and back-scatter (and half as bright to the side), Mie scattering transmits a huge amount more energy forwards. The ratio of forward to side scatter, I_{s0} / I_{s90} decreases with χ, but for typical PIV parameters will be in the order 10-1000 (Melling, 1997). It should be noted that the intensity of Mie scattered light is also dependent on the relative angle between the polarisation plane and the viewer*.

Figure 2.16 demonstrates the effect of viewing angle on the intensity of perpendicularly polarised light received from TiO_2 particles of varying diameters, in air, at both 532 nm and 633 nm. All of the following data has been generated using MiePlot v3.4†, which uses the popular BHMIE code presented by (Bohren and Huffman, 1998) to solve the underlying Maxwell's equations. Although Lorenz-Mie theory is specific to spherical particles, techniques also exist for the calculation of light scattering from irregularly shaped particles (Hulst, 1993).

* While the radial scattering intensity profiles for both *p*- and *s*-polarised light (c.f. Figure 2.26 on page 63) are equal when summed through 360°, their minima and maxima occur in different positions.

† Written by Philip Laven. Available free of charge at: http://www.philiplaven.com/mieplot.htm

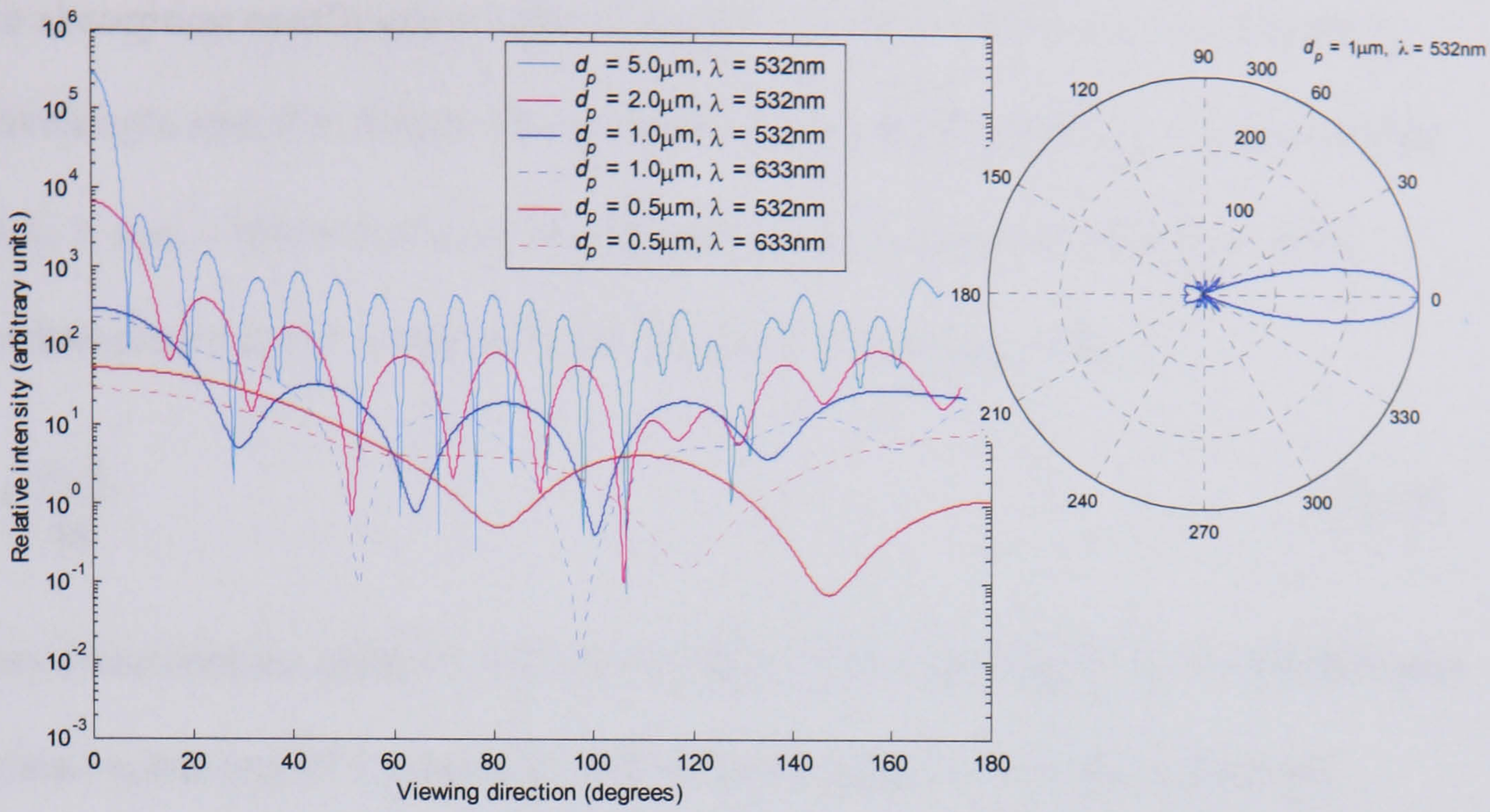

Figure 2.16 – Mie scattering of TiO_2 particles in air (note logarithmic scale).

The linear-axis polar plot is included above right to emphasize the large difference (×30) between the amounts of side- and forward-scattered energy. Figure 2.17 demonstrates the change in power law as d_p increases (c.f. Figure 2.14) using simulated 90° scattering intensities.

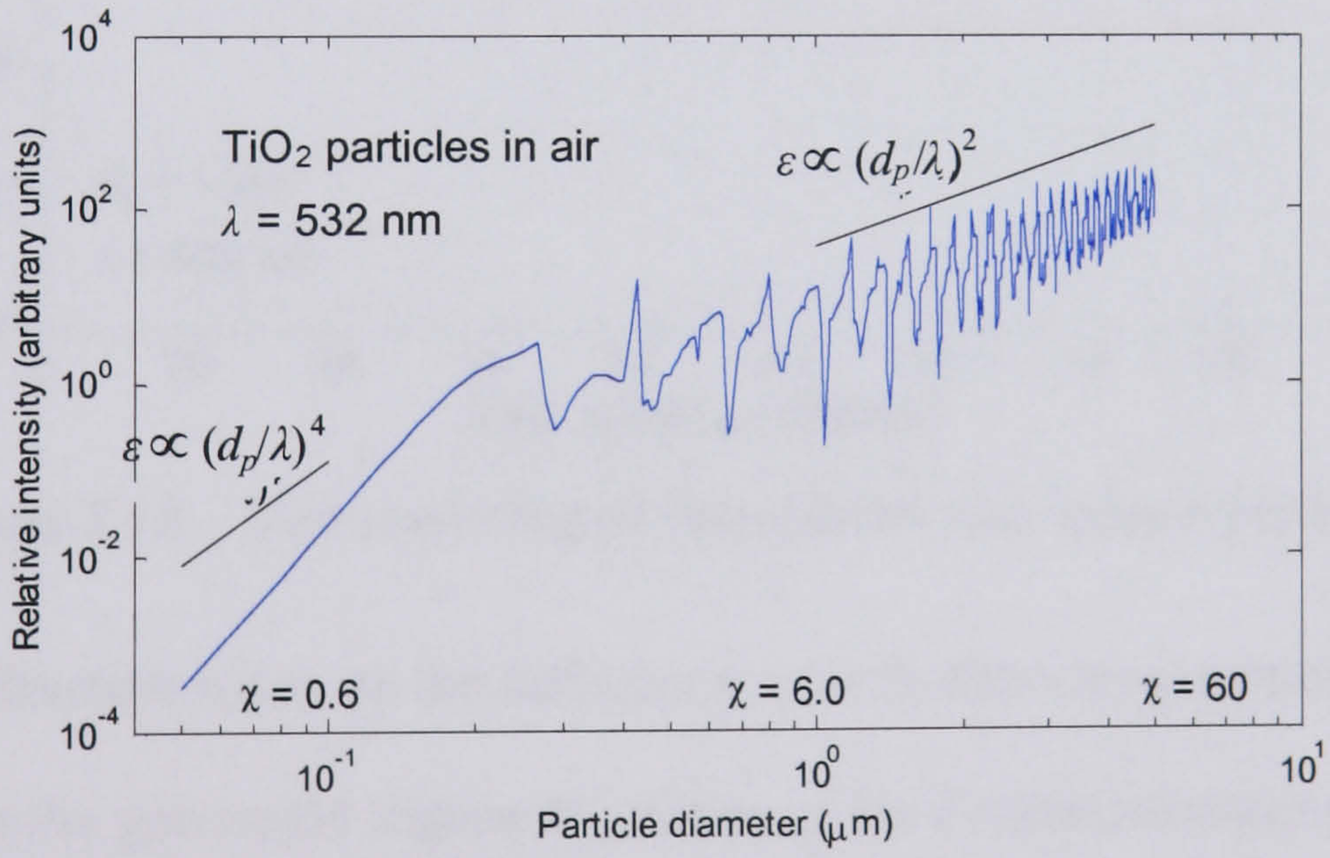

Figure 2.17 – 90° Mie scattering intensity of TiO_2 particles in air.

While the figures above illustrate the effects both of d_p and λ on the angular scattering profile, the *total* energy scattered (as a proportion of that supplied) is dependent on the particles' absorption coefficient, and the relative refractive indices of the particle and

fluid. The absorption coefficient α varies between complete translucency and opacity, and is wavelength specific. It may be expressed volumetrically (m^{-1}) or by mass (m^2kg^{-1}), where $\alpha_v = \rho_p \alpha_m$. Absorbance can be represented by a complex refractive index, where the imaginary part k is related to the volumetric absorbance by:

$$k = \frac{\alpha_v \lambda}{4\pi} \tag{2.25}$$

Mie theory encompasses complex refractive index values, and Figure 2.18 demonstrates the simulated scattering of 2 materials with different opacities. Notably, there are relatively few naturally occurring materials with anything more than a negligible opacity (e.g. $k_{water} \approx 2\times10^{-9}$ at 532 nm), exceptions including the mineral hematite and the element carbon.

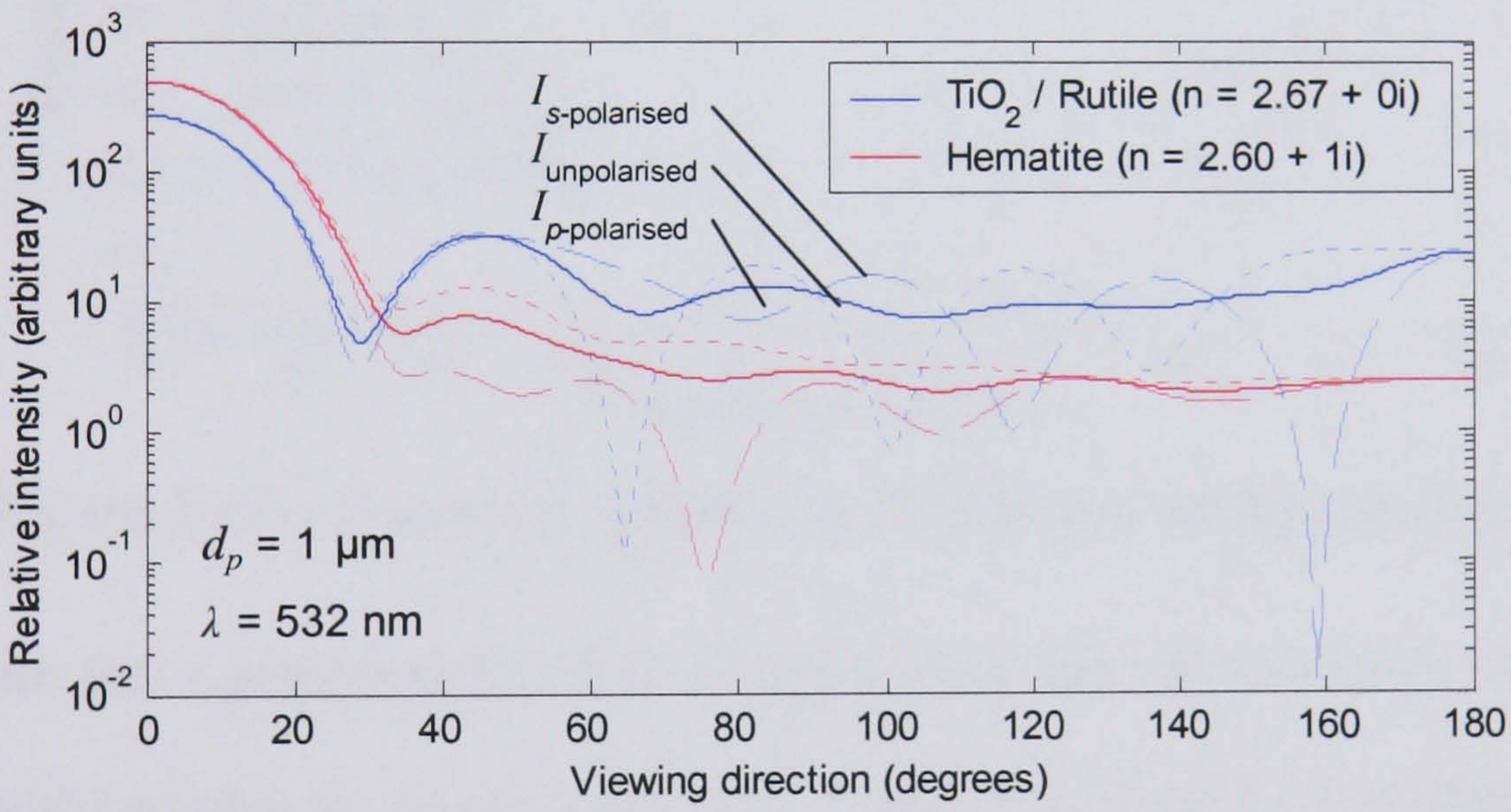

Figure 2.18 – Mie scattering of transparent and opaque particles.

The effect of refractive index on the reflectivity of non-absorbing particles can be demonstrated in the geometric regime by means of the Fresnel equations. It should be noted that, as with absorbance, refractive indices are wavelength dependent, though only strongly so for a small number of materials such as TiO_2 (DeVore, 1951). The Fresnel equations provide the proportion of energy (both *p*- and *s*-polarised) reflected from a dielectric surface:

$$R_{p-polarised} = \left(\frac{(n_0/\cos\theta) - (n_1/\cos\Theta)}{(n_0/\cos\theta) + (n_1/\cos\Theta)} \right)^2 \tag{2.26}$$

$$R_{s-polarised} = \left(\frac{(n_0\cos\theta) - (n_1\cos\Theta)}{(n_0\cos\theta) + (n_1\cos\Theta)} \right)^2 \tag{2.27}$$

…where n_0 and n_1 are the refractive indices of the fluid and particle, θ the angle of incidence, and Θ the angle of refraction ($\Theta = (n_0/n_1)\sin\theta$). Figure 2.19 illustrates the amount of light reflected from 3 common seeding material and fluid combinations.

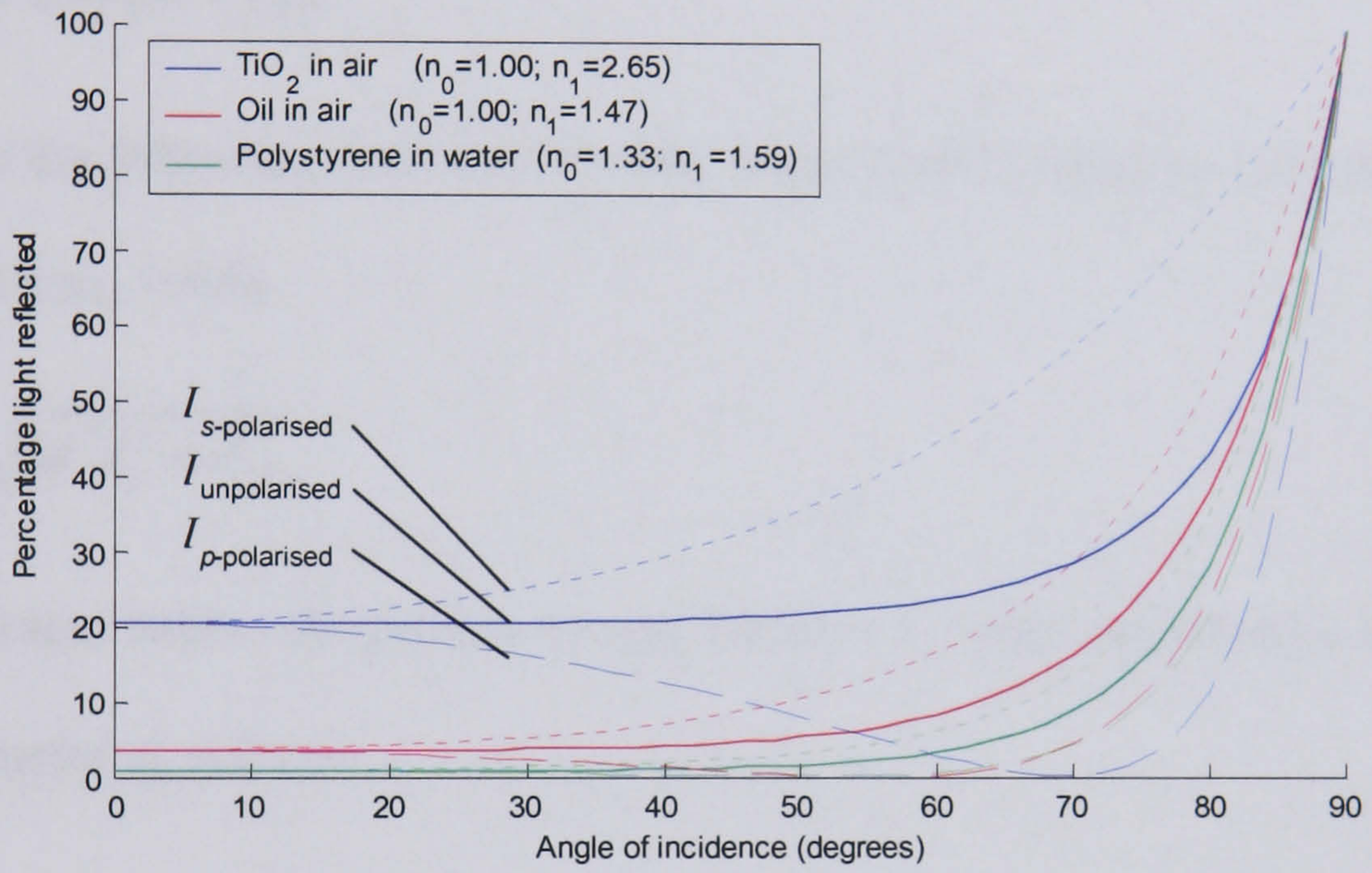

Figure 2.19 – Geometric reflectivity for selected seeding materials.

It can be seen that a greater proportion of light is reflected (per boundary transition) when the ratio between the seeding and fluid's refractive index is at its highest. Not only does this demonstrate that seeding should be chosen on the basis of a maximal refractive index, but also that fluid flows require larger particles in order to maintain the same amount of light scattering as an air flow. As demonstrated in Section 2.2.1.2 however, this increased size requirement is countered by an improvement in the seeding's flow following ability.

2.2.3. Recorded Particle Image Size

In the geometric regime, the diameter d_τ of a particle's image on the camera sensor plane is proportional to the physical particle size, i.e. $d_\tau = M.d_p$. At smaller scales however, particles produce Airy ring images, caused by Fraunhofer diffraction (Guerrero, et al., 2000). For suitably high quality (i.e. diffraction limited) lenses, the diameter d_{Airy} of the bright, central Airy disc may be estimated as:

$$d_{Airy} = 2.44(M+1)\lambda f^{\#} \tag{2.28}$$

…leading to the following definition for the image-plane diameter of any particle:

(Adrian and Yao, 1985)

$$d_\tau = \sqrt{M^2 d_p^2 + d_{Airy}^2} \tag{2.29}$$

As demonstrated below, the particle image diameter d_τ tends towards d_{Airy} as the real particle diameter d_p reduces:

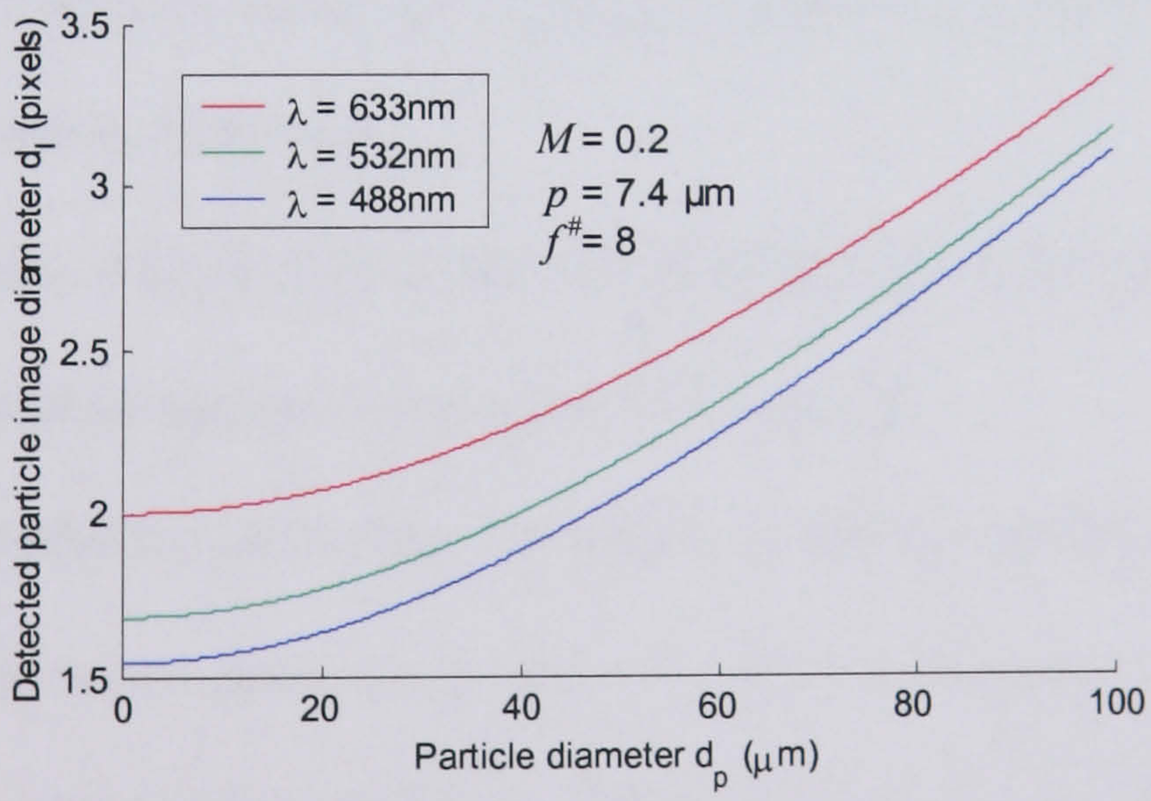

Figure 2.20 – Imaged particle diameter (in pixels) vs. actual particle diameter.

This leads to the interesting observation that – for small particle sizes – a switch from blue to red light would necessitate a seeding generator's output to be almost halved, in order to maintain a constant seeding source density N_S (c.f. page 15).

2.2.4. Summary of Seeding Requirements

We may conclude that seeding should be chosen on the following bases:

- The seeding should be supplied at a low enough mass density that:
  - Inter-particle interaction becomes unlikely;
  - The potential for turbulence modification is reduced (relevant if $d_p > 1\mu m$).
  - The seeding source density $N_S \ll 1$.
- The seeding should however be dense enough that $N_I > 15$ (c.f. page 15).
- The size distribution of the particles should be as narrow as possible, to minimise a low velocity bias caused by the disproportionate brightness of larger particles, which follow the flow less accurately.
- The particle density should be as close as possible to that of the surrounding fluid, in order to avoid buoyancy or gravitational effects, particularly if d_p is large. Seeding particles for fluid flows may be sorted by means of a settling chamber.
- The particles' diameters should be as large as possible, in order to maximise light scattering, but not so large that:
  - Their diameter is equivalent to the size of structures in the flow. All sides of a particle should be subject to the same fluid motion.
  - Particles in turbulent flows lose the ability to follow oscillations of a frequency of interest. Maximum values for d_p and ρ are given by equation (2.21) on page 43.
  - Particle velocities lag behind those of laminar flows due to the fluid's acceleration. Maximum values for d_p and ρ are given by equation (2.10) on page 41.
- The particle material's refractive index should have a high real component and low imaginary component, in order to maximise the amount of scattered light.

2.2.5. Recognised Seeding Materials

Lists of seeding materials, as used for PIV studies by various authors, are provided by (Kasagi and Nishino, 1991; Meinhart, et al., 1998; Melling, 1997; Weitbrecht, et al., 2002). Table 2.1 consolidates references from these (and other) papers, in order to provide an indication of the range of available seeding materials and characteristics. The popularity of each seeding type, for both gas and liquid flows, is indicated to the right of the table.

	Material	ρ (kg/m^3)	Typical d_p (μm)*	Refractive index†	Melting / Boiling point	Used in…	
						Gas	Lqd
Minerals / Oxides	Zirconium oxide (ZrO_2)	5890	≥ 0.7	1.95	T_m = 2715°C	✓	✓
	Aluminium oxide (Al_2O_3)	3970	0.18-100	1.76	T_m = 2054°C	✓	✓
	Titanium dioxide (TiO_2)	3500	≥ 0.1	2.65	T_m = 1775°C	✓✓	✓
	Chalk ($CaCO_3$) dust	2830	10-50	1.59	T_m = 825°C	✓	
	Silica (SiO_2)	2650	5	1.46	T_m = 1830°C	✓	✓
	Zinc chloride ($ZnCl_2$) smoke pellet	2500	0.5		T_m = 275°C	✓	
Polymers / Plastics	Polyamide / Nylon	1060	20-200	1.53	$T_m \approx$ 180-265°C		✓✓
	Polystyrene	1050	0.2-1000	$1.59+3\times10^{-4}i$	$T_m \approx$ 190-260°C	✓	✓✓
	Eliokem Pliolite resin	1020	40-60				✓
	Thermoplastics	1020	6-200	1.54	$T_m \approx$ 150-400°C		✓
	Polyethylene	960	5	1.52	$T_m \approx$ 100-130°C		✓
Liquids	Glycerol fog	1260	0.1-3	1.47	T_b = 290°C	✓✓	
	Water droplets	1000	50	$1.34+2\times10^{-9}i$	T_b = 100°C	✓	
	Atomised water fog	1000	20	$1.34+2\times10^{-9}i$	T_b = 100°C	✓	
	Vegetable oil droplets	970	0.6-5	1.47	T_b = 299°C	✓✓	
	Oil smoke (produced at 190-240°C)	970	0.02-1.6	1.47	T_b = 299°C	✓	
	Styrene	900	0.5	1.56	T_b = 145°C	✓	
	Acetone	800	1	1.36	T_b = 56°C	✓	
	Blood cells		5				✓

* Values given are ranges found in the literature, and not necessarily indicate of available sizes.

† At 532nm, or as close as possible, where a choice given in the literature. Unless shown, values for complex part k were not found, and can be considered negligible.

Other	Glass spheres	2600	0.5	1.51	$T_m \approx 1500°C$	✓	
	Burnt toast smoke	2000	0.4	$1.46+0.015i$		✓	
	Incense / Tobacco smoke	1200	0.01-0.3	1.43-1.59		✓	
	Fluorescent particles	900-1100	60-100				✓
	Pollen	1000	10-100	1.42, $k > 0$			✓
	Hollow glass balloons	100-1100	10-100		$T_m \approx 1500°C$	✓	✓✓
	Hollow nylon balloon		30		$T_m \approx 180\text{-}265°C$	✓	
	Hollow silica balloons	200-800	40-50	1.70	$T_m = 1830°C$	✓	
	Hydrogen bubbles (H_2)	0.09	40-500	1.00	-		✓

Table 2.1 – Seeding materials and typical physical characteristics.

It should be noted that while the physical characteristics listed above (where available) are sufficient to allow calculation of that seeding's flow following ability, there may be additional issues associated with each material. Styrene, for example, is a carcinogen, and although TiO_2 is one of the cheapest and brightest solid oxide seeds, Al_2O_3 is less likely to conglomerate.

2.2.6. Seeding Generators

Seeding generators are responsible for the homogenous dispersion of seeding particles within a flow medium, and – depending on the material used – generation of those particulates (Melling and Whitelaw, 1973). Ideally, a generator should produce a monodisperse particulate suspension at a high (but controllable) enough rate to fulfil the $N_I > 15$ criterion for the particular imaging parameters used.

The seeding of liquid flows, which typically involves solid particles of either very small diameter or of a density close to that of the liquid, is most straight-forward. When (as in most cases) the flow recirculates, a simple sprinkle and stir is all that is required, whereas non-recirculating flows need only a simple mechanical dispenser (Weitbrecht, et al., 2002). Gas flows prove more difficult to seed, and there are substantial differences between the performance and generation of the appropriate liquid and solid seeding particulates, as summarised below:

	Liquid seeding	**Solid seeding**
Pro's & Con's	• Easy to generate at a consistent rate. • Difficult to generate in large quantities. • Particles are spherical, therefore capable of being modelled accurately. • May cause films on wind tunnel windows, causing refractive bending.	• More likely to agglomerate, due to moisture, electrostatic forces and irregular shape. • Can be used in flames and high-temperature gas flows.
Generation	• Evaporation / condensation (e.g. glycerol fog). • Air jet atomisation (e.g. oil droplets). • Ultrasonic atomisation (e.g. water fog).	• Atomisation of solid / solvent suspension (e.g. TiO_2 in alcohol). • Fluidisation (e.g. Al_2O_3). • Ultrasonic vibration (e.g. glass spheres). • Combustion (e.g. incense). • Chemical (e.g. the reaction of $TiCl_4$ with water vapour to produce TiO_2).

Table 2.2 – Summary of liquid and solid seeding for gas flows.

2.2.6.1. Liquid Seeding Generation

Liquid seeding particles are normally generated for PIV studies by means of atomisation, due to the process's simplicity and the consistency of the results. Typically a nebuliser or Laskin nozzle is used: both devices operate on the principle of liquid entrainment and shearing within a high speed jet of air (c.f. Figure 2.21).

Either type of atomiser design may incorporate an impactor, added just in front of the jet to filter out any large droplets that appear (only those particles with a low Stokes number are capable of moving around the obstruction, instead of hitting it). By virtue of being operating underwater (or more commonly, oil), the aerosol produced by a Laskin nozzle may experience additional separation, due to larger particles combining with the wall of their surrounding bubble before reaching the surface of the fluid.

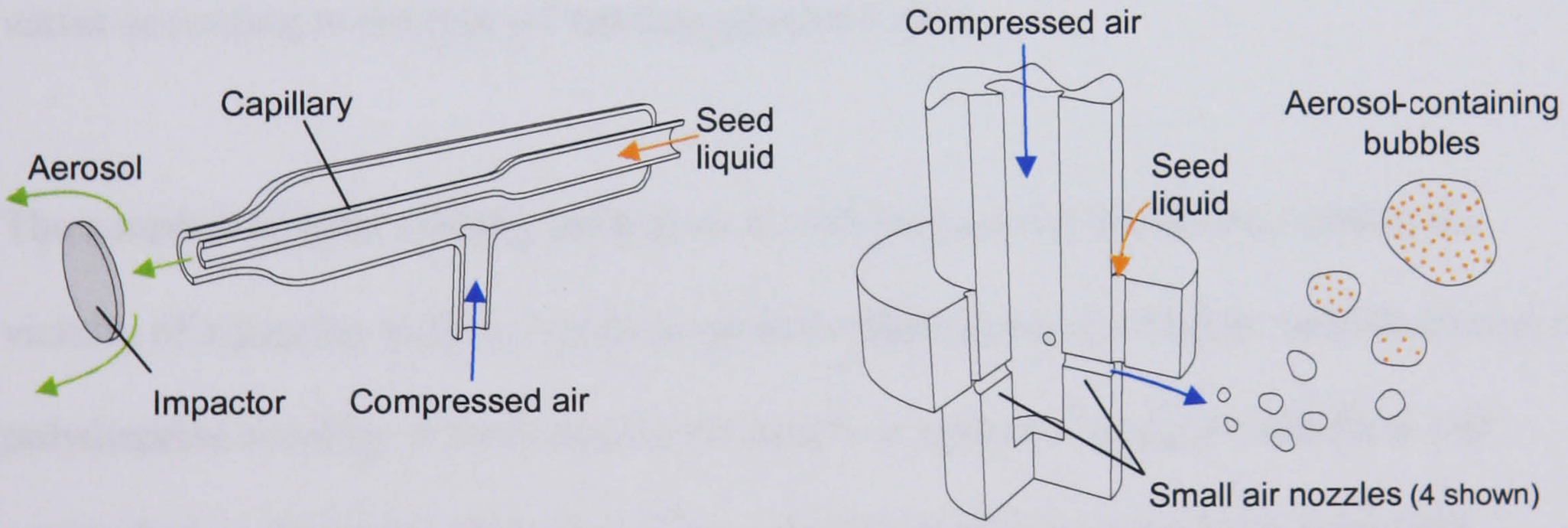

Figure 2.21 – Liquid particulate aerosol generators: a) Nebuliser; b) Laskin nozzle.

The size distribution of particles produced by 4 and 12-nozzle nebulisers was measured by (Kähler, 2003). As shown in Figure 2.22, the size distribution is tightened significantly when an impactor is added, and – perhaps surprisingly – the smallest of the nozzle diameters tested (0.5 mm) was found to produce the greatest number of larger-than-intended particles.

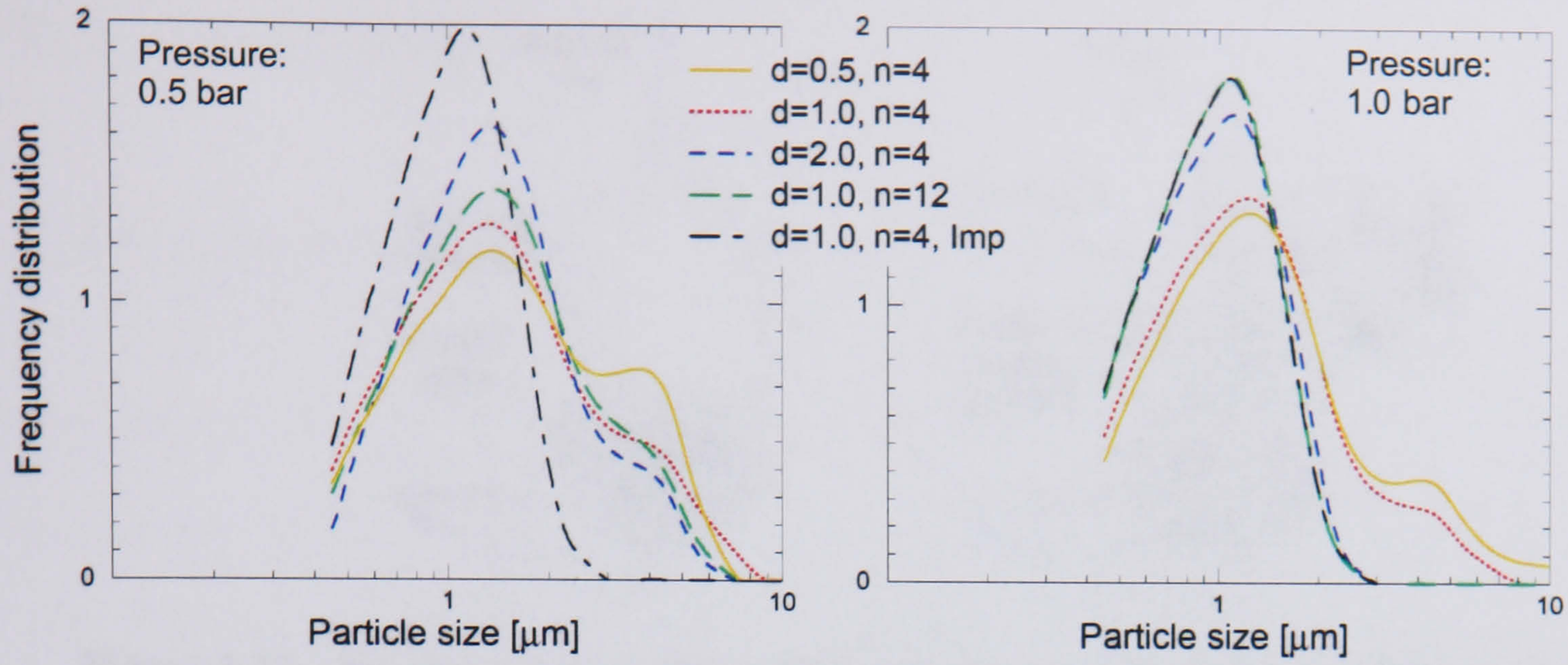

Figure 2.22 – Atomised particle size distributions, from (Kähler, 2003).

2.2.6.2. Solid Seeding Generation

With a few exceptions (e.g. smoke), solid seeding particulates are invariably supplied in ready-to-use form, and as a result, their size can be measured prior to use. Damp or non-spherical particles will however agglomerate during their dispersion, to a degree that varies according to the type of seeding generator used.

The simplest of solid seeding generators merely palpate the particulates within the vicinity of a passing airflow, but these devices often produce a highly variable stream of polydisperse seeding. A more consistent supply is achieved using the fluidised bed seeder design depicted in Figure 2.23 on page 58, in which air passes *through* the seeding, and only those particles that become entrained in the rising bubbles of gas exit the seeder. The monodispersity of the seeder's output may be further improved by adding a second phase of 'host' beads (of ≤ 0.5 µm diameter or so), which encourage any agglomerated particles to divide before reaching the top of the bed (Melling, 1997).

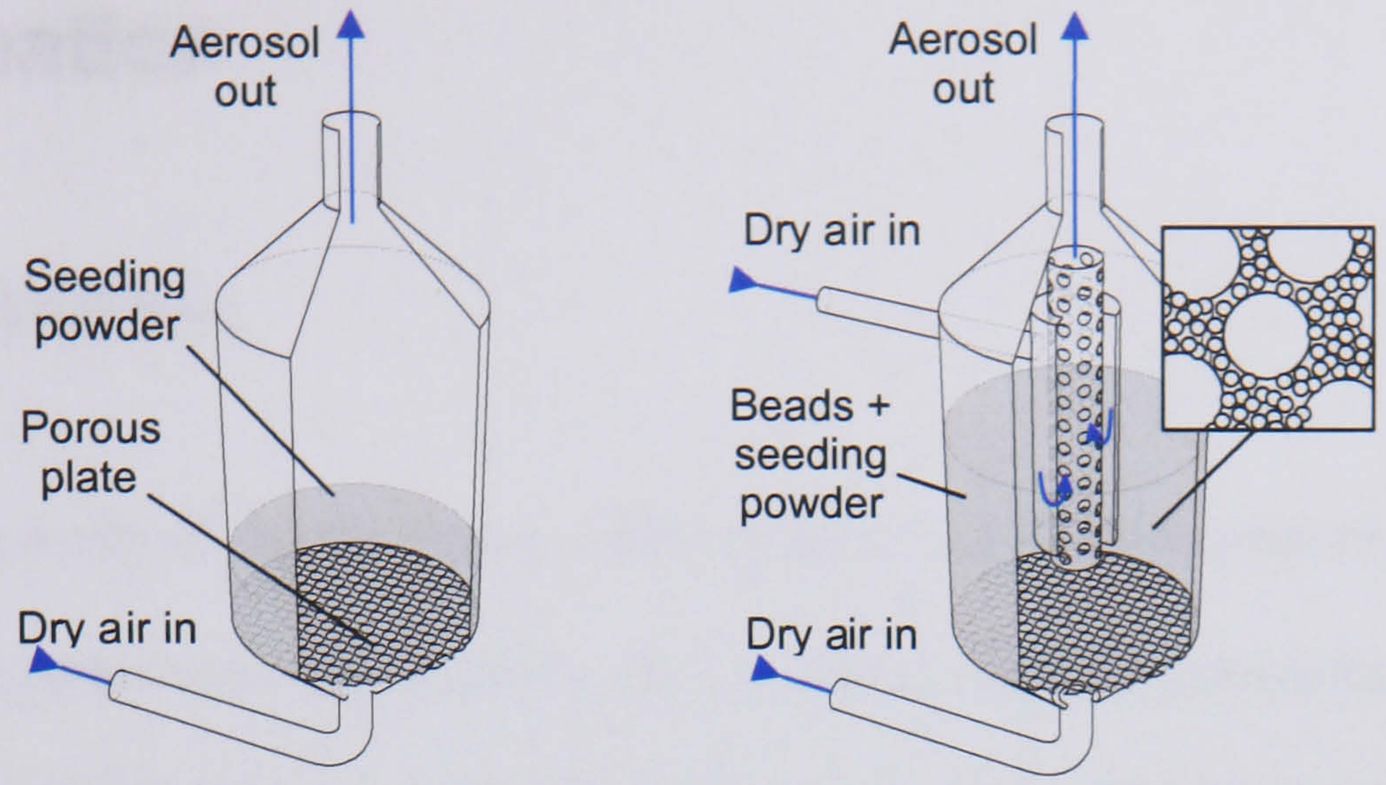

Figure 2.23 – Single, and dual-phase fluidised bed seeders, from (Melling, 1997).

For applications requiring very fine control over the size of the seeding, solid particles may be suspended in a liquid, then atomised. By choosing a solvent that evaporates quickly in the flow medium (e.g. ethanol), the maximum effective (agglomerated) particle size should be no greater than the size of the atomised fluid particles.

2.3. Illumination

2.3.1. Introduction

By cross-correlating every n^{th} frame from a video camera, it is possible to perform PIV on slow flows using continuous illumination, such as that from cheap, powerful incandescent lamps (Weitbrecht, et al., 2002). Similarly, a sensitive high-speed camera with a very short exposure time can be used (Pereira, et al., 2004; Tsushima, et al., 2004), but given the typical unavailability of suitable cameras, such an approach often proves impractical. Given the need therefore for pulsed illumination, a PIV experiment will almost always make use of either a pulsed light source or a means of modulating a continuous one.

Mechanical choppers (often comprising a wheel or solenoid) are a common form of modulation device, but their minimum 'on' times are usually limited to the order of milliseconds (Willert and Gharib, 1991; Zhao, et al., 2001). While the use of a mechanically shuttered laser with a traditional light sheet might therefore lead to blurred particle images, a scanned light sheet (discussed on page 66) can instead be used to provide an effective and cheap illumination system for low speed flows (Cosgrove, et al., 2001).

(Vogel and Lauterborn, 1988) used a non-mechanical acousto-optic deflector to modulate a CW argon ion laser, by steering the beam into and out of an aperture, thereby achieving pulse trains of up to 1 MHz, but with very low energy (3 μJ for a 1 μs duration pulse).

While LEDs can be pulsed for nanoseconds, their low power density means that they are only rarely used for PIV (Chételat and Kim, 2002), more often finding application in flow visualisation (Stüer, et al., 1999) or pulsed planar background illumination (Estevadeordal, 2005). Xenon flash-lamps, on the other hand, are capable of emitting hundreds of Joules per flash, and have been used successfully for low cost PIV on a number of occasions (Coupland, 1990; De Ponte, et al., 2001). Their use is only limited by the difficult of forming an efficient, high-quality, collimated light sheet, and their relatively long pulse duration (anywhere between 1μs and 1ms), which limits their suitability for very high speed flows.

2.3.2. Lasers

Not surprisingly, lasers are the most commonly used PIV light source, due to their high power, potentially very short pulse durations, and collimated monochromatic output. Table 2.3 lists several laser types commonly used in PIV studies, alongside specifications for *typical* high-end commercial systems available at the time of writing.

	Lasing medium	**Wavelength (nm)**	**Power**	**Pulse duration**	**Repetition rate**
Diode	Semiconductor e.g. AlGaInP	400 - 1000	20 mJ	Arbitrary	n/a
Solid State	Nd:YAG	1064 (→ 532)	300 mJ	5 ns	50 Hz
	Nd:YLF	1053 (→ 527)	20 mJ	5 ns	20 kHz
	Ruby	694	10 J	20 ns	1 Hz
Gas	Argon Ion	457 / 488 / 514	5 W	Continuous	n/a
	Copper Vapour	511 / 578	30 mJ	5 - 185 ns	50 kHz

Table 2.3 – Common PIV lasers with typical characteristics.

All the lasers listed above share a common operating principle, namely the stimulation of light emission from a lasing medium, using some form of external energy pump. Light will be emitted for as long as the amplifying medium is pumped*, which for the 3 types of laser shown above, is achieved by means of electric current, flash-lamp illumination, or electrical discharge. As a result, semiconductor lasers may be directly modulated at very high speed, whereas a simple flash-lamp pumped Nd:YAG might lase for around 300 μs (the typical flash-lamp pulse duration).

* The copper vapour laser (CVL) is an exception, as its emission is 'self-quenching'. A typical CVL's pulse length and repetition rate is consequently determined by the cavity, and not by modulation of the pump. CVL PIV experiments therefore require a laser-centric approach to camera triggering.

2.3.2.1. Q-Switching

In order to achieve the short pulse lengths listed in Table 2.3 (and necessary for high speed PIV measurements) solid state lasers incorporate Q-switching* devices in their laser cavities:

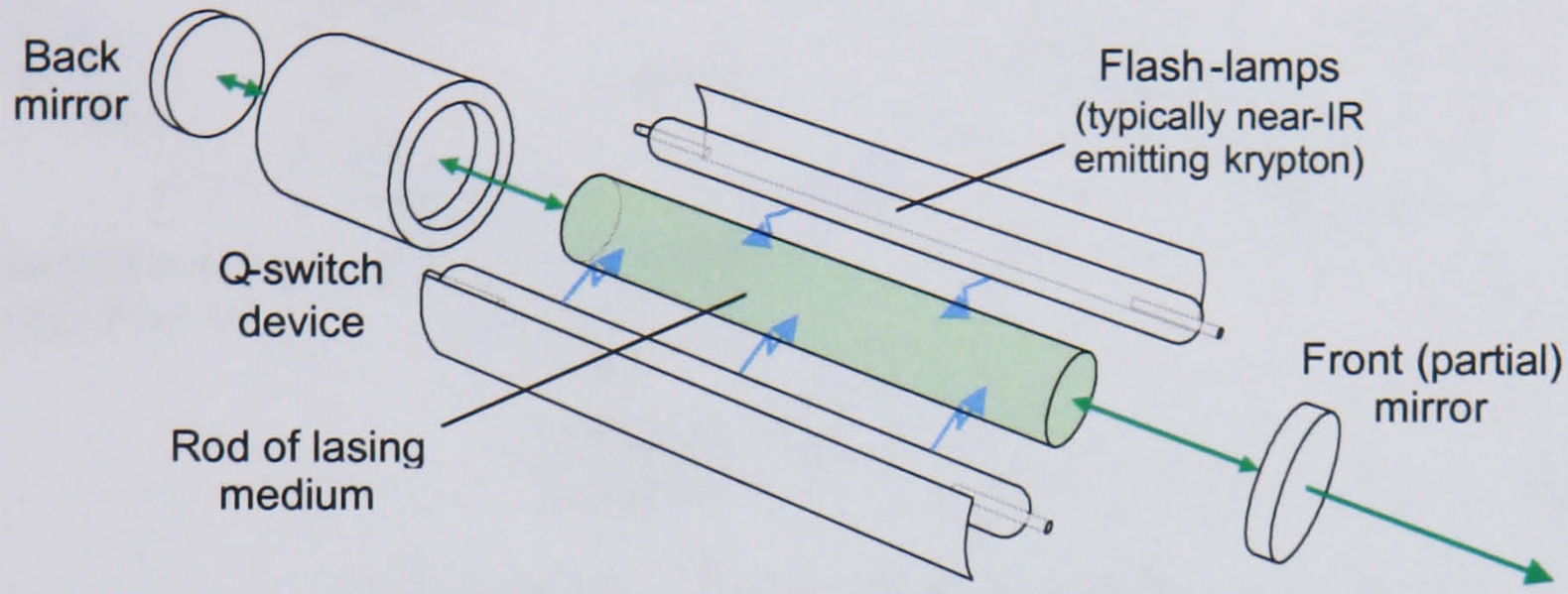

Figure 2.24 – Q-switched flash-lamp pumped solid state laser cavity.

The Q-switch serves to prevent lasing whilst the laser medium is being pumped with energy. This is achieved by placing an adjustable attenuator between the laser rod and back mirror, thereby preventing any optical feedback within the cavity, and the associated stimulated emission of light. At the point when the medium contains its maximum possible amount of energy, the attenuation is removed, resulting in a fast, bright discharge.

While a Q-switch could comprise a simple electro-mechanical shutter, or even completely passive components, Pockels cells are almost invariably used in PIV lasers due to their high switching speed. Pockels cell are constructed using any crystal (e.g. KD*P (KD_2PO_4)) that exhibits the Pockels effect, whereby the material's level of birefringence is proportional to the electric field induced across it. As a result of this

* The Q refers to the cavity 'quality factor'. The Q-factor is large when intra-mirror losses are low.

phenomenon, it is possible to arbitrarily rotate an incident light beam's axis of (linear) polarisation at will, and it is this ability that is exploited in a Q-switched laser, as demonstrated below:

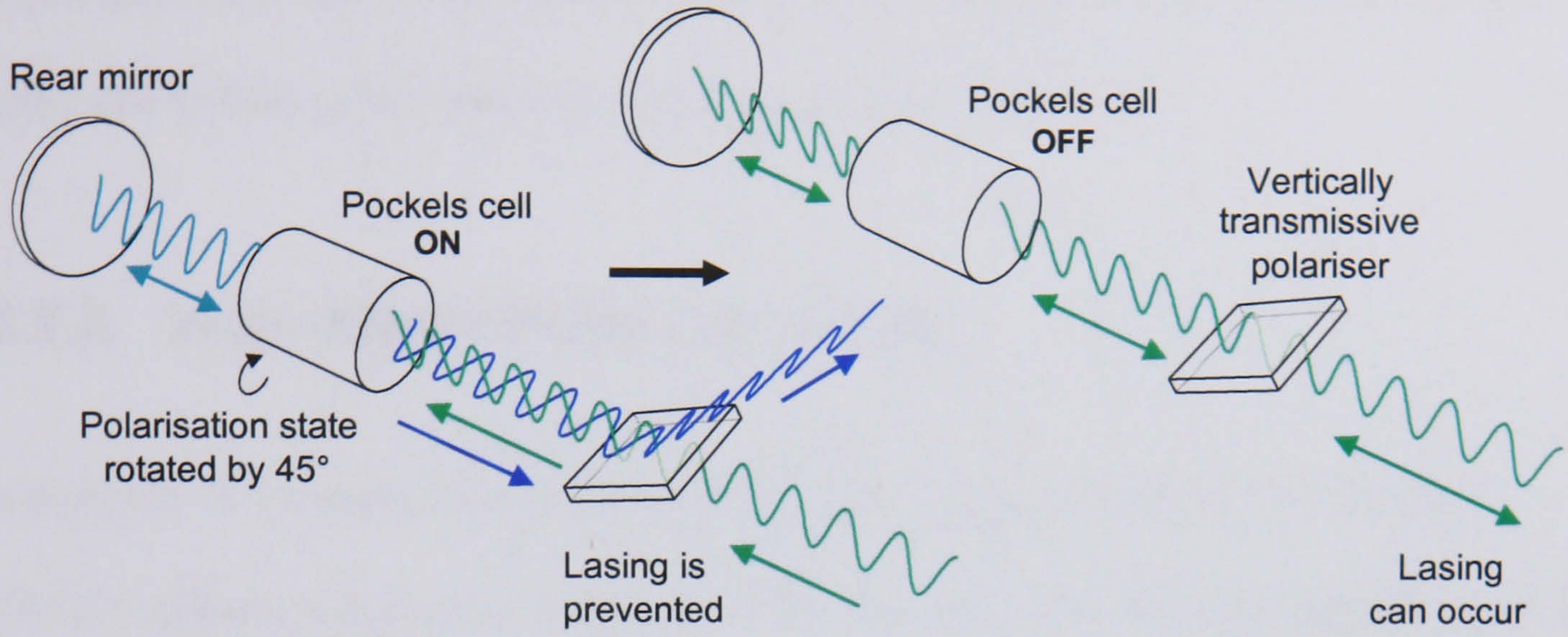

Figure 2.25 – Pockels cell Q-switching.

The polariser used in conjunction with a Pockels cell often works by taking advantage of the phenomenon of Brewster's angle. Using Snell's law for the refraction of light between two media, it can be shown that at an angle of incidence of Brewster's angle θ_B, no light polarised perpendicular to the plane of incidence will be reflected from the interface:

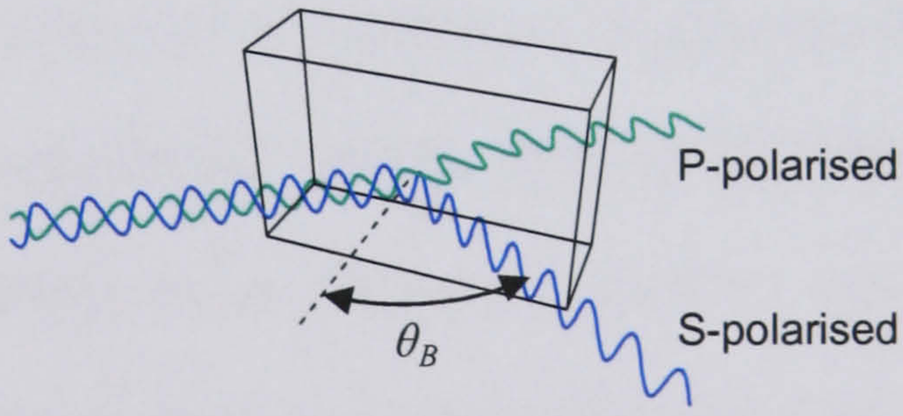

Figure 2.26 – Brewster's angle.

Brewster's angle can be calculated from the ratio of the materials' refractive indices, according to equation (2.30) below. For glass in air; $n_m = 1.52$, $n_a = 1.00$, and $\theta_B \approx 57°$. It should be noted however that refractive index values are wavelength dependent, but for a monochromatic laser this is of course unimportant.

$$\theta_B = \tan^{-1}\left(\frac{n_m}{n_a}\right) \tag{2.30}$$

The Q-switching arrangement depicted in Figure 2.25 may be simplified, incidentally, by cutting and polishing the Pockels cell crystal at the appropriate Brewster's angle, thereby incorporating the polariser into a single optical element.

2.3.2.2. High-Speed Pulse Generation

The majority of commercially available PIV laser systems comprise two separate Nd:YAG cavities, mounted in the same enclosure along with optics to spatially combine the beams, and a frequency-doubling crystal to convert the output from 1064 to 532 nm. Pulse pairs, with an arbitrary time separation, can be produced at up to kHz rates, providing the drive electronics are capable of providing sufficient power to the flash-lamps.

The copper vapour laser (CVL) offers significantly higher pulse powers and repetition rates however, and it has been used in a number of high-speed PIV studies: turbulent flame fronts at 10kHz (Lecordier and Trinite, 1999), and *Re* 3900 wind tunnel flows at 20kHz (Williams, et al., 2003), for example. Even the CVL is unsuitable for ultra-fast pulsing though, in part because of its non-triggerable nature. In such situations, the pulse 'slicing' technique may be used.

As shown in Figure 2.25, a Pockels cell is usually used to rotated the polarisation angle of incoming light by 45°, such that the twice-rotated beam is incapable of passing through the adjoining polariser. At the point when the cavity should lase, this angle is

reduced to 0°. If however, the angle is reduced in small steps, by applying a decreasing voltage across the cell, then a proportion of the emitted light will be transmitted through the polariser, and a limited amount of lasing will occur. Through careful adjustment of the voltages sent to the Pockels cell, arbitrary pulse trains may be generated, but of a maximum length equal to the pump's impulse duration. Figure 2.27 demonstrates both a well adjusted pulse train, as well as one in which the pulse amplitude remains representative of the amount of energy stored in the laser medium at the time.

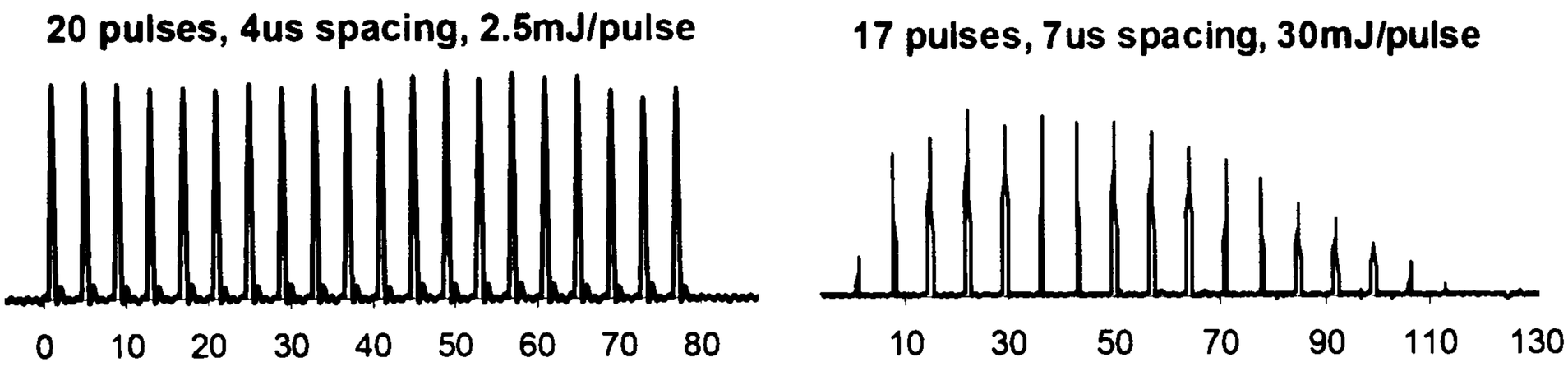

Figure 2.27 – 'Sliced' Nd:YAG laser pulses, from (Lempert, et al., 2002).

Variations on the Pockels cell slicing method have been used to visualise flow structures in an asymmetric Mach 2.0 jet at 10 kHz (Lempert, et al., 2002; Thurow, et al., 2000), as well as a pulse-excited Mach 1.3 jet at 500 kHz (Wernet and Opalski, 2004).

2.3.3. Light Sheet Generation

The production of a light plane from a coherent laser beam may be achieved in one of three ways:

- Using an arrangement of cylindrical lenses.
- By scanning a (switched) continuous laser beam with a rotating mirror.
- By means of a prismatic light sheet forming optic.

Cylindrical lenses, which transform light in one axis only, are the simplest and most commonly used method of light sheet production. The fact that most lasers have a beam diameter greater than the 1 – 2 mm sheet thickness typically required for 2D PIV however necessitates additional optics to focus the light sheet to a thin "waist" within the camera's field of view. Two such arrangements are shown below, with others described by (Diemunsch and Prenel, 1987; Prenel, et al., 1989).

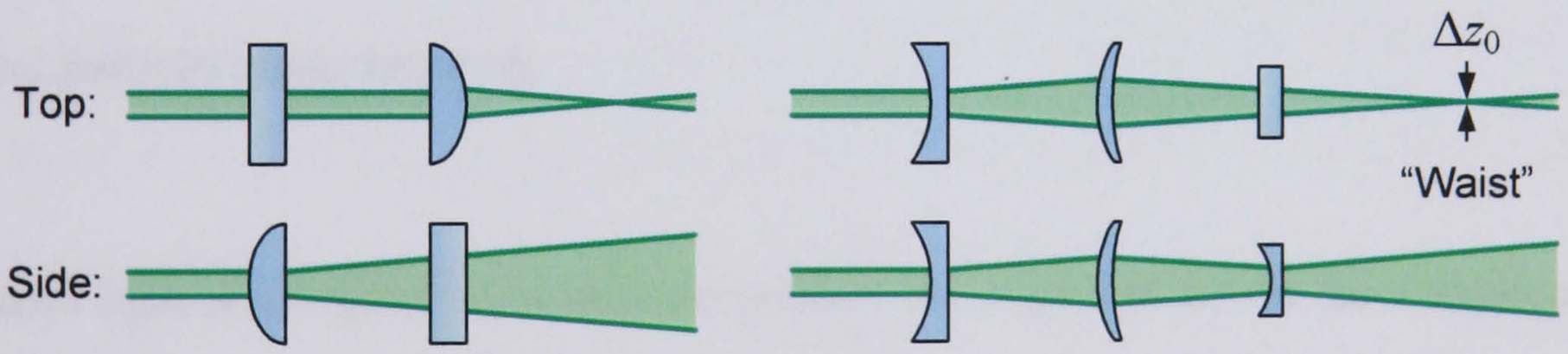

Figure 2.28 – Cylindrical lens sheet forming optics, from (Stanislas and Monnier, 1997) and (LaVision FlowMaster system manual).

Rotating multi-faceted mirrors, or scanning galvanometers (Prenel and Jeudy, 1998), are an alternative means of producing a light sheet. (Cosgrove, et al., 2001) used an octagonal mirror, in combination with a parabolic mirror, to illuminate a 10 cm^2 measurement area with parallel sweeps of laser light every 0.5 – 2.5 ms. Such scanning systems either illuminate each of two exposures with a single sweep (Jakobsen, et al.,

1997) or – more commonly – several sweeps of the beam, where the sweeps either follow each other so quickly as to reveal seeding particles in a single "frozen" position, or with slower sweeps that allow particles time to move between illuminations. This inter-sweep separation (which should be such that the particles do not simply appear blurred) is a function of the flow speed and mirror rotation rate, and can yield measurements that are considered either instantaneous or time-averaged.

In both cases, the timing accuracy of the PIV system is dependent on the responsiveness of the external beam switching mechanism, be it a solenoid or acousto-optic deflector. For this reason, scanned light sheets are rarely used for high speed flows, which require two very short pulses a short, and accurately defined, time apart. For slower speed flows however, scanned light sheets can produce significantly brighter particle exposures than would be otherwise be possible with a chopped CW laser (Gray, et al., 1991). This is because the laser remains on for a much longer time, illuminating each area of the measurement volume in turn with a very high light flux, without causing the otherwise ensuing particle image blurring.

Prismatic light sheet optics have become popular amongst low power laser applications (e.g. 3D machine vision), due to their ability to generate spatially uniform light sheets (Huang, et al., 2005). A cylindrical lens, conversely, produces a Gaussian intensity distribution, with the centre of the sheet more intense than the edges. Prismatic style light sheet generators are however inefficient and rarely available with high power laser coatings, and as a result rarely used for PIV studies.

2.4. Camera Sensors

2.4.1. Introduction

At the inception of PIV, image capture was invariably performed using 35mm or larger format film cameras, the pictures from which were correlated purely in the optical domain (Farrell, 1993; Keane and Adrian, 1992; Mao, et al., 1993). Film based cameras have remained popular due to their low cost and high resolution (Lawson and Wu, 1999; Rosner, 1992), as well as the availability of high resolution film scanners that allow image analysis to be performed digitally. The unavoidable requirement for wet chemical film processing has however motivated a comprehensive shift towards the use of digital cameras for PIV image capture (Lai, et al., 1998). Not only is their resolution now comparable, if not greater, to that of film, but they also offer the possibility of online alignment and real-time processing.

Section 2.4 therefore explains the *modus operandi* of CCD and CMOS sensors only, and discusses some of the technological options available to the digital camera designer. Subsequent subsections demonstrate how different sensor designs may be applied to both two-frame cross-correlation and high-speed time-series PIV image capture.

2.4.2. Principle of Operation

Almost all digital camera sensors are based on either Complementary Metal Oxide Semiconductor or Charge Coupled Device technology. CMOS was invented in 1963 at Fairchild Semiconductor as a means of producing low power integrated circuits, but the ability to create photosensitive chips was soon exploited. The CCD was invented in 1969 at AT&T Bell Labs, and its obvious superiority halted CMOS image sensor research immediately, which only restarted after work in the early 1990's at NASA's Jet Propulsion Laboratory implemented the Active Pixel Sensor technology that some predict may eventually overshadow CCD's current high-end market stronghold.

Both sensors employ the photoelectric effect, whereby photons hitting a pixel release a number of electrons that is proportional to the illumination intensity. In order for an electron to be released however, the incoming photon must have an energy greater than that of the bandgap of the photo-detector material which, in the case of silicon, is 1.12 eV or 1100 nm. Upon being hit by sufficiently energetic light, electrons in the detector enter the conduction energy band, allowing them to move freely through the material and as such constitute an electric current. By introducing an electric field across the detector, it is possible to separate the electrons and electron-holes in the material, thereby isolating the generated negative charge for subsequent measurement.

CCD and CMOS sensors differ in the way in which this charge is read. A CCD chip typically has no more than one or two sets of charge measuring electronics, with the packets of electrons being transferred from pixel to pixel before leaving the chip via a single charge to voltage converter. Conversely, each pixel in a CMOS sensor contains

its own set of electronics to handle charge to voltage conversion, digitisation, and even noise cancellation.

2.4.3. CCD Sensors

CCD sensors most often comprise a rectangular array of pixels of around 6 – 20 μm square. One notable exception is FujiFilm's Super-CCD™ family (shown below) which uses both low and high light sensitive pixels in a hexagonal pattern to maximise the sensor's signal to noise ratio.

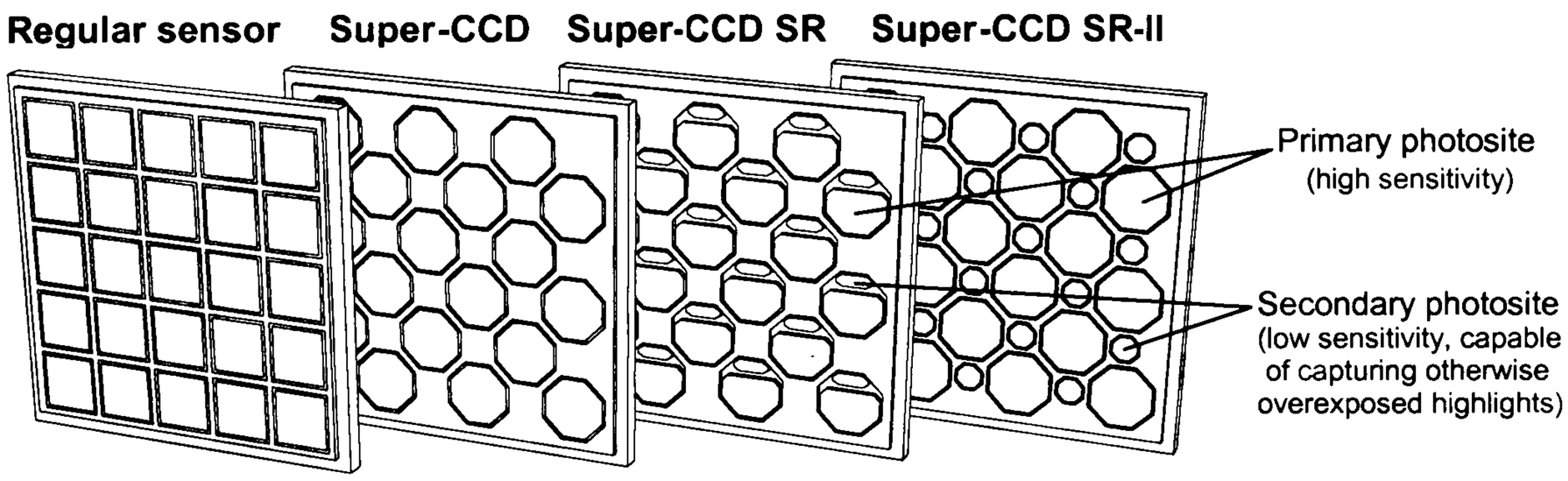

Figure 2.29 – The FujiFilm Super-CCD family, along side a regular sensor.

However the pixels are arranged, each one can be thought of as a well capable of collecting and storing a finite amount of charge, defined as the 'well capacity'; typically around 50,000 electrons. While image sensors with complex pixel arrangements comprise spatially separate areas of photosensitive silicon, the simplest of CCD sensors – as shown in Figure 2.30a on page 71 – define pixel location primarily by an electric field within the photo-detector material.

All illustrations in this section depict the accepted 'buried-channel' arrangement of silicon, in which the diffusion of electrons from *n* to *p*-type doped semiconductor generates an electric field through the depth of the sensor. The maxima of this field, i.e.

the electron well, lies just under the surface of the sensor, amplified in any position under a positively charged surface electrode.

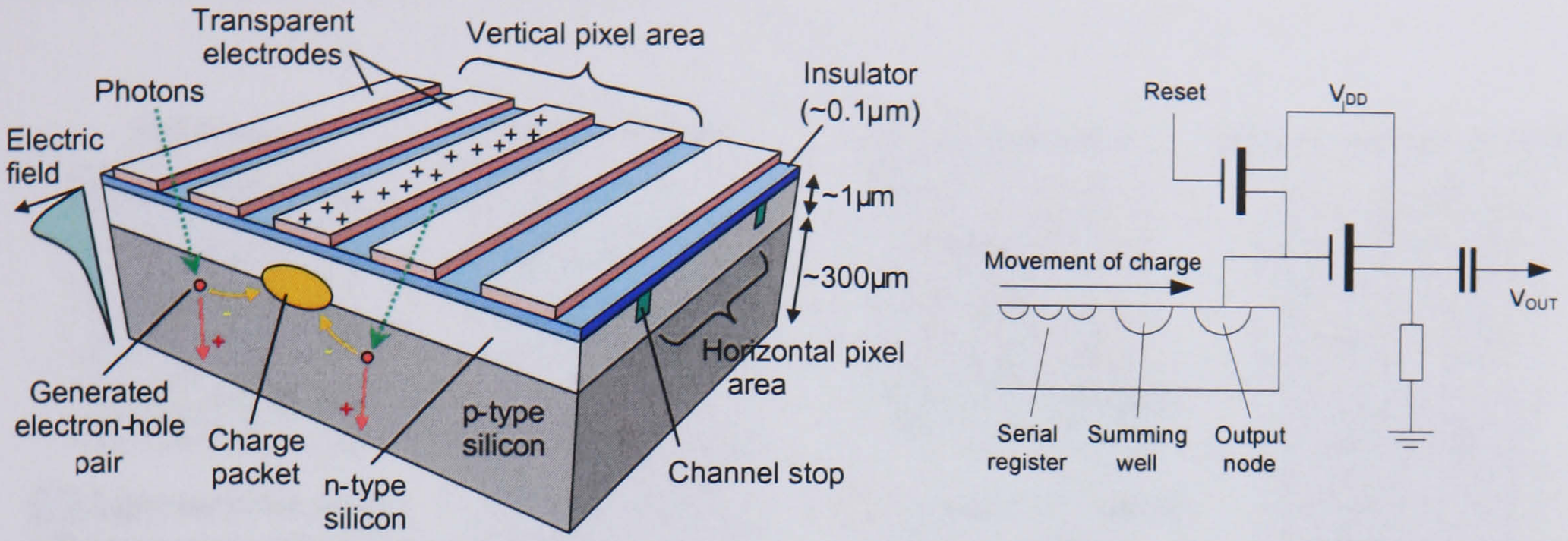

Figure 2.30 a) Simple CCD structure; b) CCD pixel readout electronics.

As photons generate electron-hole pairs within the silicon, the electrons migrate towards the most positively charged centre of each pixel, horizontal segregation being achieved using strips of p-type doping, called channel stops. In the common 3-phase electrode arrangement shown below, only the centre of each pixel's 3 electrodes is held high during integration, the others being used for readout, in which sequential charging of adjacent electrodes 'drags' the charge towards the readout electronics. Unlike the earlier surface channel sensors, buried-channel designs have a charge transfer efficiency (CTE) of around 99.999%, meaning that only around 1 electron in 100,000 gets left behind during the pixel-to-pixel readout process.

The readout electronics can be as simple as those shown in Figure 2.30b, as their primary purpose is merely to convert charge into voltage, which is subsequently digitised. In reality however, an amplifier is often included, the gain of which is measured in electrons per analog-to-digital unit (ADU), otherwise known as 'counts'.

While all CCD sensors use the same method of charge transfer and measurement, the route taken from pixel to digitiser varies according to the readout mode. The four main readout designs are shown in Figure 2.31.

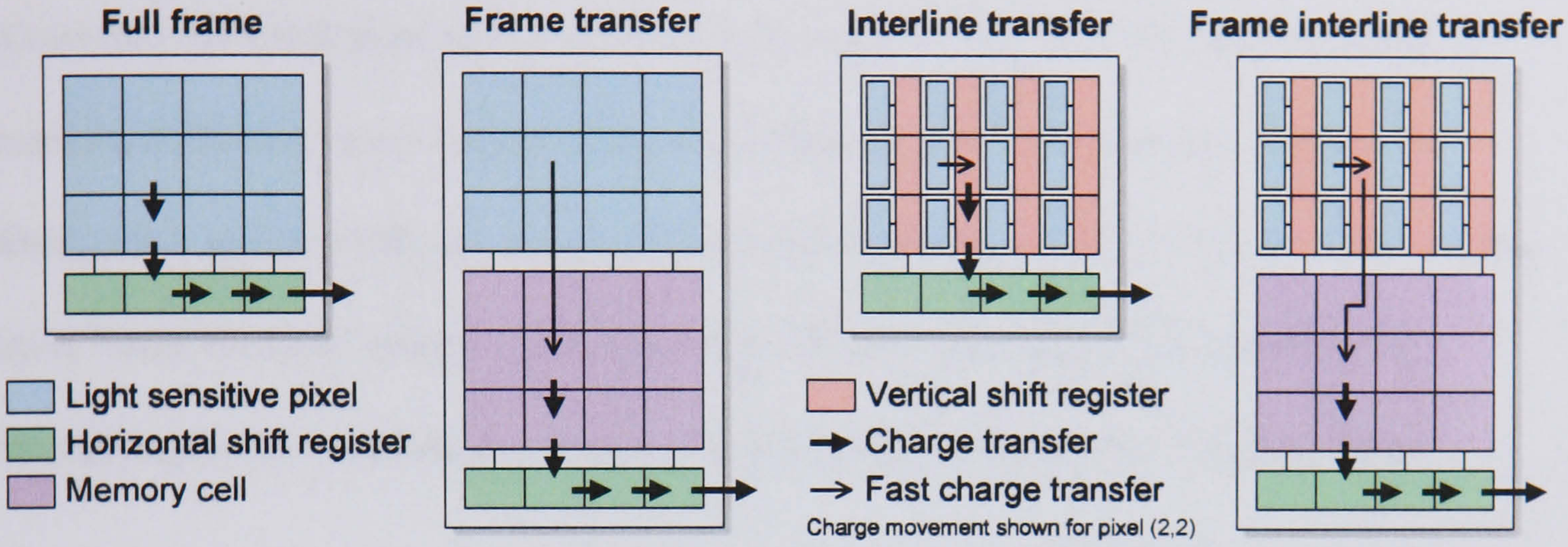

Figure 2.31 – Types of CCD sensor readout, adapted from (Lai, et al., 1998).

2.4.3.1. Full Frame CCD Sensors

Full frame (FF) sensors are the earliest and simplest of CCD designs, though still in use by today studio photographers, due to their high fill factor and resulting image quality. As with all of CCD designs, the bottom of every column of pixels feeds into a horizontal shift register, the end of which is attached to the readout electronics. After exposure, charge within each pixel is moved down one place, for all columns, in parallel. The horizontal shift register transfers each row of charge to the electronics in serial, at a rate determined by the 'pixel clock' – typically 30 MHz or so.

Due to the simplicity of the FF sensor design, the pixels collect charge constantly, even during readout. This means that without some form of external exposure control (be it pulsed illumination or a mechanical shutter), the resulting images will suffer vertical smearing.

2.4.3.2. Frame Transfer CCD Sensors

Frame transfer (FT) sensors are twice the size (and therefore expense) of FF sensors, due to the inclusion of a light-shielded memory array, in between the light-sensitive pixels and the horizontal shift register. Charge can be moved from the pixels into the memory cells very quickly (typically in less than 1 μs), meaning that a constantly illuminated sensor produces a significantly less smeared image. A design variant – the 'split frame transfer' sensor – decreases the transfer time further by dividing the memory array in two; one above and one below the imaging area (Taylor, 1998).

2.4.3.3. Interline Transfer CCD Sensors

Interline transfer (IT) sensors were invented in 1973 and are the most common CCD design in use today. Like FF sensors, each light-sensitive pixel has an associated light-shielded memory cell, but it is directly next to the pixel, thereby allowing very fast transfers without the charge having to travel through a whole column of adjacent pixels. Furthermore, the charge can be readout through the resulting vertical shift register while the next exposure is being integrated.

A disadvantage of the IT design is the reduction in each light sensitive pixel's physical area, which is often described in terms of the sensor's 'fill factor' (typically of the order 50%). While the amount of light incident on the photosensitive part of each pixel may be maintained through the use of a microlens array, mounted on top of the sensor, the smaller pixel size invariably results in a reduced well capacity which in turn impacts the sensor's dynamic range.

2.4.3.4. Frame Interline Transfer CCD Sensors

Frame interline transfer (FIT) sensors are often used in professional broadcast cameras, and were introduced to address one potential problem with IT sensors: when subjected to extreme glare, both light and charge can escape into the vertical shift register, resulting in a bright vertical "streak" in the image. FIT sensors combine the best of FT and IT sensors by both minimising the time charge is held in the pixel, and minimising the time charge is held *next* to the pixel. The result is a sensor with both low noise and high dynamic range (Hynecek, 1988; Itakura, et al., 1993).

2.4.3.5. CCD Sensor Sensitivity

While its spectral range and sensitivity makes silicon ideal for the detection of visible wavelengths, the material's high refractive index means that around ⅓ of the photons hitting it are reflected. The opacity of the electrodes deposited onto the sensor surface also increases as light moves towards the blue, imposing a lower detection limit of around 400nm. In an attempt to improve the photon detection sensitivity, back-illuminated sensors have been developed which, together with the original front-illuminated sensor, form the two basic CCD architectures.

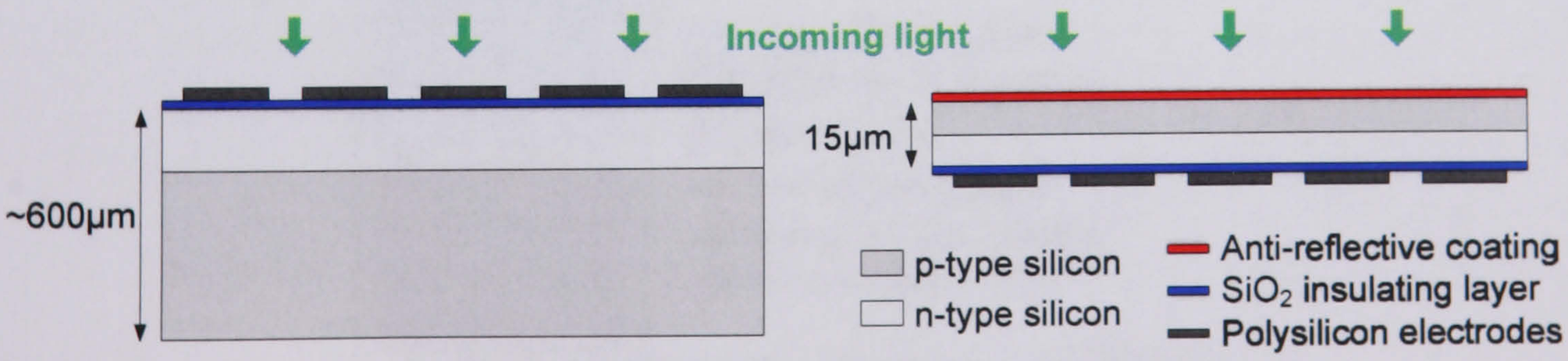

Figure 2.32 – Front (left) and back (right) illuminated CCD sensors.

In order for a back-illuminated sensor to operate successfully, the silicon must be thin enough to allow electrons to travel freely from the illuminated surface to the readout electrodes. The necessary chemical etching to ~15 μm thickness results however in an extremely delicate wafer, and the sensors are extremely expensive as a result. It is also nigh-on impossible to manufacture an interline transfer back-illuminated sensor.

The smooth rear side of a back-illuminated sensor can however be coated with a transparent antireflective coating (typically hafnium dioxide), which can reduce reflections (of a chosen wavelength) to less than 1%. The lack of electrodes in front of the sensor also results in a vastly improved blue response, though Kodak went some way to improving this problem in front-illuminated sensors with the release of their Blue Plus chip in 2000, which uses a truly transparent electrode material.

Electronic-multiplication CCDs use a completely different method to improve the sensitivity of front-illuminated sensors. By using higher-than-normal voltages to 'drag' the charge packets along an extended horizontal shift register, it is possible to multiply (by up 1000 times) the number of electrons at each transition, by means of 'impact ionisation' (Tubbs, 2003).

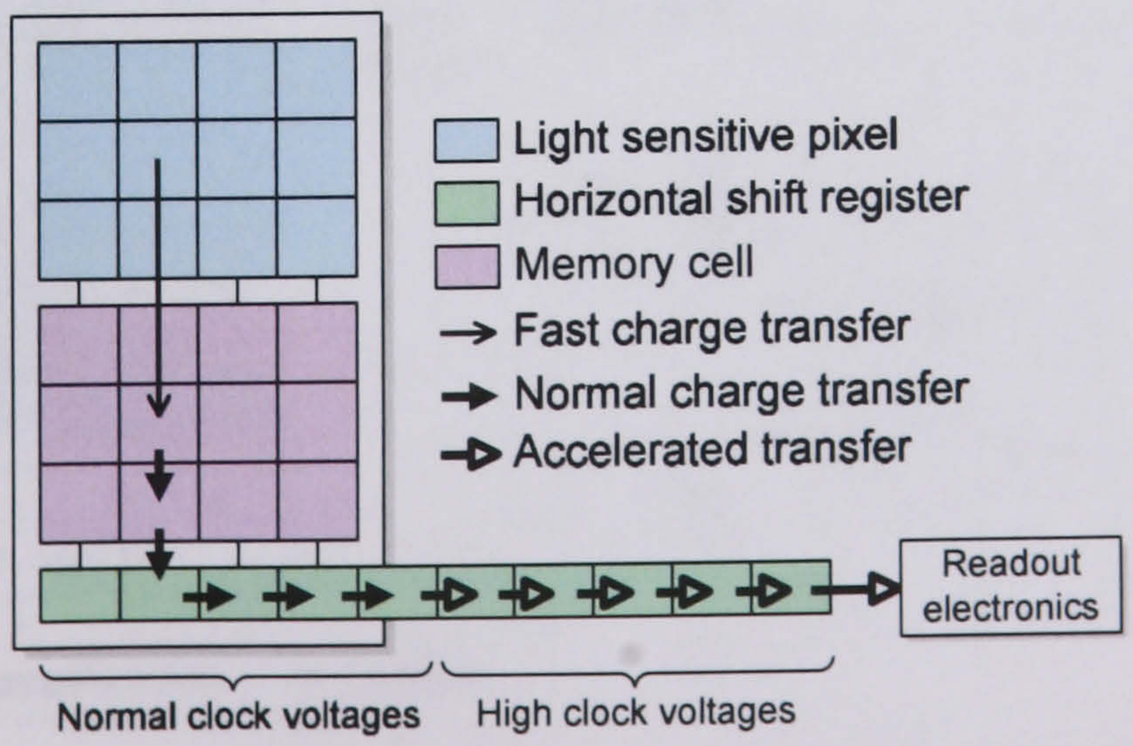

Figure 2.33 – An EM-CCD frame-transfer sensor.

2.4.4. CMOS Sensors

While historically, CMOS image sensors have been unable to match the quality and sensitivity of their CCD counterparts, new 'active pixel' designs are enabling this to change. CMOS sensors offer a number of advantages over CCD, namely lower power consumption; lower cost (they can be made in the same foundry as any other IC); greater on chip functionality (thereby allowing miniaturisation of the encompassing camera); random pixel access; high-speed read-out; and a total lack of the blooming and smearing artifacts that can occur with CCDs.

Unlike the capacitative electron well of a CCD sensor, each pixel of a CMOS sensor comprises a silicon photodiode and associated readout electronics. While the earliest 'passive' CMOS designs contained just one transistor per pixel, which switched the diode between charge amplifiers at the bottom of every column, modern 'active' pixel sensors (APS) include charge to voltage conversion electronics within each pixel, the results of which may be read in an arbitrary order, using the row and column selection arrangement illustrated below:

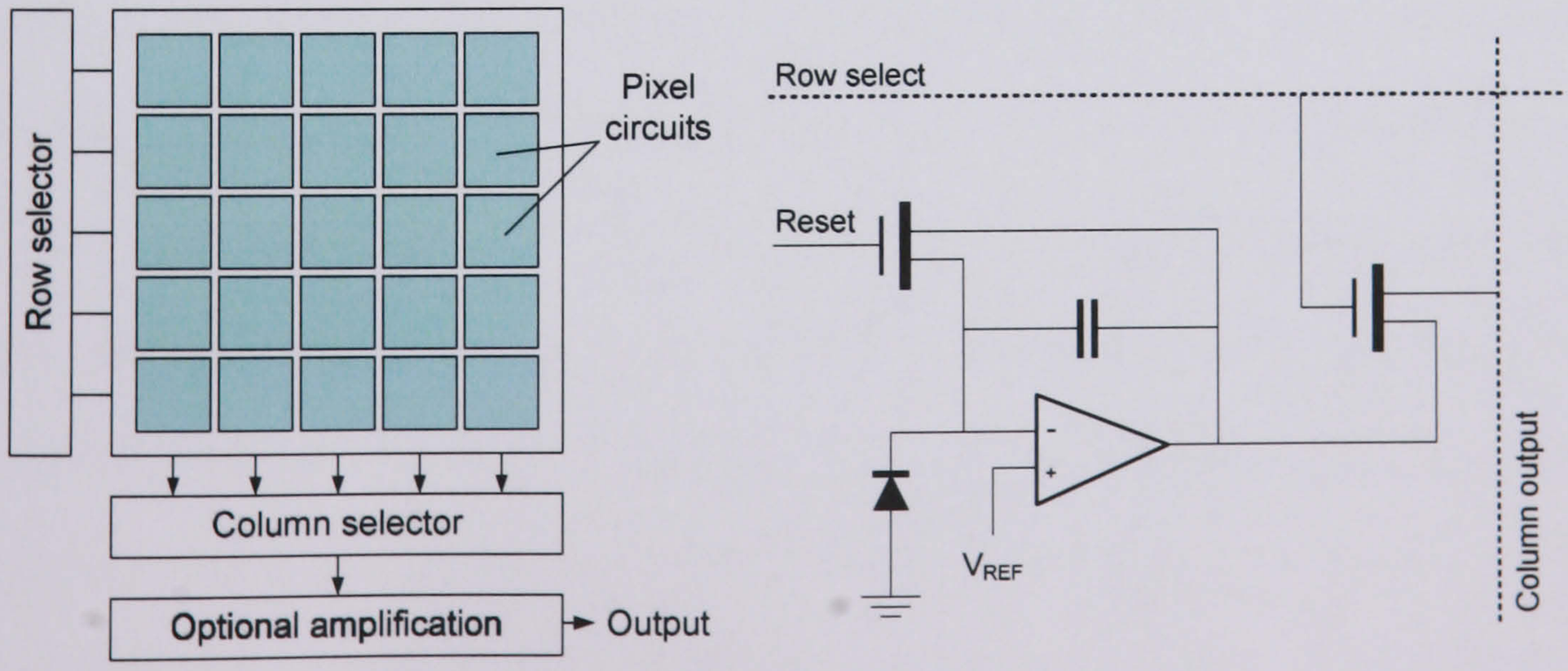

Figure 2.34a) CMOS sensor architecture; b) Typical APS (CTIA) readout electronics, from (Bigas, et al., 2006).

Due to the amount of circuitry inside each pixel, the fill factor of a typical CMOS sensor is only 30% or so. While microlenses can minimise the effect this has on the device's sensitivity, manufacturers consistently attempt to increase the fill factor in order that the sensor's dynamic range may be improved. While modern APS pixels often contain 4 transistors, for example, Micron Inc. have reduced this count to 2.5, by means of a unique readout circuit that is shared between two pixels.

Further problems to have dogged CMOS sensors, such as high fixed pattern noise (in which manufacturing irregularities across the sensor's surface cause there to be differences between each pixel's gain and bias) are now routinely countered using techniques such as 'double differencing sampling', and logarithmic readout electronics have allowed CMOS' dynamic range to equal that of CCD technology (Bigas, et al., 2006). As will be shown in Section 2.4.7, these cumulative improvements to CMOS sensors mean that they are now increasingly finding application amongst PIV studies.

2.4.5. Colour Sensing

While the vast majority of flow visualisation and PIV studies use monochrome cameras, the multi-coloured multi-dimensional measurement techniques discussed in Section 2.1.2 prove an exception. Such polychromatic experiments typically use a number of monochrome cameras, each fitted with its own bandpass filter (Brücker, 1996a), but commercial 'all-in-one' colour cameras have also been successfully deployed (Gogineni, et al., 1998; Jaw, et al., 2003).

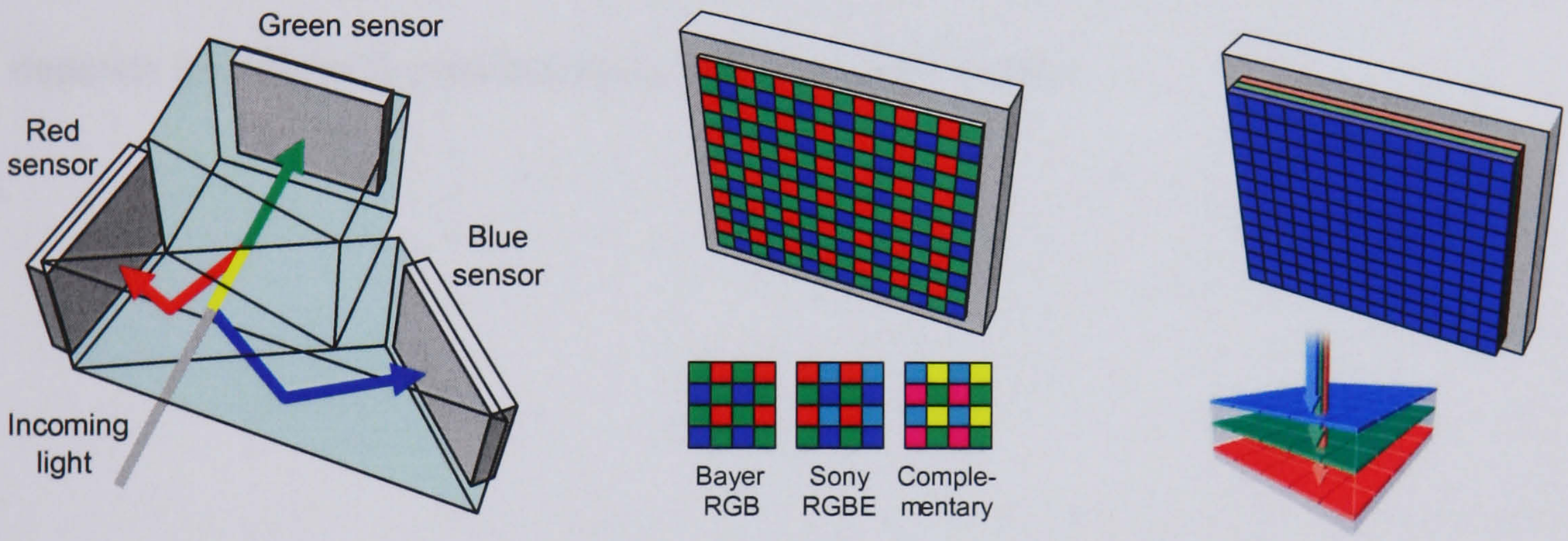

Figure 2.35a) Trichroic prism separation; b) Mosaic filtering; c) Vertically integrated.

Professional '3CCD' colour cameras use three sensors and a trichroic prism arrangement to split incoming light into its 3 component colours, as shown above left. In order to reduce expense however, most cameras instead use just one sensor, covered in a mosaic of filters, thereby providing colour detection at the expense of spatial resolution. Bryce Bayer invented the most commonly used filter mosaic arrangement (shown above centre), in which twice as many pixels are used to detect green light as red or blue, in order to better match the receptivity of the human retina. In 2004, Sony introduced an improved set of filter colours (comprising an additional 'emerald' pixel), while complementary filters are often used in cheap cameras as they let around 30% more light through (albeit at the expense of colour reproduction).

The third type of colour camera considered uses a 'vertically integrated' sensor, the best known example of which is the Foveon™ X3, released in 2003. Like a 3CCD system, each pixel of the recorded image contains RGB information from 3 discrete photosites, but they are located on top of each other, on the same chip. Such designs take advantage of the wavelength dependence of silicon's absorption coefficient, meaning red light penetrates further than blue. The Foveon sensor creates 3 electron wells by the fabricating 2 n- and 2 p-type layers per pixel (cf. Figure 2.30a), though alternative implementations have been proposed (Steibig, et al., 2006). In all cases, photo-electrically generated electron-hole pairs migrate into one of the 3 wells; which one depends on the depth penetrating by the associated photon.

2.4.6. Cameras for Cross-Correlation

As discussed in Section 2.1.1.1, the cross-correlation of dual-frame PIV images offers a number of advantages over the auto-correlation of a single image, but it does require two images to be recorded within the space of Δt. This can be achieved using 'frame-straddling', in which two laser pulses are timed to occur at the start and end of adjacent camera exposures. In this way, (Lecordier, et al., 1994) demonstrated the recording of pulses with separations down to 10μs, using a particular model of Sony video camera.

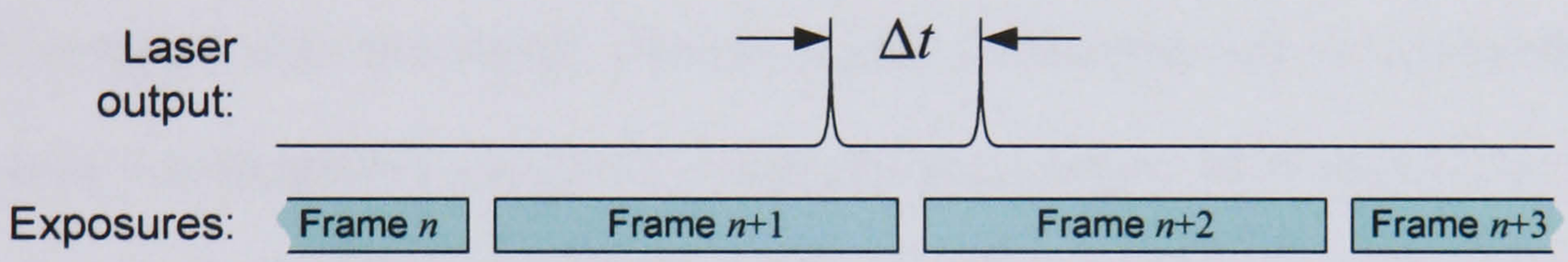

Figure 2.36 – The 'frame-straddling' technique.

(Gogineni, et al., 1998) and (Jaw, et al., 2003) used differently coloured laser pulses and a colour camera to achieve arbitrarily short pulse separations; the consecutive exposures being isolated by splitting each individual image into its red and green components. (Riou, et al., 2000) instead placed two image-intensifier shuttered cameras in a face-to-face orientation, thereby allowing images to be acquired from each less than 50 ns apart.

The vast majority of PIV images are however now acquired using specially designed "double-shutter" cameras, based on the interline transfer CCD sensor design described on page 73. Upon receiving a trigger, such cameras start to expose the first of two frames (commonly referred to as 'frame A') for a user-defined period, before transferring the collected charge into the vertical shift register, from which it is gradually read out. As soon as the charge is moved however, the photosensitive pixel areas can start to be exposed once more, thereby allowing the second 'frame B' to be

exposed as little as 200 ns after the first. As a result of this arrangement however, frame B's exposure will be of the same duration as frame A's readout, which is equal to the inverse of the camera's readout rate. For this reason, such cameras must either be used in darkened surrounding, or with a bandpass filter fitted to the front, to prevent the second exposure from becoming saturated.

2.4.7. Cameras for High-Speed Time-Series Acquisition

While interline-transfer sensors, or multi-coloured lasers can be used to capture 2 (or even 3) images a short time apart, they are unable to acquire a sequence of images at high speed. As discussed on page 19, and in the next chapter, high-speed time-series video has proven invaluable in studying the evolution of spasmodic flow phenomena, and the ideal camera system should be capable of recording at extremely high speed for an arbitrary length of time. Table 2.4 lists the high speed camera technologies available at the time of writing, along with typical characteristics. Examples of commercially available cameras, from each category, are illustrated on page 350.

Technology	**Frame rate**	**Resolution**	**Frame count**	**…dependent on**
Sub-windowable CMOS	2 kHz 250 kHz	1 Mpx <1 kpx	3,000 2,000,000	The amount of image storage RAM.
In-situ image storage (ISIS)	1 MHz	0.1 Mpx	100	Intrinsic sensor design.
Rotating mirror	25 MHz	1 Mpx	100	Number of sensors.
Multiple gated sensors	500 MHz	1 Mpx	8	Number of sensors.

Table 2.4 – High-speed camera technologies and typical performance characteristics.

2.4.7.1. Sub-Windowable CMOS Sensors

The readout rate of a CCD or CMOS camera is directly proportional to the speed of the pixel clock used to drive the shift registers, or row and column selectors (c.f. Figure 2.31 and Figure 2.34). In the case of a CCD however, higher clock rates result in a shorter time available for each pixel's charge to voltage conversion, which in turn means higher noise. CCD sensors are therefore rarely clocked above 40 MHz, but their overall frame rate can be increased by means of multiple readout 'taps'. By using 2 or more horizontal shift registers in parallel, it becomes possible to run CCDs at 100's of Hz with only a limited reduction in image quality (Hoffberg, et al., 1997).

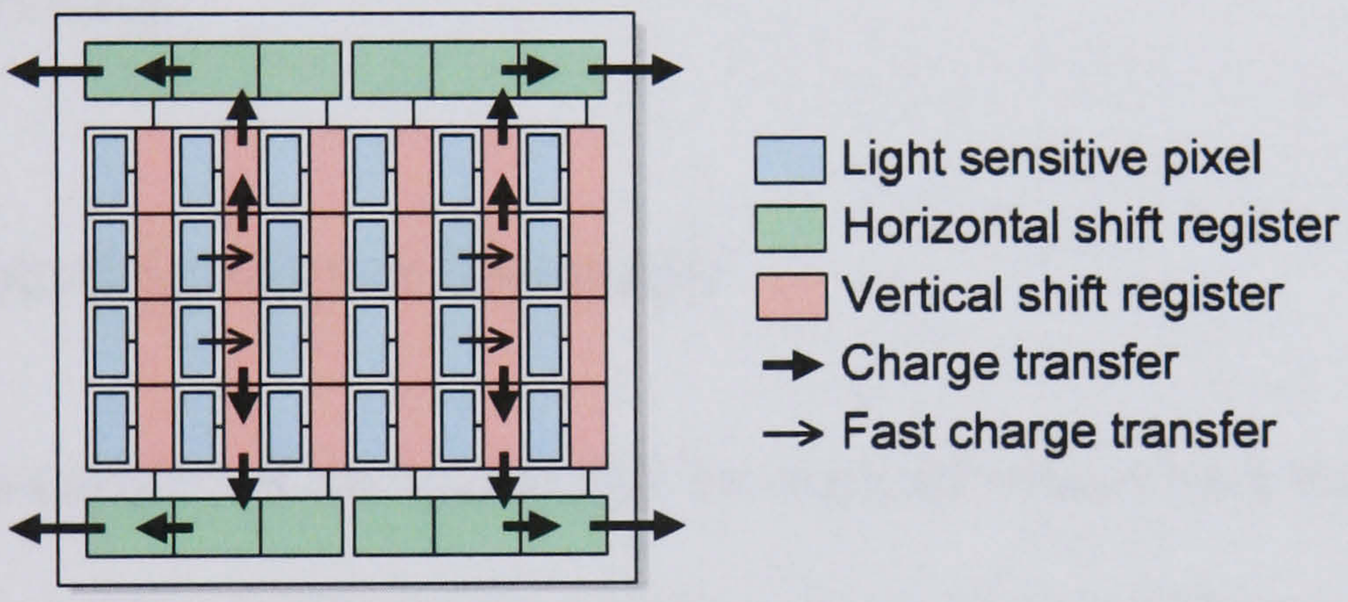

Figure 2.37 – CCD interline sensor with 4 separate readout taps.

Beyond a certain point however, it becomes impractical to produce high-resolution, high-speed CCD sensors. Because each pixel of an APS CMOS sensor produces a pre-amplified *voltage* though, the readout rate of a CMOS sensor may be approximately double that of a CCD, without any associated reduction in image quality. By combining such elevated clocking rates with as many as 2000 parallel readout taps (Krymski, et al., 2003), cameras with bandwidths of the order of Gpx/s may be produced (Fossum and Krymski, 2000; Hillebrand, et al., 2000). The potentially non-sequential manner of CMOS sensor readout also facilitates 'sub-windowing', in which only a user-defined

subset of the pixels is read out, with an associated increase in the frame rate (e.g. 96 × 8 pixels can be imaged at 154 kHz using the industry-leading Phantom v9.1 camera).

In the case of all high-speed cameras, the bandwidth of the video output is far higher than that which can be saved to disk, or even transmitted to a standard PC. This is of particular pertinence to CMOS cameras, as they would otherwise be capable of recording ad infinitum. Such cameras therefore incorporate solid-state FIFO memory, which can be written to at high speed, but simultaneously read out more slowly to the host computer. The number of frames that may be acquired then becomes a function of both the amount of sub-windowing (i.e. the image size), and the quantity of RAM installed in the camera.

2.4.7.2. Rotating Mirror Systems

Historically, the majority of time-series PIV measurements have been made using rotating drum or rotating mirror (or prism) film cameras (Lin and Rockwell, 1994; Williams, et al., 2003). While digital sensors cannot be attached to the inside of a spinning drum in the same way as a strip of film, rotating mirror cameras *can* be extended to the digital domain.

As can be seen in Figure 9.17 (page 350), rotating mirror systems scan a projected image across an array of digital sensors, using a mask to ensure that the image does not become blurred as it spins round. By evacuating the camera chamber and using a high-speed gas turbine to spin the mirror, such cameras are able to achieve frame rates as high as 25 MHz, but with only as many exposures as there are image sensors.

2.4.7.3. In-Situ Image Storage (ISIS) Sensors

ISIS sensors are capable of MHz framing rates, but without any moving components. They work in almost exactly the same way as the interline transfer CCD design (c.f. Figure 2.31, page 72) but using a subdivided vertical shift register, which provides each pixel with a number of memory cells into which charge can be transferred at high speed.

Most commercially available ISIS sensors are made using a standard CCD full frame sensor, covered by a separate metal mask. In this way, adjacent light-shielded pixels can act as the vertical shift register, and the standard readout mechanism can be used to transfer the charge. The Dalsa 64K1M sensor, for example, comprises a 960 × 960 pixel array covered by a mask that exposes just 1 in 16 pixels, resulting in a 240 × 240 sensor capable of capturing 17 frames at up to 1 MHz. While such designs often suffer as a result of their low fill factor ratios (around 3% for the 64K1M), they have been successfully deployed in PIV studies of jet shear layers (Lempert, et al., 2002) and large-scale turbulent structure evolution (Thurow, et al., 2000),

Dedicated ISIS sensor designs first appeared when (Kosonocky, et al., 1996) implemented a 2D serial-parallel-serial memory array next to each pixel, and a sensor based on this design was subsequently produced by Princeton Instruments (Lowrance, et al., 2004). While this device could frame at up to 5 MHz, its resolution was limited to 300 × 300 px. The ISIS concept has since been heavily developed by work at Kinki University, Japan (Etoh, et al., 2005), resulting in the production of the HyperVision HPV-1 camera, manufactured by Shimadzu Corp. An innovative slanted pixel

arrangement (shown in Figure 2.38 below) allows the HPV-1 to capture over 100 frames at 1 MHz.

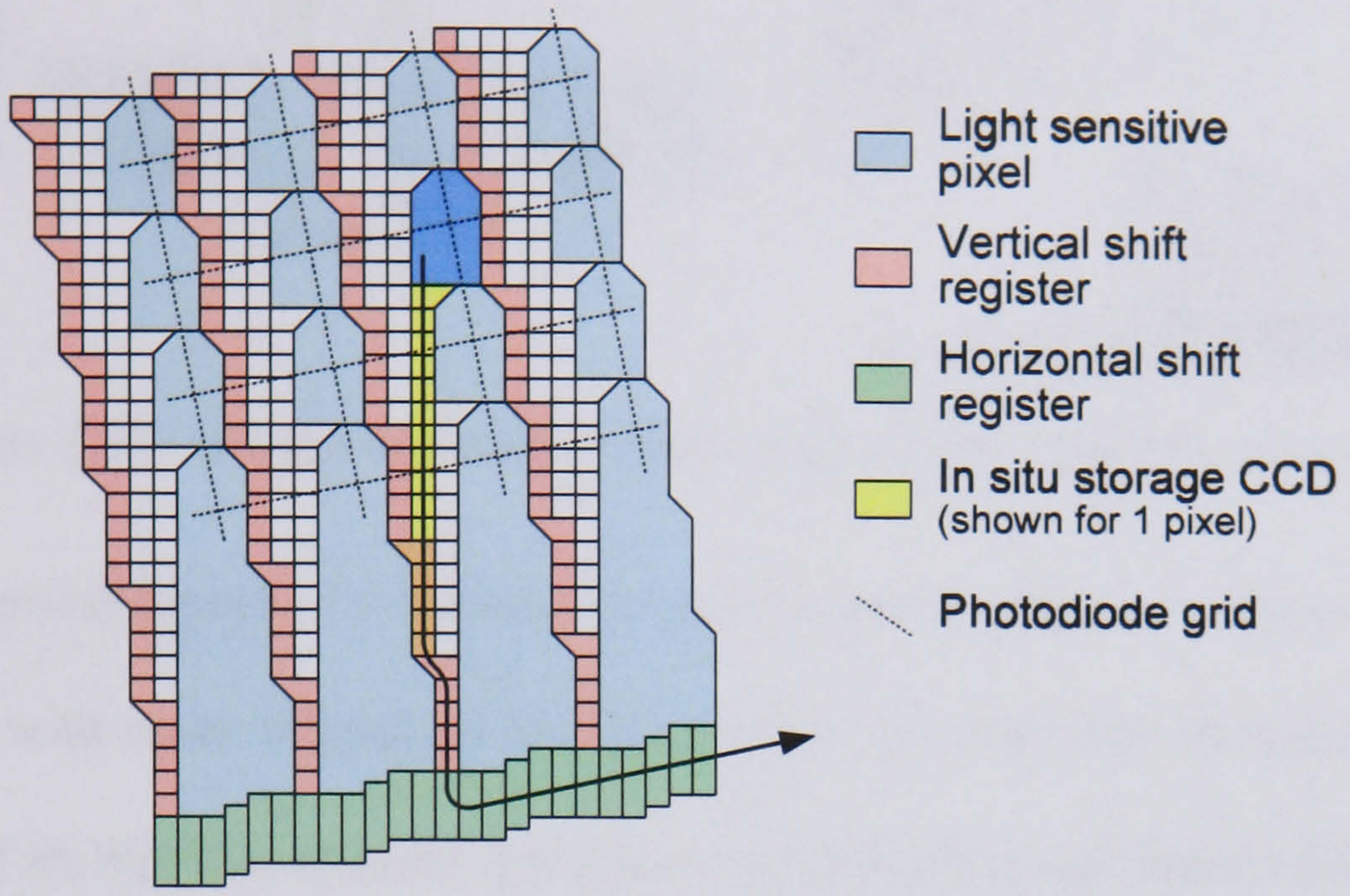

Figure 2.38 – The Shimadzu HPV-1 sensor layout, from (Etoh, et al., 2003).

ISIS sensors are still in their infancy, with the current low spatial resolution proving a limiting factor in their applicability to PIV. Their solid state design, high speed and frame count do however mean that they are the most suitable technology to meet the imaging requirements of future high-speed time-series PIV (Etoh, et al., 2002).

2.4.7.4. Multiple Gated Sensors

High-speed imaging using multiple camera sensors, each equipped with a fast non-mechanical shutter, is a tried and tested technique. Harold Edgerton developed the Kerr-cell shuttered Rapatronic camera in the 1940's, banks of which were used to acquire the iconic 10 ns exposures of nuclear explosions. More recently, image intensifiers – which can be energised for less than 1 ns – have been used to gate digital sensors, arranged in front of beam splitters or prisms in such a way as to simultaneously image a single optical input (c.f. Figure 2.39 on page 86). In this way, a small number of frames can be acquired at up to GHz rates.

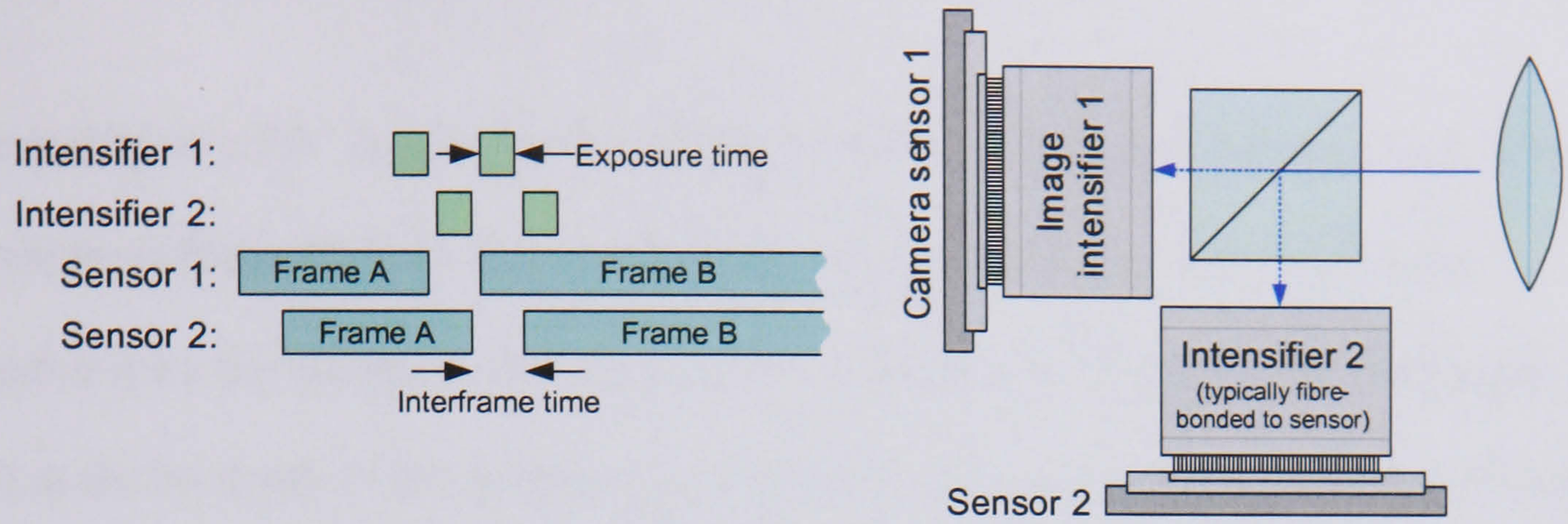

Figure 2.39 – Image intensifier gated dual-sensor high-speed camera.

The internal optical layout of a typical 4 sensor camera is shown in Figure 9.17 on page 350, but units with up to 16 sensors and intensifiers are available. Furthermore, by using both frames of an interline transfer sensor, and interleaving and frame-straddling the exposures as shown above, it is possible to take twice as many exposures as there are sensors, at a maximum frame rate of (n/f) where each of the n sensors have an interframe transfer time of f. It is also possible to install ISIS sensors in such cameras, thereby further increasing the frame count (Eisenberg, et al., 2002).

2.4.8. Image Quality

The quality of a PIV image may be defined in terms of its signal-to-noise ratio, which should be sufficiently high that the particles are clearly visible, while any noise introduced by the camera is not. The linearity of the sensor's photometric response, as well as the bit depth of the output, may also affect the quality of the subsequent image correlation, but these factors are of lesser concern (Mullikin, et al., 1994).

2.4.8.1. Sensitivity

The sensitivity of a CCD or CMOS sensor may, in part, be described using the quantum efficiency (QE), which is defined as the percentage of incident photons (of a particular wavelength) that generate an electron-hole pair within the photo-detector material (c.f. page 71). Typical CCDs, at the time of writing, tend to peak at around 50% QE, while back-illuminated sensors (c.f. Section 2.4.3.5) may produce electrons from as many as 90% of the incident photons. The *overall* sensitivity of a camera, and its output for a particular amount of incident illumination, is however the product of several other parameters relating to the readout electronics, as indicated below:

	Incident photons	**Quantum efficiency**	**Conversion efficiency**	**Readout gain***	**ADC rate***
Units:		%	V/e^-		V/count
Typical example values:	10,000	60	10×10^{-6}	5	100×10^{-6}
	10,000 photons	→ 6,000 electrons	→ 60 mV	→ 300 mV	→ 3000 counts

Table 2.5 – The calculation of overall image sensor efficiency.

* In some cameras, these parameters are variable. In the case of the A/D conversion however, it is often only the *effective* digitisation rate that changes (by virtue of the subset of bits that are transferred) when the camera is switched between (say) 8 and 12-bit readout modes.

2.4.8.2. Noise

The vast majority of camera sensor noise can be divided into the 3 categories listed below. As discussed on page 77, CMOS sensors can additionally suffer from fixed pattern noise, in which the signal varies according to the pixel used to detect it.

Noise source	**Changes with…**
Photo shot noise.	Illumination intensity, and exposure time.
Dark current noise.	Sensor temperature, and exposure time.
Read-out noise.	Pixel clock frequency.

Table 2.6 – Sources of image noise.

The production of photons, and therefore their arrival rate at a given pixel, is an inherently random, Poisson process, in which the photons only share the same *probability* of arriving somewhere in a given time period. As such, no camera in the world is capable of truly repeatable operation, and photon shot noise is the term given to describe the resultant variation in an image's brightness. This deviation (which has an RMS proportional to the square root of the illumination intensity) does however prove negligible for all but the shortest exposures, or dimmest images.

Just as visible photons create electrons pairs in a sensor's silicon, so does any innate thermal energy. For CCD sensors, this is a particular problem as the resultant charge is captured and interpreted in exactly the same way as the 'true' signal, when in fact it merely results in random noise (with the same temporal Poisson distribution as the shot noise). The average 'dark current' noise at a particular temperature may be quantified (in e^-/px/s) by recording images with the lens cap on, but it can only be removed by

lowering the temperature of the sensor. Liquid nitrogen cooling (as used in professional astronomical applications which require very long exposures) can reduce dark current noise to almost non-existent levels, while the more practical Peltier heat pump is sufficient for the majority of high-end PIV camera sensors.

It should be noted that just as the performance of a CMOS sensor's pixels can vary, so can the dark current noise produced by different pixels of a CCD sensor. Slight differences in the silicon's thickness, introduced during manufacture, can lead to pixels with an above average dark current, which in turn produce bright than average image values. Such 'hot pixels' can however be corrected for, assuming the exposure time and dark current noise is known.

Readout noise is introduced during the sampling of the sensor's readout amplifier, and it increases with the rate at which data is read out. Typical readout noise (and related) characteristics for a high-end CCD PIV camera – 2048 px^2 pco.2000 – are given in Table 2.7, from which it can be calculated that 1,000 532 nm photons, collected during a 2 second exposure, would *on average* result in an output of 271 counts, 3% of which will be due to noise.

Readout noise	Grade 0 sensor at 10 MHz readout	10 e^- rms
	Grade 1 sensor at 40 MHz readout	18 e^- rms
Dark current noise	At 20°C	0.50 e^-/px/s
	At -20°C	0.01 e^-/px/s
Combined conversion efficiency		2.1 e^-/count
Quantum efficiency at 500 nm		55%

Table 2.7 – Noise and sensitivity related characteristics for the pco.2000 camera.

2.4.9. Imaging Lenses

The camera lens is an important part of the PIV experiment, as it not only determines the potential measurement volume, but also the quality of the recorded images.

2.4.9.1. Magnification Factor

The distance X covered by a lens of focal length f, at a distance a, is given by:

$$X = x\left(\frac{a}{f} - 1\right) \tag{2.31}$$

…where x is the width (or height) of the image sensor (equal to the number of pixels multiplied by the pixel pitch p). A 2000 px^2 sensor with p = 7.4 µm, fitted with a 50 mm lens for example, will result in a 0.28 m wide FOV at 1 m. This relationship between x and X may be expressed both in terms of the magnification factor M, and *for a particular* a, the number of pixels per millimetre Z:

$$M = \frac{x}{X} = pZ_a \tag{2.32}$$

2.4.9.2. Depth of Field

The lens' f-number $f^{\#}$ relates the focal length f to the aperture size D_a:

$$f^{\#} = \frac{f}{D_a} \tag{2.33}$$

A smaller f-number increases the amount of light that reaches the sensor ($I \propto f^{\#-2}$) but also reduces the depth of field. The use of Scheimpflug mounts enables users to choose lenses based on the largest possible D_a, though it rare to find a lens with an f-number

less than 1. Several definitions have been proposed for the depth of focus δz, with (Adrian, 1991) using:

$$\delta z = 4\left(1+\frac{1}{M}\right)^2 f^{\#2}\lambda \tag{2.34}$$

For the values $f^{\#} = 8$, $\lambda = 532$ nm, and $M = 0.2$, for example, $\delta z = 4.9$ mm. Outside $a \pm \delta z/2$, the particle images will be blurred by ≥20% of the in-focus diameter. Any angular camera arrangement not featuring Scheimpflug correction should therefore use lenses with an f-number large enough that $\Delta z_0 < \delta z$. (Meinhart, et al., 2000) demonstrated an exception to this requirement, by defining the measurement volume for microscopic PIV studies of MEMS devices by means of the focal depth.

2.4.9.3. Lens Quality

Cheaper lens, or those with a small f-number (which requires that the glass lens elements be bigger), are likely to introduce distortions into the recorded image. Radial barrelling, as shown below, is particularly common, though shearing and 'pinching' can all occur to a variable degree. This is of particular pertinence to stereoscopic camera arrangements in which a simple geometric calibration (c.f. page 28) is unable to account for all of the image- to object-plane transformations. As will be shown in Chapter 3 however, more complex camera calibration can mitigate such problems.

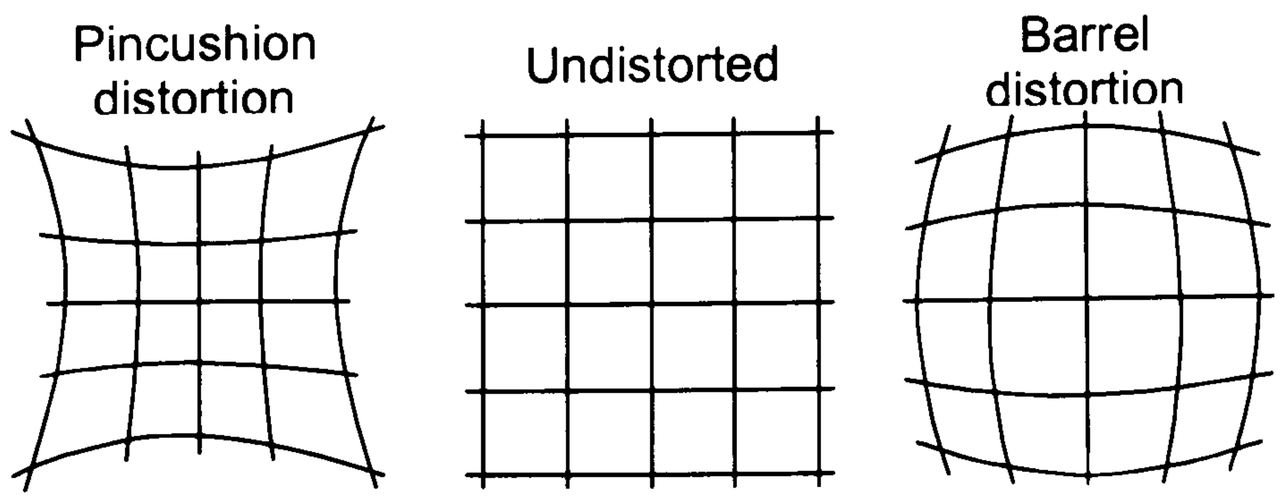

Figure 2.40 – Examples of radial distortion.

2.5. Image Analysis

2.5.1. Introduction

Many different computational methods have been developed for the analysis of PIV images: (Landreth, et al., 1988) used simple orthogonal image compression to find the position of individual particles; while (Grant and Pan, 1997) demonstrated the application of a neural network, which was able to associate relative particle positions with a particular flow vector. Morphological binary image analysis techniques, based on both the Hausdorff distance and approximation to a Voronoï diagram have also been demonstrated (Capart, et al., 2004; Chetverikov, 2001).

Almost all commonly used analysis techniques, however, are based on a singular underlying principle: the recorded image is examined on a sub-region by sub-region basis, with a single particle displacement measurement made at each of the positions considered. The particle displacement within each 'interrogation window' (which has area A_I) may be found by either Fourier transformation of the PIV image(s) onto the frequency domain, or direct numerical calculation of the correlation between two displaced images (Perez, 2005).

2.5.2. Optical Correlation

Until the mid-1990's, the majority of film-based PIV images were analysed optically, as limited computing power and low scanner resolution meant that there was little advantage to performing correlation in the digital domain. Such optical analysis is based on the fact that the image formed by a lens at a distance of 1 focal length is the Fourier transform of whatever object is placed 1 focal length in the other direction.

Fourier transformation of a sub-region of an auto-correlation PIV image results in a series of 'Young's fringes' whose orientation and spacing is proportional to the direction and magnitude of the particles' travel (Adrian, 1991; Keane and Adrian, 1990). While such fringe patterns can be measured and analysed directly, using techniques such as the Hough transform (Greenhill and Jones, 1997), it is also possible to calculate the particle displacement by further Fourier transformation of the fringe pattern. This may be achieved either numerically, using a digitised video image of the fringes (Prasad, et al., 1992), or again optically (Jakobsen, et al., 1993).

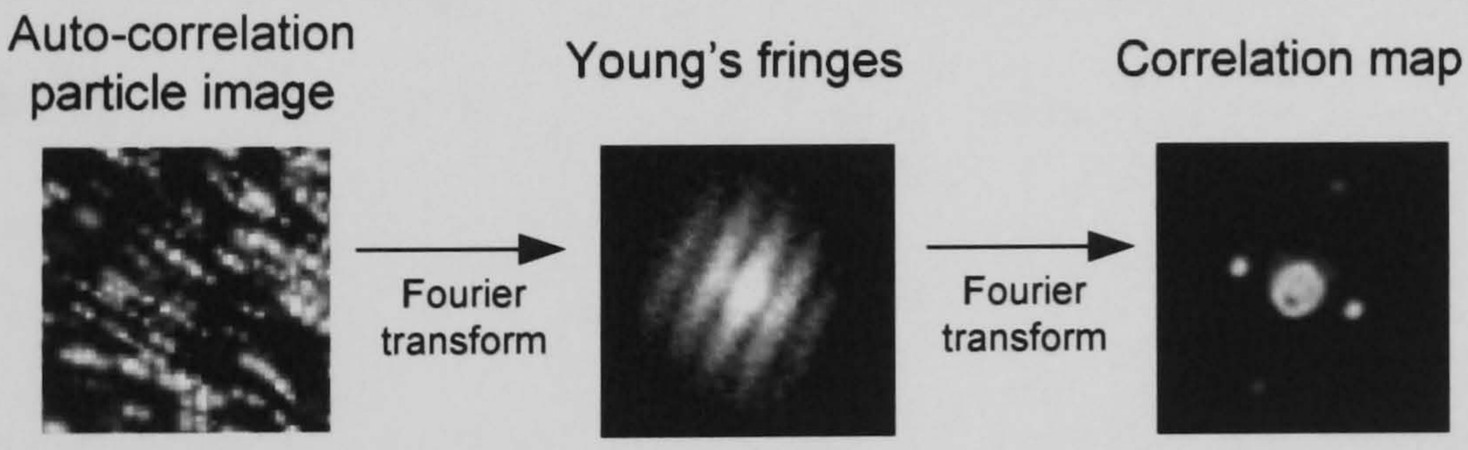

Figure 2.41 – Fourier transformation of an auto-correlation PIV image.

The Fourier transformation of the Young's fringes is referred to as the 'correlation map', and contains peaks whose positions relate directly to the original particle displacement. Auto-correlation maps therefore contain 3 peaks; one in the centre

(caused by correlation between each dot and itself) and two smaller symmetrical peaks, caused by correlation between particles in their displaced positions.

Figure 2.42 shows a set of auto-correlation maps produced by both optical and numerical transformation of a projected Young's fringe, as well as a map produced numerically, from a digital PIV image. Despite the slightly lower quality of the map produced by purely optical means, such analysis was at one time popular due to its (theoretically) instantaneous nature (Coupland and Halliwell, 1988).

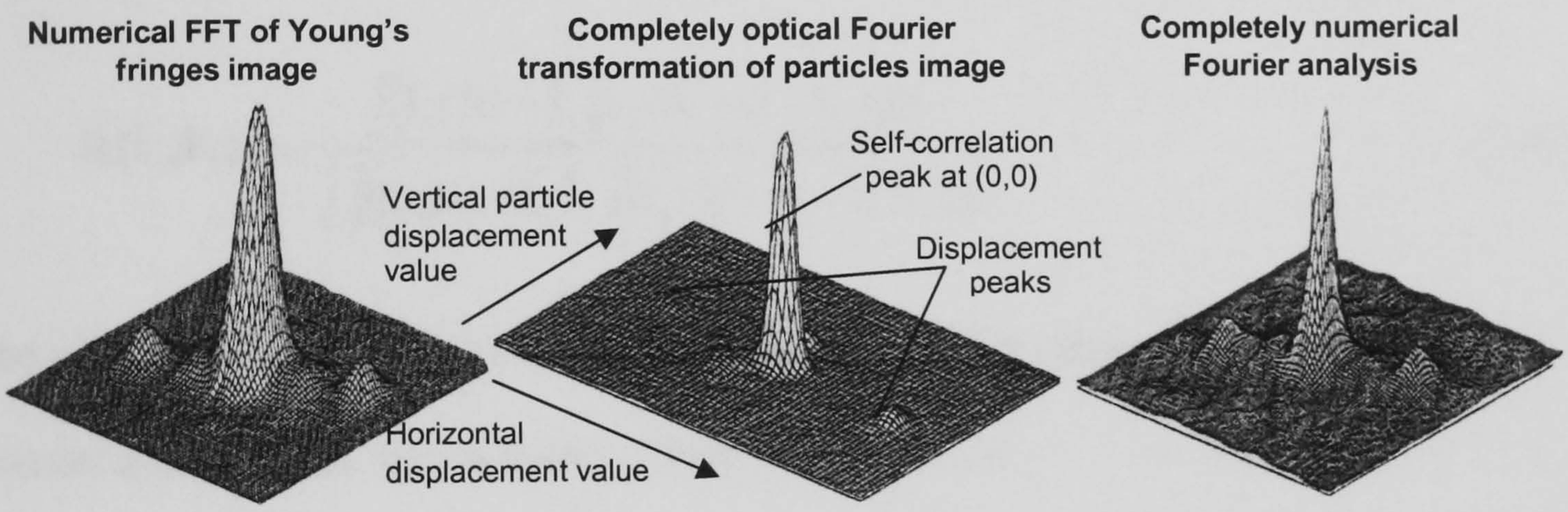

Figure 2.42 – Auto-correlation maps produced by 3 methods, from (Westergaard and Buchhave, 1993).

Further details of the theory and practise of optical correlation are given in Appendix 9.1.1 on page 329.

2.5.3. Digital Cross-Correlation

Given the power of modern computers, and the wide-spread use of digital interline-transfer PIV cameras, all modern DPIV images are analysed by means of digital cross-correlation (Willert and Gharib, 1991). (Keane and Adrian, 1992) define the degree of correlation **R** between the sub-regions **X** of two images $\mathbf{I}_1$ and $\mathbf{I}_2$ as:

$$\mathbf{R}(\mathbf{I}_1,\mathbf{I}_2)_{\mathbf{s}} = \int \mathbf{I}_1(\mathbf{X})\mathbf{I}_2(\mathbf{X}+\mathbf{s})\,d\mathbf{X} \tag{2.35}$$

…but alternative, normalised definitions, are also frequently used: (Hu, et al., 1998)

$$\mathbf{R}(\mathbf{I}_1,\mathbf{I}_2)_{\mathbf{s}} = \frac{\int\left(\mathbf{I}_1(\mathbf{X})-\overline{\mathbf{I}_1}\right)\left(\mathbf{I}_2(\mathbf{X}+\mathbf{s})-\overline{\mathbf{I}_2}\right)d\mathbf{X}}{\sqrt{\int\left(\mathbf{I}_1(\mathbf{X})-\overline{\mathbf{I}_1}\right)^2 \int\left(\mathbf{I}_2(\mathbf{X}+\mathbf{s})-\overline{\mathbf{I}_2}\right)^2 d\mathbf{X}}} \tag{2.36}$$

The correlation function given in equation (2.35) may be approximated using a finite Fourier transform, as shown below: (Press, et al., 1992)

$$\mathbf{R}(\mathbf{I}_1,\mathbf{I}_2) \Leftrightarrow \hat{\mathbf{I}}_1 \cdot \hat{\mathbf{I}}_2^{*} \tag{2.37}$$

…where ˆ represents the Fourier transform and * the complex conjugate. The majority of PIV image analysis is performed using this FFT correlation estimate, due to the reduced number of mathematical operations required in its calculation: $N^2 \log_2 N$ as opposed to N^4 (where N is the number of pixels within the interrogation-region **X**).

All 3 of the correlation functions above have been implemented in Matlab M-code (provided in Appendix 9.4.1, page 403) and, as shown in Figure 2.43 on page 96, there is negligible difference between the output of the normalised direct correlation function and the FFT analogy. The maps were produced by applying the functions to a simulated PIV image, produced as part of the J-PIV project (Okamoto, et al., 2000).

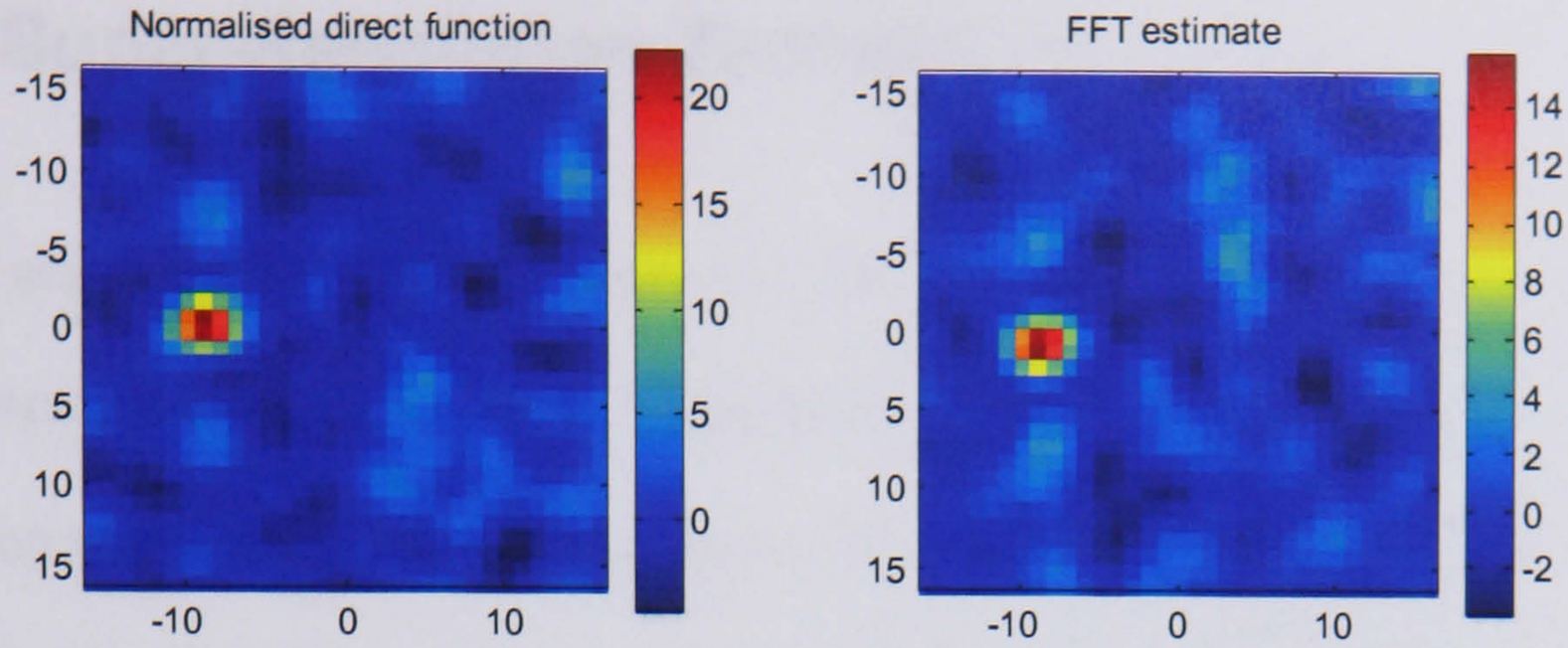

Figure 2.43 – Typical direct and FFT cross-correlation maps.

The FFT correlation function has also been applied to 2 different areas within the same image, to illustrate the effect of the interrogation window size on the correlation map quality. Position B in the original image (shown below) contains a range of particle displacements and as a result, correlations from that area are noisier than those from Position A. As demonstrated by (Hu, et al., 1998), the correlation map's SNR can be improved by enlarging the interrogation window size, but the resulting velocity measurement then becomes spatially averaged over a larger area, as demonstrated by the altered position of the correlation map peak (annotated with white text).

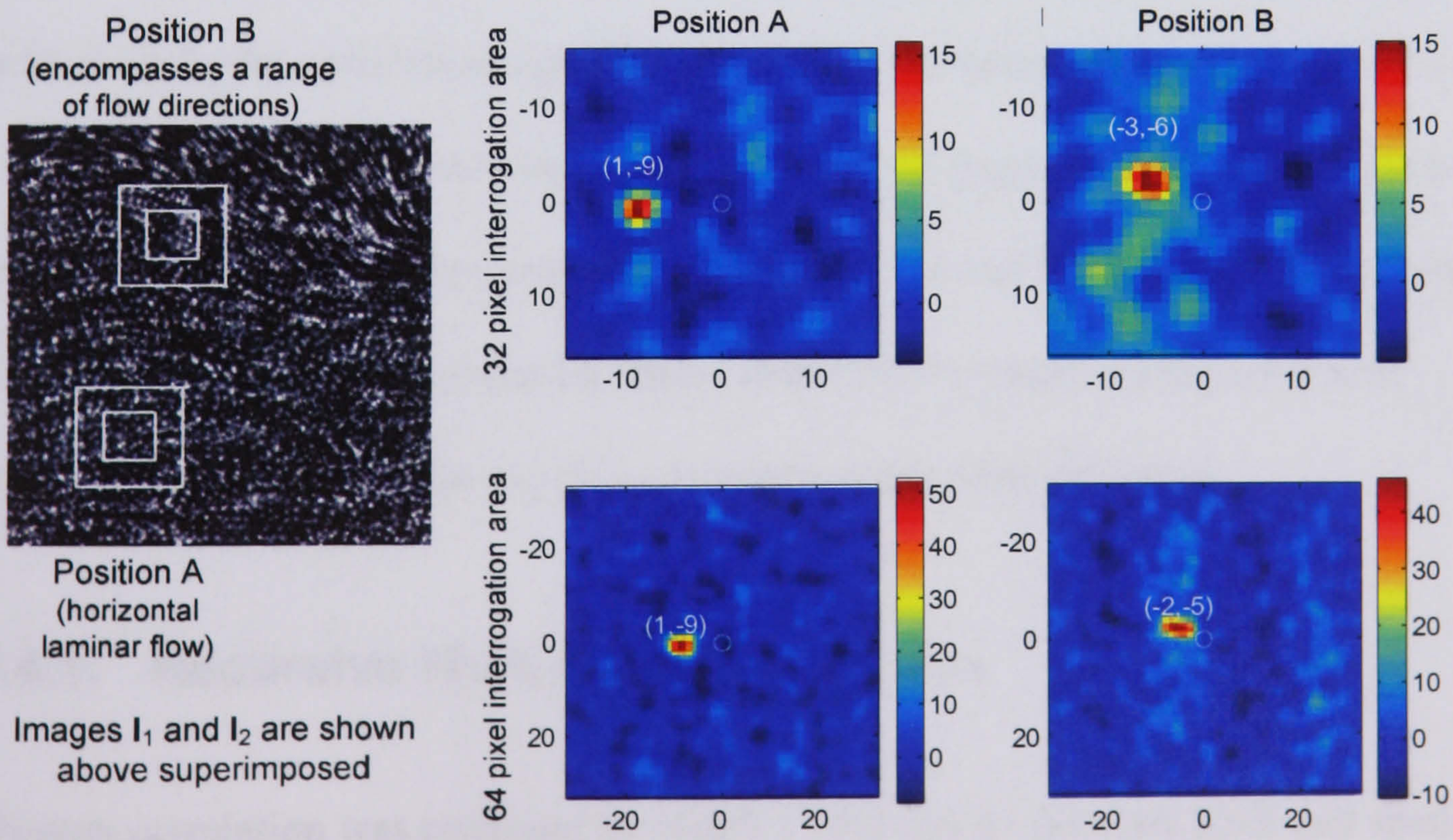

Figure 2.44 – The effect of interrogation window size.

2.5.4. Super-Resolution Techniques

In order to maximise the dynamic range of a PIV measurement, particle displacements must be extracted from the correlation map with sub-pixel accuracy, as opposed to merely using the position **p** of the maximum value (Willert and Gharib, 1991). Each component of the sub-pixel displacement **s** is therefore typically calculated using 3 adjacent correlation values, as per equation (2.38) below, although a number of alternative more accurate algorithms have been presented (Nobach, et al., 2004; Roesgen, 2003). The accuracy of the detected displacement may also be increased by tracking individual particle images, post-correlation, using hybrid PTV-PIV (Keane, et al., 1995).

$$\mathbf{s}_x = \mathbf{p}_x + \frac{\log(\mathbf{R}_{\mathbf{p}_x-1,\mathbf{p}_y}) - \log(\mathbf{R}_{\mathbf{p}_x+1,\mathbf{p}_y})}{2\log(\mathbf{R}_{\mathbf{p}_x-1,\mathbf{p}_y}) - 4\log(\mathbf{R}_{\mathbf{p}_x,\mathbf{p}_y}) + 2\log(\mathbf{R}_{\mathbf{p}_x+1,\mathbf{p}_y})} \tag{2.38}$$

For conventional correlation algorithms, the successful measurement of small flow structures is dependent on the use of a small interrogation window. As demonstrated on page 96 though, the correlation signal-to-noise ratio decreases with window size – a fact that is corroborated by Adrian's image density rule (c.f. page 15). The use of time-series techniques, such as correlation map summing (Meinhart and Wereley, 2000), or 'single pixel resolution' intensity correlation (Billy, et al., 2004), enables a high dynamic measurement range, but at the expense of instantaneous measurements.

2.5.4.1. Recursive Multi-Pass Correlation

Multi-pass correlation was proposed by (Hart, 1999) and it offers the SNR and spatial benefits of both large and small interrogation window sizes. The correlation process starts as normal, except that a very large interrogation window size can be used, thereby

ensuring a pronounced correlation map peak. During the next stage, smaller interrogation windows are considered, with their position in the second image offset by whatever amount was found during the previous correlation; (Wereley and Meinhart, 2001) suggest a improvement to the technique in which both windows are offset by equal amounts. If the flow under study is completely laminar, then the second interrogation map will result in a single peak in its centre; if not, then any small-scale deviation found may be subtracted from the previously calculated value.

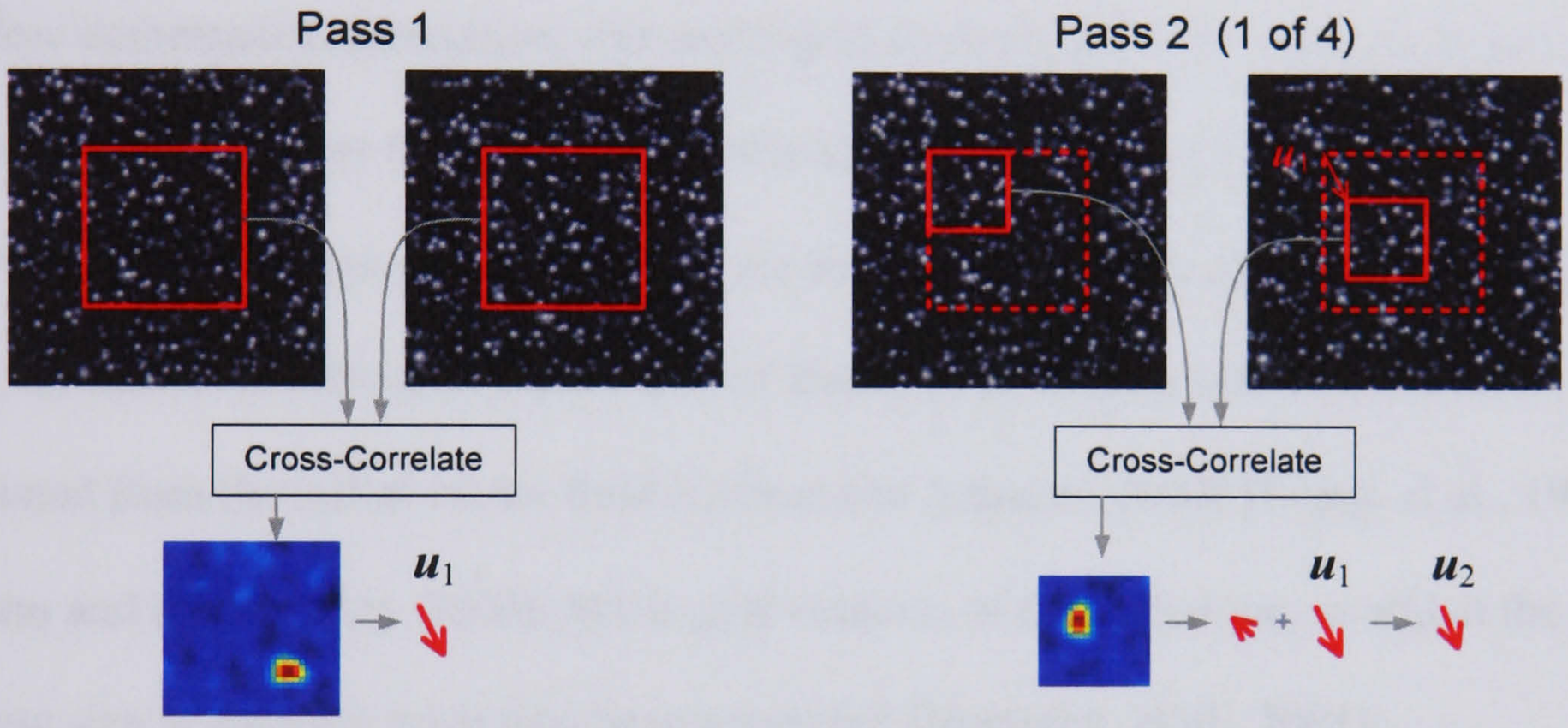

Figure 2.45 – The first 2 stages of recursive multi-pass correlation.

The multi-pass technique offers particular benefit to correlations calculated using the FFT function described on page 95. Because a proportion of particles will 'drop off the edge' of the interrogation window, the SNR at the edges of an FFT correlation map will be lower than in its centre. As a result, Gaussian windowing functions are often applied to suppress noise in the corners, but as a result, such correlations maps then become slightly biased towards low displacements (Westerweel, 1997). The improvements that thus result from using multi-pass processing, such as the reduction in the so-called 'peak locking' effect, are examined in detail by (Gui and Wereley, 2002; Westerweel, et al., 1997).

2.5.4.2. Window Deformation Correlation

PIV images from flows with high velocity gradients can prove difficult to analyse, as the interrogation windows contain a range of particle displacements, which can in turn lead to stretched, or multiple correlation peaks (Bolinder, 2000). Even extremely small interrogation windows, applied as part of multi-grid analysis, are unable to resolve the motion in the centre of a vortex, for example (Huang, et al., 1993a).

Window deformation correlation, like multi-grid analysis, starts by calculating an initial estimation of the vector field, using regularly spaced interrogation windows. In the next pass however, the interrogation windows are both translated *and* deformed (c.f. Figure 2.46), by means of various combinations of shearing, stretching and rotation, as calculated from the initial vector field (Gilbert and Johnson, 2003; Huang, et al., 1993b; Scarano and Riethmuller, 2000). Multi-grid versions of the technique, in which the window size is reduced, have also been presented (Nogueira, et al., 2001).

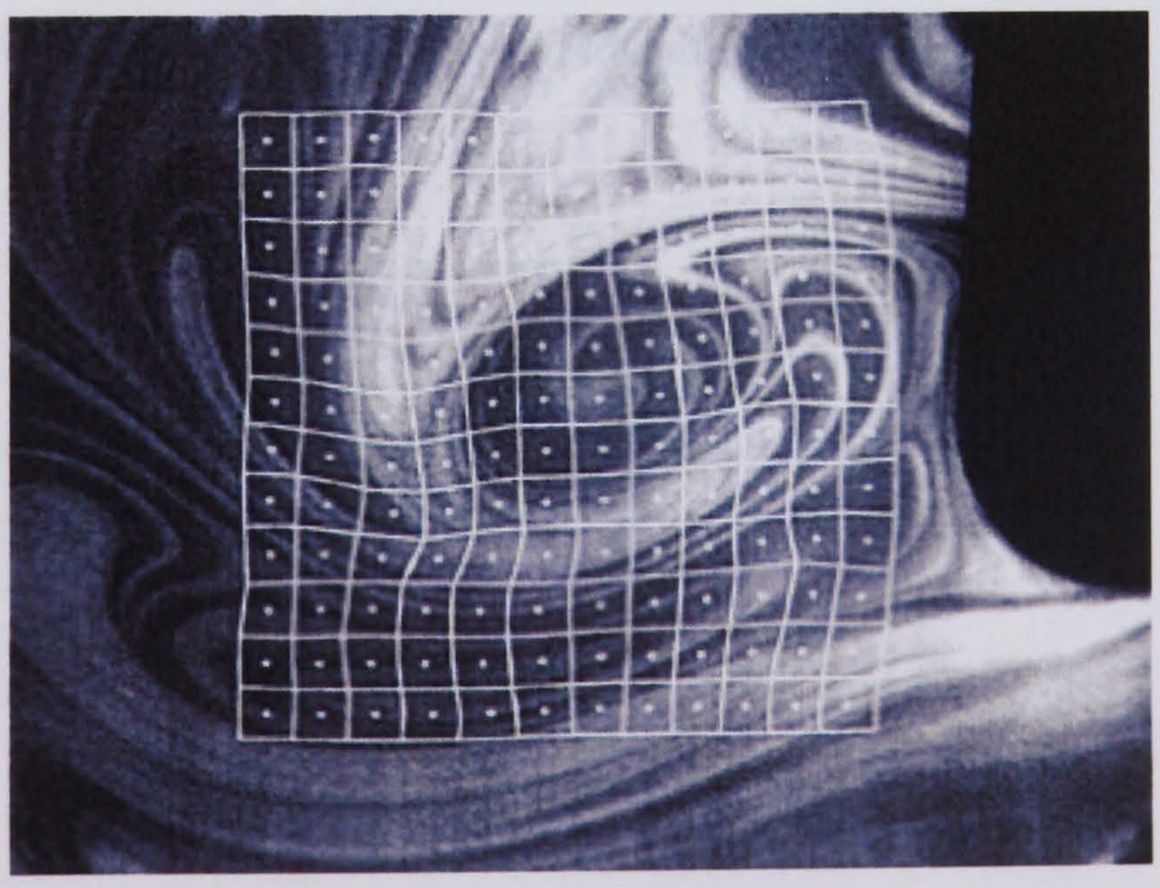

Figure 2.46 – Deformed interrogation windows, from (Scarano, 2002).

2.5.5. Vector Validation

For good quality PIV images, captured in accordance with the guidelines described in Section 2.1.1.2 (page 19), the RMS of the detected particle image displacement error, using standard cross-correlation, is less than 0.1 pixels (Huang, et al., 1997; Megerle, et al., 2002). Put another way, the ratio of u_{max}:σ_u, where u_{max} is the maximum flow velocity and σ_u the minimum resolvable velocity fluctuation, is typically of the order 150:1 (Adrian, 1997). The increased spatial resolution achievable with multi-grid and deformation correlation techniques is discussed by (Nogueira, et al., 2005).

In practise, noisy images, captured with a low seeding density or inappropriate Δz_0 or Δt value, will result in correlation maps with a low SNR, which in turn produce spurious displacement values as shown below. Vector maps are therefore typically post-processed to remove such spurious vectors, by considering either the strength of the originating correlation peak, or the variation between a vector and its neighbours.

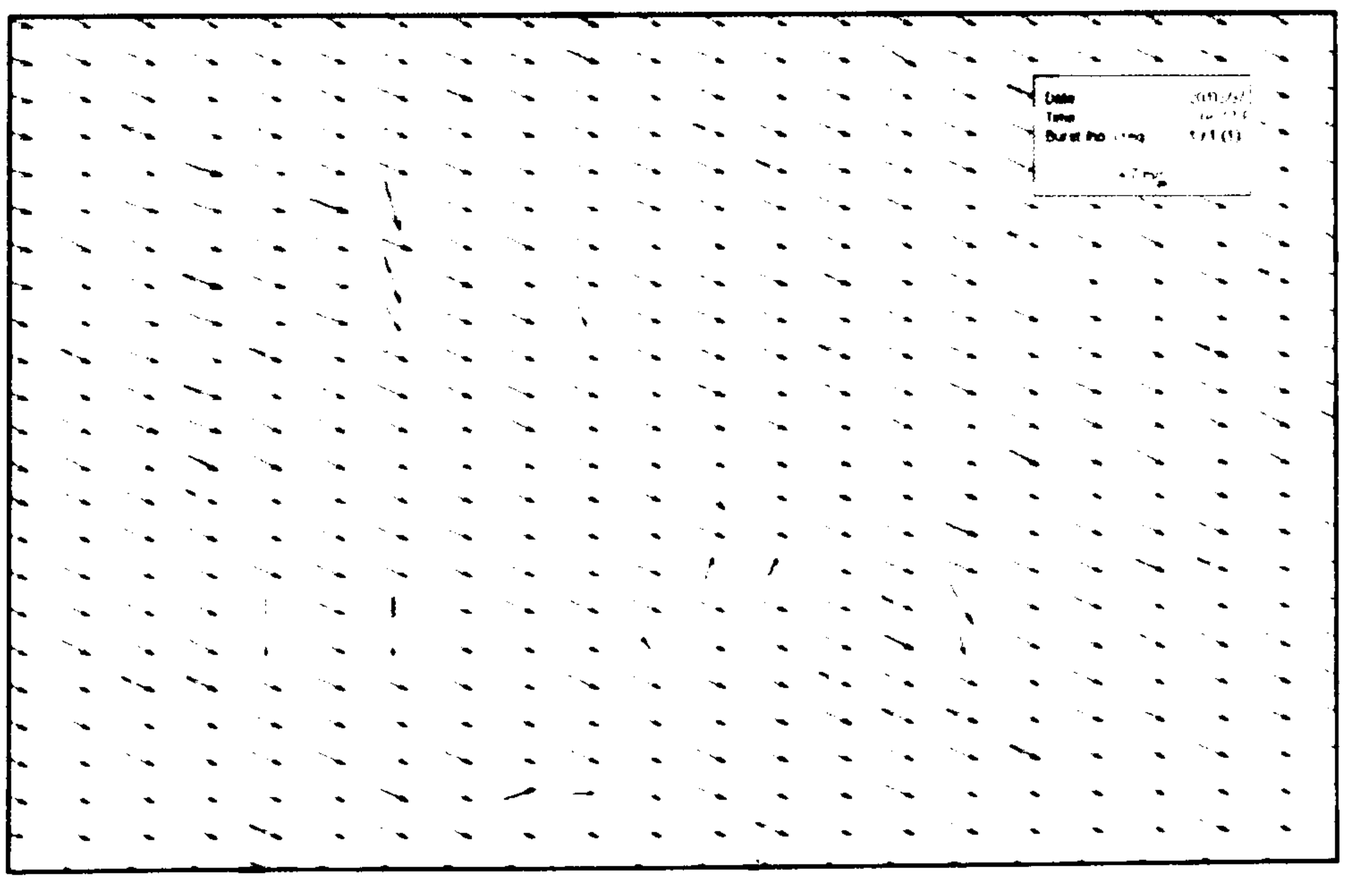

Figure 2.47 – Spurious vectors, from (Nogueira, et al., 1997).

2.5.5.1. Correlation Strength Filtering

As shown in the top right correlation map of Figure 2.44 on page 96, interrogation windows containing high velocity gradients can result in multiple peaks appearing in the correlation map. In the case of extremely noisy images, random peaks will appear, with spurious vectors resulting whenever a 'noise' peak is found to be the highest.

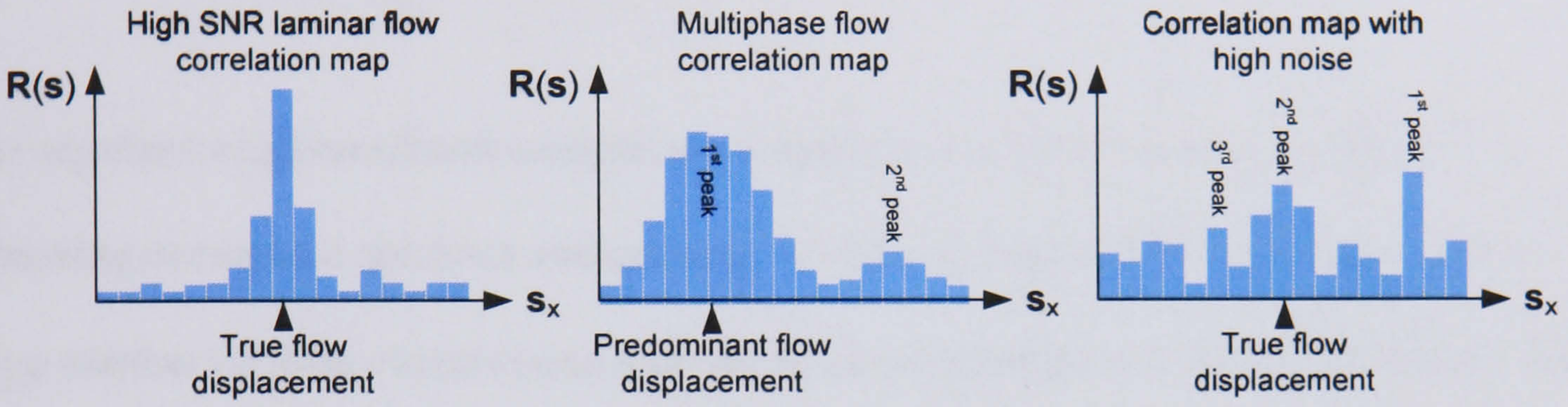

Figure 2.48 – Multiple peak correlation map (profiles).

Given the obvious difference between a 'good' and 'bad' correlation map, it is possible to discount vectors based on the height of their map's 1st peak relative to the 2nd, though such ratios tend to be chosen arbitrarily. Given the random nature of noise within a correlation map, it is also possible to reinforce the 'true' peak, by multiplying two maps (offset by a small amount) together, as proposed by (Hart, 2000). While data processing times are doubled, the improvements in vector quality can be marked.

2.5.5.2. Spatial Vector Filtering

As stated by (Westerweel, 1994), the validity of a particular vector may be quantified by comparing its values with either the mean of the whole vector map; the mean of a subset of neighbouring vectors; or – as has proved most effective – the median of the surrounding neighbourhood. Typically, 3 × 3 subsets of the map are considered, with the central vector considered valid only when:

$$\mathbf{U}_{median} - n.\mathbf{U}_{RMS} \leq \mathbf{U}_{2,2} \leq \mathbf{U}_{median} + n.\mathbf{U}_{RMS}$$

and $$\mathbf{V}_{median} - n.\mathbf{V}_{RMS} \leq \mathbf{V}_{2,2} \leq \mathbf{V}_{median} + n.\mathbf{V}_{RMS}$$

…where **U** and **V** are the horizontal and vertical components of the 3 × 3 neighbourhood. While the multiplier *n* will normally be chosen on a trial-and-error basis, (Westerweel and Scarano, 2005) suggested the use of a 'normalized median' test, in which *n* is varied depending on the values of the surrounding flow.

The standard neighbourhood comparison technique has been proven to work well at removing occasional spurious vectors such as those in Figure 2.47, but maps with a large number of false vectors pose a problem, as represented in Figure 2.49 below. The central vector in this example *should* be discarded as spurious, but the high RMS of the 3 × 3 region would therefore require *n* to be chosen with extreme preciseness.

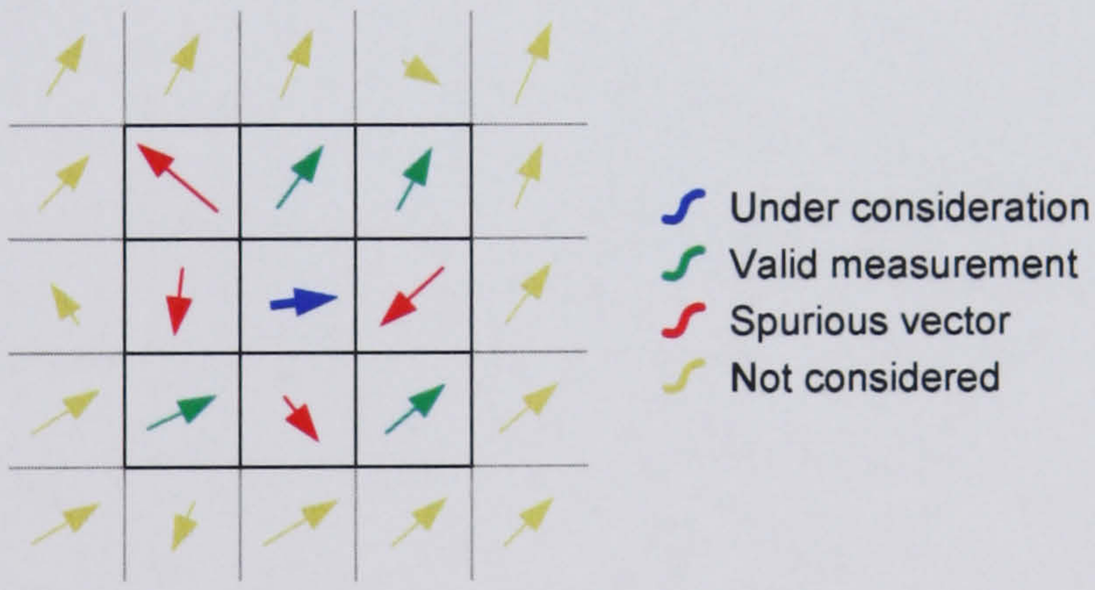

Figure 2.49 – Local vector comparison and filtering.

As a solution to this problem, (Nogueira, et al., 1997) proposed a multi-pass filtering strategy, in which the most-obviously incorrect vectors are removed on an iterative basis. It is further possible to reinsert vectors into the holes left by filtering, by considering the 2nd and 3rd peaks of the correlation map (c.f. Figure 2.48), thereby further improving the quality of the resultant vector map.

3. A Novel Method for the Acquisition of High Speed TR-PIV Data

3.1. Introduction

3.1.1. High-Speed Time-Series Acquisition

Sequential, continuous visualisation is necessary in order to fully understand any time-dependent flow phenomenon, and time-series PIV allows the evolution of such flows to be quantified. Furthermore, time-space correlation of TR-PIV data allows fundamental flow characteristics, such as vortex convection velocities and turbulence integral length and time scales, to be calculated.

Interesting flow structures, however, typically evolve in all but the slowest flows at a rate too high to be captured by standard $\leq$ 30 Hz cameras. While temporal interpolation of the flow using POD is possible to a certain degree (Druault, et al., 2005), the acquisition of most TR-PIV is dependent on the high-speed sensor technologies explained in Section 2.4.7, as well as the high repetition rate lasers discussed in Section 2.3.2.2. Table 3.1, on the next page, lists a representative sample of high-speed time-series studies, along with the sampling rate and camera and laser equipment used. As can be seen, the majority of high-resolution ($\geq$ 1 Mpx) high-speed ($\geq$ 10 kHz) time-series data is still captured using film-based rotating drum cameras; a fact due to both their greater availability, and the high cost of the only current alternative (multiple gated sensor based cameras).

This chapter therefore discusses the feasibility of an alternative time-series acquisition technique, in which standard double-shutter PIV cameras are used – without any additional hardware – to acquire high-speed contiguous particle image sequences.

	Camera output			Laser*	Application example
	Rate† (kHz)	Frames	Size (Mpx)		
Rotating drum camera	20	66	6.8 (film)	Copper vapour	Fundamental TR-PIV for LES code validation (Williams, et al., 2003).
	10	300	Film	CW Ar^+ with AOD	TR-PIV of cavitation bubble collapses (Vogel and Lauterborn, 1988).
	10	70	1.8 (film)	Copper vapour	TR-PIV of burner flames (Honoré, et al., 2000).
	10	50	6.0 (film)	Copper vapour	TR-PIV of turbulent impinging jets (Zhang, 1999).
CMOS	27	1000s	0.07	High rep. Nd-YAG	Power spectrum measurements in Re = 4000 turbulent jets (Tanahashi, et al., 2004).
	1	4096	0.26	CW Ar^+	$Re = 5\times10^5$ oceanic flow simulation PIV measurements (Tsushima, et al., 2004).
CCD	9	200	0.03	High rep. Nd-YAG	Velocity autocorrelations in a methane jet flame (Kawanabe, et al., 2000).
ISIS	100	16	0.33	High rep. Nd-YVO_4	Visualisation of gasoline injection sprays (Eisenberg, et al., 2002).
	1000	17 32	0.06 0.01	Pockels 'slicing'	Visualisation of fast axisymmetric jet flows (Lempert, et al., 2002; Thurow, et al., 2000).
Multiple aligned sensors	32	4	0.37	Swept CW Ar^+ beam	The comparison of Lagrangian and Eulerian fluid flows (Jakobsen, et al., 1997).
	100	4 16	1.31 0.33	High rep. Nd-YAG	TR-PIV of turbulent air using 4 ISIS sensors (Wieneke and Reckers, 2000).
	2000	8	1.31	Multiple cavities	TR-PIV of Mach 1.3 pulse-excited jet flow (Wernet and Opalski, 2004).

Table 3.1 – Representative selection of high-speed time-series studies.

* In the cases where it is not stated, the laser used was a frequency doubled Nd:YAG.

† This is the fastest rate achievable with the equipment used; not necessarily the sampling rate of the actual flow measurements.

3.1.2. Proposed Technique

As discussed in Section 2.1.2.2, the use of 3-dimensional camera calibration is well established for both stereoscopic PIV image analysis and 3D-PTV (Maas, 1990). By back-projecting the images captured from a number of closely packed cameras onto the plane of a pulsed light sheet (as per 'mapping'), it is therefore possible to recreate the overlapping views achieved using a specialised multiple sensor high-speed PIV camera.

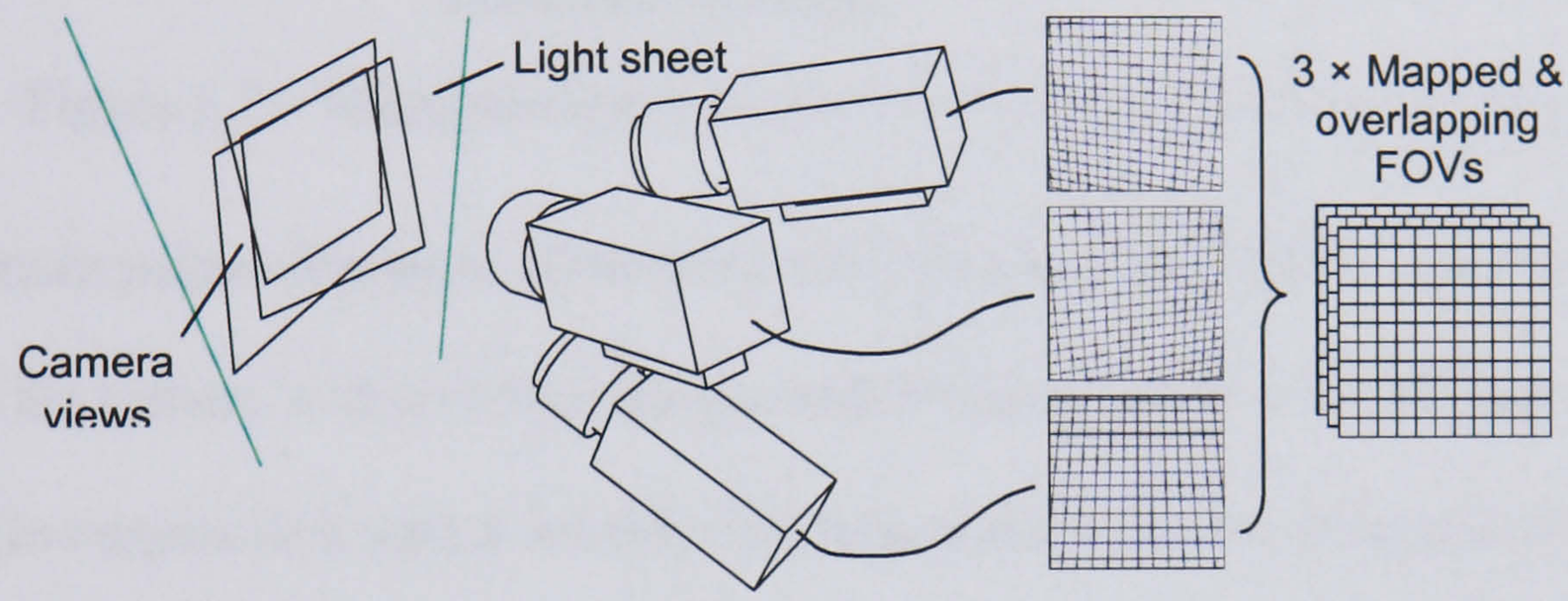

Figure 3.1 – The mapping of separate cameras' views onto a common FOV.

By capturing a single, short exposure from each of n cameras, a total of n frames of video may be acquired, at a maximum rate of just under $2/a_{min}$ Hz, where a_{min} is the minimum permissible exposure time. Furthermore, by using 'double-shutter' PIV cameras, the n^{th} camera can be used to acquire an additional, final frame, as shown below:

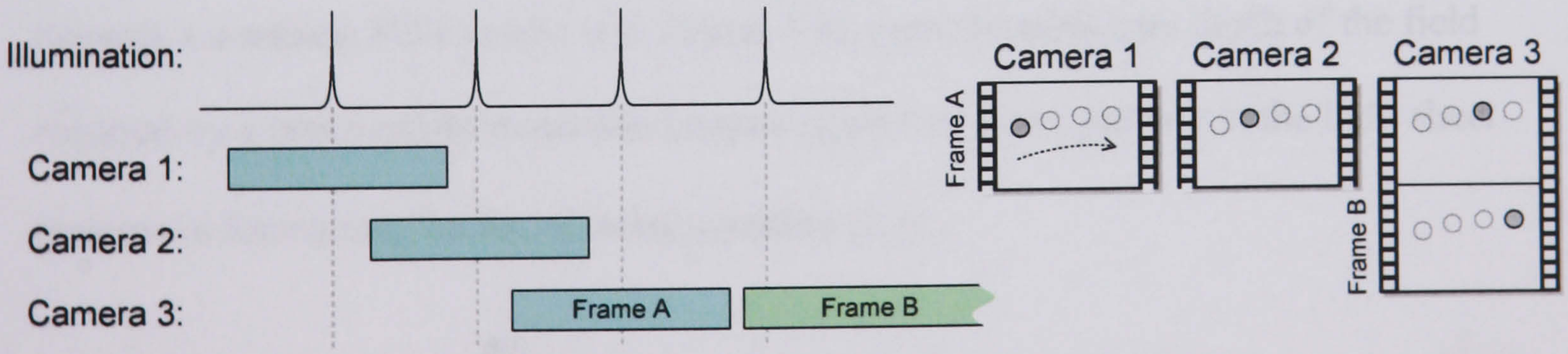

Figure 3.2 – Single exposure multi-sensor acquisition.

It is hereby proposed that it might also be possible to acquire an additional n-1 frames, by multiply-exposing each camera, as illustrated below, and subtracting the back-

projected images from one another. In this way, the position of the seeding during every odd pulse is captured directly, while an even numbered image *i* is generated by subtracting both of camera ($^{i}/_{2}$+1)'s exposures from camera ($^{i}/_{2}$)'s second.

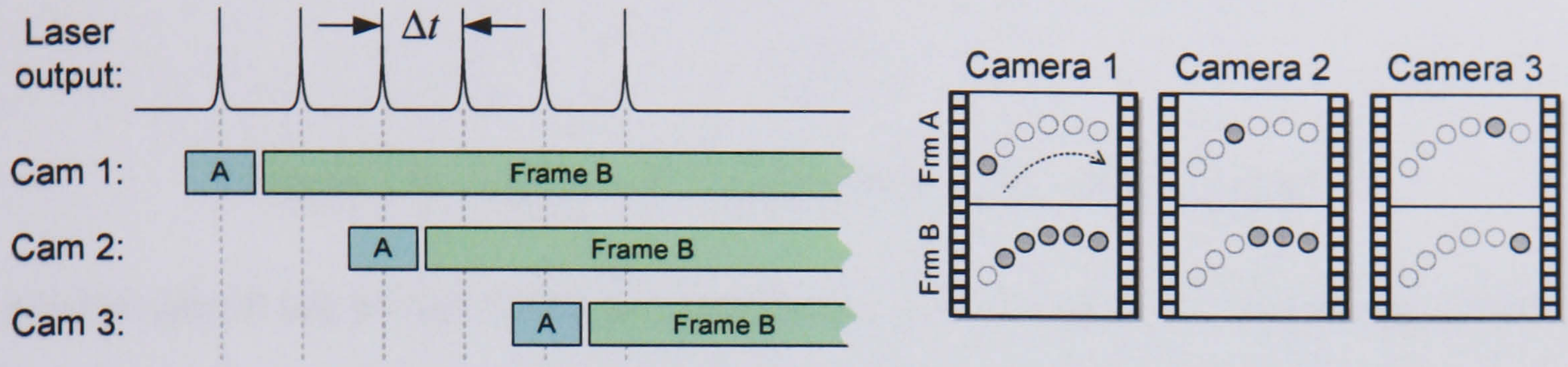

Figure 3.3 – Multiple-exposure multi-sensor acquisition technique.

The minimum pulse separation allowed by this technique is given by equation (3.1), where *f* is the camera's inter-frame charge transfer time. Using pco.2000 cameras, for example (in conjunction with a suitably fast laser system), it would be possible to acquire time-series data at up to 4 MHz.

$$\Delta t > \max\left\{\frac{a_{\min}}{2}, f\right\} \tag{3.1}$$

The validity of the single or multiple-exposure technique is dependent upon a number of factors, one of which being the requirement that the cameras have sufficient depth of field. Assuming that they are used without Scheimpflug lens mounts, and are all pointed towards a common FOV centre (c.f. Figure 3.4), then the minimum depth of the field required by a horizontally translated camera (such that every particle in the light sheet remains in focus) may be found using equation (3.2):

$$\delta z_{\min} = \Delta X \tan\theta + \frac{\Delta z_0}{\cos\theta} \tag{3.2}$$

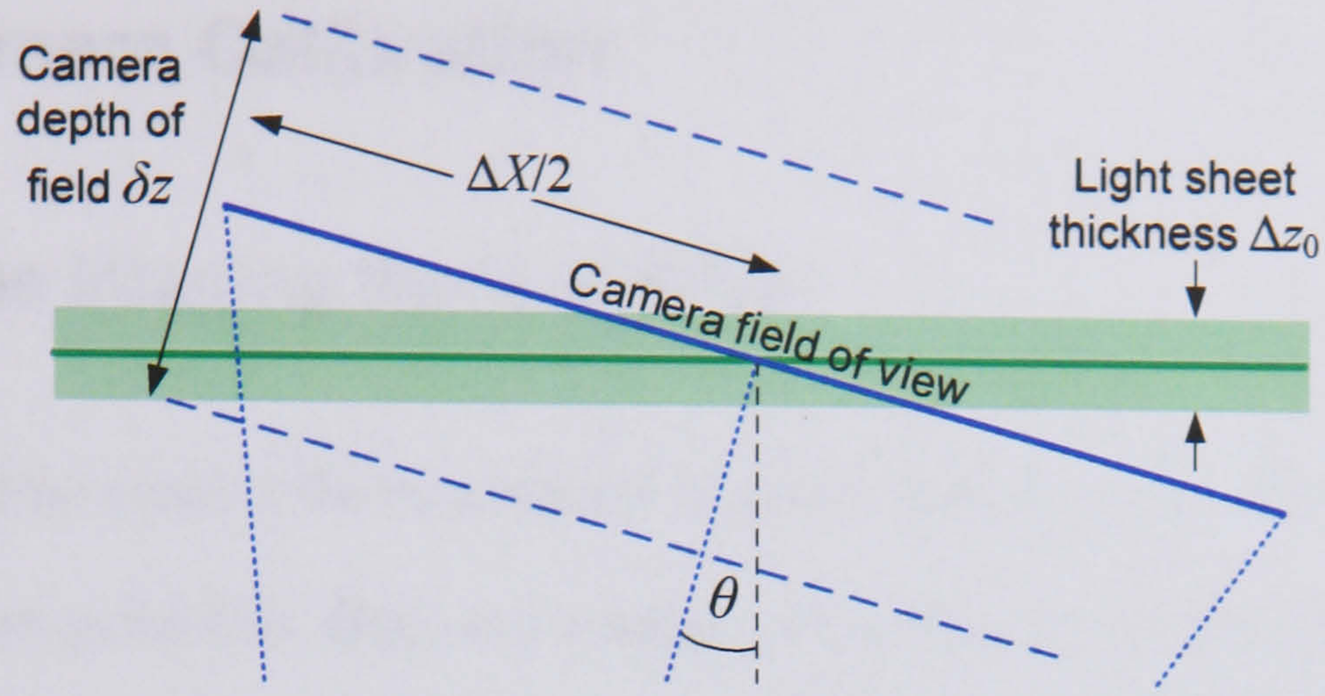

Figure 3.4 – Light sheet thickness and camera depth of field.

Accordingly, it can be calculated (using equation (2.34) on page 91) that two pco.2000 cameras with 10 cm wide FOVs, mounted 50 cm from a 2 mm thick 532 nm light sheet, must be equipped with lens of *f*-number no smaller than *f*/9.9, in order that the particles remain in focus. Clearly, the more cameras that are used, the higher $f^{\#}_{\min}$ becomes.

An additional requirement of the multiple-exposure technique is that light scattered from the seeding must be sufficiently evenly distributed amongst the cameras (which must also have a large enough dynamic range) that it is possible to distinguish between (2*n*-1) unchanging exposures. The seeding particles should therefore be as spherical as possible, with the cameras oriented around the axis of the light sheet (as shown in Figure 3.1) in order to minimise the effect of Mie scattering's angular dependency.

3.1.3. Camera Calibration

3.1.3.1. The Imaging System Model

Camera calibration enables the relationship between the real-world and camera image-coordinates to be quantified. Once this mapping is known, a recorded image can be back-projected onto any plane by calculating the pixel coordinates associated with each point of an equispaced grid on that plane. Most calibrations are founded on the 'pin-hole' (or 'linear') camera model, in which every point is projected onto the image plane by means of a straight line passing through the 'projection centre' (Clarke and Fryer, 1998).

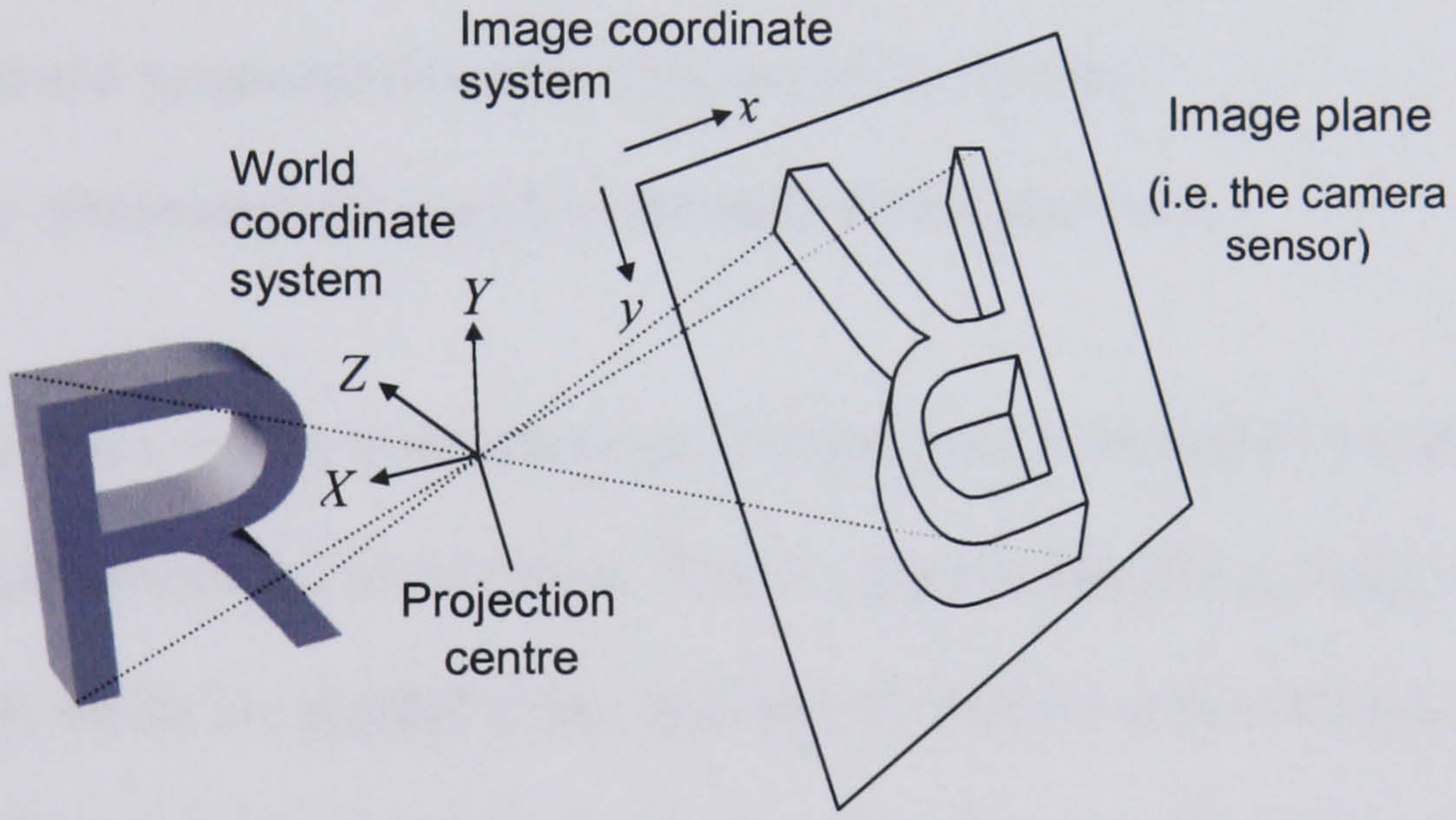

Figure 3.5 – The pin-hole camera model.

If the position and orientation of the image plane (within the world-coordinate system) is known, then a transformation matrix can be calculated to describe the relationship between the two. (Fu, et al., 1987), for example, defined a 4 × 4 calibration matrix in which the values are given in terms of the pan and tilt of a gimbal-mounted camera, the derivation of which is given in Appendix 9.1.2 (page 331).

The pin-hole model by itself is not however a particularly accurate representation of a camera system. As discussed in Section 2.4.9.3, lenses often introduce unwanted distortion into an image, and it is even possible that a camera sensor's axes may not be completely orthogonal. Complete camera calibration models therefore comprise 2 parts: a set of extrinsic parameters, which describe the position and orientation of the camera, and a set of intrinsic parameters, which may include coefficients to describe any of the following:

- The focal length of the lens.
- The sensor's horizontal and vertical pixel spacing.
- The image centre (or 'principle point'), i.e. the pixel position that lies on the camera's optical axis (not necessarily the central pixel).
- Radial and tangential distortion introduced by the lens.
- Linear distortions introduced in the sensor's manufacture.

As shown by (Tsai, 1987), most sensors and lenses can be accurately modelled using only the radial component of distortion. This is typically described using 1 or 2 coefficients *k*, which are applied in the form shown below. More complex camera models may however involve the use of up to 10 intrinsic parameters, e.g. (Lucchese, 2003).

$$\begin{bmatrix} x_i \\ y_i \end{bmatrix} = \begin{bmatrix} x_i\left(1 + k_1 r_i^2 + k_2 r_i^4 + k_3 r_i^6 + \ldots\right) \\ y_i\left(1 + k_1 r_i^2 + k_2 r_i^4 + k_3 r_i^6 + \ldots\right) \end{bmatrix} \quad \text{where:} \quad r_i = \sqrt{x_i^2 + y_i^2} \tag{3.3}$$

3.1.3.2. Optical Model Calibration

As stated in Section 2.1.2.2, most camera calibration is performed optically, and not geometrically. As such, the coefficients of the camera calibration model cannot be calculated directly, but must instead be estimated such that the model fits actual observations as closely as possible. This is typically achieved by means of an iterative least squares error minimisation routine.

As is shown by (Heikkilä and Silvén, 1997), the model parameters may be estimated using either a 'direct linear transformation' (in which radial and tangential distortions are ignored, or calculated post-calibration), or a slower but more accurate non-linear approach. In the case of the DLT, as is shown in Appendix 9.1.2.3 (page 334), a minimum of 6 paired image- and world-coordinates are needed for the extrinsic-parameter transformation matrix to be calibrated.

3.1.3.3. Calibration Point Measurement

Accurate optical camera calibration is dependent on using accurately measured calibration points. While the world-coordinate of a calibration feature will usually be known to micron precision, camera noise can limit the accuracy with which the associated image-coordinate is found (Lavest, et al., 1998). (Lucchese and Mitra, 2002) demonstrated that if a checkerboard calibration pattern was used, its corners could be found to the nearest 0.01 pixels, but manufacturing considerations mean that most calibration targets comprise circular marks.

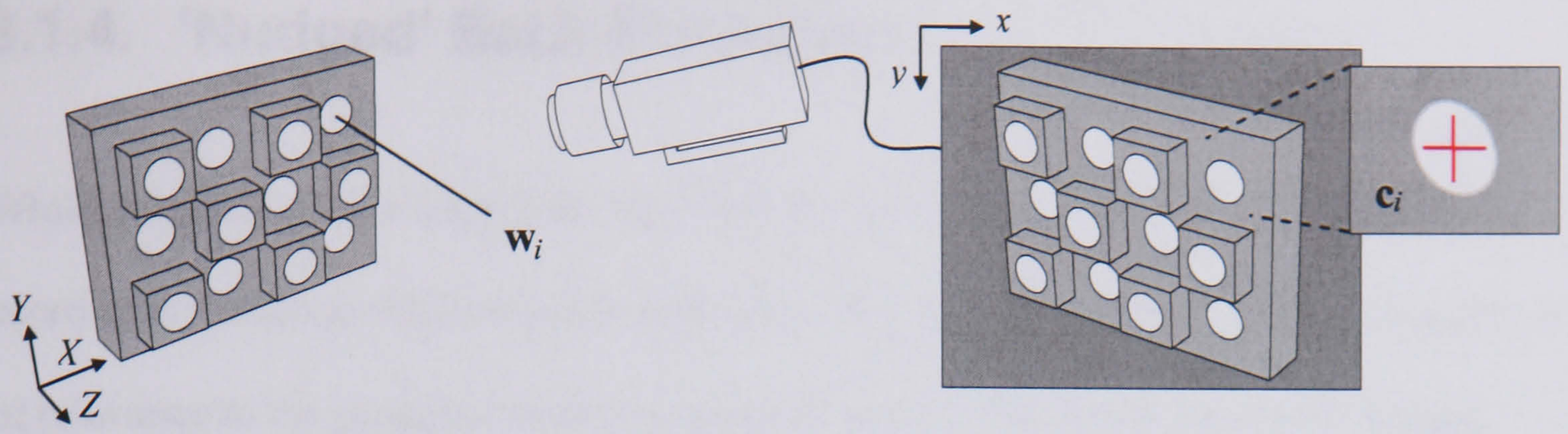

Figure 3.6 – 3D camera calibration using circular markers.

As however demonstrated by (Mateos, 2000), the image-plane centre of an obliquely viewed circle may be perceived as being in a different position to its back-projected true centre. This problem can be minimised by using a large number of smaller calibration dots, with centres calculated according to their weighted centroid, as defined below:

$$\bar{x} = \frac{\iint x\mathbf{I}(x, y)\,\mathrm{d}x\mathrm{d}y}{\iint \mathbf{I}(x, y)\,\mathrm{d}x\mathrm{d}y} \tag{3.4}$$

$$\bar{y} = \frac{\iint y\mathbf{I}(x, y)\,\mathrm{d}x\mathrm{d}y}{\iint \mathbf{I}(x, y)\,\mathrm{d}x\mathrm{d}y} \tag{3.5}$$

3.1.4. 'Nudged' Back-Projection

While the position of a laser light sheet will typically be known within the world-coordinate system to millimetre (or less) accuracy, even the smallest of discrepancies is of relevance to the proposed acquisition techniques. As shown in Figure 3.7 below, back-projection of multiple cameras' images onto a plane other than that of the light sheet can result in individual particles being perceived as occupying completely different positions.

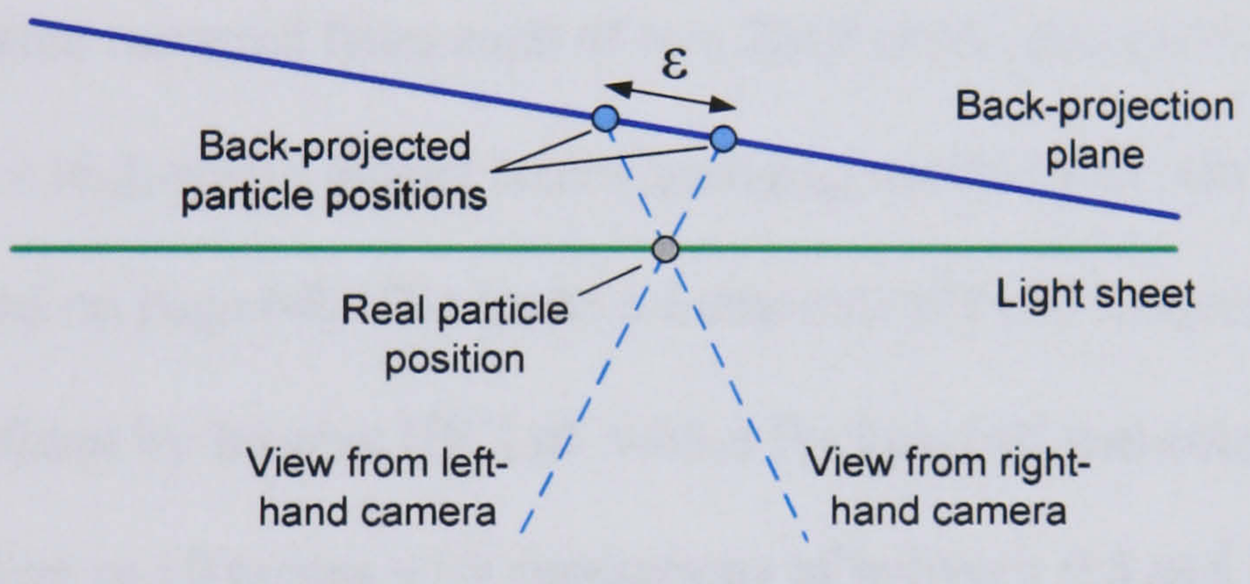

Figure 3.7 – Particle positioning error due to an unknown light sheet position.

The error ε between such cameras' back-projected images may be quantified by cross-correlating simultaneous exposures from each of the cameras against each other. (Riou, et al., 2000) used the resulting 'error maps' to correct velocity measurements acquired using two cross-facing single-exposure cameras, but in the proposed techniques, the images themselves are translated (or 'nudged') by the calculated error. This bears some similarity to the method proposed by (Okamoto, et al., 1995) who did away with camera calibration completely, though not without an associated reduction in the measurement's spatial resolution.

3.2. Experimental Application and Results

The feasibility of the multiple-exposure acquisition technique described on page 108 was tested by recording a sequence of 4 frames, from 2 cameras, at 67 kHz. This section describes not only the results but also the back-projection software used, which was similarly applied to processing the data discussed and presented in Chapters 4 – 6.

3.2.1. Experimental Apparatus

Pairs of images were captured from each of two 2048 pixel^2 pco.2000 PIV cameras, in conjunction with a high-speed pulsed laser (operating on the Q-switch 'slicing' principle described on page 64). The laser; a Lumonics HY400 frequency-doubled Nd:YAG, was refitted by Innolas UK Ltd. with a Pockels cell and controller to enable the production of up to 10 pulses with separations of between 0.5 and 30 μs. The system components are shown in Figure 3.8a on page 116, with further details given in Appendix 9.1.3 (page 336).

For a given pulse separation and number, the laser's Pockels cell controller must be carefully adjusted in order to provide pulses of equal intensity. Figure 3.8b shows the mean and standard deviation of the intensity of a typical 200 kHz 10-pulse sequence, as measured using a photodiode connected to a Tektronix TDS 1002 oscilloscope. It can be seen that the brightness of the final pulses, in particular, deviates significantly from trigger to trigger.

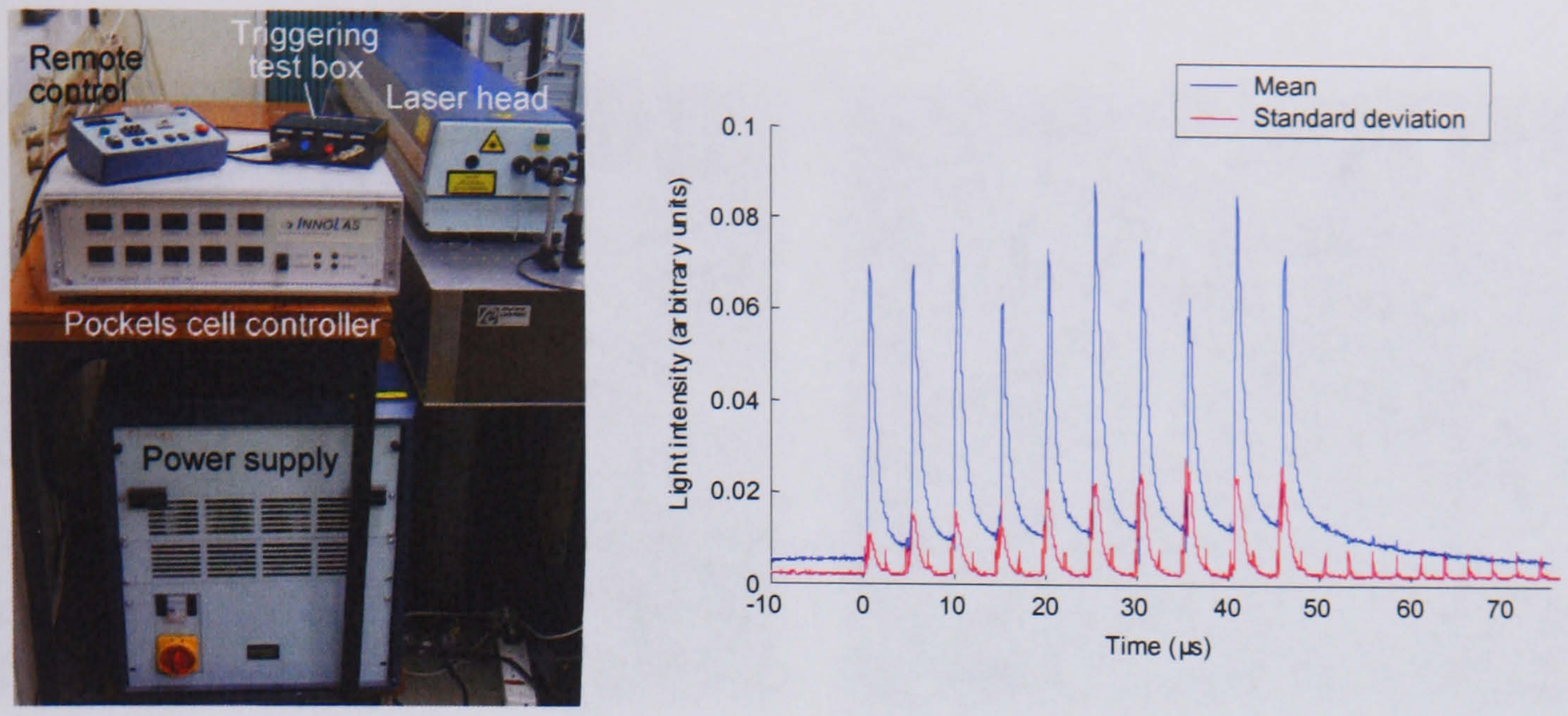

Figure 3.8a) The Innolas 10-pulse laser system; b) Statistics from 100 10-pulse sequences.

For the purposes of testing the multiple-exposure technique, 4 pulses (with separation Δt = 15 μs) were used to illuminate a simple high-speed flow, generated by passing 4 bar compressed air through a 5 × 45 mm constriction, as shown below. 1 μm diameter vegetable oil seeding particles, generated using an Oxford Lasers Laskin nozzle atomiser, were mixed with the compressed air inside the flow constrictor. The two cameras were then placed next to each other, approximately 600 mm away from the 2 mm thick light sheet, thereby subtending a half angle of 4.8°.

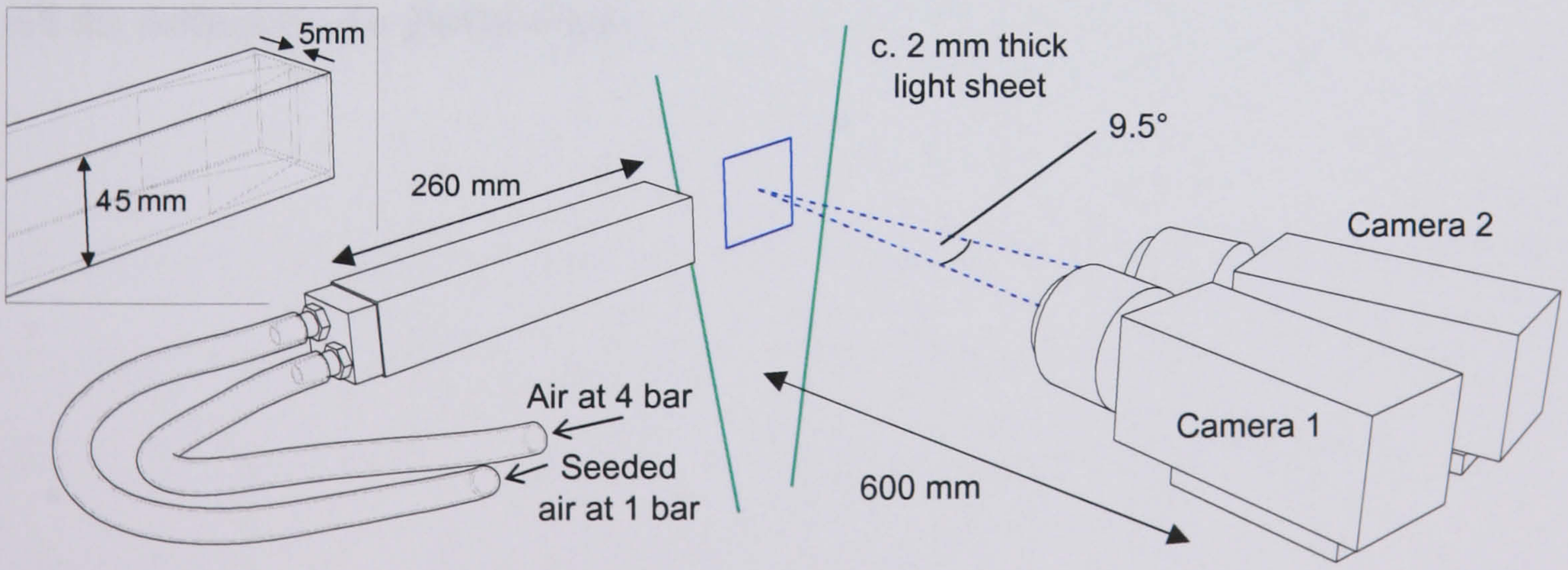

Figure 3.9 – High-speed flow experiment.

A typical pair of images from the first camera, showing an average inter-pulse particle displacement of 8.7 pixels (which equates to a flow speed of 29 m/s) are shown below:

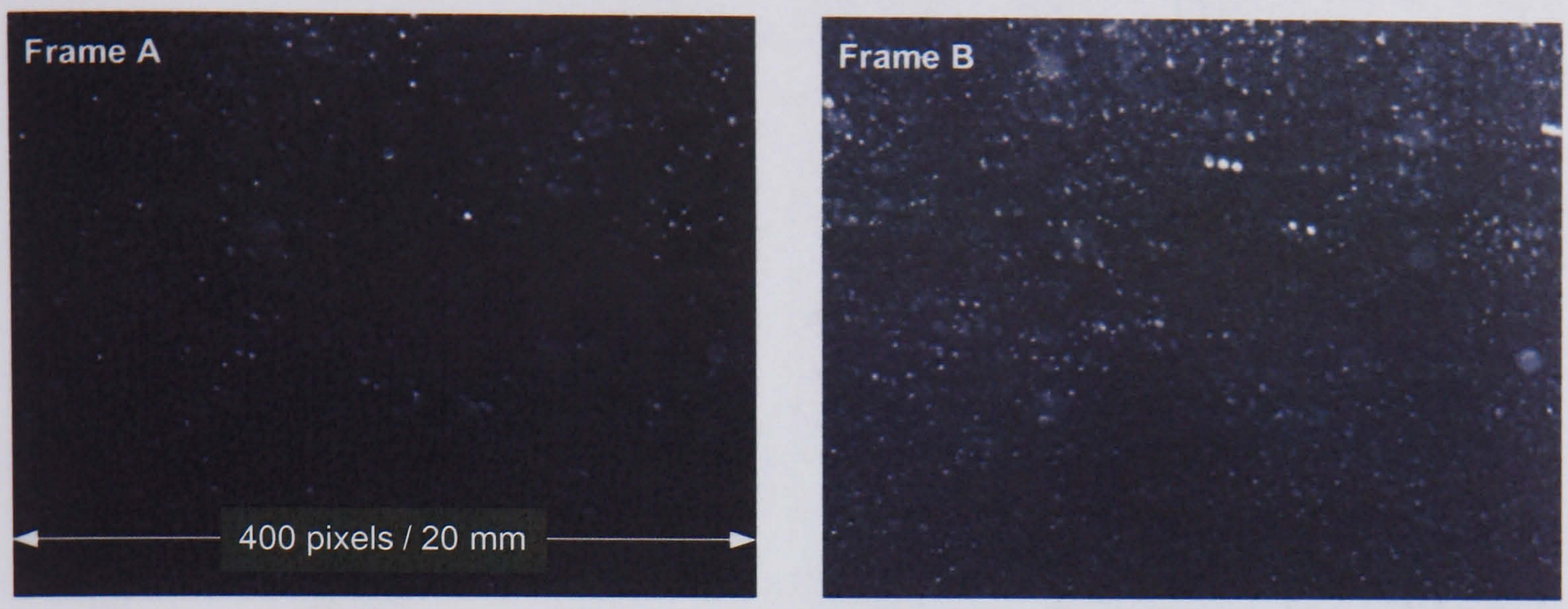

Figure 3.10 – Multiply-exposed high-speed flow images.

3.2.2. Calibration Image Analysis

The cameras were calibrated using a custom-machined, dual-level calibration plate, placed within the light sheet such that the illuminated particles would be in the same plane as its front face. The black-anodised aluminium target comprises 75 × 49 small white marker dots* spaced on a regular 2 mm grid, with alternate columns of dots spaced 2 mm apart in the z-direction. One of the front-most dots is removed in order to aid the definition of a global origin.

* Each mark is a circular, conical indentation (placed by the CNC machining tool) which was in turn filled with white paint.

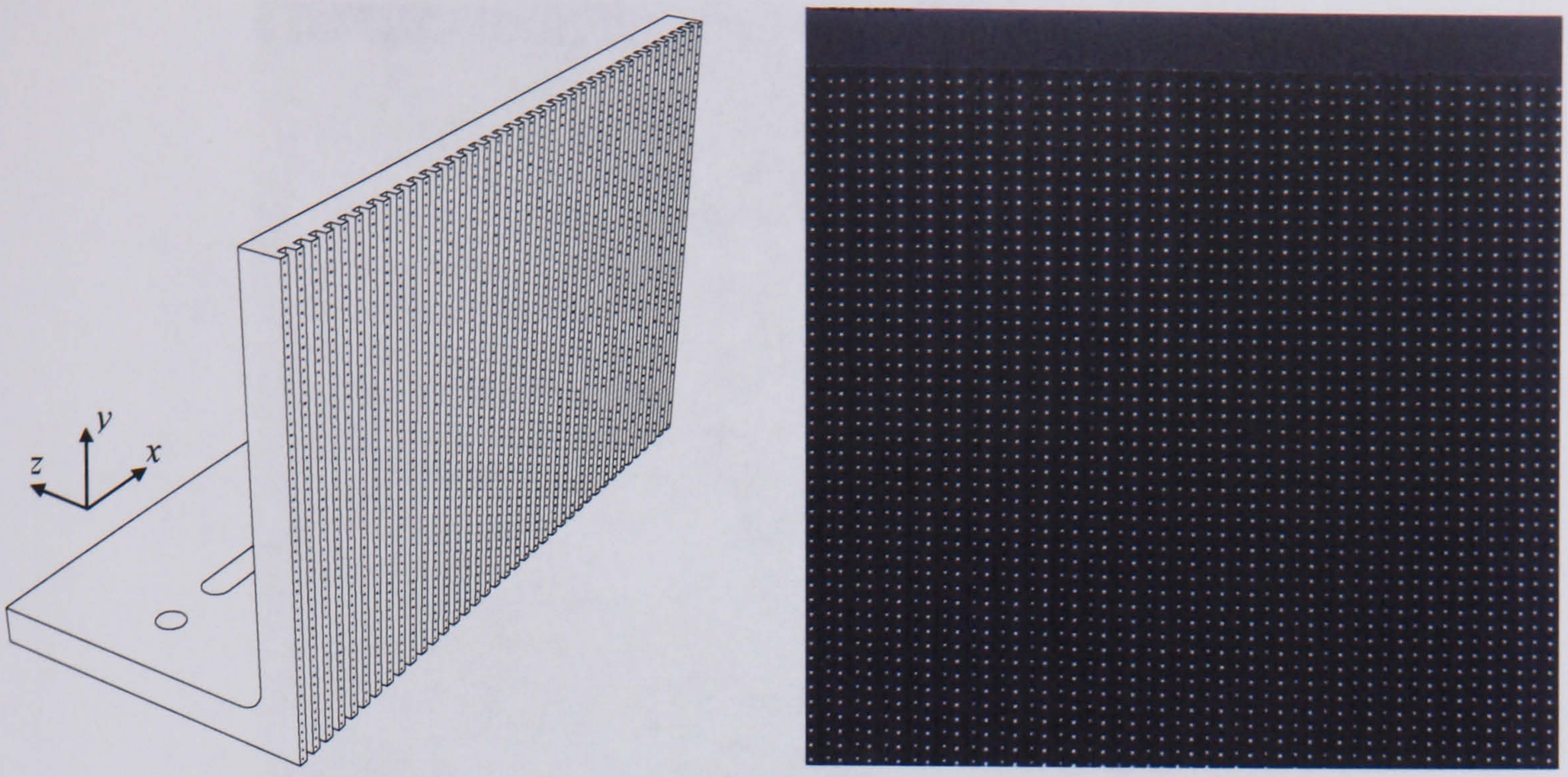

Figure 3.11a) 3D calibration plate; b) Typical calibration plate image.

Isolating each calibration point within the captured images is a relatively straight forward exercise; establishing the associated real-world coordinates is however slightly more complicated. This geometric analysis may be performed in part using the Hough transform, which is able to extract multiple features (such as lines) from a binarised image (Ehrenfried, 2002). By using the line Hough transform (which is described in Appendix 9.1.4 on page 338), the position and orientation of each row and column of the calibration plate can be found, thereby enabling every individual dot to be assigned a global coordinate.

All of the calibration images referred to in this thesis were analysed using the Matlab script that is given in Appendix 9.4.2 (page 404). The code's user interface, through which parameters such as the calibration dot spacing are set, is shown in Figure 3.12, with the script's processing operations explained in detail in Appendix 9.1.5 (page 341).

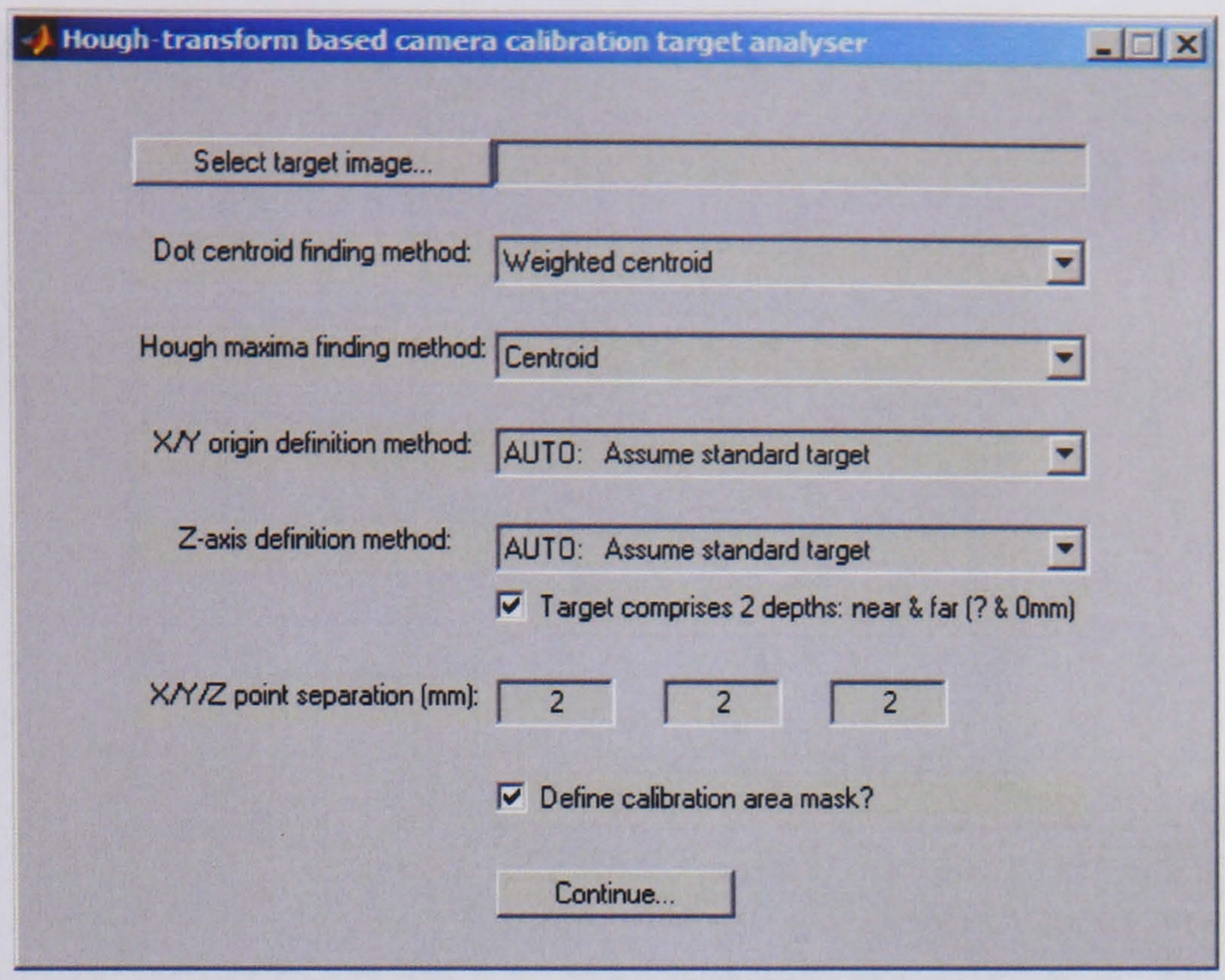

Figure 3.12 – Matlab calibration plate image analysis application.

Figure 3.13 on page 120 shows the graphical output of the script along with the form of the CSV dot position file that is written to disk. The accuracy with which the weighted centroid algorithm (given on page 113) is able to extract the dot image-coordinates may be quantified by calculating the deviation in dot separation along a whole column of dots. As shown in Figure 3.14 the standard deviation of this variation is typically of the order 0.2 pixels.

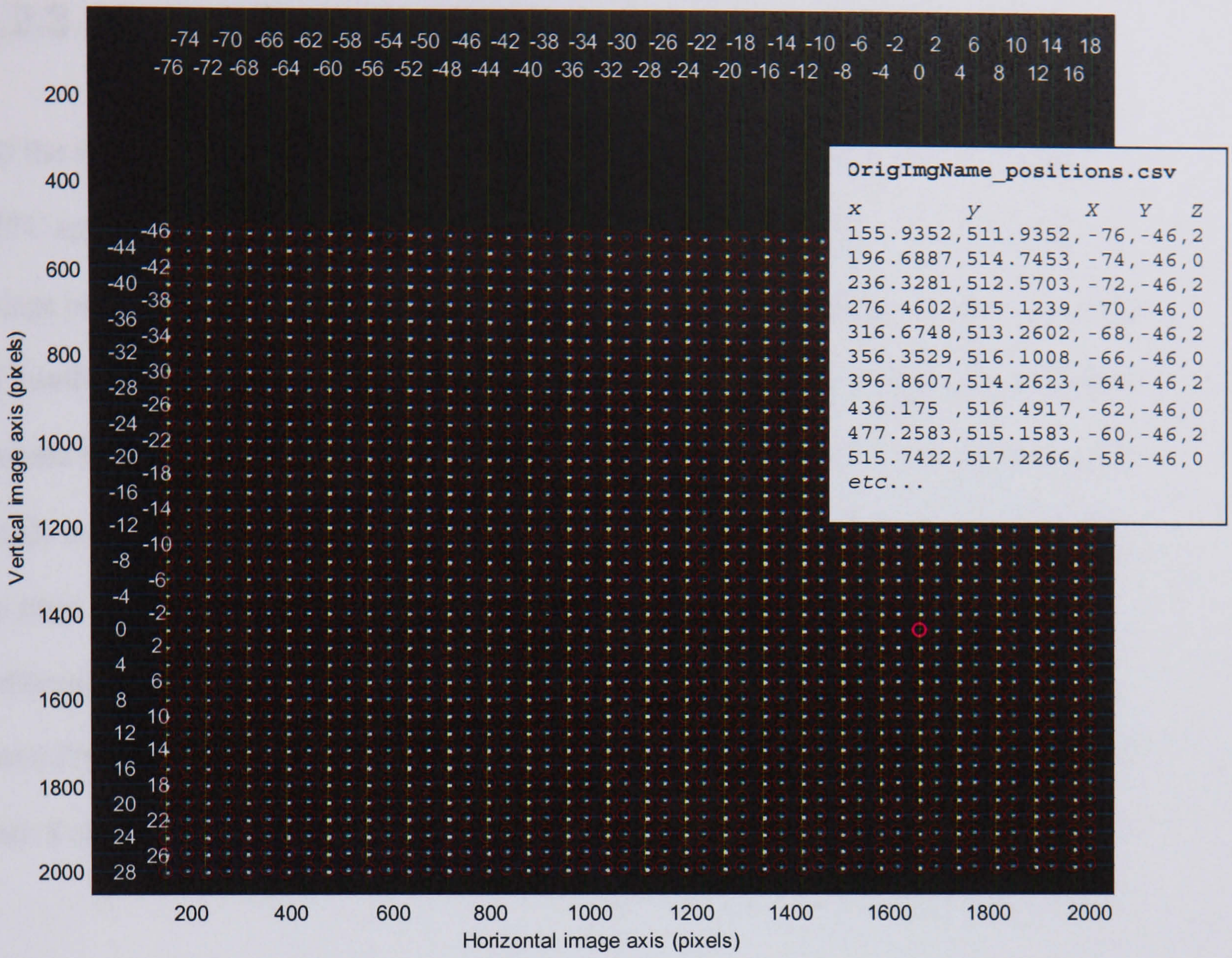

Figure 3.13 – Graphical and CSV output of the calibration image analysis script.

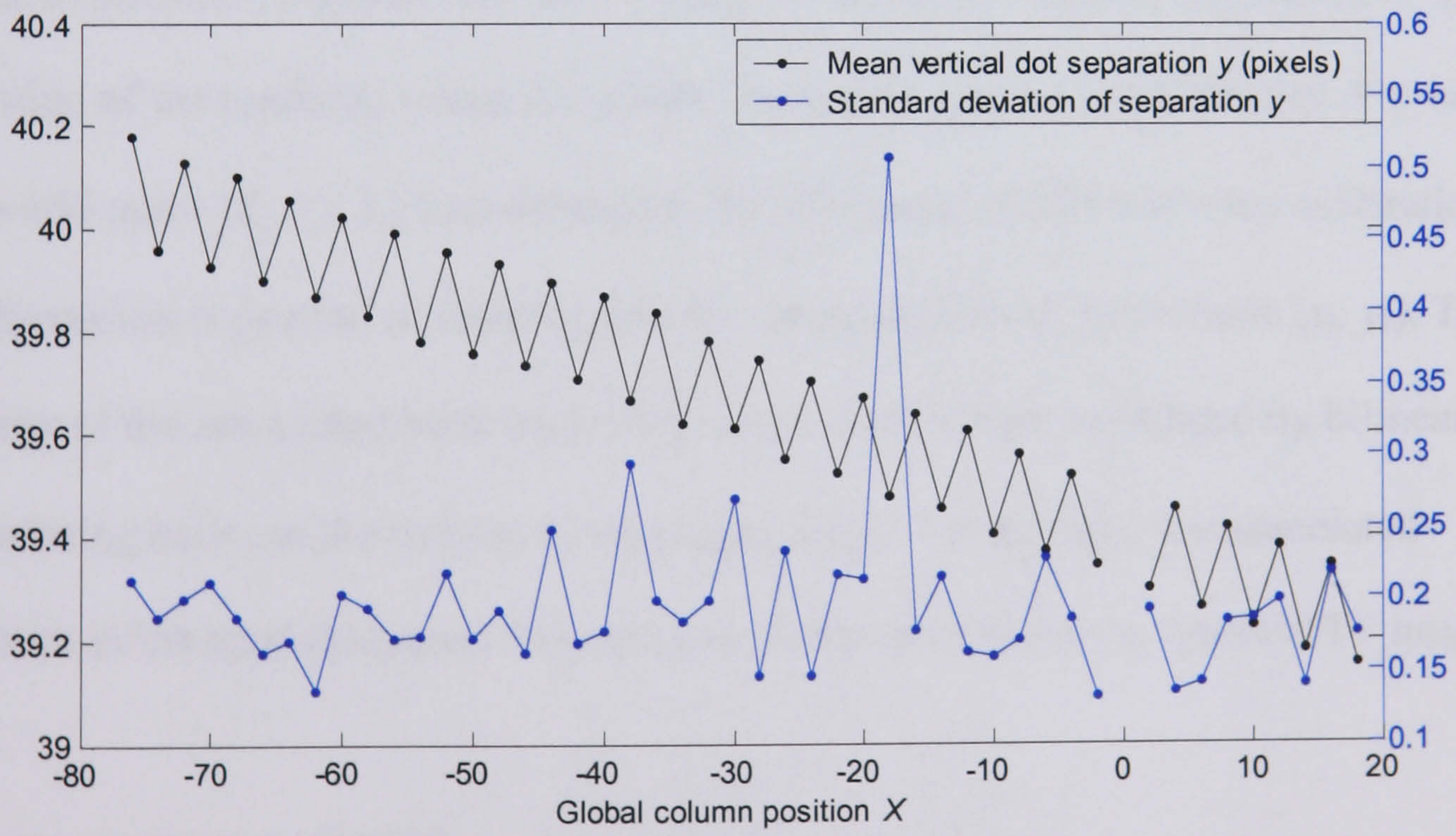

Figure 3.14 – The vertical dot separation for each column of Figure 3.13.

3.2.3. Image Back-Projection

All the PIV data described in this thesis was back-projected using a custom-written MFC application (named 'BatchProcess'), which in turn makes use of the IPL98 C++ image processing library, created by members of The Maersk Institute at the University of Southern Denmark*. IPL98's 'CPerspective' class provides an implementation of the camera calibration model provided by (Gonzales and Woods, 1993), with an additional single coefficient radial distortion correction factor, applied according to equation (3.3) on page 111. Furthermore, the class includes a linear estimation routine, to enable calibration of the model using dot coordinate pairs such as those listed in Figure 3.13. BatchProcess also makes use of the FreeImage library† to enable the back-projection of both 8 and 16-bit images, in a variety of formats.

As can be seen from Figure 3.15 on page 122, the software allows directories full of images to be back-projected onto an x-y plane of any size, with any z-coordinate. The resolution of the rendered image (in pixels / mm) may also be set arbitrarily. For each real-world point (X_i, Y_i, Z_i) thus deemed to be of interest, IPL98's inverse calibration transformation is queried in order to find the associated image coordinate (x_i, y_i). The intensity of the associated back-projected image pixel is then calculated by bilinearly interpolating between the nearest 4 raw image pixels. Fortunately, the associated reduction in the spatial Nyquist frequency is rarely of relevance to typical PIV images.

---

* IPL98 is available for download, under a GNU Lesser General Public License (LGPL), from:

http://www.mip.sdu.dk/ipl98/

† FreeImage is available under a GNU GPL from: http://freeimage.sourceforge.net/

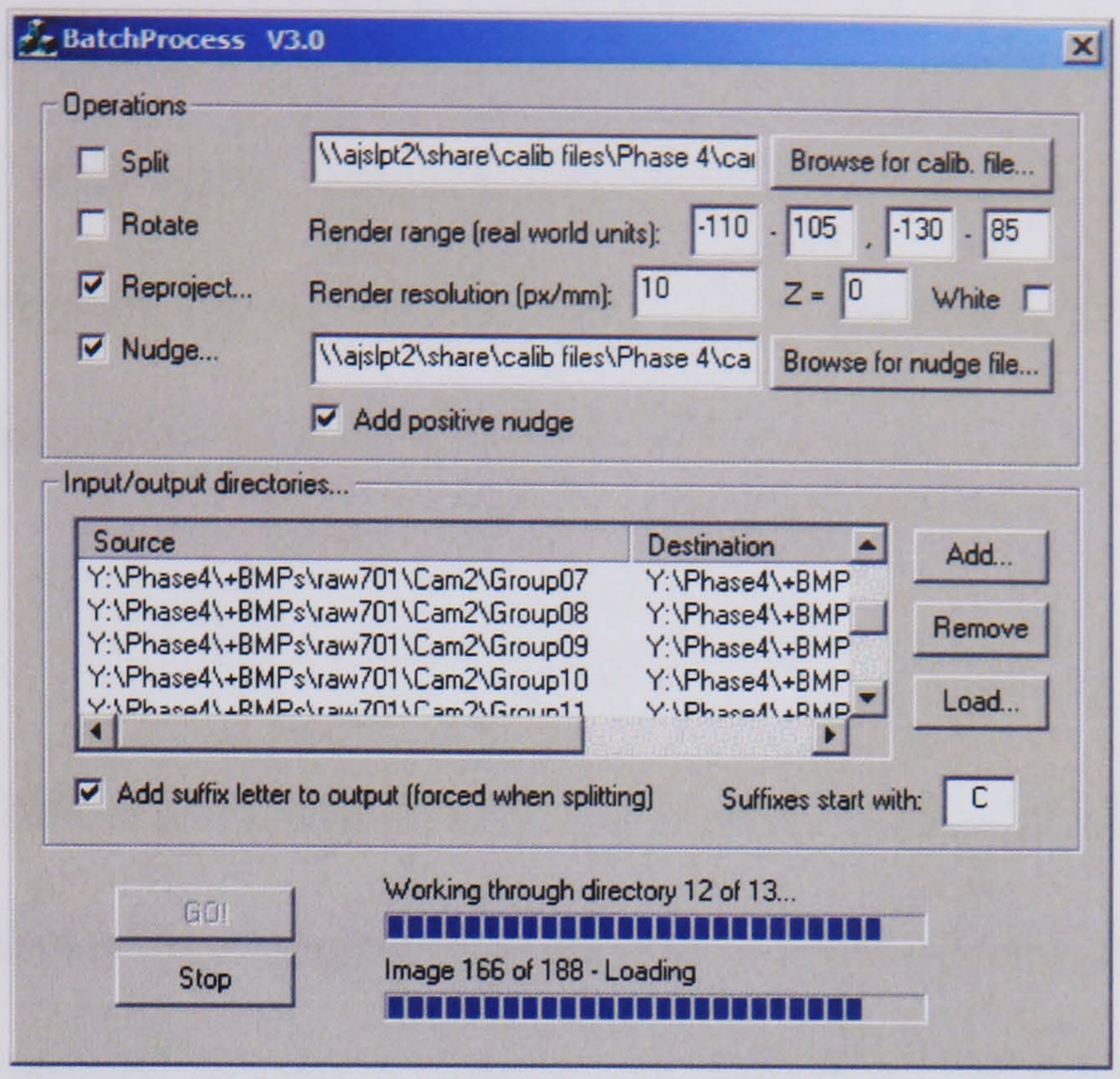

Figure 3.15 – The BatchProcess software.

The accuracy of the back-projection process, and the validity of using only 1 radial distortion coefficient, can be tested by comparing back-projected versions of the calibration plate images acquired from both cameras. Figure 3.16 demonstrates that the dots lying on the back-projection plane overlap perfectly, even in the images' corners.

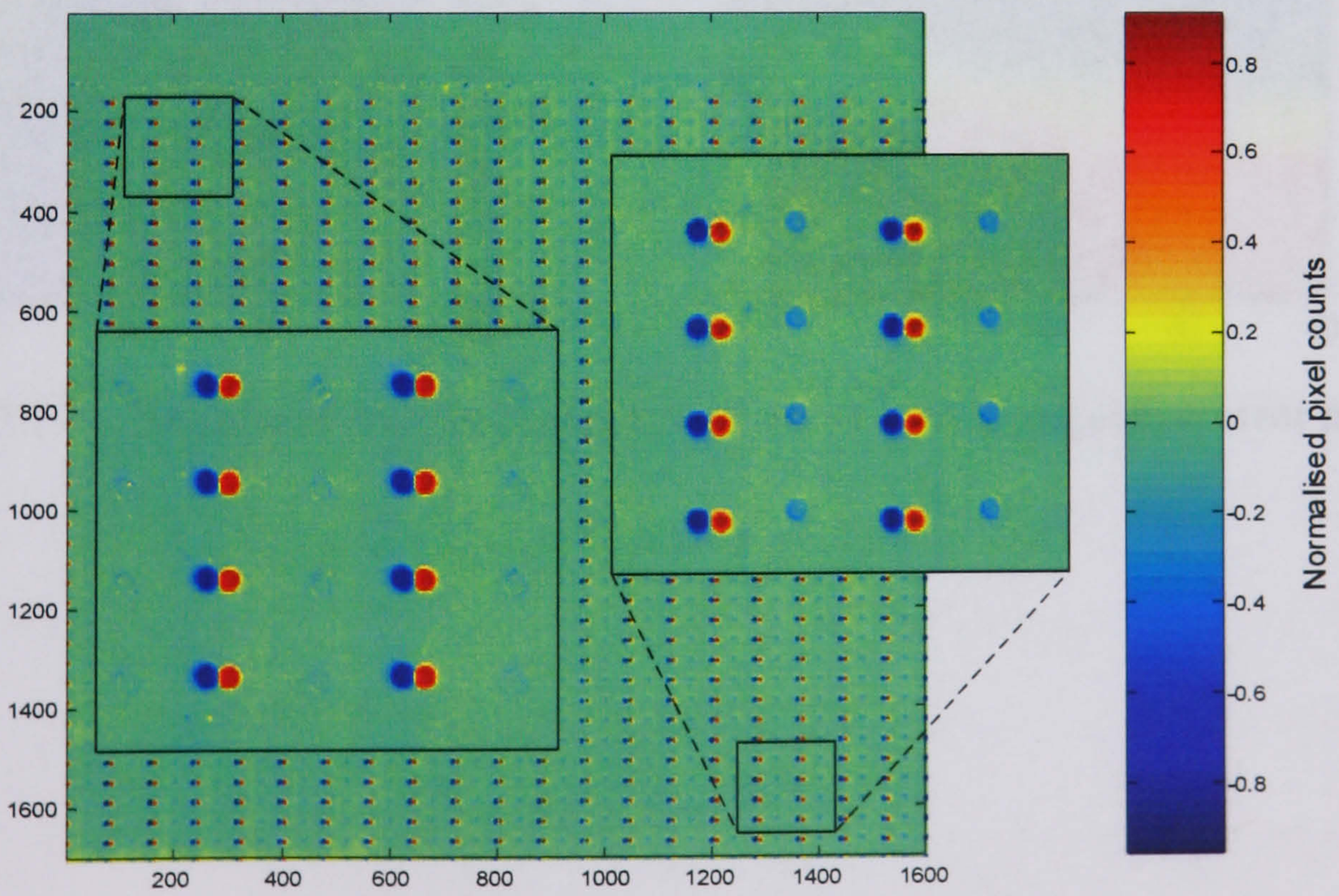

Figure 3.16 – The difference between back-projection calibration images.

The BatchProcess software is also able to 'nudge' images (as explained in Section 3.1.4) using vector 'error maps' exported from any popular correlation application. For each back-projection point considered, the value of the supplied error map at (x_i, y_i) is extracted using bilinear interpolation and the image-coordinate incremented by that amount.

Figure 3.17 shows the back-projection error map for the setup described on page 116. The map was calculated by averaging 20 instantaneous-exposure cross-correlations, and it reveals a notable angular deviation between the light sheet and calibration plate, about an (almost) vertical axis.

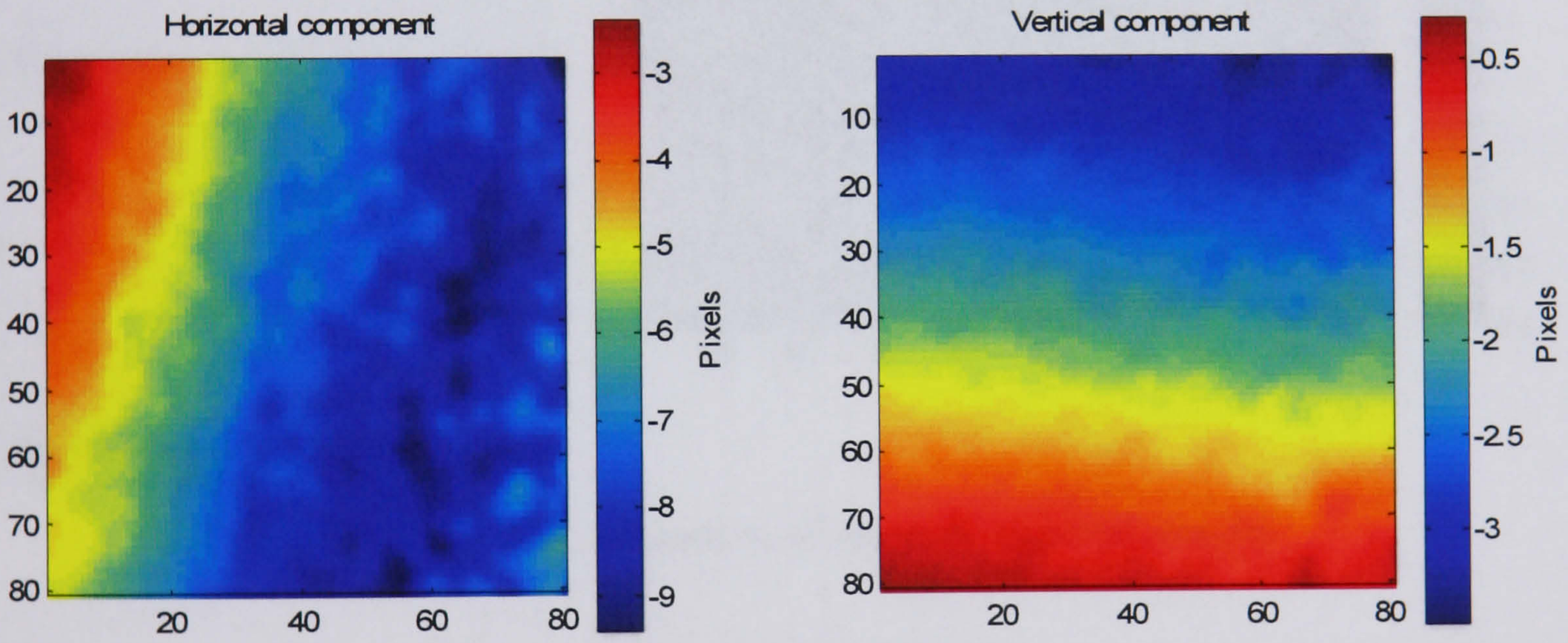

Figure 3.17 – Horizontal and vertical components of a back-projection error map.

3.2.4. Image Subtraction

In order to test the most crucial stage of the multiple-exposure technique – image subtraction – pairs of double-exposures were captured from the cameras in 16-bit, then back-projected and 'nudged' using the error maps shown in Figure 3.17. Inverted 180 × 120 pixel subsections of a typical coincident image set are shown below, with the last two exposures – acquired by camera 2 – shown added together. The difference in intensity between the two is shown on the right.

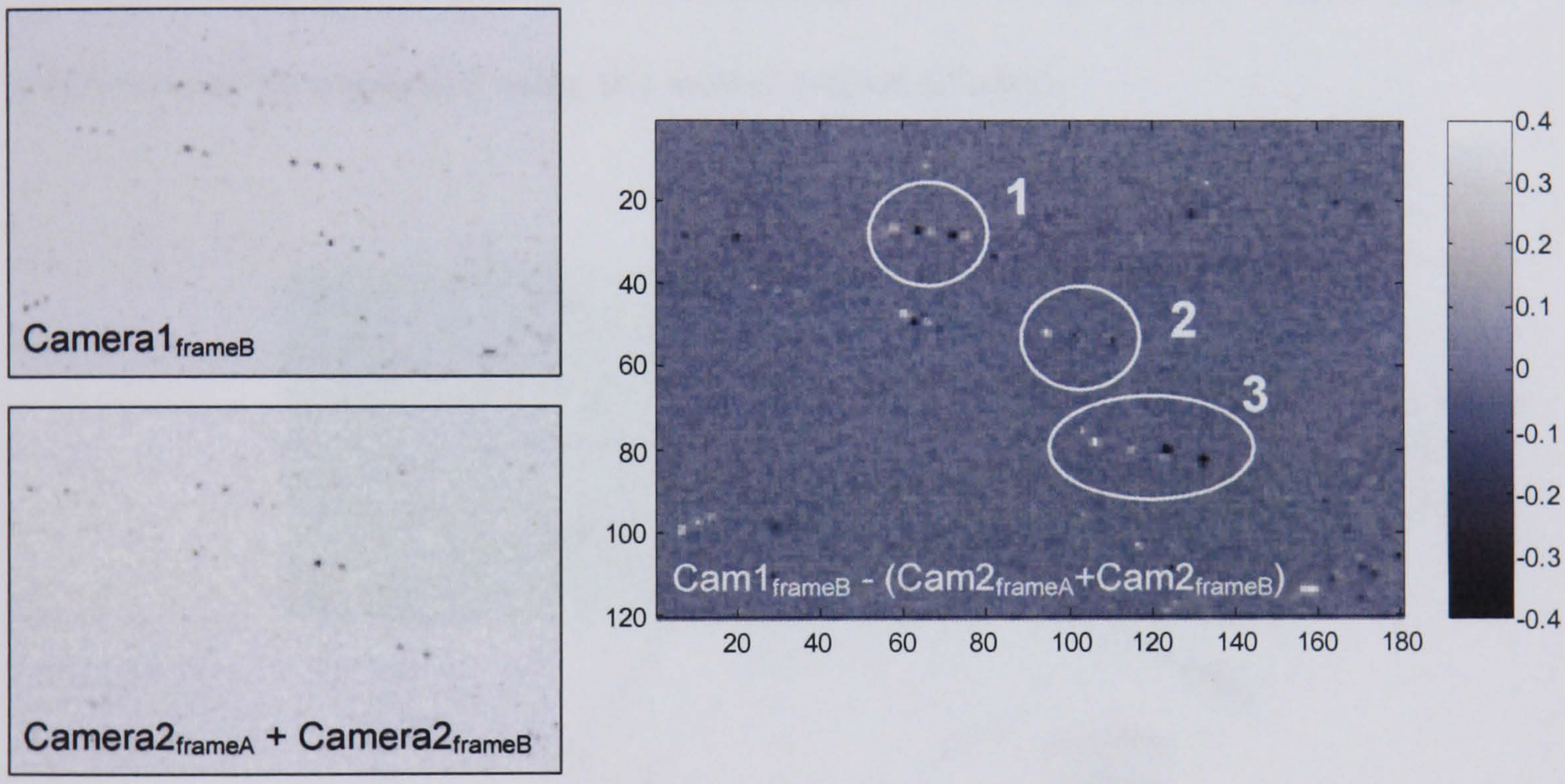

Figure 3.18 – The subtraction of multiply-exposed images.

For the example shown above, it can be seen that the multiply-exposed particles in the circled position labelled '2' overlap almost perfectly, while those in positions 1 and 3 are out of alignment by up to 10 pixels horizontally. While binary morphological image processing operations could be used to subtract such offset particles, this approach would require an unfeasibly low particle density, and an unattractively high inter-pulse particle separation.

3.3. Conclusions

3.3.1. Light-Sheet Limitations

The non-overlapping of particles in Figure 3.18 has shown that the multiple exposure time-series acquisition technique is impractical for the camera arrangement shown on page 116. This problem arises from the fact that even completely accurately back-projected images will show particles in different positions if the light sheet is anything more than a negligible thickness. This maximum error ε in the particles' perceived positions can be estimated using the model presented below:

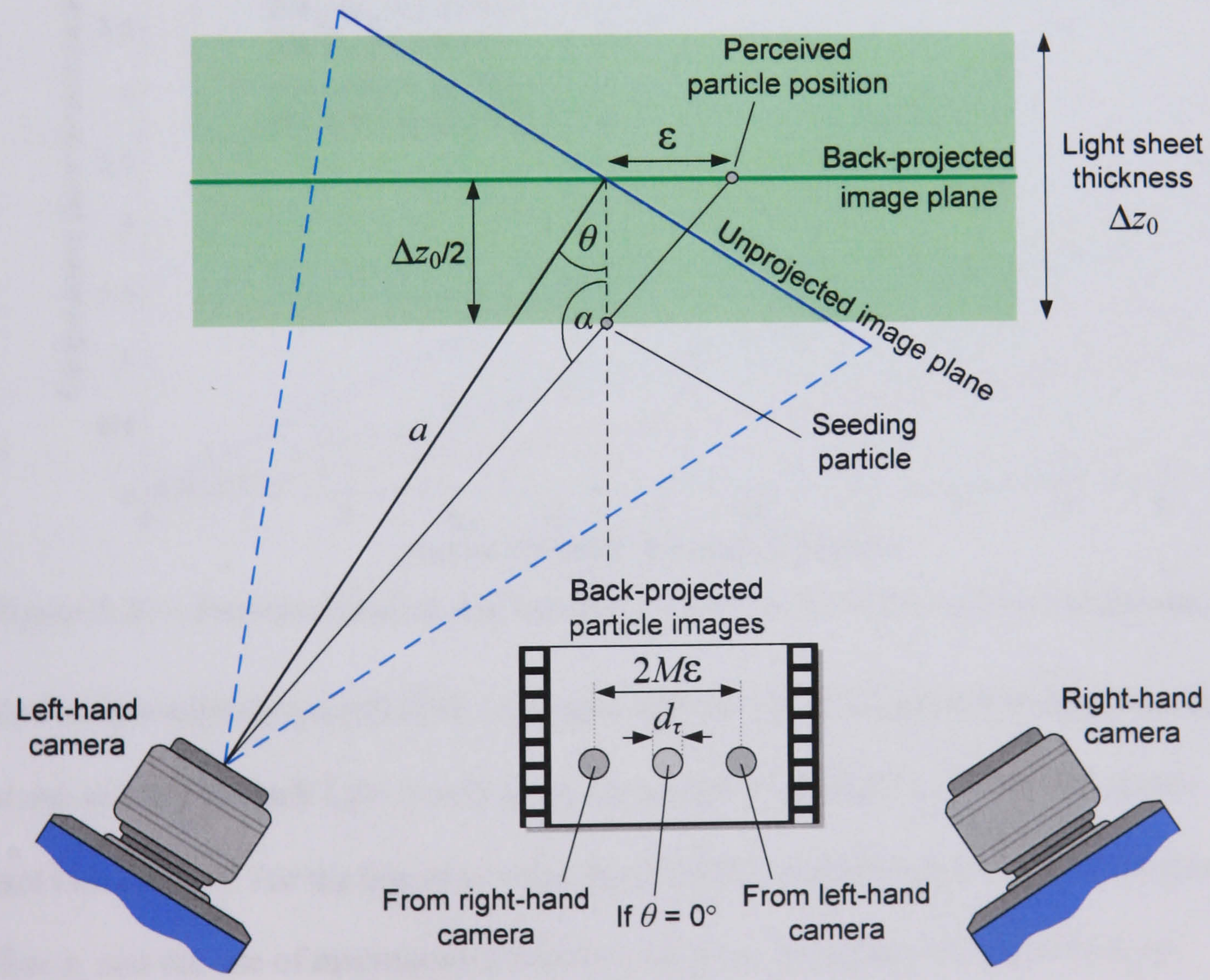

Figure 3.19 – Particle image positioning error, caused by a thick light sheet.

$$\varepsilon = \frac{\Delta z_0 \sin(\pi - \alpha)}{2\sin(\alpha - 0.5\pi)} \quad \text{where:} \quad \alpha = \pi - \sin^{-1}\left(\frac{a\sin\theta}{\sqrt{a^2 + 0.25\Delta z_0{}^2 - a\Delta z_0\cos\theta}}\right) \tag{3.6}$$

Figure 3.20 compares the recorded particle image diameter d_τ (calculated using equation (2.29) on page 51), with the maximum particle position error $2M\varepsilon$, for a 2048 px^2 camera with 7.4 μm pixels, positioned 0.5 m from a 532 nm light sheet. Values are given for a number of sheet thicknesses and lens parameters, over a range of camera angles:

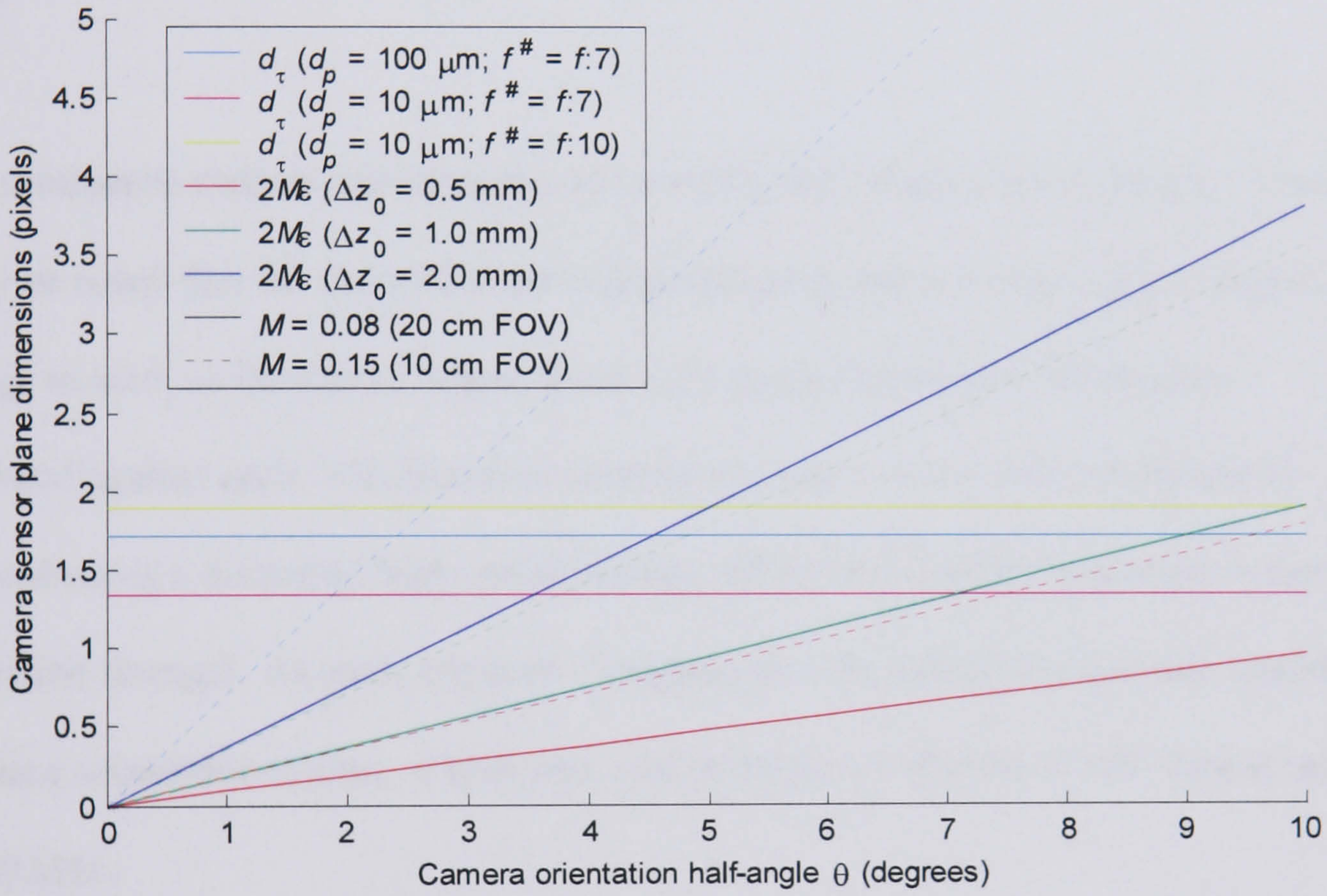

Figure 3.20 – Particle diameter and maximum position error for various camera angles.

The multiple-exposure acquisition technique therefore only becomes feasible (assuming the use of a 2 mm thick light sheet) when the camera half-angle $\theta \leq 2°$ as it is at this point that $M\varepsilon < d_\tau$. For the laboratory test described, this would entail a 1.5 m camera offset a, and the use of macroscopic lenses to maintain a reasonable magnification factor.

3.3.2. Single Exposure Acquisition

Single exposures acquired from physically separate cameras (c.f. Figure 3.2, page 107) suffer from exactly the same particle positioning errors as multiply-exposed images. For this reason, the few TR-PIV studies that do use separate cameras involve either light-sheets of differing polarisation, such that individual vector maps may be correlated using 2 frames from the same camera (Humphreys and Bartram, 2001; Wernet, et al., 2003), or a face-to-face arrangement of 2 cameras, thereby enabling $\theta = 0°$ (Riou, et al., 2000).

With symmetric camera orirentations, and a sufficiently high seeding density, however, it may be noted that the individual particle positioning errors within a given region average to zero, as illustrated below. Such back-projected images, when cross-correlated against each, will therefore produce the same vector fields as would be achieved using a dedicated high-speed camera, albeit with a slight reduction in the correlation strength. As such, the next 3 chapters discuss the application and results of a 5 camera acquisition system, which was used to capture 6 frames of PIV data at rates of up 330 kHz.

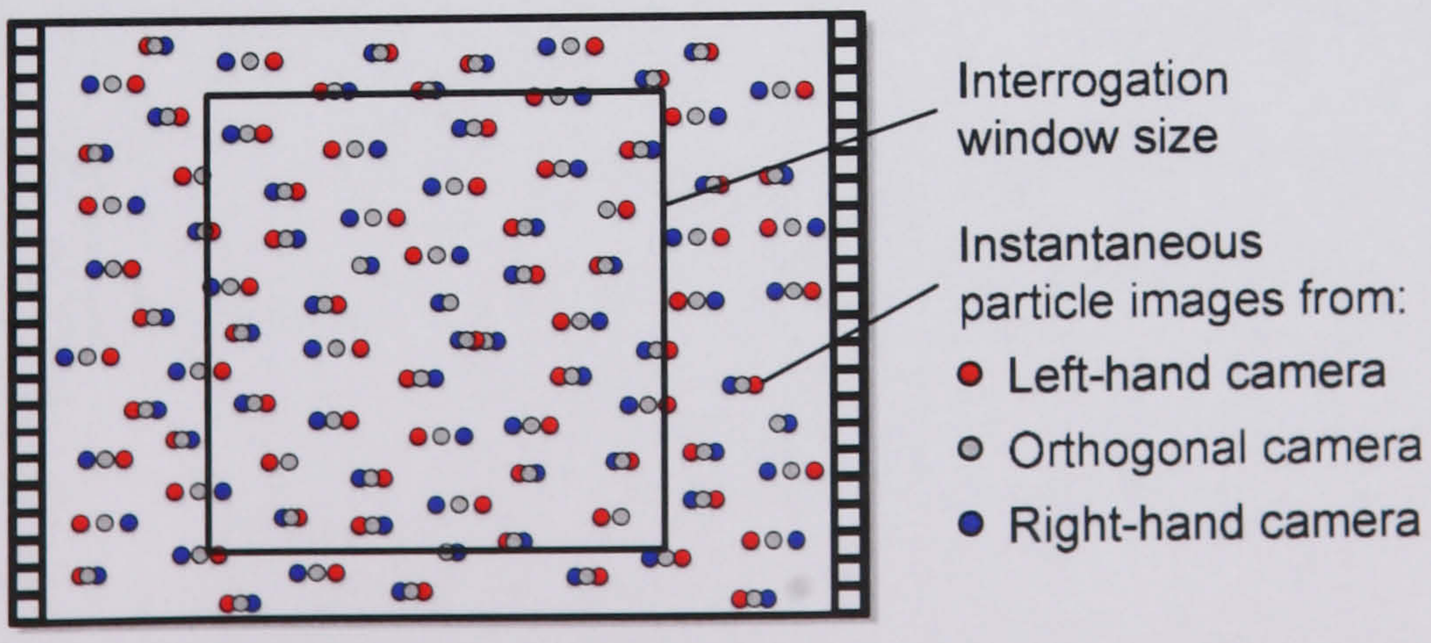

Figure 3.21 – 3 overlapped views of particles in a thick light sheet.

4. Coaxial Jet Noise Project: Introduction

4.1. Introduction

The CoJeN (Computation of Coaxial Jet Noise) project is a €5.7m EU 6th framework research programme, in the category 'Aeronautics and Space'. CoJeN will run for 38 months from 1st February 2004, and is being managed and coordinated by QinetiQ Ltd.

4.1.1. Aims & Objectives

As stated on the associated European Union webpage*, the principle objective of CoJeN is:

> *'To develop and validate prediction tools which can be used by the aerospace industry to assess and optimise jet-noise reduction techniques.'*

Noise levels from the jet engines of commercial aircraft are currently the biggest obstacle to the expansion of the air transport industry. As explained in Chapter 1, the plight of residents living around airports has already led to expansion plans being rejected, night curfews being imposed, and several major airports thus operating at the limit of their capacity. In an attempt to reduce this constraint on the industry's growth, and help meet the objectives of the EU's 2001 'European aeronautics: a vision for 2020' report (namely that Europe should become the '*uncontested world leader in the field of aeronautics by 2020*'), the Advisory Council for Aeronautics Research in Europe (ACARE) initiated the X-Noise initiative.

* http://ec.europa.eu/research/aeronautics/projects/article_3691_en.html

As part of the '2020 Vision', ACARE proposed a 10 dB reduction in new aircraft noise levels between 2000 and 2020, and the X2-Noise project (it is now in its 2nd phase) is responsible for designing and delivering an appropriate technology roadmap. This consists primarily of the development of low-noise aircraft components, designed by means of enabling technologies such as Computational Fluid Dynamics (CFD), Computational Aero-Acoustics (CAA), experimental databases for validation, and the associated technology transfer.

The CoJeN project, and its framework 5 predecessor JEAN (Jet Exhaust Aerodynamics and Noise), serve to supply these enabling technologies, namely CFD, CAA and experimental data sets. Specifically, whereas JEAN dealt only with single-stream jets, CoJeN will extend the developed codes and noise prediction methodologies to coaxial jets of arbitrary nozzle geometries, thereby bringing the research further in line with industry's requirements.

The technical objectives of CoJeN are thus defined in the project proposal:

- *'To identify and improve optimal CFD techniques for the prediction of jet flow development from coaxial nozzles of arbitrary geometry.*
- *To develop aero-acoustic codes which can predict the acoustic fields from the CFD results.*
- *To acquire aerodynamic and acoustic data with which to validate these codes.'*

4.1.2. Project Structure

The CoJeN project involves 24 academic and industrial partners from all over Europe, a complete list of which is available in Appendix 9.1.6 (page 347). The partners and workload were divided between 4 work packages, which align closely with the technical objectives of the project listed on the previous page. The tasks assigned to each group, and their scheduling within the project, are shown below:

	Year 1				Year 2				Year 3			
	Q1	Q2	Q3	Q4	Q1	Q2	Q3	Q4	Q1	Q2	Q3	Q4
WP0 – Project Management												
0.1 – Management												
0.2 – Specifications												
0.2 – Assessment												
WP1 – Flow Prediction												
1.1 – RANS simulation												
1.2 – LES/DES simulation												
1.3 – Vortex methods												
1.4 – Technology transfer												
WP2 – Generation & Propagation												
2.1 – Acoustic analogy												
2.2 – Direct methods												
2.3 – Hybrid methods												
2.4 – Technology transfer												
WP3 – Meas. Tech. & Experiments												
3.1 – Develop advanced meas. tech.												
3.2 – Test preparation & campaign												
3.3 – Data analysis												

Table 4.1 – CoJeN project schedule.

The University of Warwick (and therefore the author) was a WP3 partner, involved in the 'Measurement Techniques and Experimentation' work package.

4.2. Jet Noise

4.2.1. Background

Near-ground aircraft noise originates from a number of airframe components, such as the landing gear, auxiliary power unit and high-lift slats and flaps, but the most significant source is the jet engine, shown in Figure 4.1 below. Turbofan engine noise is produced both internally and externally, with internal noise originating primarily from the inlet duct, combustor, compressor and (most notably) fan, which produces both narrow and broadband sound. During takeoff however, the fan noise is equalled by that originating from the exhaust.

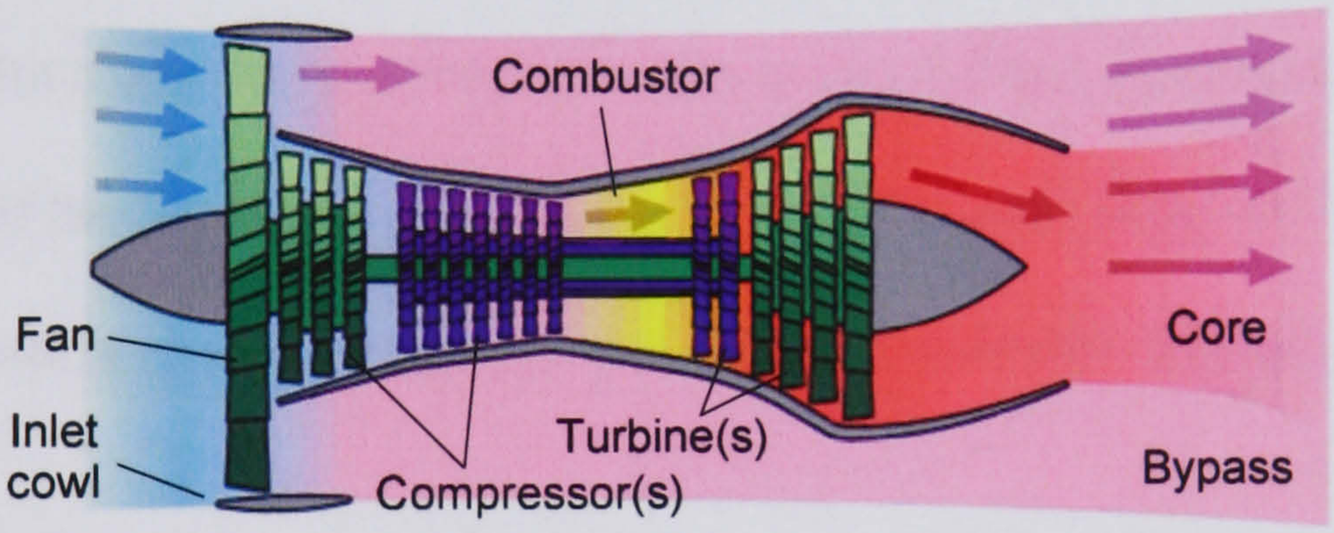

Figure 4.1 – A turbofan engine (Wikipedia website).

While supersonic jets will produce 'shock noise' from within the core flow, the primary source of exhaust noise in commercial airliners stems from the end of the primary potential core, where high speed air is forced to mix with the ambient flight-stream. Figure 4.2 on the next page illustrates the 4 main mixing regions in a coaxial flow, each of which produces noise of a different frequency range and intensity, the perception of which also differs depending on angle. Exhaust noise 'source regions', and the measurement thereof, are discussed in detail by (Smith, 2004).

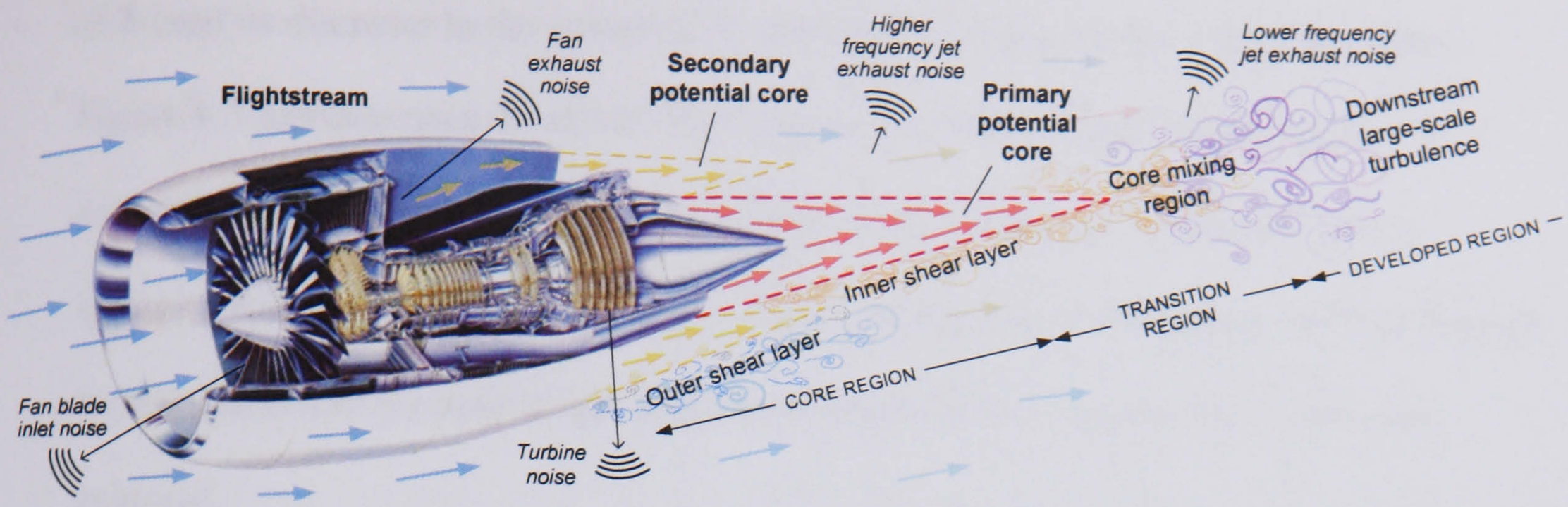

Figure 4.2 – Coaxial jet mixing regions.

4.2.2. Noise Reduction Techniques

Reductions in internally produced engine noise have been achieved by applying linings to the inlet lip and interior of the cowl and nacelle (which houses the engine); by modifying the fan blade design; even by active control of the pressure field inside the inlet cowl and of the flow around the blades tips (Krothapalli, et al., 2004). The CoJeN project is however primarily concerned with reducing the noise originating from the exhaust.

Since their introduction, the bypass ratios* of turbofan engines have steadily increased, leading to a continuous improvement in fuel efficiency. Higher bypass ratios also mean that a greater proportion of the exhaust flows at 'low' speed. As stated by Lighthill's eighth power law, the sound produced by a jet is proportional to its speed to the power

---

* Defined as the ratio between the bypass and core stream's mass flow rate. Engines with a higher bypass ratio are able to extract closer to 100% of the power generated by the engine (for a given amount of fuel), by providing thrust to both the core *and* bypass streams. The result is an engine with a high total mass flow rate, but a small, 'lean' burn in the combustion chamber.

of 8 (and its diameter to the power of 2), meaning that large noise reductions ensue. Figure 4.3 demonstrates the effect that bypass ratio improvements have had on commercial aircraft engine's perceived noise levels (measured in EPLdB*). As is apparent from recent progress however, future increments in the bypass ratio are limited by the associated increase in fan diameter or turbine blade temperature resistance required.

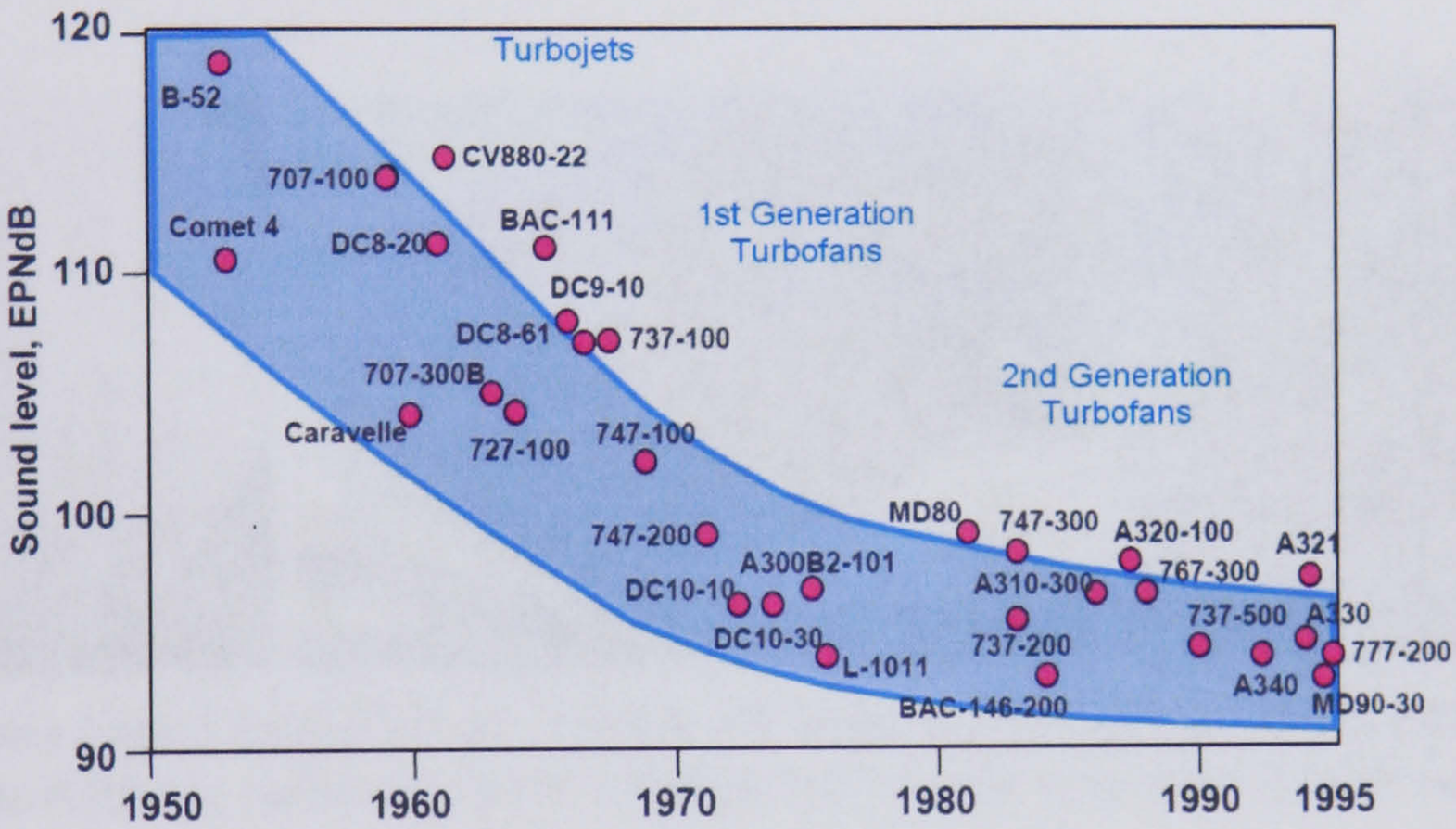

Figure 4.3 – The effect of increasing bypass ratios on jet noise, from (Neise, 2004).

For a given bypass ratio, it is therefore necessary to reduce exhaust noise by minimising the area over which the flow is turbulent. At the most basic level, this is achieved by designing a nozzle with a geometry that encourages the flight-stream, bypass and core flows to mix as soon after the engine as possible. An extended 'long' cowl which places the secondary nozzle exit *downstream* of the core (c.f. Figure 4.4a on page 135) will also stimulate such inner shear layer mixing, as will an eccentric arrangements of the two nozzle exits (Papamoschou and Debiasi, 2002).

* Based on Fletcher and Munson's lines of Equal Perceived equal loudness, c.f. (Rossing, et al., 2001).

An alternative (or additional) approach to mixing enhancement uses asymmetric features such as vanes, lobes, serrations or chevrons, to introduce vortices into the jet, which in turn encourage the exhaust's energy-rich large-scale structures to interfere with each other. Such devices are typically applied as part of 'hush kits' (used to quieten older, low-bypass ratio engines) and they have been shown have reduce noise by up to 4 dB; the effect on the flows themselves having been demonstrated using PIV by (Bridges, et al., 2003; Bridges and Wernet, 2004).

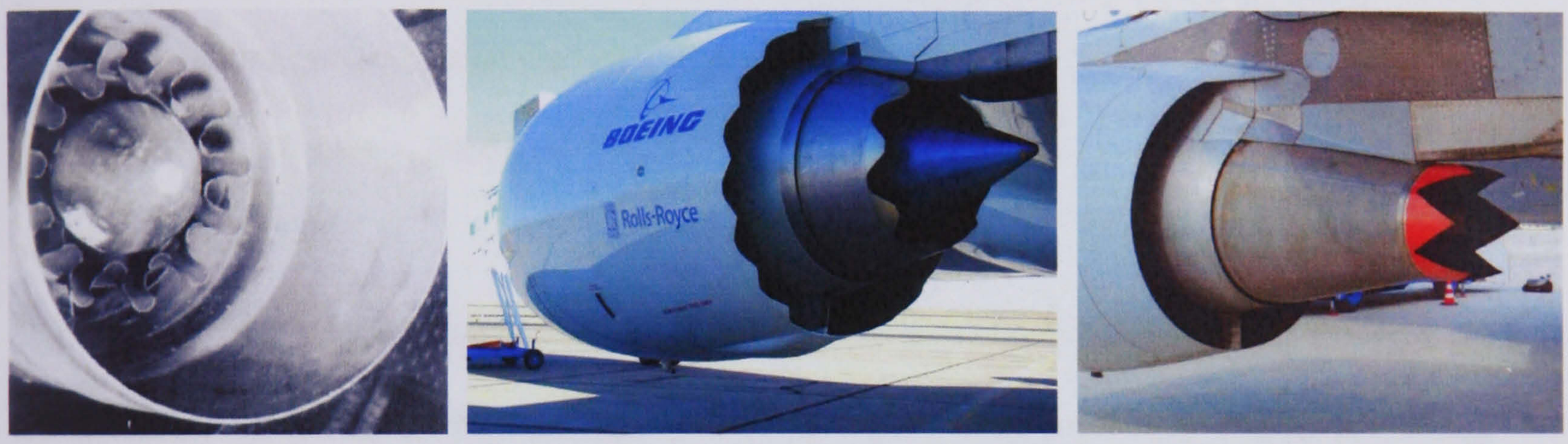

Figure 4.4a) Lobed forced mixer (NASA AT website); b) Serrated Rolls Royce Trent 800 engine (Qinetiq website); c) GE CFM56-5a5 engine with chevrons (Neise, 2004).

4.2.3. Noise Prediction Techniques

The high cost of building and testing engine prototypes means that progress in noise reduction is dependent upon the ability to theoretically model and predict the sound produced by a given nozzle geometry. Research into the generation of noise from turbulent flows was pioneered by (Lighthill, 1952), and his Acoustic Analogy still forms the heart of most aeroacoustic research. The analogy is based on the Navier-Stokes equations, rearranged in a form that gives the integrated noise field in terms of 'Lighthill's stress tensor', which contains terms for the spatial distribution of the flow's velocity, pressure and viscosity (Tam, 1998).

The Lighthill Analogy has been modified and improved many times in order to incorporate terms that represent the latest in jet noise understanding – the fact that turbulent structures are of different sizes (and therefore produce different frequencies), and the way that noise is refracted, for example. As computational power has grown however, it has become possible to calculate the acoustic pressure field *directly*, by means of CFD on a very small scale. Unfortunately, such direct numerical simulations (DNS) currently take many months to produce enough 'frames' of data to calculate noise spectra, meaning that current CAA is still mainly based on analogy or 'hybrid' approaches (Bodony, 2005).

The accuracy of noise prediction and CFD are directly related, as the former is based on the output of the latter. As such, the first of the CoJeN work packages is dedicated to the expansion and application of the latest codes for the 4 main (non-DNS) turbulence models (c.f. Table 4.1). While time-averaged RANS modelling is well established and has been shown to agree well with experimental single-stream jet measurements (Farassat, et al., 2004), instantaneous LES and DES models (which can be thought of as being analogous to multi-pass correlation techniques) should be better able to simulate the small-scale turbulence in a complex, hot coaxial jet flow.

4.3. CoJeN Experimental Work

4.3.1. Test Nozzles

In consultation with Rolls Royce (the experimental work package leader) a series of three $^{1}/_{10}$ scale engine nozzle geometries were specified. The coplanar nozzle, shown on the right of Figure 4.5, comprises a simple parallel design intended to produce a 'model' coaxial flow, thereby enabling comparisons between the acquired data and previous fundamental research. The short cowl nozzle, shown on the left, is instead representative of a modern commercial high bypass ratio engine, where convergent walls and a central 'bullet' are included to encourage early mixing between the streams. A 20-serration cowl was also designed, in order to test its effect on the short cowl geometry.

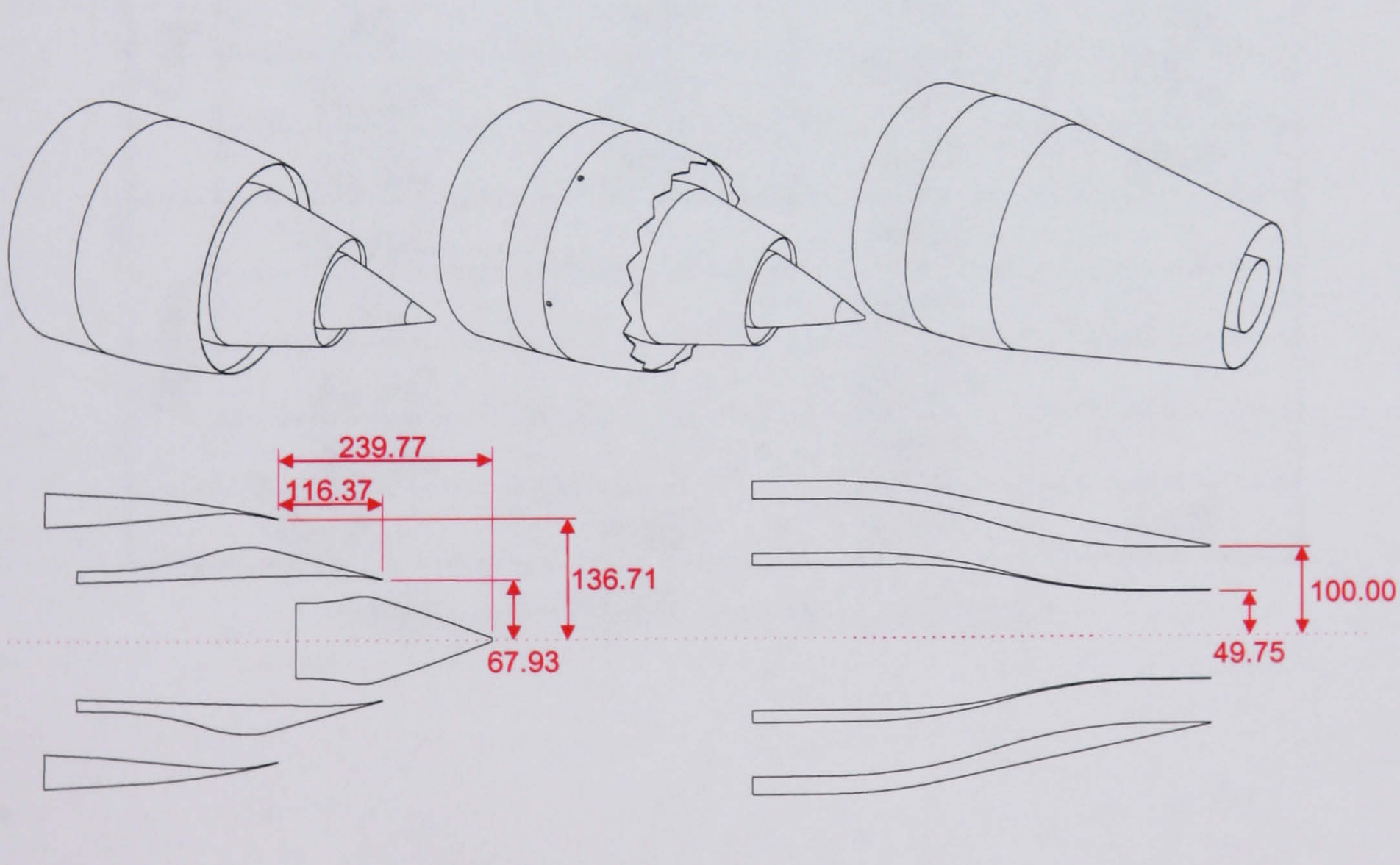

Figure 4.5 – Plain and serrated short cowl and coplanar nozzle geometries.

The reference diameters D_{REF} used for flow non-dimensionalisation in Chapter 6 are those of the secondary nozzle exit, i.e. 200 and 273 mm.

4.3.2. Test Operating Conditions

The jet conditions considered for the CoJeN test were designed to be representative of those used during aircraft takeoff – the period of greatest exhaust noise production. In order to test the prediction codes as completely as possible however, a wide range of flow conditions were considered, such that the relative influence of each noise source region (c.f. Figure 4.2 on page 133) would differ. Table 4.2 shows the operating points decided upon, with the fully-expanded jet velocity V, Mach number M, static temperature T_s, and total temperature T_p given for both the primary and secondary (core and bypass) flows:

Operating Point:		**1.1**	**1.2**	**1.3**
Core	V_p (m/s)	340.3	404.5	480.7
	M_p	0.621	0.738	0.877
	T_{sp} (K)	775.6	775.6	775.6
	T_{tp} (K)	827.9	849.5	879.9
Bypass	V_s (m/s)	306.8		
	M_s	0.902		
	T_{ss} (K)	288.14		
	T_{ts} (K)	335.0		
V_S / V_P		0.902	0.759	0.638

Table 4.2 – CoJeN operating conditions.

4.3.3. Flow Measurements

The CoJeN experiment was divided into 6 test phases, during which the work package 3 project partners performed a variety of acoustic and aerodynamic measurements. In this way, a complete picture of the jet could be assembled, and any CFD or acoustic predictions compared with actual measurements of velocity or noise. As can be seen from Table 4.3, a large volume of acoustic data was collected, both near to jet (thereby enabling location of the individual noise sources) and far from the jet (to establish the ensemble sound heard on the ground). Aerodynamic measurements comprised time-series LDA data, taken from single points within the flow, and PIV surveys performed by both the author and José Nogueira, of Universidad Carlos III de Madrid.

Test phase	Measurements (and responsible project partner)
1	• Far-field polar microphone array measurements (Qinetiq). • Far-field azimuthal microphone array measurements (ISVR).
2	• Volumetric PIV (Warwick). • 2D PIV nozzle-exit survey (Madrid).
3	• 2D PIV exhaust mapping with simultaneous LDA (Warwick). • Limited 3D PIV exhaust mapping (Madrid).
4	• 2-point LDA measurements (Dantec). • Near-field linear microphone array measurements (ISVR).
5	• Cross-plane 3D PIV (Madrid). • Near-field circular microphone array measurements (DLR). • Near-field linear microphone array measurements (ISVR).
6	• Internal pressure & temperature nozzle survey (Qinetiq).

Table 4.3 – The CoJeN measurement programme.

The planes of both Warwick and Madrid's PIV measurements are shown in Figure 4.6 below. As illustrated on the right of the diagram, Warwick's phase 2 volumetric PIV measurements – whose purpose was to confirm the angular alignment of the jet –

comprised a series of radial planes, which could be reconstructed to give a cross-axial view. During phase 3, Warwick was responsible for the production of mean and RMS time-averaged statistics for the whole of the jet exhaust. During this 2D mapping, LDA time-series data was also collected from within Warwick's PIV field of view. By virtue of being synchronised with each other, these combined LDA and PIV measurements could be used to assemble an ultra high speed reconstruction of the flow, using the interpolation technique described by (Kerhervé and Fitzpatrick, 2006b).

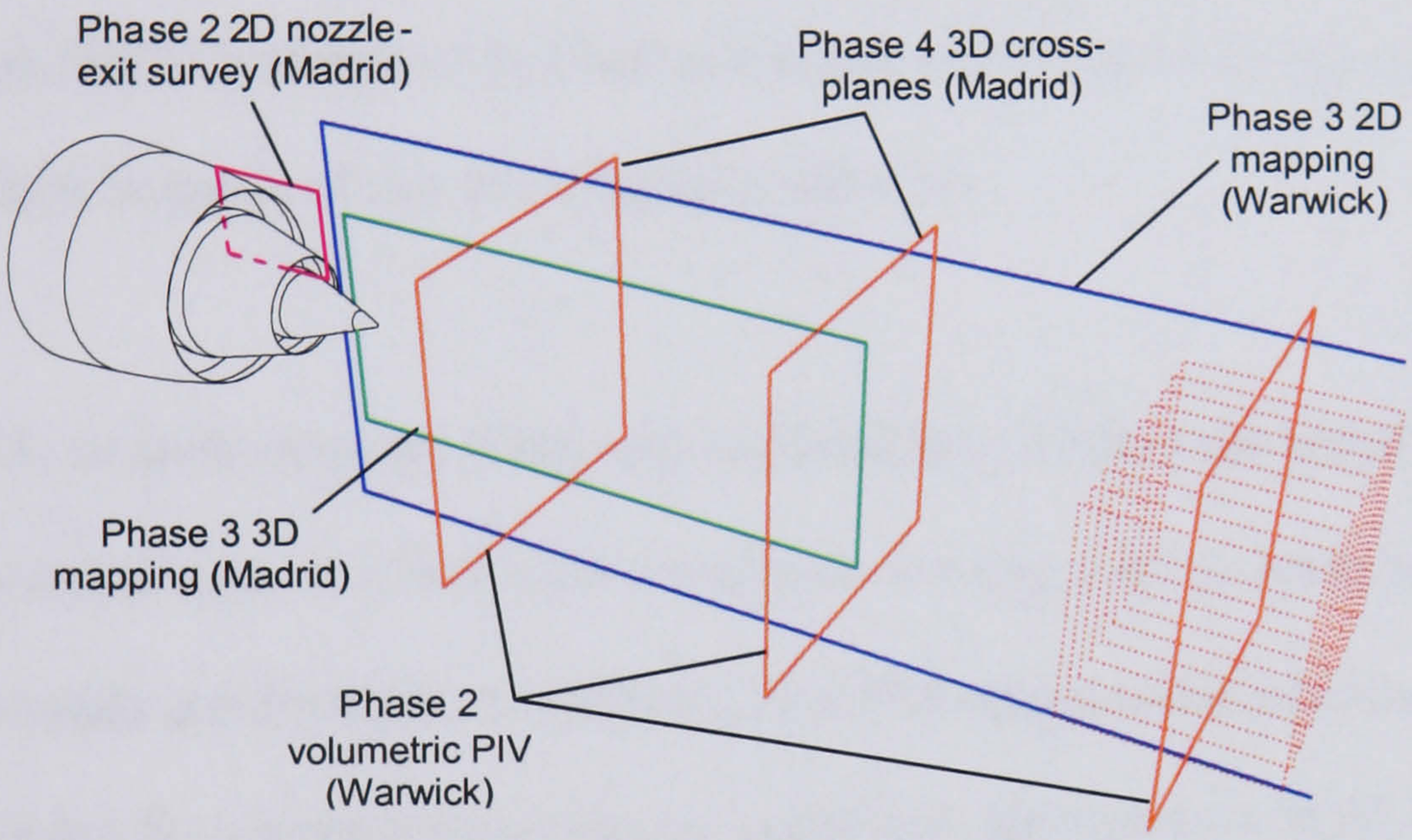

Figure 4.6 – PIV measurement planes.

4.3.4. Time-Space Correlation

As shown in Table 4.3, test phase 4 involved the collection of 2-point LDA data, in which time-series velocity measurements were acquired simultaneously from two sets of velocimeters, offset by means of a small motorised axial traverse. By comparing the similarity between the signals, it is possible to establish the rate at which the jet's structures decay as they travel downstream – information that is analogous to the efficiency with which the flow's kinetic energy is converted to sound. Such 'time-space' correlations are of particular relevance to jet-noise prediction because, as shown by (Seiner, 2003), a model of far-field sound intensity based on Lighthill's Analogy can be re-written in terms of this de-correlation directly.

Dual LDA, or deflectometry (Doty and McLaughlin, 2005) time-series measurements allow the calculation of a flow's de-correlation over time for as many points in space as the LDA heads are driven to. Correlating two PIV measurements however allows the de-correlation **R** to be calculated for *any* point **x** in the camera's FOV, for as many time delays τ as the lasers are triggered to. PIV-based time-space correlations therefore offers far greater insight into the jet's behaviour, but at the expense of an increased measurement acquisition time, due to the vastly different sampling rates of PIV and LDA, and the need for convergence in the time-averaged correlation values.

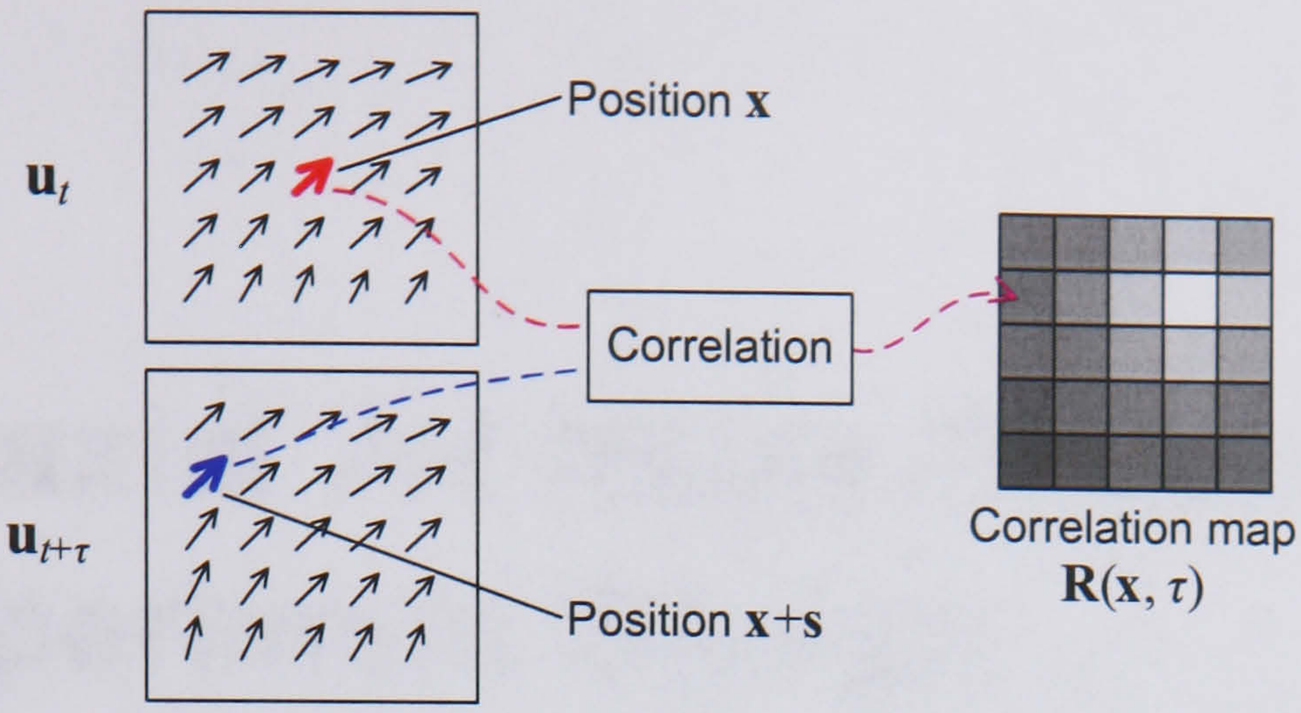

Figure 4.7 – Time-space correlation using PIV vector maps.

The time-space correlation **R**, and related length and time scales L and T are defined as follows, where typically only the horizontal component of the vector maps **u** is used. (Kerhervé and Fitzpatrick, 2006a)

$$\mathbf{R}(\mathbf{x},\tau,\mathbf{s}) = \frac{\overline{\mathbf{u}_t'(\mathbf{x})\mathbf{u}_{t+\tau}'(\mathbf{x}+\mathbf{s})}}{\sqrt{\overline{\mathbf{u}_t'(t,\mathbf{x})^2}\cdot\overline{\mathbf{u}_{t+\tau}'(\mathbf{x}+\mathbf{s})^2}}} \tag{4.1}$$

$$L = \int_0^\infty \mathbf{R}(\mathbf{x},0,s)\,\mathrm{d}s \tag{4.2}$$

$$T = \int_0^\infty \mathbf{R}(\mathbf{x},\tau,s_{peak})\,\mathrm{d}\tau \tag{4.3}$$

Previous PIV time-space correlation studies have been dependent upon using either a high-speed time-series camera, e.g. (Lempert, et al., 2002; Schröder, et al., 2004), or liquid-crystal or polarisation based shuttering of two, accurately aligned cameras (Ganapathisubramani, et al., 2005; Guibert and Lemoyne, 2002). During CoJeN test phase 4 however, it was decided to apply the multiple-camera acquisition technique described in the previous chapter, thereby enabling time-space correlations to be made without the constraints on τ inherent to LCD shuttering, or the reduction in image quality or intensity that results from image intensification or polarising optics.

5. Coaxial Jet Noise Project: Experiment Design

5.1. Requirements and Specification

5.1.1. Exhaust Measurement Volume

The jet exhaust region defined as being of interest to the aerodynamic CoJeN project partners is shown in yellow in Figure 5.1, i.e. one half of the jet exhaust, extending to (at least) 3m from the secondary nozzle exit. To enable coverage of the whole length, all experimental equipment would be mounted on an axial traversing system, as described in Section 5.3. The secondary nozzle exit diameter (and reference diameter D) was taken to be 0.2 m, with the radial-component of the measurement volume predicted to increase at a rate of 1 in 10.

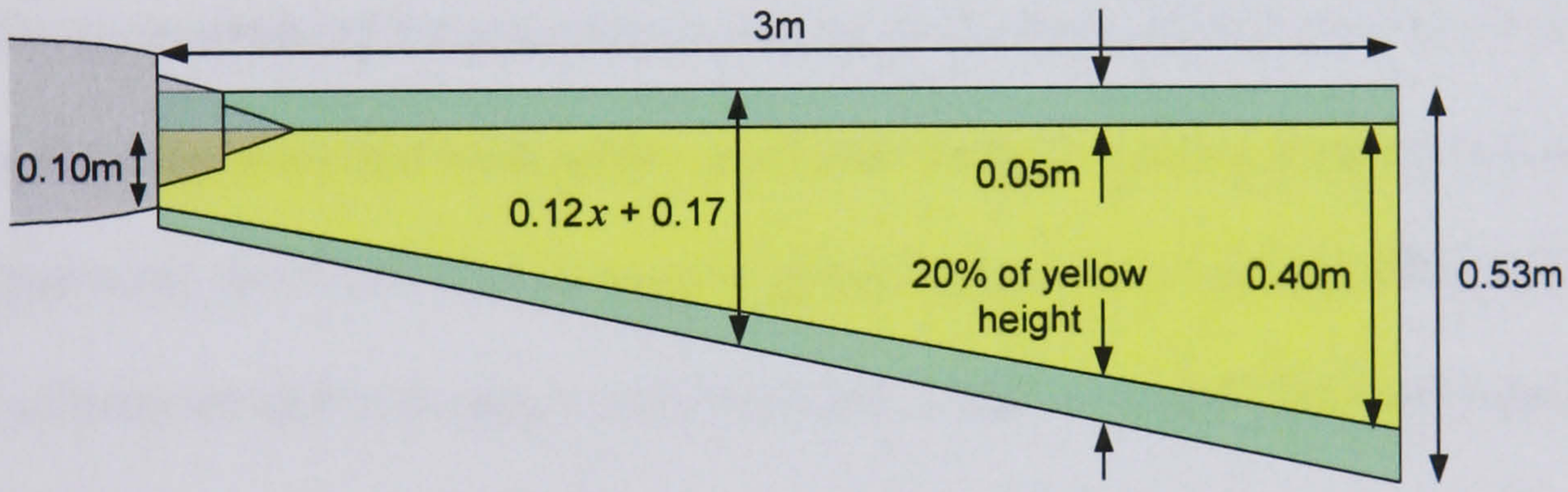

Figure 5.1 – CoJeN measurement area of interest.

The measurement area was defined on the assumption of axially symmetric flow, and for this reason its angle (about the jet centreline) was not defined. It was however considered shrewd to base the requirements for Warwick's phase 3 PIV rig on a slightly expanded region, as shown in green.

5.1.2. Measurement Parameters

The number of samples required during each test phase differed: during phase 2 it was only required that the mean velocities converged, whereas in phase 3 convergence of the RMS values was required. Based on these requirements and discussions with project partners, it was agreed that 300 samples would be taken per cross-axial position during phase 2, and 1000 samples taken during phase 3. It was also agreed that the PIV should be capable of resolving the near-nozzle fine-scale turbulence with a spatial resolution down to approximately 5 mm.

5.1.3. Temporal Constraints

One of the most pressing considerations during the CoJeN experiment was time. With facility operating costs (for both rental, staff and energy) running at many thousands of pounds per hour, the time taken to acquire phase 2 and 3 data directly affected the number of nozzles and operating conditions that could be tested. The high running costs also highlighted the importance of overall system reliability and remote rig diagnostic abilities.

Camera acquisition times, specifically, may be put in context by considering a typical medium-scale PIV experiment, comprising a camera with a 0.10 × 0.12 m field of view, running at 10 Hz. When scaled to the CoJeN experiment dimensions, such a setup would take around 5 hours to acquire 1000 vector maps from the 1.05 m^2 exhaust area. In contrast, it was suggested that phase 3 acquisition should take no longer than 1 hour.

The relationship between camera frame rate, field of view, and acquisition time is explored in Section 5.2, as is the method that was employed to provide higher-than-normal measurement speeds. This in turn determined the requirements of the rig's computing system, which is discussed in Section 5.7.

5.1.4. Physical Constraints

As with any PIV experiment, the CoJeN rig had to be designed in such a way that it would not interfere with the flow under examination. Given the high speeds and temperatures involved, consideration also had to be given to protecting the cameras and lasers from undue damage.

Preliminary RANS predications of the jet exhaust velocity and temperature were performed by Volvo Aero; one of the CoJeN CFD partners. As exemplified by Figure 5.2a though, a typical camera's operating temperature range was only exceeded (at 40°C or 315K) around 0.4 m from the jet centreline, at the far end of the measurement volume.

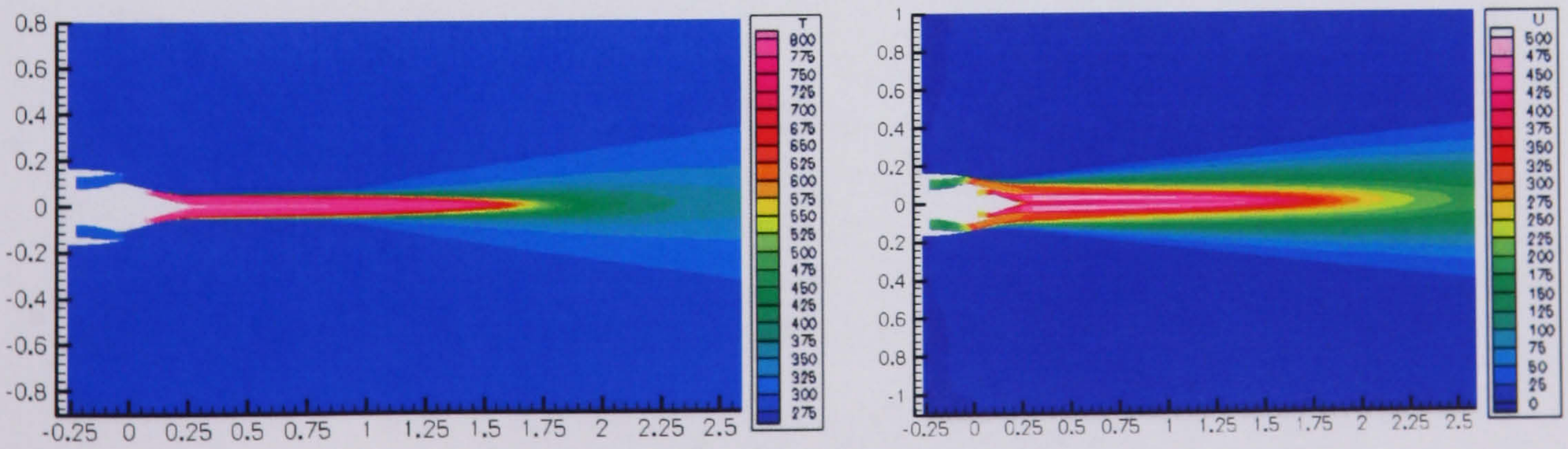

Figure 5.2 – RANS predictions for short cowl nozzle, OP.1.3: a) Temperature; b) Horizontal-component velocity. (Volvo Aero)

Early CFD predictions of the horizontal component of velocity (c.f. Figure 5.2b) also served to confirm the estimated 1-in-10 gradient of the edge of the outer shear layer. Extending this relationship to 6.0 m from the nozzle (the most downstream position equipment would likely ever be placed) suggested the air would be disturbed up to 0.84 m from the jet centreline. It was therefore decided to maintain a 0.9 m safety offset between all measurement equipment and the jet centre line.

5.2. Imaging System

5.2.1. Requirements and Options

The imaging system – comprising both camera(s) and lenses – formed the heart of the Warwick PIV rig. Its requirements were:

- The ability to acquire data from the whole of the measurement plane.
- …as quickly as possible.
- The ability to record images of sufficient resolution that:
  - ≥ 5 mm flow structures can be identified at the nozzle exit.
  - Adrian's source and image density requirements for successful PIV are met.
- To provide results of good accuracy.

Bearing in mind the 1:16 volumetric expansion between the start and end of the measurement region, and an increase in the size of flow structures of interest, it is possible to define three applicable imaging methods:

1. The camera(s) are equipped with zoom lenses such that their field of view (FOV) can be increased from 193 to 530 mm in height.
2. The camera(s) have a constant, large FOV with a height of at least 530 mm. No moving parts are required.
3. The camera(s) have a constant but small FOV, only capable of covering the far end of the jet exhaust by means of vertical mosaicing.

In the following sections the viability of each option is considered.

5.2.2. Variable Zoom Imaging System

Given the increasing area yet decreased resolution required at the far end of the jet exhaust, PIV cameras equipped with variable zoom lenses appeared an attractive option, and a Matlab script (given in Appendix 9.4.4, page 417) was written to simulate such a system. Figure 5.3 shows the result of one such exercise, using a 2048^2 pixel camera, whose FOV can be seen to increase from 227 – 596 mm in 9 steps:

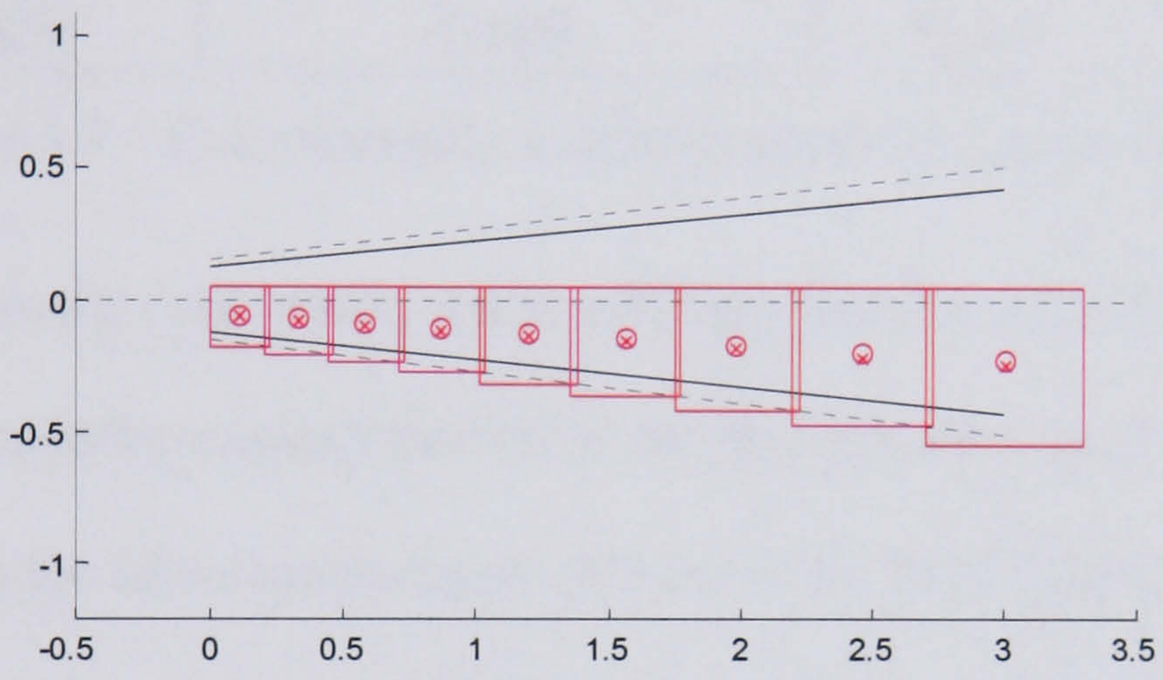

Figure 5.3 – Variable-zoom imaging system example.

Given a frame-rate of 15Hz, the resulting 18,000 images would take 24 minutes to acquire, allowing 30 seconds to move from one position to the next. Table 5.1 lists simulation results for a variety of popular camera sensor sizes and frame rates. With the exception of sensor E, the acquisition times are all significantly below 1 hour.

Sensor	Sensor resolution (px) & frame rate	Number of recording positions	Phase 3 acquisition time	Magnification factor *Z* (px/mm)
A	1600 × 1200 @ 30 Hz	7	10 minutes	5.0 – 1.8
B	1200 × 1600 @ 30 Hz	12	19 minutes	7.3 – 2.8
C	2048 × 2048 @ 15 Hz	9	24 minutes	9.0 – 3.4
D	4072 × 2720 @ 5 Hz	6	42 minutes	11.1 – 4.3
E	2720 × 4072 @ 5 Hz	14	100 minutes	18.7 – 7.0

Table 5.1 – Variable-zoom imaging system simulations.

Despite the evident suitability of a variable-zoom imaging system, its notable Achilles' heel is the lack of suitable motorised zoom lenses. Those that are available may be divided into the following categories:

Application	Availability & Choice	Quality	Price
Photography	Extremely poor*	Fair	n/a
CCTV	Good	Poor	≥ £200
TV cameras & cinematography	Good	Excellent	≥ £3000
Scientific	Good	Good	≥ £1000

Table 5.2 – Commercially available motorised zoom lenses.

More important than the cost/quality trade-off is the fact that all commercially available motorised zoom lenses have either limited or no magnification factor feedback. Furthermore, given the drive mechanisms often used by such lenses, it would be difficult to envisage an encoder capable of giving feedback to the resolution necessary for PIV (where the measured velocity is directly proportional to the magnification factor).

Possible solutions to this problem included custom-engineered lenses and/or mounts, or faintly illuminated calibration targets in the background of every image. (Chen, et al., 2001) have shown that servo-driven zoom lenses can be build with high accuracy, and their system was additionally calibrated for the variation in the intrinsic camera

---

* While the lack of motorised lenses for film or digital camera bodies may seem surprising, particularly given the abundance of both ultrasonic ring driven auto-focus separates and all-in-one digital cameras with optical zoom, there is simply no market for them: professional photographers prefer the speed of manual adjustments. Canon, for example, made just one motorised zoom lens (the EF 35-80 mm *f* 4-5.6 Power Zoom) and it was aimed at the low end of the market, with a related low optical quality.

parameters with the changing magnification factor. Given however the experimental nature of such solutions, it was decided that variable zoom imaging was inappropriate for the CoJeN PIV system.

5.2.3. PIV Image Quality

With reference to Section 2.1.1, we recall that Adrian suggests successful PIV is best achieved by ensuring the seeding densities $N_S \ll 1$ and $N_I > 15$. The imaging system's magnification factor M should therefore be chosen on this basis. However, by scanning a camera with a fixed magnification down the jet, both N_S and N_I will change, as the seeding densities are a function of the seeding concentration C, which drops by a factor of approximately 16 as the jet expands from 0.1 to 0.4 m radius. It therefore had to be confirmed that a constant FOV size is viable, given a constant seeding supply.

Equations (2.1) and (2.2) from page 15 can be rearranged to find the seeding concentration (in particles / m^3) necessary to give a particular source or image density:

$$C_{N_S} = \frac{4 N_S M^2}{\Delta z_0 \pi d_\tau^2} \tag{5.1}$$

$$C_{N_I} = \frac{N_I M^2}{\Delta z_0 A_I} \tag{5.2}$$

Table 5.3 lists the acceptable range of seeding concentrations for imaging system options 2 and 3. These are the values of C that give $N_S = 0.5$ and $N_I = 20$ for a 2048^2 pixel sensor with 7.4μm pitch, $p_d = 0.3\mu m$, $\lambda = 532nm$, $\Delta z_0 = 2mm$, $f^\# = 6$ and $A_I = 32px^2$. d_τ is given by equation (2.29) on page 51.

	Imaging system option 2	**Imaging system option 3**
FOV	530 × 530 mm	220 × 220 mm
M	(2048×7.4μm / 0.53m) = 0.029	(2048×7.4μm / 0.22m) = 0.069
$C_{N_S=0.5}$	4.05×10^{9} m^{-3}	2.18×10^{10} m^{-3}
$C_{N_I=20}$	1.46×10^{8} m^{-3}	8.46×10^{8} m^{-3}
C-ratio	27.8	25.8

Table 5.3 – Acceptable seeding concentrations for CoJeN imaging system.

The large C-ratio demonstrates the huge range of seeding concentrations that should provide acceptable PIV images (for the parameters given above). Not only does this suggest that adjustment of the seeding levels will be a relatively straight-forward task, but it also makes clear that a reduction in C of one sixteenth does not necessitate a reduction in PIV image quality. It should however be noted that the C-ratio (and whether or not it is greater than 16) is highly sensitive to both the lens f-number, and cross-correlation interrogation window size, as demonstrated in Table 5.4. The sensor resolution and FOV is of limited consequence in this respect.

		$f^{\#}=4$	$f^{\#}=5$	$f^{\#}=6$	$f^{\#}=7$	$f^{\#}=8$
1024 px^2 sensor	$A_I = 16\text{px}^2$	16.1	10.3	7.2	5.3	4.0
	$A_I = 32\text{px}^2$	64.4	41.2	28.6	21.0	16.1
2048 px^2 sensor	$A_I = 16\text{px}^2$	15.6	10.0	7.0	5.1	3.9
	$A_I = 32\text{px}^2$	62.6	40.0	27.8	20.4	15.6

Table 5.4 – C-ratios for different imaging system parameters (0.53m FOV).

5.2.4. Spatial Resolution

Given the requirement to identify 5 mm structures in the flow near the nozzle exit, it is possible to define constraints upon the magnification factor M for a particular distance a between camera and light-sheet. As shown on page 90, the magnification factor at a may be represented by $Z_a = M$ / pixel pitch. Because (A_I / Z_a) must be smaller than or equal to the size of flow structures of interest, we find that:

For $A_I = 16$ px^2: $Z_a \geq 3.2$ px/mm

For $A_I = 32$ px^2: $Z_a \geq 6.4$ px/mm

As revealed in Table 5.4 however, were $A_I = 16$ px^2 it would be difficult to fulfil Adrian's PIV criteria without constantly adjusting the seeding levels in the jet. For this reason, we shall conclude that $A_I = 32$ px^2 and $Z_a \geq 6.4$ px/mm as a result. With this in mind, it becomes clear that imaging option 2 (in which the camera FOV is at least 530 mm) is conceivable only when using a rotated 2720 × 4072 pixel sensor (the largest PIV sensor currently commercially available), resulting in $Z_a = 7.7$ px/mm. Given however the unrepresentatively high cost of these sensors, not to mention the 'wasted' near-nozzle pixels, option 2 was disregarded.

It was therefore established that the CoJeN rig would comprise camera(s) with fixed magnification, mounted on a vertical traverse. In order to quantify the effect of sensor size and magnification factor on the overall phase 3 acquisition time, a Matlab script (given in Appendix 9.4.5, page 422) was written to calculate the number of measurement positions required in order to cover the measurement volume for a particular size of FOV. Figure 5.4 shows the 31 positions calculated as being required

when a 2048 × 2048 px sensor is used with a magnification factor of 9 px/mm (i.e. a FOV of 228 × 228 mm). It can be seen that in this example, the rig would have to be equipped with a vertical traverse of at least 416 mm (20 mm overlap is provided between views).

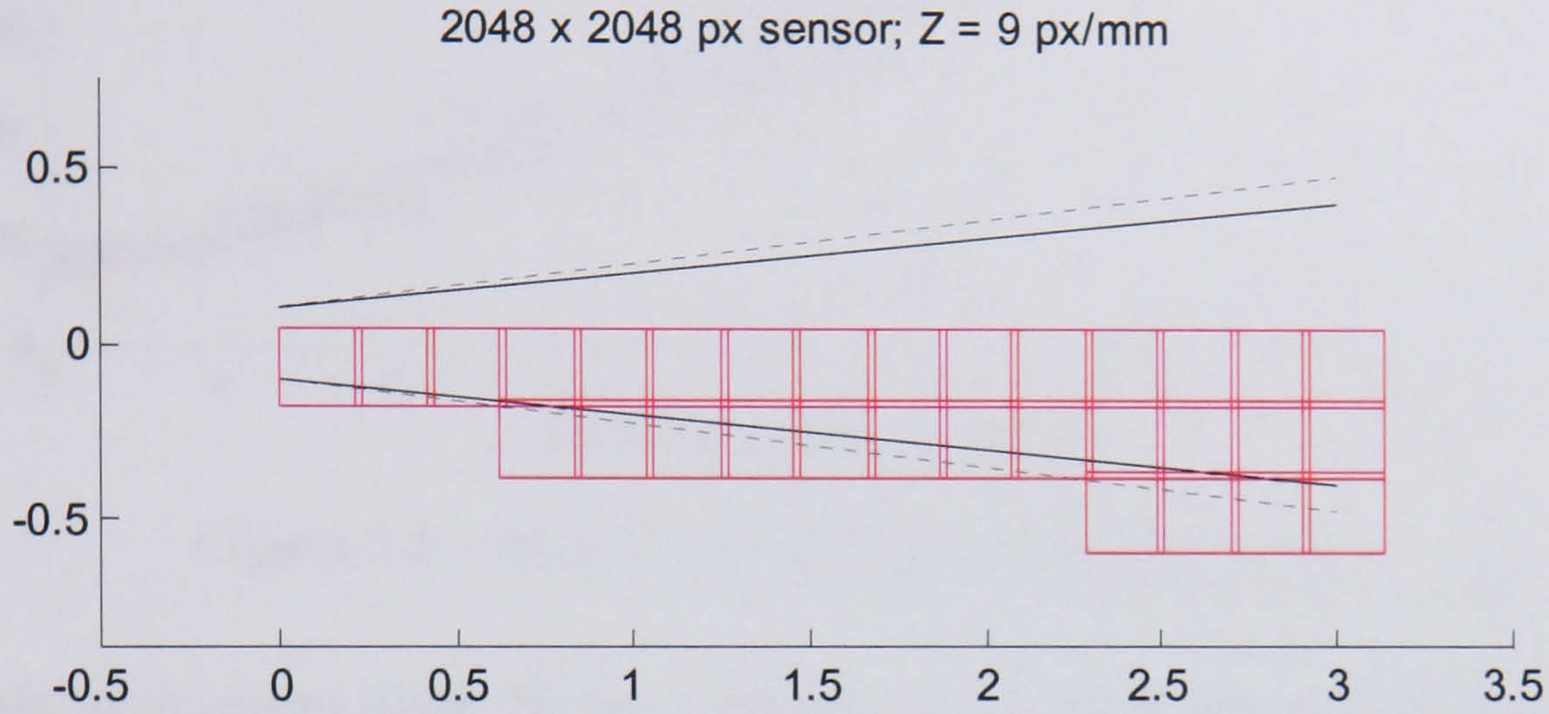

Figure 5.4 – The 31 positions calculated as required for Phase 3 if $Z_a = 9$ px/mm.

Based on the FOV positions thus calculated, Figure 5.5 gives the total time required for phase 3 data acquisition vs. the magnification factor Z_a for 3 typical sensor resolutions*. The sensor frame rates have all been normalised to give a bandwidth of 61.7 Mpx/s, and it has been assumed that axial traverse movements take 20 seconds, and radial traverse movements (which are kept to a minimum) take 40 seconds. It can be seen that for $Z_a \geq$ 6.4 px/mm, average acquisition times ≥ 50 minutes.

* In the case of non-square sensors, the orientation that yields the lowest acquisition time is plotted. In the case of both rectangular sensors shown, this is horizontal.

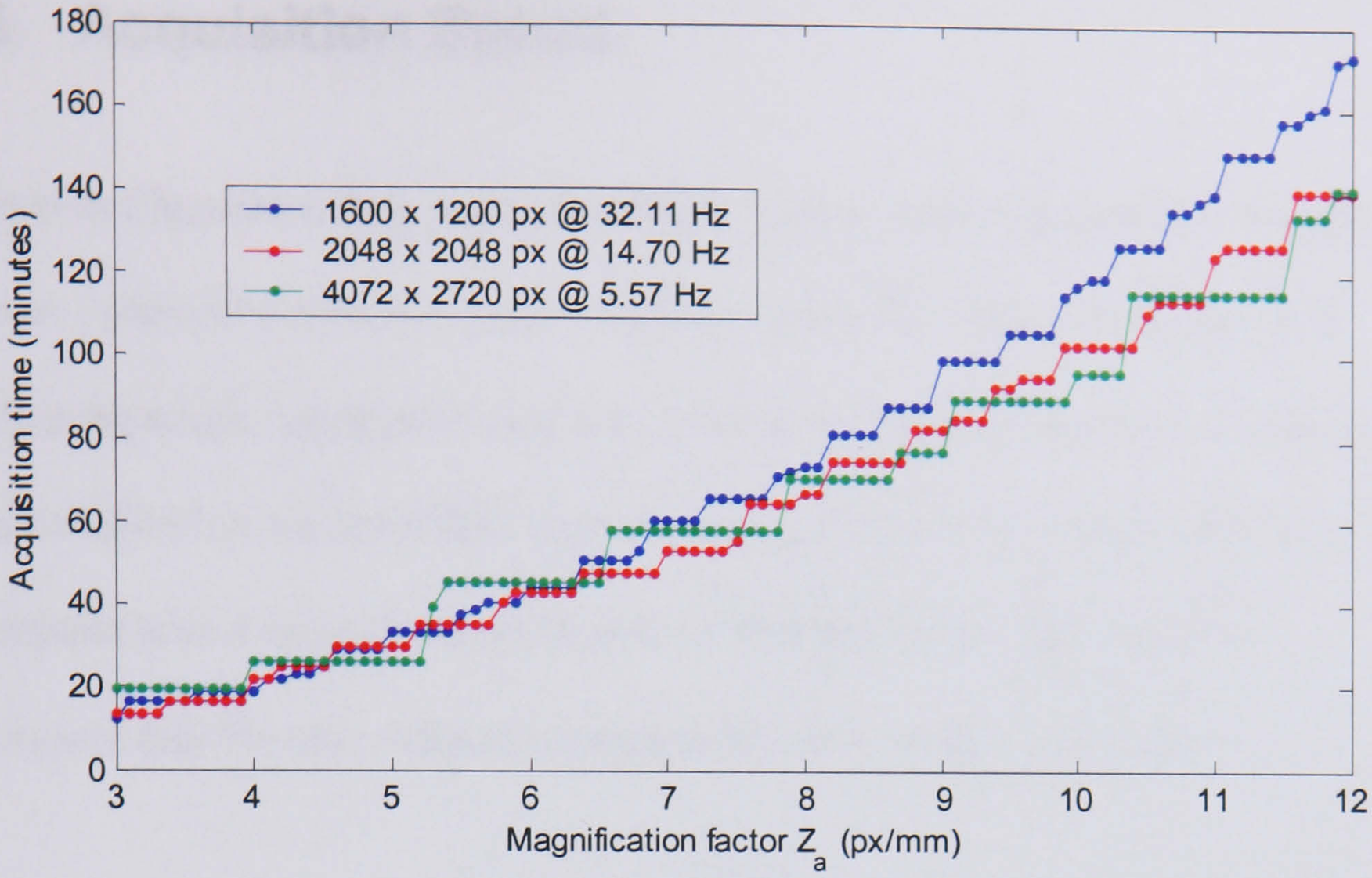

Figure 5.5 – Simulated Phase 3 acquisition times.

On the whole, acquisition times for the 3 sensor sizes considered rank in order of the sensor area, in pixels. This is due to the reduced number of axial and radial traverse movements required for the larger sensors to able to cover the measurement volume. In order to maximise acquisition speed therefore, it was shown that the cameras used during CoJeN should be of the highest possible resolution.

5.2.5. Acquisition Speed

As shown in Chapters 2 & 3, multiple sensors – when carefully corrected for geometric distortion – provide a means of acquiring time-series PIV data at high speed. A simplified approach, using just 2 sensors, is similarly capable of almost doubling standard acquisition times without such strict calibration requirements. Figure 5.6 demonstrates how a second camera is able to 'interleave' an additional PIV measurement into the time taken to complete the first camera's read-out.

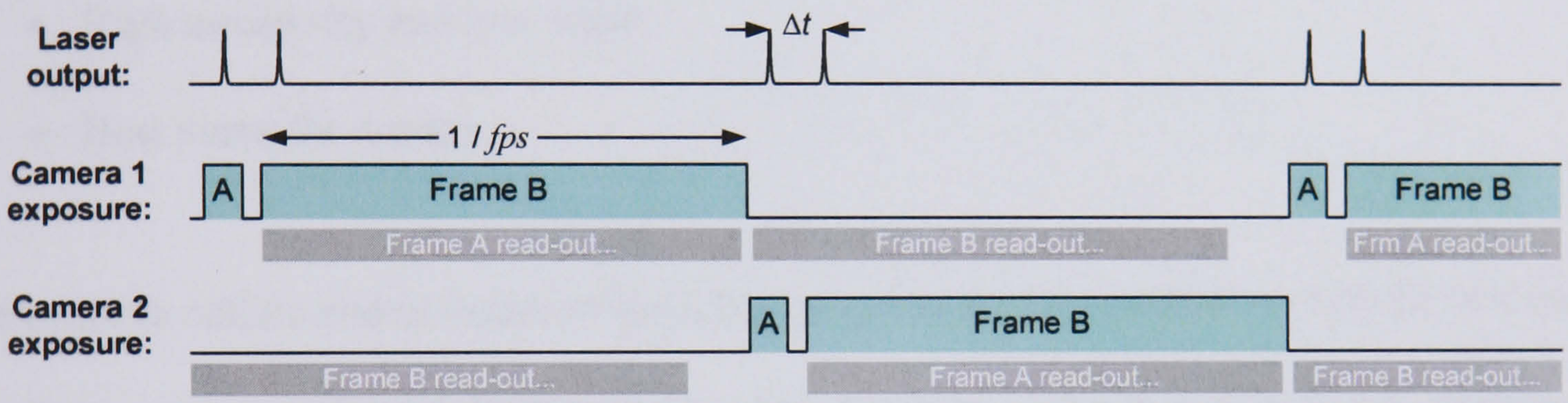

Figure 5.6 – Interwoven PIV acquisition.

Given the ability to almost halve the acquisition times shown in Figure 5.5, it is clear that the magnification factor Z_a could be as great as 11 px/mm (for a 2048 × 2048 sensor) before phase 3 acquisition times exceed 1 hour. This value was therefore considered the upper limit for Z_a when choosing lenses for the cameras.

5.2.6. Camera Selection

The requirements for the CoJeN cameras may be summarised thus:

- As large a sensor as possible.
- An interframe transfer time no greater than 2 μs.

  This requirement was based on an evaluation of the minimum Δt likely to be required for the CoJeN flows. Using $Z_a = 10$ px/mm, $U_{max} = 400$ m/s, and $\Delta x_{max} = ¼ A_I = 8$ px; $\Delta t_{min} = \Delta x / Z_a U \approx 2.5$ μs.
- High sensitivity and low noise.
- Best value for money.

In order to collate and compare information about available cameras, a mySQL powered website was created using PHP scripting. The database – shown in Figure 5.7 – displays both quotes and up to 30 parameters per camera (a full list is given in Appendix 9.1.7, page 348), as well as allowing the cameras to be sorted and filtered in any number of ways. Secondarily derived information is also calculated and displayed for each entry; for example, the camera's dynamic range (calculated as a function of full well capacity and read noise), bandwidth (in Mpx/s), and value for money (in £/bandwidth).

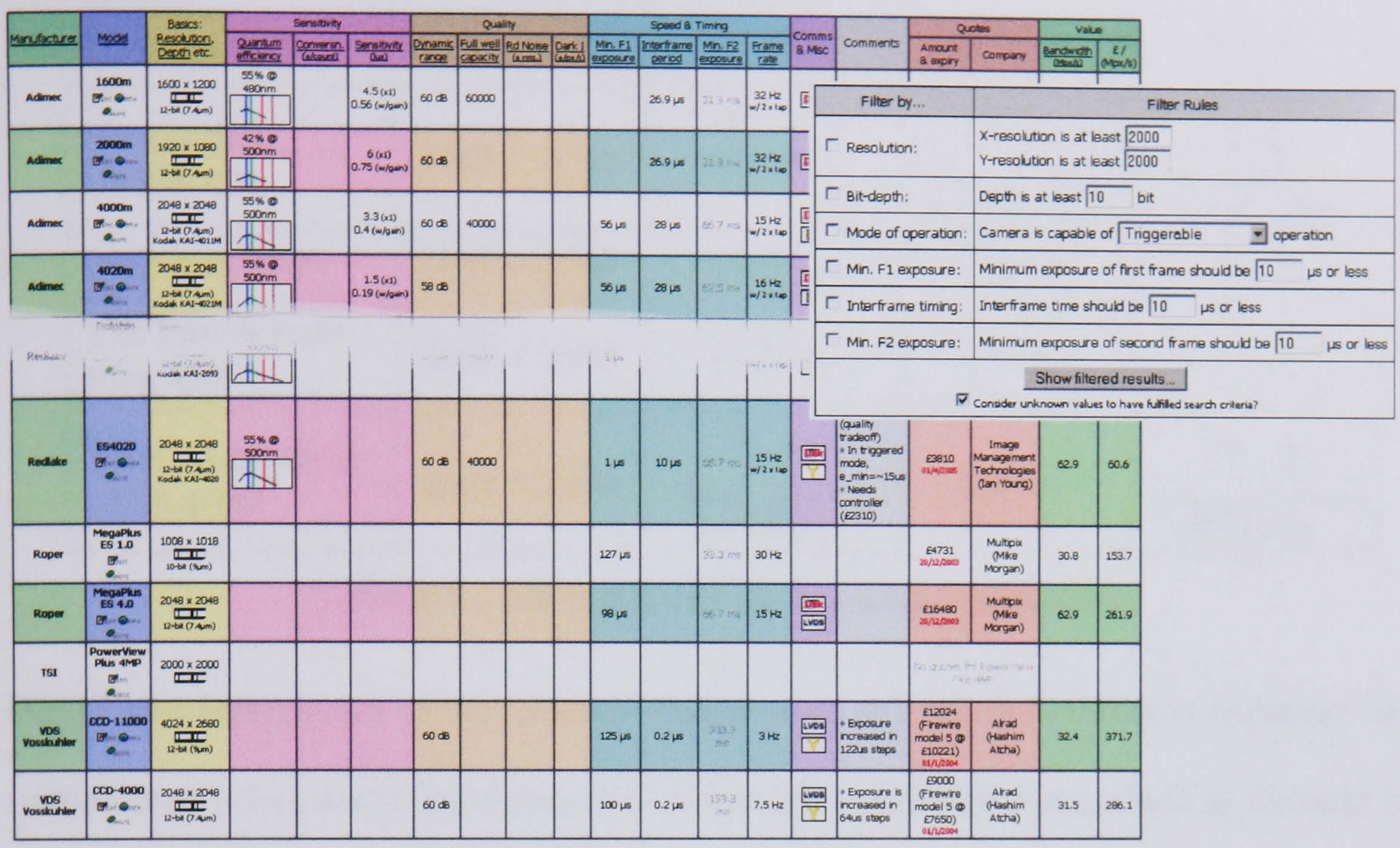

Camera Database

This database is biased towards those cameras suitable for CoJeN (i.e. > 1Mpx PIV cameras). Click here for a brief explanation of the columns.

If you wish to reduce the number of cameras visible, use the form at the bottom of the page to filter the database. You can also sort the database, by clicking on the appropriate column header. You are currently viewing all 49 cameras in the database.

Click here if you wish to add a new camera to the database.

Manufacturer	Model	Basics: Resolution, Depth etc.	Sensitivity: Quantum efficiency	Sensitivity: Conversn. (e/count)	Sensitivity: Sensitivity (lux)	Quality: Dynamic range	Quality: Full well capacity	Quality: Rd Noise (e rms)	Quality: Dark I (e/px/s)	Speed & Timing: Min. F1 exposure	Speed & Timing: Interframe period	Speed & Timing: Min. F2 exposure	Speed & Timing: Frame rate	Comms & Misc	Comments	Quotes: Amount & expiry	Quotes: Company	Value: Bandwidth (Mpx/s)	Value: £ / (Mpx/s)
Adimec	1600m	1600 x 1200 12-bit (7.4µm)	55% @ 480nm		4.5 (x1) 0.56 (x/gain)	60 dB	60000				26.9 µs		32 Hz w/ 2 x tap						
Adimec	2000m	1920 x 1080 12-bit (7.4µm)	42% @ 500nm		6 (x1) 0.75 (x/gain)	60 dB					26.9 µs		32 Hz w/ 2 x tap						
Adimec	4000m	2048 x 2048 12-bit (7.4µm) Kodak KAI-4011M	55% @ 500nm		3.3 (x1) 0.4 (x/gain)	60 dB	40000			56 µs	28 µs		15 Hz w/ 2 x tap						
Adimec	4020m	2048 x 2048 12-bit (7.4µm) Kodak KAI-4021M	55% @ 500nm		1.5 (x1) 0.19 (x/gain)	58 dB				56 µs	28 µs		16 Hz w/ 2 x tap						
Redlake	ES4020	2048 x 2048 12-bit (7.4µm) Kodak KAI-4020	55% @ 500nm			60 dB	40000			1 µs	10 µs		15 Hz w/ 2 x tap	LVDS	(quality tradeoff) • In triggered mode, e_min=~15us • Needs controller (£2310)	£3810 01/4/2005	Image Management Technologies (Ian Young)	62.9	60.6
Roper	MegaPlus ES 1.0	1008 x 1018 10-bit (9µm)								127 µs			30 Hz			£4731 20/12/2003	Multipix (Mike Morgan)	30.8	153.7
Roper	MegaPlus ES 4.0	2048 x 2048 12-bit (7.4µm)								98 µs			15 Hz	LVDS LVDS		£16480 20/12/2003	Multipix (Mike Morgan)	62.9	261.9
TSI	PowerView Plus 4MP	2000 x 2000																	
VDS Vosskuhler	CCD-11000	4024 x 2680 12-bit (9µm)				60 dB				125 µs	0.2 µs		3 Hz	LVDS	• Exposure increased in 122us steps	£12024 (Firewire model 5 @ £10221) 01/1/2004	Alrad (Hashim Atcha)	32.4	371.7
VDS Vosskuhler	CCD-4000	2048 x 2048 12-bit (7.4µm)				60 dB				100 µs	0.2 µs		7.5 Hz	LVDS	• Exposure is increased in 64us steps	£9000 (Firewire model 5 @ £7650) 01/1/2004	Alrad (Hashim Atcha)	31.5	286.1

Filter by...	Filter Rules
Resolution:	X-resolution is at least 2000 Y-resolution is at least 2000
Bit-depth:	Depth is at least 10 bit
Mode of operation:	Camera is capable of Triggerable operation
Min. F1 exposure:	Minimum exposure of first frame should be 10 µs or less
Interframe timing:	Interframe time should be 10 µs or less
Min. F2 exposure:	Minimum exposure of second frame should be 10 µs or less

Show filtered results...

Consider unknown values to have fulfilled search criteria?

Figure 5.7 – PIV camera database webpage (insert: filtering parameters).

Several observations stemmed from analysis of the camera database:

- Cameras employing ~4000 × 2700 pixel sensors* provide, on average, half the value for money than 2048 × 2048 pixel cameras from the same range.
- For a given product family, the highest bandwidth is invariably offered by the 2048 × 2048 pixel sensor product.
- Approximately half the PIV cameras in the database have an interframe time greater than 2 µs, and were as such unsuitable for CoJeN.

Table 5.5 shows the short-list of cameras considered both reasonable value for money, and technically suitable for the CoJeN experiment. It is interesting to note that all the cameras listed use the same Kodak KAI-4020 (or 4010) image sensor.

* In almost all cases, the Kodak KAI-11000.

Camera	Resolution	Maximum frame-rate	Interframe time	Min. frame A exposure
Dantec HiSense 4M	2048 × 2048	11.0 Hz	200 ns	4.5 µs
Hamamatsu C9300-024	2048 × 2048	11.4 Hz	500 ns (Non-standard, unproven option)	25 µs (Non-standard, unproven option)
PCO pco.2000	2048 × 2048	14.7 Hz	180 ns	0.5 µs
TSI PowerView Plus 4MP	2048 × 2048	16.0 Hz	200 ns	42 µs
VDS Vosskühler CCD-4000	2048 × 2048	7.5 Hz (Only 1 read-out tap available)	200 ns	100 µs (Increased in 64 µs increments)

Table 5.5 – Short-list of CoJeN camera candidates.

Based on a comparison of the cameras' frame-rates, minimum first frame exposure time (which is of relevance to the time-series acquisition techniques described in Chpater 3) and price, it became clear that PCO's pco.2000 was the most appropriate choice. As such, 2 cameras (in the form of their Imager Pro Plus alter-ego) were purchased from LaVision, with an additional 3 units lent for the duration of the CoJeN test. The full camera specification can be found in Appendix 0 (page 349).

5.2.7. Lens Selection

As demonstrated in Sections 5.2.4 and 5.2.5, the camera lenses' magnification factor Z_a was to lie between 6.4 and 11.0 px/mm. Taking the average as a guide, and the previously stated 0.9 m safety stand-off as the distance between the cameras and light sheet (thereby maximising the light received), we can calculate the lens focal length required. From equations (2.31) and (2.32) on page 90:

$$f = \frac{a}{\frac{1}{pZ_a} + 1} \tag{5.3}$$

…where p is the pixel pitch of the camera sensor. For p = 7.4 μm, a = 0.9 m, and Z_a = 8.7 px/mm, we find that $f \approx$ 54mm.

In considering the lens f-number required, there are a number of factors to consider, as summaried in Table 5.6:

Advantages to a low $f^\#$ lens	**Advantages to a high $f^\#$ lens**
• Increased amount of light transmitted. • Increased range of acceptable seeding levels (see Table 5.4, page 152). • $f^\#$ can always be increased, by closing the iris.	• Increased depth of focus. • Decreased lens cost.

Table 5.6 – Factors affecting the choice of lens f-number.

By considering the depth of focus required for a particular experiment, it is possible to place a lower limit on the f-number required, thereby potentially minimising costs.

Figure 5.8 depicts a simple angled camera arrangement, for which the minimum depth of focus required is:

$$\delta z_{\min} = \Delta X \tan\theta = \Delta X \tan \sin^{-1} \frac{s}{a} \tag{5.4}$$

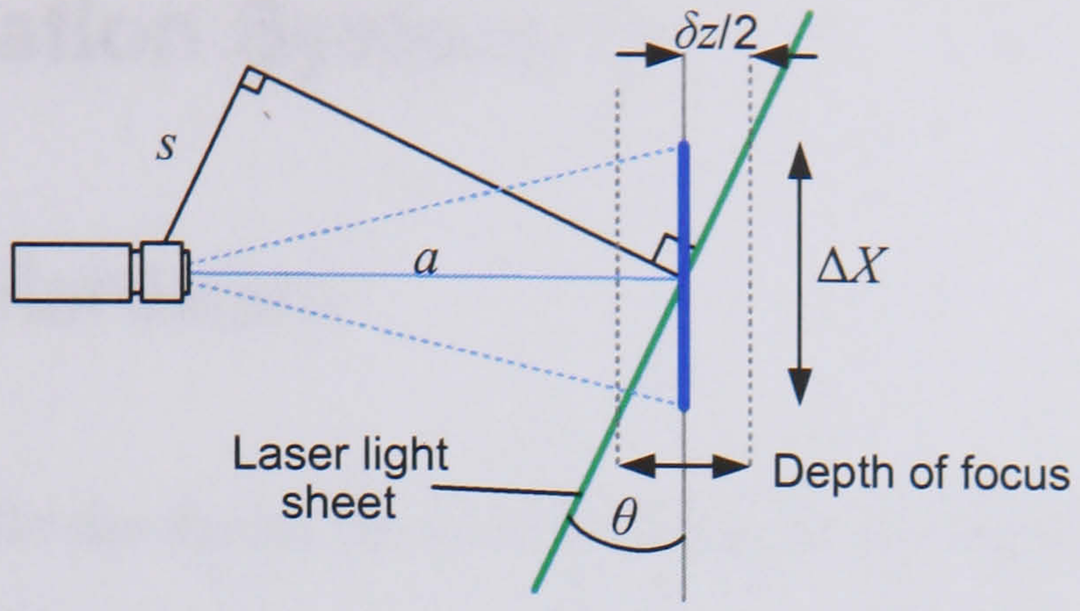

Figure 5.8 – Lens DOF requirements as a function of camera angle.

For the simplified non-orthogonal camera arrangement shown in Figure 5.8, the minimum depth of focus required for the values shown above, and a camera separation s of 50 mm (based on the width of a pco.2000) $\delta z_{min} = 13$ mm. Using equation (2.34) on page 91, the associated f-number is given by:

$$f^{\#} = \sqrt{\frac{\delta z}{4\lambda\left(1+\frac{1}{M}\right)^2}} \tag{5.5}$$

…which in this case equates to $f/4.7$. Given that the f-number is adjustable, and would normally be set as low possible, the lenses chosen for CoJeN should have an f-number of less than $f/4.7$.

Based on the considerations above, availability and pricing, 5 Nikon Micro Nikkor 55mm $f/2.8$ lenses were purchased. The associated FOV size and magnification factors (for a 2048^2 px, 7.4 μm sensor) at different object distances are shown in Table 5.7:

Distance a (m)	0.7	0.8	0.9	1.0	1.1
FOV (mm)	178	205	233	260	288
Magnification factor Z_a (px/mm)	11.52	9.98	8.80	7.87	7.11

Table 5.7 – Object distance vs. FOV for a 55 mm lens.

5.3. Illumination System

5.3.1. Laser Hardware

The lasers available for use during the CoJeN project were 3 NeoPIV Nd:YAG double-headed units, supplied by Oxford Lasers Ltd*. The laser heads each contain two separate 1064 nm cavities (thereby allowing $\Delta t \rightarrow 0$) and a single frequency-doubling crystal, which converts the 3 mm diameter beam into vertically polarised 532 nm light. The optical arrangement used to combine the two beams is shown in Figure 5.11 on page 164.

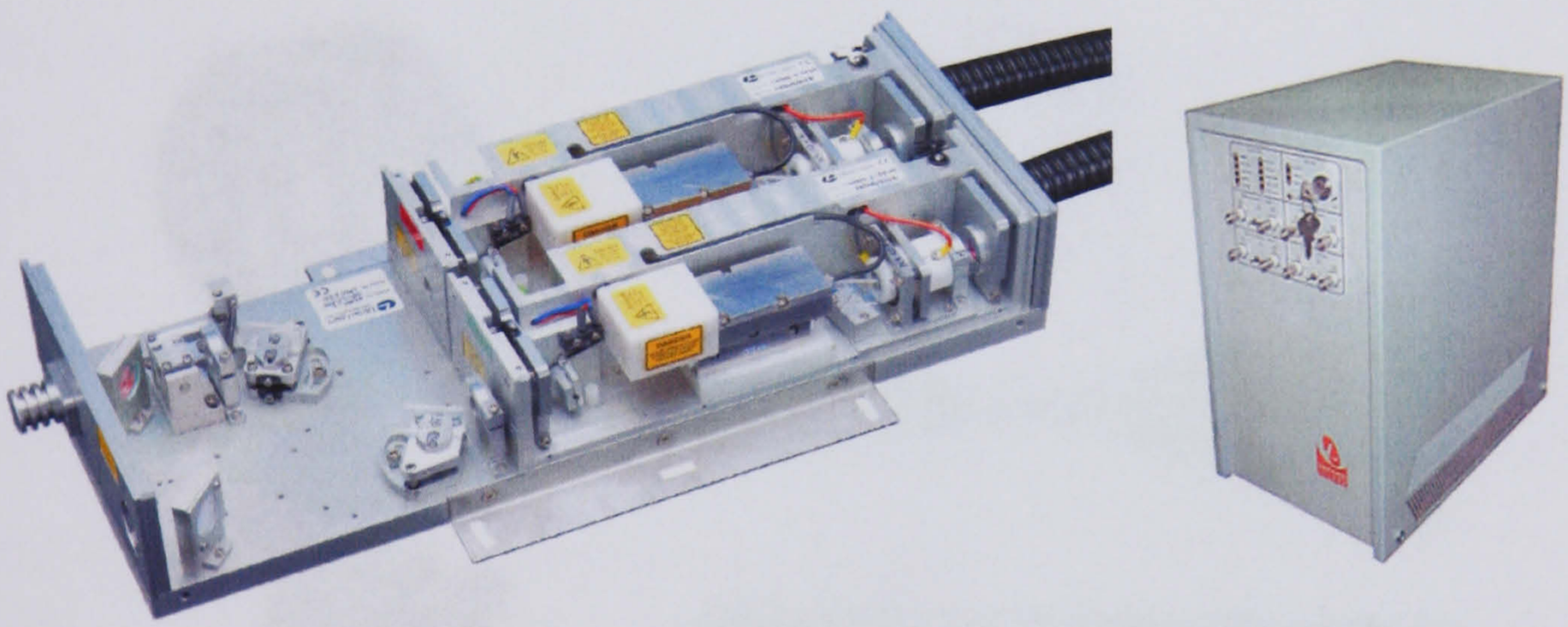

Figure 5.9 – NeoPIV head and power supply. (Litron; Oxford Lasers)

Each of the lasers were rated at 600 mJ at 1064 nm, with an actual measured output of, on average, 140 mJ at 532 nm. The lasers produce 4 ns long pulses at up to 15 Hz, using either an internal clock, or external triggers, and the power supplied to each of the two sets of flash-lamps can be controlled separately. Each laser head's PSU contains a closed-loop water cooling system, and BNC connectors for the TTL level flash-lamp and Q-switch triggers.

* The lasers are in fact re-badged Litron 'Nano S PIV' systems.

5.3.2. Light Sheet Formation and Combination

5.3.2.1. Sheet Formation

The conventional means of generating a light sheet have been discussed in Section 2.3.3, but the author has found that the combination of two cylindrical lenses, slightly rotated relative to each other, can produce a high quality sheet. As such, the CoJeN light sheet was generated using two cylindrical lenses (f/25 mm and f/40 mm) mounted in rotating holders, as shown below. Details of the lenses and mounts are given in Appendix 9.3.5.1 (page 388).

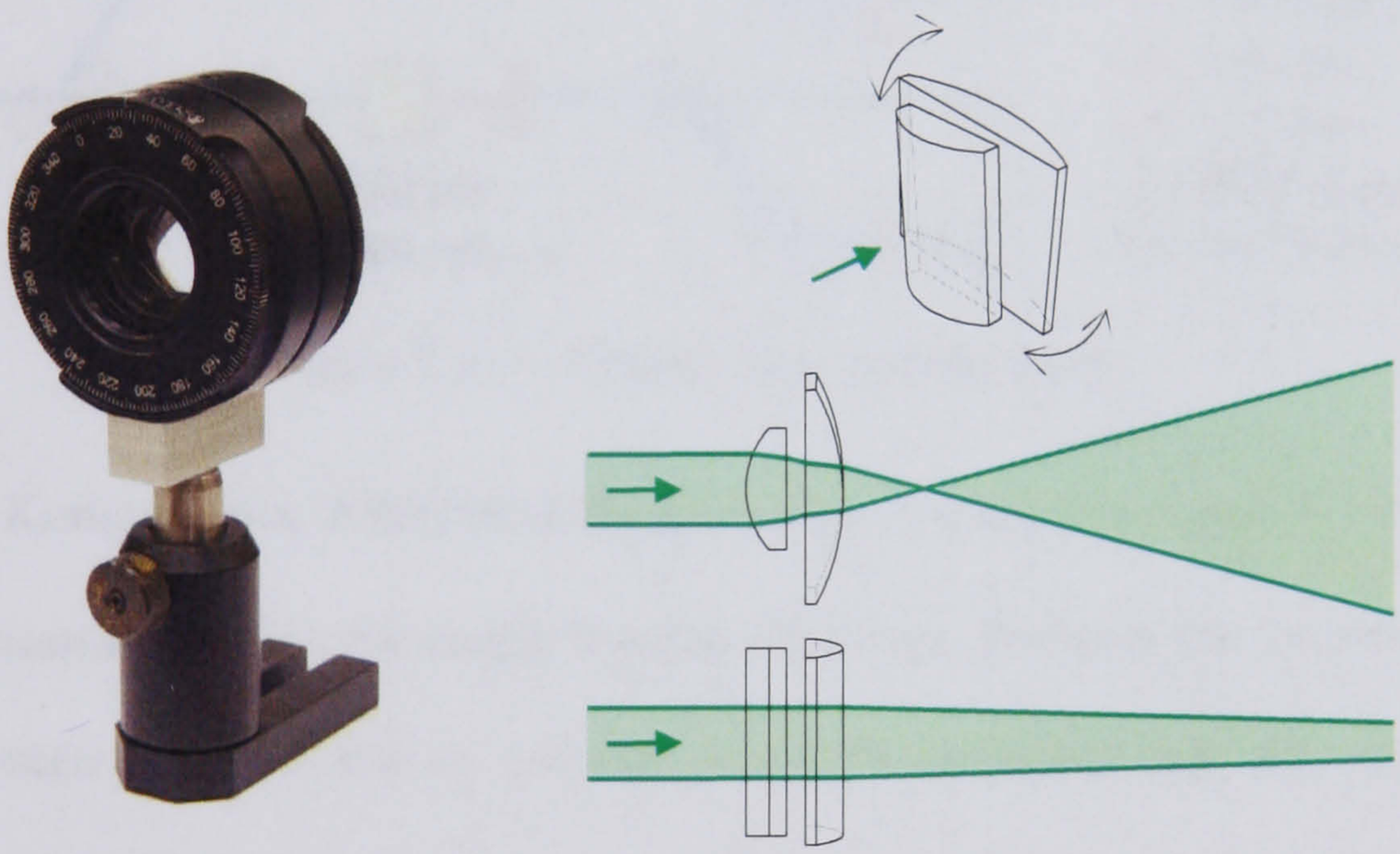

Figure 5.10 – Dual cylindrical lens sheet forming optics.

By rotating the lower power lens relative to the other, the waist of the sheet can be focussed with ease, thereby allowing the light sheet to be focussed accurately to 2 mm in the camera's field of view. As is explained below, the ability to rotate the orientation of the sheet as a whole was also necessary for accurate sheet alignment.

5.3.2.2. Beam combination

Given 6 individual lasers, and the requirement that their outputs all be formed into a single coincident light sheet, it might be considered most logical to spatially superimpose the beams, then use a single set of light sheet optics. Multiple beams, such as the two in the dual-head NeoPIV laser head shown in Figure 5.9, can be combined relatively easily by taking advantage of the Brewster's angle phenomenon described in Section 2.3.2.1 (page 62).

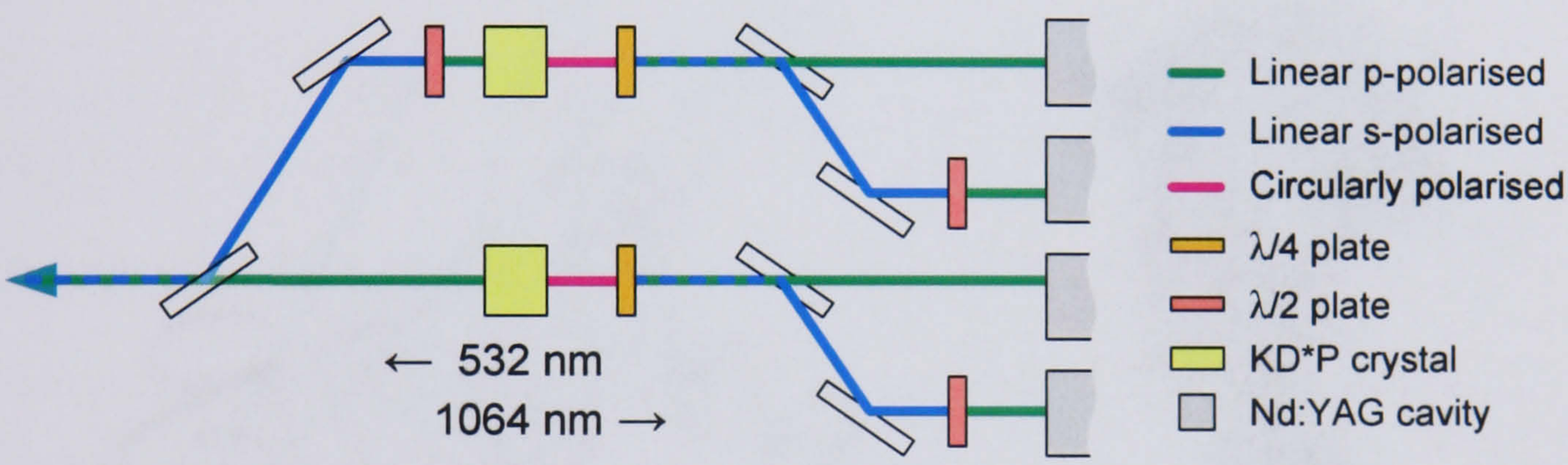

Figure 5.11 – 4-beam laser combination.

(Kähler and Kompenhans, 2000) used the arrangement shown in Figure 5.11 to combine 4 Nd:YAG beams into one, for multiple pulse PIV work. Because the frequency doubling crystals used was able to 'convert' circularly polarised light into single-state linearly polarised light, both the 1064 nm and 532 nm beam pairs could be combined using a λ/2 plate and a dielectric oriented at Brewster's angle. The arrangement does however require n frequency conversions when scaled to 2^{n+1} number of beams. The same authors also demonstrated an alternative combination technique, in which additional Pockels cells were used to rotate polarisation states in between individual pulse emissions.

5.3.2.3. Geometric Sheet Combination

A simpler alternative to the beam combination arrangements presented above is to generate multiple light sheets independently, then redirect them in such a way that they overlap and occupy the same plane. This arrangement, which was adopted for CoJeN, is achieved by slight rotation of the outer two cylindrical lens pairs, and tilting of the associated mirrors:

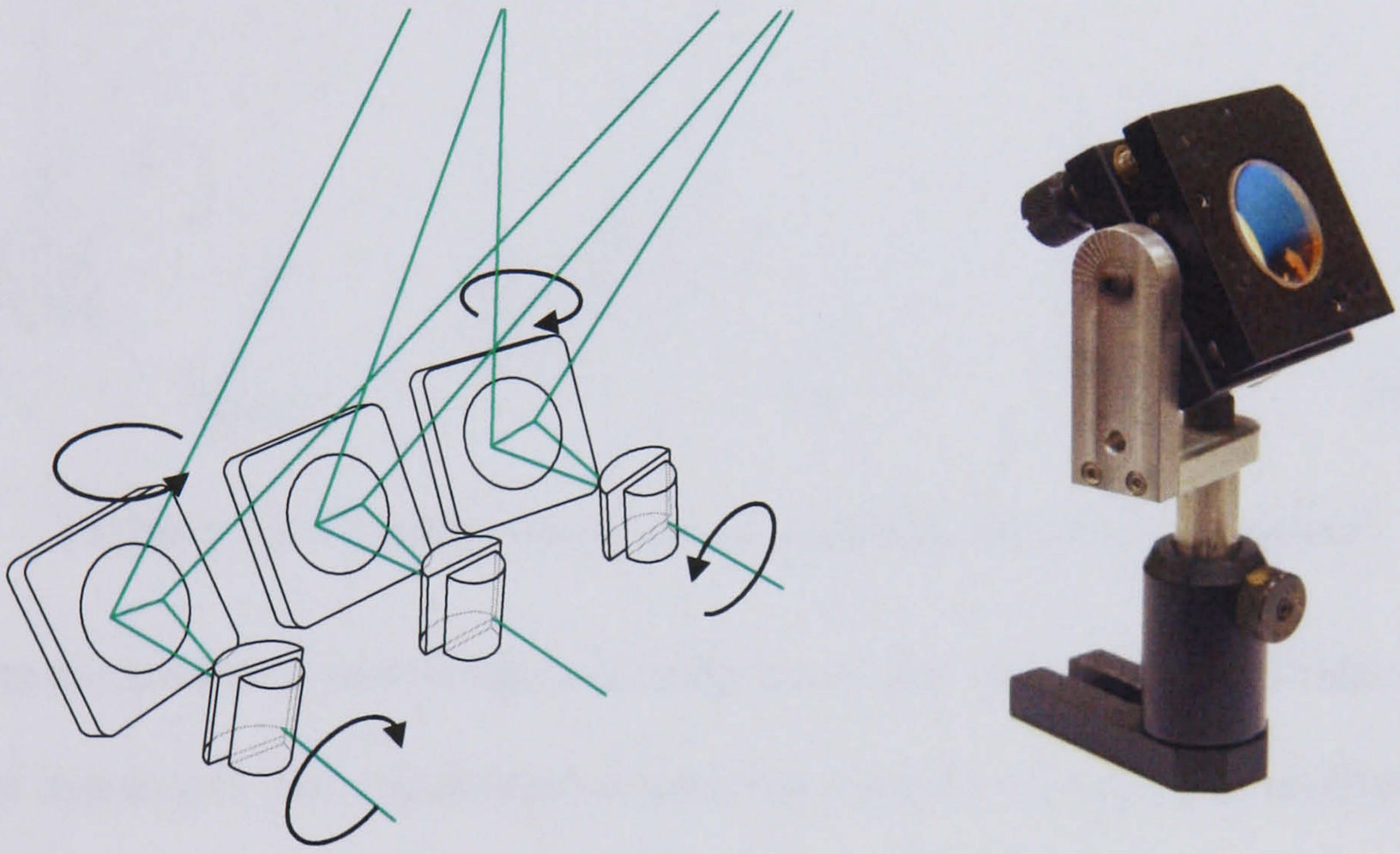

Figure 5.12a) Three laser light-sheet combination; b) Mirror gimbal mount.

In order to confirm that the sheet can indeed be placed in exactly the same plane, a mathematical model was formulated, and the results checked with a Matlab ray-tracing script. These are presented, and discussed, in Appendix 9.4.3 (page 414). Details of the mirrors and mounts, shown in Figure 5.12b, are given in Appendix 9.3.5.2 (page 389).

5.3.3. Light Sheet Alignment

The use of separate light sheet generation optics introduces the possibility of relative light sheet misalignment, meaning that each laser will illuminate a different measurement volume. Figure 5.13 demonstrates three methods by which the light sheet planes might lose their coincidence: by tilt introduced at either the projection origin or by the mirror, or roll introduced by rotation of the light sheet forming optics.

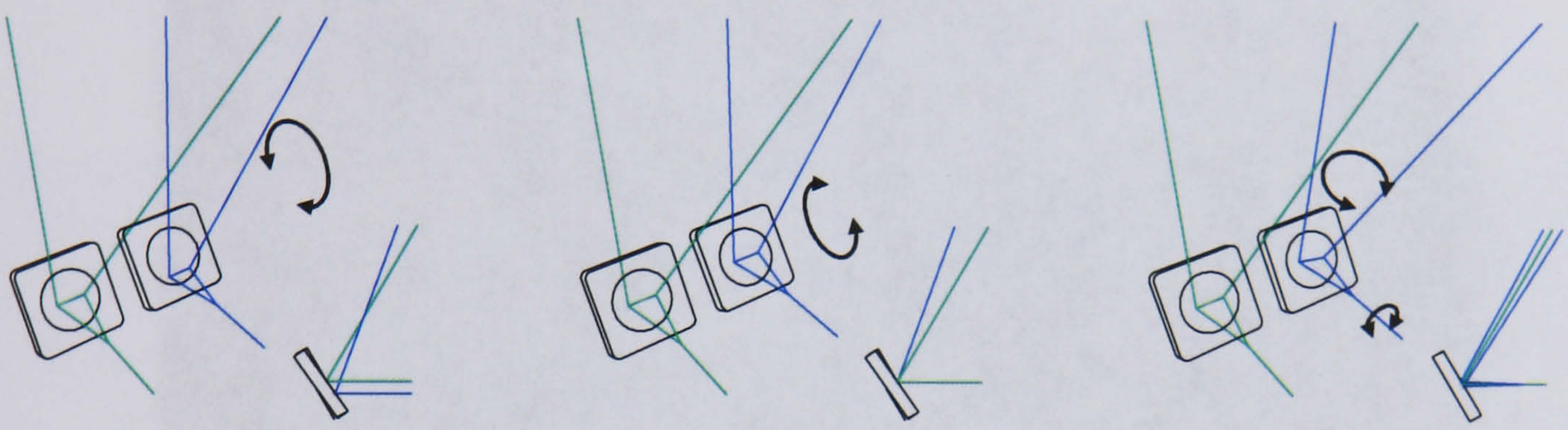

Figure 5.13 – Possible methods of laser light sheet misalignment.

In order to measure any such relative misalignment, the CoJeN rig was fitted with an automatic inspection tool, based on the real-time analysis of video frames from a camera aimed at a screen placed perpendicular to the light sheet. The camera arrangement can be seen in Figure 5.26 on page 179. While this system could not detect the first of the misalignments shown above, errors caused by such mismatched mirror rotation will be small (it would be obvious if the laser was hitting the cylindrical lens more than ~2 mm above or below the expected position, and on that basis any resulting angular sheet error is limited to 0.15° or less).

The operation of the software, and a detailed description of the image processing it performed is given in Appendix 9.1.9 (page 355). The application is shown during use in Figure 5.14, where it can be seen that laser 2 (labelled in yellow) needs to be

increased in power and moved to the left, and laser 6 (magenta) needs to be rotated clockwise in order to become aligned with laser 3 (green) with a rotational accuracy of 0.1° and horizontal accuracy of 0.2 pixels.

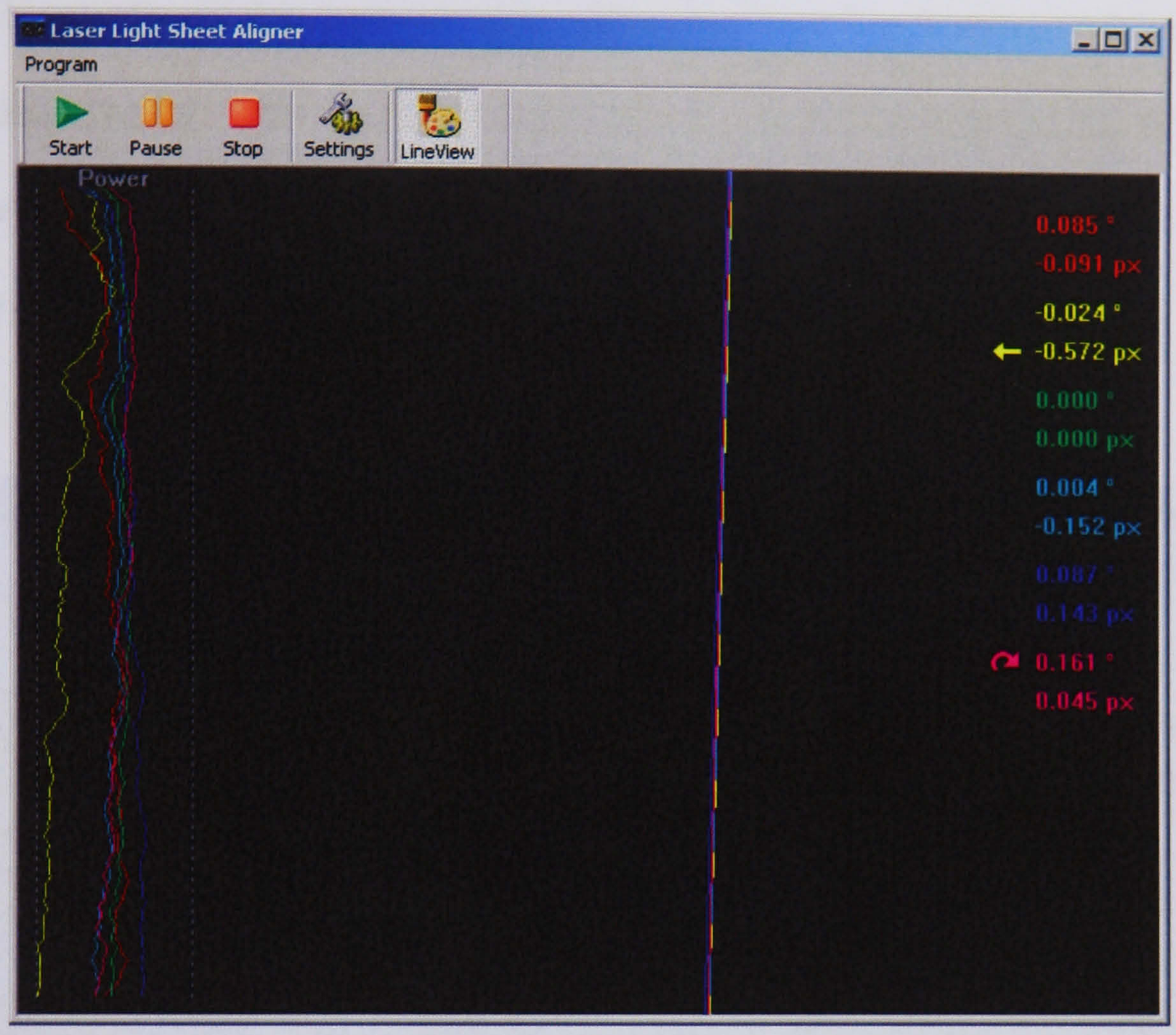

Figure 5.14 – The laser light sheet alignment application.

The lasers were aligned every morning, to an angular accuracy of 0.1° and 0.2 pixels orthogonal spatial accuracy, an amount equivalent to approximately 15 μm in the cameras' FOV (less than 1% of the 2 mm light sheet thickness).

5.4. Experimental Facility

5.4.1. The NTF at Qinetiq

The CoJeN experiment was performed at Qinetiq's Noise Test Facility in Farnborough, near London. The 26 × 26 × 14 m anechoic chamber, shown in Figure 5.15, is still one of the world's largest aero-engine exhaust noise research facilities, despite being originally constructed in the 1970's.

Figure 5.15 – The NTF at Qinetiq, Farnborough. (Qinetiq website)

The facility is capable of generating 3 airstreams for the testing of coaxial nozzles, i.e. the core and bypass jets (both of which can be heated) and an unheated flightstream. Furthermore, the entire chamber is capable of constant evacuation, to ensure the cleanliness of the air intake.

5.4.2. Rig Support Structure

During the course of the CoJeN test phases 2-5, a 6 m high support structure was erected inside the NTF chamber to provide instrument access to the jet centre line, which is 8.7 m above ground level. The top of the structure was fitted with two 1.5 × 2.5 m bogeys (centred on the jet centreline), capable of moving measurement equipment along the length of the jet exhaust.

The corners of each bogey were mounted on linear bearings, which ran along two 7.5m long rails. Motorised belts, wrapped around each of the rails, pulled the bogeys independently, by means of the arrangement shown in Figure 5.16. Magnetic incremental motion sensors and limit-switches enabled absolute position control to the nearest 10 μm. The entire support was mounted on surveyed concrete pedestals, to ensure the coincidence of the guide rails with the nozzle's frame of reference.

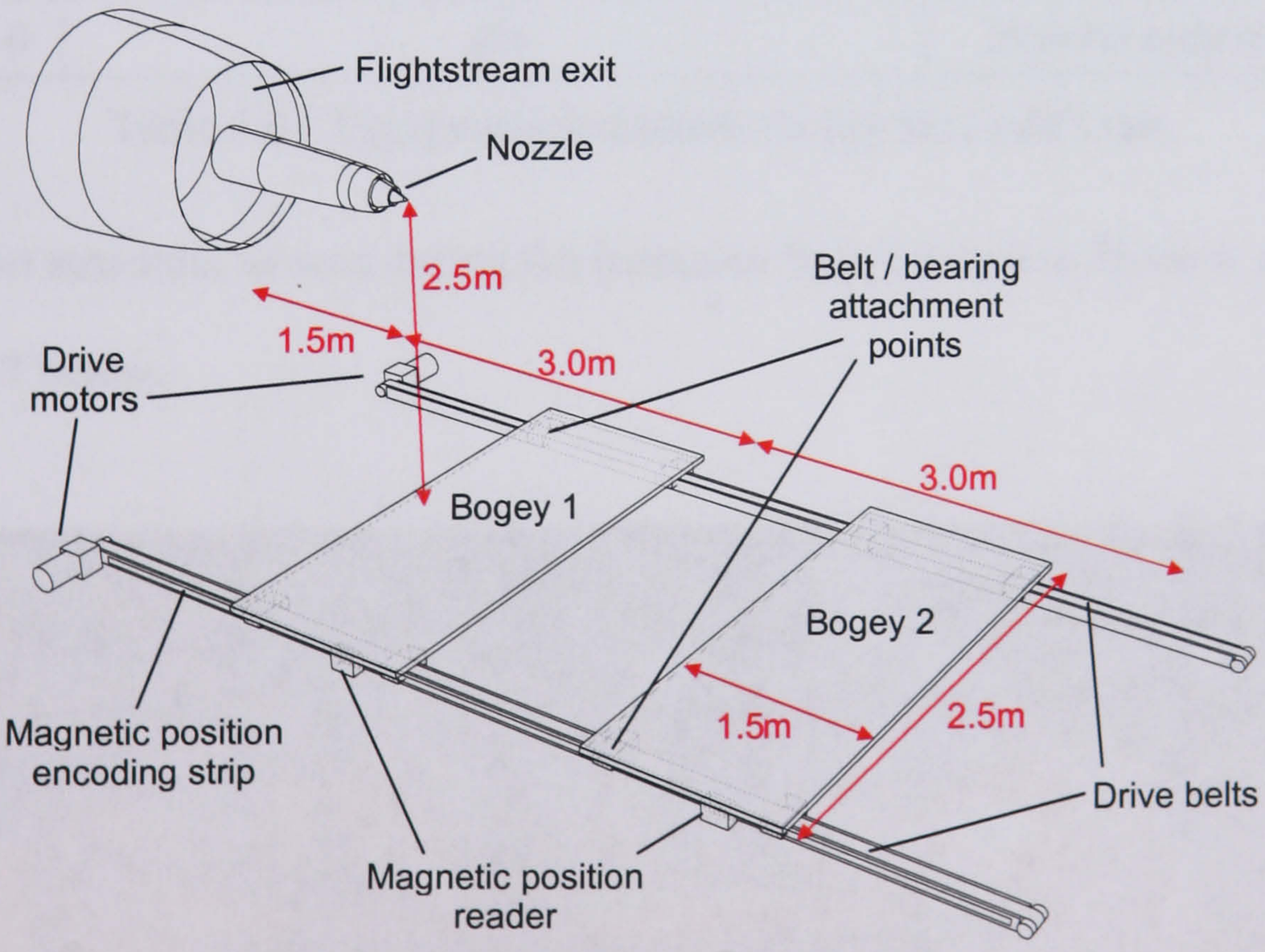

Figure 5.16 – The bogeys and drive system.

Engineering drawings for the support structure, which was designed and built by a Farnborough engineering company, are included in Appendix 9.3.1 (page 377). It can be seen that the 7.5 m traverse is separated into 3 sections: a 1.5 m long 'front storage zone', a 3.0 m 'measurement zone', and a 3.0 m long 'back storage zone'. The purpose of the 'storage zones', was to allow both 1.5 m wide equipment-laden bogeys unhindered access to the entire length of the 3.0 m measurement zone. The equipment placed on the two bogeys during each test phase is listed below:

	Equipment on bogey 1	**Equipment on bogey 2**	**Non bogey mounted equipment**
Phase 1	n/a		Far-field azimuthal and polar microphone arrays
Phase 2	Madrid PIV	Warwick PIV	
Phase 3	Madrid PIV	Warwick PIV & LDA	
Phase 4	2-point LDA	Warwick PIV	Near-field linear microphone array
Phase 5	Near-field circular microphone array	Madrid PIV	Near-field linear microphone array
Phase 6	n/a		Internal nozzle probe

Table 5.8 – Equipment placement during the CoJeN test.

The support structure, as seen during the transition from Phase 3 to Phase 4, is shown in Figure 5.17 below:

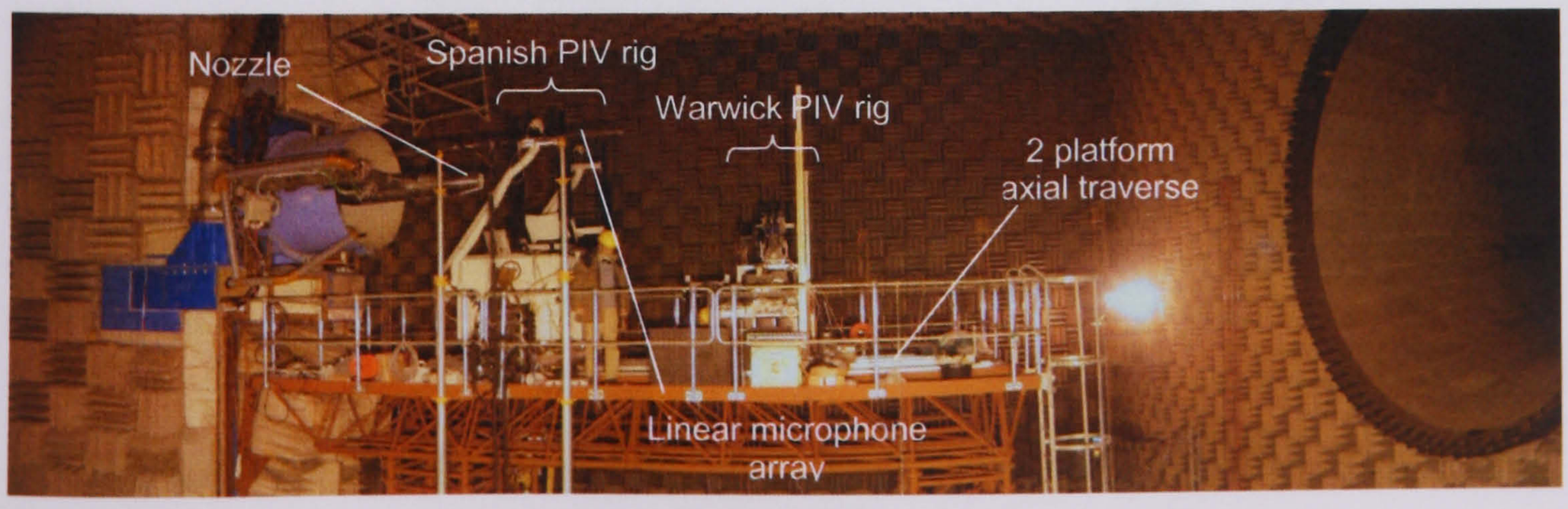

Figure 5.17 – NTF, with support structure and CoJen rigs.

5.5. Mechanical Rig Design

5.5.1. Component Layout

The world-orthogonal arrangement of camera and light sheet, as shown in Figure 5.18a, is well established for 2D PIV studies. It is however difficult to incorporate the appropriate camera support structure into a compact rig that is both mechanically stable and capable of being lifted into place using a crane. Furthermore, it was initially understood that near-field microphone measurements would be taken during CoJeN test phases 2 & 3, meaning that the acoustic impact of the PIV rig at jet height needed to be minimised. This is most easily achieved by reducing the number and height of vertically protruding surfaces, which would otherwise be capable of reflecting sound from the jet to the microphones.

For these reasons, and given the assumed unimportance of measurement plane angle, it was decided that an angled camera and light sheet arrangement, as shown in Figure 5.18b, would be most appropriate.

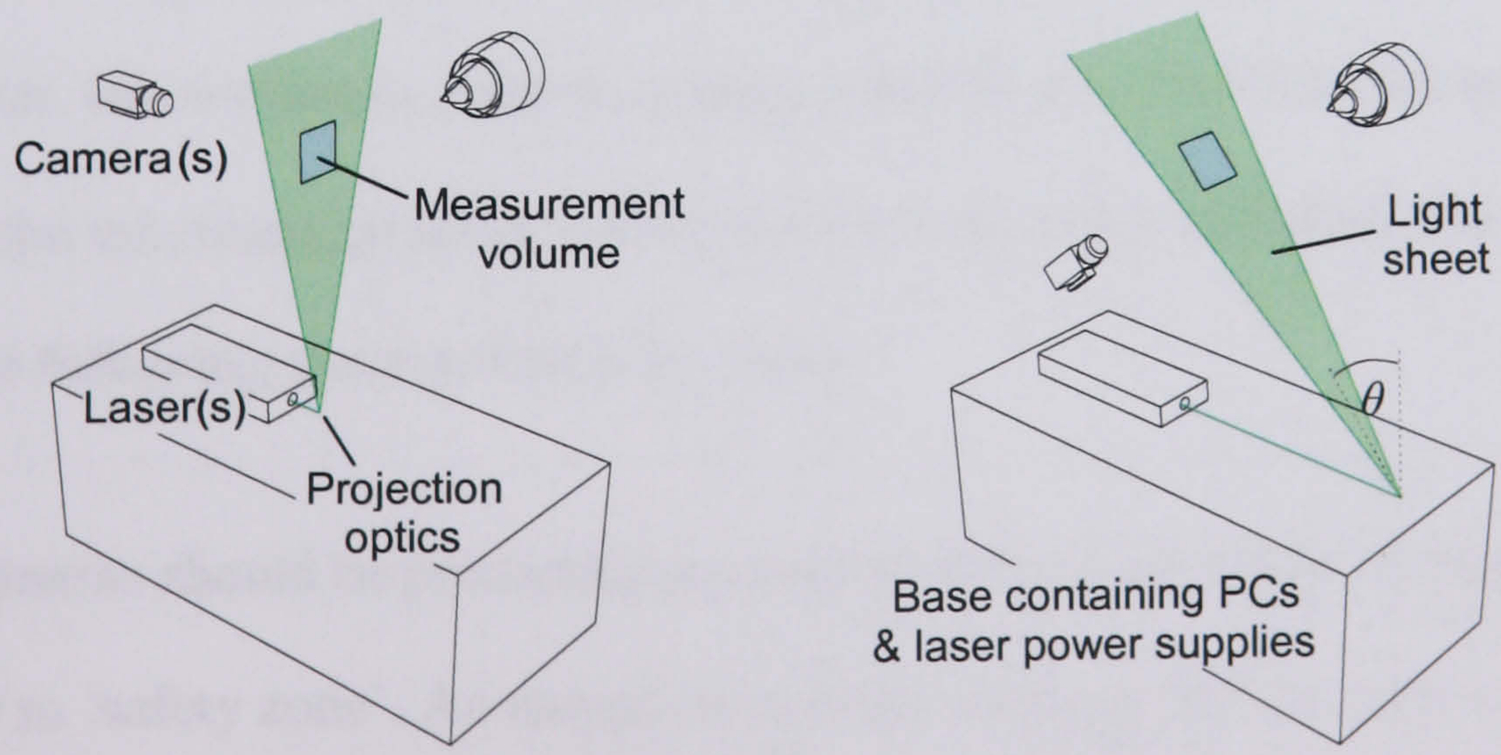

Figure 5.18a) World-orthogonal CoJeN rig arrangement; b) Angled arrangement.

While a highly rotated measurement volume reduces the overall height of the equipment, it also forces the light sheet projection optics ever further towards the edge of the rig. With the axial traverse bogeys only 1.5 × 2.5 m in size, it can be seen that the amount of space available for phase 2 cross-axial traversing is directly dependent on θ – the angle between the light sheet and vertical.

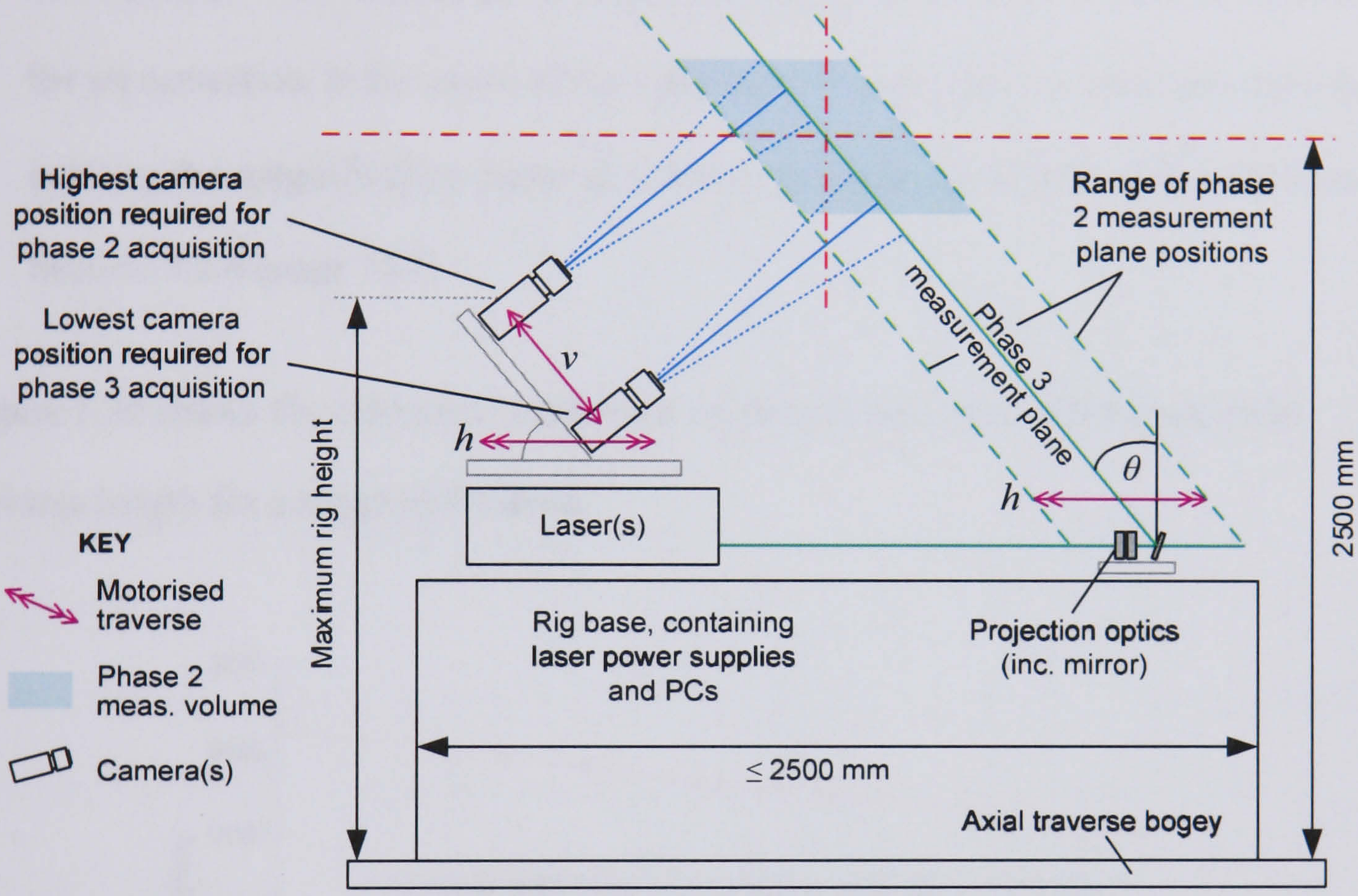

Figure 5.19 – Downstream view of CoJeN rig components.

A Matlab script (given in Appendix 9.4.6, page 424), based on the component layout shown above, was written in order to quantify the effect of θ on both the maximum rig height and the maximum possible cross-axial traverse length (labelled h in the figure above). The following assumptions were made:

- The cameras should be positioned as close to the jet as possible without entering the 0.9 m 'safety zone'. An exception is made during phase 2 cross-axial acquisition, when the cameras are allowed up to 0.6 m from the jet centreline.

- The projection optics and cameras should never move more than 1150 mm from the centre of the rig.
- As a result of being mounted on a base which is tall enough to hold the laser power supplies (but short enough that the lowest camera position can be accommodated), the laser exit ports are 1.1 m from the rig bottom.
- The cameras' FOV should be traversed between 116 mm above, and 492 mm below the jet centreline, in the plane of the light sheet. These values were determined by entering the magnification factor $Z_a = 8.8$ px/mm into the Matlab script presented in Section 5.2.4 (page 154).

Figure 5.20 shows the calculated maximum rig height and permissible cross-axial traverse length for a range of θ values:

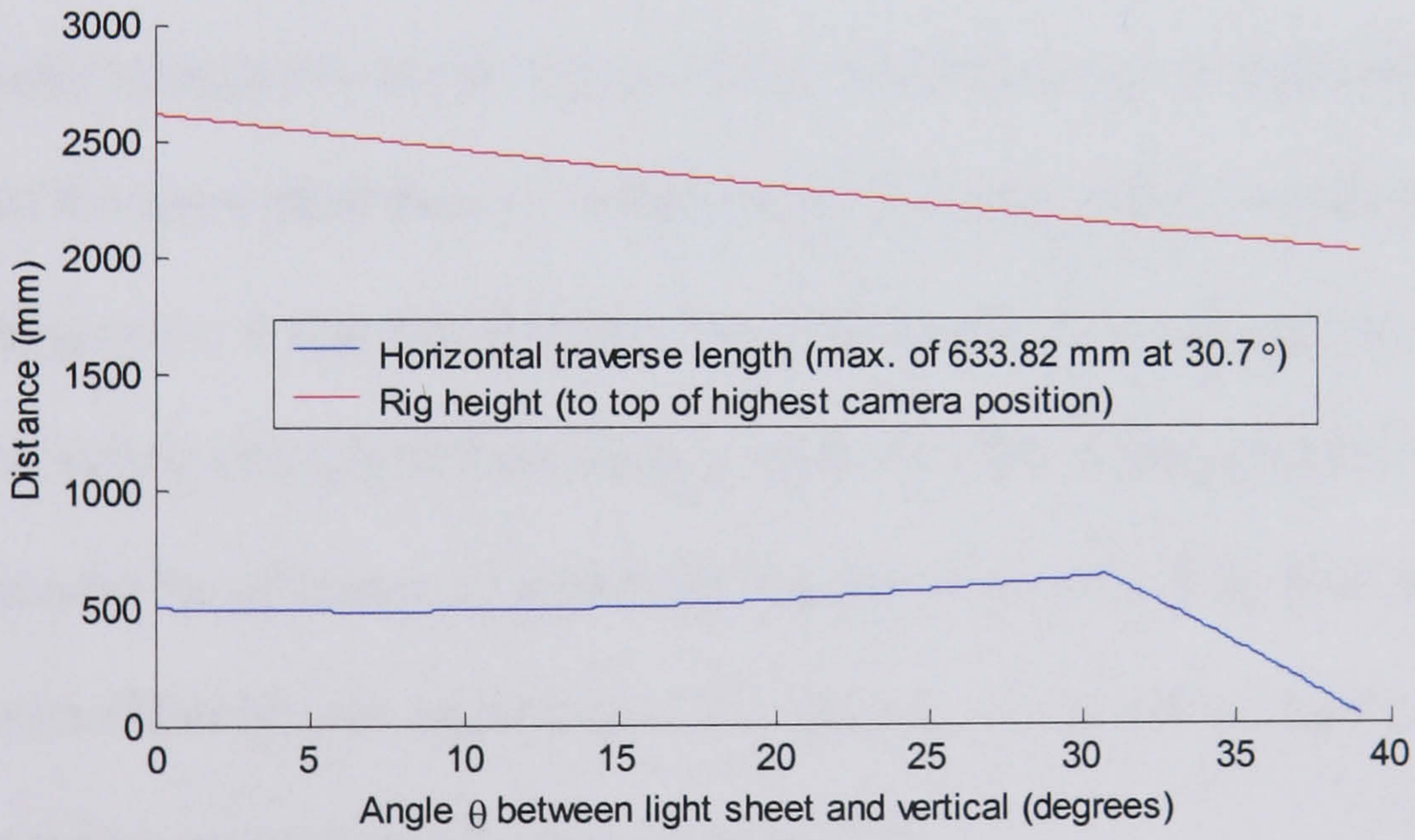

Figure 5.20 – CoJeN rig light sheet angle optimisation.

Figure 5.21 shows the rig layout as calculated for $\theta \approx 31°$; the value that can be seen to offer the best compromise between horizontal and vertical compactness. This value was accordingly used during the construction of the CoJeN rig.

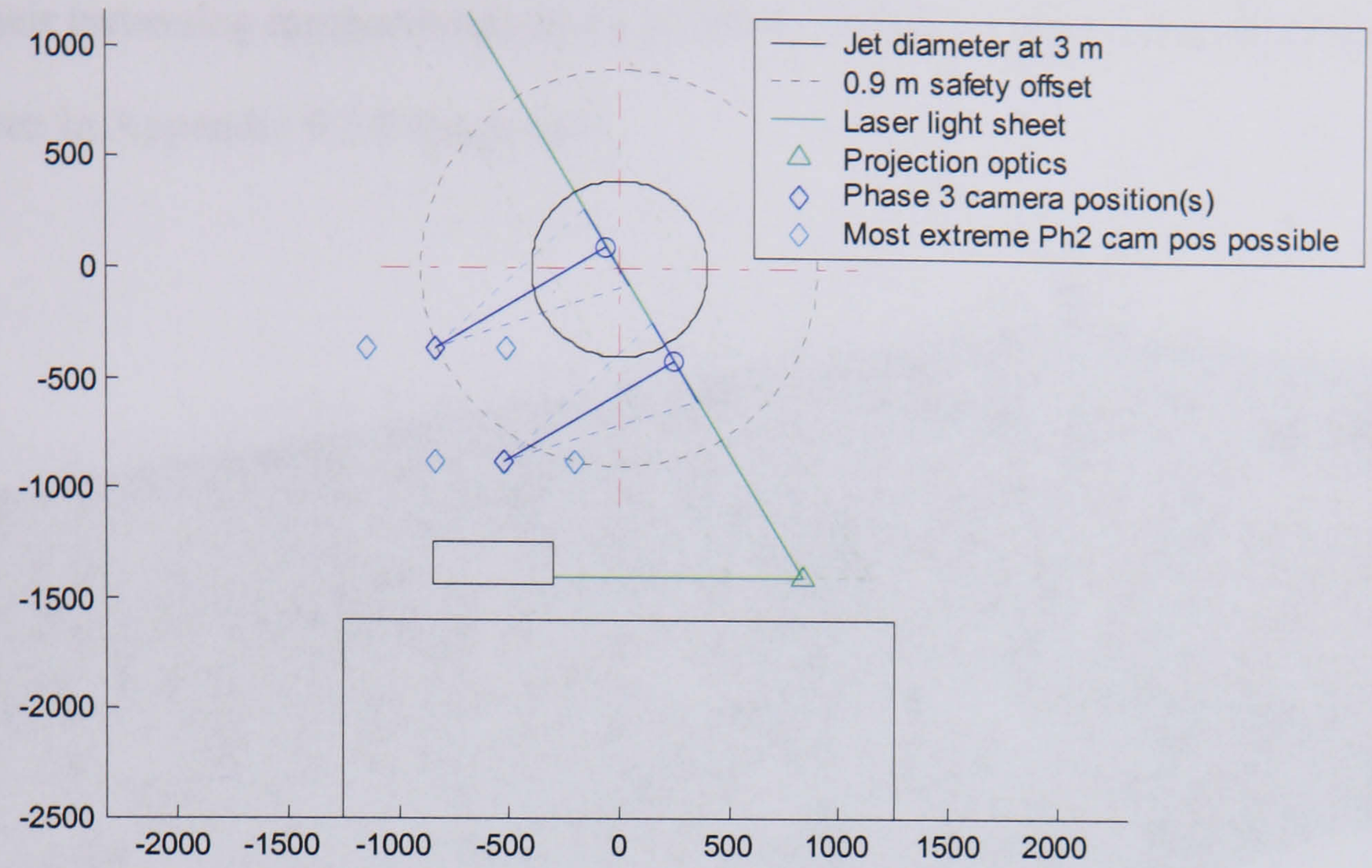

Figure 5.21 – Downstream view of CoJeN rig component layout, with $\theta = 30.7°$.

5.5.2. Rig Construction

It was originally intended to build the base of the CoJeN rig out of extruded aluminium profile, due to the associated ease of construction. However, after consulting several mechanical engineers, it was decided that the joints used with such extrusions would not necessarily be strong enough for compliance with the 1998 Lifting Operations and Lifting Equipment Regulations, to which the rig had to comply. The final design therefore used welded 50 mm square steel box section, as shown in Figure 5.22. Details of the design are given in Appendix 9.3.2 (page 379).

Half of the top surface of the rig was covered with a tapped aluminium optical table, while the other half was used to support the laser enclosure shown in Figure 5.23. The enclosure, which was made from 45 mm square extruded aluminium profile, not only supported the 3 NeoPIV laser heads, but also provided a base onto which the cameras

(and their traversing mechanisms) could be fitted. Details of the laser enclosure design are given in Appendix 9.3.3 (page 380).

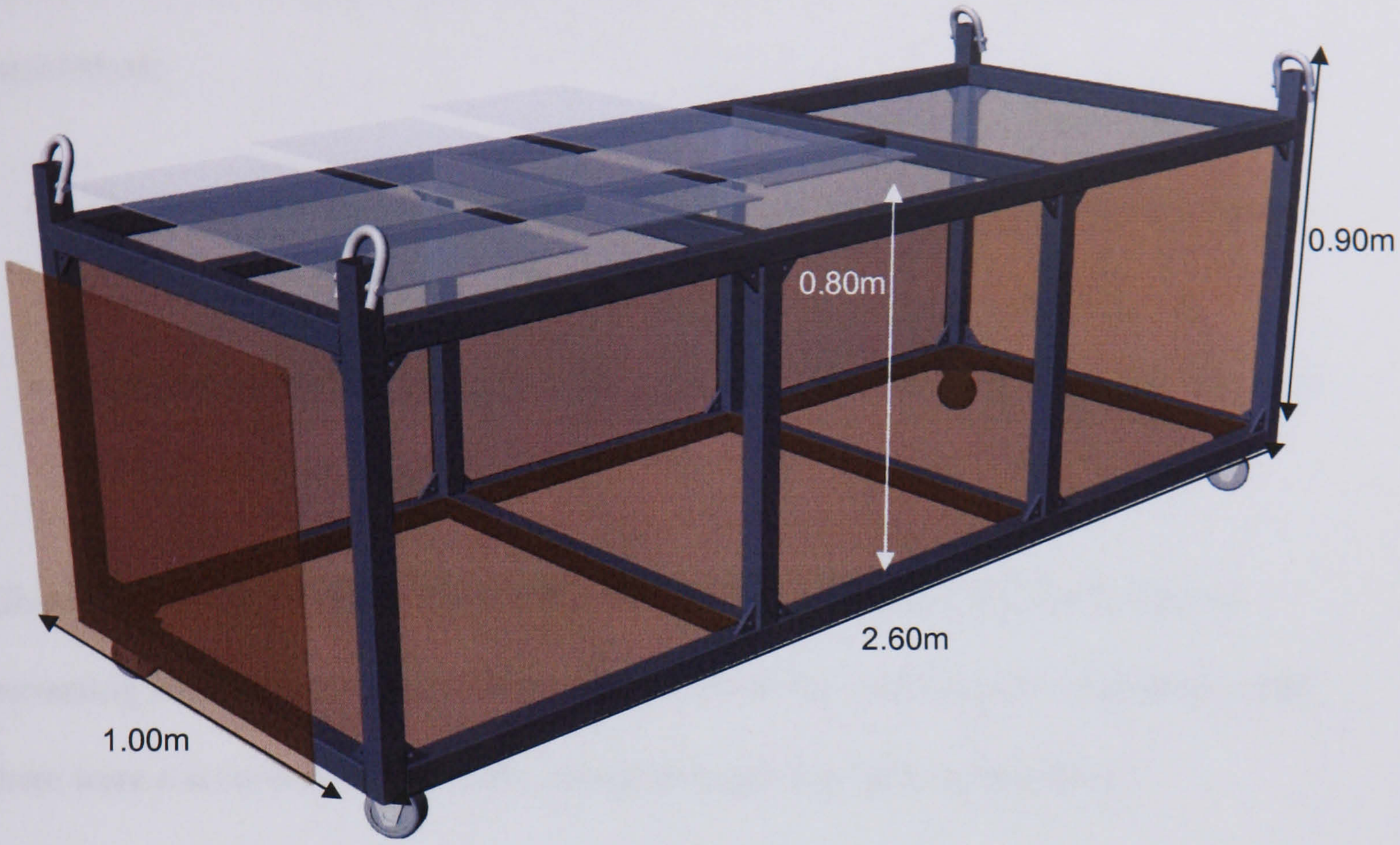

Figure 5.22 – The CoJeN rig steel framework.

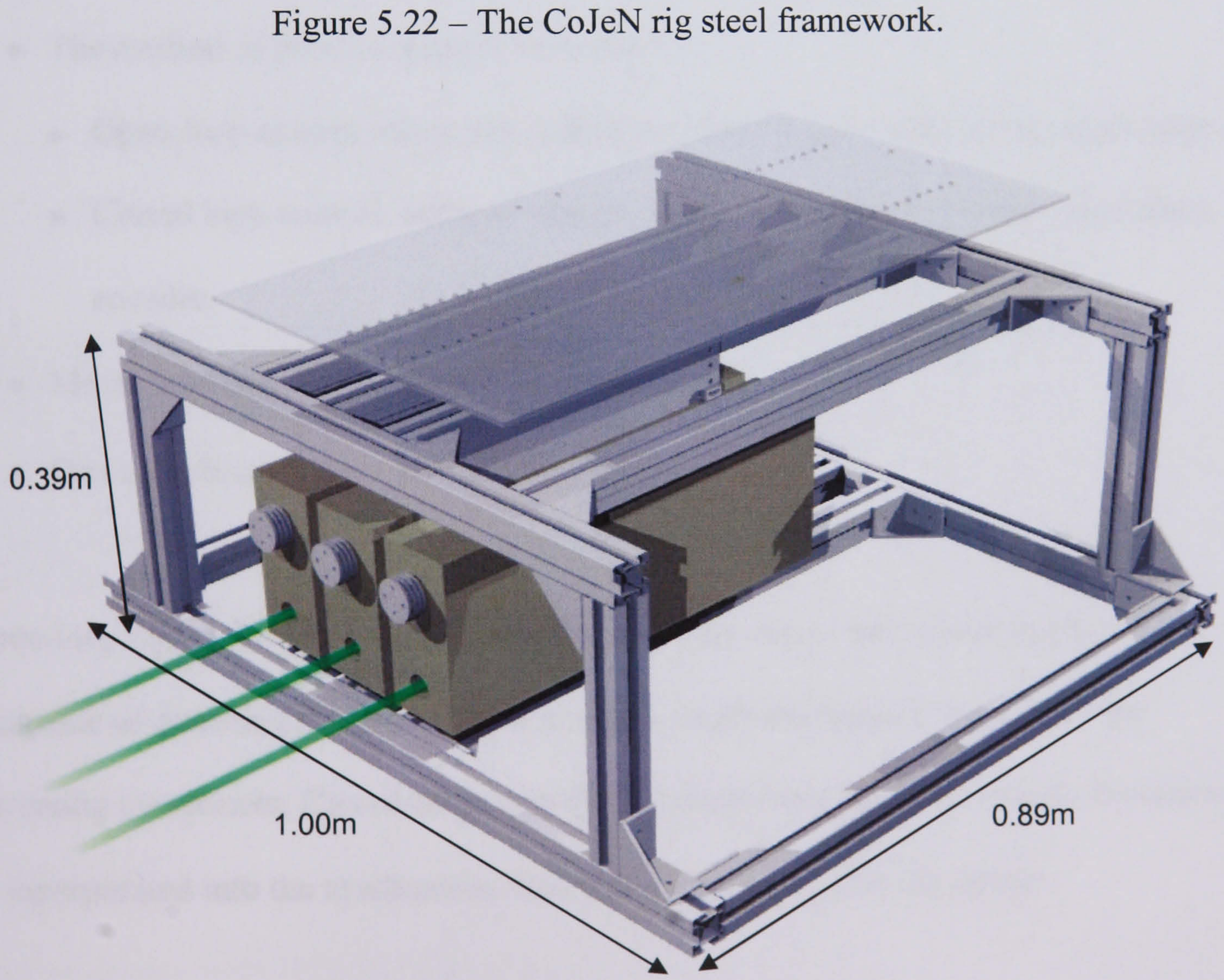

Figure 5.23 – The CoJeN rig laser enclosure.

5.5.3. Motorised Traverses

From the Matlab script presented in Section 5.5.1 the following requirements were established:

- The cameras required a traverse capable of moving at least 608 mm in the same plane as the light sheet (i.e. ~31° to the vertical).
- Both the projection optics and cameras must be mounted on cross-axial traverses of up to 633 mm in length.

Given the rig component layout presented in Figure 5.19, it is clear that 3 separate traversing sections were required. Putting the traverses' mechanical design to one side, there were a several questions to be answered regarding their motorisation:

- The method of position control to be used:
  - ▸ Open-loop control using, say, a stepper motor or piezoelectric linear actuator.
  - ▸ Closed loop control, using an optical or magnetic, rotary or linear quadrature encoder.
- Motor type (e.g. DC, stepper or linear motor).
- Drive mechanism (e.g. lead screw or belt drive).

Open-loop motor drivers are invariably cheaper than closed-loop controllers, but are incapable of detecting motor slippages or stalls, or obstructions in the way of the traversing component. Closed-loop controllers, while more accurate, require encoders to be incorporated into the mechanism, which adds further cost to the design.

Given the assumption that no unexpected obstructions would appear in the way of the CoJeN rig components, it was decided to power the traverses using bipolar stepper motor driven lead-screws, running under open-loop control. By using un-encoded stepper motors, costs were minimised, but the use of a lead-screw and a bipolar motor* reduced the possibility of motor slippage caused by insufficient torque.

The motor driver selected for use with the CoJeN traverses (Milford Instruments; model 5-595) is shown in Figure 5.24a, alongside the 75Ω 200 step/rev. motor it was used to power. Four of the drivers were daisy-chained together and mounted (along with 2 × 12V 1A power supplies) in the enclosure shown in Figure 5.24b.

Drive capabilities:	Bipolar windings; 500mA at 12V.
Stepping speed:	$\frac{1000}{2^n}$ Hz, where $n = \{0,1,2,3,4,5,6,7\}$.
Communications:	9600 baud (8-N-1) RS-232 serial protocol.

Table 5.9 – Milford Instruments 5-595 motor driver specification.

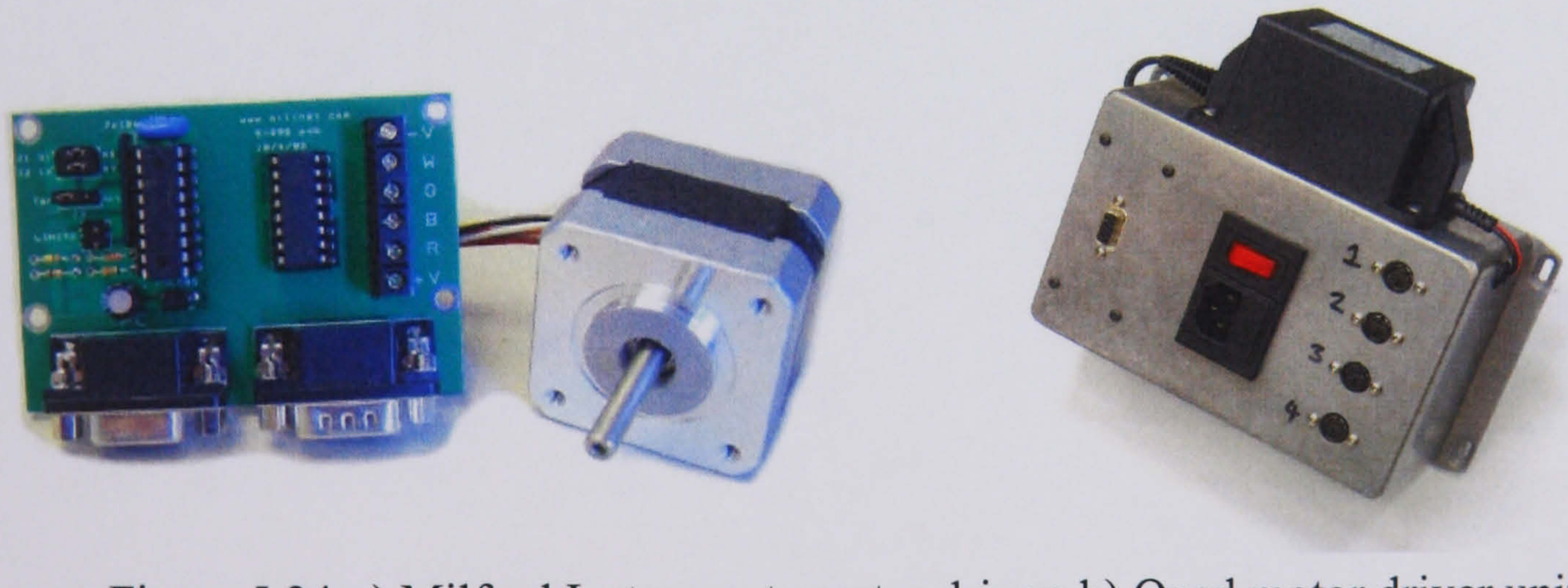

Figure 5.24 a) Milford Instruments motor driver; b) Quad motor driver unit.

* Bipolar stepper motors, by virtue of energising 2 of their 4 coils at a time, provide more torque than unipolar motors. The difference however, often lies only in the drive electronics and not the motor itself.

While the 5-595 motor driver lacks an encoder interface, it does offer a limit switch input, which was used to datum the traverses' positions. Slotted optical switches (RS; 304-560) were mounted at each end of the traverses, and the motors rotated until contact was made. Figure 5.25 details the OR-gate junction box that had to be fitted to each traverse to enable the optical switches to be interfaced with the controller.

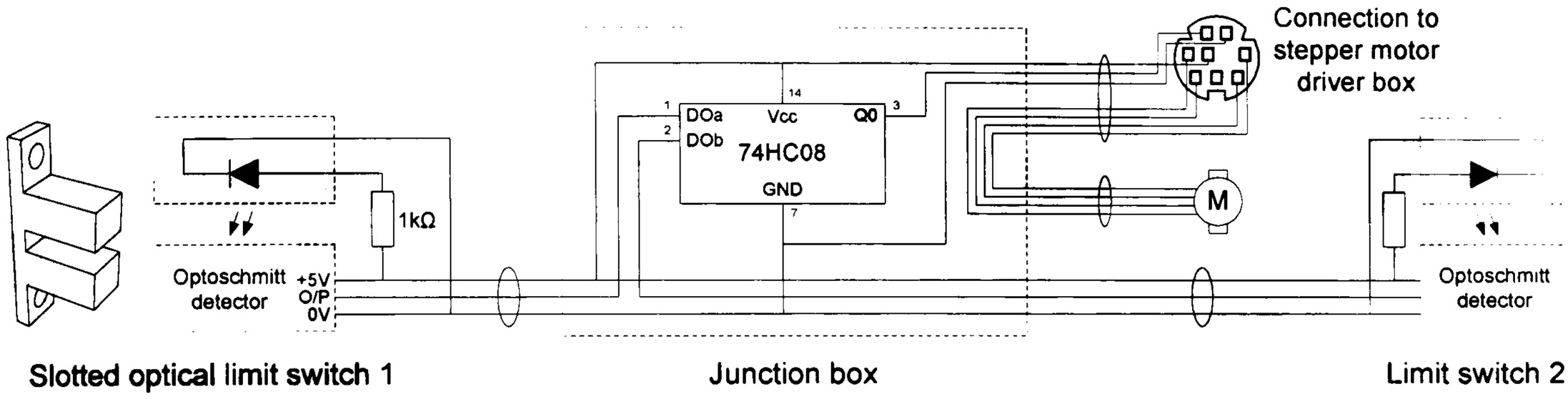

Figure 5.25 – CoJeN traverse limit switches and junction box.

5.5.4. Projection Optics Traverse

The projection optics traverse comprised a 200 × 300 mm platform (covered with M6 tapped holes on a 20 mm grid) mounted atop a 460 mm long linear guide rail. The platform was driven using an M10 lead-screw which was connected to the stepper motor via a 1:2.5 timing belt arrangement. Full engineering drawings for all components of the traverse can be found in Appendix 9.3.4 (page 382).

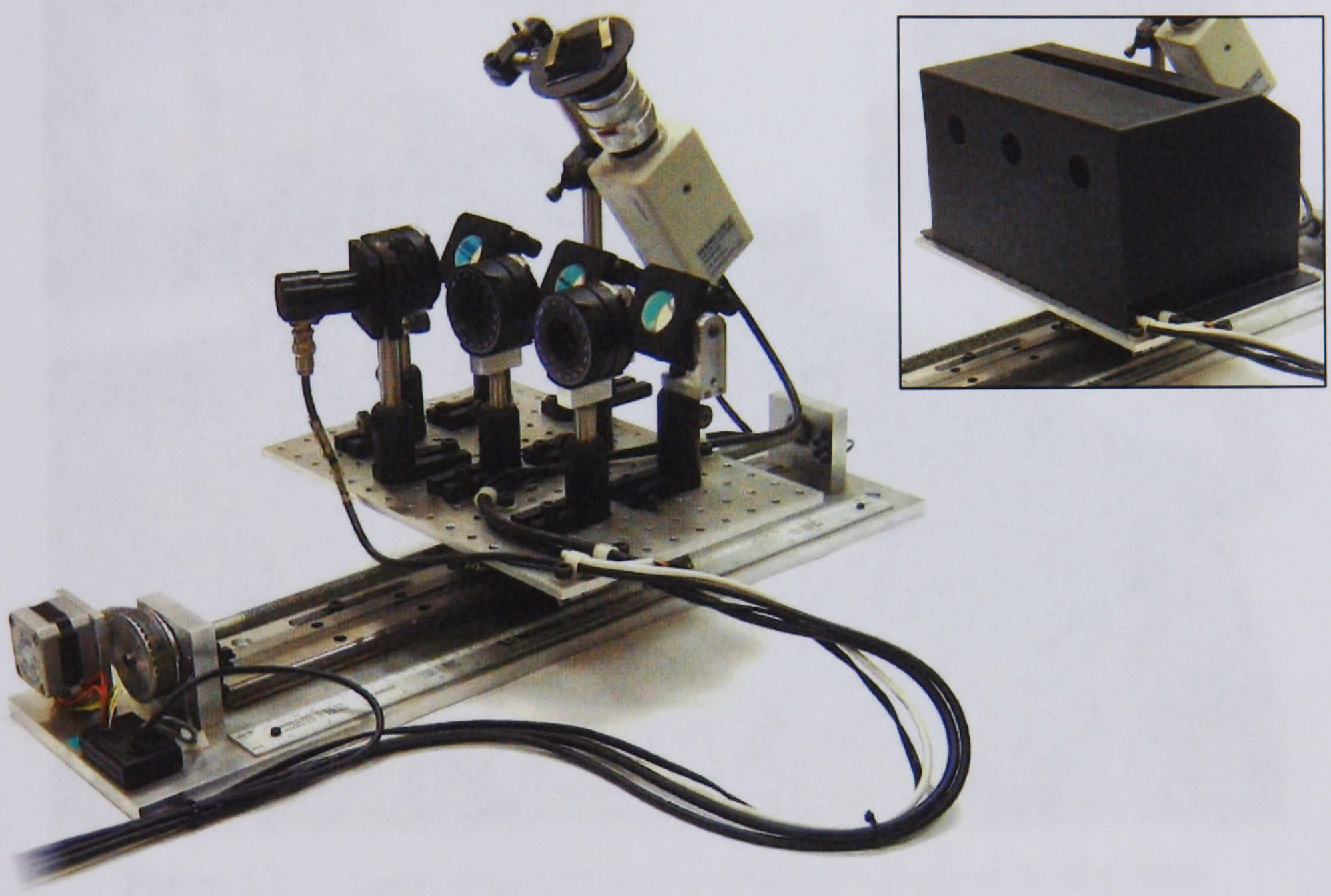

Figure 5.26 – The light sheet projection traverse (insert: with dust shield).

Figure 5.26 shows the platform with its payload of cylindrical sheet-forming lenses and projection mirrors. A photodiode (used for laser power monitoring during setup) and the sheet alignment camera discussed in Section 5.3.3, are also shown. During testing, the projection optics were covered with a dust shield (shown above right) to minimise the ingress of seeding particles.

5.5.5. Laser Alignment Mirrors

One downside to traversing the light sheet optics during phase 2 was the requirement that the laser beams be completely orthogonally to the traverse axis. In order to facilitate this alignment, an additional 3 pairs of Nd:YAG mirrors (ThorLabs; NB05-H12) were mounted between the laser heads and cylindrical lenses, as shown in Figure 5.27:

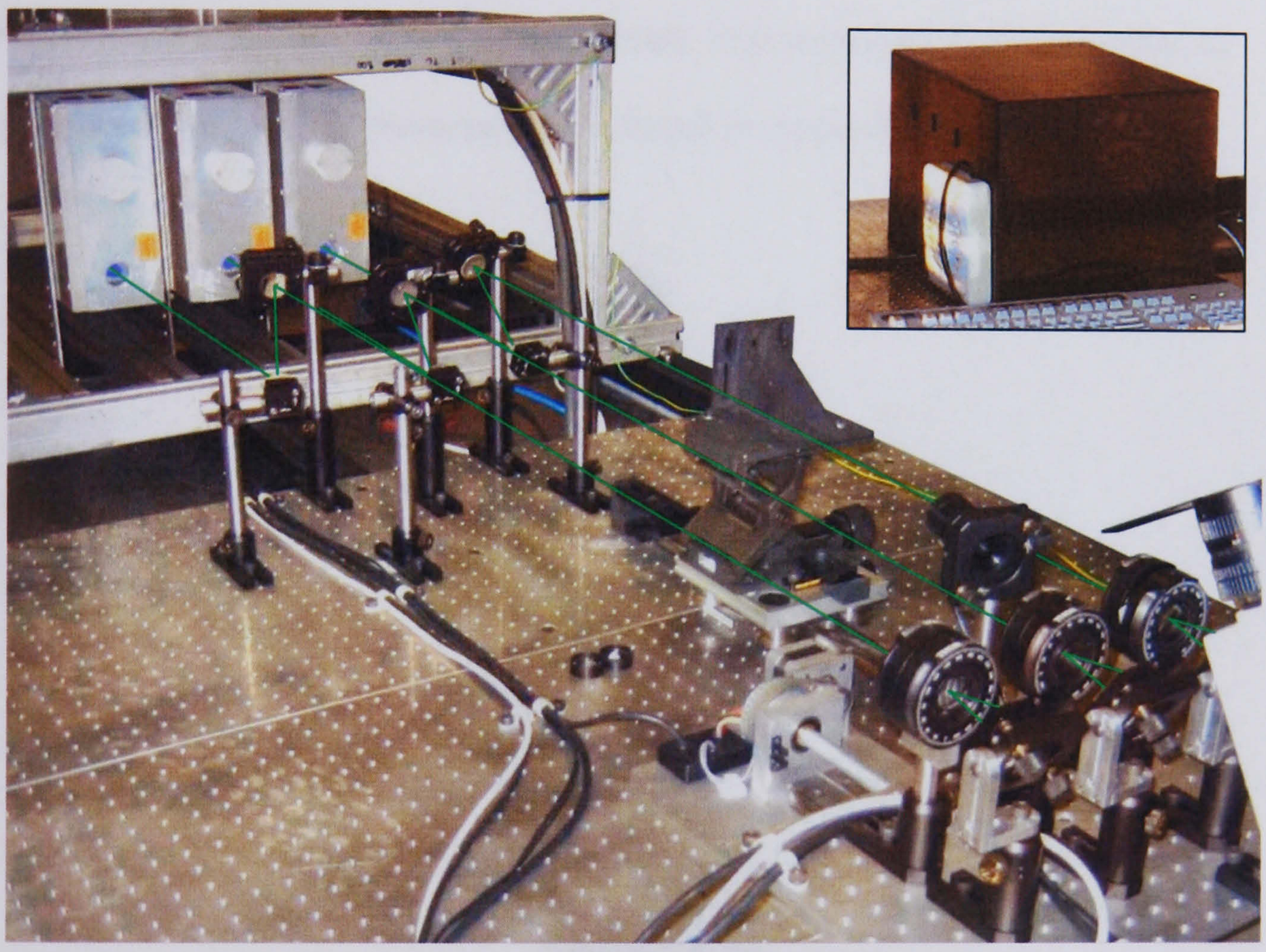

Figure 5.27 – Laser alignment mirrors (insert: ventilated dust cover).

Not only did this ease the adjustment of both the beams' height and angle, but it also allowed the projection optics to be mounted closer together than the laser heads themselves. Similarly, the heads could be mounted lower down than they would have otherwise had to be. As before, these mirrors were covered with a dust shield during testing, with a filtered fan added to provide positive pressure ventilation.

5.5.6. Camera Traverse

The 'vertical' section of the camera traverse, shown in Figure 5.28 below, comprised a 290 × 260 × 10 mm platter (covered with Ø 6.1 mm holes) mounted on a 700 mm long guide rail, which could be locked at any angle between 0 and 90° to the vertical. The horizontal base traverse comprised two 600 mm long guide rails, spaced 200 mm apart for stability. Both sections were driven using M10 lead-screws which were connected to their motors via 1:3.3 timing belt arrangements. Full engineering drawings for all components of the vertical traverse can be found in Appendix 9.3.6 (page 390).

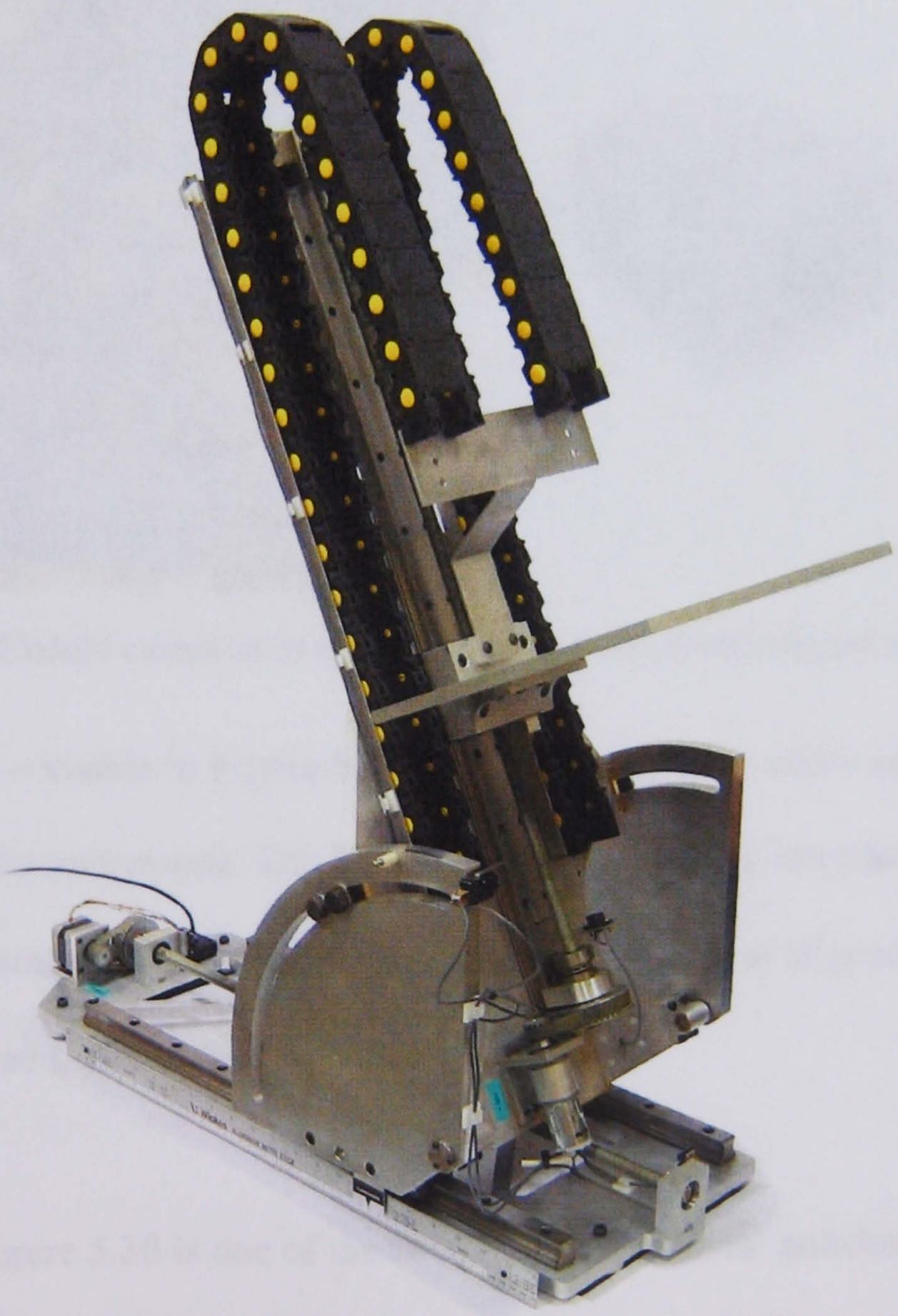

Figure 5.28 – The CoJeN camera traverse.

5.5.6.1. Camera Mounting

The PIV cameras (numbered 1 through 5) were mounted to the camera traverse in the positions shown in Figure 5.29a. If the cameras were aligned orthogonally with the platter however, and bolted directly to it, the fields of view would be offset by up to 200 mm. To allow adjustment of their positions, to maximise FOV overlap, angled camera mounts were manufactured: 3 with a fixed 5.5° inclination and 2 of variable angle. Engineering drawings for the mounts are given in Appendix 9.3.6 (page 401).

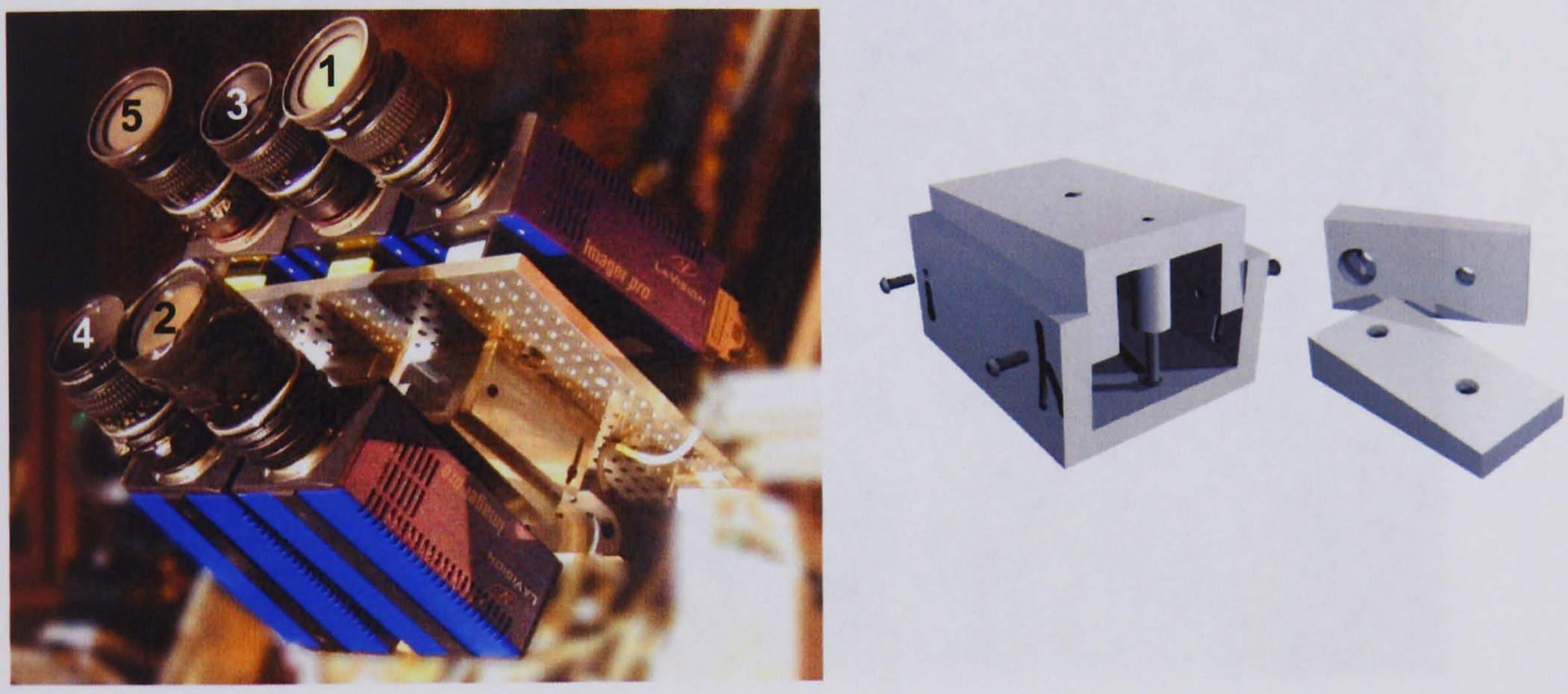

Figure 5.29a) CoJeN cameras in situ; b) Variable and fixed angled camera mounts.

A further bracket – visible in Figure 5.30 – was constructed to allow an LDA head to be attached to the camera traverse. The LDA system, used during test phase 3 to acquire measurements from a point within the PIV cameras' FOV, was aligned, calibrated and operated by Dantec Dynamics.

Also visible in Figure 5.30 is one of the two 'alignment rulers' attached to the camera traverse to ensure that it was oriented at the same angle as the light sheet. By moving the traverse between its highest and lowest positions, and ensuring that the light sheet

hit both rulers at the same point, the inclination and rotation of the light sheet relative to the camera FOVs could be confirmed as being zero. These rulers also served to hold the 3D camera calibration plate described in Section 3.2.2 (page 118), and also a black cardboard 'projection screen', for use during the light sheet alignment described in Section 5.3.3.

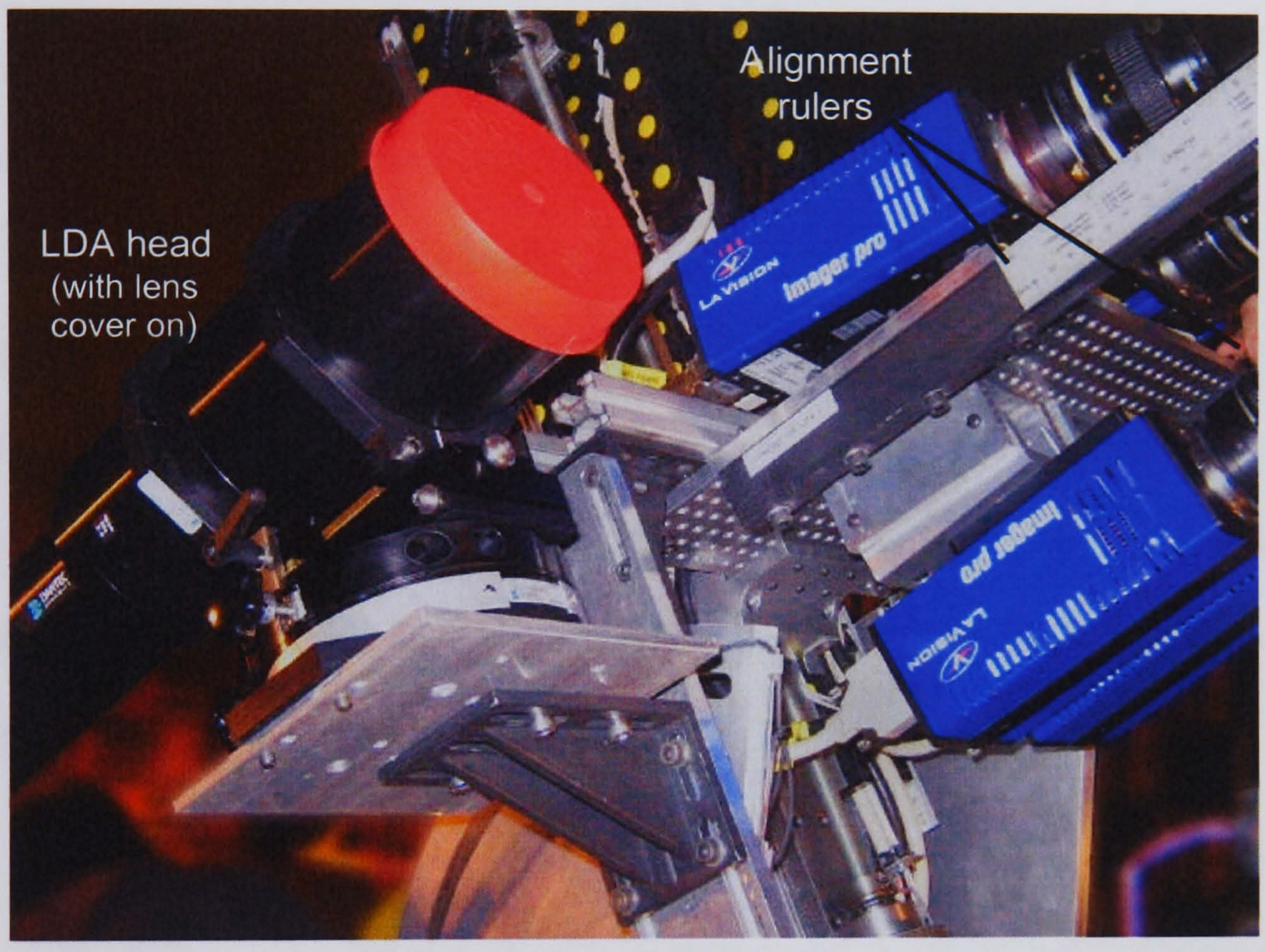

Figure 5.30 – LDA head and alignment ruler, mounted on the camera traverse.

5.5.7. Traverse Positioning Accuracy

It was imperative to ensure that the stepper motors described in Section 5.5.3, running under open-loop control, would be suitable for powering the mechanisms described above. The assembled traverses were therefore weighted down with their payloads, and driven forwards and backwards (by equal amounts) 100 times, in order to test overall positional accuracy.

While both horizontal traverses returned to their exact original position, the stepper motor did not have enough torque to raise the vertical section of the camera traverse without skipping a significant number of steps. The motor's torque could be increased by reducing its speed, but this was considered unacceptable, as was replacing the driver such that a higher current stepper motor could be fitted.

The step-skipping problem was successfully solved using a counterweight (see Appendix 9.3.6, page 400), but it was eventually decided to replace the stepper motor with a more powerful 12V epicyclically geared DC motor (RS; 417-9661). Unlike the stepper motor of course, the DC motor had to be controlled manually, using the system described in Section 5.8.3 (page 209). Due to the relatively small number of 'vertical' movements required throughout the test however, this did not prove to be a problem. Additionally, the traverse limit switches had to be replaced with the diode protection system detailed below:

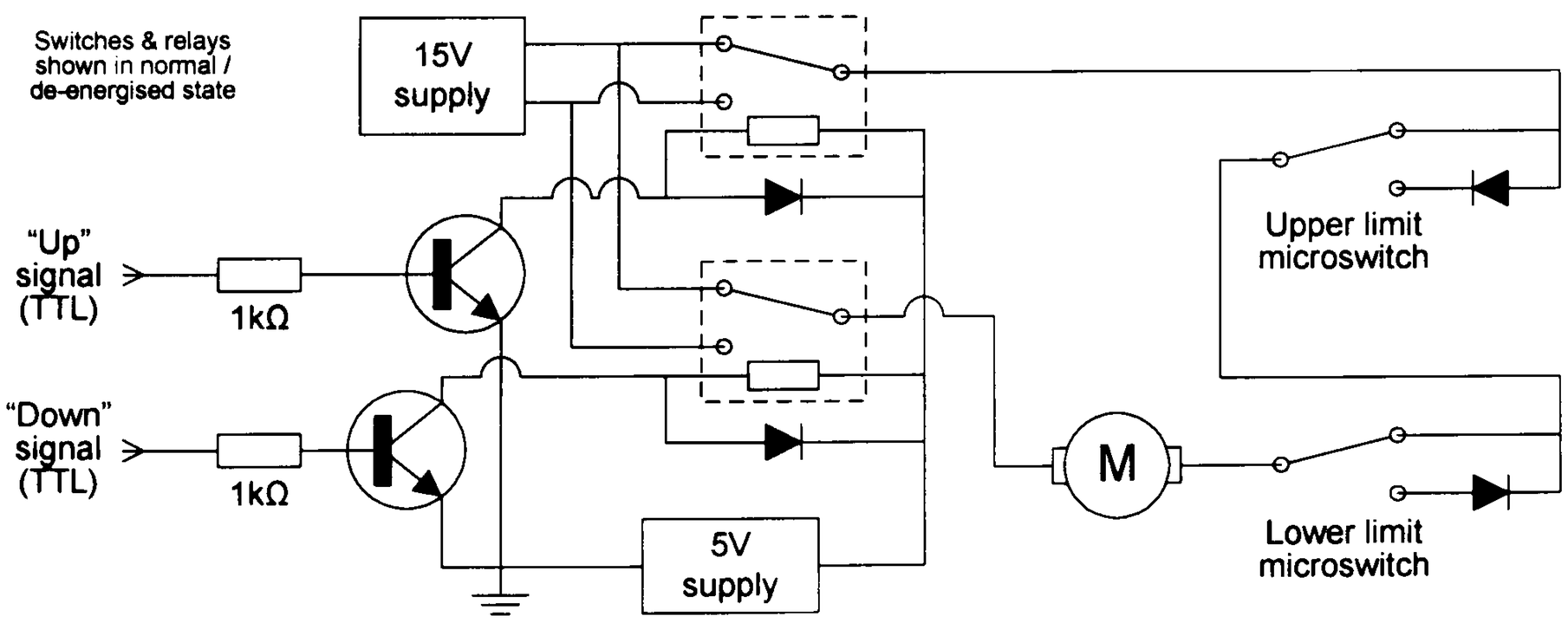

Figure 5.31 – DC motor control electronics.

5.6. Control System

Software applications serve a number of roles in a PIV experiment:

- To control the firing of lasers and triggering of cameras (in the case of CoJeN; 5 cameras and 6 lasers).
- To synchronise any associated hardware (e.g. motorised traverses) with the laser firing.
- To receive and store images from the cameras.
- To correlate and otherwise process the acquired images.

5.6.1. Software Options

Commercial software is available which can fulfil all the roles listed above, thereby making experimental execution extremely straight-forward. Popular applications include DaVis (by LaVision GmbH), InSight (by TSI Inc.), and FlowManager (by Dantec Dynamics), but in all cases the software is limited to working with the manufacturer's own cameras and timing hardware. As a result, the PIV applications compatible for use with the pco.2000 cameras were limited to DaVis and VidPIV (by ILA GmbH), the latter of which can only be used with a 5-channel timing synchroniser.

While DaVis is a highly respected and functional software package, it was decided that a custom control application created by the author would be used, for the following reasons:

- While the timing parameters for a simple single camera PIV experiment can be controlled using DaVis' user-friendly GUI, more complex measurements (such as those performed during phase 4 of the CoJeN test) must be defined in an 'ACQ' file, written in DaVis' CL programming language. While allowing complete flexibility, this approach makes on-the-fly timing adjustments difficult.
- Non-LaVision electronic components, such as motor drivers, can only be controlled using low level serial output CL commands, and devices requiring a custom API for control must be integrated using a convoluted, inefficient method.
- High bandwidth camera data acquired using DaVis is subject to computationally intensive processing as part of the file writing process. This results in a number of technical challenges for multiple camera setups.
- LaVision's Programmable Timing Unit, and a license for DaVis's hardware control functionality together cost almost £10,000.

5.6.2. Custom Control Software

The PIV control application used – YAPP* – was designed primarily to facilitate the design, and execution, of complex software and hardware 'action' sequences. An 'action' might comprise the firing of a laser, the moving of a traverse, or the writing of a file for example. YAPP has since evolved into a multi-functional application containing a hierarchical image processing framework, with multiple camera interfacing currently being implemented. The application, written by the author in C++ using the MFC MDI framework, is shown in Figure 5.32.

* Yet Another PIV Program.

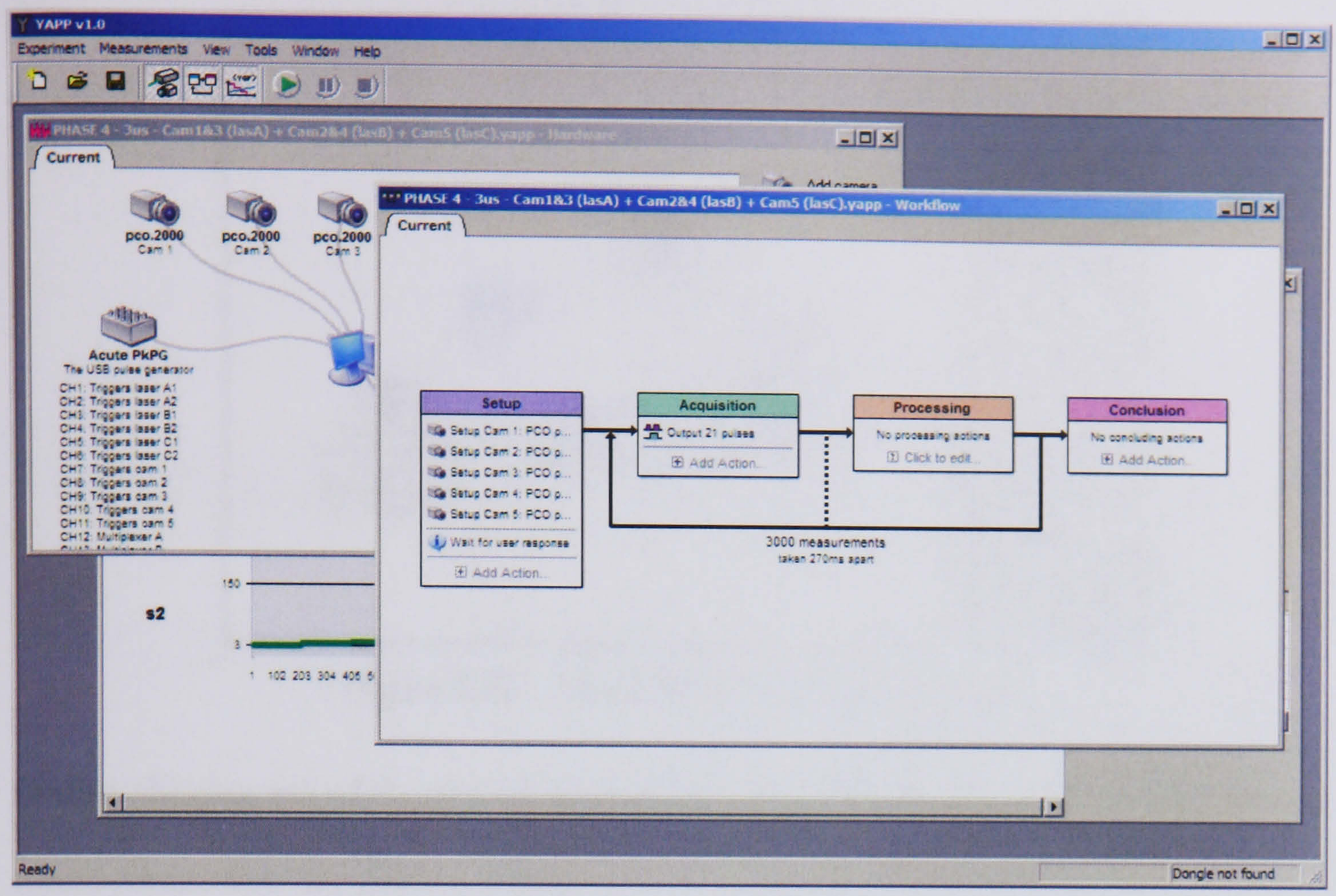

Figure 5.32 – YAPP control software interface.

Visible in the figure above are the three main windows – *Workflow*, *Hardware* and *Variables* – used to edit a YAPP experiment. These interfaces, and the way in which they are used to create an experiment, are described below:

5.6.2.1. Hardware View

The YAPP *Hardware* window comprises a visual representation of the apparatus involved in the PIV experiment. These devices are divided into four categories: cameras, timing synchronisers, motor drivers, and measurement devices (such as DAQ cards or GPIB oscilloscopes). A typical experimental setup is shown in Figure 5.33, with a more detailed view of the associated dialogs available in Appendix 9.1.10 (page 359).

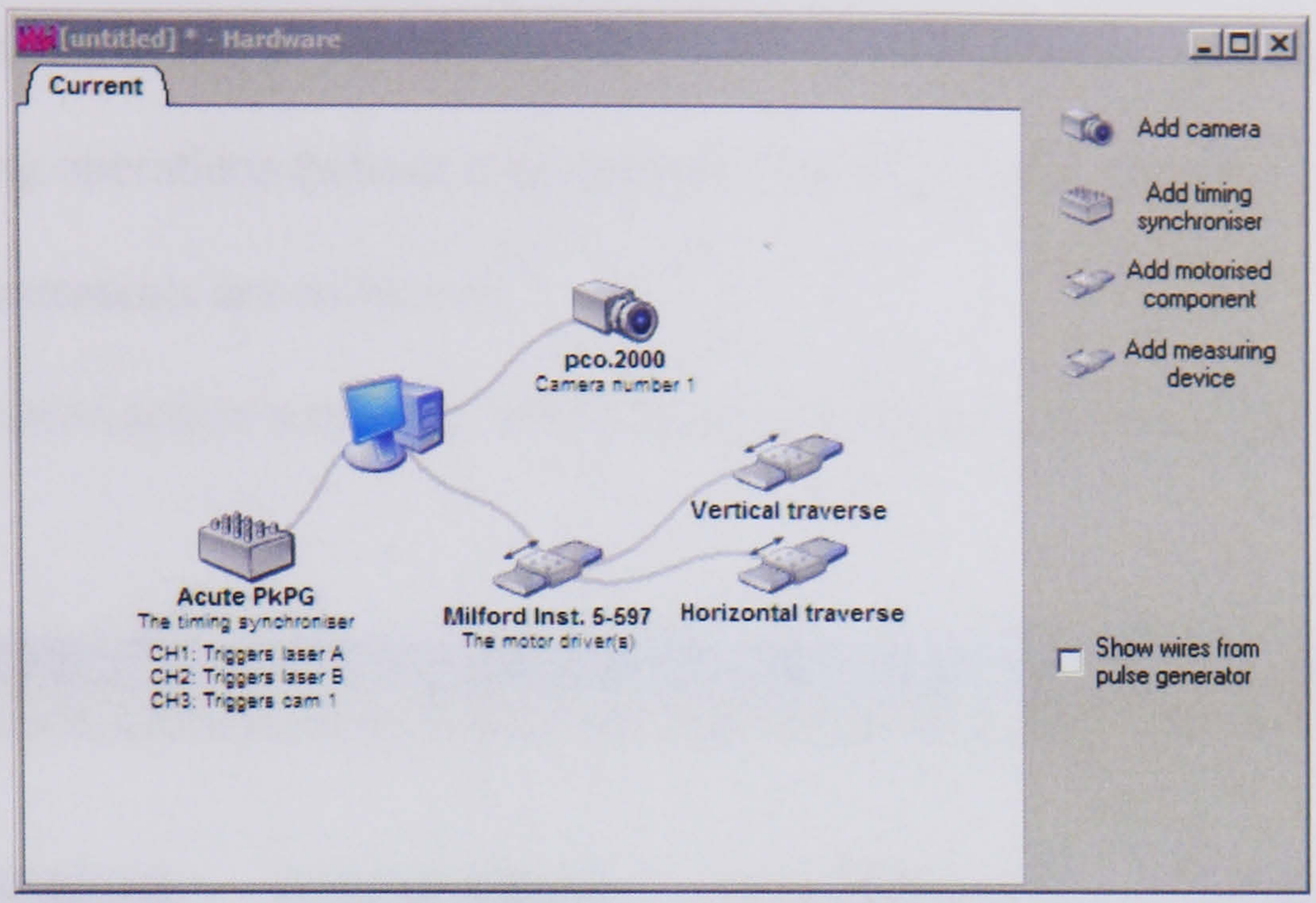

Figure 5.33 – The YAPP *Hardware* window.

Double clicking any of the devices shown brings up their configuration dialog, through which parameters like camera exposure time, or traverse speed, may be set.

5.6.2.2. Workflow View

At the heart of YAPP is the experimental workflow diagram, comprising:

- A *Setup* action sequence, which is executed just once at the beginning of the experiment. Commands to turn on a wind tunnel, or arm a laser safety system, might be included in this block.
- An *Acquisition* action sequence, which is repeated an arbitrary number of times, at a user-defined frequency. The actions in this block would typically comprise those necessary to trigger the cameras and lasers for one measurement.

- A *Processing* block, to process acquired data using an arbitrary number of processing operations (whose results are delivered in either real-time, or after all the measurements are collected).*
- A *Conclusion* action sequence, which is run just once at the end of the experiment.

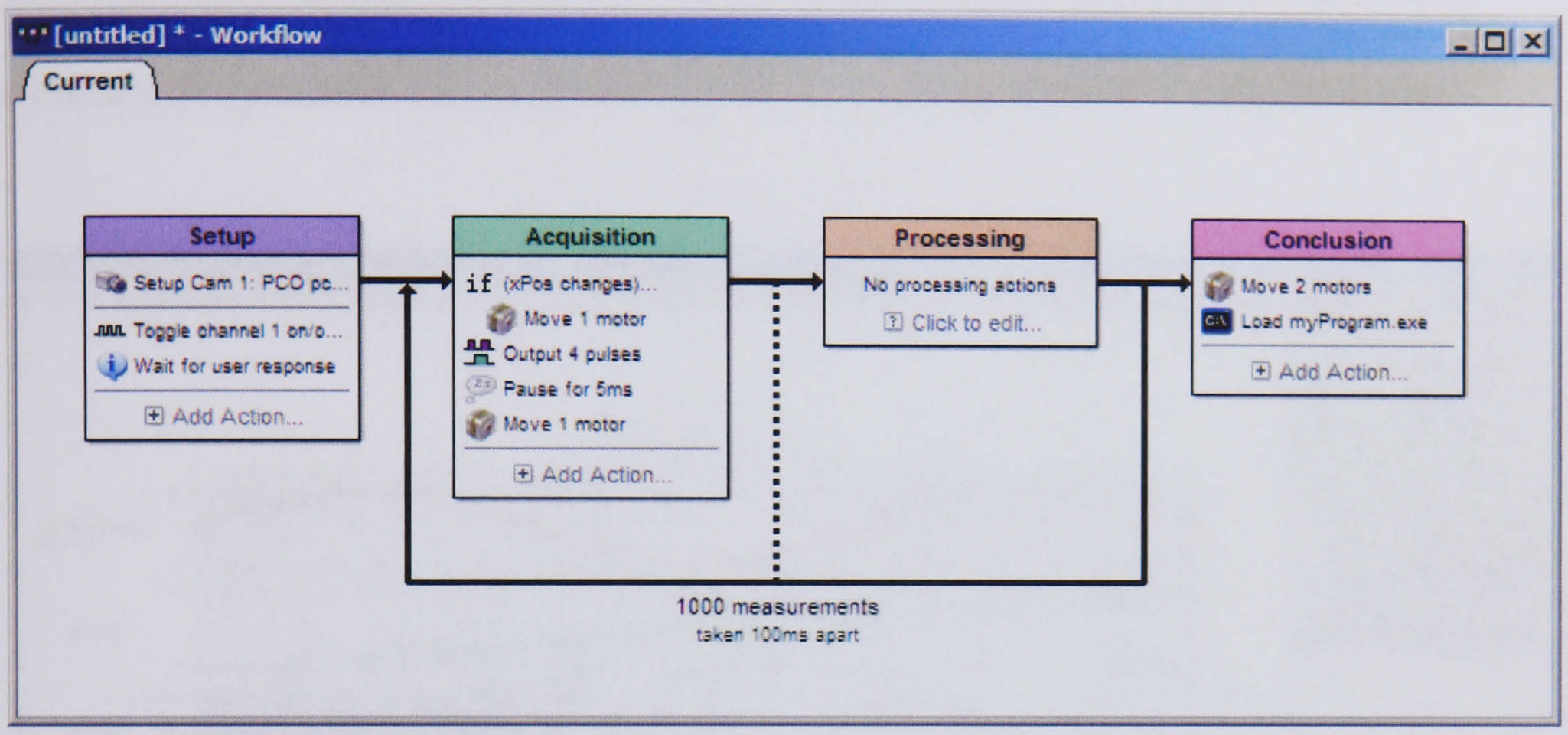

Figure 5.34 – The YAPP *Workflow* window.

YAPP is written in such a way that all hardware-related actions may be used with *any* of the devices (of the appropriate type) shown in the *Hardware* view. A 'motor move' action, for example, can be used to control an encoded DC motor connected to a Solutions Cubed MicroPID controller, *or* a stepper motor connected to the PC's parallel port, by virtue of the genericised nature of the internal action/hardware relationship. Further screenshots associated with the *Workflow* view (shown in Figure 5.34) may be found in Appendix 9.1.10 (page 358).

* While the processing framework (responsible for scheduling and executing the operations) was complete at the time of writing, only the most basic (not particularly useful) processing operations had been coded.

5.6.2.3. Variables View

Much of YAPP's usefulness comes from its implementation of variables. Most actions' parameters of interest (e.g. the position to move a traverse to) can take the form of an alphanumeric variable, rather than a statically defined number. The *Variables* window (c.f. Figure 5.35) displays all of the variables thus defined within the experiment's actions, and the values they will take for each of the experiment's measurements.

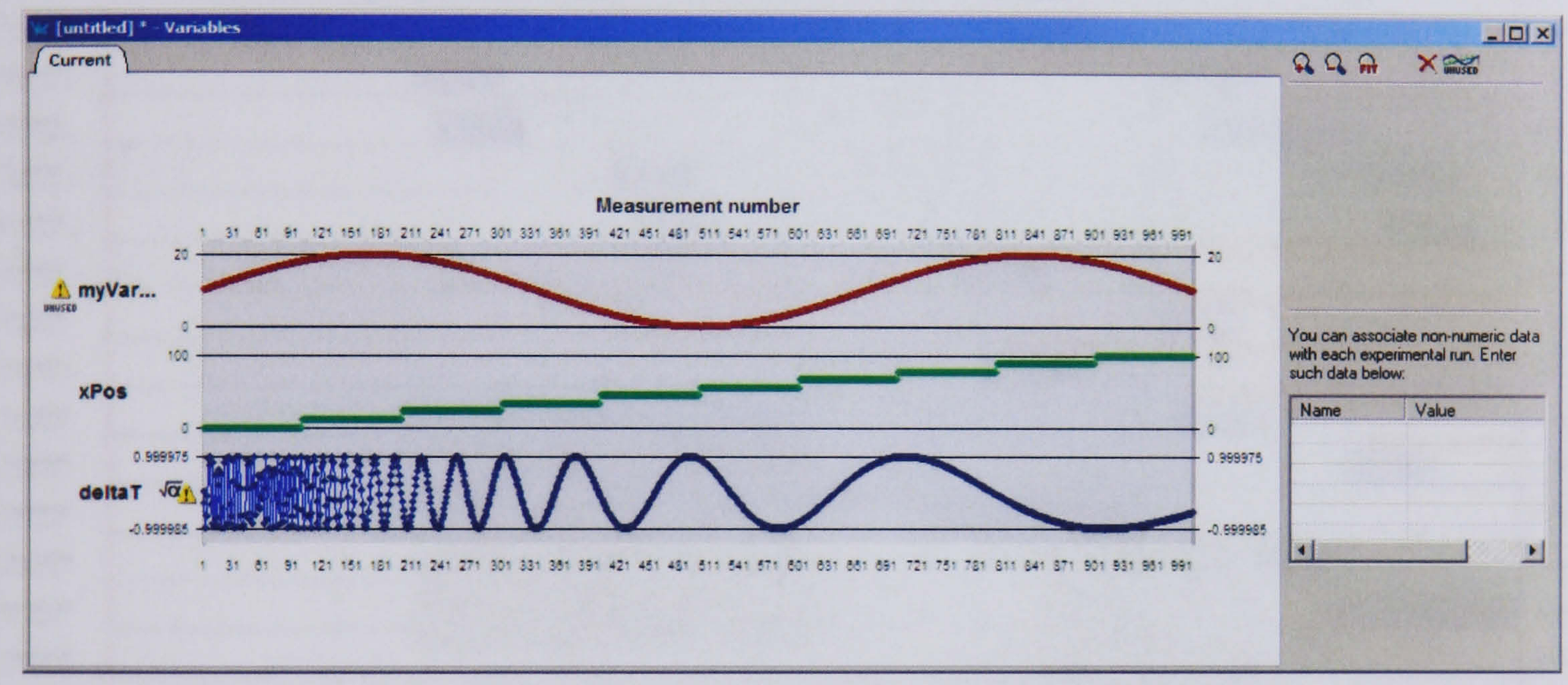

Figure 5.35 – The YAPP *Variables* window.

As can be seen in Appendix 9.1.10 (page 360), the variables can be defined in 1 of 4 ways: as a constant, as a stepped linear progression, using values from a user-supplied list, or according to an arbitrary mathematical formula.

5.6.2.4. Pulse Train Generation using YAPP

One of the more powerful features of YAPP is its ability to generate arbitrary trigger pulse trains (using the 'pulse train output' action) that can change over the course of the experiment, according to variable values.

Figure 5.36 shows the pulse train output action that was used during phase 4 of the CoJeN test. Two variables were used in the YAPP experiment: *s1* (defined as a constant) represented the Δt interval between laser pulse pairs, and *s2* (defined using a 15 value look-up list) determined the time interval between the 3 pulse pairs.

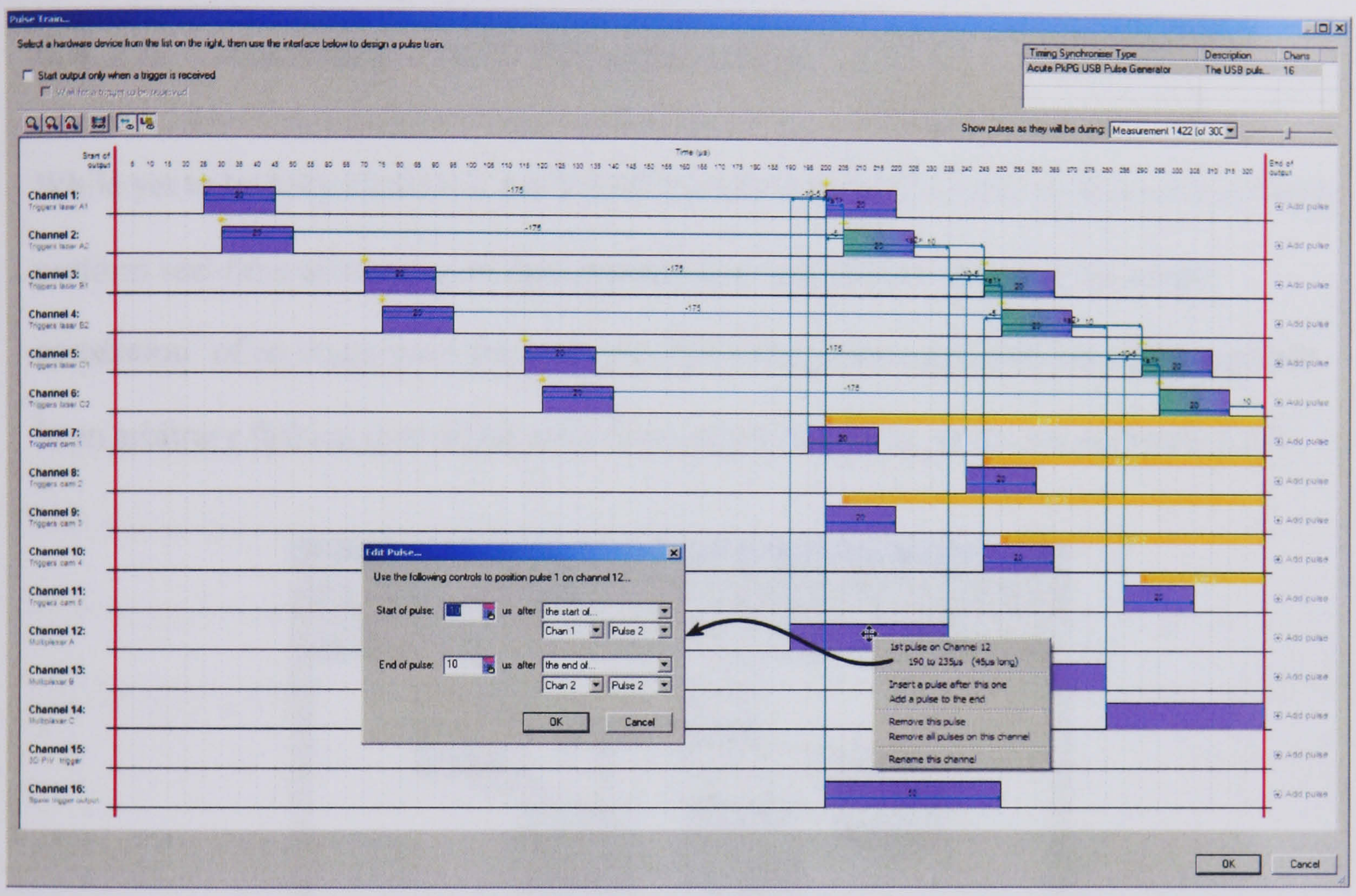

Figure 5.36 – YAPP pulse train output action interface.

The pulse train action's interface colours each pulse's edge according to whether its position is defined by a constant or a variable (the former, purple, pulses can be moved around by dragging with the mouse), and it also able to illustrate where in time laser pulses and camera exposures occur.

While the position of the pulse's edges may be defined in absolute terms, it is also possible to position each edge of a pulse relative to any edge of any other pulse. This functionality was used in the phase 4 pulse train to ensure that the cameras were triggered at the right time relative to the lasers, even though the time between pulses

(*s2*) changed through the course of the experiment. Although Δt remained constant throughout the phase 4 experiments, it too was defined using a variable (*s1*) to assist adjustment. A single click in the *Variables* window allowed Δt to be set to a level that ensured the recorded particle movement $\leq$ 8 pixels (¼ A_1).

5.6.2.5. Ancillary YAPP Functionality

While yet to be fully exploited, the YAPP workflow execution code includes the ability to perform real-time processing of data collected by 'acquisition actions'; the rough correlation* of an image pair, for example. Processing operations may be wired together in an arbitrary fashion (providing node colours are matched), as shown in Figure 5.37:

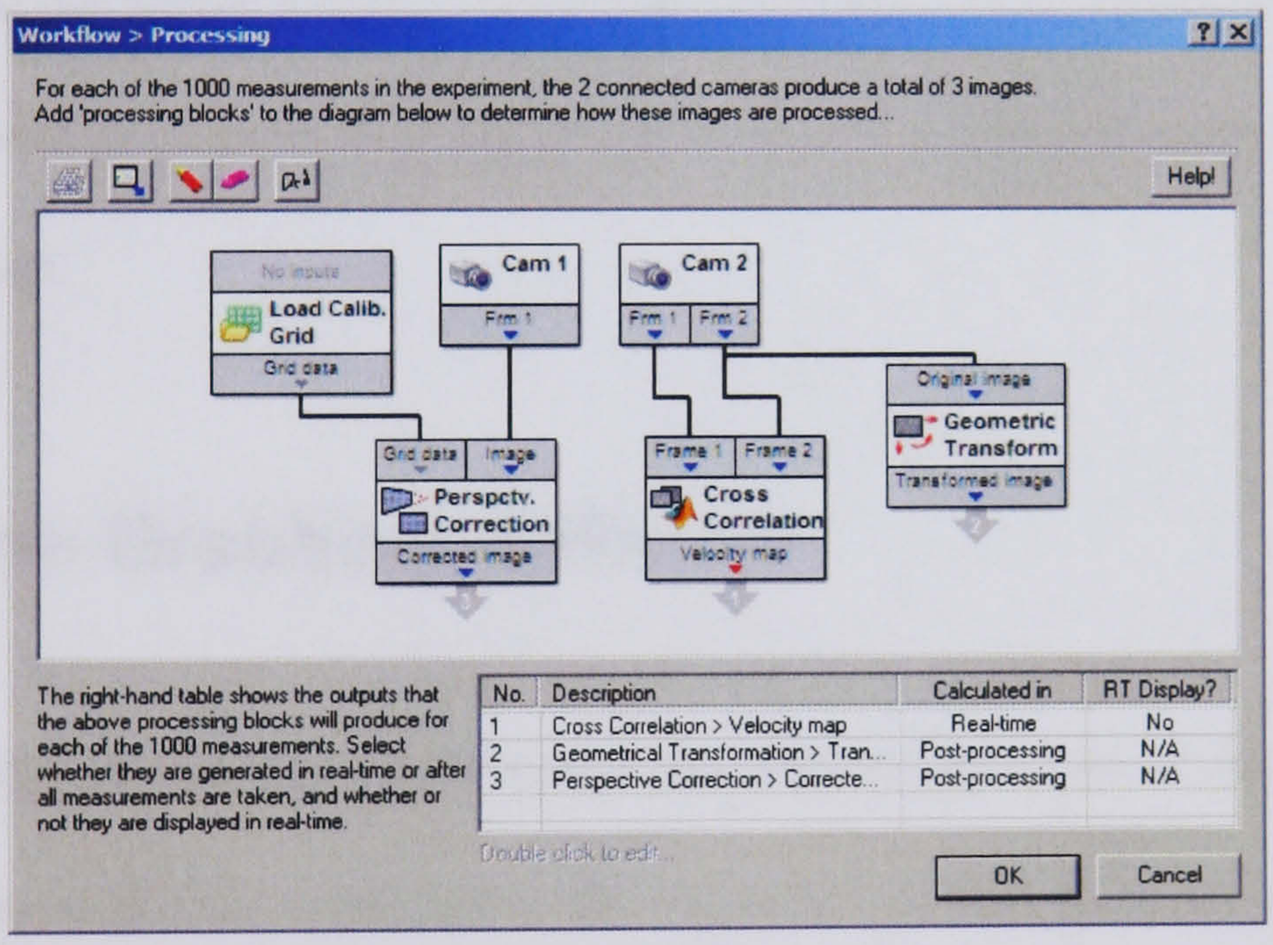

Figure 5.37 – YAPP hierarchical data processing.

By virtue of offering the image processing framework in an offline form, YAPP proved useful as a simple paint program, capable of loading and editing 16-bit greyscale TIFFs without conversion to 8-bits, as is often the case.

---

* Implemented on an experimental basis using the extremely fast FFTW library.

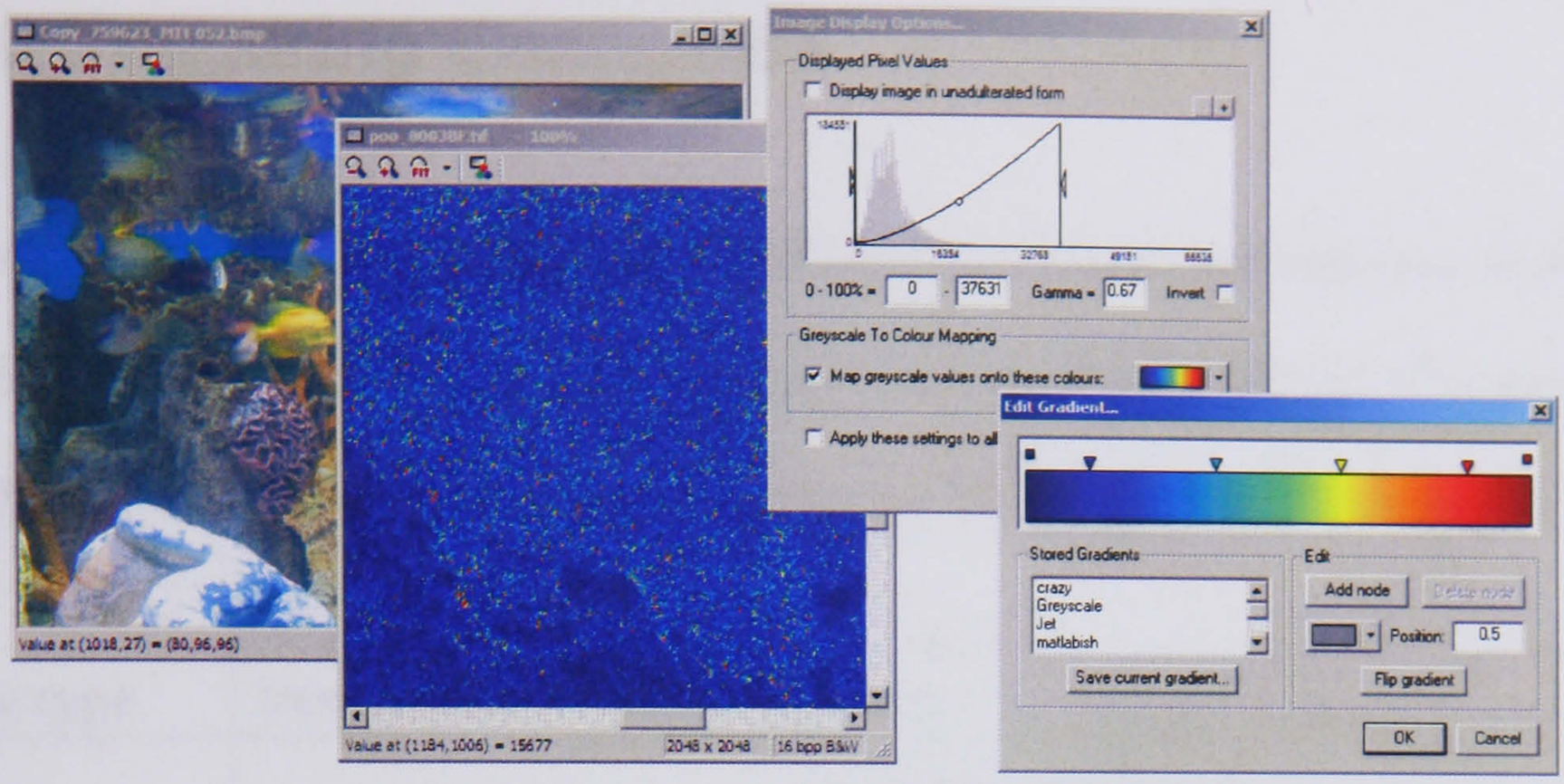

Figure 5.38 – 16-bit image viewing and manipulation in YAPP.

Of more relevance to the CoJeN experiment was the historical execution record maintained within the XML .yapp experiment file. This feature enabled an exact record to be kept of *every* action executed throughout the test (as well as the variable definitions used at the time). Finally, the multi-threaded nature of the application enables experiments to be paused at any point: a function that is surprisingly rare in similar applications.

5.6.3. Frame-Grabbing Software

Because, at the time of writing, YAPP could not directly interface with the pco.2000 cameras, a separate software application was required to save their images to disk. CamWare v.2.13, written and supplied by PCO with the cameras, is an elegantly simple application which was used for just that purpose. In order to reduce disk space requirements, the 14-bit raw data was saved in the form of 8-bit BMPs (rather that 16-bit TIFFs) with the image converted according to a user-defined LUT.

5.6.4. Triggering Electronics

Reference has been made to the triggering of the CoJeN lasers and cameras, and an appropriate timing synchroniser with which to do this had to be chosen. Computer controlled pulse generators, suitable for control by YAPP, fall into 3 categories:

Device type	Description	Notes
PC bus I/O (e.g. a DAQ or the PC's parallel port)	Output channel states are set directly by the host PC.	• Low – medium timing accuracy. • Arbitrary pulse train output. • Lots of output channels possible. • Very low cost.
Programmable delay generator	Programmable comparators examine the state of a dedicated clock driven counter.	• High – very high timing accuracy. • Typically only 1 pulse/channel/trigger. • Typically relatively few channels.
Pulse sequencer	A dedicated clock is used to readout a pre-programmed bit pattern from FIFO memory.	• High timing accuracy. • Arbitrary pulse train output. • Limited pulse train duration.

Table 5.10 – Pulse generator varieties, as suitable for PIV experiment triggering.

Given the short Δt values required during CoJeN, and the number and flexibility of output channels required, it was decided that a pulse sequencer would be the most appropriate device. Accordingly, the Acute PkPG-2116 'pattern generator' was sourced.

Designed primarily for use in IC testing, the PkPG is both powered and programmed over USB, and is able to output an arbitrary waveform on each of 16 channels. The on-board clock can run at up to 100 MHz, meaning pulses can be as short as 10 ns, with only 20 ns between triggers. The PkPG's full specification can be found in Appendix 9.1.11 (page 361) along with details of its command structure, which had to be backward engineered to allow integration with YAPP.

5.6.4.1. Trigger Channels

With 5 cameras, 6 laser flash-lamps, and 6 laser Q-switches, it can be seen that the 16 output channels of the Acute PkPG were insufficient to trigger all of the equipment directly. While it would have been possible to operate the NeoPIV lasers using just 6 triggers, it was found that the internal delay generator were unacceptably variable (c.f. Appendix 0, page 364). An attempt to construct more accurate delay lines failed.

The issue was finally resolved by multiplexing the trigger signals. For each of the 3 laser heads, a single PkPG output channel determined whether another 2 channels triggered flash-lamps *or* Q-switches. As such, only 9 channels were required for laser triggering. The logic used to implement this arrangement is shown in Figure 5.39:

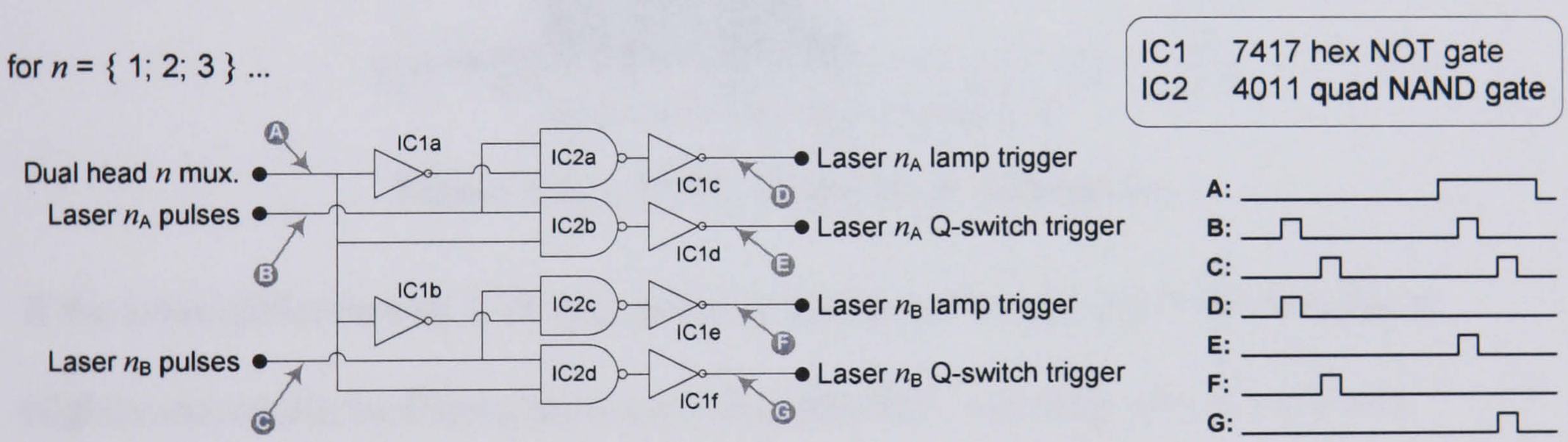

Figure 5.39 – Multiplexed laser triggering circuit.

The laser trigger de-multiplexer is shown in Figure 5.40, alongside the Acute PkPG (as supplied, and as packaged for use during CoJeN):

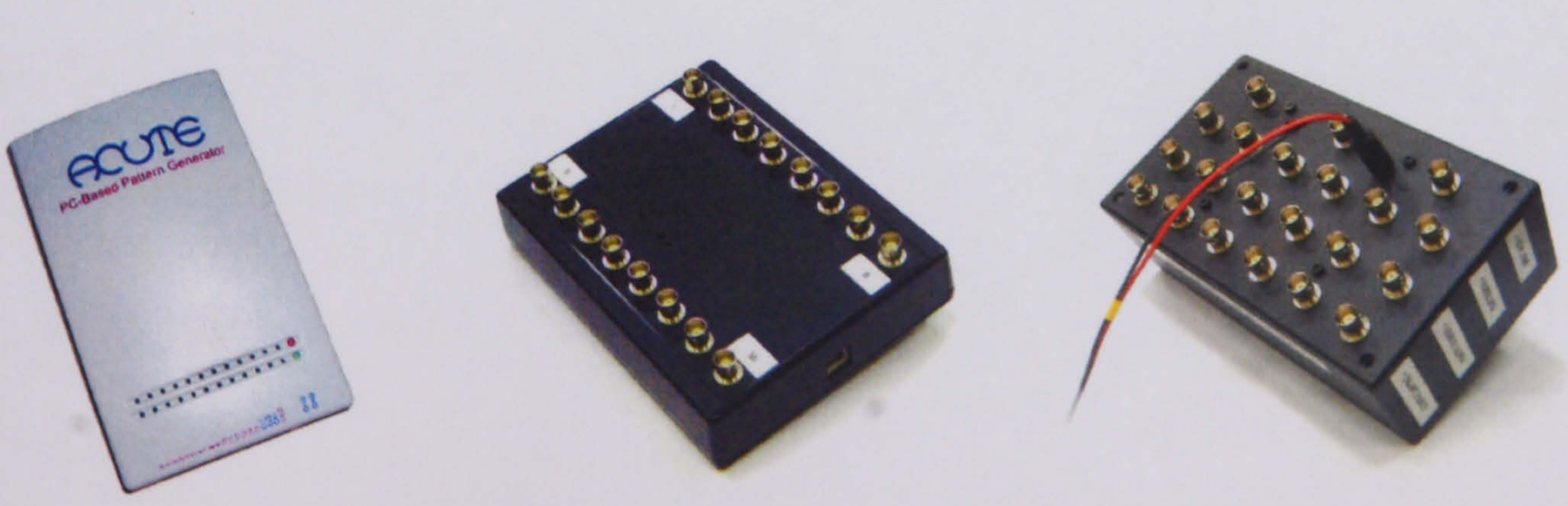

Figure 5.40a,b) The Acute PkPG sequencer; c) Laser trigger demultiplexer.

5.6.4.2. Timing Accuracy

The PkPG's accuracy was tested by measuring the time between 2 pulses (outputted 159 μs apart, on different channels) 1000 times, using a Tektronix TDS 1002 oscilloscope and a variation of the Matlab script given in Appendix 9.4.8 (page 430). Figure 5.41 shows the distribution of the difference between the expected and measured time delays:

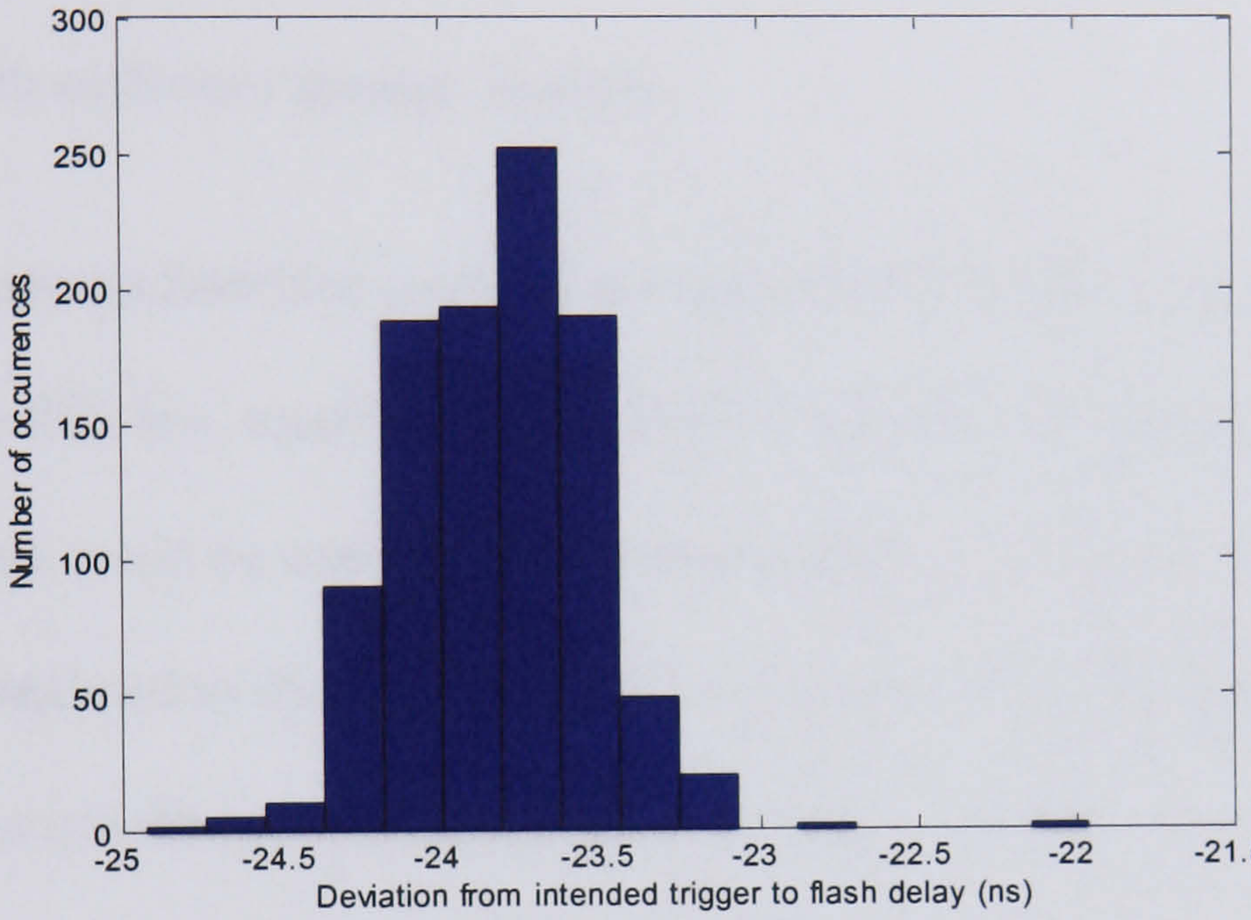

Figure 5.41 – PkPG timing error distribution.

If the mean difference of 23.8 ns is taken as being real (and not just the result of a slightly inaccurate oscilloscope clock), then the PkPG's timing error is ~0.015%. Furthermore, the standard deviation of the data shown above is just 0.29 ns, which clearly compares well with the device's advertised 3 ns jitter.

5.7. Computer System

The CoJeN computer system served 2 main purposes:

- To run YAPP, and thereby control the rig's electronic components.
- To receive and store PIV image data from the 5 cameras
  - ...at a sufficiently high rate.
  - ...with sufficient storage capacity.

The number of camera interface computers required was initially defined by the bandwidth of the PCI bus, used by the pco.2000's CameraLink cards. While PCO claimed 2 cameras could be used on 1 PC consecutively, less optimistic advice from the vendor, and the realisation that the CamWare software lacked necessary functionality when used with multiple cameras, led to the decision to install 1 PC per camera.

Therefore, the preliminary computing requirement became:

- 5 × camera interface PCs.
- 1 × control PC (HP Compaq dc5100 microtower; 2.66 GHz P4 processor; 256 Mb RAM). This was used to run YAPP, the light sheet alignment software, and several other minor control applications which are described in Section 5.8.

All PCs would run Microsoft Windows XP Professional. While the control PC had a number of responsibilities though, the camera interface PCs existed purely to run the CamWare frame-grabbing software and in turn record the image stream to disk. Due to the speed and volume of image acquisition, the hard disks of these PCs required special consideration.

5.7.1. Acquisition and Storage Requirements

5.7.1.1. Capacity Requirements

The CoJeN test specification constantly evolved, but at the time of designing the computer system, predictions of the (maximum) quantity of data collected during each test phase stood at the amounts shown in Table 5.11, i.e. a total of 4.30 Tb.

Phase 2	Phase 3	Phase 4
• 9 × nozzle / operating condition combinations • 3 × axial measurement positions • 12 × cross-axial planes • 2 × in-plane 'heights' • 300 × measurements per position = 194,400 measurements = 1.48 Tb of data*	• 9 × nozzle / operating condition combinations • 31 × measurement positions (c.f. Figure 5.4, page 154) • 1000 × measurements per position = 279,000 measurements = 2.13 Tb of data	• 1 × nozzle / operating condition combination • 5 × measurement positions • 15 × phase • 200 × 3 measurements per position per phase = 90,000 measurements = 0.69 Tb of data

Table 5.11 – Predicted number of CoJeN measurements.

* Each measurement = 2 frames × (2048 × 2048 pixels) × 8-bit = 8.00 Mb

5.7.1.2. Speed Requirements

The pco.2000 cameras, running in full frame mode (2048 × 2048 pixel) at their maximum frame rate of 14.7 Hz produce a video stream with bandwidth 58.8 MBps. Tests conducted using a typical hi-spec PC (Dell Dimension 8400; 3.06 GHz P4 processor) equipped with a 80 Gb SATA-150 hard disk drive revealed however a maximum sustainable write speed of only 28 MBps, compared to a theoretical maximum of 49 MBps.

In order to enable the cameras to be used at their maximum frame rate, it was clear that a faster method of disk storage, namely a RAID disk array, would be required. Given the high cost of RAID storage systems though*, it was decided that the CoJeN computers would comprise both high-speed RAID storage (to be used during acquisition) *and* a slower, cheaper, storage medium which could be used to 'archive' each day's measurements.

* Despite being an acronym for Redundant Array of Inexpensive Disks, the majority of RAID controller cards are for use with SCSI disk drives, which are significantly more expensive than IDE or SATA disks.

5.7.2. RAID Disk Array Machines

5.7.2.1. Design and Construction

The measurements taken during each of the test phases may be summarised thus:

	Phase 2	Phase 3	Phase 4
One cycle of measurement(s) comprises:	• 2 frames from ≥ 2 cameras	• 2 frames from ≥ 2 cameras	• 1 frame from cameras 1, 2, 3, 4 • 2 frames from camera 5

Table 5.12 – Distribution of measurements by each CoJeN camera.

Based on the distribution of the measurements, it might be concluded that there should be either:

- 1 very fast RAID disk array, to which all 5 cameras can write.
- 5 not-so-fast arrays (1 per camera), each of which would have different capacity and write-speed requirements.
- Either 2 or 3 disk arrays, with equal capacity and write-speed requirements for each test phase.

For reasons of both simplicity and economy, it was decided that it would be best to build 3 separate RAID disk arrays, thereby determining that 3 cameras (numbers 1, 3 and 5) would be used for acquisition during test phases 2 and 3. Data collected from cameras 2 and 4 during phase 4 would be written onto a network drive, mounted on either PC 1 or 3, as illustrated in Figure 5.42:

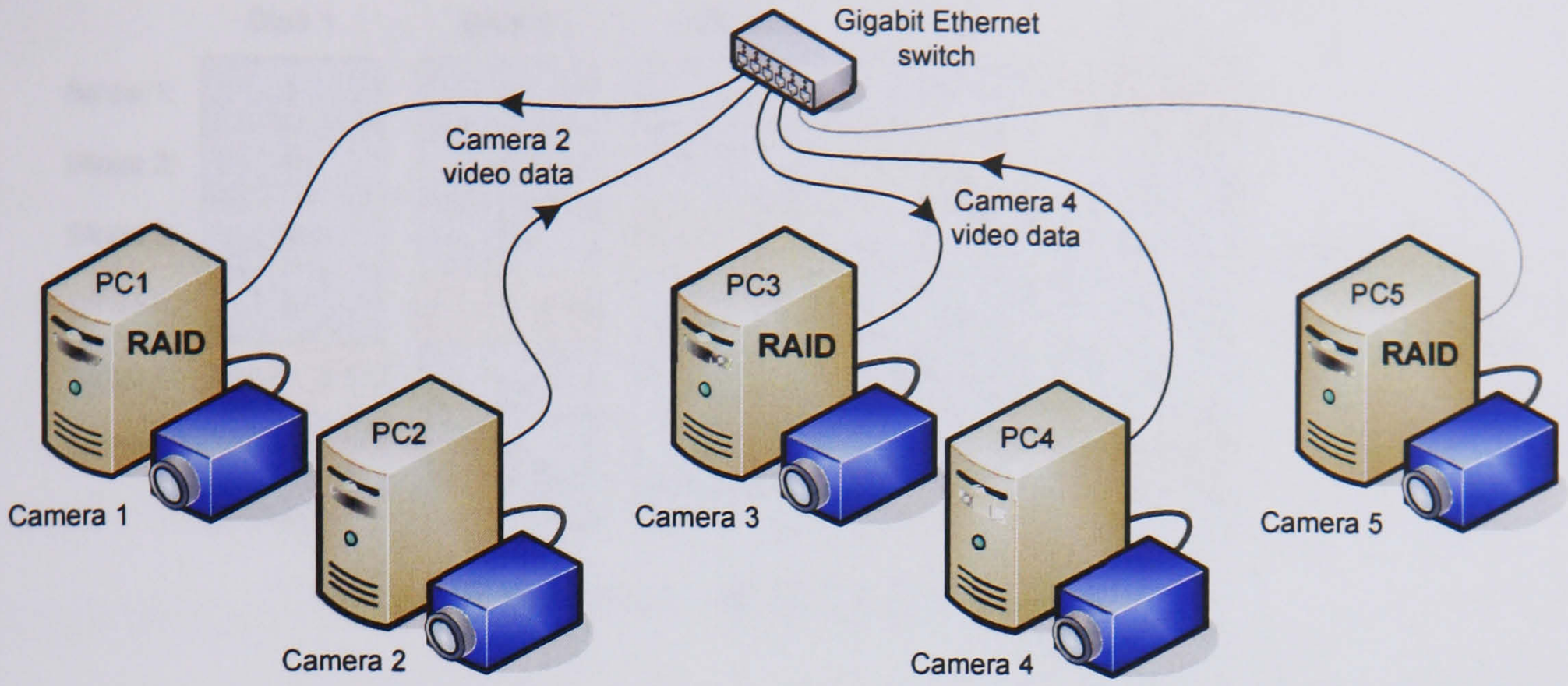

Figure 5.42 – CoJeN camera and RAID PC arrangement.

The 5 camera PCs were specified and built by members of a Warwick University MEng student team. The resultant design comprised:

- Intel SE7210TP1-E server motherboard.
- 3.0 GHz Intel Pentium 4 CPU.
- 512MB PC3200 DDR SDRAM.
- Maxtor Diamond Max Plus 80 Gb SATA hard disk.
- For 'high-speed' PCs 1, 3 and 5:
  - 5 × Maxtor Atlas V 73.5 Gb U320 SCSI hard disk drives.
  - Adaptec 2130SLP U320 (single channel) SCSI RAID controller card.

For each of the 'high-speed' PCs, the 5 SCSI hard drives were configured as a RAID 5 array, meaning that 20% of their capacity was used to store parity data (typically the XOR of the data). This redundancy enabled the array's contents to be restored should one of the disks fail. The way in which data and parity blocks are distributed over 5 RAID 5 disks is shown in Figure 5.43:

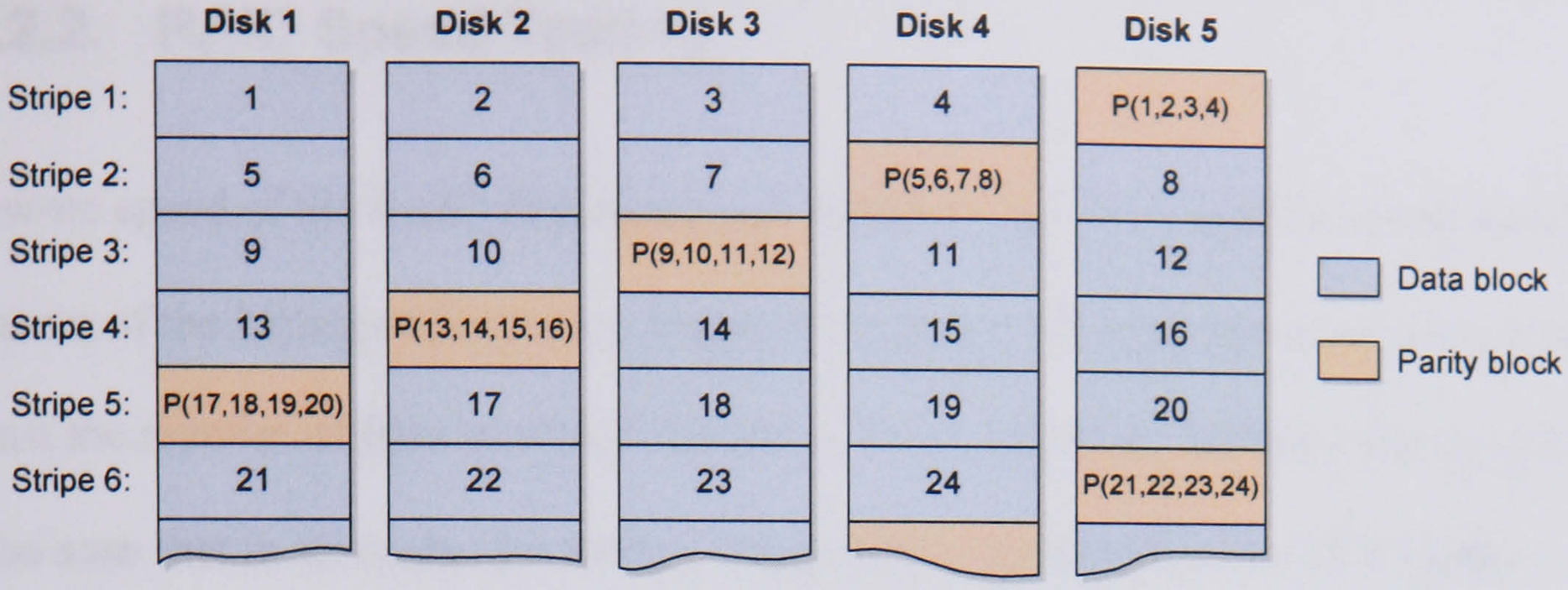

Figure 5.43 – RAID 5 data storage.

Clearly the write speed for the array shown in Figure 5.43 is 4 times that possible using just 1 of the disks (assuming a hardware RAID controller card is used, calculating and writing the parity block adds no overhead). The formatted capacity of the Maxtor Atlas disks used was therefore 273.8 Gb, when running in a RAID 5 configuration. While both the capacity and write speed of the array could be increased by 125% by switching to a RAID 0 configuration, any damage to the disks (which will be shown to be a pertinent issue) would prove irreparable.

5.7.2.2. RAID Speed Testing

The write speed of the RAID disk array was tested using a C++ application written by members of the MEng student team. Figure 5.44 shows the average write speed plotted against the number of files written to the array, for a number of different file sizes*. It can be seen that in all cases, the writing bandwidth is greater than the 58.8 MBps capable of being produced by the pco.2000 camera.

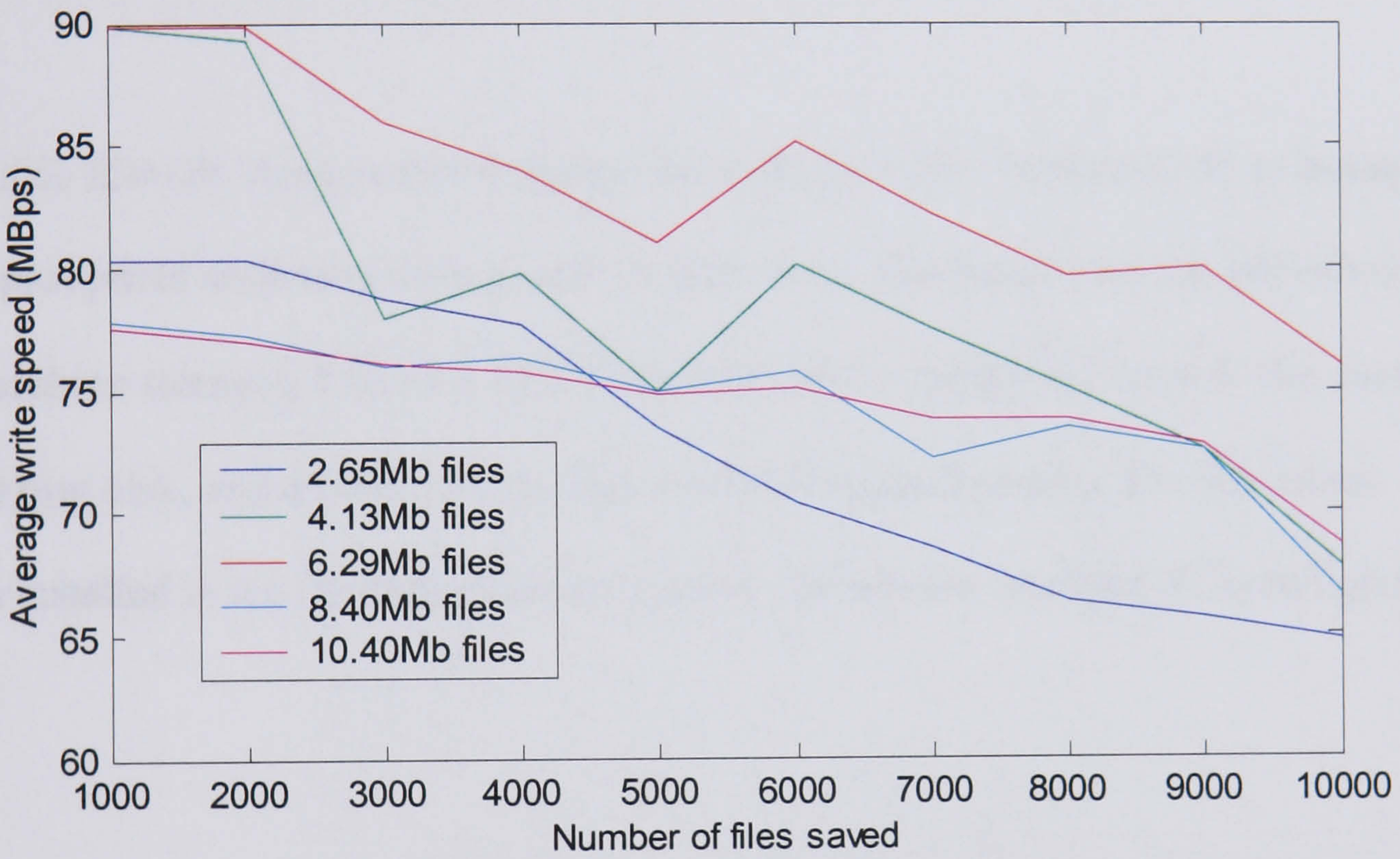

Figure 5.44 – CoJeN RAID array write speed.

* The image pairs acquired during test phases 2 & 3 were saved as (2048 × 4096 pixel) × 8-bit = 8.00 Mb files. The single frames acquired by cameras 1 – 4 during phase 4 were 4.00 Mb in size.

5.7.3. Archive Storage

Based on the assumed 4.30 Tb of data being collected (c.f. Table 5.11), and the RAID arrays being able to hold 3 × 274 Gb, it can be seen that an additional 3.50 Tb of storage was required. A review of commercially available internal and external hard disk drives was performed by the MEng team, with the aim of finding the lowest cost (per Gb) storage device. DVD and CD storage was not considered, due to the amount of manual intervention required to change disks.

The LaCie 250 Gb 'designed by Porsche' external hard drive was selected as being the most appropriate archiving device, and 15 units were purchased (thereby providing 3.75 Tb of archive storage). The 35 × 112 × 188 mm drives, shown in Figure 5.45a, comprise a 7200 rpm disk, and a USB 2.0 interface with 8Mb transfer cache. The drives are shown installed in the rig (alongside the control and camera interface PCs) in Figure 5.45b.

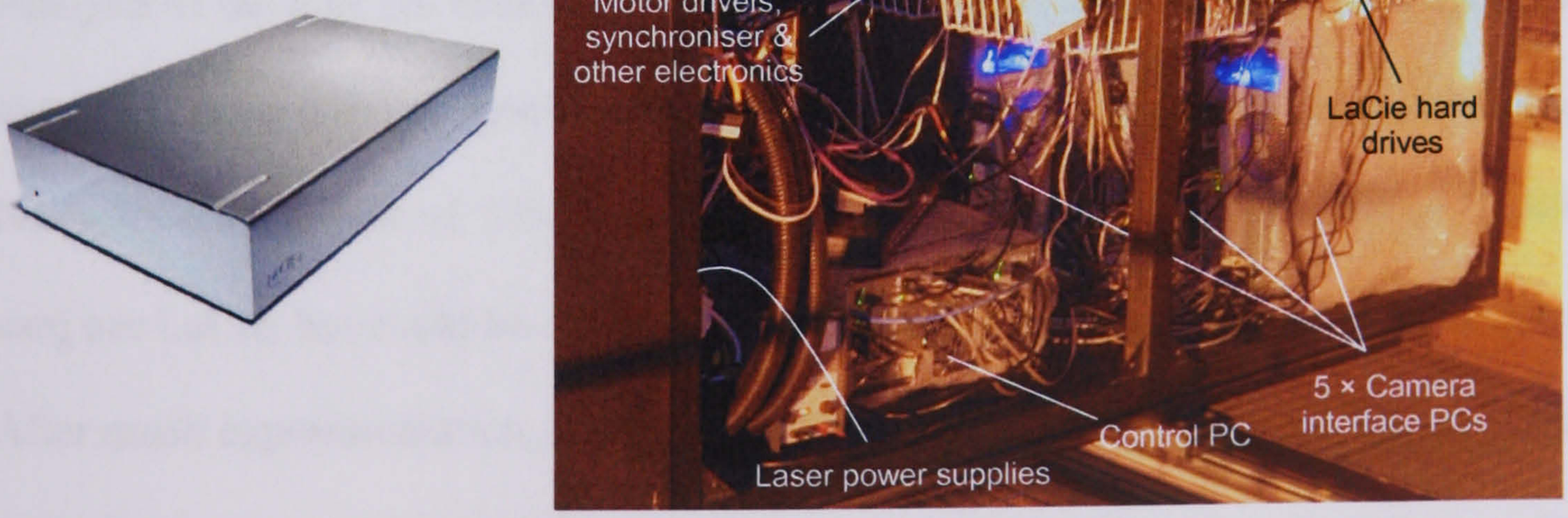

Figure 5.45 – LaCie 250 Gb external hard drive: a) alone; b) in situ.

5.7.3.1. Archive Transfer Speed

The 821 Gb capacity of the RAID disk arrays was sufficient to store a total of 105,000 PIV measurements, or 3.4 phase 3 nozzle / operating condition combinations (c.f. Table 5.11). At one point prior to the test however, it was envisaged that 4 such combinations might be tested in 1 day. For this reason, the speed at which data could be transferred from the RAID disks onto the external drives had to be benchmarked.

It was initially intended that 5 LaCie disks would be attached to each PCs 1, 3 and 5. A multi-threaded application (c.f. Figure 5.46) was written to move the files as efficiently as possible between a number of destination and output drives, whilst logging the time taken.

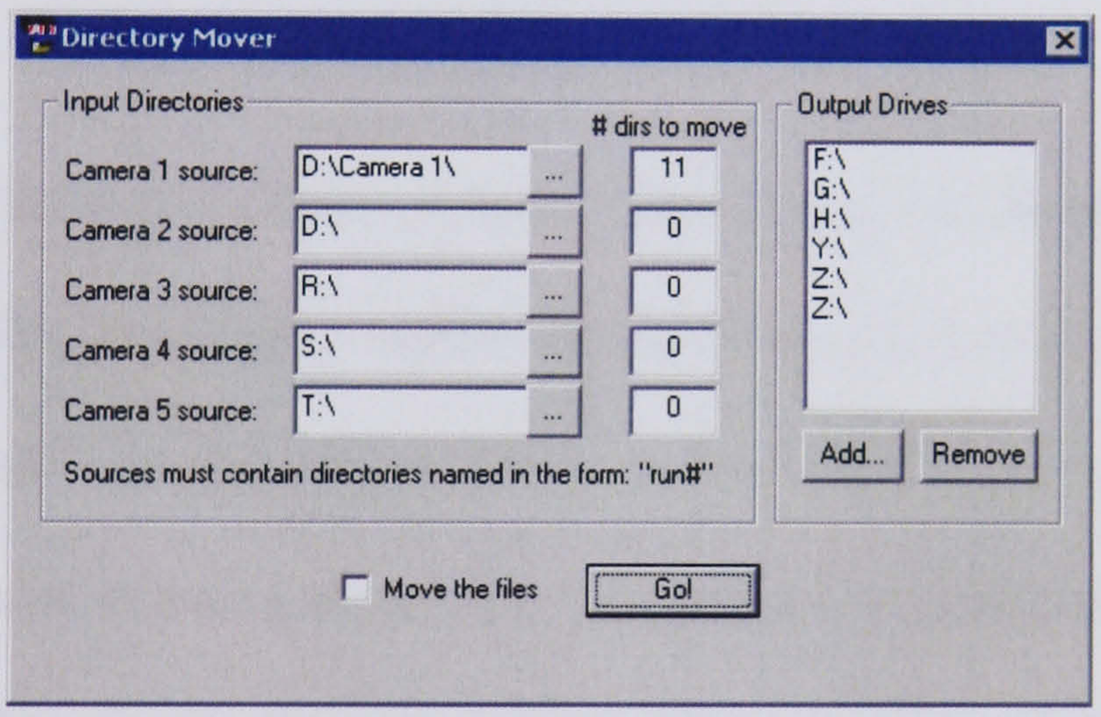

Figure 5.46 – Directory moving software.

Analysis of the logs (an example of which is included in Appendix 9.1.13, page 366) showed that the transfer speed was only of the order of 10 MBps; far slower than the hardware was capable of. This transfer rate was unaffected by the addition of 1 USB card per LaCie, but could be raised slightly by connected the external drives via a hub. After much experimentation, it was found that a more significant speed increase could be achieved by connecting 2 of the 5 drives to a different PC, and accessing them over the network. In this way, the archive transfer time for a typical set of phase 3 data was reduced to approximately 1 hour.

5.7.4. Machine Networking

As discussed in Section 5.7.2.1, the camera interface PCs needed to be networked together using Ethernet and, to this end, an 8-port Gigabit switch (Belkin; F5D55141-8) was installed inside the CoJeN rig, with connections made to each of the enclosed PCs. The LAN was also used to provide remote control of both the control and camera interface PCs using Microsoft's Remote Desktop Connection VNC client. A 5-port Gigabit switch (Belkin; F5D55141-5) was placed in the NTF control room and connected to the rig via 100 m of CAT6 cable. By virtue of assigning static IP addresses to all PCs involved in the test, the whole of the rig could be controlled using a single laptop in either location.

A backup communication and control system, comprising a keyboard/video/mouse (KVM) switch was also installed to negate any software glitches or crashes. All PCs in the rig were connected to an OmniView PRO2 8-Port KVM Switch (Belkin; F1DA108T), which was in turn connected to a monitor, keyboard and mouse in the control room via an OmniView CAT5 Extender system (Belkin; F1D084), with 100m of standard CAT5 network cable between the two. While two further reasons for installing the KVM proved superfluous (it was feared that the Gigabit switch's bandwidth might be exceeded, plus a KVM was required to access the 3D system described on the next page), it nevertheless provided a useful method of viewing multiple PC screens at once.

5.8. Ancillary Systems

5.8.1. 3-Component PIV System

The opportunity arose to borrow a stereo PIV system from Dantec Dynamics for the duration of the CoJeN test. The system, comprising 2 HiSense 1M (1280 × 1024 pixel) cameras with Scheimpflug mounts, a processor unit, and FlowManager software, was duly incorporated into the rig along with its own control PC. Despite being otherwise independent, the triggering of the 3D system was controlled by YAPP. Figure 5.47 shows the HiSense cameras mounted on the vertical traverse, 1.1m apart.

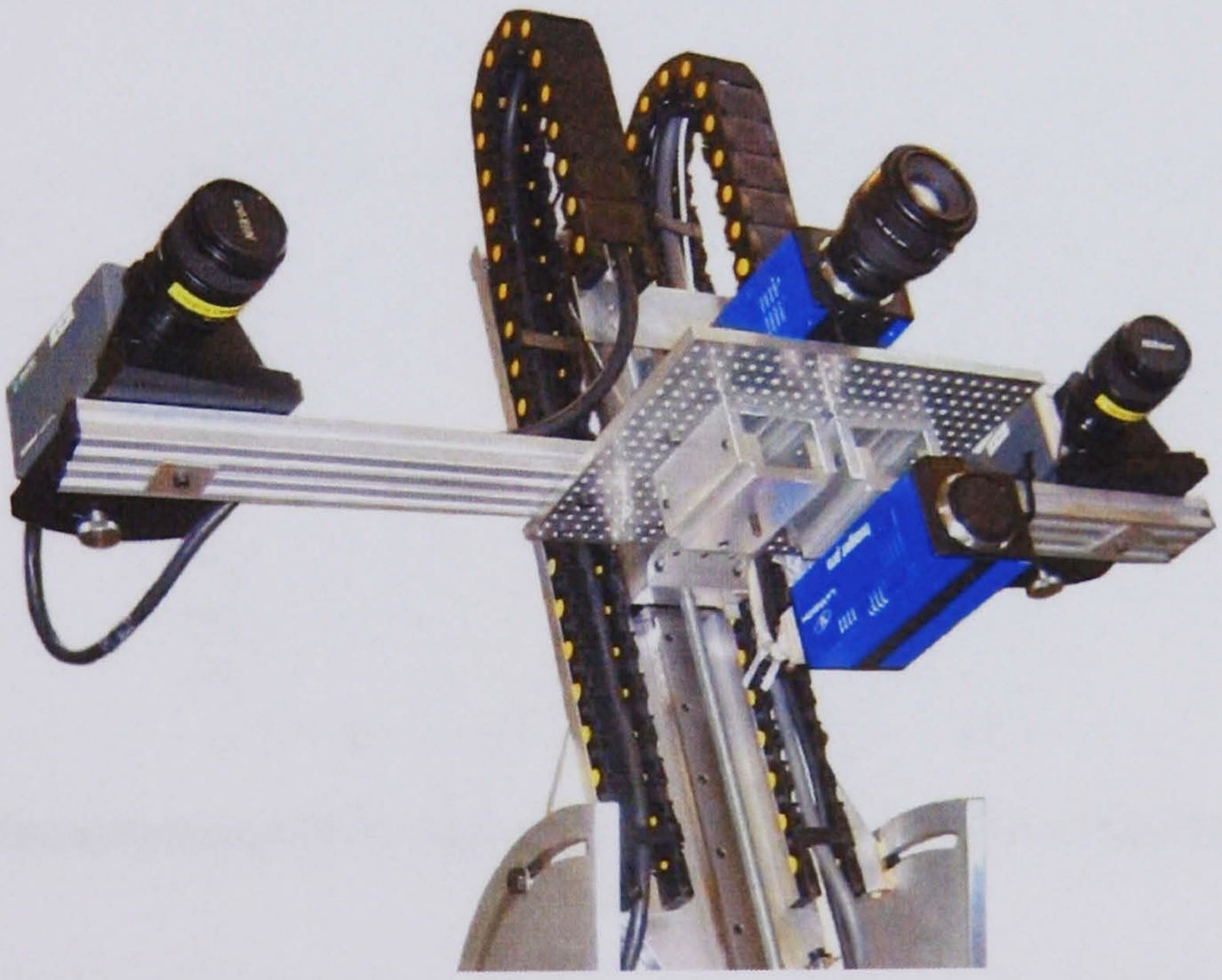

Figure 5.47 – 3D PIV cameras mounted on the CoJeN rig.

Unfortunately, due to delays in the CoJeN schedule, the 3D system's loan period ended before the test started, meaning that no 3D data could be collected from the jet exhaust. This description is therefore included purely for reasons of completeness.

5.8.2. Background-Oriented Schlieren

In addition to the 2D and 3D PIV cameras, a Background-Oriented Schlieren (BOS) system was added to the rig as a test of feasbility. BOS is an optical technique capable of measuring density gradients within a fluid field, be they caused chemically, or by pressure or temperature. In many respects, BOS is a variation on shadowgraphy, which has been proven to be a simple, low-cost means of visualising high speed flows (Skeen, et al., 2003), with results that are proportional to the amount of refractive light bending in multiple paths through the flow (c.f. Figure 5.48). (Richard and Raffel, 2001) for example, used BOS to study helicopter blade wakes, and they describe the technique in detail.

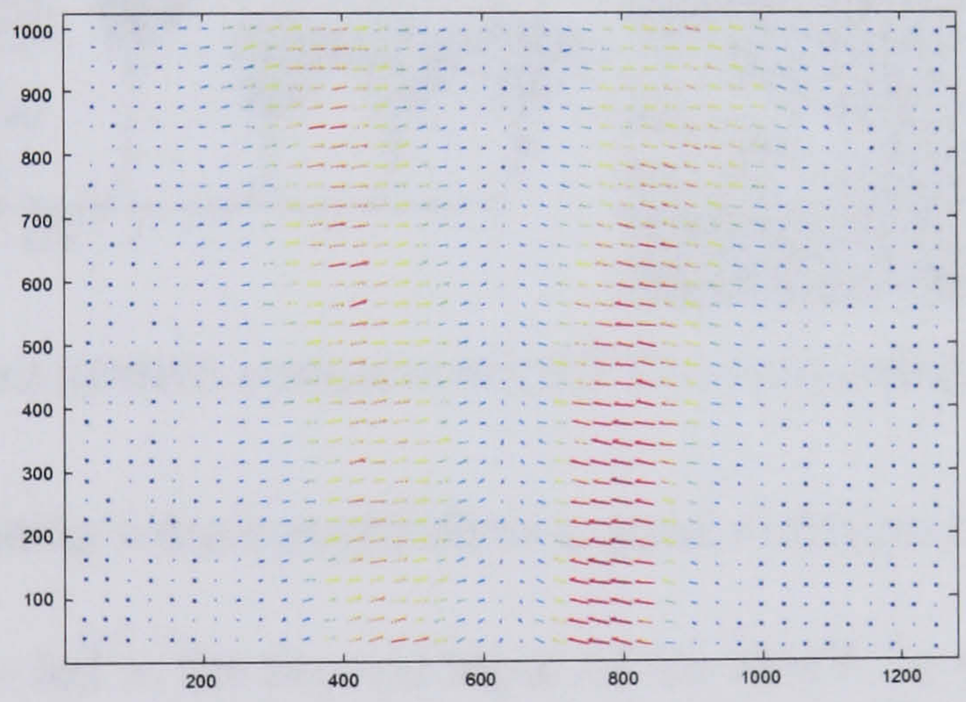

Figure 5.48 – Instantaneous BOS vector map; part of a high-speed helium jet study by the author.

The 1-dimensional BOS system employed during the CoJeN test, and the results obtained from it, are described in Appendix 9.1.14 (page 367).

5.8.3. Observation Cameras

In order to provide confirmation of the open-loop controlled traverse positions, as well as allowing visual inspection of all of the apparatus during a test, the rig was instrumented with four small monochrome PAL cameras, with built-in infrared LEDs to allow their use in the dark (Maplin; MS37S). Three of the cameras were attached to the motorised traverses and aimed at stationary rulers; the fourth was mounted on two model servos (Maplin; FS35Q) which could be placed anywhere on the rig's table top.

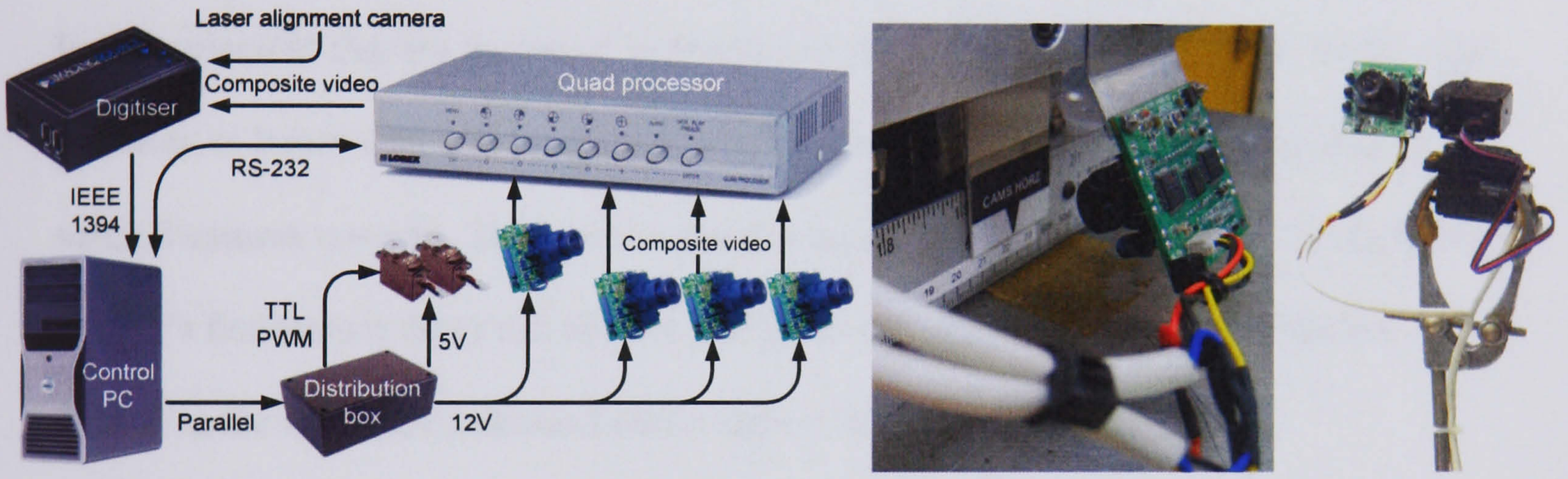

Figure 5.49 a) Camera system components; b) Traverse camera; c) Pan/tilt camera.

The four miniature cameras were connected to a quad video processor (Ganz; QD-04C), the output of which was fed to the second input of the FireWire video digitiser (Imaging Source; DWG-1) used by the light sheet alignment camera described in Section 5.3.3. An RS-232 serial link to the quad processor allowed each of the four cameras to be remotely switched to full-screen, while two channels of the control PC's parallel port were used for direct PWM control of the pan and tilt servos.

The video stream was viewed using software supplied with DWG-1 digitiser, and small C++ applications were created to control the servos and quad processor. The software interfaces are shown in Figure 5.50.

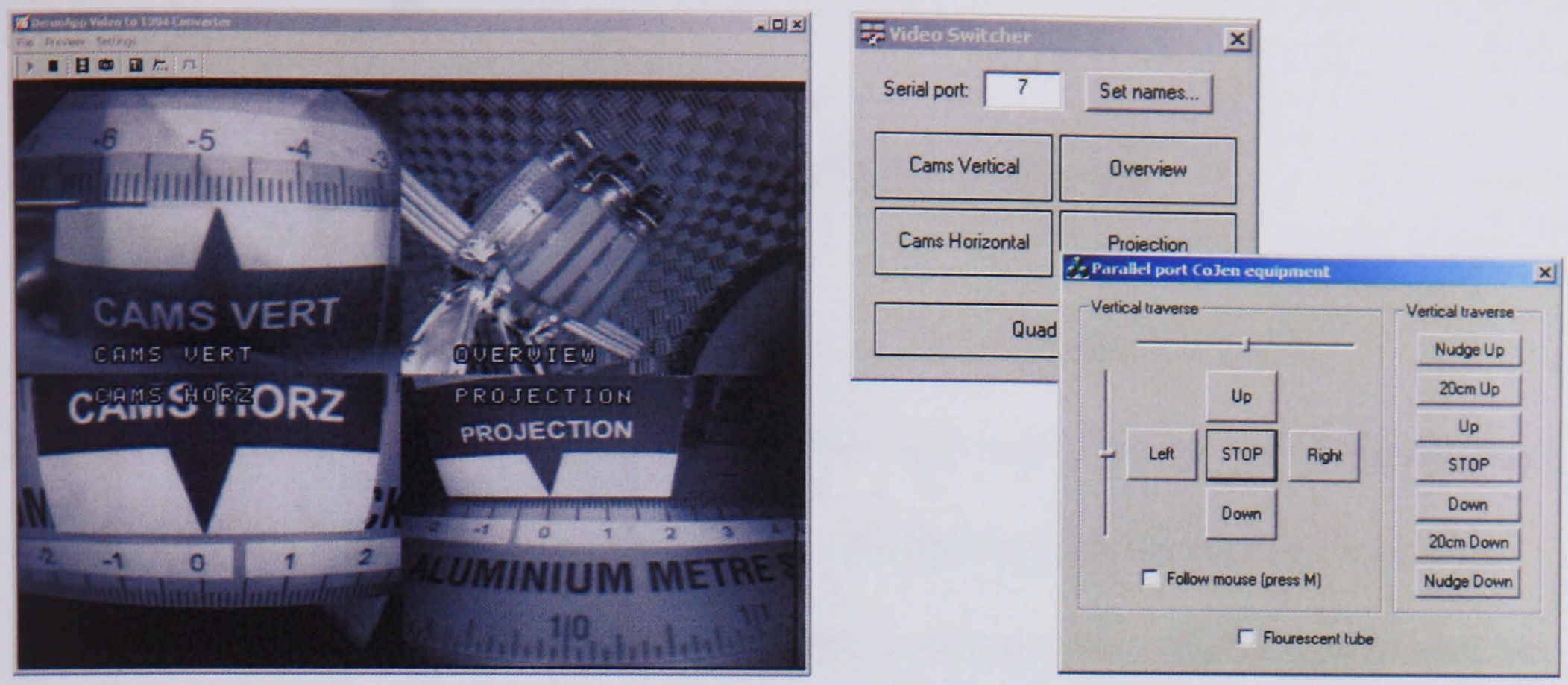

Figure 5.50 – Software to view, select, and move the observation cameras

It was estimated that the traverses' cameras and rulers allowed confirmation of the stage positions to better than 250 μm, which was of relevance to the manually controlled vertical camera traverse. The controls for this traverse's DC motor (as well as the BOS system's fluorescent tube) can be seen alongside the observation camera's pan/tilt control in the application shown bottom right of Figure 5.50.

5.8.4. Automatic PC Starter

Due to the enclosed nature of the CoJeN rig's base, a means of automatically starting the enveloped PCs was required. A timer circuit, shown in Appendix 9.1.15 (page 370), was built to simulate the momentary closing of each PC's power button, approximately 5 seconds after power was applied to the rig. It was found that a shorter delay was insufficient time for the PC power supplies to stabilise, leading to unpredictability in the computer start ups.

5.9. Seeding

5.9.1. Considerations and Requirements

The ease of providing suitable seeding for a large PIV experiment is often underestimated, as was demonstrated during the CoJeN test. Not only must the seeding be delivered at a high – yet controllable – rate, with uniform particle sizes, but it must also be introduced into the flow at a point where it will become suitably mixed with the fluid under study. Consideration must also be given to the pressure that may be required in order to inject particles into the flow, as well as the practicality of the system's operation.

Seeding for all of the CoJeN experiments was provided by Qinetiq who, through consultation with the experimental partners, chose to use titanium dioxide (TiO_2) particles, due to their low cost, brightness and solid form. As discussed in Section 2.2 (page 35), the choice of particulate diameter is invariably a trade-off between the accuracy of flow depiction required, and the amount of light needed by the measurement technique. This was particularly pertinent given that the CoJeN test comprised both PIV and LDA measurements (the latter of which is much more light-sensitive), and only 1 type of seeding was to be used through the experiments.

Prior to the test, it was hoped that the LDA surveys might achieve data-rates of up to 20 kHz, thereby allowing the measurement of turbulence of up to 10 kHz. As revealed by equation (2.19) on page 43, TiO_2 particles in air should have a diameter no greater than 0.22 μm if they are to follow 10 kHz oscillations with 95% amplitude accuracy. Given

the stock particle sizes available however, and concerns regarding the amount of light available for PIV, it was finally decided to use the ever popular 0.3 μm diameter seeding, 300 kg of which was ordered.

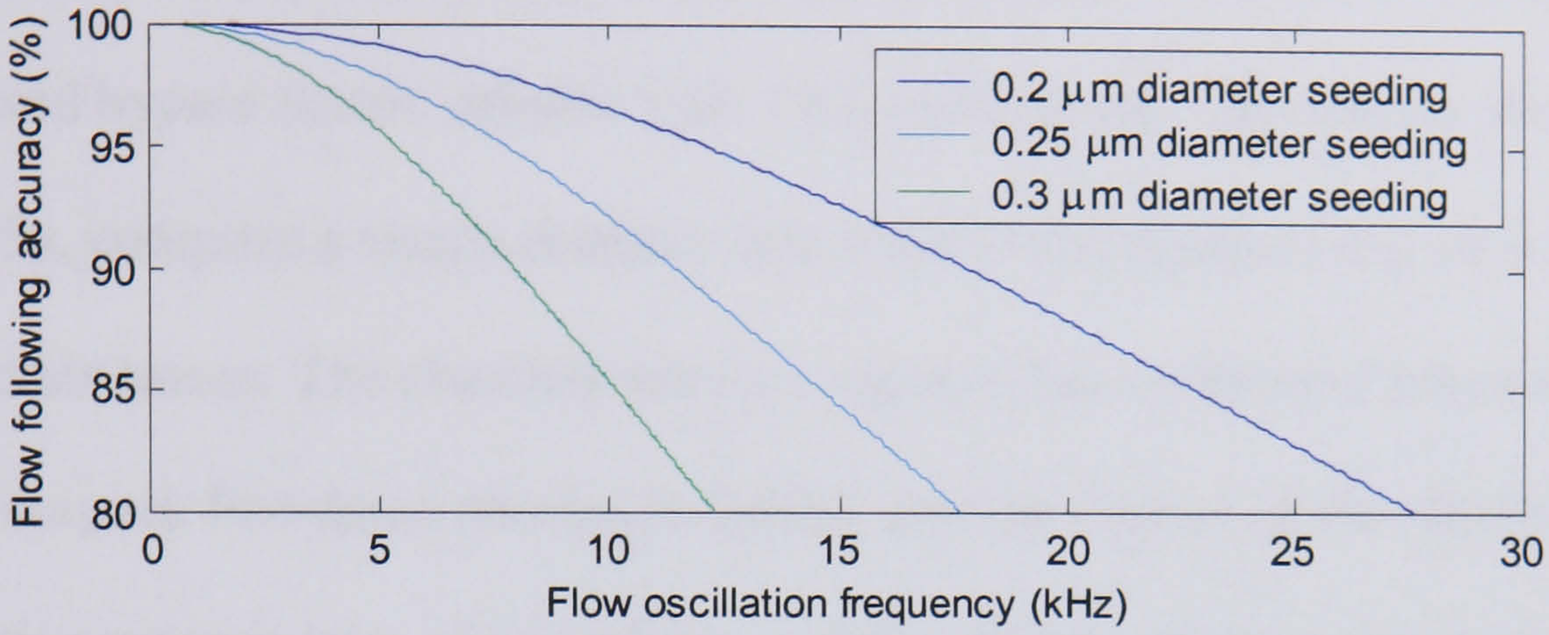

Figure 5.51 – The performance of TiO_2 seeding in air, based on equation (2.19).

It is of note that when seeding samples from both Kronos Inc. and Huntsman LLC were examined under an SEM, the average particle diameter was found to be around 0.20 μm and 0.25 μm respectively, thereby improving the seeding responsiveness by the amounts shown in Figure 5.51, but reducing the amount of scattered light by 2 to 3 times (c.f. Section 2.2.2, page 45).

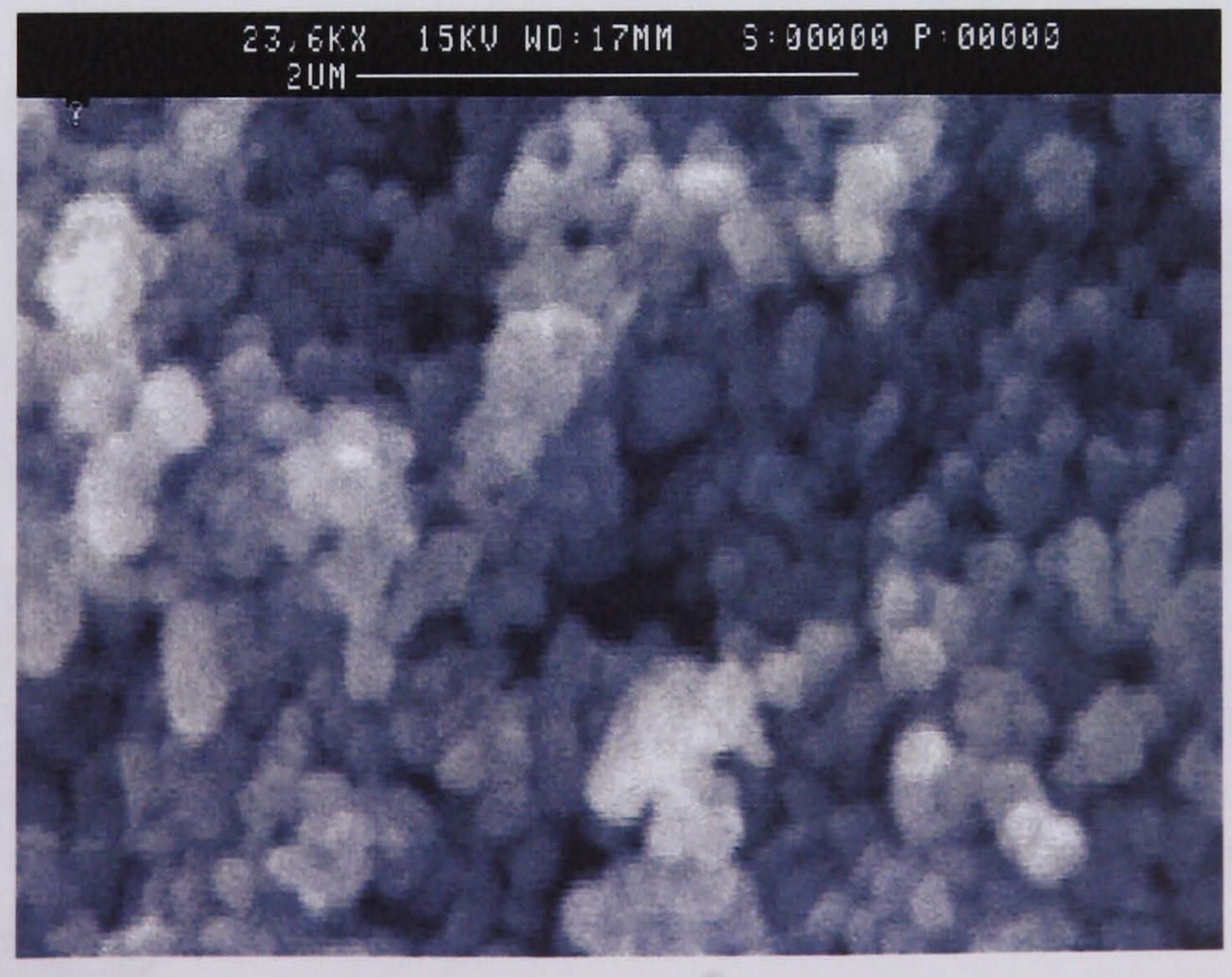

Figure 5.52 – 0.3 μm Huntsman Tioxide TR38 particles.

5.9.2. Seeding Generation

5.9.2.1. Core & Bypass Seeding

Qinetiq initially intended to use 4 powder seeders manufactured by LaVision to provide both core and bypass nozzle streams with TiO_2 particulates. The seeders, shown in Figure 5.53a, comprise a single chamber into which high-pressure dry air is injected, and seeded air leaves. The chamber sits on a separate base (coloured blue) which houses a rotating magnet. Powdered seeding is loaded into the bottom of the chamber along with a stirring magnet (aka. 'flea') which – when rotated – kicks a cloud of dust into the passing stream of air.

Tests at Warwick University, and manufacturer advice, both stressed the importance of correct seeding preparation, to avoid agglomerated particles (which the seeder is unable to filter out). To this end, a number of ovens were installed in the NTF to allow the each day's seeding to be dried over the course of the previous night.

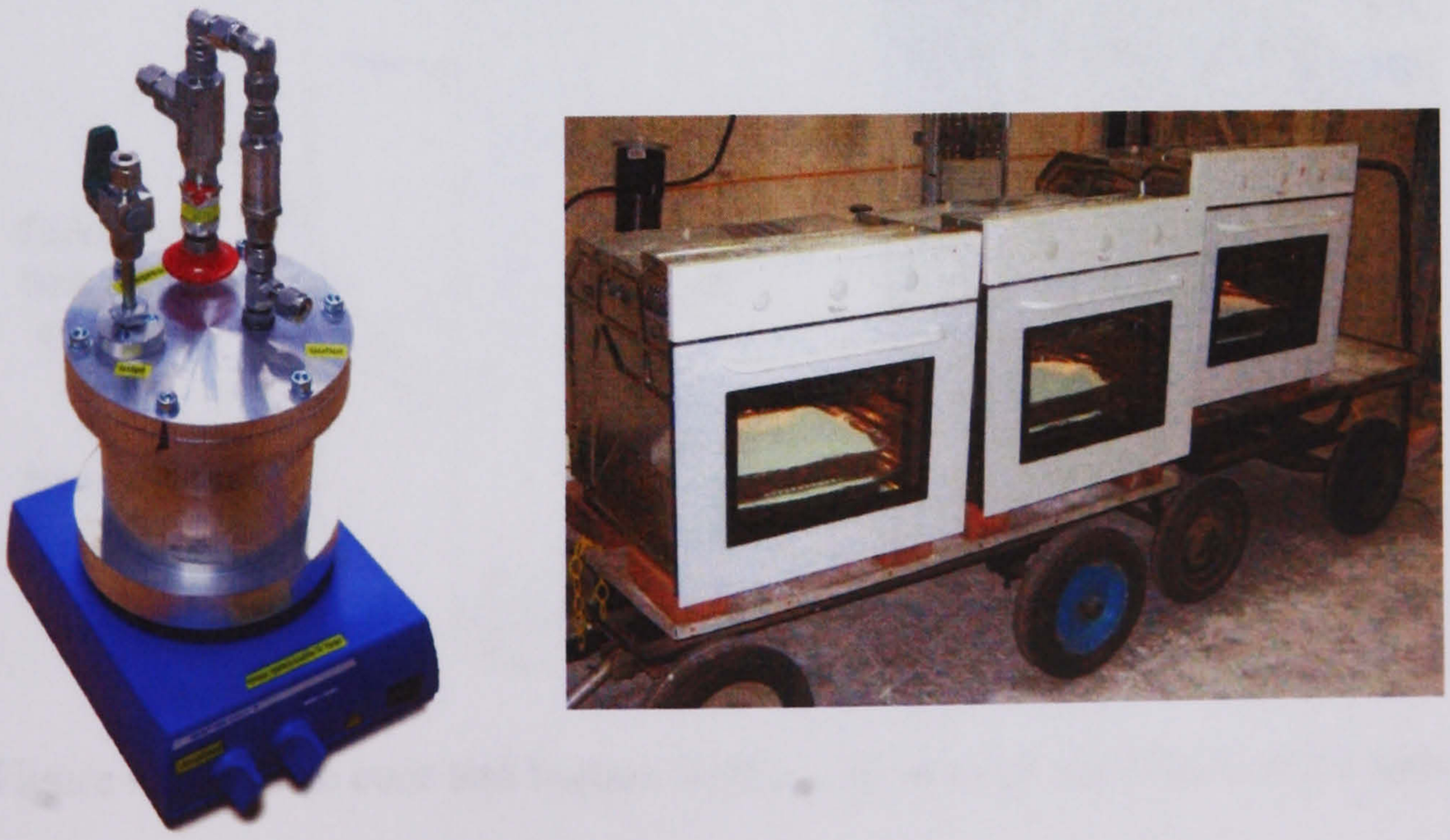

Figure 5.53a) LaVision seeding generator; b) The TiO_2 drying facilities.

During pre-test trials, the LaVision seeders worked well but one fundamental flaw was revealed: at the flow rates required to fully seed the jet, the chambers emptied after only 10 minutes or so. In an attempt to increase the running time (by allowing larger amounts of seeding to be loaded at a time), the magnetic flea was replaced with a stirred attach to an electric drill, but to little benefit. For this reason, it was felt necessary to source larger seeding generators.

Given the non-scalable nature of the LaVision design, two seeders were rapidly designed and constructed based on a fluidised bed design that had been used successfully at the NASA Glenn jet facility. Constructed from 4" diameter pipe, the new design comprised both a standard fluidised bed and a cyclonic particle separator, allowing large agglomerated particle clumps to be removed from the output by means of centrifugal force. After a typical day's running, around ¼ of the seeding used would be found, separated, at the bottom of the cyclone chamber.

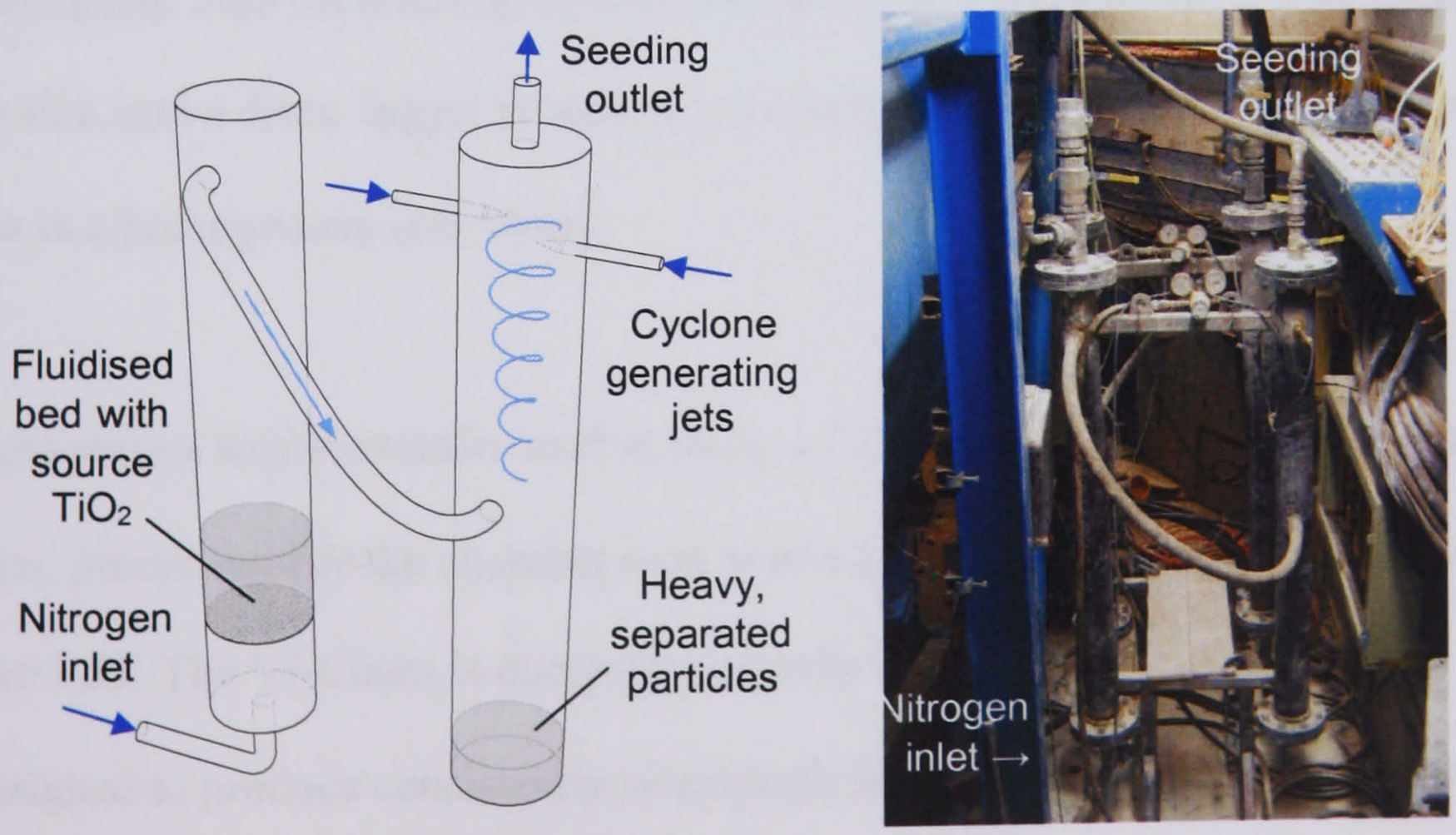

Figure 5.54 – The core and bypass seeding generators used for CoJeN tests.

5.9.2.2. Flight-stream seeding

The flight-stream in which the nozzles were tested should comprise completely laminar flow, and is therefore of little interest in itself. The purpose of seeding the flight-stream is rather to improve the quality of measurements made in the outer mixing layer of the exhaust, where air will be exchanged between the jet bypass and the flight-stream. Based on the assumption that *some* core/bypass seeding would be present in the areas of interest, and budgetary considerations based on the large cross-sectional area of the flight-stream, it was felt that certain compromises could be made in the flight-stream seeding.

The flight-stream was therefore initially seeded using a Dantec Dynamics glycol atomiser, positioned slightly upstream of the nozzle. Not only did this unit suffer from limited output, but it was also difficult to disperse the fog sufficiently throughout the whole of the flight-stream, even after the construction of a drain-pipe rake. Two oil-based atomisers from Oxford Lasers suffered from low visibility due to their small particle size, and a disco fogger produced too much seeding, which appeared to the PIV cameras as a homogenous grey cloud.

The flight-stream was eventually seeded using a Concept Vi-Count Compact aerosol generator, placed outside the chamber next to one of the flight-stream intakes, as shown in Figure 5.55. The Vi-Count is designed primarily for use in filter testing, and is as such designed to produce consistently sized particles, of between 0.2 – 0.3 μm diameter.

The smoke is generated by the vaporising a mist of white-oil*, produced using externally supplied pressurised inert gas (in this case, nitrogen).

Figure 5.55 – Vi-Count aerosol generator, as used for flightstream seeding.

* A highly-refined (typically food-grade) mineral oil.

5.9.3. Seeding Performance

The Vi-Count and fluidised bed seeders proved capable of generating very good seeding, with similarly sized particles, concentrations and intensities. Figure 5.56 demonstrates such homogeneous seeding, as witnessed just downstream of the short-cowl nozzle.

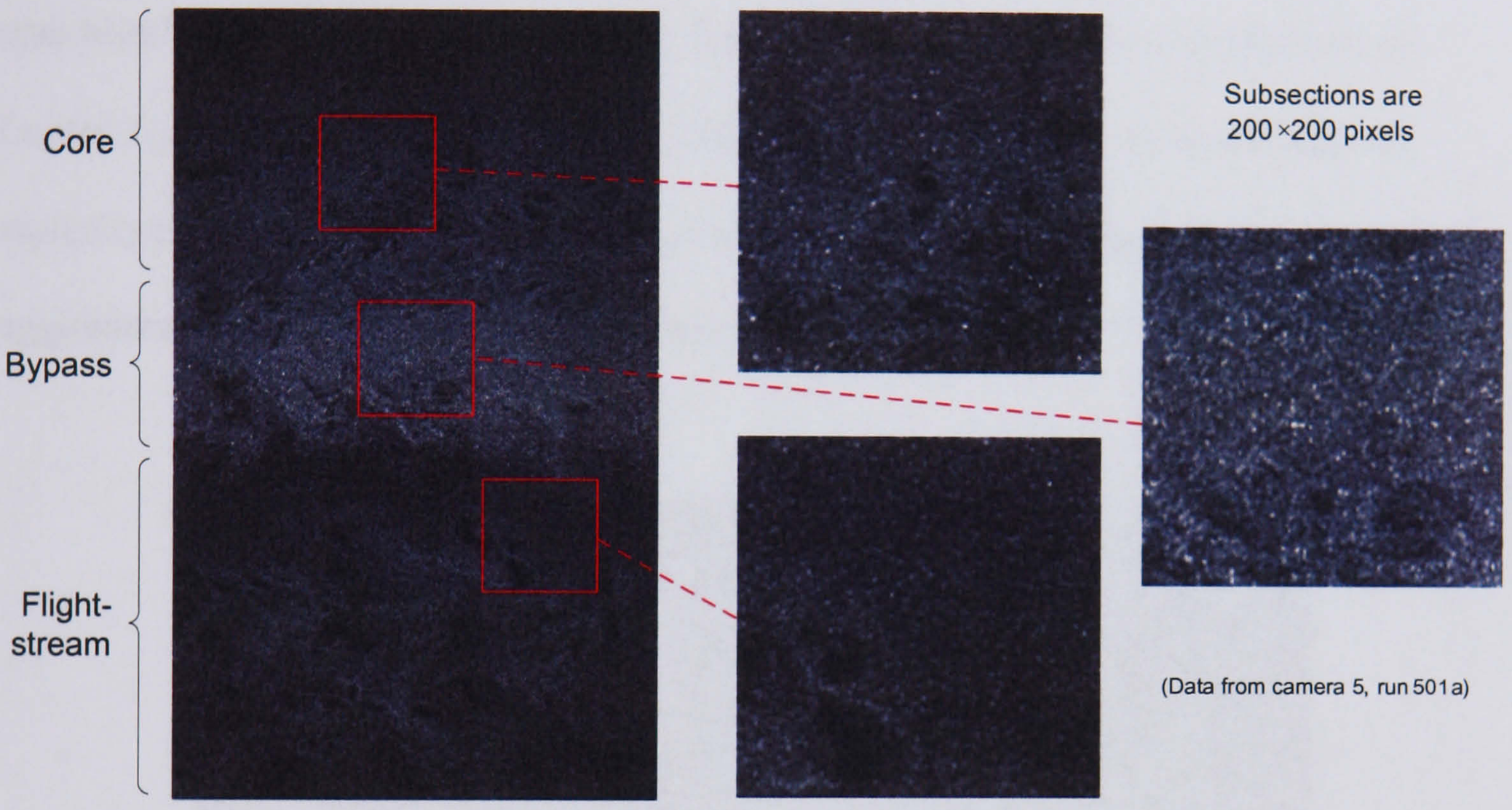

Figure 5.56 – Good CoJeN seeding, as seen by the PIV cameras.

Problems were however caused by the inconsistency of the TiO_2 seeding levels. In addition to downtime necessitated by refills, it also proved extremely difficult to adjust the nitrogen feed pressure to the (relatively low) accuracy required. There were also occasional surges caused the detachment of layers of built up particles on the side of the pipes which carried seeding to the nozzle. Figure 5.57 shows three frames taken from a video recorded by the rig-mounted observation camera during a Phase 3 experiment. The core, bypass, and flight-stream (along with the LDA beams) can all be clearly distinguished as they falter on and off.

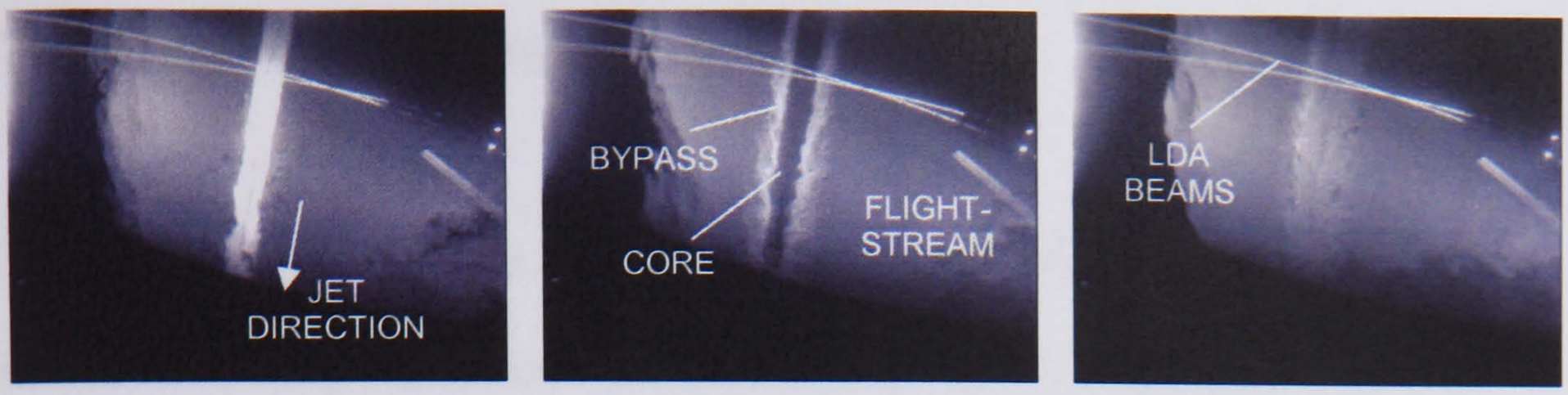

Figure 5.57 – Intermittent jet seeding.

It should be noted that after the test, concerns were raised over the level of TiO_2 seeding agglomeration. These worries arose from the observation of particle clumps around the core nozzle stream instrument rake (c.f. Figure 5.58), and a sieve test performed by Dantec Dynamics. As is apparent from Figure 5.56 however, the TiO_2 seeding was typically no brighter than the 0.2 – 0.3 μm oil particles, suggesting that any agglomeration occurred on a temperamental basis.

Figure 5.58 – Agglomerated seeding around the instrumentation rake.

5.10. Systems Overview

An image of the CoJeN rig (as it stood during test phase 4) and schematics of the electronic computing and systems, are included in Figures 5.59 – 5.61 below:

Figure 5.59 – The CoJeN rig in situ.

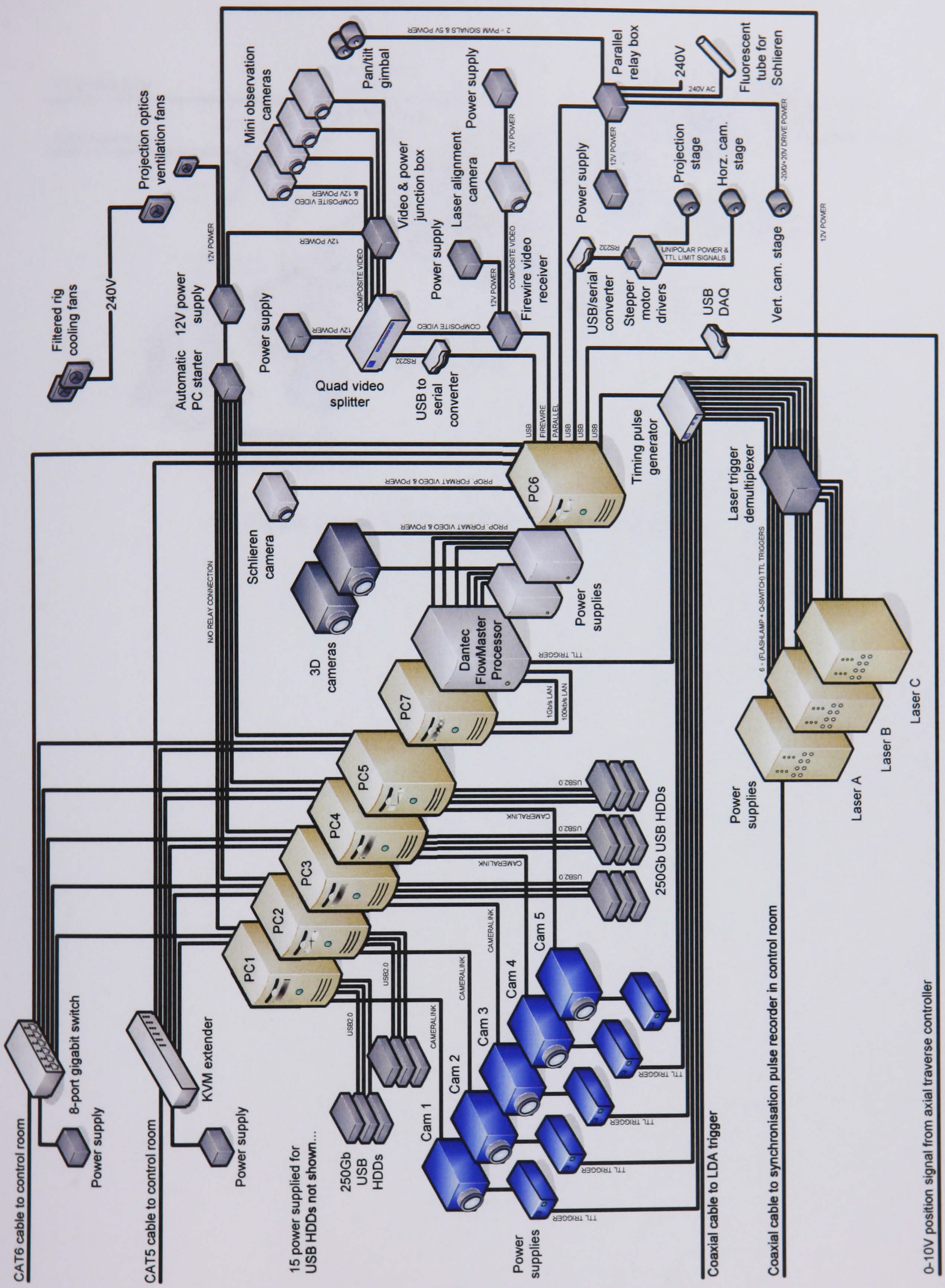

Figure 5.60 – CoJeN rig electronics.

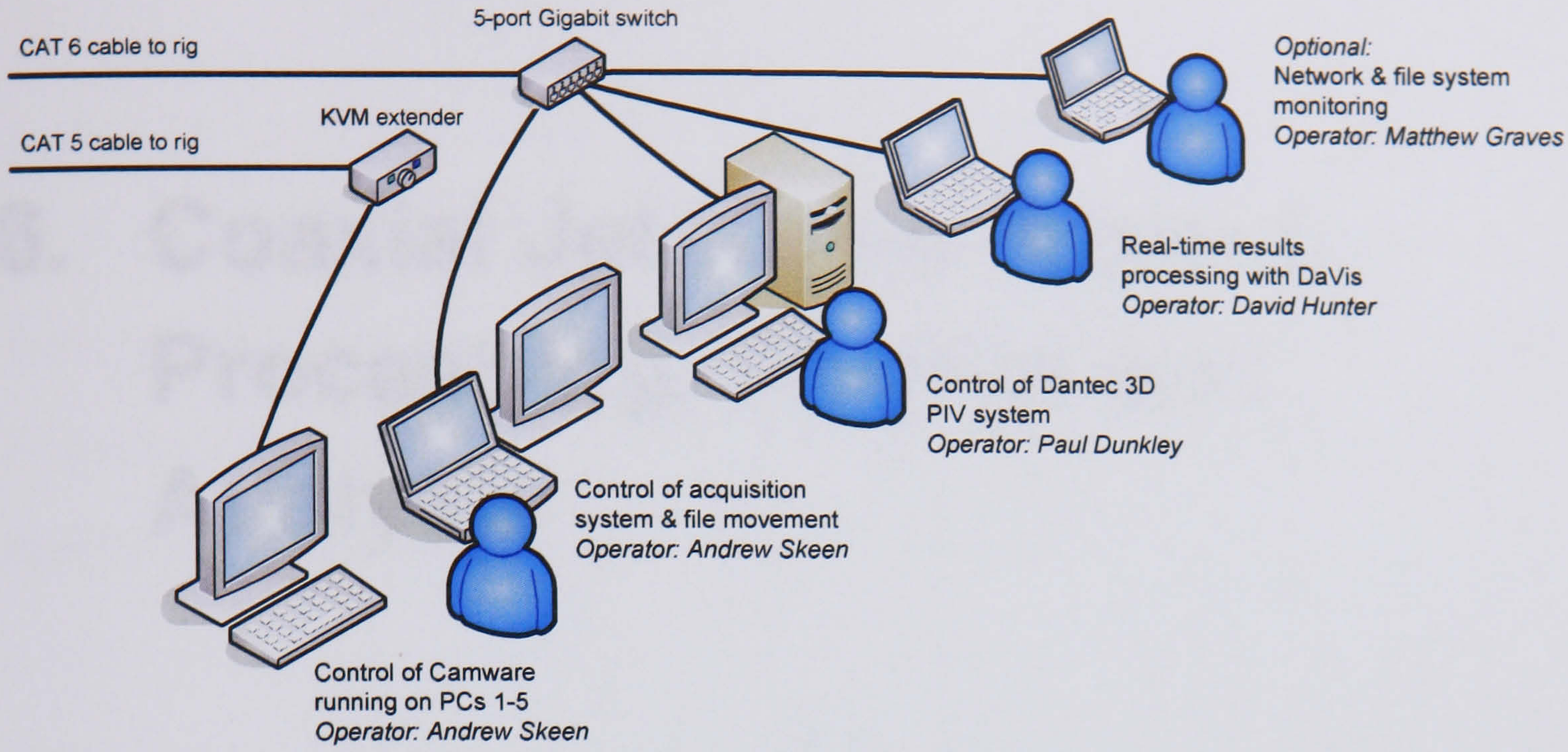

Figure 5.61 – Control room computer systems.

6. Coaxial Jet Noise Project: Processing, Results and Analysis

6.1. Datasets Collected

Sections 6.1.1 through 6.1.3 detail the amount of data that was collected during each of the CoJeN test phases. It will be noted that – in phase 3 specifically – fewer nozzles and operating conditions were tested than planned (c.f. Table 5.11, page 198). This was due to delays in the test schedule caused, in part, by the difficulties experienced with the seeding. That said, there were still over ⅓ million PIV measurements made.

Every set of data collected during the test was assigned a 'run number', which differentiates samples based on the positions of the axial and radial (i.e. 'vertical' camera) traverses*. Information pertaining to each run number (which are referenced throughout this chapter), such as the traverse positions and Δt value, are given in Appendix 9.2.1 (page 371).

6.1.1. Phase 2: Volumetric Cross-Planes

Based on consideration of the associated compromise between cross-axial resolution and acquisition speed, it was decided that the phase 2 volumetric PIV measurements would comprise 2 cross-axial 'scans' of 11 'slices', one above the other, as shown in Figure 6.1. These double scans were to be repeated in 3 different positions down the jet, namely 5D, 10D, and 15D.

* A single run number was used to label the phase 2 cross-axial 'scans'. The run number itself comprises a 3-digit numeral (incremented every time CamWare recording was started) and an optional character, generated when subdividing contiguous recordings into different measurement positions.

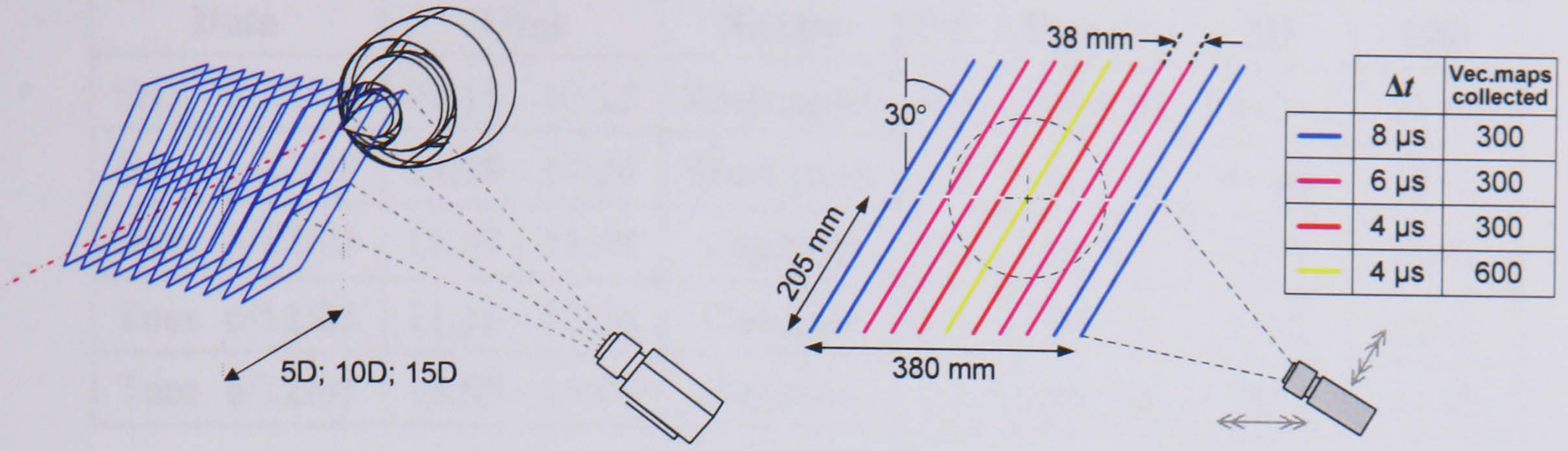

Figure 6.1 – Phase 2 measurement positions.

The PIV measurements were made at 12 Hz, using 3 cameras as described in the previous chapter. Adding the time taken for the traverses to move, it took a little over 20 minutes to complete 2 scans, as shown above. Figure 6.2 details the relative camera and laser timing, as controlled (along with the cross-axial traverses) by YAPP. For most of the datasets collected, Δt was altered depending on the 'slice' position; typical values used are listed to the right of Figure 6.1.

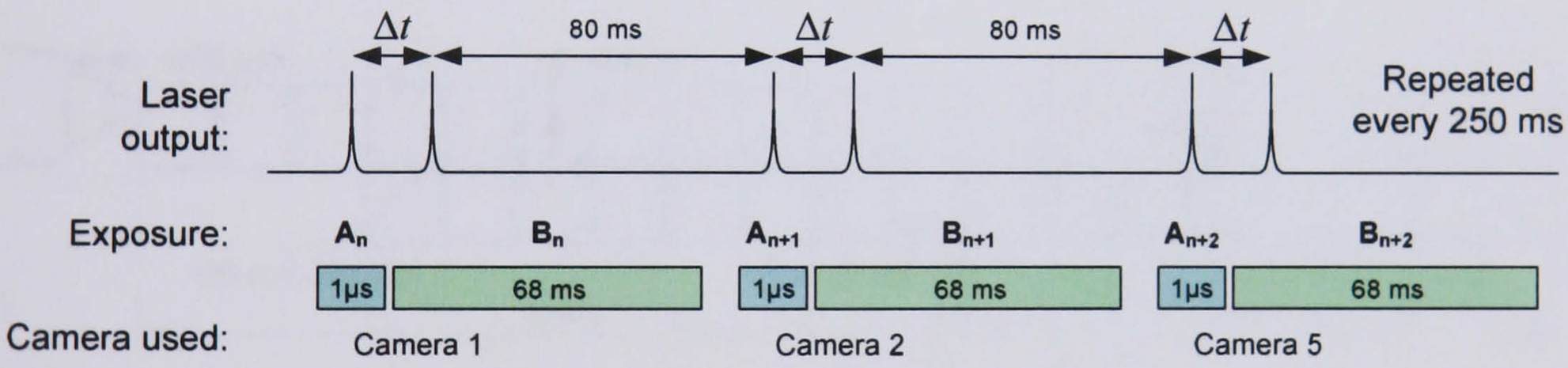

Figure 6.2 – Phase 2 measurement timing.

A total of 4 nozzle / operating condition combinations were tested, as listed in Table 6.1 (OP 1.8 is a cold variant of OP 1.2). Time constraints also meant that some of the measurements comprised only single, centred scans, instead of the intended double 'high and low' scans. Furthermore, no data whatsoever could be collected at 15D due to a combination of time constraints and a computer problem, which is discussed in Section 6.2.4. The total quantity of data collected was 404 Gb.

Date	Time	Nozzle	OP	Run #'s	5D	10D
Fri 2/12/05	09:15 - 10:23	Short cowl	1.8	101-108	11×1×2	11×1
Fri 2/12/05	14:08 - 14:24	Short cowl	1.2	111-112	No data	11×2
Mon 5/12/05	15:07 - 15:49	Coplanar	1.2	120-123	11×1	11×1
Tues 6/12/05	11:16 - 12:26	Coplanar	1.3	130-135	11×2	11×2
Tues 6/12/05	13:55 - 15:09	Coplanar	1.2	136-141	11×2	11×2

Table 6.1 – Phase 2 data acquired during the CoJeN test.

6.1.2. Phase 3: Full Exhaust Mapping

Because the 'interleaved' measurement technique described in Section 5.2.5 enabled data acquisition at a relatively high speed, it was decided amongst CoJeN partners that the length of the measurement volume should be increased by approximately 0.8 m. These additional measurement positions are marked below in turquoise:

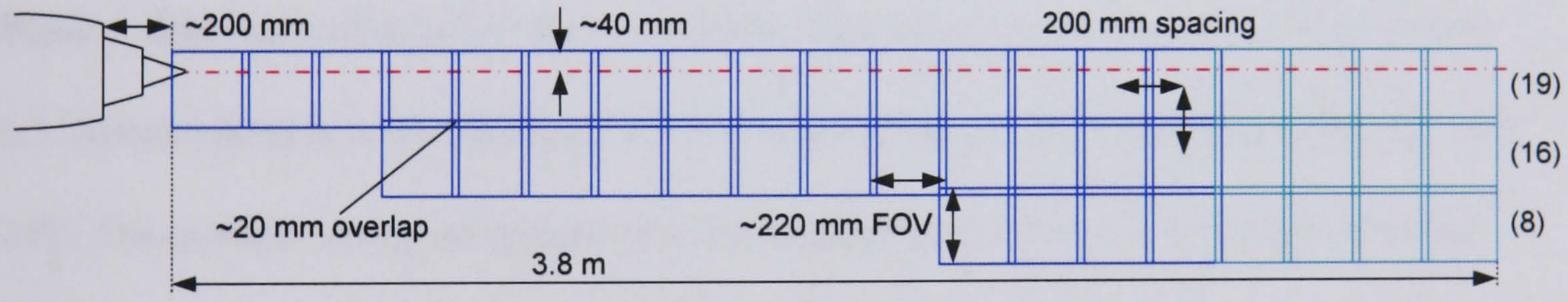

Figure 6.3 – Phase 3 measurement positions.

The first measurement's axial position was determined by the upstream bogey's inability to move as close to the nozzle as intended, due to interaction between the equipment on it and the flight-stream cowl (c.f. Figure 5.16, page 169). As with phase 2, the measurements were made using 3 of the cameras, operating at 12 Hz (c.f. Figure 6.2), with $3 \times 350 = 1050$ vector maps collected in each position. As such, it took a little over an hour to cover the whole of the measurement volume shown above. The 4 nozzle / operating condition combinations measured are listed in Table 6.2, where it can be

seen that the short cowl / OP.1.2 measurement had to be performed over the course of 2 days. Time constraints also meant that serrated nozzle measurements were dropped from test phase 3.

Date	Time	Nozzle	OP	Run #'s	Exhaust Coverage
Fri 9/12/05	12:43 - 14:39	Short cowl	1.1	500-509	Complete
Mon 12/12/05	14:12 - 15:42	Short cowl	1.2	520-529	Top & middle row
Tues 13/12/05	14:41 - 15:28	Short cowl	1.2	544-550	Top & bottom row
Tues 13/12/05	09:46 - 13:21	Short cowl	1.3	530-543	Complete
Wed 14/12/05	09:33 - 13:05	Coplanar	1.2	560-570	Complete

Table 6.2 – Phase 3 data acquired during the CoJeN test.

A total of 397,434 images were collected during phase 3, equaling 1552 Gb of data.

6.1.3. Phase 4: Time-Resolved PIV

Phase 4 data was collected in the same plane as phase 3; along the top row of Figure 6.3. Measurements were taken at a total of 6 different axial positions between 6D and 11D, this number being determined by the available time as well the position of the other axial traverse bogey. Each PIV measurement comprised 6 exposures, acquired at approximately 11 Hz (for reasons explained in Section 6.2.1).

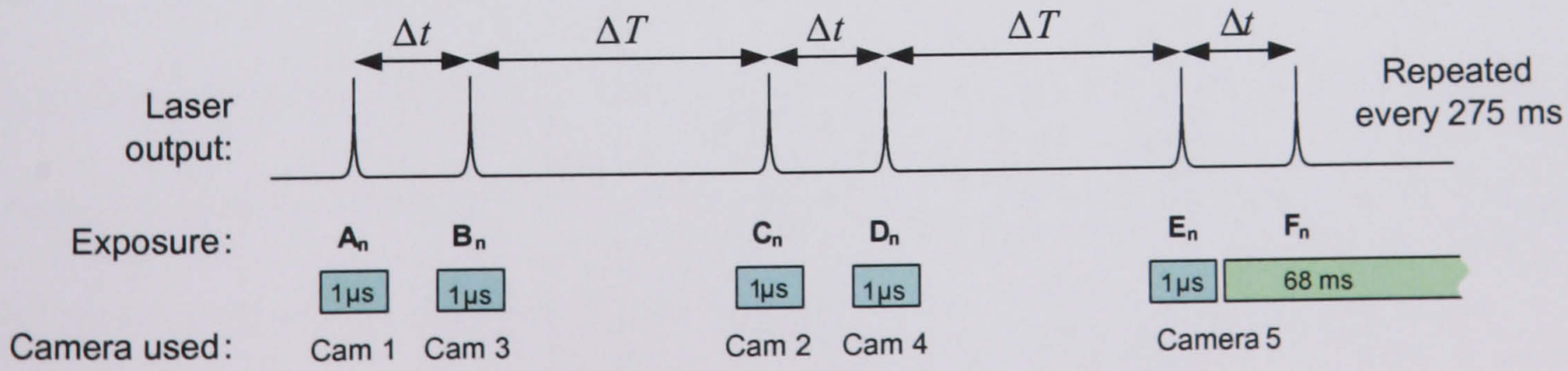

Figure 6.4 – Phase 4 measurement timing.

The time between the end of one pulse pair and the start of the next, ΔT, was defined as:

$$\Delta T = n\Delta t \quad \text{where} \quad n = \{\ 1\ 2\ 3\ 4\ 5\ 6\ 7\ 8\ 9\ 10\ 15\ 20\ 30\ 40\ 50\ \} \tag{6.1}$$

For each of the 15 n values, 200 measurements were taken; a value based on the time-space correlation experiments performed by (Wernet, et al., 2003). The Δt values used for each dataset are given in Table 6.3, along with each measurement's centre axial position. All of the phase 4 data was taken on Friday 16/12/05 (from 09:39 – 14:22) whilst the short cowl nozzle was installed, and operating under OP 1.3.

Run #	701	702	703	704	705	706	708	709	710	712	713
Δt (μs)	5	5	3	3	3	3	3	3	3	3	3
X (m)	2.30	2.11	1.91	1.71	2.31	1.61	2.31	3.01	1.61	1.90	2.31*
X (D)	8.4	7.7	7.0	6.3	8.5	5.9	8.5	11.0	5.9	7.0	8.5

Table 6.3 – Phase 4 data acquired during the CoJeN test.

Runs 708 – 710 consisted of only 4 images (exposure pairs AB & CD), but all other runs comprised close to 18,000 images, resulting in a total of 152,741 images (or 597 Gb of data) being collected.

* Run 713 was acquired at a radial position 100 mm lower than the others.

6.2. Issues Encountered

In common with most experiments, a significant proportion of the CoJeN data processing related to the factoring out and correction of errors that found their way into the measurement. Given their importance, Section 6.2 comprises an account of these problems, namely two camera faults and problems caused by rig vibration and optical interference.

6.2.1. Camera Clock Performance

The pco.2000 cameras used for the CoJeN tests were chosen, in part, because of their ability to acquire full-frame images at 14.7 Hz. In common with every other similar camera however, this framing rate is only achieved when using both of two available read-out taps (c.f. Section 2.4.7.1, page 82) and the higher of two possible pixel clock frequencies (40 MHz as opposed to 10 MHz). While a faster pixel clock is expected to increase noise by a marginal amount, the use of well balanced multiple taps should have no discernable effect on a camera's image quality.

During the course of the CoJeN test, the image quality of cameras 3 and 4 was found to steadily degrade under 40 MHz operation, particularly when using 2 read-out taps. On some days, the noise-levels were such that these two cameras were rendered unusable without switching to the slower 10 MHz pixel clock. Extreme examples of the image degradation experienced are shown in Figure 6.5:

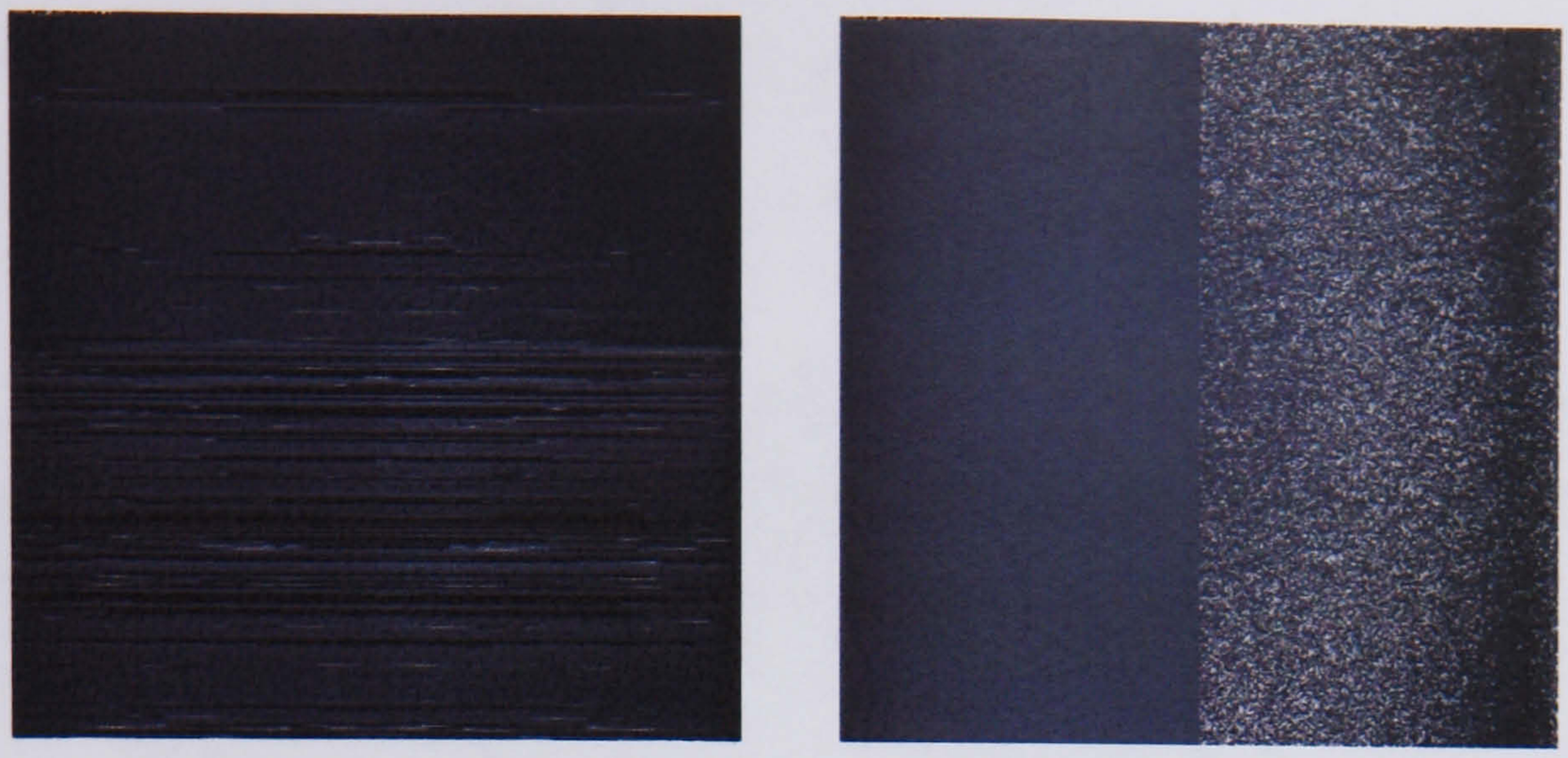

Figure 6.5 – Camera 4 images, using 1 and 2 taps, with a 40 MHz clock.

No such malfunctions had been visible during previous camera use in a laboratory setting, so given that the only change in operating condition (upon installation in the NTF) was environmental, it was concluded that this behavior was the result of extreme cold and humidity. That said, it is believed that the operating and overnight storage temperatures in the NTF did not exceed the camera manufacturer's recommended limits, as shown in Table 6.4. Nevertheless, in an attempt to mitigate environmental effects, it was decided to wrap the cameras every night in a tarpaulin 'tent', the air inside of which was warmed by a small fan heater.

Operating temperature	5 – 40 °C
Operating humidity	10 – 90 %
Storage temperature	-20 – 70 °C

Table 6.4 – pco.2000 camera environmental requirements.

For the majority of the CoJeN test, perhaps as a result of the fan heater, images from cameras 3 and 4 produced 'useable' images under all operating conditions, but – as can be seen in Figure 6.6 below – the dark noise (that measured with the lens cap on) of these two cameras' images approximately doubled when the pixel clock was switched from 10 to 40 MHz. The histogram of camera 1's dark noise is indicative of normal

operation, and it is interesting to note that cameras 3 – 5 were the hired units, while cameras 1 and 2 were brand new.

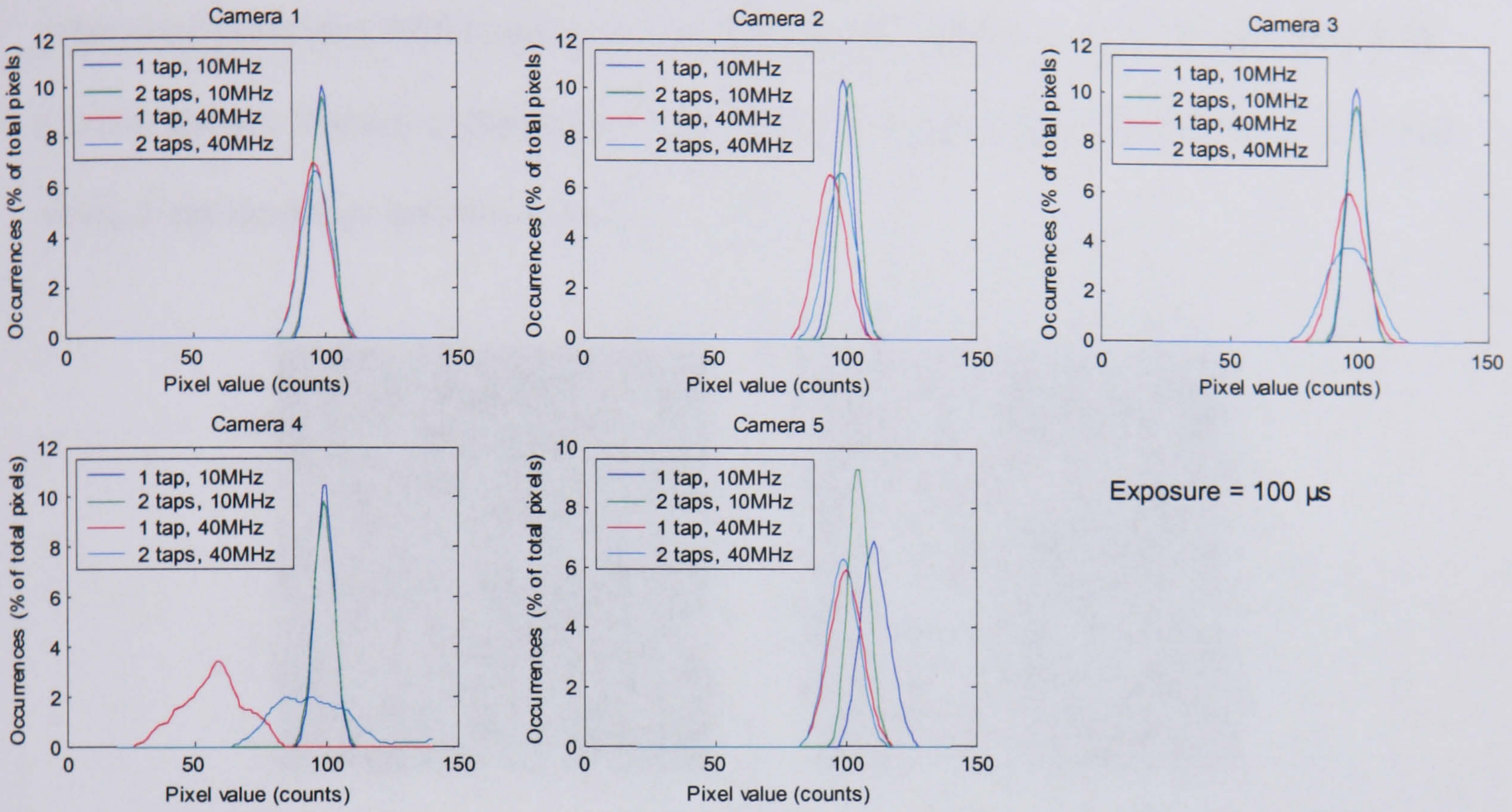

Figure 6.6 – Dark noise histograms for cameras 1-5, for all operating modes.

Due to the increased noise and unpredictable bouts of severe image degradation, cameras 3 and 4 were never used with a 40 MHz pixel clock, meaning that cameras 1, 2 and 5 (not 1, 3 and 5) had to be used for phase 2 and 3 acquisition (c.f. Figure 6.2)*. During phase 4 acquisition, cameras 1 to 4 could be run with a 10 MHz pixel clock and 2 tap read-out, with only a slight reduction in the overall measurement rate; from 4.0 Hz to 3.7 Hz.

* Because of the RAID machine distribution (c.f. Figure 5.42, page 201) this involved swapping the connections between cameras 2 and 3 and PCs 2 and 3; the non-sequential phase 4 camera order shown in Figure 6.4 is an indirect result.

6.2.2. Left / Right Velocity Bias

While, in a laboratory setting, there is negligible visible difference between the images acquired from a pco.2000 running in 1 or 2-tap mode, the same could not be said of the CoJeN images. Typical instantaneous and time-averaged images from phase 3, acquired using 2-tap read-out, are shown below:

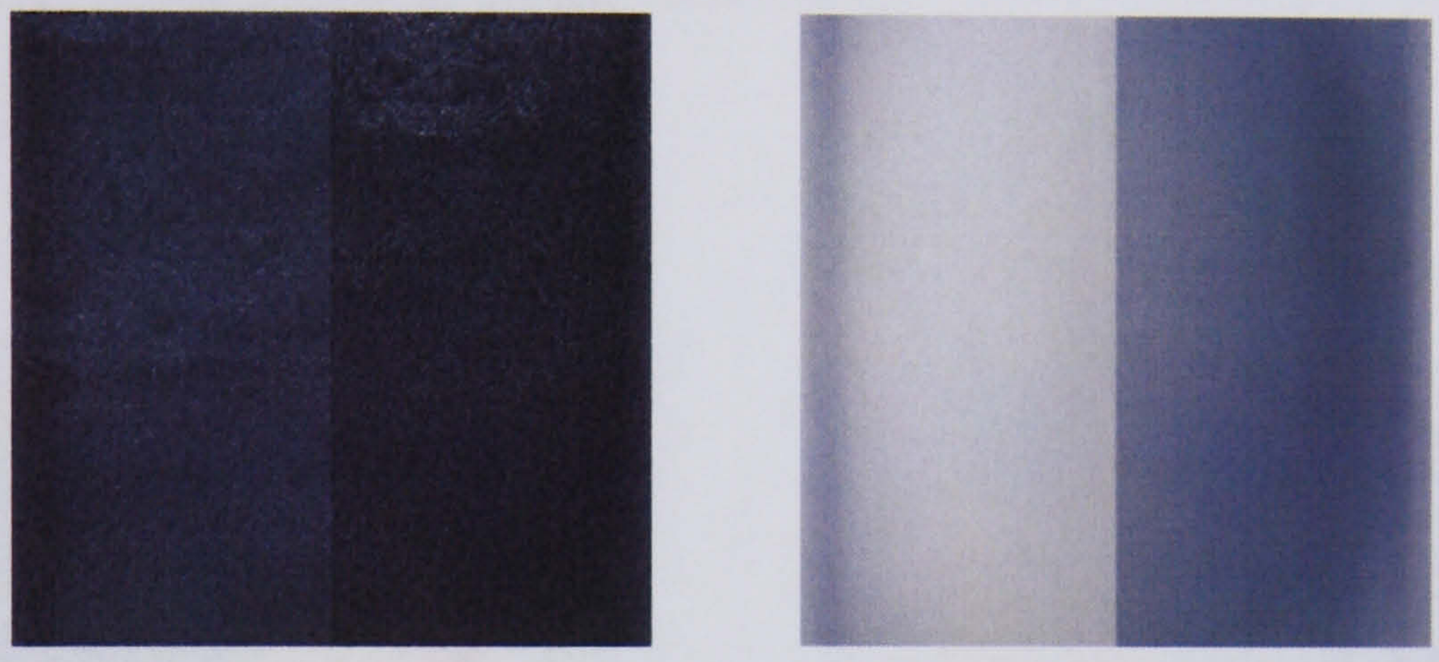

Figure 6.7 – Instantaneous and (enhanced) time-averaged* phase 3 images.

Table 6.5 quantifies the intensity difference for cameras 1, 2 and 5, using phase 3 data from 9th December. The value quoted is the average intensity of a thin vertical strip to the left of centre of a time-averaged image, minus the equivalent right-hand average. The units are rounded 8-bit counts, considered over all 43 jet measurement positions.

	Camera 1		**Camera 2**		**Camera 5**	
	Frame A	Frame B	Frame A	Frame B	Frame A	Frame B
Range:	-2 – 13	-5 – 24	-37 – -3	-21 – -1	-2 – 1	-6 – 1
Average:	8	16	-12	-6	-1	-1

Table 6.5 – Left / right intensity differences, from raw Phase 3 image data.

* Time-averages referred to in Chapter 6 comprise 350 samples.

It can be seen in Figure 6.8 that the relationships between left and right-hand side brightness differ for each camera, and also changes in polarity and magnitude for different measurement positions. By considering the left / right intensity difference for each of 17 adjacent axial measurement positions (along the top row of Figure 6.3) in conjunction with the average image intensity, it becomes clear that the two are at least partially related. The left / right intensity difference was also significantly more noticeable during phase 3, whose images were much dimmer (for reasons that are discussed in the next section).

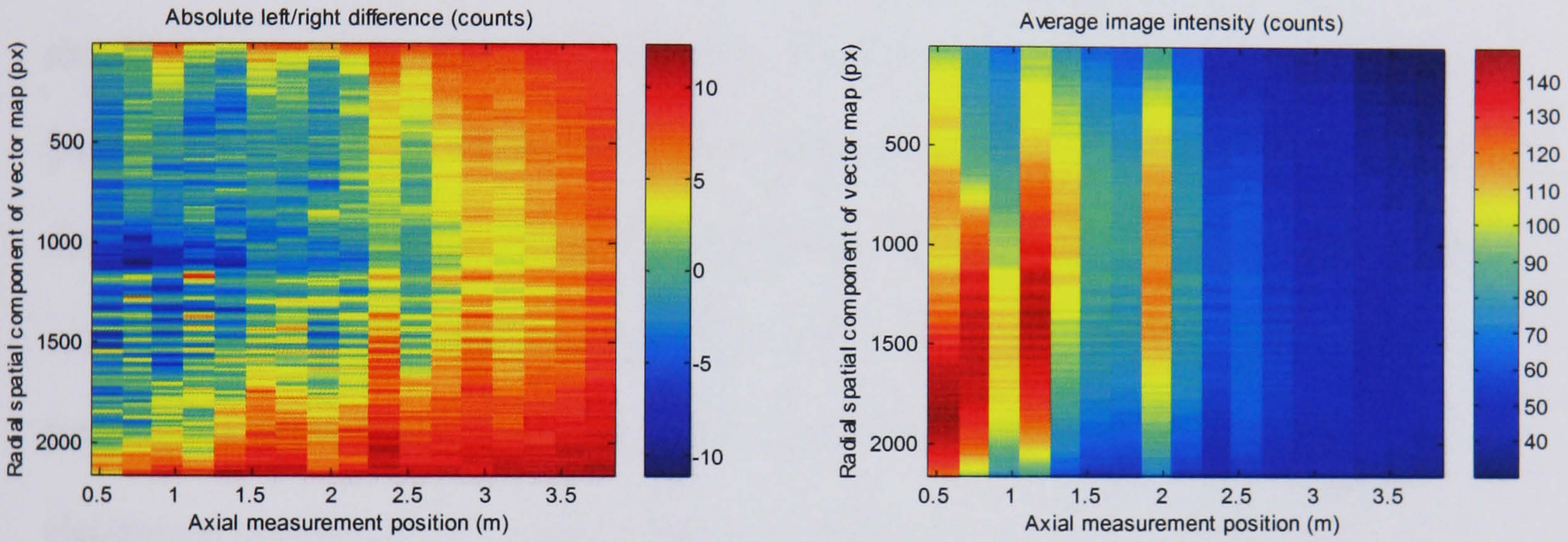

Figure 6.8 – Left/right difference, and average intensity for camera 1, frame A.

In addition to the relatively minor intensity differences between the left and right of the captured images (which *should* have a negligible effect on the cross-correlation process) it also became apparent that correlated, time-averaged vector maps were exhibiting a difference between the two sides! This difference is barely visible in the vertical vector component, instead manifesting itself in the horizontal-component, as exemplified by Figure 6.9:

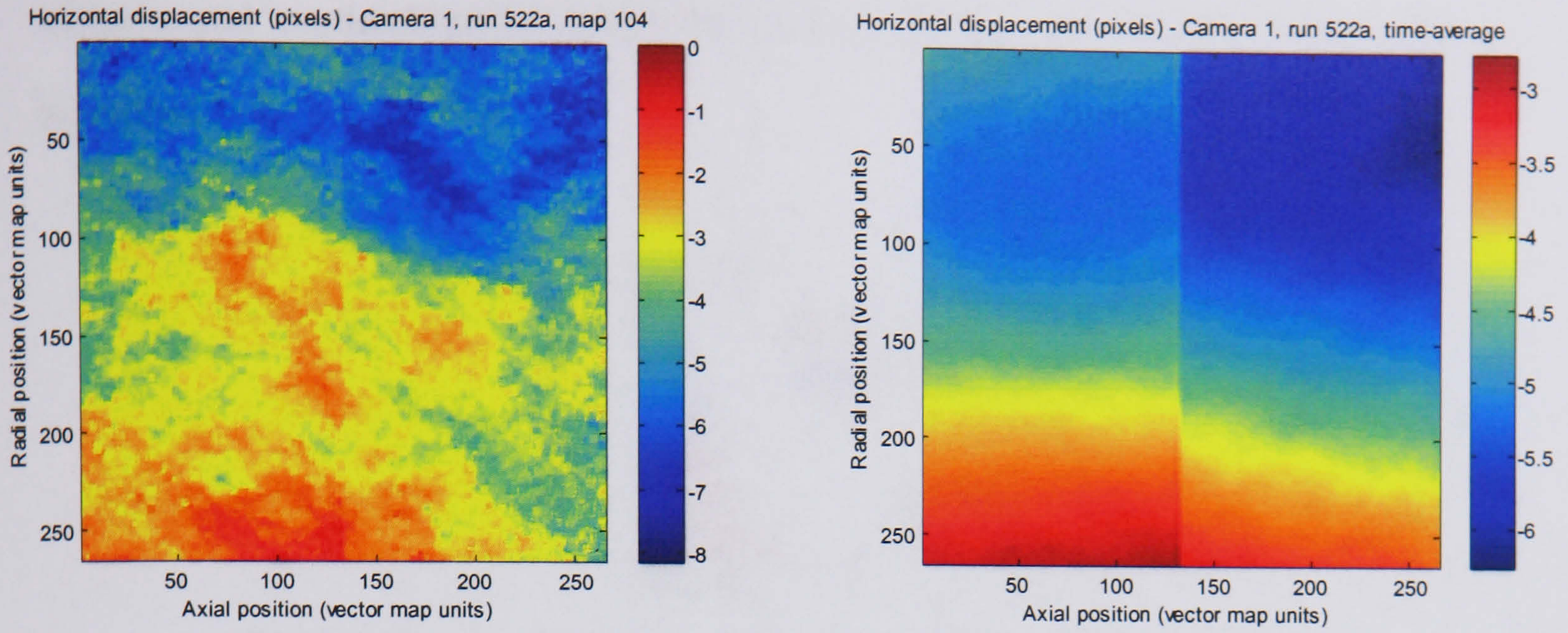

Figure 6.9 – Instantaneous and time-averaged vector maps (horizontal component).

That the underlying image fault affects only the horizontal component of the vector map should come as no surprise, due to the way in which the camera sensor is read-out (c.f. Section 2.4.3, page 72). Cross-talk between adjacent *vertical* pixels is only possible if the digital signal becomes mangled, or the sensor's charge transfer efficiency degrades severely (something Kodak presumably ensures is unlikely). Given their potential temperature dependency, it is likely that the fault instead lies with the analogue electronics associated with sensor readout, amplification and digitization, all of which receive a stream of adjacent *horizontal* pixel charge packets.

Despite being aware of the problem, and having updated the design of the electronics as a result, neither the camera manufacturer nor vendor were able to suggest specific means by which the velocity (or intensity) bias might be corrected, or provide a description of the underlying cause. It is interesting however to compare the image intensity distributions for frames A and B, as demonstrated in Figure 6.10 on page 234. With the longer exposure time, it might be expected that frame B's intensity distribution would be wider, but the opposite was found to be true. While this might be suggestive

of horizontal 'motion blurring' within the frame A image, no such effect was visible to the naked eye.

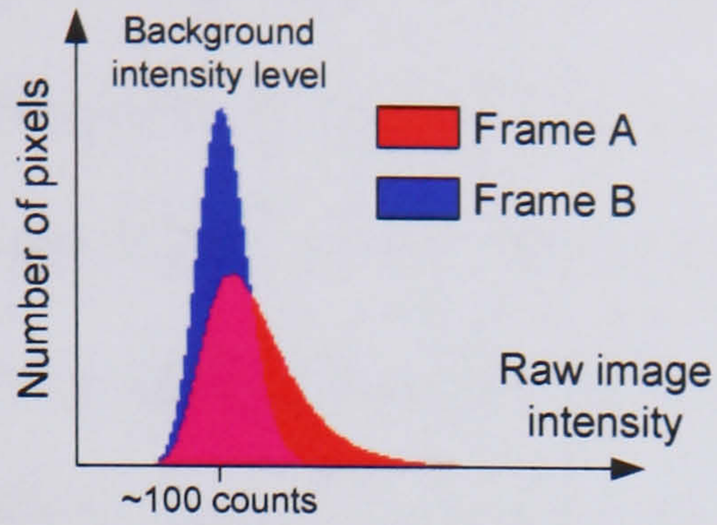

Figure 6.10 – Typical phase 3 frame A & B intensity histograms.

It may be noted that the final results indicate a slight discontinuity within the vertical velocity component, but this is believed to be due only to the slight rotation inherent to the pre-correlation image back-projection that was performed. It is also likely that some cross-over between horizontal and vertical image displacement occurs during the cross-correlation process. Finally, it is of note that identical horizontal-component velocity differences were observed, albeit to a lesser extent, in 1 of the 4 separately tapped quarters of the cameras being used by the Spanish PIV team (for whom it was also a new phenomenon).

The approximate magnitude of the horizontal-component displacement discontinuity is indicated in Table 6.6. The left/right difference (expressed in pixels) is defined as the measured particulate displacement just left of centre minus that from the right, averaged vertically, and considered for all phase 3 measurements.

	Camera 1	**Camera 2**	**Camera 5**
Range:	0.20 – 1.75	0.16 – 1.01	0.29 – 2.17
Average:	0.73	0.51	1.03
Standard deviation:	0.26	0.11	0.19

Table 6.6 – Left/right horizontal displacement difference in Phase 3 vector maps.

All three cameras therefore share a fairly significant leftwards-bias on the right-hand half of the sensor (and/or a rightwards-bias on the left half). A cursory examination of the statistics also revealed there to have been a clear increase in the average left/right difference with time: the discontinuity for data from the 14th December (the final phase 3 test) is – for all cameras – over double that for data from the 9th (the first phase 3 test). This increasing difference is consistent with an observed decline in image signal-to-noise ratio (SNR), due to a gradual reduction in laser output power, which is discussed on page 238.

It is interesting to observe that, for the discontinuity quantifier considered above, the relationship between left and right-hand sides is always of the same polarity: invariably positive. This contrasts with the relative left / right *intensity* difference listed in Table 6.5: camera 1 usually (but not always) had a darker right-hand side, but camera 2 in all cases had a darker left-hand side, for example.

Finally, it should be noted that despite the different camera orientations used during the CoJeN test, the relative effect on the perceived flow velocity is the same for all cameras used in phases 2 and 3. For the purposes of annotating Figure 6.11 below, it has been assumed that *both* sides of the vectors maps are incorrect, with biases relative to the true jet velocity (*a* and *b*) of opposite sign.

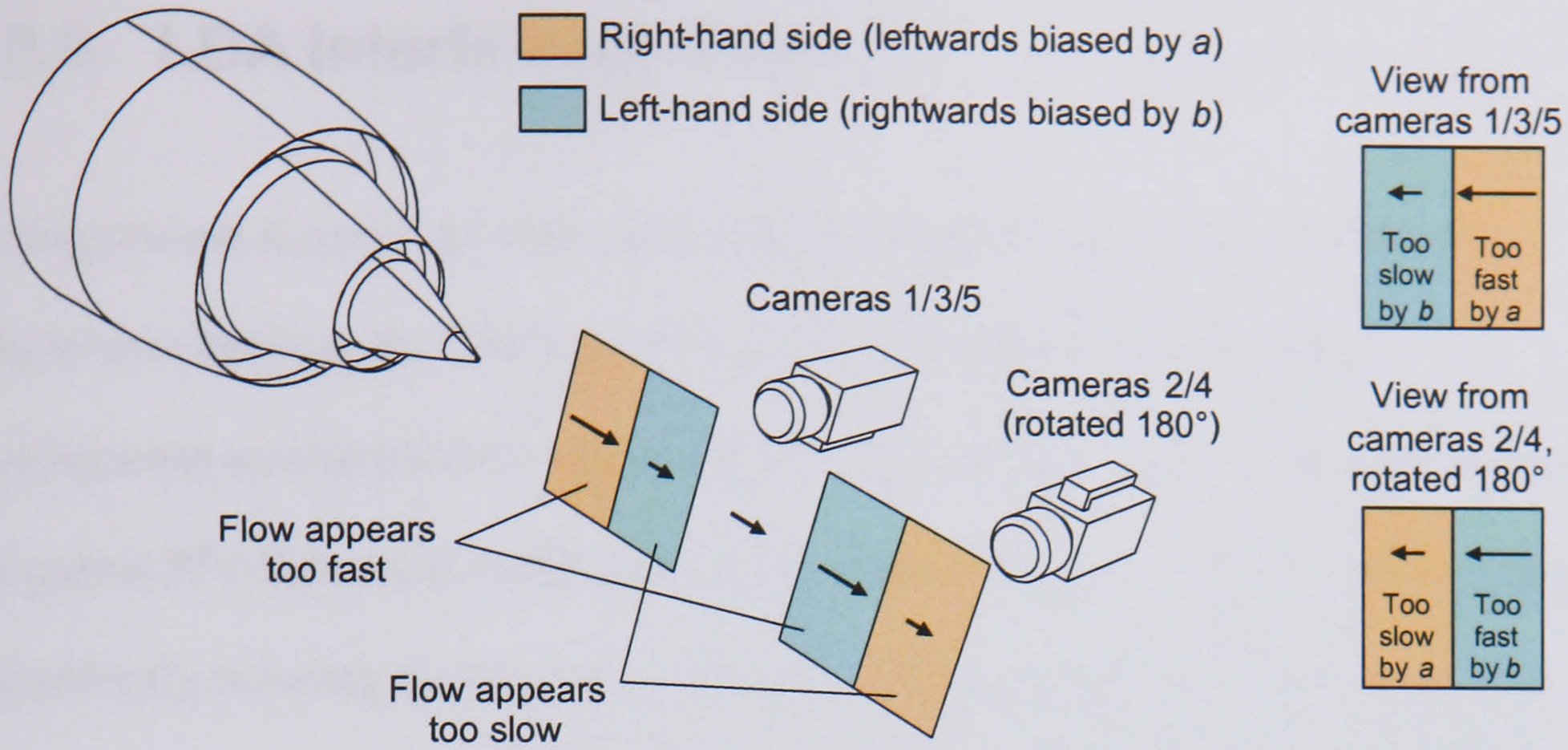

Figure 6.11 – Camera sides, as arranged during the CoJeN tests.

A more detailed analysis of the left / right velocity bias and the means by which it was corrected are given in Section 6.5.2.

6.2.3. LDA Interference Filter

During pre-test discussions with CoJeN project partners, the matter of optical interference between the PIV and LDA systems (as used during the phase 3 simultaneous measurements) was brought up. Specifically, the fear was expressed that the pulsed PIV light sheet could temporarily 'blind' the LDA photomultipliers, thereby significantly reducing the data rates. In order to counter these concerns, the author sourced an appropriately tight notch filter (Semrock 532nm StopLine; NF01-532U-25) to allow 97% of the 514.5 nm LDA light to pass, whilst blocking 99.9999% of scattered 523 nm PIV light.

During these discussions, the possibility that the PIV cameras would need filtering from the LDA beams was also raised, but the Warwick team was advised that this would not be necessary, and as such the system was designed and tested without filters (having first checked that the chamber could be completely darkened for the tests). Unfortunately, as is obvious with hindsight, the LDA beams proved highly visible in the 68 ms duration 2nd frame exposures, and 532 nm bandpass filters therefore had to be fitted to the cameras for the duration of phase 3.

The transmittance of a bandpass filter is dependent on its quality, bandwidth and the angle of incidence. The transmission efficiency of a ≤10 nm bandwidth filter (at 0° incidence) is typically between 40% and 90%, but non-perpendicular illumination will reduce the central bandpass wavelength λ, according to the following equation:

$$\lambda_\theta = \frac{\lambda_0}{N}\sqrt{N^2 - \sin^2\theta} \tag{6.2}$$

…where θ is the angle of incidence and N is the effective refractive index of the filter coating (typically between 1.45 – 2.00).

If the angle of incidence is calculated for light coming from one edge of the CoJeN cameras' field of view ($\theta = \tan^{-1}(0.1\text{m}/0.9\text{m}) = 6.3°$) and we assume $N = 1.7$, it can be calculated that the central bandpass wavelength of a 532 nm filter is reduced by more than 1 nm. The filters available for the CoJeN test had only a 3nm bandwidth* and an advertised maximum transmittance of 60%, meaning that the light transmittance at the edge of each camera's field of view approached 30%; even less in the corners. This radial effect is visible in the images below:

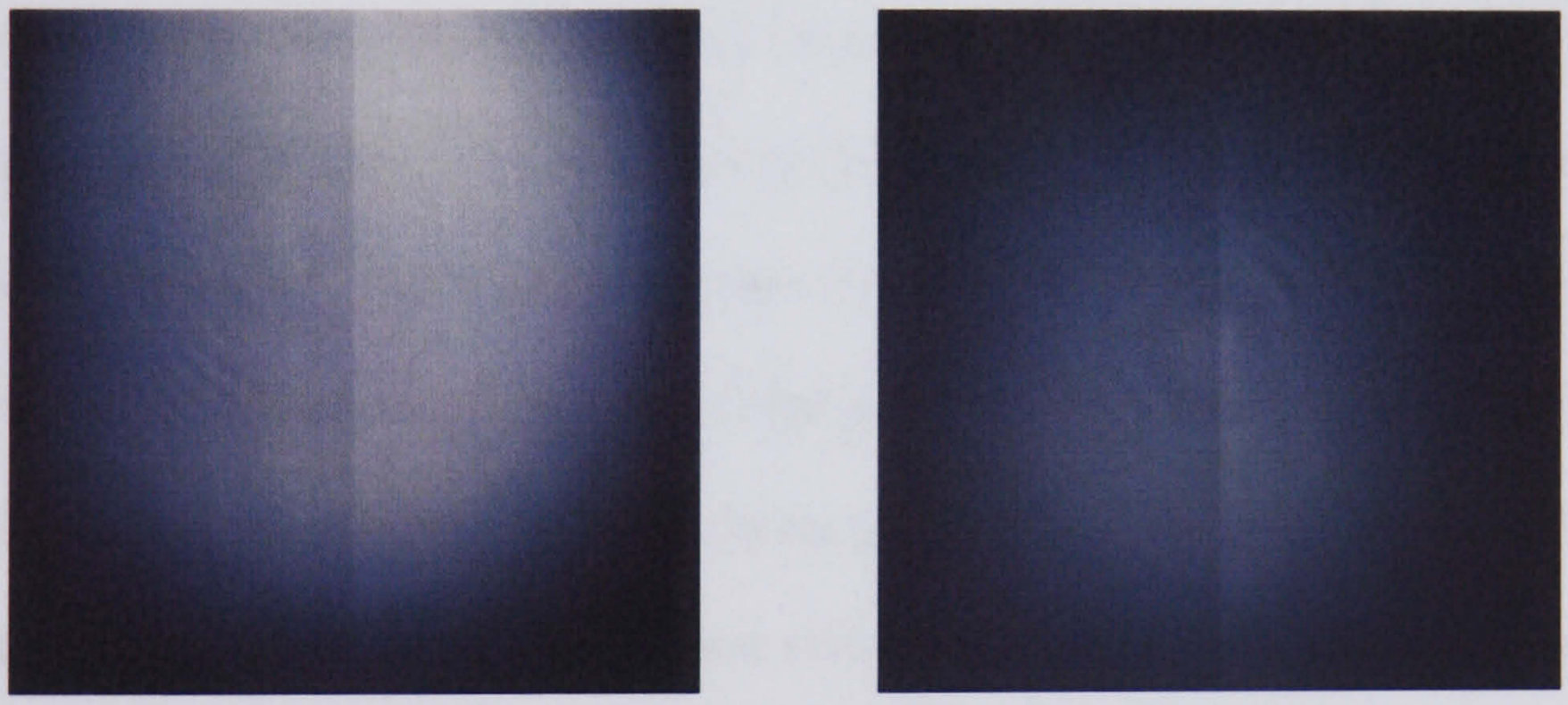

Figure 6.12 – Average of 350 phase 3 PIV images, from cameras 2 and 5.

The reduction in received light intensity of ≤ 60% was further compounded by a gradual reduction in laser output power during the course of the CoJeN test. This was initially thought to be due to laser flash-lamp wear (each having been fired many millions of times by the end of the test), but a subsequent service by the laser manufacturer revealed

* Defined as the width between a threshold of 50% of peak transmittance, i.e. for wavelengths below 530.5 nm and above 533.5 nm, less than (peak transmittance)/2 of the incident light is transmitted.

two alternative reasons. Not only had the matched laser heads and power supplies been paired incorrectly by the vendor, thereby leading to electronic wear, but the levels of refractive index matching fluid in the Pockels cells were found to be low, thereby reducing the optical efficiency of the cavity.

As a result of the filter specifically, some cameras' images' SNR was reduced to such an extent that the seeding particles could not be distinguished from the camera noise, especially in the corners of the images. This in turn led to a high proportion of spurious vectors in the correlated maps, which required special attention during the post-correlation vector filtering, as explained in Section 6.3.5.

As may have been observed in Figure 6.12 (and Figure 6.8b on page 232), a further result of applying the interference filters was the appearance of Newton's rings* around the centre of the frame. These rings are also visible in the correlated velocity maps, more noticeably in the vertical-component (as shown below), but to an equal extent in the horizontal-component, (c.f. Figure 6.9b on page 233). Figure 6.13 on page 240 shows a time-averaged vertical-component vector map with a pronounced ring pattern, and a displacement profile (marked in black) taken through the rings' radius.

* The result of constructive and destructive interference between a spherical and flat surface. The spherical surface in this case was more likely a filter cover glass than the front of the camera lens.

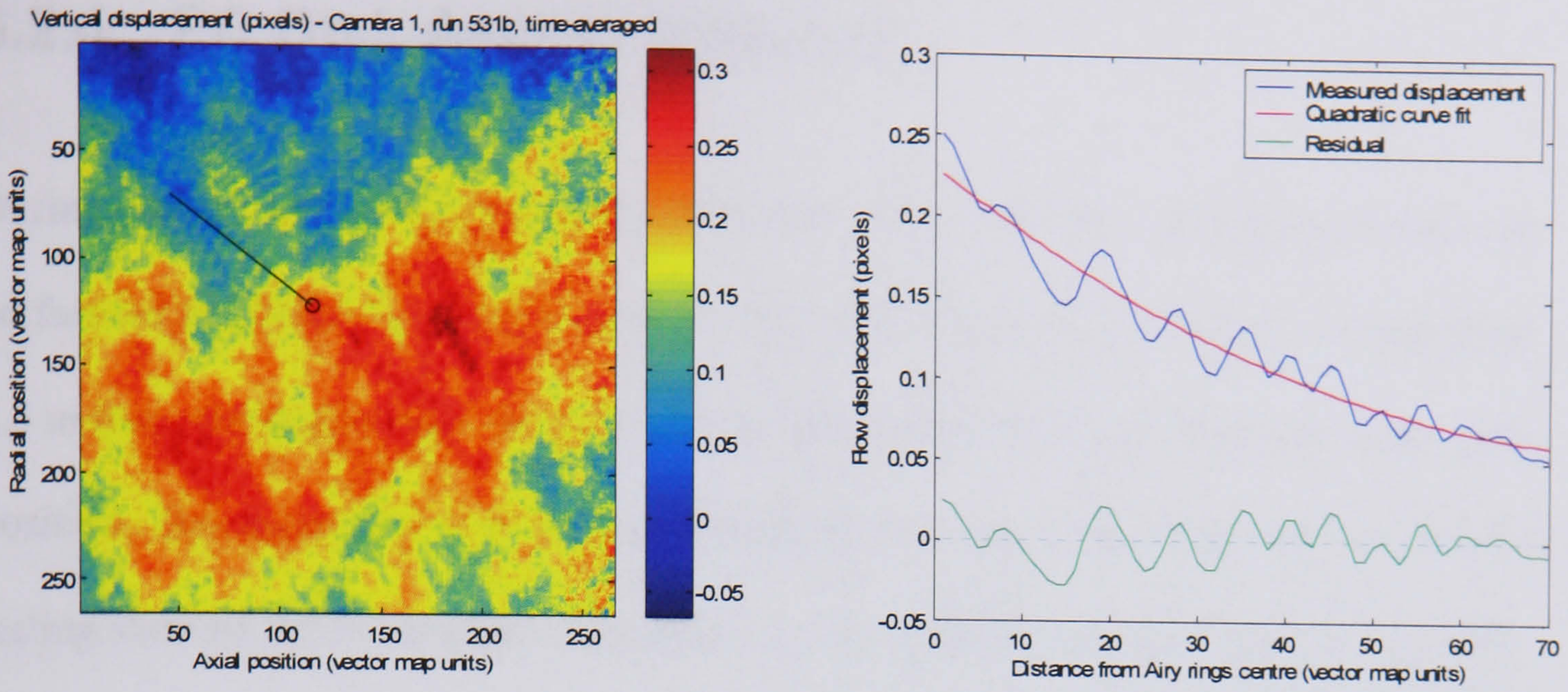

Figure 6.13 – Effect of Newton's rings on the vertical-component displacement.

For the data shown above, the average deviation between the measured and curve-fitted displacement, along the profile shown, is just under 0.01 pixels. For a horizontal displacement of 8 pixels, this equates to a relative error of less than 0.2%.

The small variation in the intensity of the rings (c.f. Figure 6.12) suggests that this phenomenon is not an artifact of the cross-correlation process itself. It is rather believed to be due to the multiple reflections between the filter surfaces causing a small 'motion blur' effect on the particle images, the strength of which may change as the particles move. To create a velocity error of 0.01 pixels, for example, the difference between the measured and real displacements as indicated on the right of Figure 6.14 below, would only have to be 74 nm.

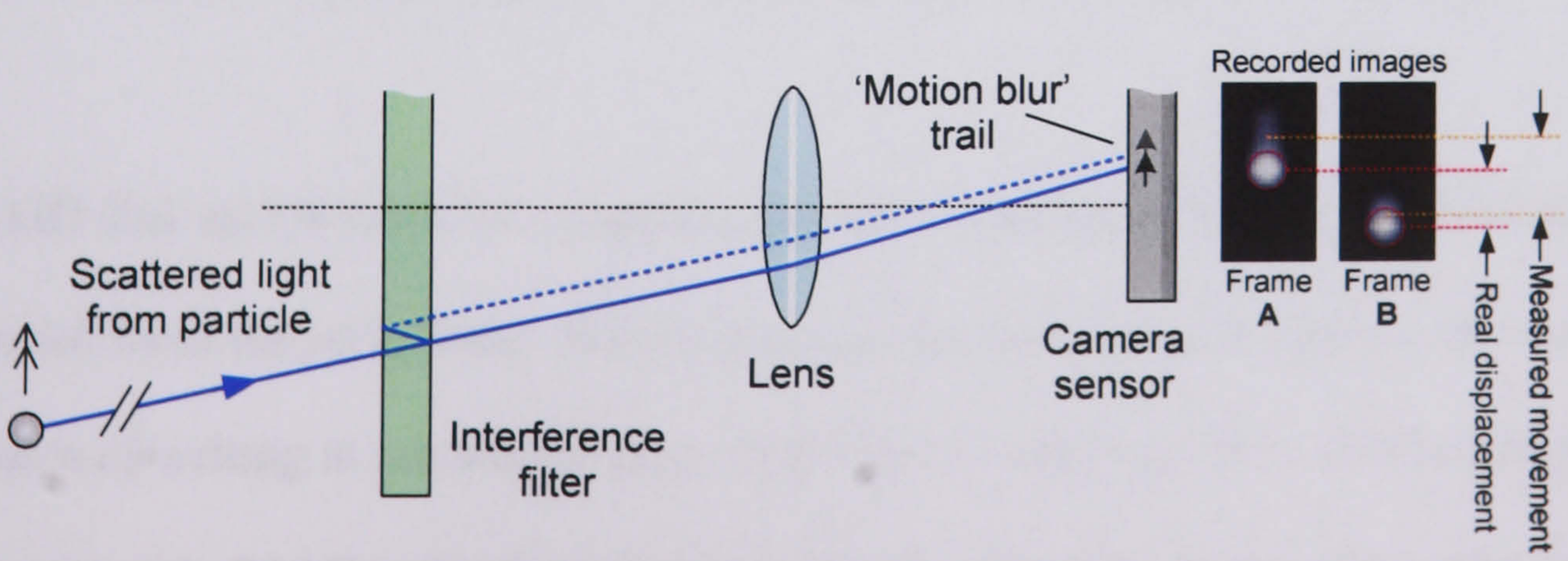

Figure 6.14 – Internal interference filter reflections.

6.2.4. PC Disk Access Failures

During phase 2 of the test, it was observed that the control PC – which had previously performed faultlessly – became unresponsive whenever the rig was moved more than 2.5 m from the nozzle exit. As such, it was impossible to acquire any data at the 15D position. This behaviour was initially thought to be coincidental, but subsequent days' testing showed the PC to crash repeatedly, with a Windows stop screen (colloquially known as the 'blue screen of death') being generated at the same axial position every time.

Analysis of the Windows log files revealed the failures to be due to an inability to read and write to the hard disk drive. It was concluded that this was most likely a result of vibrations being transmitted from the jet exhaust, which – by 2.5 m – had expanded sufficiently to impinge on the wall of the rig. The control PC was therefore 'vibration isolated' prior to phase 3 testing, using layers of bubble wrap packaging.

The 5 camera interface PCs were similarly protected, but space constraints limited the amount of padding that could be applied. Consequently, PC4 crashed during phase 4 testing: a result of the same inability to access the C:\ drive whilst at the far end of the jet. It is for this reason that runs 708 – 710 have only 4 consecutive exposures.

The RAID disk arrays used for image storage were similarly affected by vibration transmitted from the jet exhaust. While testing in the laboratory had shown the arrays to be capable of writing at around 80 Mbps (c.f. Figure 5.44, page 203), this had dropped to approximately 25 Mbps by the end of the test. For this reason, the phase 4 repetition

rate of 275 ms, shown in Figure 6.4, had to be slowly increased, to a maximum value of 290 ms (i.e. a 10.3 Hz measurement rate).

Buffers in the cameras and RAID controller cards, and CamWare's silent tolerance of slow disks, meant that a disparity between the laser firing rate and disk write speed could only be identified by reviewing the number of BMP files saved. As such, some datasets contain slightly fewer images than intended. While this is of negligible importance to the time-averaged statistics, the simultaneous phase 3 PIV and LDA, and phase 4 time-series measurements were directly affected. Section 6.3.1 (page 243) explains the method by which skipped images were identified and corrected for.

6.3. Generic Processing Workflow

All data collected during the CoJeN test was subject to a common set of processing operations, as depicted below. Section 6.3 details each of these steps.

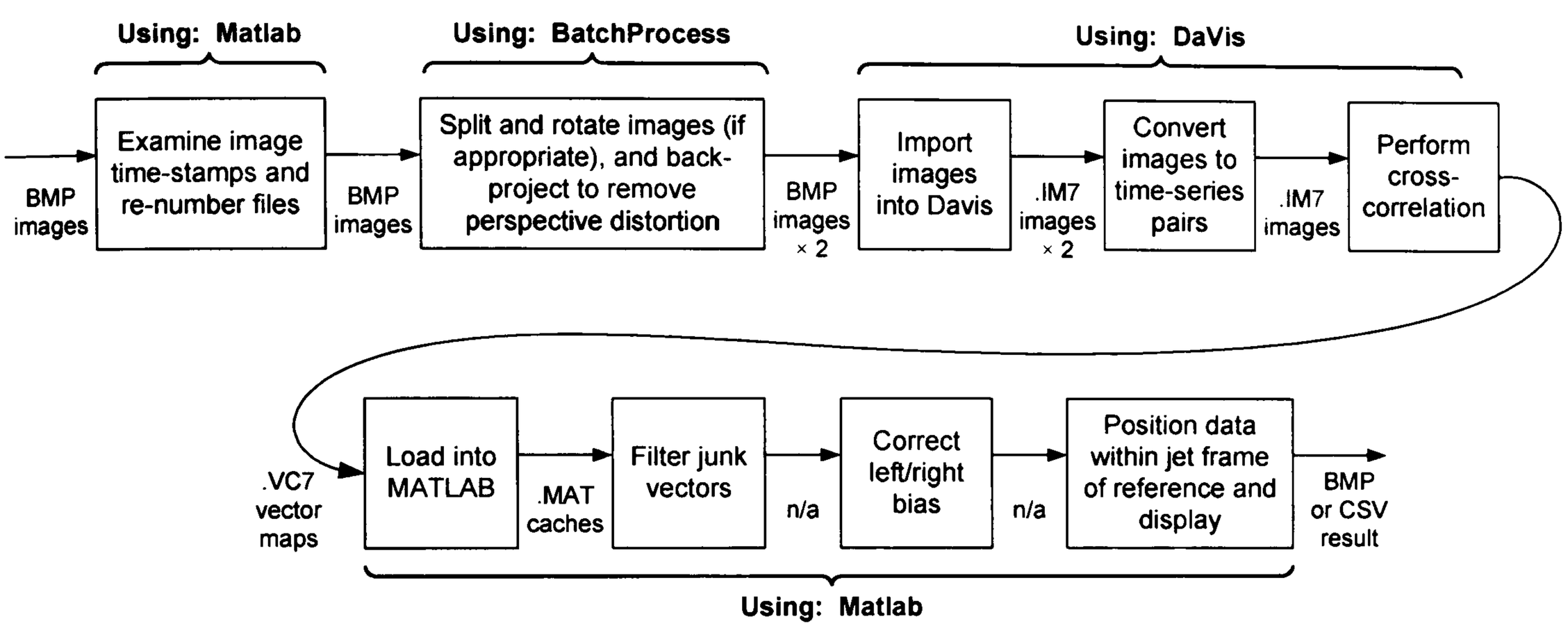

Figure 6.15 – Generic processing workflow for CoJeN data.

6.3.1. File Renumbering

The loss of some images (due to the reduction in RAID write speed) was compounded by the sequential manner in which CamWare numbers saved image files. If 1 in 2 of n triggered camera images are saved to disk, the resulting $n/2$ files will be numbered 1 to $n/2$, rather than being assigned their originating trigger count (between 1 and n).

Fortunately, CamWare offers the ability to add a time stamp to the top-left corner of the saved images, in the form of either binary encoded pixels (which requires 16-bit file saving), or black and white text, as shown in Figure 6.16. Time-stamping was enabled for all images acquired during the CoJeN test.

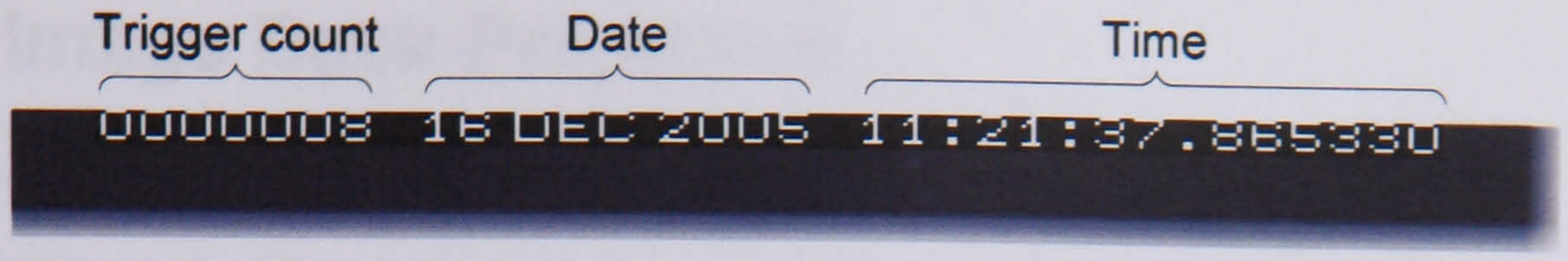

Figure 6.16 – An embedded timestamp in an image's top left corner.

A Matlab script (given in Appendix 9.4.9, page 433) was written to perform automatic character recognition on every image's timestamp. In addition to writing the 3 parameters shown above to a CSV spreadsheet, the file's name, number therein, and 'time written' attribute were also saved. A further Matlab script was written to confirm that the trigger count shown in the timestamp is indeed consistent with the triggering time.

The CSV tables could thus be used to find coincident Phase 4 image quintuplets, as well as synchronising the phase 3 PIV and LDA measurements. They also revealed the potentially non-sequential nature of CamWare image recording, even when the disk write-speed was sufficient. Table 6.7 illustrates a severe (and fortunately rare) example of file repetition and skipping. It can be seen that the 2172nd image has been lost, despite ample disk bandwidth. Repeated images, such as img_2171.bmp were deleted in order to avoid skewing of the time-averaged statistics.

File	Timestamp (s)	File #	Correct frame #
img_2169.bmp	35640.914945	2169	2169
img_2170.bmp	35641.456950	2170	2171
img_2171.bmp	35641.456950	2171	2171
img_2172.bmp	35641.185948	2172	2170
img_2173.bmp	35641.998842	2173	2173
img_2174.bmp	35642.269730	2174	2174

Table 6.7 – An example of non-sequential image saving.

6.3.2. Image Back-Projection

One of the two most important image processing operations was back-projection, in which the images were transformed onto a real-world coordinate system. While back-projection is a prerequisite of the acquisition technique used during phase 4, images from phases 2 and 3 were also transformed, for the following reasons:

- To remove perspective distortion by means of warping rather than mapping (c.f. Section 2.1.2.2, page 29).
- To ensure that all cameras' images shared a common coordinate system, with any relative displacement between FOVs known.

The back-projection was performed using the BatchProcess software described in Chapter 3,. This software was also used to split CamWare's 2048 × 4096 pixel double-exposure images into frames A and B, as well as rotating the images from cameras 2 and 4 by 180°.

Given the large number of images involved, several features of the BatchProcess software were designed to assist; notably the ability to read and write to network folders, and load pre-existing lists of data sources and destinations. In this way, the back-projection processing effort could be quickly expanded to take advantage of a number of networked computers.

The images were all back-projected using a resolution of 10 pixels per millimetre and, for each test phase, the same set of 3D calibration data. Although calibration plate images were captured from each camera every morning and evening of the CoJeN test,

it was found that (as intended) the relative camera orientations never changed mid-phase. This could be checked by ensuring that calibration plate images from any day, when back-projected, always overlapped. The back-projection parameters, including the calibration plate image's acquisition date and time, are given below:

Phase	3D calibration plate image	Back-projected image size	Relative FOV offsets* (mm)	Nudged?
2	11:06 05/12/05	2021×2048 px 202.0×204.7 mm	Cam 1: (0, 0) Cam 2: (0, 8) Cam 5: (0, 0)	✗
3	08:54 09/12/05	2201×2201 px 220.0×220.0 mm	Cam 1: (0, 0) Cam 2: (0, -7) Cam 5: (-1, -5)	✗
4	06:56 16/12/05	2151×2151 px 215.0×215.0 mm	All images were re-projected onto the same area.	✓

Table 6.8 – CoJeN image back-projection.

It can be seen that the image sizes differ for each phase, and that each phases 2 and 3 camera's back-projected images occupy slightly different real-world positions. The decision to maintain the slight differences in the cameras' FOV positions was made for the following reasons:

- The area of overlap between adjacent measurement positions is increased.
- The whole of the captured image is used, without the edge being 'thrown away'.

The phase 3 back-projected images are larger for a similar reason: whereas every pixel of the phase 2 back-projected images contain data from the original image, the 2201 ×

* The sign of the offset is such that in phase 3, camera 5's view was *above* and to the *left* of camera 1's.

2201 pixel phase 3 images contain small 'gaps', for which no raw image data exists (c.f. Figure 6.17). As a consequence of allowing gaps, less data was wasted from the edges of other camera's images.

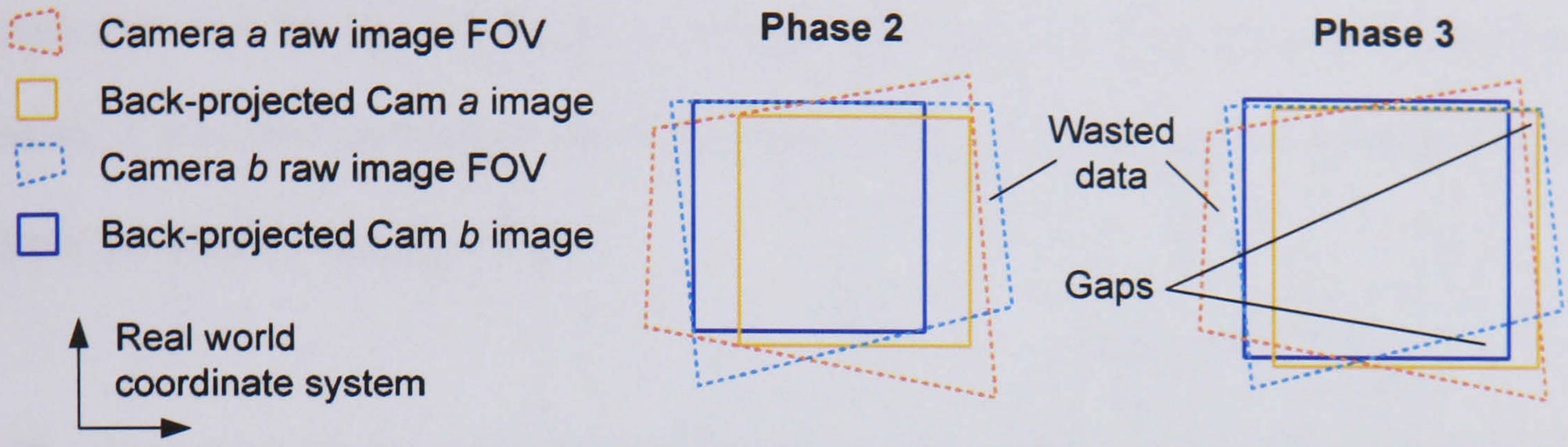

Figure 6.17 – CoJeN image back-projection.

Simultaneously exposed seeding images were captured every day of the CoJeN test, but they were only correlated and used for high-resolution back-projection correction (a.k.a. 'nudging'; c.f. Section 3.1.4) of the phase 4 images, due to the large associated increase in processing time. Even without 'nudging', the back-projection stage of the CoJeN processing took almost as long as the correlation: around 1 month, using an average of 7 × 3.0 GHz PCs.

6.3.3. Spatial Calibration

To aid comparison, every CoJeN project partners' test measurements were to share a common frame of reference, with the origin defined as the intersection of the secondary nozzle exit with the jet centre line. In addition to aligning all PIV data to this coordinate system, it was also necessary to establish the position of the LDA measurement volume within the phase 3 cameras' FOV.

Both calibrations were achieved by recording images of the feature of interest, namely the nozzle and the LDA measurement volume (visualised by means of a 1 second long exposure). A Matlab–based line intersection measurement application was written to aid accurate measurement of the images' datum points, as shown in Figure 6.18 below.

In the case of the LDA, the image of the beams was traced to give the position of the measurement volume in the image plane (i_{LDA}, j_{LDA}) directly. The short cowl nozzle was instead measured by tracing the edges of the bullet to an 'imaginary' datum point (i_0, j_0), located 244.29 mm from the secondary nozzle exit. The coplanar nozzle, being outside the cameras' field of view, was initially calibrated using a ruler attached to the nozzle. Having however confirmed that the cameras did not move relative to each other during test phase 3, the short cowl nozzle's calibration data was used instead.

Figure 6.18 a) Long-exposure image of LDA beams; b) Image of nozzle tip.

With knowledge of the axial traverse position a_0 and vertical camera position v_0 used during acquisition of each nozzle calibration image, the real-world position (x, y) of any pixel (i, j) in an image captured at (a, v) could be found using equation (6.3):

$$\begin{bmatrix} x \\ y \end{bmatrix} = \begin{bmatrix} 244.29 + (a - a_0) - 0.1(i - i_0) \\ (v - v_0) - 0.1(j - j_0) \end{bmatrix} \tag{6.3}$$

The calibration images were all back-projected in the same way as the main PIV images, meaning that the vector (m, n) associated with a particular image point (i, j) could be found using equation (6.4). This relationship is dependent on both the interrogation window size A_I, and the vector overlap ov %. Both the top-left pixel and vector indices start (0, 0).

$$\begin{bmatrix} m \\ n \end{bmatrix} = \left(\begin{bmatrix} i \\ j \end{bmatrix} - \frac{sp}{2} \right) \Big/ sp \qquad \text{where:} \qquad sp = A_I \left(1 - \frac{ov}{100} \right) \tag{6.4}$$

The calibration images were all taken using camera 3, and the pertinent datum point positions given in Table 6.9. The images were back-projected onto the same space as camera 1, meaning the offsets given in Table 6.8 remain valid.

Measurement set	i_0	j_0	a_0	v_0	i_{LDA}	j_{LDA}
Phase 2; Runs 101-141	720	935	2.4	5.2	n/a	n/a
Phase 3; Runs 500-529	1914	353	120.5	175.0	1270	645
Phase 3; Runs 530-570	1872	387	142.4	175.0	1837	566
Phase 4; Runs 700-714	As above				n/a	n/a

Table 6.9 – Calibration points from camera 1's perspective.

Because the Warwick PIV rig was mounted on the downstream bogey during test phase 4, it was not possible to take any calibration images of the nozzle during this time. The last calibration images from phase 3 were therefore used instead.

6.3.4. Cross-Correlation

There are a multitude of software packages, code libraries and Matlab scripts available (both free and commercially) for the cross-correlation of PIV images. After comparison of its competitors however, LaVision's DaVis 7 package was selected for the processing of the CoJeN PIV data. The software not only offers image deformation correlation as standard, with access to a large number of related parameters, but it also provides a whole raft of associated vector and image processing operations.

One disadvantage to using DaVis to process images acquired using CamWare is the requisite conversion of the files from BMP format to LaVision's proprietary IM7 format. This conversion comprises two stages:

- Importation of the individual BMPs, which are in turn saved as IM7 files.
- Transformation* of the $2n$ 'single frame' IM7 files into n 'double frame' files. Without this operation, Davis will interpret the files as a very long time-series of individual images.

Unfortunately, these two stages must be performed separately†, meaning that approximately 16 Gb of IM7 files (half of which can be subsequently deleted) are created for every 8 Gb of BMPs.

---

* Within DaVis batch processing: "Copy and reorganize" group → "Create multi-frame buffer from time series" operation → "Mode: create (n/2) images: 1+2, 3+4, 5+6..." parameter.

† The buffer operation can be selected as a batch command within the *Import* dialog, but when importing several directories, *all* BMPs are first stored as single IM7s in a temporary directory, before being saved as

Every runs' images (for a given nozzle / operating condition combination) were imported into a single DaVis project. In this way, the 'hyperloop' function could be used to select and successively correlate all of the data associated with a particular day's measurements in one go.

To reduce the time taken for the images to be cross-correlated, DaVis' distributed processing functionality was engaged, though not without some difficulty. By spreading the computational load over an arbitrary number of networked PCs (on average, around 7 units of c. 3.0 GHz), the time taken was reduced to a little over a month. Table 6.10 lists the cross-correlation settings used for each test phases' images:

	Phase 2	**Phase 3**	**Phase 4**
Correlation function:	Multi-pass correlations, with reducing window size. Standard FFT based I1*I2 correlation. Zero initial offset.		
Iterations:	128px (50%) × 1 → 32px (0%) × 1	128px (0%) × 1 → 32px (75%) × 1	128px (50%) × 1 → 32px (50%) × 2
Resultant vector grid:	63 × 64 vectors spaced 32 px apart	275 × 275 vectors spaced 8 px apart	134 × 134 vectors spaced 16 px apart

Table 6.10 – CoJeN cross-correlation processing parameters.

The notation "*a*px (*b*%) × *c*" is used to denote the number of passes *c* performed using an interrogation window of size *a* × *a* pixels, where the windows overlap by *b*%. In DaVis, as with most PIV software, the window size reduces by a factor of 2 at a time.

---

double IM7s in the final destination. Unfortunately, *Streaming Mode* (which ensures that the operations execute on a directory by directory basis) was not properly implemented in the available software release.

6.3.5. Vector Filtering

Due to the use of 3 (or 4) correlation passes, with a very large initial interrogation window size (c.f. Table 6.10), the quality of the phase 2 and 4 vector maps was extremely good. The interference filters fitted to the cameras during phase 3, and the associated reduction in image SNR however did impact the quality of the phase 3 vectors maps; an issue that is discussed further in Section 6.5.1.

All of the CoJeN vector maps were spatially filtered within DaVis, using the following post-processing operations:

Operation		**Parameters**		
		Phase 2	**Phase 3**	**Phase 4**
Median filter ('Strongly remove & iteratively replace')	Remove if > rms ×	1.5	1	2
	Insert if < rms ×	2.5	1.5	3
Remove groups of less than … vectors		5	20	15
Fill up [with interpolated vectors]		Once	Once	All

Table 6.11 – CoJeN vector filtering parameters.

The median filter used the multi-pass algorithm from (Nogueira, et al., 1997), which was described in Section 2.5.5.2 (page 101). The median filter's parameters (as with those for all of the operations) were established primarily on a trial and error basis. It may be noted however that the amount of variation allowed within each vector's neighbourhood is related to both the spacing between adjacent vectors (c.f. Table 6.10), and the amount of turbulence in the measurement region. Although the phase 4 vector maps were twice as dense as phase 2's, for example, the samples were taken much further down the jet.

Because it is possible for neighbourhood median filters to interpret large areas of self-similar vectors as valid, the CoJeN maps were further processed to remove small isolated groups of vectors that might therefore arise. Finally, an interpolation operation was included to insert vectors into any empty spaces. For phases 2 and 3, vectors were only interpolated from immediate neighbours, whereas the phase 4 maps (which contained few empty spaces to start with) were iteratively filled to completion in order to aid their subsequent analysis.

Figure 6.19 demonstrates the effect of the 3 post-processing operations on a phase 2 vector map, acquired from a poorly seeding point near the edge of the jet. While a large number of vectors have simply been removed, vectors have also been generated by interpolation (e.g. the vector in black), or been changed (e.g. the vector in red) either by virtue of removal and subsequent interpolation, or because a non-tallest correlation map peak was selected during the median neighbourhood operation.

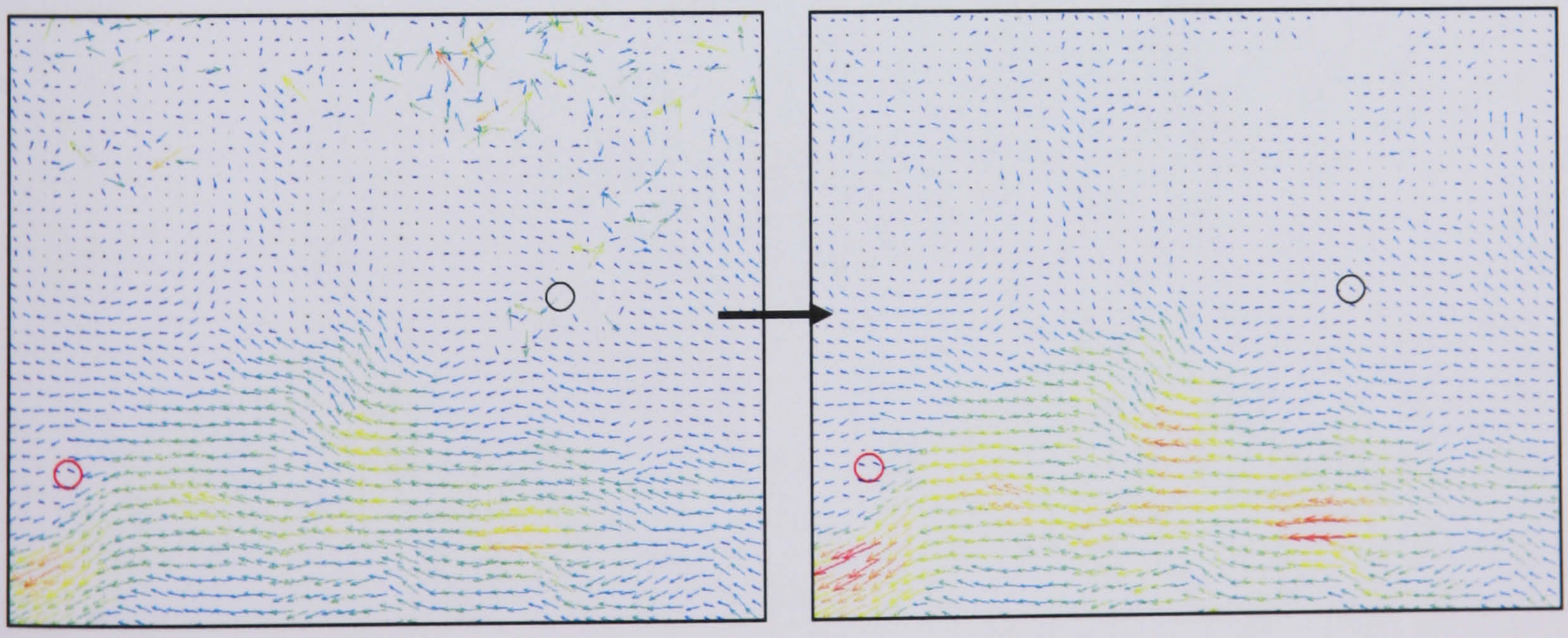

Figure 6.19 – Spatial filtering applied to a phase 2 vector map.

Table 6.12 demonstrates the overall effect of the filtering operations on the total number of vectors within each phase 2 vector map*. It can be seen that the removal of spurious vectors far outweighs their replacement with interpolated data:

	Camera 1	**Camera 2**	**Camera 5**	**Average**
Before:	95.77 %	96.93 %	92.00 %	94.90 %
After:	91.93 %	94.46 %	90.91 %	92.43 %
Difference:	-3.84 %	-2.47 %	-1.09 %	-2.47 %

Table 6.12 – Phase 2 vector coverage, before and after filtering.

* The statistics shown exclude a single scan that suffered from extremely low seeding.

6.4. Phase 2 Processing & Results

All of the CoJeN data processing and analysis was performed using Matlab, and for this reason the spatially-filtered vectors from DaVis were first converted from .VC7 file format into .MAT arrays, using LaVision's MatlabIMX DLL. This approach was significantly faster than using DaVis' export function, and the resultant .MAT files could be used to decrease the time taken to load and process data*. The phase 2 file conversion script is given in Appendix 9.4.10 (page 436), alongside all of the other code described in this section. When executed, the phase 2 scripts provide a graphical user interface (c.f. Figure 6.20) through which the data may be both reconstructed and displayed.

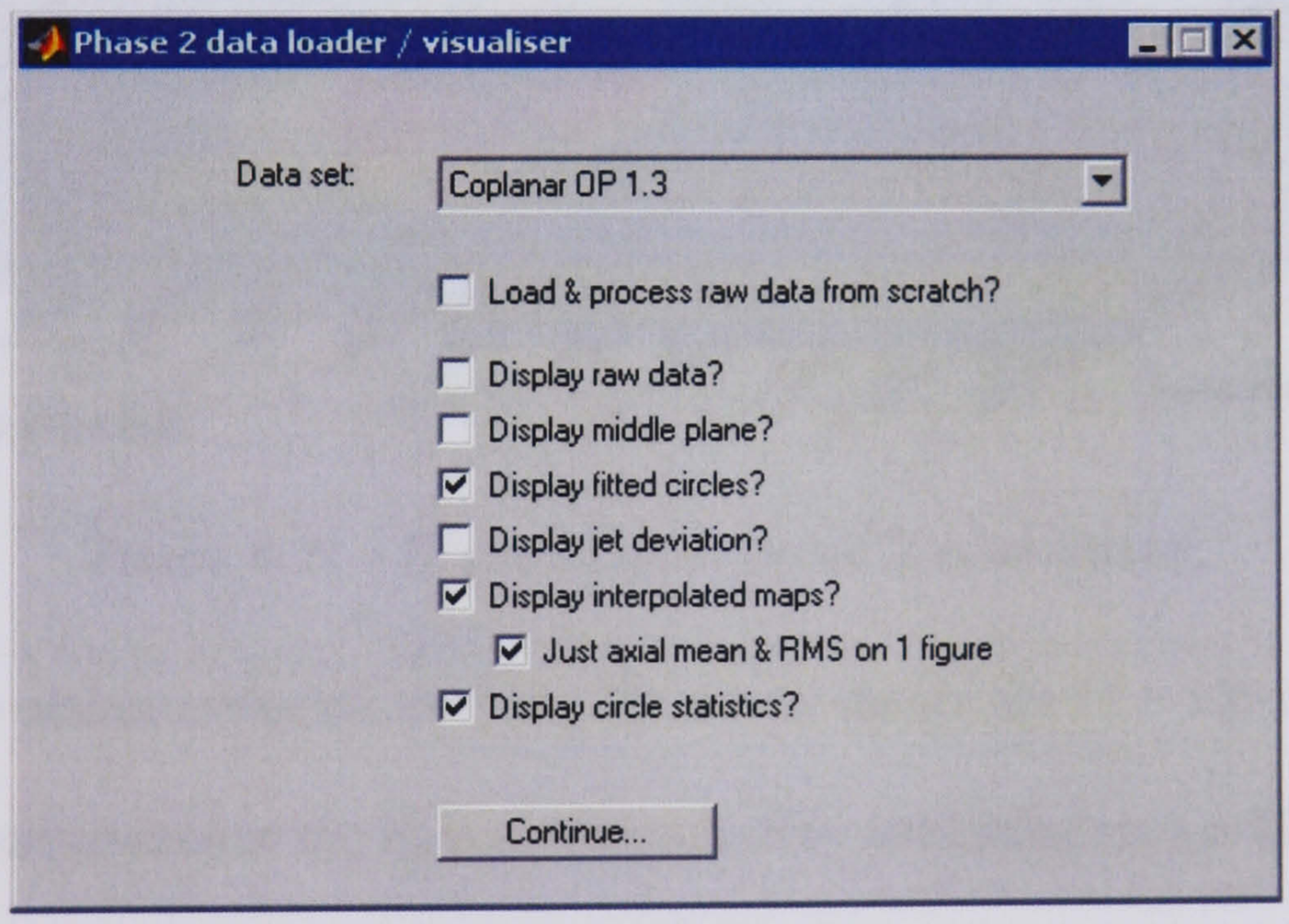

Figure 6.20 – Phase 2 processing script interface.

* Not only because the .MAT arrays were smaller than the contributory .VC7 files (which contain data for up to 4 correlation peaks), but also because disk access times were reduced by virtue of reading just a single file, instead of several hundred at a time.

6.4.1. Cross-Plane Reconstruction

Having been loaded and suitably sorted, the phase 2 displacement vector maps were converted into velocities (using the appropriate Δt value), and the mean, RMS and vorticity values calculated for each of the 11 slices. These time-averaged statistics were then vertically positioned according to both their camera's back-projection offset (listed in Table 6.8 on page 246), and whether they constituted a 'high', 'low' or 'central' scan.

Figure 6.21 illustrates the resultant (mean axial velocity) data matrix:

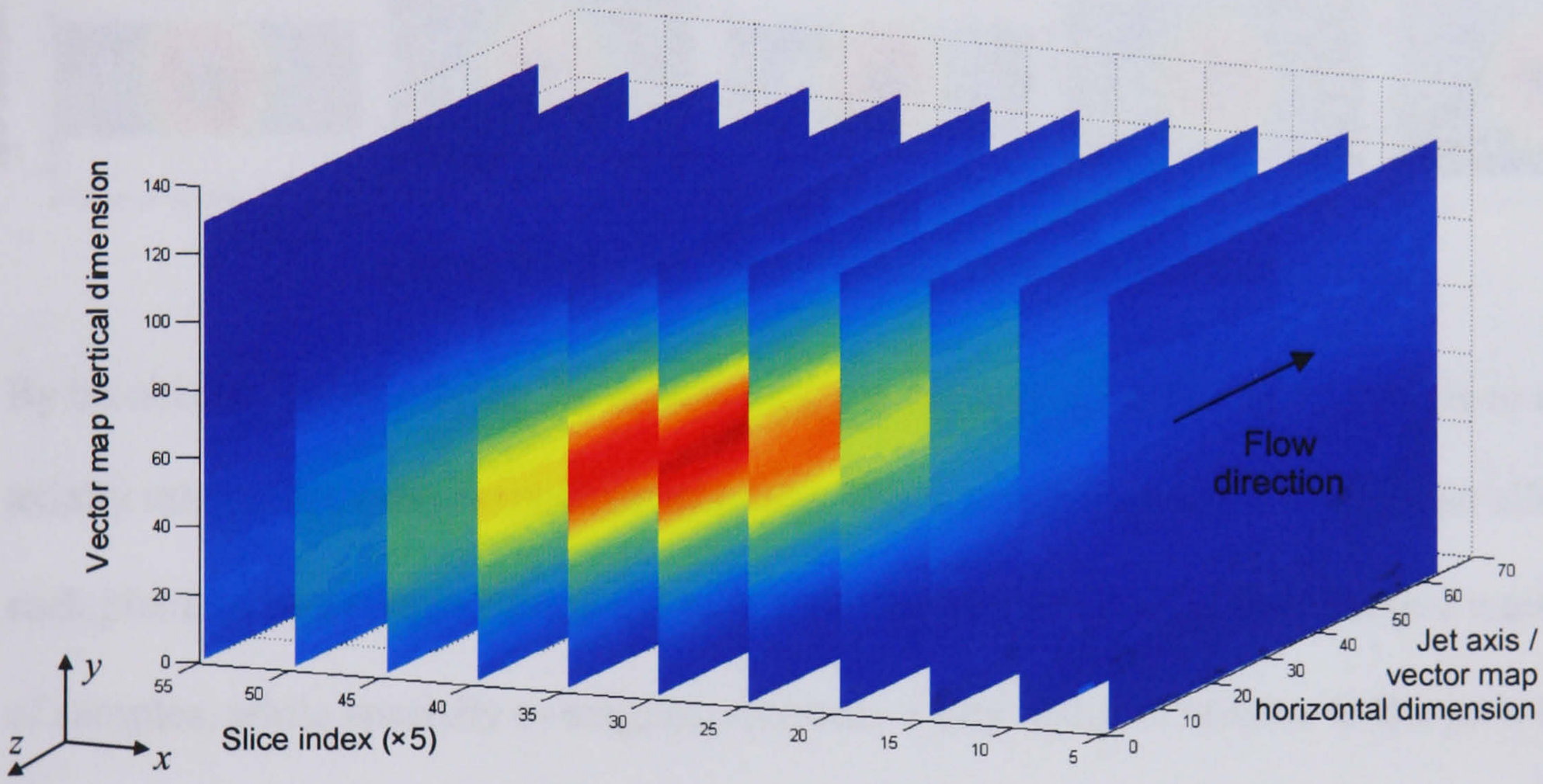

Figure 6.21 – Representative phase 2 axial dataset.

Cross-axial x-y planes extracted from the 3D matrix shown are 11 × 129 in size. The slices were reconstructed at the light sheet angle θ by stretching such a 2D cross-axial matrix until it was ($38 / 3.2\cos\theta$) units wide*, then offsetting each row of the matrix by $j\tan\theta$ units, where j is the row index.

* Although the numbers 38 and 3.2 refer to the scan length and vector spacing in mm, the units of the array itself are not mm. The figures are instead scaled using mm-scale axes.

Reconstructed planes of mean axial velocity, for all of the phase 2 data acquired, are shown in Figure 6.22. As suggested by the data's appearance, the lower half of the 5D sample taken on 06/12/05 was acquired at a time when the seeding generators were being adjusted. All figures presented depict the view downstream.

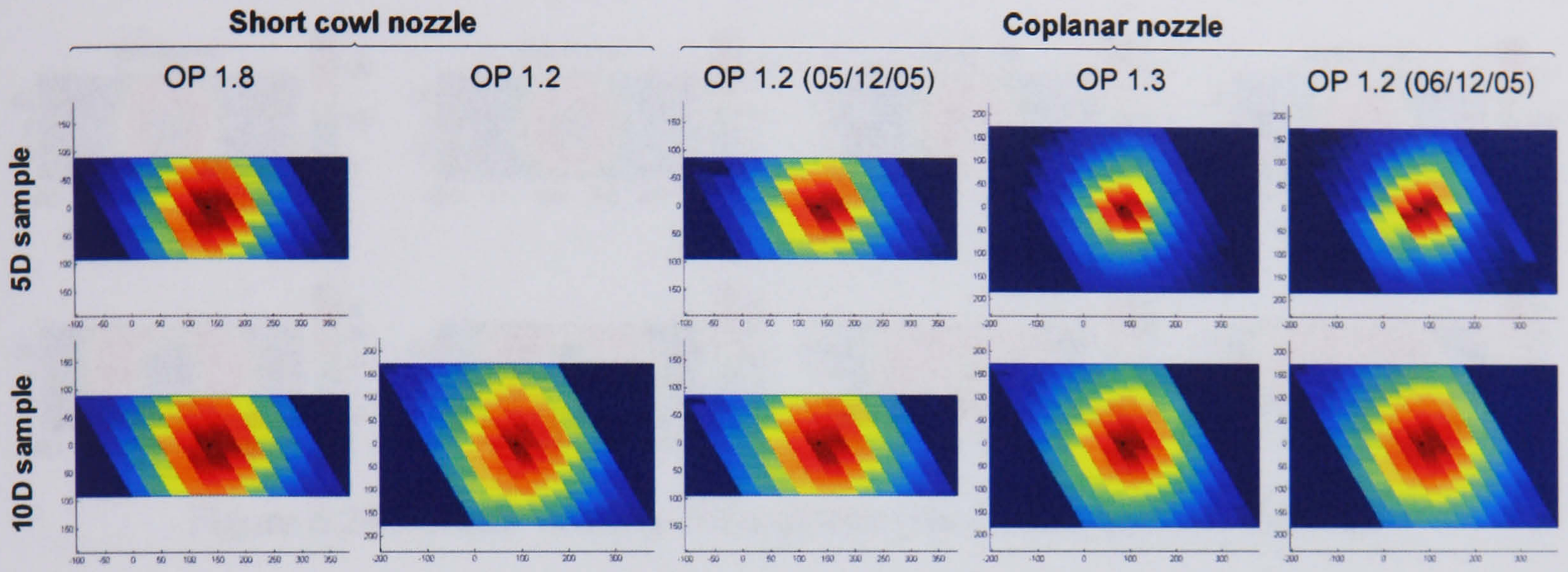

Figure 6.22 – All phase 2 data; non-interpolated.

By bicubically interpolating the data during the 'stretching' stage, it is possible to cross-axially interpolate each reconstructed plane. The script in Appendix 9.4.10 also allows each plane to be averaged along the jet's axis, thereby increasing the effective number of samples, while spatially averaging over only a tiny distance relative to the jet's time-averaged structure lengths. All data presented in this section is therefore averaged over 16 mm of the exhaust; Figure 6.23 exemplifies each of the calculated statistics, thus interpolated:

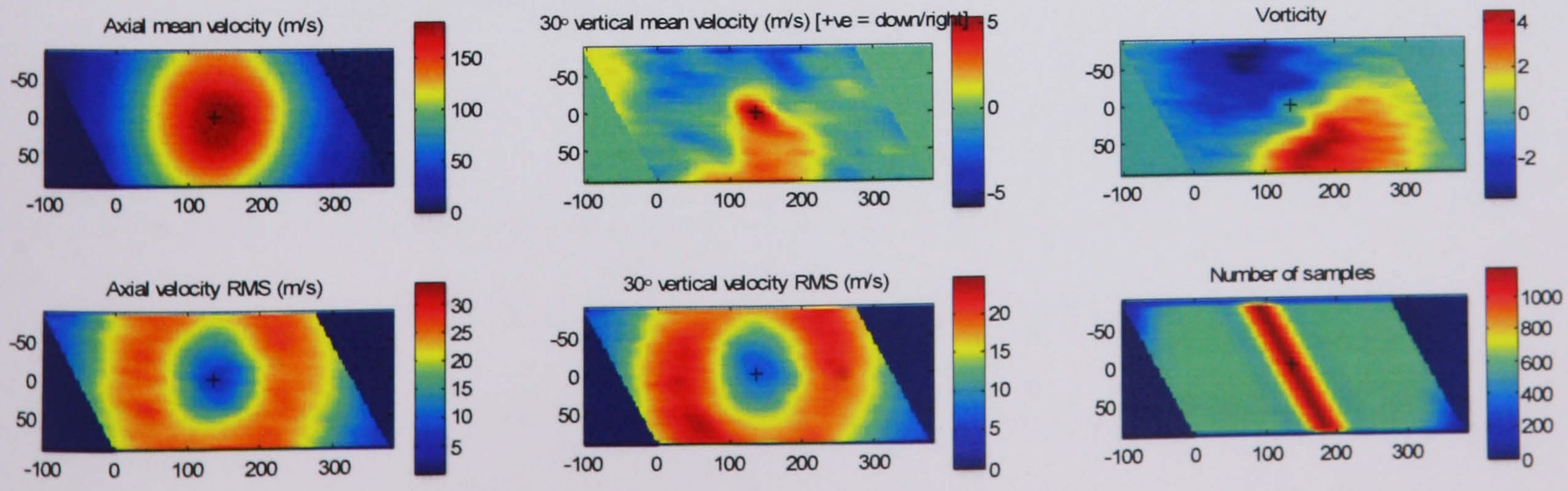

Figure 6.23 – Cross-axial statistics (short cowl nozzle / OP 1.8, at 897 mm).

By extracting cross-axial planes from the upstream and downstream edges of the 3D matrices, it is possible to examine cross-axial planes from 4.5D, 5.5D, 9.5D and 10.5D. The jet-wise progression of the mean and RMS axial velocities for both a short cowl and coplanar nozzle dataset are shown below:

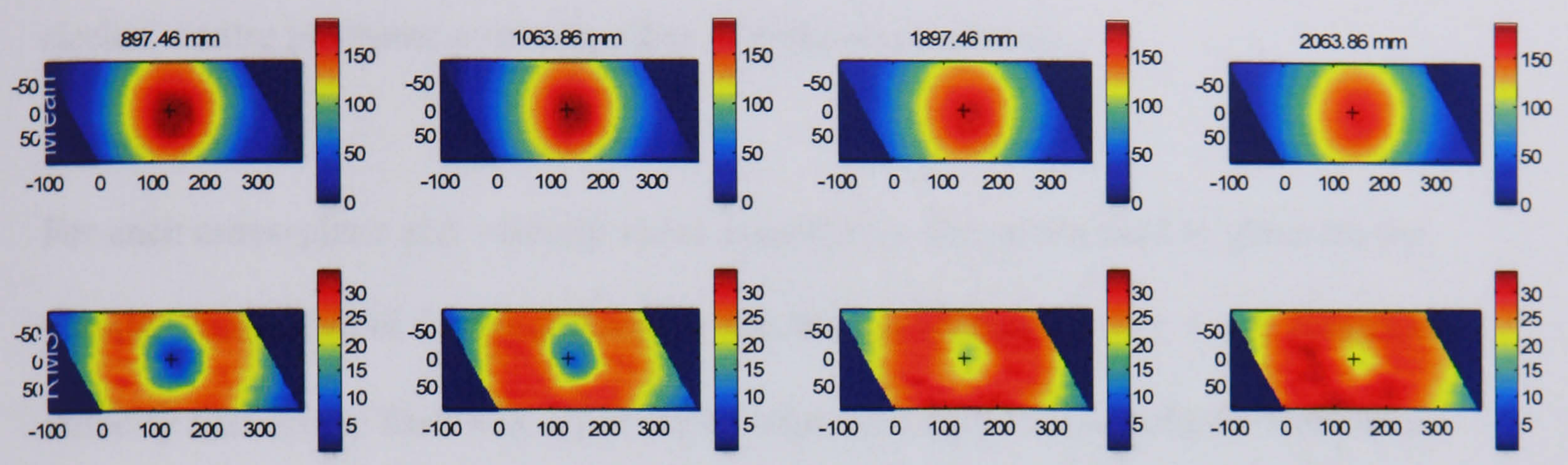

Figure 6.24 – Axial velocity cross-planes (short cowl nozzle / OP 1.8).

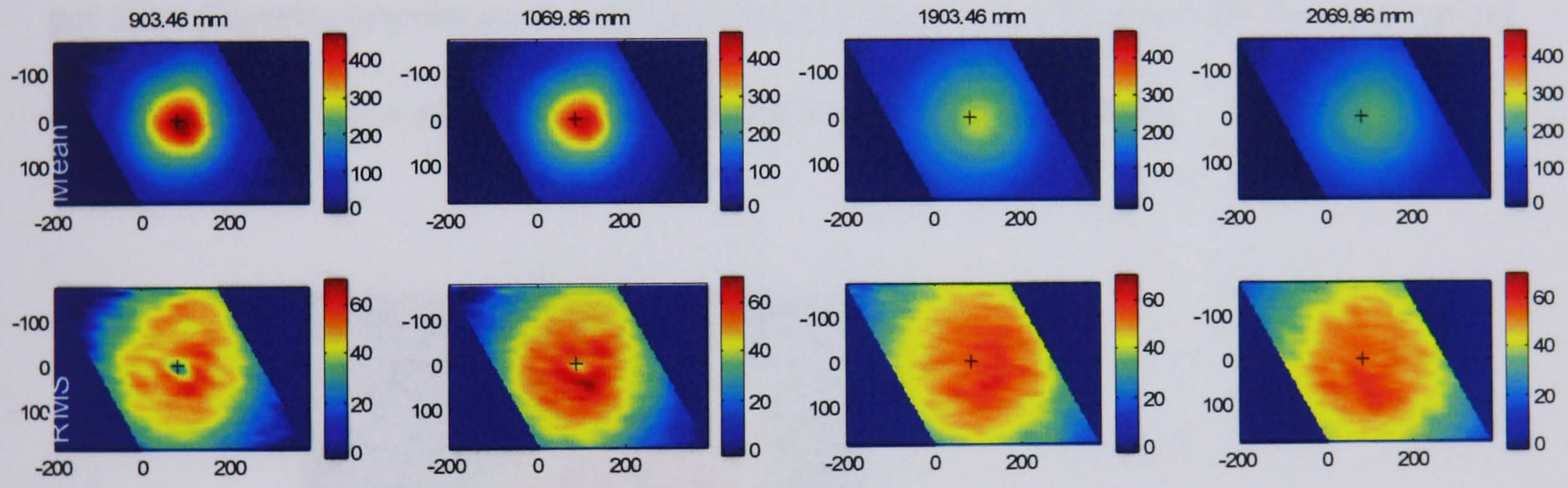

Figure 6.25 – Axial velocity cross-planes (coplanar nozzle / OP 1.3).

A complete set of cross-plane time averaged statistics, for all phase 2 datasets, is available in Appendix 9.2.2 (page 372).

6.4.2. Circle Fitting

The primary objective of the phase 2 measurements was to identify any deviation between the jet centerline and the axial traversing mechanism. This was achieved by fitting up to 60 circular contours to the mean axial velocity data, and comparing the circles' centre positions over a number of cross-axial planes.

For each cross-plane and velocity value considered, the points used to generate the circular contour were first found within the raw, un-interpolated 11 × 129 mean axial velocity data array. This was achieved by interpolating between velocity transition points within each slice, in such a way as to ensure that only 2 points were generated per slice (thereby improving the circle fitting of noisy data). Figure 6.26 shows a typical un-interpolated cross-plane, with 10 contour points marked by dots.

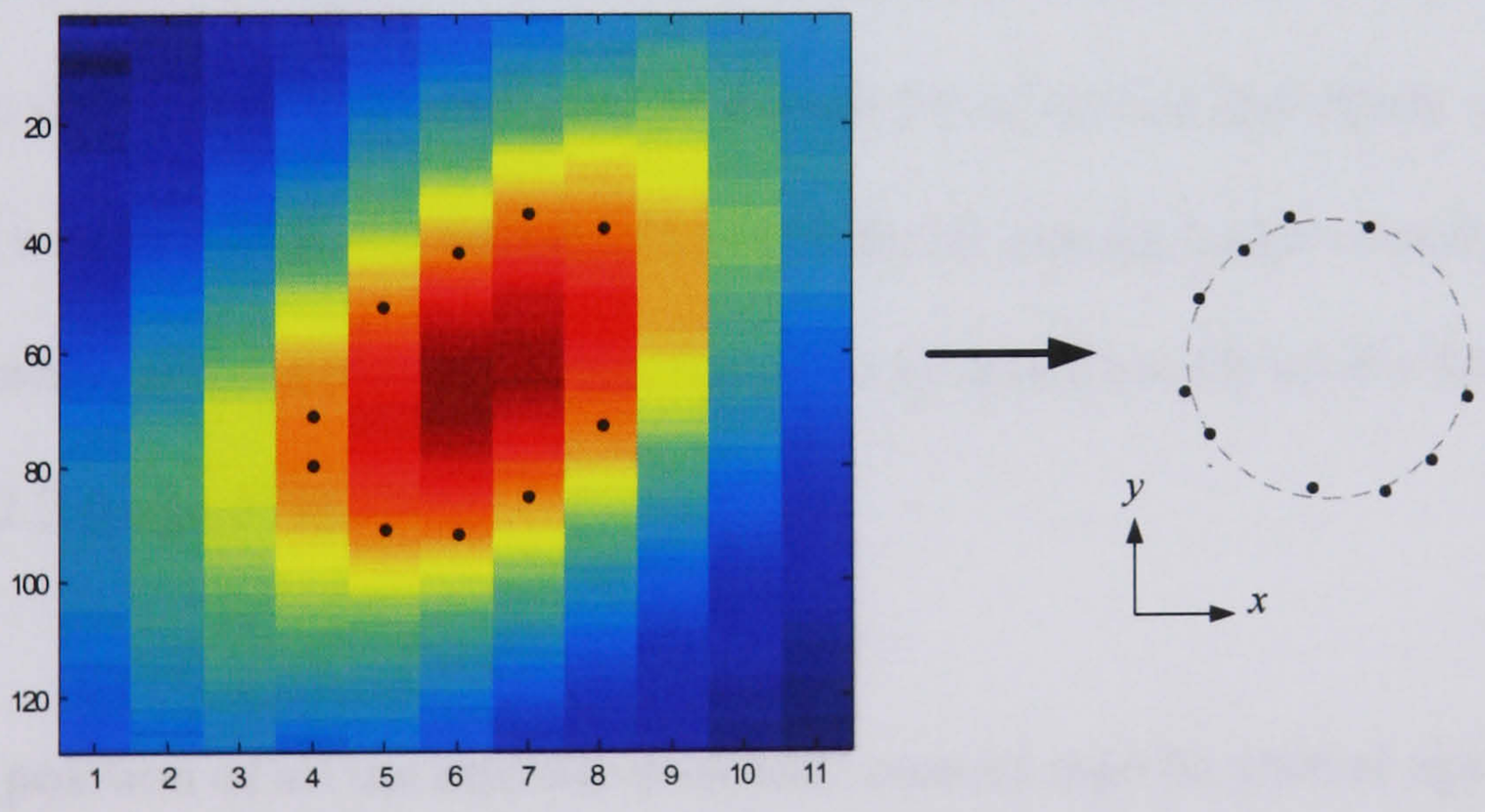

Figure 6.26 – Cross-axial circle fitting points.

The position of each contour point was transformed into real-world units using the calibration data described in Section 6.3.3, and then (providing there were at least 6 such points) used as an input coordinate for a linear least squares iterative circle fitting

algorithm*. Figure 6.27 illustrates the fitted circular contours and associated centre point positions for 2 cross-planes from the coplanar nozzle / OP 1.3 dataset:

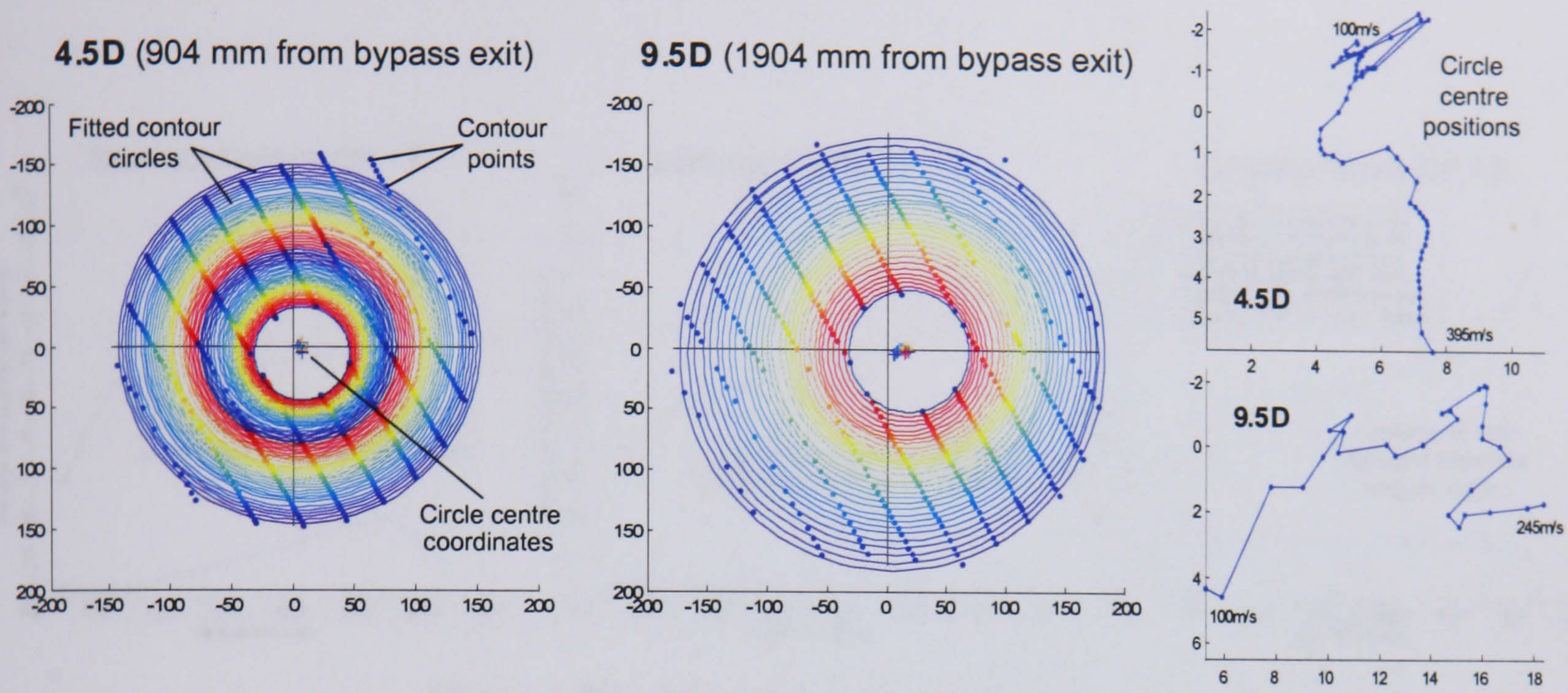

Figure 6.27 – Cross-axial circular axial velocity contours (coplanar nozzle, OP 1.3).

It is interesting to observe that for the 4.5D axial plane shown above left, the 395 m/s contour is 7 mm *below* the 100 m/s contour, while for the 9.5D cross-plane, the 245 m/s contour is 12 mm to the *right* of the 100 m/s contour. In both cases, the contours' centres are to the right of their expected positions. Fitted circles and centre coordinate positions, as well as additional information such as the change (with velocity) in circle radius, fit quality, and contour point circularity, is all available for all the datasets in Appendix 9.2.2 (page 372).

The average position of all the circular contours' centres may be plotted against the axial planes position to reveal any overall angular jet divergence, relative to the rig's

---

*The Matlab scripts in Appendix 9.4.10 make use of the LSGE library 'ls2dcircle' fitting function. The Least Squares Geometric Elements library was produced as part of the EuroMETROS EU 'software tools for metrology' project, and may be downloaded at: http://www.eurometros.org/metros/packages/lsge

traverse. Figure 6.28 plots the horizontal and vertical components of this deviation (in black and blue respectively) over 4 axial positions, for each of the nozzle / operating condition combinations that were measured at both 5D and 10D:

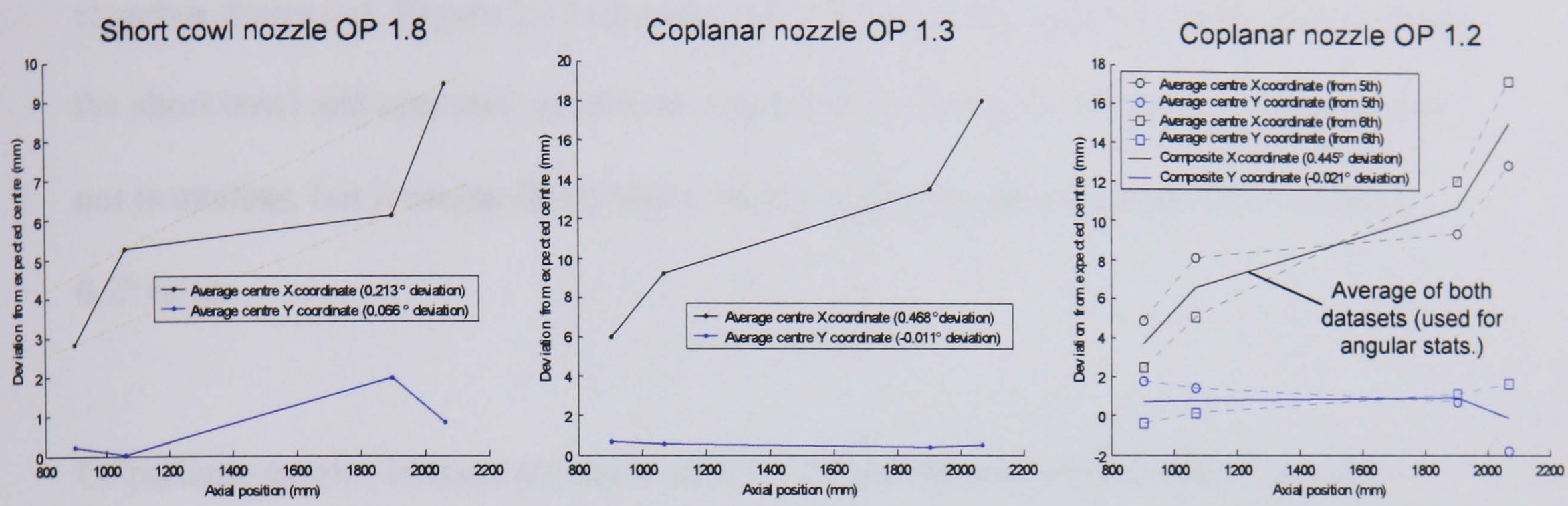

Figure 6.28 – Jet position vs. axial distance.

The 'Z' shape shared by all of the *x*-coordinate plots is most probably due to slight light sheet misalignment of ± 1.5 mm at each edge of the cameras' FOV. The horizontal jet deviation was therefore measured by averaging the gradients of pairs of lines, as shown in orange above. This approach is validated by the fact that the averaged *x*-coordinates, when extrapolated back to the nozzle, equal 0.38 mm and 0.36 mm for OPs 1.8 and 1.3 respectively – a low and consistent figure. The *y*-coordinate divergence was measured in the originally intended manner; using a line fit through all 4 points. The results of both measurements are presented in Table 6.13:

	Short cowl OP 1.8	**Coplanar OP 1.3**	**Coplanar OP 1.2**	**Mean**
Horizontal deviation:	0.21°	0.47°	0.45°	0.38°
Vertical deviation:	0.07°	-0.01°	-0.02°	0.01°

Table 6.13 – Jet divergence results from phase 2 measurements.

6.4.3. Discussion

As shown in Table 6.13, the overall divergence of the jet was found to be negligible; specifically a horizontal deviation of less than 0.5° towards the direction of the NTF chamber doors (c.f. Figure 5.15 on page 168). Whether the apparent difference between the short cowl and coplanar nozzle results is within the limits of experimental error or not is unclear, but it seems likely that a nozzle refit may alter the exhaust's angle by 0.2° or so.

Of perhaps greater interest are the asymmetries visible within the exhaust's cross-section. Figure 6.29 shows the interpolated 4.5D and 10.5D mean axial velocity cross-planes in contour form, for the OP 1.3 dataset. As indicated in black, there are significant deviations from the expected circular flow symmetry, but in different orientations. It should be noted that the circles contours shown below are spaced wide enough apart that the 'bulges' are the result of interpolation between more than 2 different slices. The fact that there is no discontinuity visible between the temporally separated upper and lower scans, adds credence to the assertion that these bulges are real flow phenomena, and not merely the result of variations in seeding, for example.

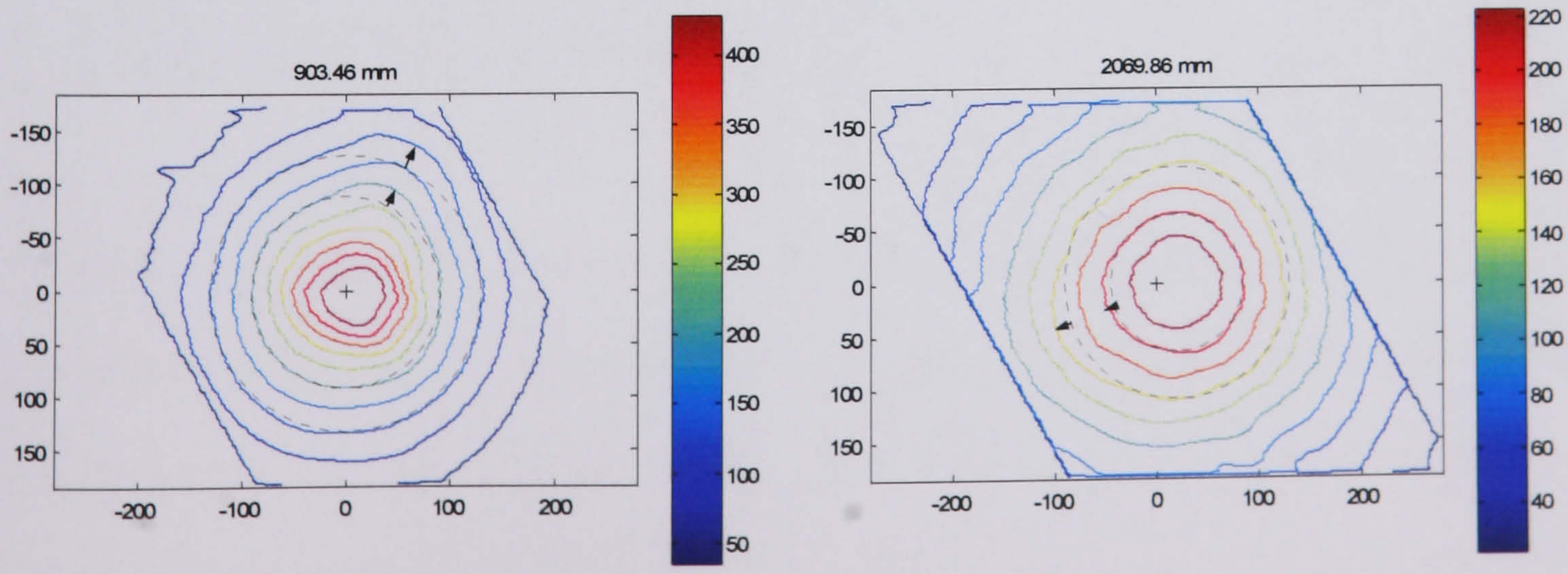

Figure 6.29 – Non circular mean axial velocity contours (coplanar nozzle, OP 1.3).

The jet's asymmetry is most noticeable in its RMS values: all datasets demonstrate an increased turbulence in the lower (and slightly right-hand) half of the exhaust. Figure 6.30 plots the mean and RMS axial velocity values along the centre of the scans' 11 slices, and it be seen that the turbulence in the lower outer mixing layer of the coplanar exhaust is approximately 120% greater than the top layer, at 4.5D.

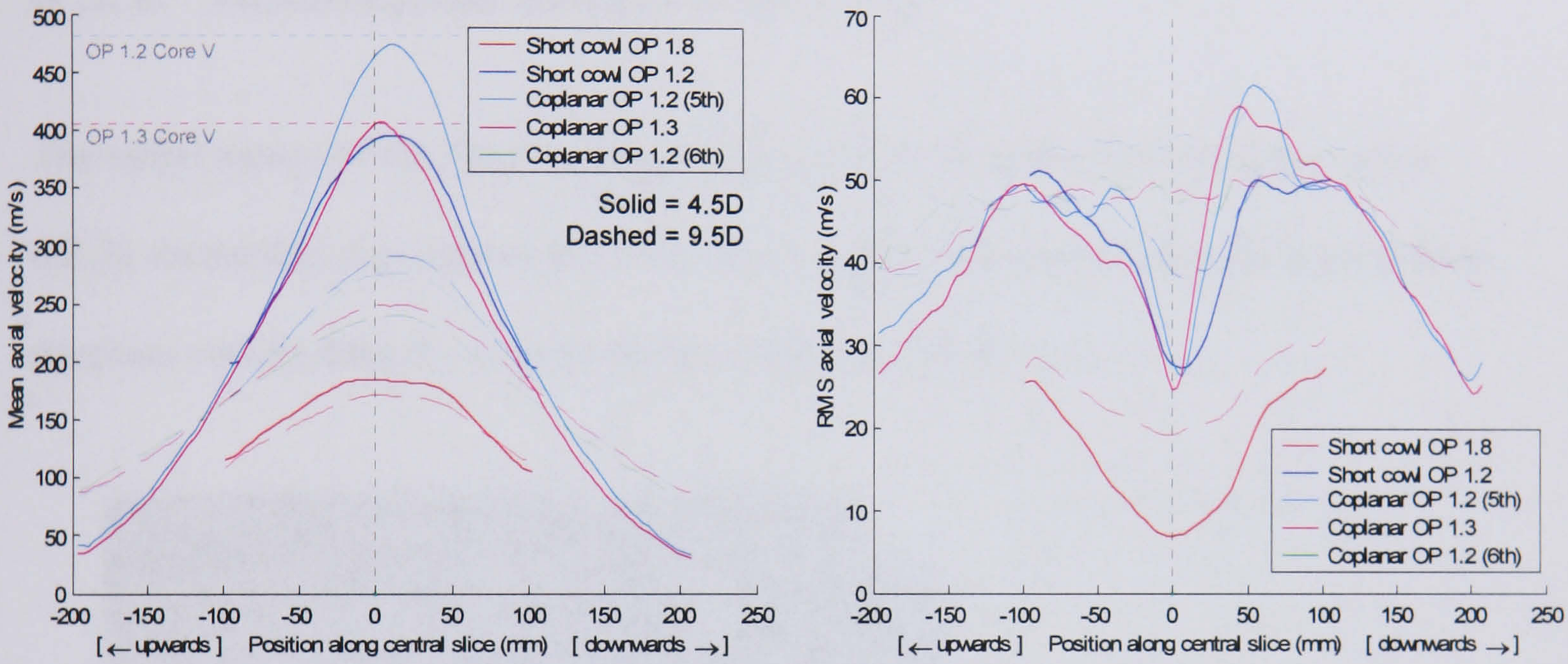

Figure 6.30 – Central slice axial mean & RMS profiles for all phase 2 data.

6.5. Phase 3 Processing & Results

While the phase 3 planar PIV data was superficially the simplest to acquire, the effects of the interference filter that was fitted over the cameras during this part of the test necessitated a number of additional processing stages.

6.5.1. Additional Vector Filtering

The radial nature of the filter's effect on the images' SNR (as discussed in Section 6.2.3), meant that the corners of the phase 3 vector maps contained significantly more spurious vectors than the centres, as demonstrated in Figure 6.31:

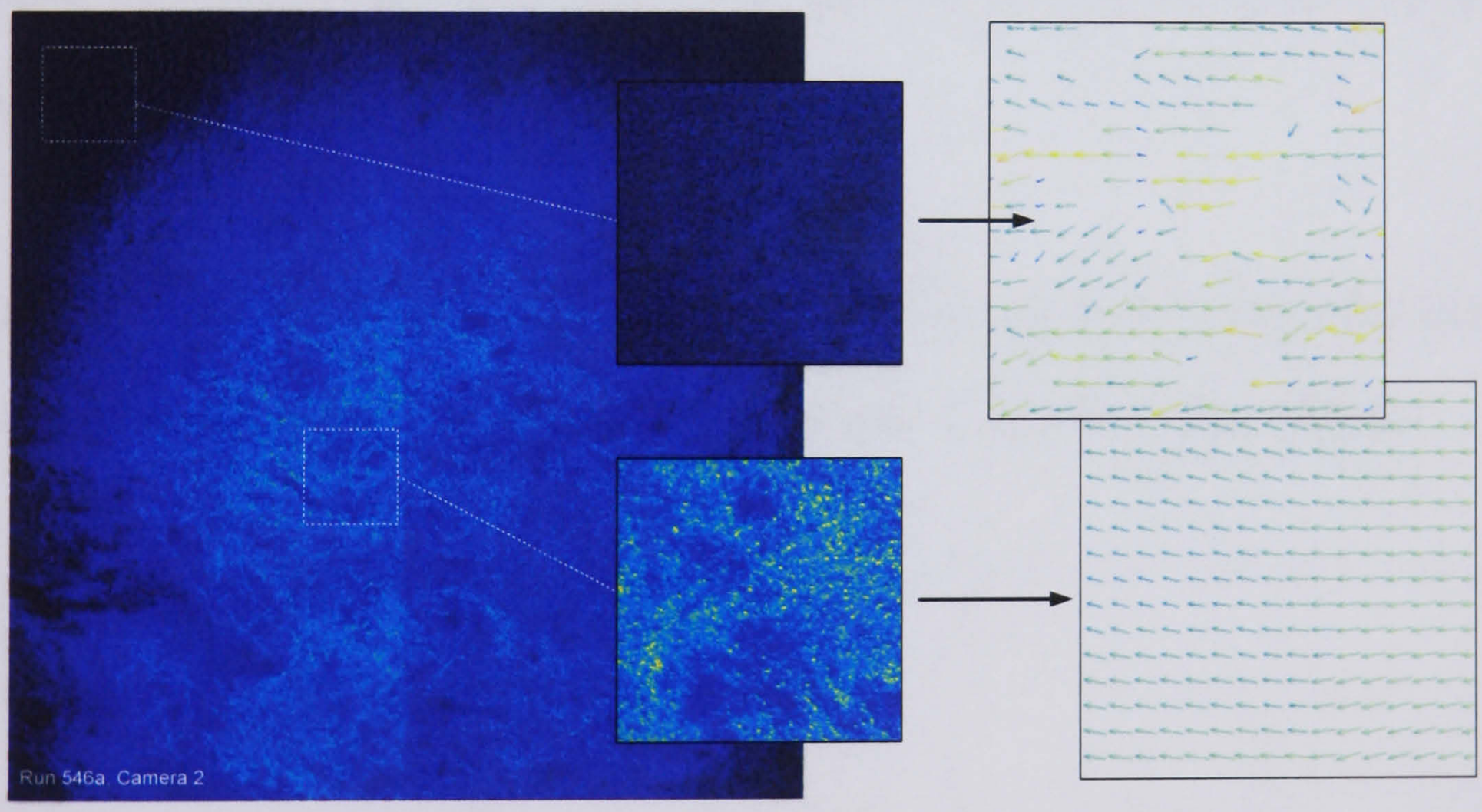

Figure 6.31 – Spurious vectors, from a phase 3 CoJeN image.

The effect of the spatial filtering operations (described in Section 6.3.5) on the horizontal component of the PIV data shown above, is illustrated in Figure 6.32. It can be seen that the majority of spurious vectors in the top left corner have been removed, as well as other, smaller defects such as that highlighted in black.

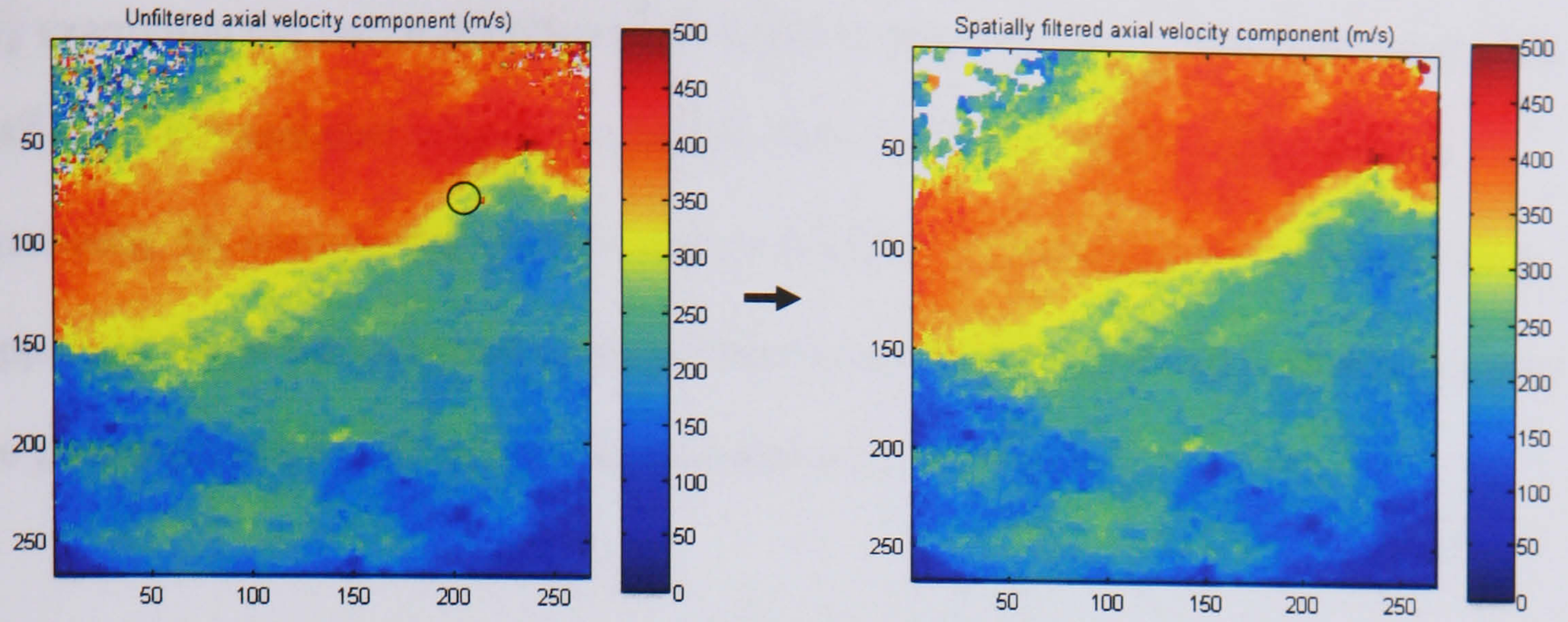

Figure 6.32 – The spatial filtering of a phase 3 instantaneous axial-velocity map.

It may however be noted that *some* spurious vectors remain in the corners of the map. This is because the range of vector values within an extremely poorly correlated region constitutes a meaningless criterion upon which to judge the validity of an individual vector. For this reason, the phase 3 CoJeN vector maps were also filtered temporally, whereby the range of valid vector values was established by considering their variation over time.

Figure 6.33 plots a time-series 'history' for the axial component of vector (50, 50) from the dataset shown above. The mean displacement of -10.8 pixels is also marked.

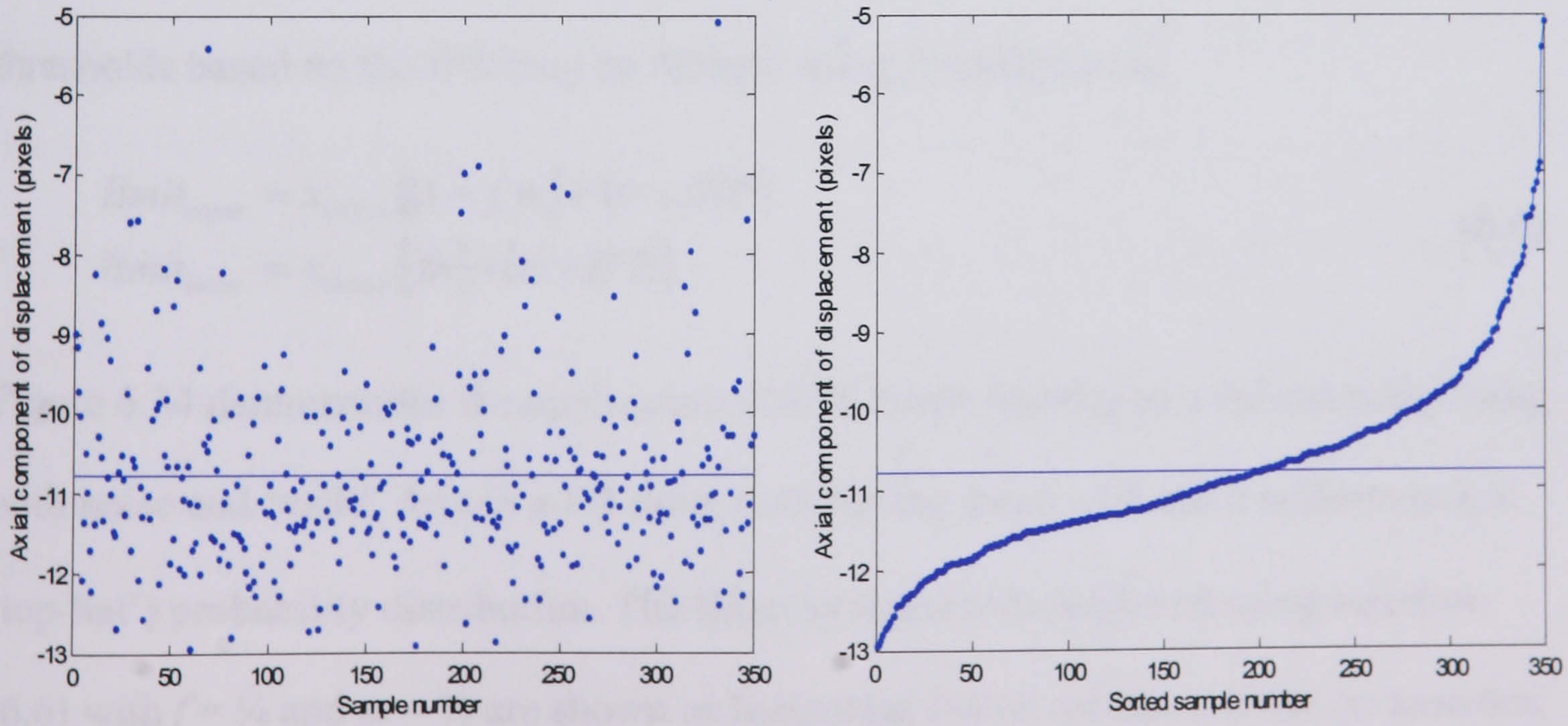

Figure 6.33 – Unsorted and sorted vector time-series (run 546a, camera 2).

By examining the vector distribution, it might be surmised that – at the very least – the 68th and 331st samples' vectors (for which the axial displacement > -6 pixels) are erroneous. By considering the time history in this way at every single vector position, upper and lower limits for the permissible axial and radial components of velocity may be generated, and in turn applied as filters to each of the vector maps.

6.5.1.1. Inter-Fractional Range Filtering

Filter limits could be generated from each vector's time-series by adding and subtracting a multiple of the RMS to the mean (or median) value, in the same way that the spatial filter limits are generated. Instead however, it was decided to apply filters based on a variation of the inter-quartile range – a commonly used statistical measure of outliers. The generalised inter-fractional range (IFR) for a 1-dimensional dataset x may be defined as:

$$IFR = x_{sorted}[(1-f)n] - x_{sorted}[fn] \tag{6.5}$$

…where n is the number of samples in x, f an arbitrary value between 0 – 0.5 (for the inter-quartile range $f = ¼$), and x_{sorted} is the dataset sorted into ascending order. Filtering thresholds based on the IFR may be defined using a multiplier m:

$$\begin{aligned} limit_{upper} &= x_{sorted}[(1-f)n] + (m \times IFR) \\ limit_{lower} &= x_{sorted}[fn] - (m \times IFR) \end{aligned} \tag{6.6}$$

Figure 6.34 demonstrates the application of IFR based filtering to a dataset comprising both noise and 'valid' data in a 1:5 ratio, both having mean of 0 and a uniform (a.k.a. 'top-hat') probability distribution. The filtering thresholds produced using equation (6.6) with $f = ¼$ and $m = ½$ are shown as horizontal dotted red lines. It can be seen that the majority of the noise lies outside the filter limits.

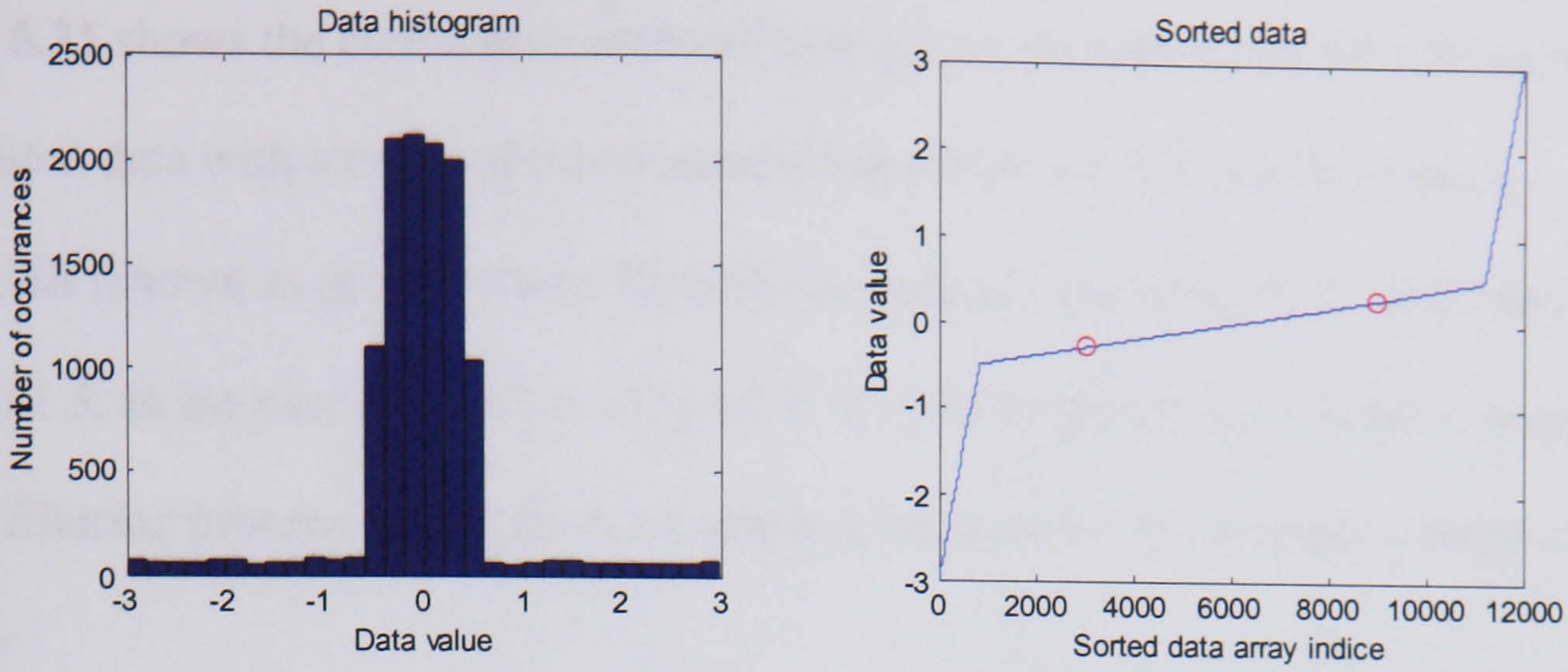

Figure 6.34 – IFR filtering example (top-hat probability distributions).

The advantage of the IFR vs. RMS approach is that only (100-200f)% of the data (i.e. that between the two red circles in Figure 6.34) is considered when formulating the filtering thresholds. Assuming symmetric noise, the thresholds will therefore be based on purely 'valid' data as long as:

$$(1-2f) < \frac{v}{n} \tag{6.7}$$

…where v is the number of non-noisy entries in x. Needless to say, this filtering method is incapable of detecting samples whose values lie within the allowed range, but which are nevertheless noise.

The choice of suitable f and m values clearly depends on the probability distribution of the data. For uniformly distributed data, such as that in the example above, it is logical to generate the filter limits by linearly extrapolating the section of data considered, i.e. $(2m+1)(1-2f) = 1$. Matters are however significantly complicated when considering data that has a unique, asymmetric (and unknown) probability distribution, with samples that may not neatly divide into 'data' and 'noise'.

Figure 6.35 shows the cumulative probability distribution function (CDF) for normally distributed data with a mean of 0 and standard deviation of 1. The IFR filtering thresholds (shown as green vertical lines) have been calculated using $f = 0.25$ and $m = 0.5$ and 1.5. In the case of $m = 0.5$, only 82.1 % of the original data would be accepted by the filtering process. The right-hand graph demonstrates how this percentage changes with m:

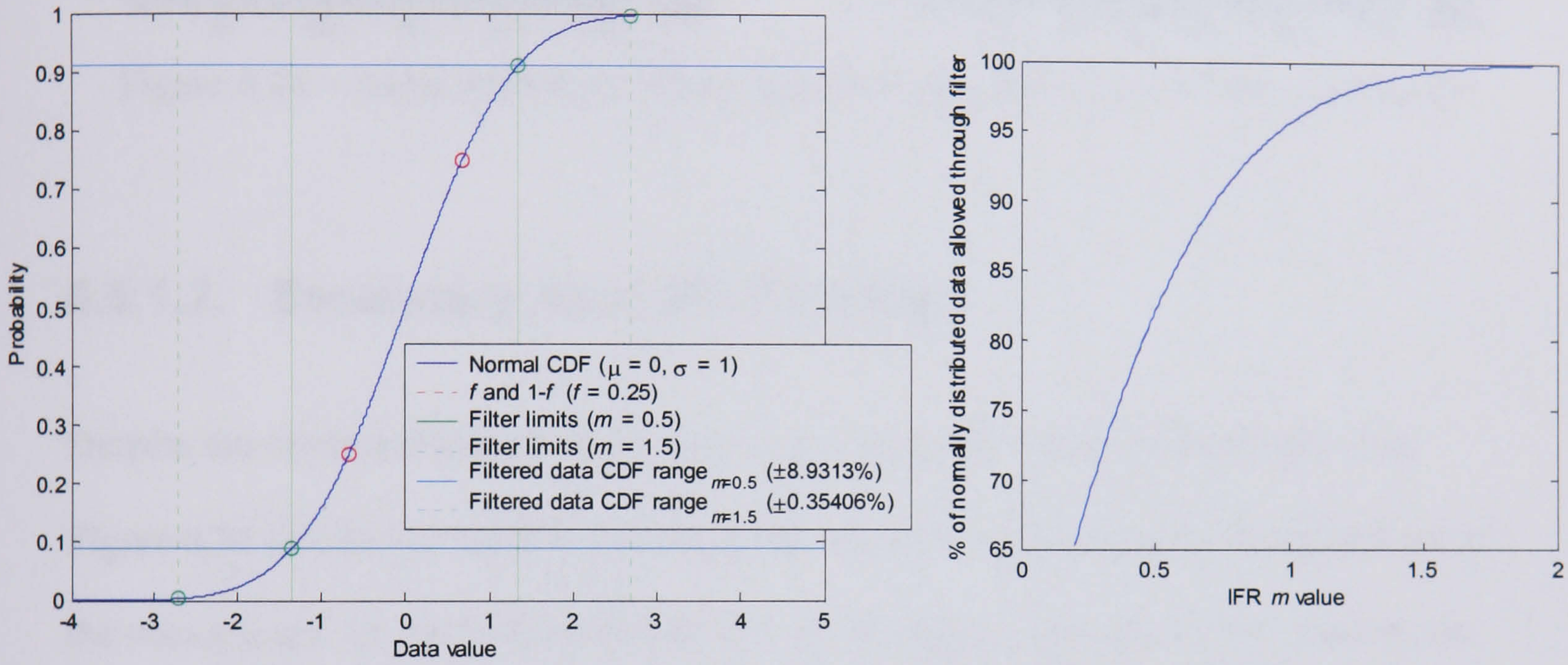

Figure 6.35 – Inter-fractional range filtering of normally distributed data.

Based on the assumption that at least 50% of the CoJeN vectors would be valid, and that the jet turbulence would be close to a Poisson process (for which the normal CDF is a good approximation when $\mu \gg 0$), it was decided that temporal IFR variable values $f = 0.25$ and $m = 1.5$ would be used, meaning that only 0.7% of purely Gaussian data would be (unfairly) rejected.

Figure 6.36 demonstrates the effect of the temporal filtering on the RMS axial velocity of the dataset shown on page 266 (acquired at the end of the potential core). It can be seen that the high values in the top left corner (i.e. those that are a measurement artifact) are approximately halved, while the lower portion of the map remains unchanged.

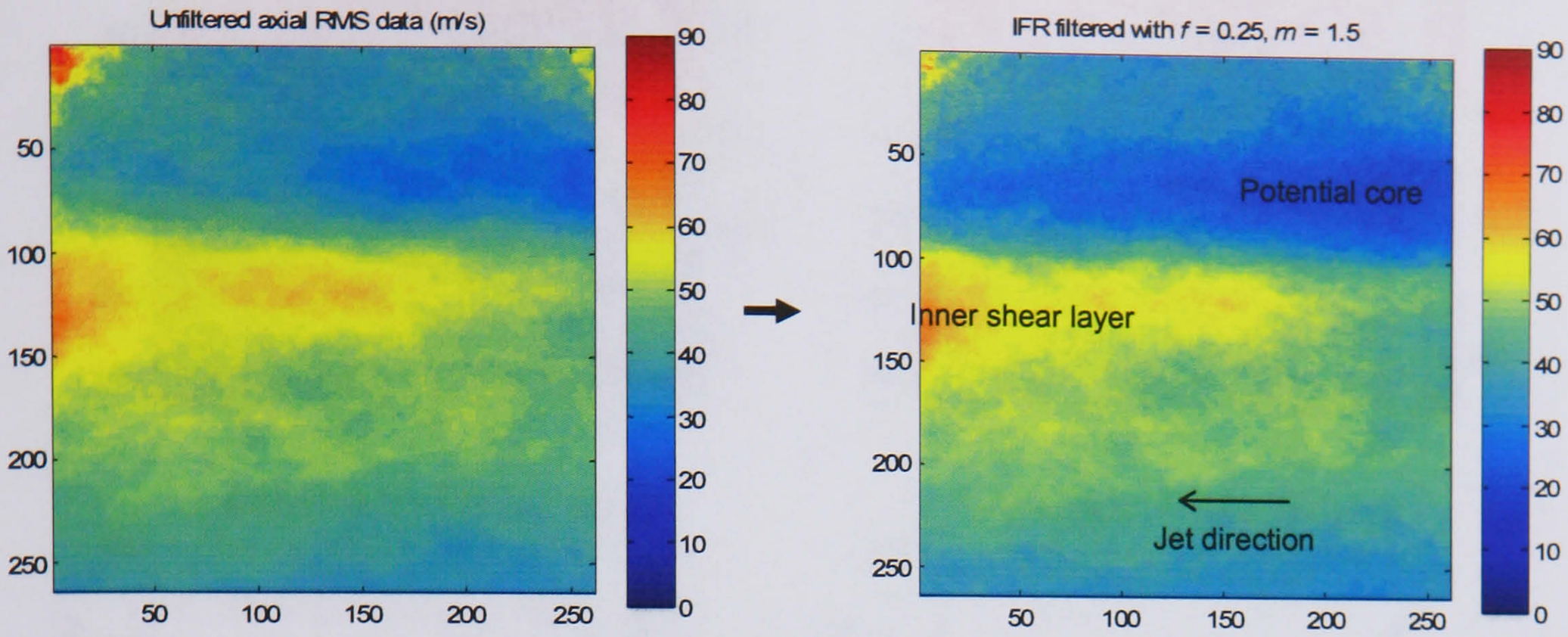

Figure 6.36 – Axial RMS data before and after IFR filtering (run 546a, camera 2).

6.5.1.2. Secondary Axial IFR Filtering

Despite the combined effects of the spatial and temporal filtering described so far, Figure 6.36 testifies to the fact that sufficient spurious vectors remain in the corners of the vector maps for the RMS values to be conspicuously inflated. For this reason, the phase 3 CoJeN data was further filtered, using a technique that relies on the flow's self-similarity in the axial dimension.

The top row of Figure 6.37 on page 271 shows the upper and lower velocity thresholds calculated using the IFR filtering method described in the previous subsection (where f = 0.25 and m = 1.5). Based on the assumption that the jet's mean and RMS values should not change significantly over 20 cm of the exhaust's length, a secondary set of IFR thresholds may be calculated for each row of the first. The middle row of Figure 6.37 illustrates such secondary thresholds (calculated using $f_2 = 0.25$ and $m_2 = 0.5$), plotted on top of sorted data from the 30th row of the limit maps shown.

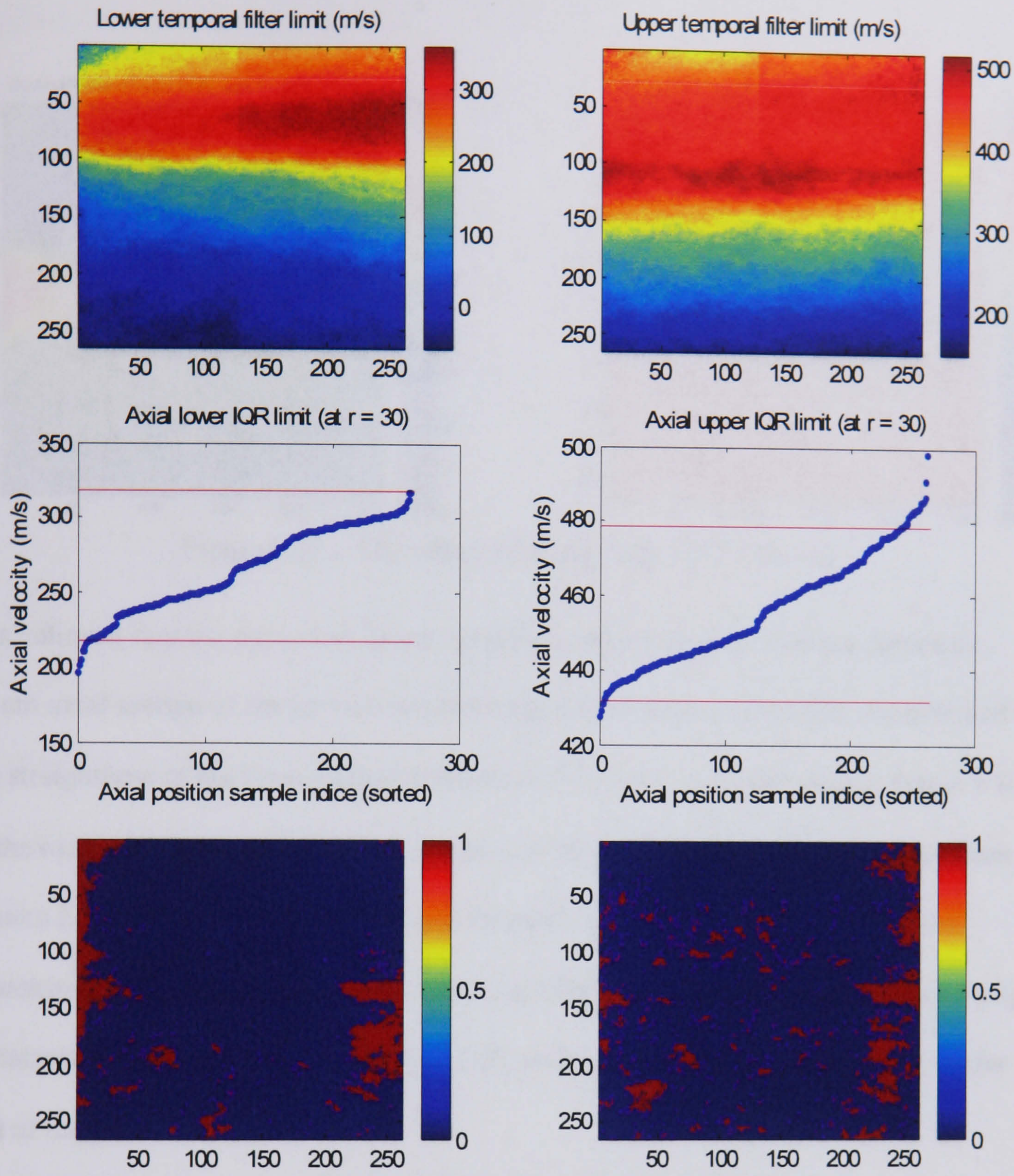

Figure 6.37 – Secondary axial IFR filtering.

The bottom row of Figure 6.37 shows (in red) the points within the original upper and lower limit maps that exceed the values set by the secondary IFR filter. Any such areas are cropped to the secondary filter's limits. In this way, the final, combined, filter limits are defined on the basis of the both the vectors' variation in time *and* space (along the axial dimension). Figure 6.38 illustrates the result of applying such double filtering to the data shown elsewhere in this section. The differences in the axial RMS values, relative to those given in Figure 6.36, are also shown.

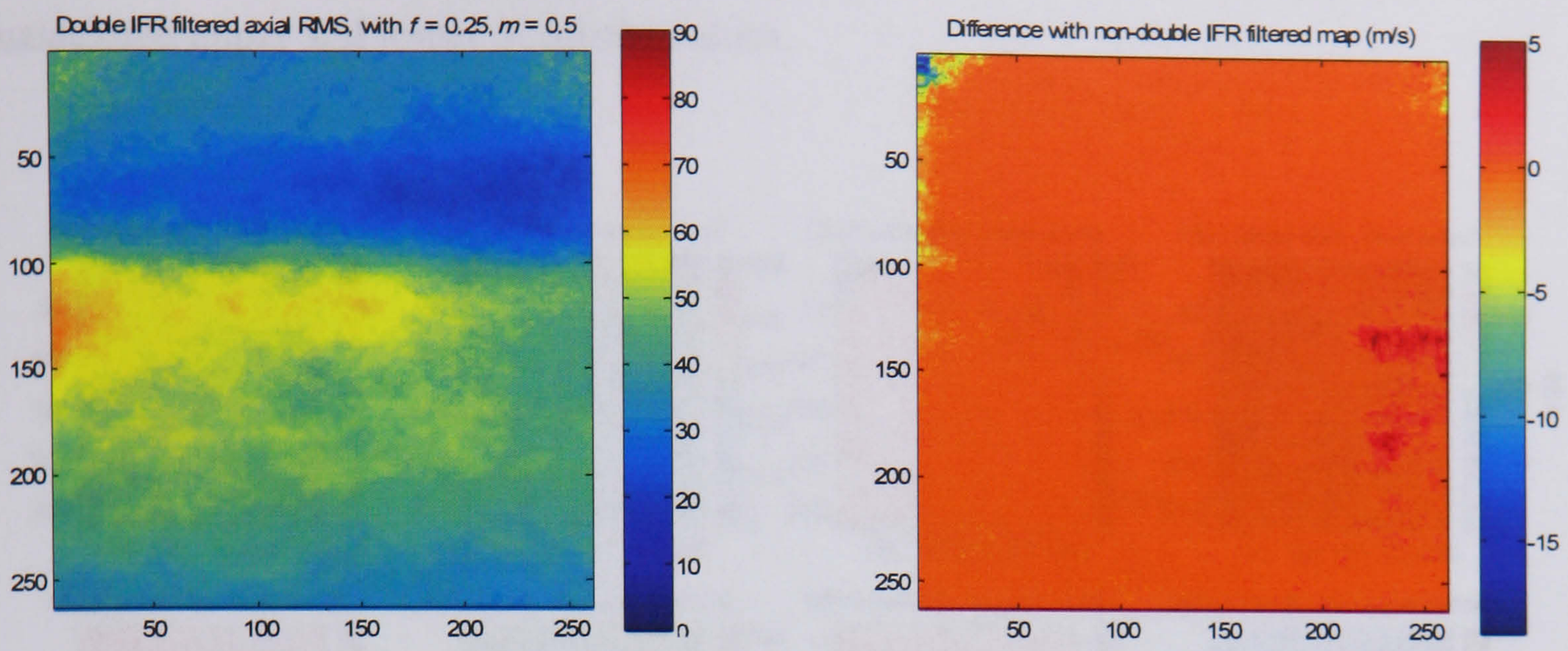

Figure 6.38 – The effect of double axial IFR filtering.

It is believed that the upper and lower ranges of valid velocities within a particular 22 cm axial section of the jet will be uniformly distributed (a belief that is confirmed by the straightness of the lines plotted in Figure 6.37), and it is for this reason that $m = 0.5$ in the example shown above. All of the data so far presented has however come from camera 2, run 546a – a relatively typical dataset with good image SNR; acquired approximately 1 m from the nozzle. The axial IFR filtering is of more relevance though to datasets with extremely poor image SNR, such as camera 5's samples from the far end of the jet.

The top row of Figure 6.39 demonstrates the upper and lower temporal filter limits calculated for a dataset with a high number of spurious vectors. As a result of the spatial filtering, there are so few (< 20) vectors left in the corners of the maps that the thresholds have had to be set to $\pm \infty$. Clearly the top few rows of these limit maps contain ‹‹ 50% 'good' data as a result. As such, the axial IFR filter parameters were adjusted to $f = 0.4$ and $m = 2$, thereby maintaining the enforced uniform probability

distribution, but basing the resultant limits on only 20% of each row's previously calculated upper and lower threshold values.

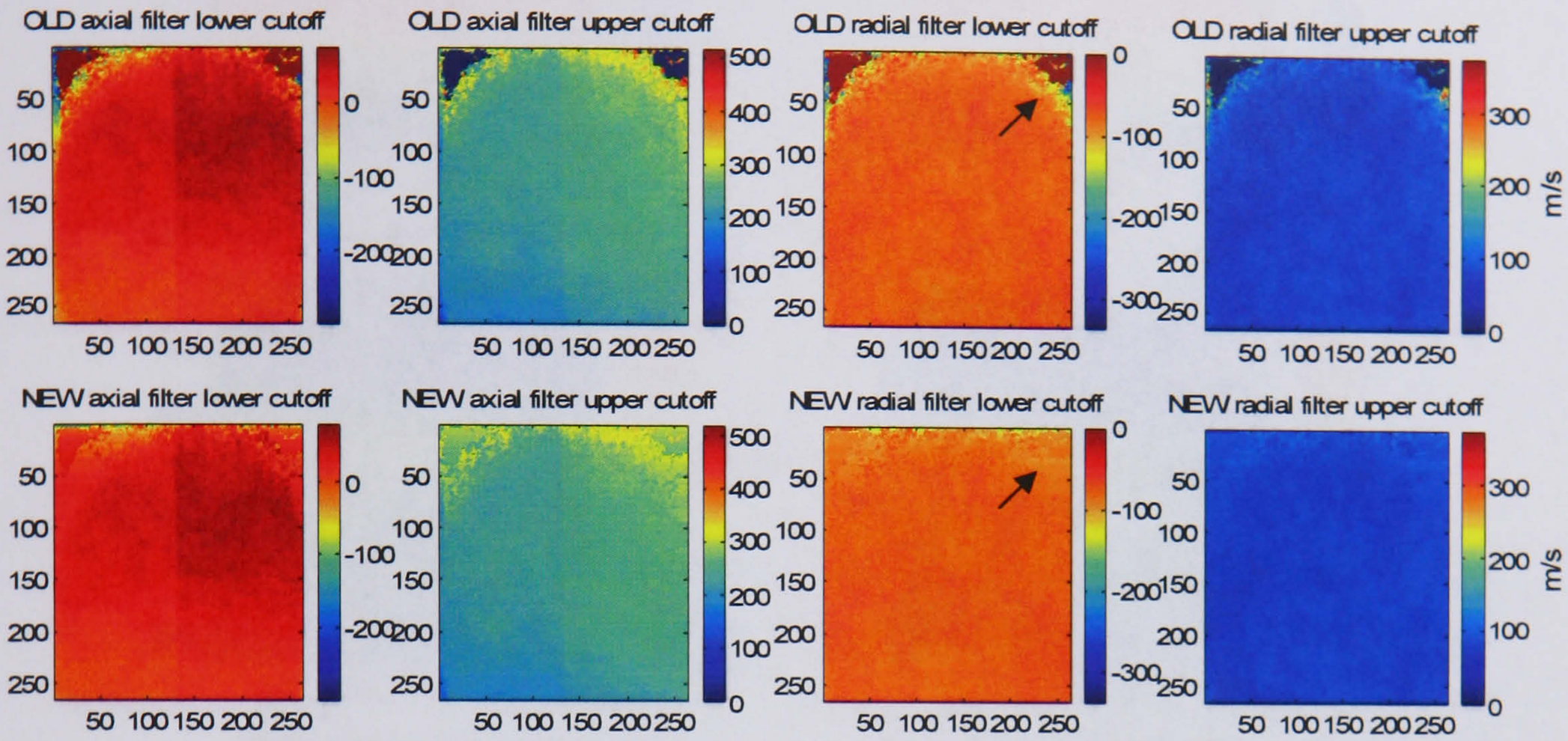

Figure 6.39 – The effect of axial IFR filtering on filter thresholds (run 535a, camera 2).

The effect of the secondary axial IFR filter on vectors located at position (250, 40) has been highlighted. Whereas the temporal-only filter would have allowed through vectors with a radial velocity component as low as -300 m/s, the adjusted filtering limits ensure that no values lower than -80 m/s may pass.

6.5.1.3. Summary of Phase 3 Vector Filtering

Figure 6.40 on page 274 illustrates the combined effect of the spatial, temporal and axial filtering on the axial mean and RMS of the dataset that has been shown throughout this section. The number of vectors removed is also shown.

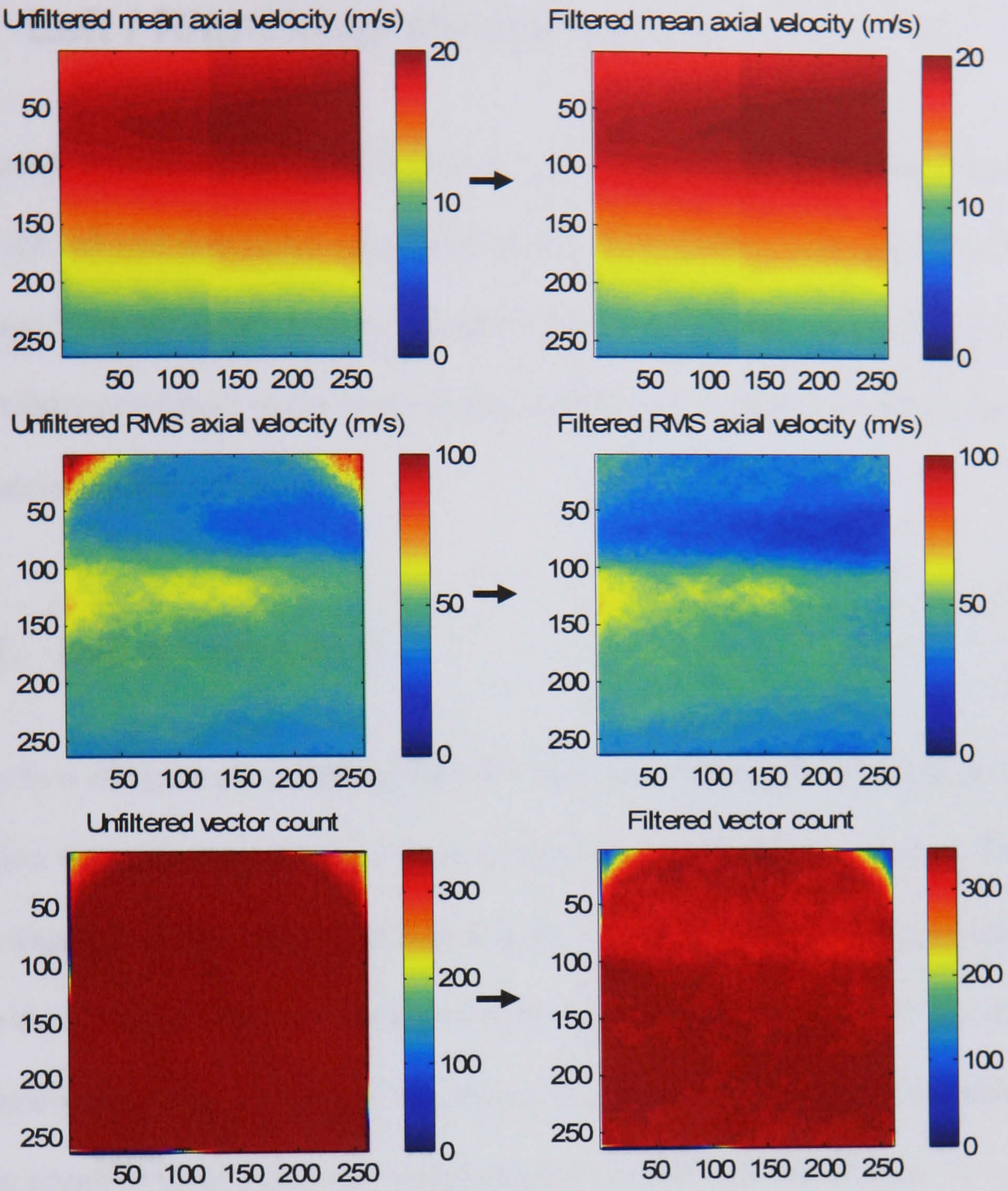

Figure 6.40 – Combined effect of all phase 3 vector filtering (run 546a, camera 2).

6.5.2. Left / Right Velocity Correction

As discussed in Section 6.2.2, the correlated vector maps displayed a clear discontinuity between the left and right hand sides of the axial-component velocity maps (c.f. Figure 6.9 on page 233). By virtue of being related to the image's brightness, this bias effect was especially prominent in the phase 3 data. Section 6.5.1 details the means by which the discontinuity was corrected.

6.5.2.1. Initial Correction

The very first attempts at correcting the left / right discontinuity were based on the assumption that only the right-hand sides of the velocity maps were 'wrong'. This was a premise founded on the observation that it is the right half the sensor that switches between the 1st and 2nd read-out taps, and only the right half of the image that changes in appearance when doing so. Clearly this theory was in turn dependent on the belief that an image acquired using just 1 tap would result in an accurate vector map.

The right hand side of each time-averaged horizontal velocity map was 'corrected' by multiplying the values by m, and adding the constant c. These corrective factors were in turn calculated using an error minimisation function, based on producing a linear progression of velocities across the left / right divide. As shown in Figure 6.41a on page 276, 3 equally spaced thin vertical strips (A, B and C) were extracted from the left and right-hand sides of the vector map, with strip C multiplied by m and added to c. The 'error quantifier' for that m and c value was then defined as:

$$\varepsilon_{m,c} = \overline{\left|\mathbf{A}_{axmean} + (m\mathbf{C}_{axmean} + c) - 2\mathbf{B}_{axmean}\right|} \tag{6.8}$$

…with the *axmean* suffix denoting averaging of each strip in the horizontal (axial) dimension. Figure 6.41b demonstrates the variation in this 'error quantifier' when calculated for a range of m and c values, with the minimum ε value marked in white. For the example shown below therefore, multiplication by 1.00 and the addition of 0.24 pixels to the right hand side of the vector map was found to result in the most linear progression of velocities from A to B to C.

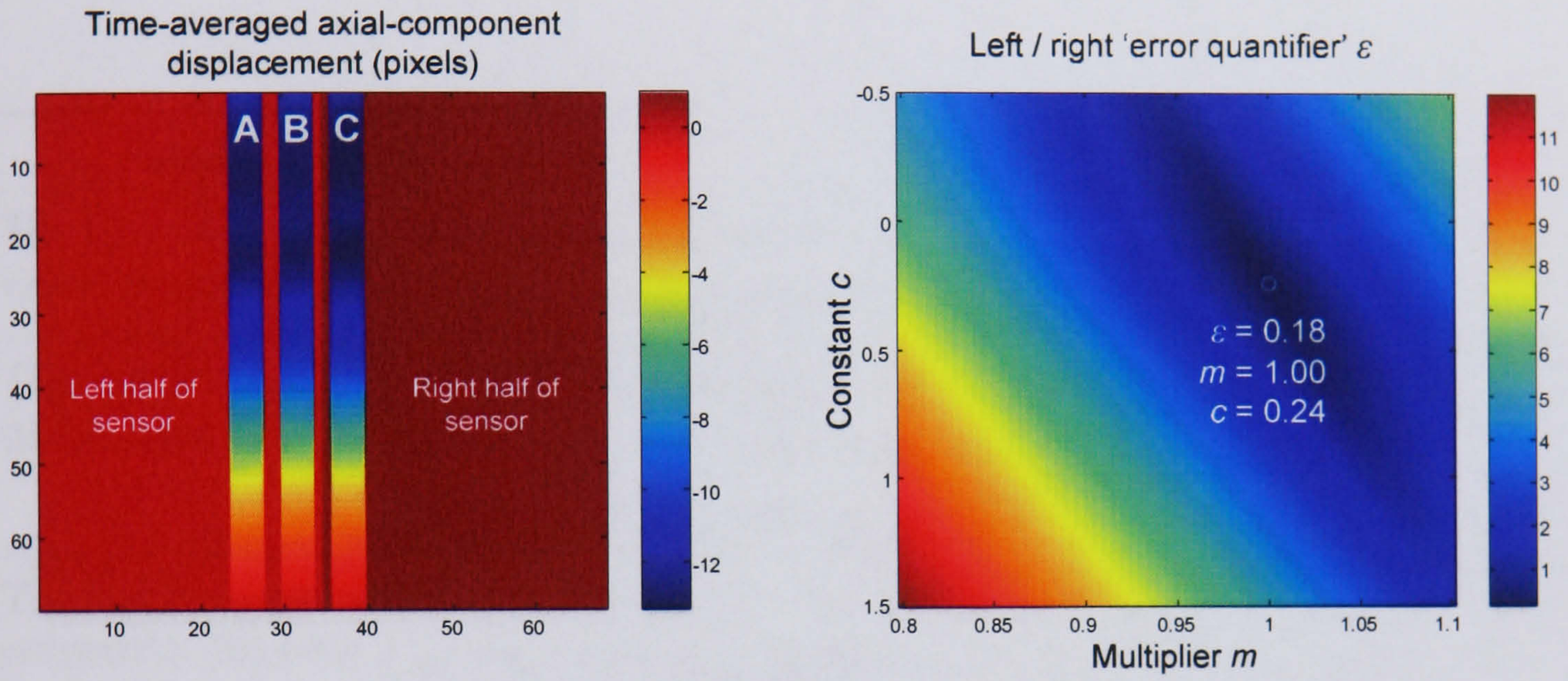

Figure 6.41a) Vector map correction strips; b) Associated 'error map'.

Figure 6.42 demonstrates the application of this correction, and the effect on an axial velocity profile, taken along the black dotted line:

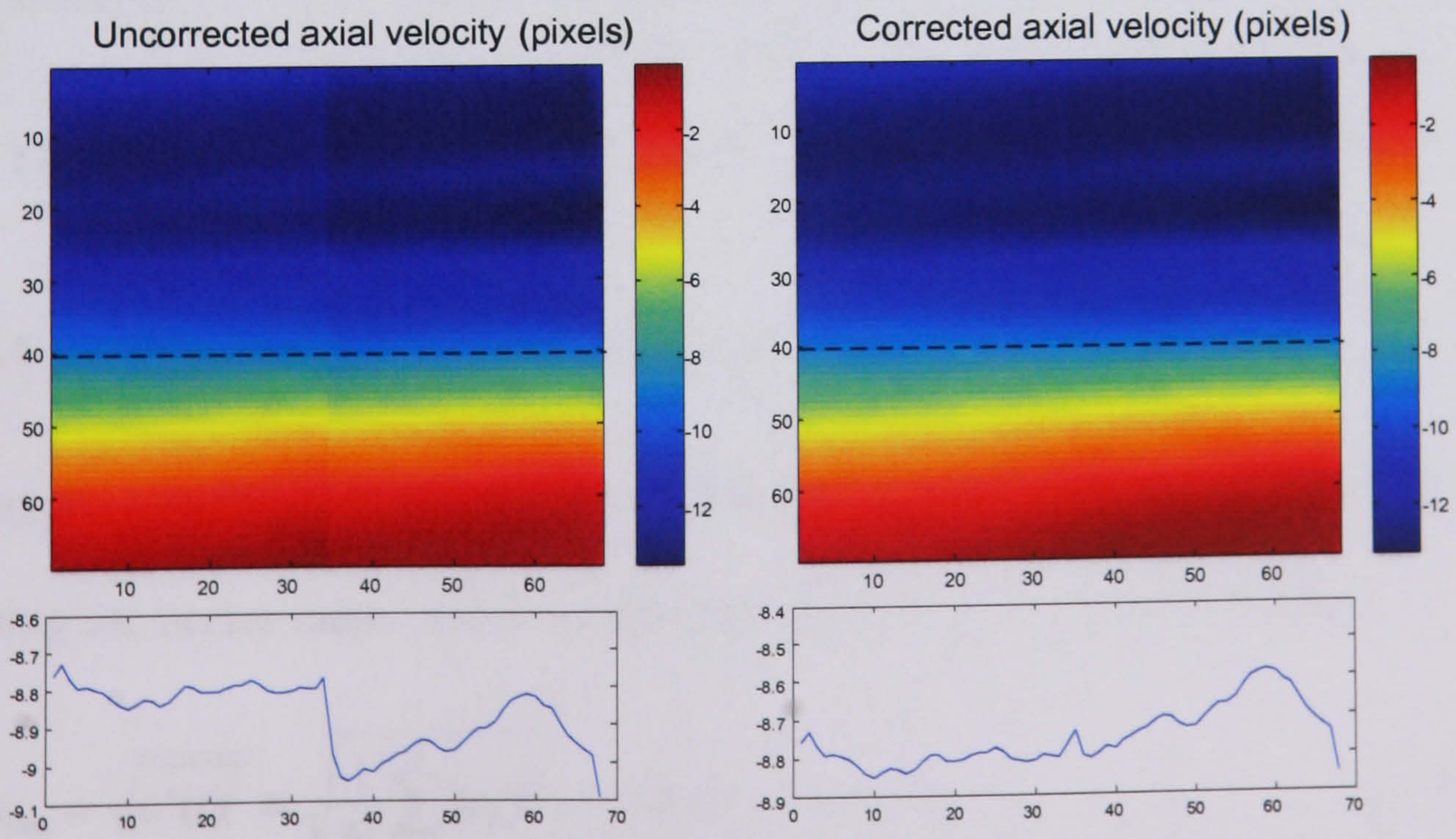

Figure 6.42 – Application of the initial left / right correction.

6.5.2.2. Analysis of the Left / Right Bias

While the correction described on the previous pages may result in an aesthetic improvement to individual vector maps, it is clear from examination of the axial velocity profile shown bottom right of Figure 6.42 that the correction is overly simplistic. In the course of determining a more accurate means of correcting of the axial velocities, a number of questions had to be addressed:

Issue	Options
The form of each vector's correction:	• Additive, i.e. $\mathbf{u} = \mathbf{u} + c$. • Additive and multiplicative, i.e. $\mathbf{u} = m\mathbf{u} + c$.
The spatial extent of the error:	• Only the right half of the vector maps need correcting. • Only the left half needs correcting. • Both halves need correcting.
The variation in correction factors c (and m) for a particular half of a vector map:	• No variation: the correction factors are scalars. • The correction factors are vectors, which vary along the map's axial dimension. • The correction factors vary along the radial dimension. • Both c and m are 2D matrices, the same size as half a map.
The variation in the correction applied to different time-averaged maps:	• The correction is the same for all cameras used. • Cameras 1, 2 and 5 each require different corrections.
	• The correction is constant for all measurement positions. • The correction varies with measurement position.

Table 6.14 – The variables associated with left / right velocity correction.

6.5.2.2.1. Form of the Vector Correction

The need for a multiplicative factor in each vector's correction may be tested by examining the vector maps' axial component RMS values, as defined below.

$$u_{rms} = \sqrt{\overline{u'(t)^2}} \equiv \sqrt{\frac{1}{N}\sum_{i=1}^{N}(u_i')^2} \quad \text{where} \quad u_i' = u_i - \bar{u} \tag{6.9}$$

Because $\bar{u}$ is factored out during the calculation of the RMS, a left / right discontinuity in the values would indicate that something more than an additive factor was required for the correction. Figure 6.43 shows a mean and RMS axial component vector map, acquired approximately 0.7 m from the nozzle. Axial profiles are presented for 4 radial positions (marked with white dashed lines), and the position of the left/right divide marked on the profiles in red.

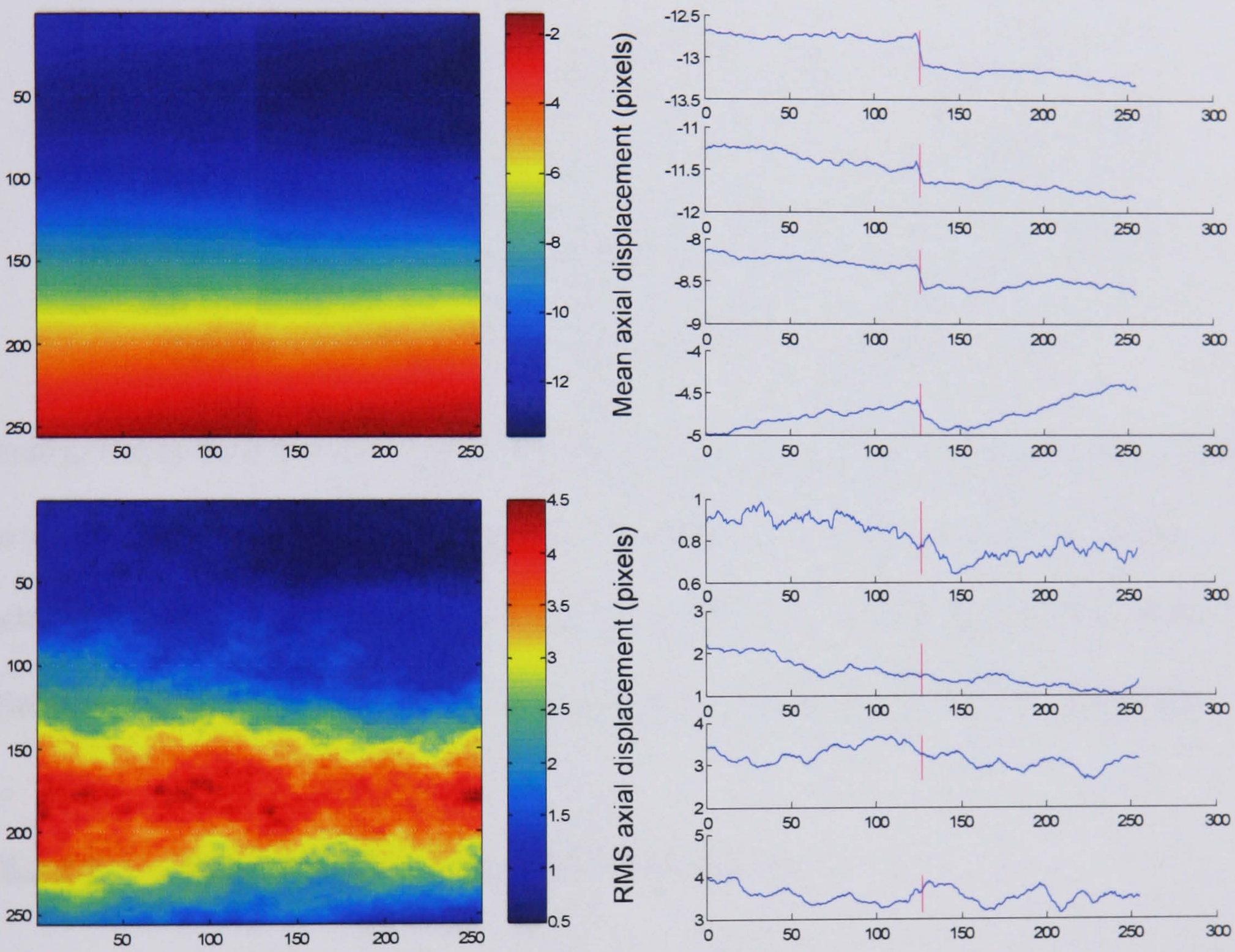

Figure 6.43 – Axial mean and RMS velocity (run 501c, camera 1).

As is apparent from the example shown above, and a representative number of other samples (from all 3 cameras), the RMS does not show the same discontinuity as the axial mean velocity. The only exception occurs, as would be expected, in measurement positions where $\bar{u} \approx 0$.

It should be noted, incidentally, that the smooth axial RMS profiles do not *prove* the absence of a multiplicative relationship between the measured and actual jet velocity. As demonstrated in Table 6.15 however, for a similar RMS to be generated from two multiplicatively adulterated datasets, highly specific additive factors must be applied as well. It is unlikely that this would occur repeatedly for multiple measurements.

	Time-series	Statistics
'True' data:	5.00, 6.00, 9.00, 4.00, 7.00, 8.00, 5.00, 6.00	Mean: 6.25 RMS: 2.44
Measured data: (1.1*true* + 0.50)	6.00, 7.10, 10.40, 4.90, 8.20, 9.30, 6.00, 7.10	Mean: 7.38 RMS: 2.95
Measured data: (0.9*true* + 0.76)	5.26, 6.16, 8.86, 4.36, 7.06, 7.96, 5.26, 6.16	Mean: 6.39 RMS: 2.95

Table 6.15 – Similar RMS values for non-similar data biasing.

Finally, it may be noted that the majority of (though not all) corrections calculated using the simplistic method described on page 275 resulted in a multiplicative correction factor $m = 0$. Based on these observations, it was therefore determined that the phase 3 axial-component velocities would be corrected by an additive corrective factor only.

6.5.2.2.2. Spatial Extent of the Left / Right Error

While the initial, simplistic left / right bias correction was based on the assumption that every vector maps' left-hand side was fault-free, wariness, and contemplation of the tap switching electronics, led to the withdrawal of this conjecture. Instead, the correction algorithm would be based on the calculation of an arbitrary sensor-wide bias, and – as will be shown – both sides of the sensor did indeed prove themselves to suffer a similar degree of biasing.

6.5.2.2.3. Variation of the Corrective Factor

Figure 6.44 comprises a contour plot of the time-averaged axial-component velocity data that was shown on page 233. The differing contour angles on the left and right-hand sides clearly demonstrate that the additive corrective factor must vary along its axial dimension. This assertion is reinforced by examination of the 'corrected' axial velocity profile shown in Figure 6.42 on page 276.

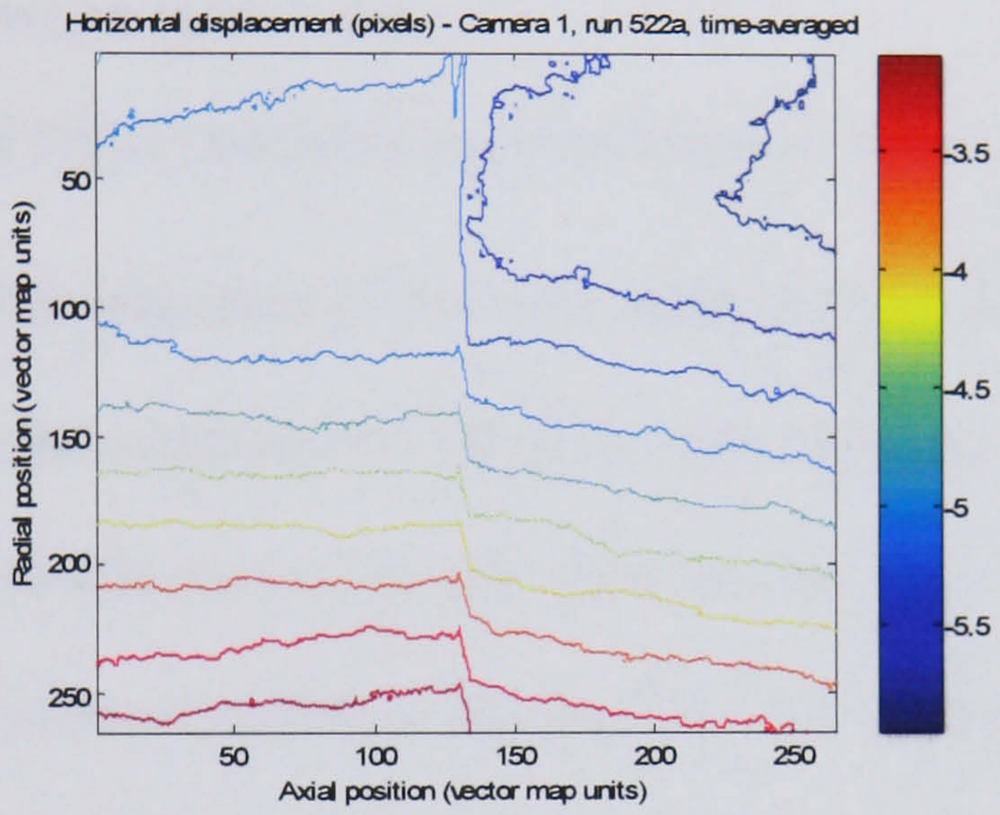

Figure 6.44 – Time-averaged axial-component velocity contours.

The variation of the required correction in the radial dimension may be established by examining the displacement discontinuity along the length of the left / right boundary. Figure 6.45 shows two radial velocity profiles taken from just left and just right of a typical vector map's centre. Both the relative and absolute velocity differences are shown; the profiles having been extracted sufficiently close to each other that these differences should be negligible.

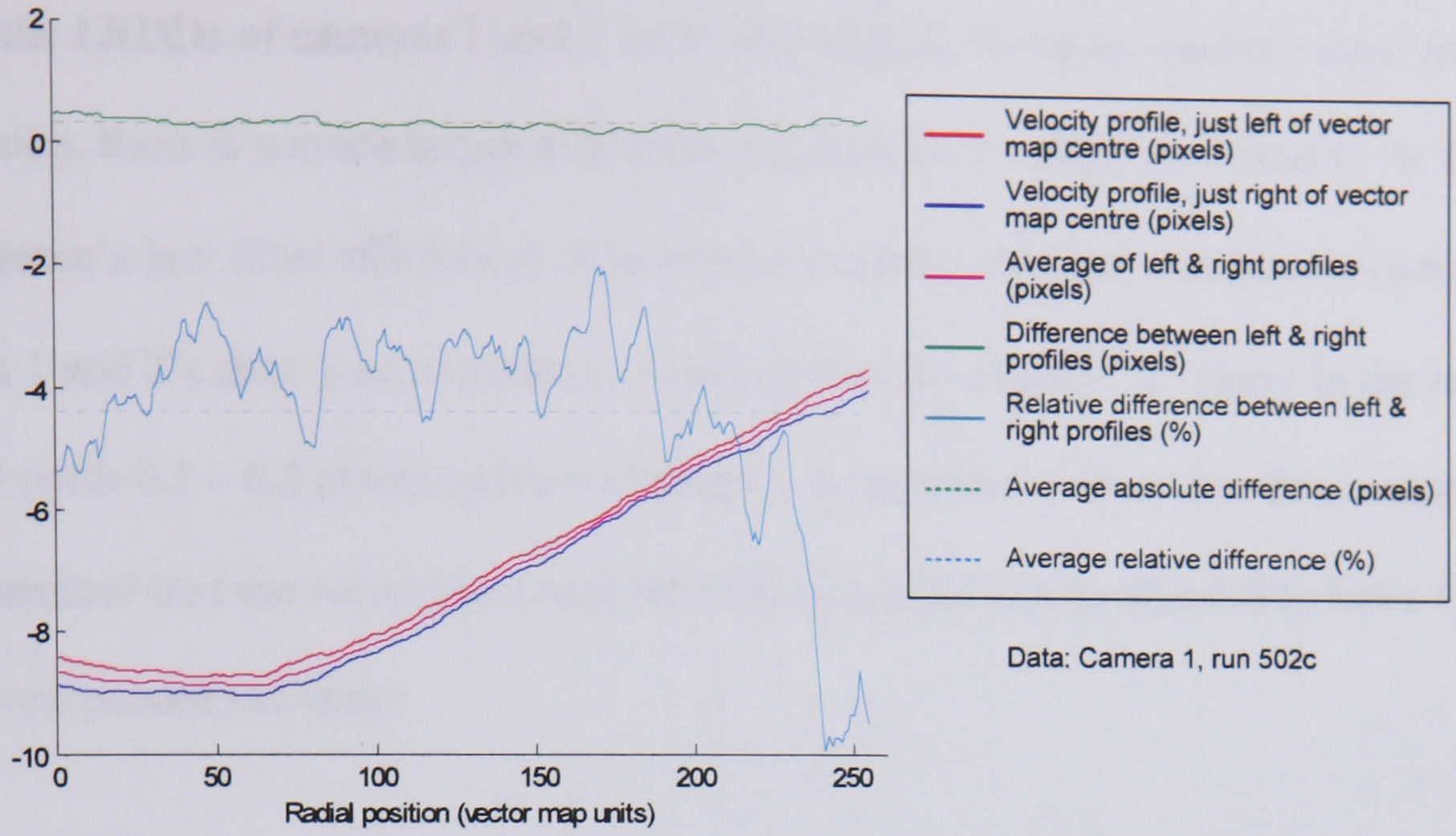

Figure 6.45 – Typical radial profile of axial-component velocity (and discontinuity).

The absolute left / right displacement difference (LRDD) thus calculated (and shown in green above), may then be compared for all of the data collected. Based on the conclusion that the correction should take an additive form only, the relative difference (shown above in cyan) is not considered. Figure 6.46 shows the mean and standard deviation of the LRDD for all data collected as part of the short cowl nozzle / OP 1.1 dataset.

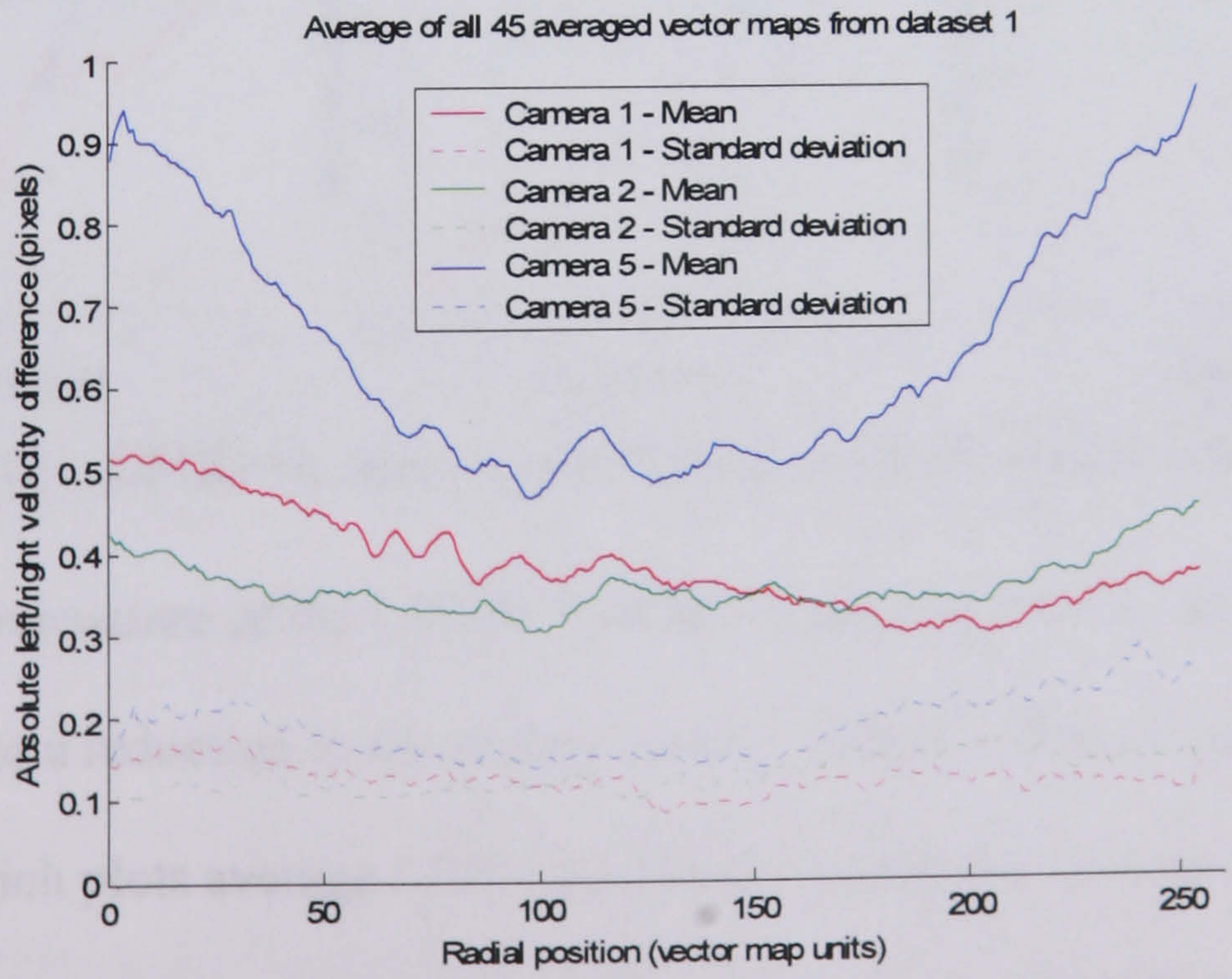

Figure 6.46 – Comparison of left / right (axial) displacement differences.

While the LRDDs of cameras 1 and 2 vary only slightly along the vector maps' radial dimension, there is a much larger difference for camera 5's maps (believed to be due to this camera's low filter efficiency). It is however notable that the standard deviation for camera 1 and 2's data is near constant, meaning that the slightly 'S' shape in the mean LRDD (with 0.1 – 0.2 pixels radial variation) is a repeatable effect. For this reason, it was surmised that the corrections applied to the maps should be allowed to have *limited* radial component variation.

6.5.2.2.4. Variation of Correction with Run Number

The fact that different cameras require different corrections is clear from Figure 6.46 on the previous page. Figure 6.47 plots the LRDD against each of the 43 measurement positions sampled, from which it becomes clear that there is also a clear difference in the bias experienced at different measurement positions.

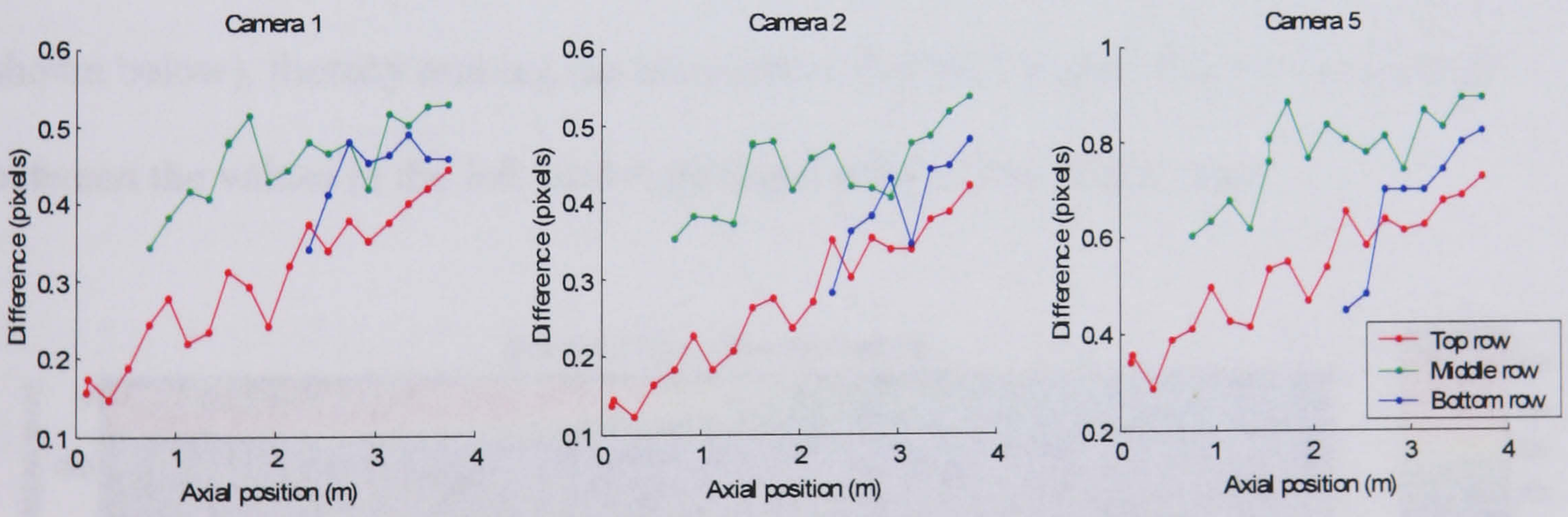

Figure 6.47 – LRDD vs. measurement position (short cowl nozzle, OP 1.1).

Given the additive nature of the LRDD, it might be assumed that its increase with axial position is due to a reduction in the source images' intensity. This is confirmed in Figure 6.48, which plots average LRDD (in black) against the average image intensity, for all of the camera 1 data shown above. The average image intensity is shown

normalised to fit the LRDD as closely as possible, and it is interesting to note that both (-intensity) and (1/intensity) fit the data just as well as each other.

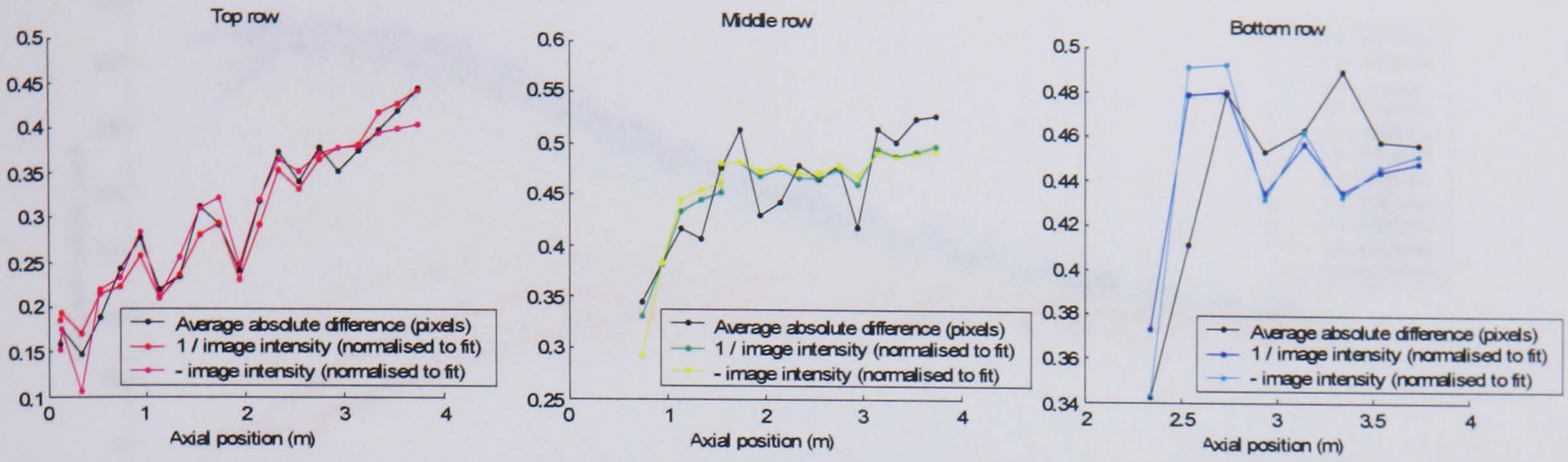

Figure 6.48 – Left/right velocity difference vs. image intensity.

6.5.2.3. Calculation of the Left / Right Correction

In order to calculate the required 2-dimensional additive corrective, a reference 'true' axial-component velocity field was required. This reference field was generated from an axially smoothed version of the PIV data itself (arranged into its mosaiced form, as shown below), thereby making the assumption that the true jet velocity lies directly between the values in the left- and right-hand sides of the vector maps.

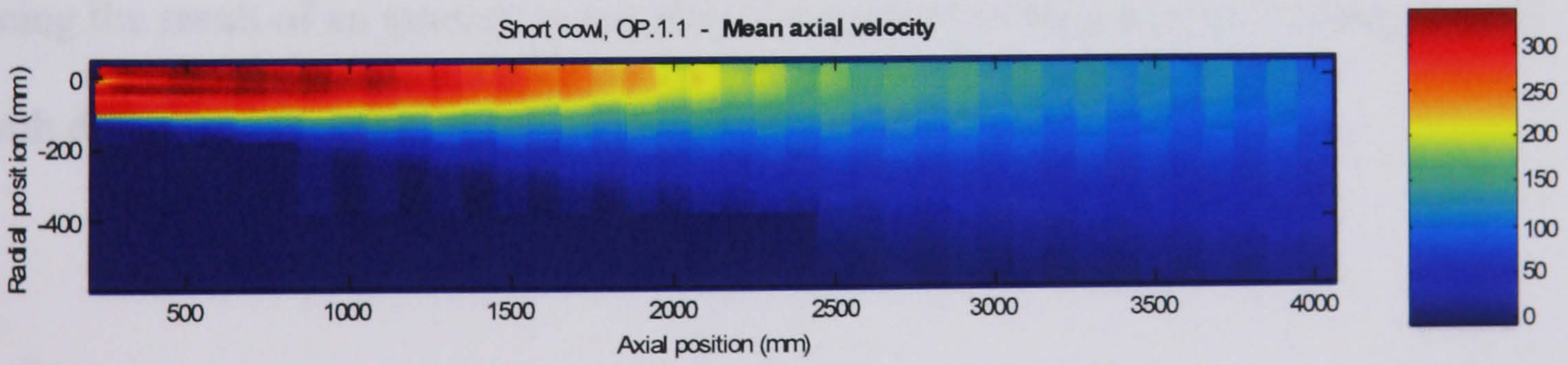

Figure 6.49 – Uncorrected mean axial velocity map (short cowl nozzle / OP 1.1).

For each of the 3 rows of measurements, 10 axial profiles (spaced 20 mm apart) were extracted, and fitted to a 5^{th} degree polynomial. 5 degrees was considered sufficient to describe the legitimate axial deviation of time-averaged jet structures, while providing

the maximum amount of smoothing possible. The raw and fitted profiles, for the top row of the dataset shown in Figure 6.49 are plotted below:

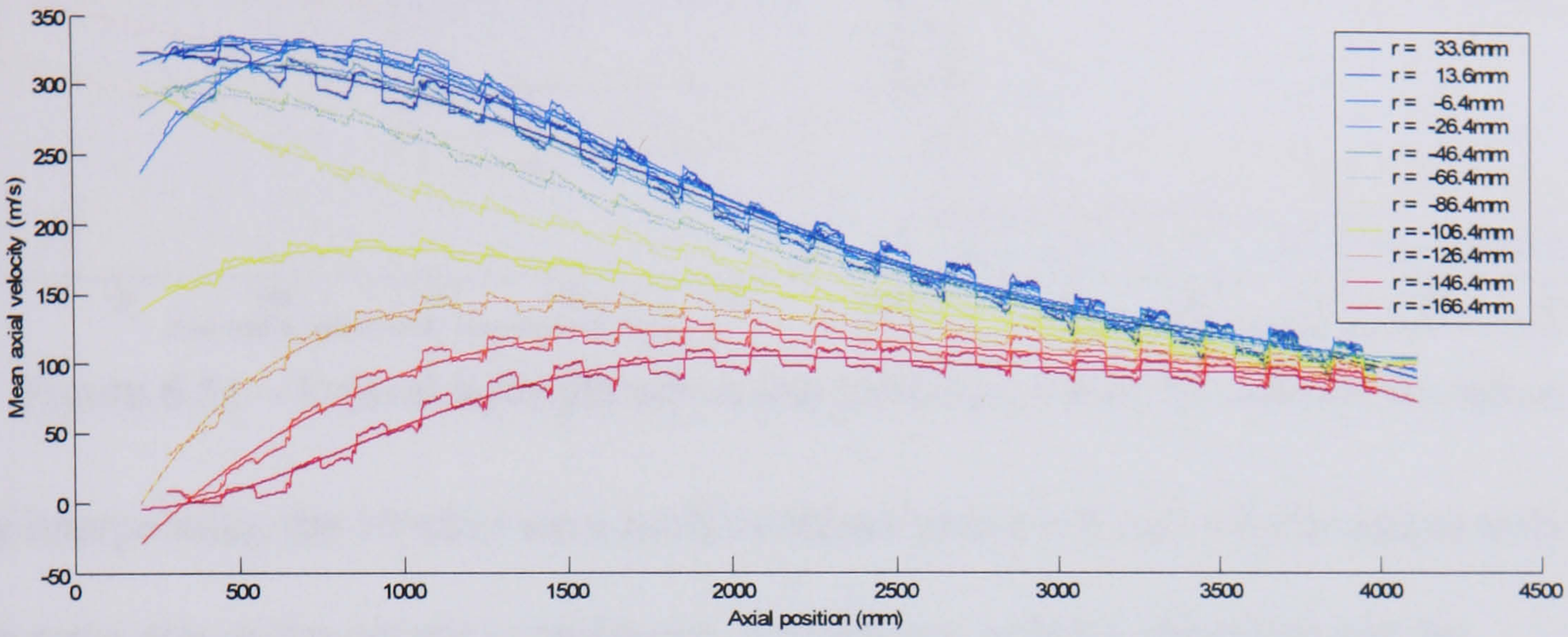

Figure 6.50 – Raw and fitted axial velocity profiles (top row, short cowl, OP 1.1).

By extracting axial profiles (in the same radial positions) from each individual vector map, the difference (or 'error') between the measured and reference velocity field can be found. Figure 6.51a shows the mean of these differences for each of the 19 vector maps acquired along the top row of data shown in Figure 6.50. The difference between the left and right-hand sides' error is obvious, and it may be observed that the profiles' values fall, then rise as the radial position of the profile increases (c.f. Figure 6.46 on page 281). It might also be noted that these values are given in m/s (not pixels), this being the result of an attempt to simplify the code's handling of overlapping samples with different Δt values*.

* Fortunately most datasets maintain a relatively constant Δt for the length of 1 row (c.f. Appendix 9.2.1)

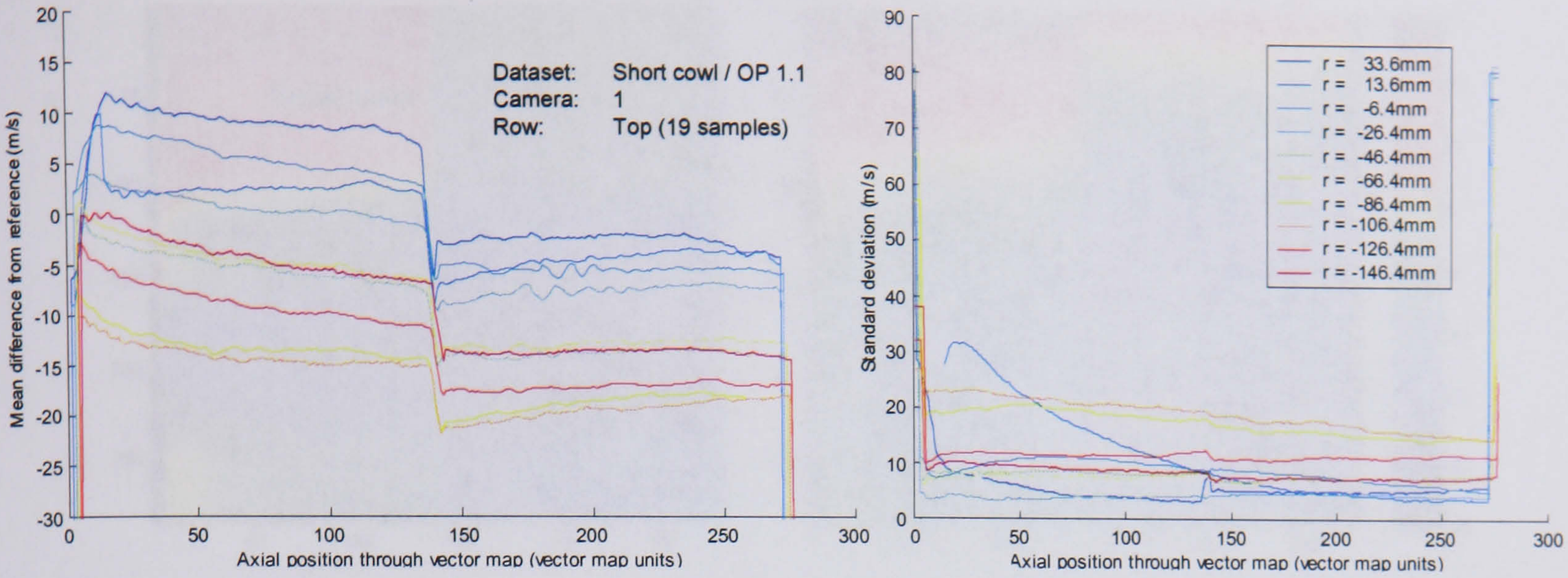

Figure 6.51 – Typical left/right correction factors; a) mean; b) standard deviation.

By interpolating the 10 axial error profiles shown above left into a 2-dimension map of the same size as the source vector maps, a simplistic additive correction may be generated. As shown in Figure 6.52a however, such a correction is heavily influenced by artefacts from upstream vector maps.

The images taken close to the nozzle contain both very bright and very dark areas, as a result of the concentration of seeding coming out of the core and bypass streams. Because the degree of vector map biasing is dependent on the raw image brightness (c.f. Figure 6.48), the resultant near-nozzle vector maps' error profiles differ significantly, depending on radial position. This is reflected in the fact that *some* of the axial profiles' standard deviation values (shown in Figure 6.51b) are much higher than others.

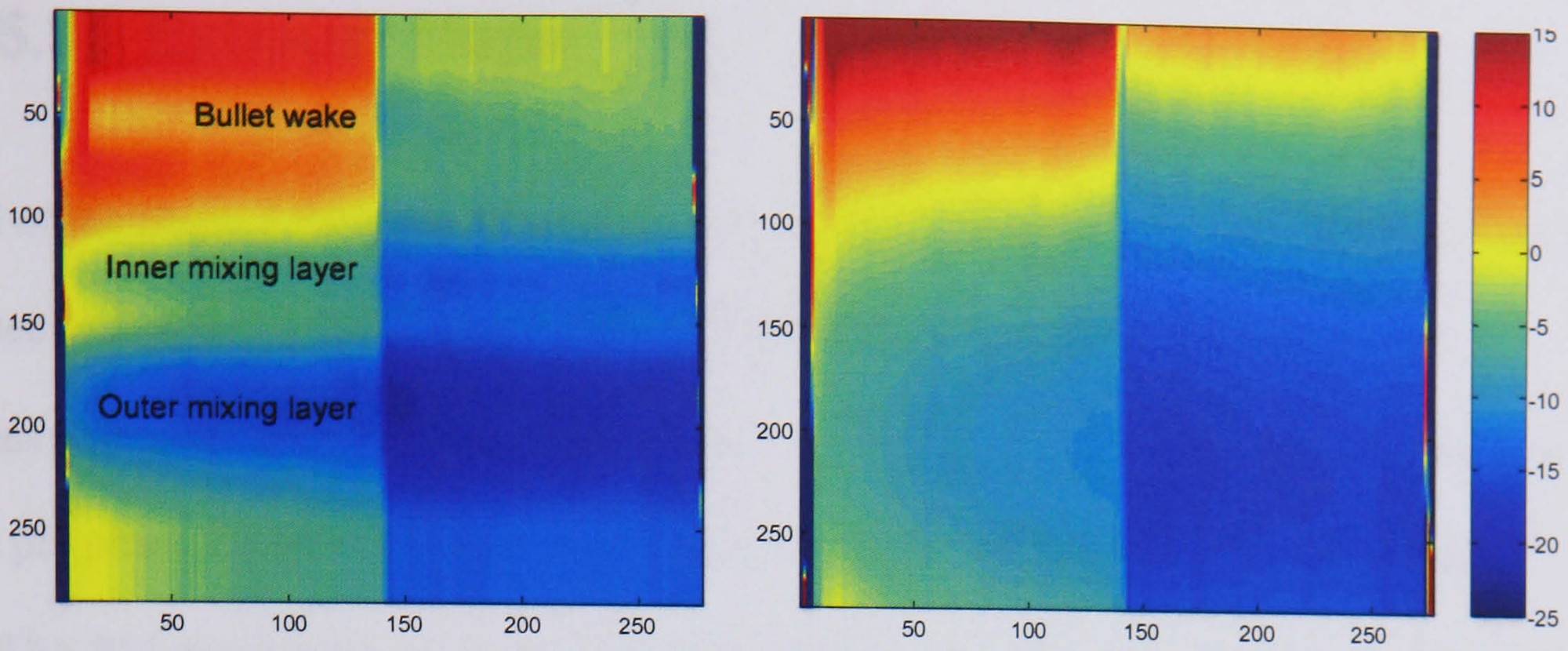

Figure 6.52a) Unsmoothed; b) Quadratically smoothed bias correction map.

In order to remove these artefacts, the correction map was instead generated by fitting a quadratic to every axial element of the mean error profiles shown in Figure 6.51, thereby producing a map with only 3 degrees of freedom in the radial ('vertical') dimension. The use of a quadratic ensures that the radial variation in the correction map may still adopt the simple curve shape depicted in Figure 6.46 on page 281.

In this way, a total of 36 (3 cameras × 4 datasets × 3 rows) axial-velocity correction map were generated, but as demonstrated in Figure 6.47, these corrections should in turn be modified according to each run's axial position, prior to being applied to the data. Based on the difficulty of producing an axially varying reference field however (due to the artefacts described above), and the relatively small (σ = 5 m/s) variation in the non-artifact areas of the error profiles (c.f. Figure 6.51b), it was decided that a correction varied according to measurement row only, would suffice.

6.5.3. Exhaust Maps

All of the phase 3 data was filtered, bias-corrected and mosaiced, using the script that is given in Appendix 9.4.11 (page 446). Due to the large quantity of data involved, extensive use is made of .MAT file 'caches', which are used to store both the raw data (as per phase 2); individual run's time-averaged statistics; and the final composited 4832 × 855 pixel maps of the jet. The data may then be displayed using the script given in Appendix 9.4.11.4 (page 460), and which is shown below:

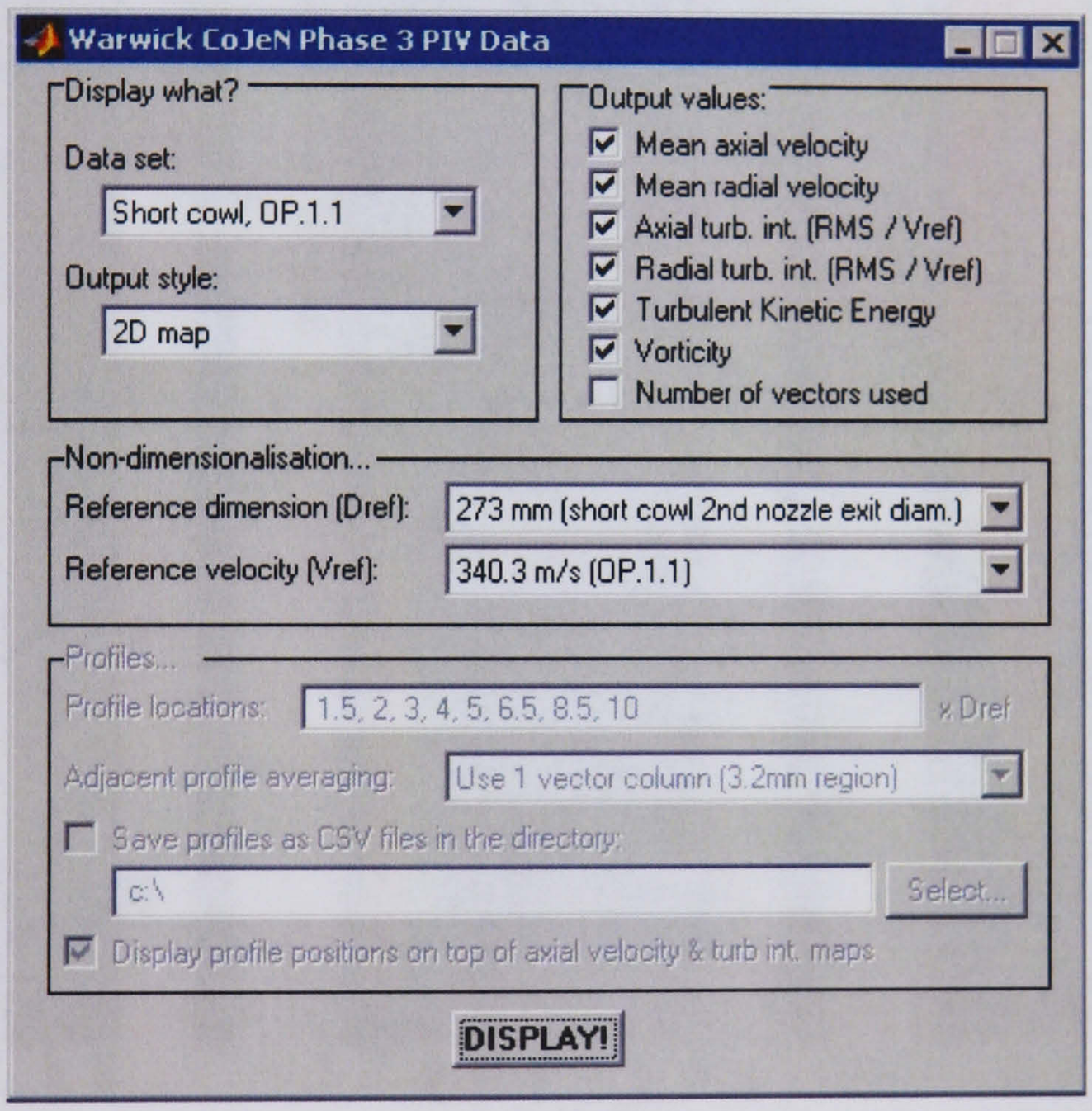

Figure 6.53 – CoJeN phase 3 display script.

Mean axial and radial, and axial turbulence velocity maps are presented on the following pages for representative short cowl and coplanar datasets. Complete sets of statistics, for all datasets, are presented in Appendix 9.2.3 on page 373.

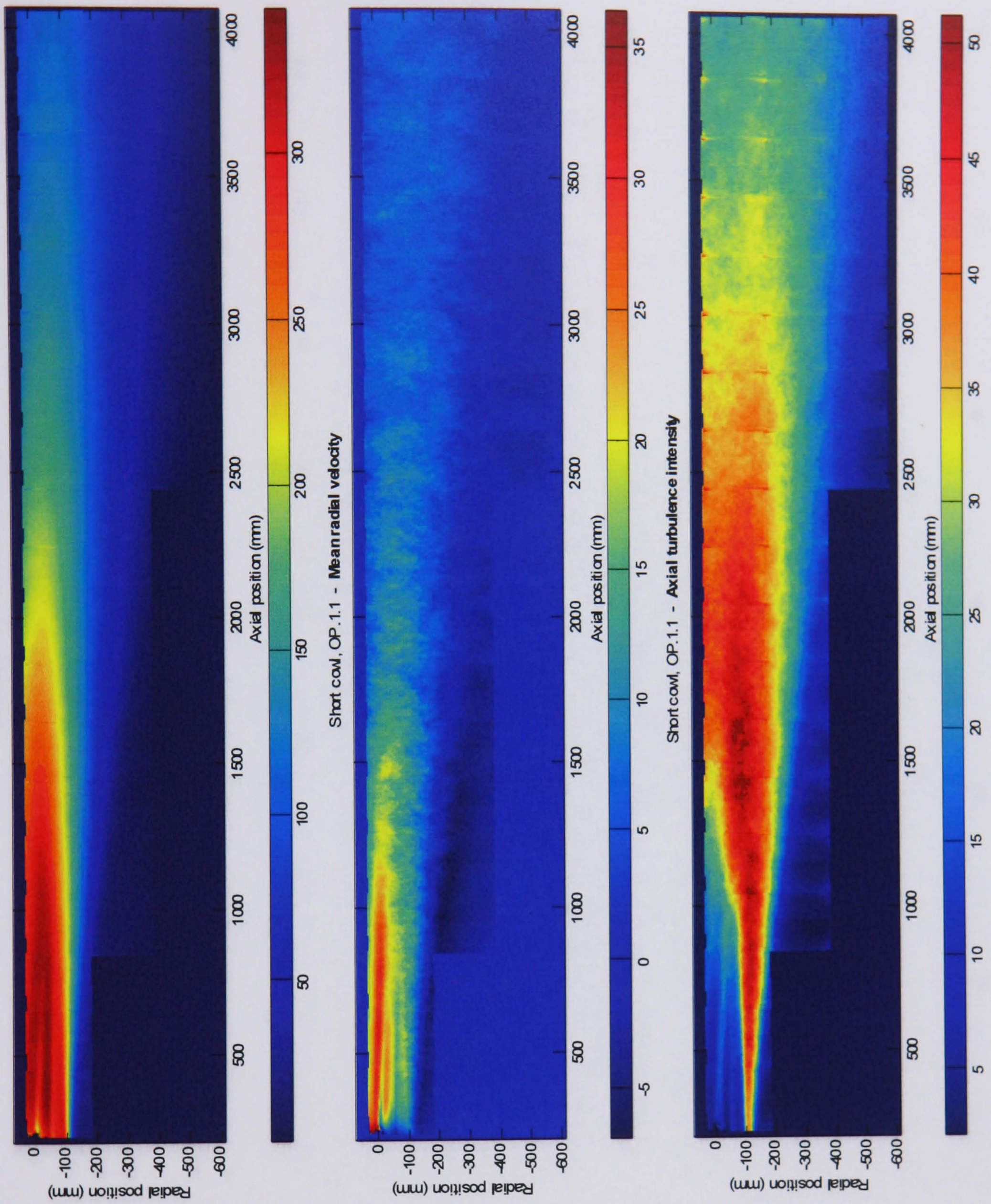

Figure 6.54 – Mean axial and radial, and axial RMS velocities (short cowl, OP 1.1).

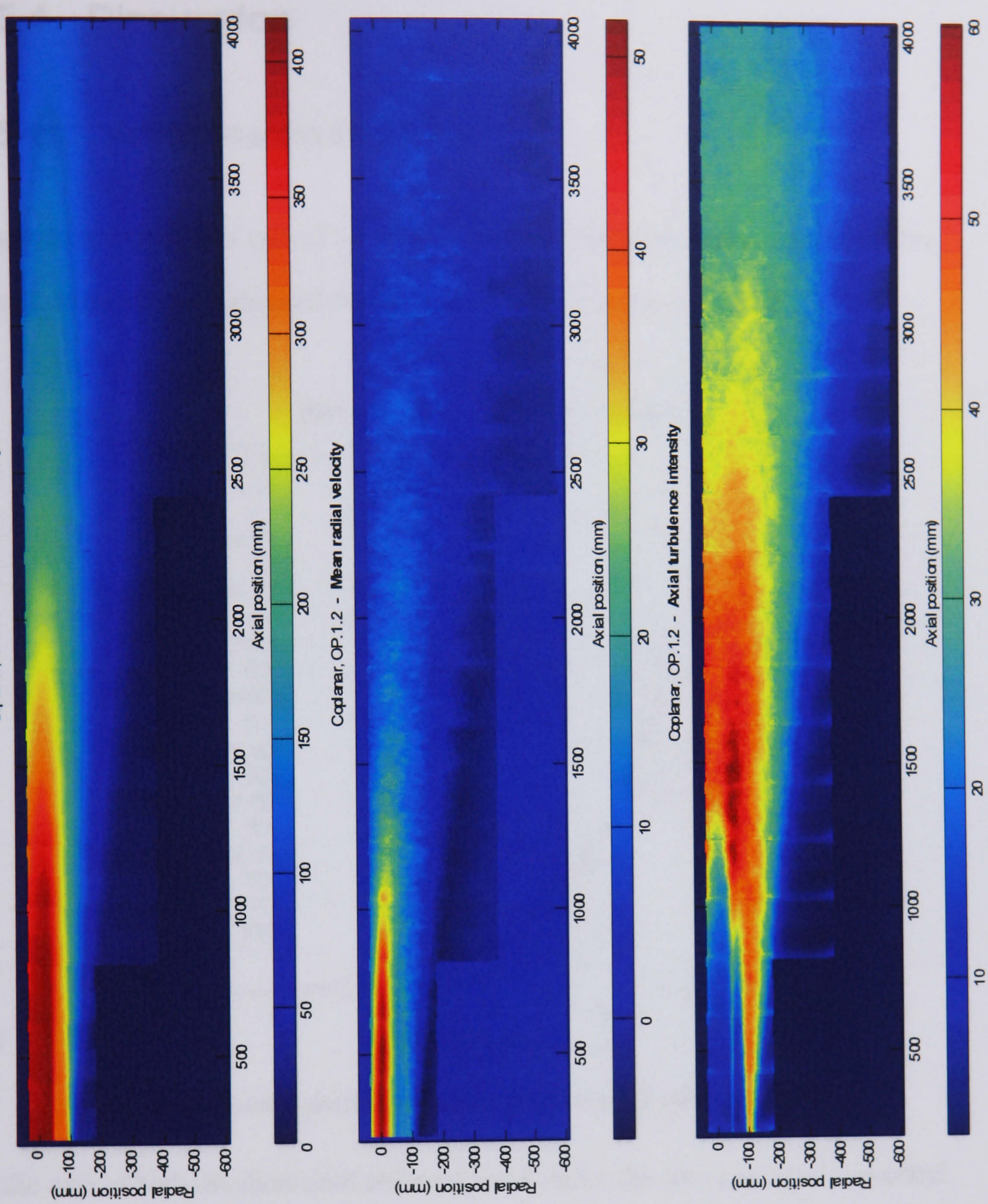

Figure 6.55 – Mean axial and radial, and axial RMS velocities (coplanar; OP 1.2).

6.5.4. Discussion

6.5.4.1. Aerodynamic Features

Figure 6.56 illustrates a typical set of normalised* mean axial velocity radial profiles, examination of which allows the potential core lengths to be measured.

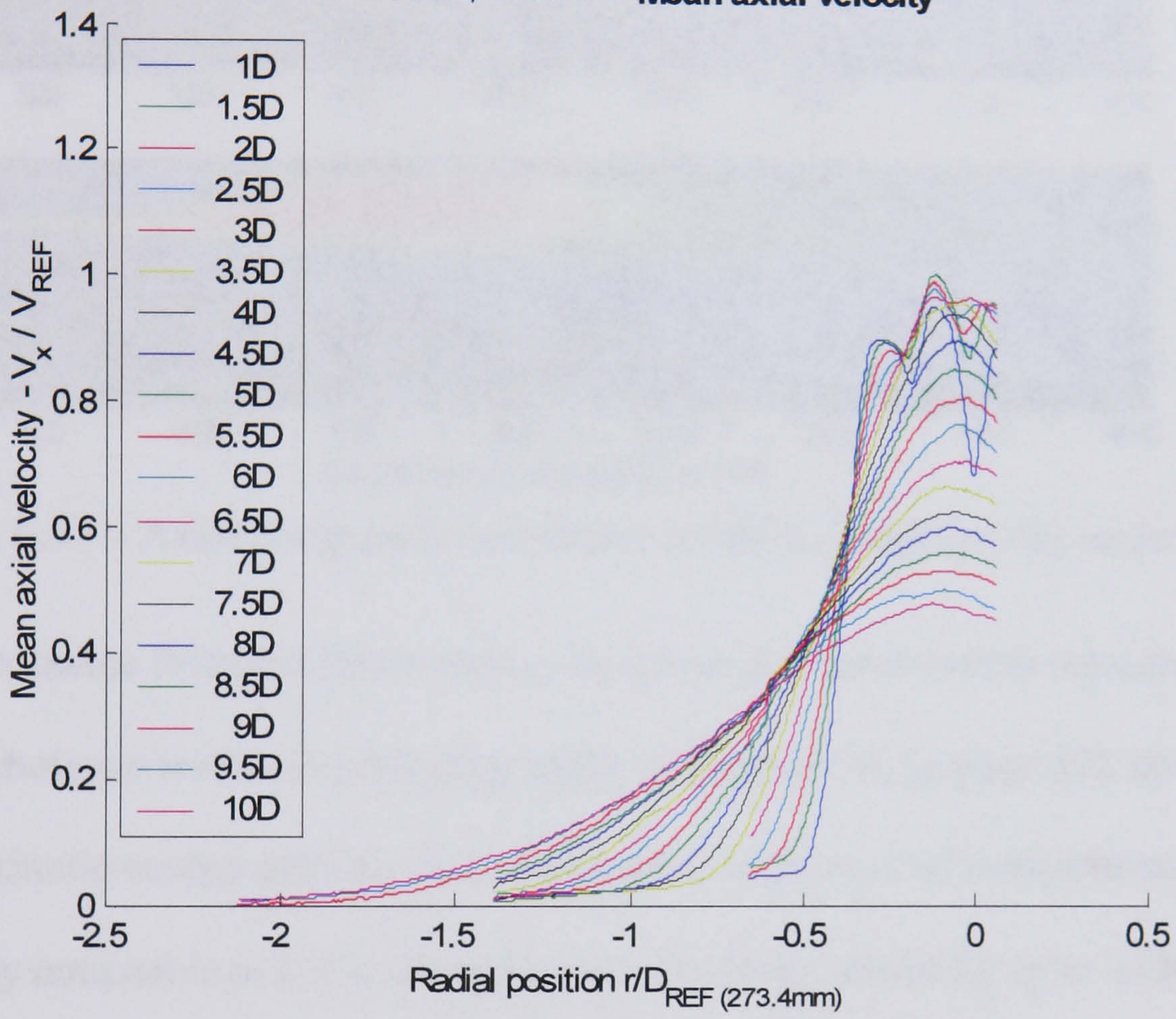

Figure 6.56 – Radial profiles of mean axial velocity (short cowl; OP 1.1).

In the case of both the short cowl and coplanar nozzles, the core and bypass potential cores were found to end around 4.0 and 2.5D from the secondary nozzle exit. The similarity between the two nozzles is reiterated in Figure 6.57, which compares the axial turbulence intensity for both nozzles, as measured under OP 1.2. It can be seen that there is only a very small increase in the turbulence produced by the short cowl nozzle,

* Data is normalised by the second nozzle exit diameter and the core fully-expanded velocity (c.f. pages 137 and 138).

and next to no difference in the position of the mixing regions. This is notable however, given the larger physical diameter of the short cowl nozzle (the camber in its inner wall meaning that its *aerodynamic* diameter is approximately the same as the coplanar nozzle).

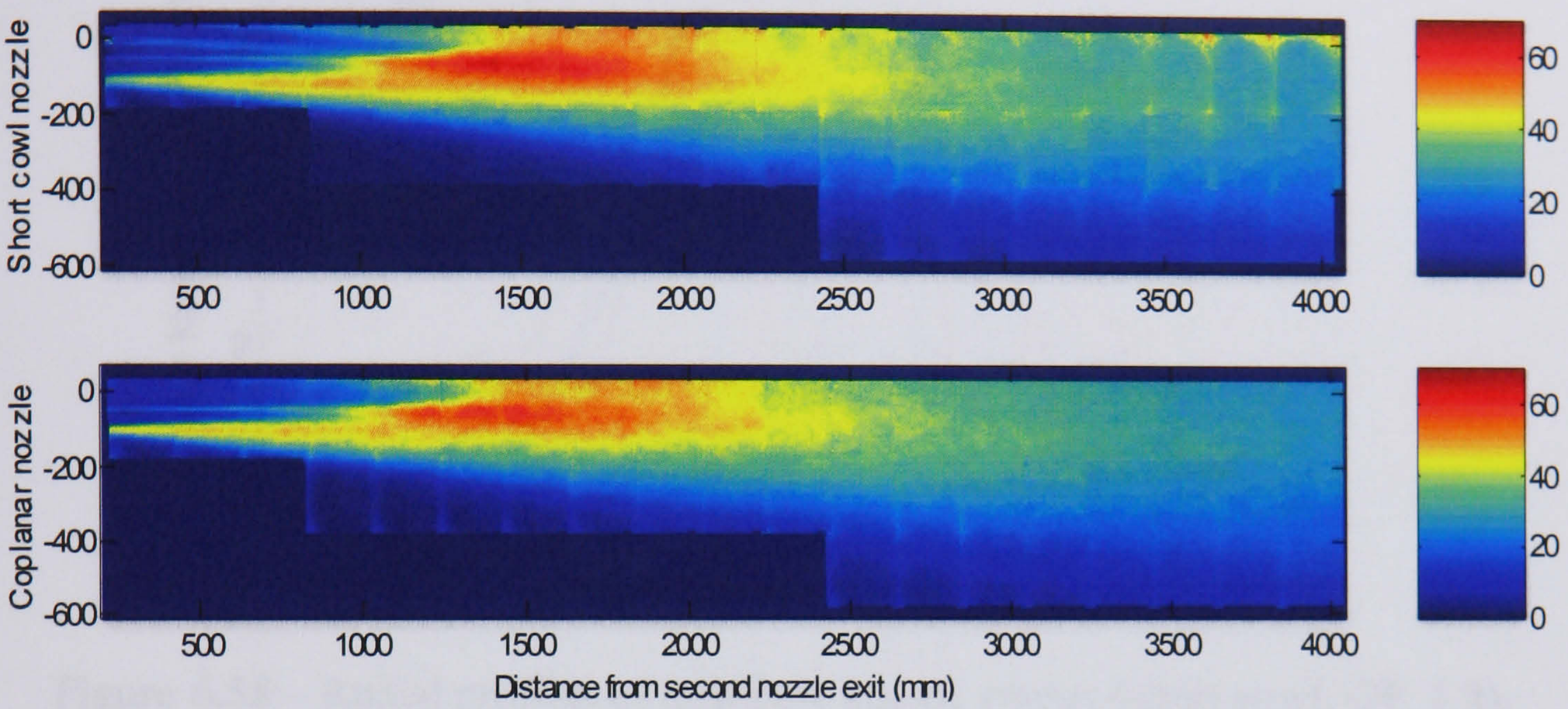

Figure 6.57 – Axial component turbulence levels for both nozzles under OP. 1.2.

As may be visible from the figure above, the phase 3 measurements corroborate the uneven turbulence levels found during phase 2. Figure 6.58 on page 292 shows a set of turbulent kinetic energy profiles for a representative short cowl measurement. As is particularly noticeable at 2.5D, the turbulence levels are anything up to 150% greater on the lower half of the jet, though unlike the phase 2 measurements (c.f. page 264) only 1 shear layer is covered by the measurement, thereby preventing a comparison.

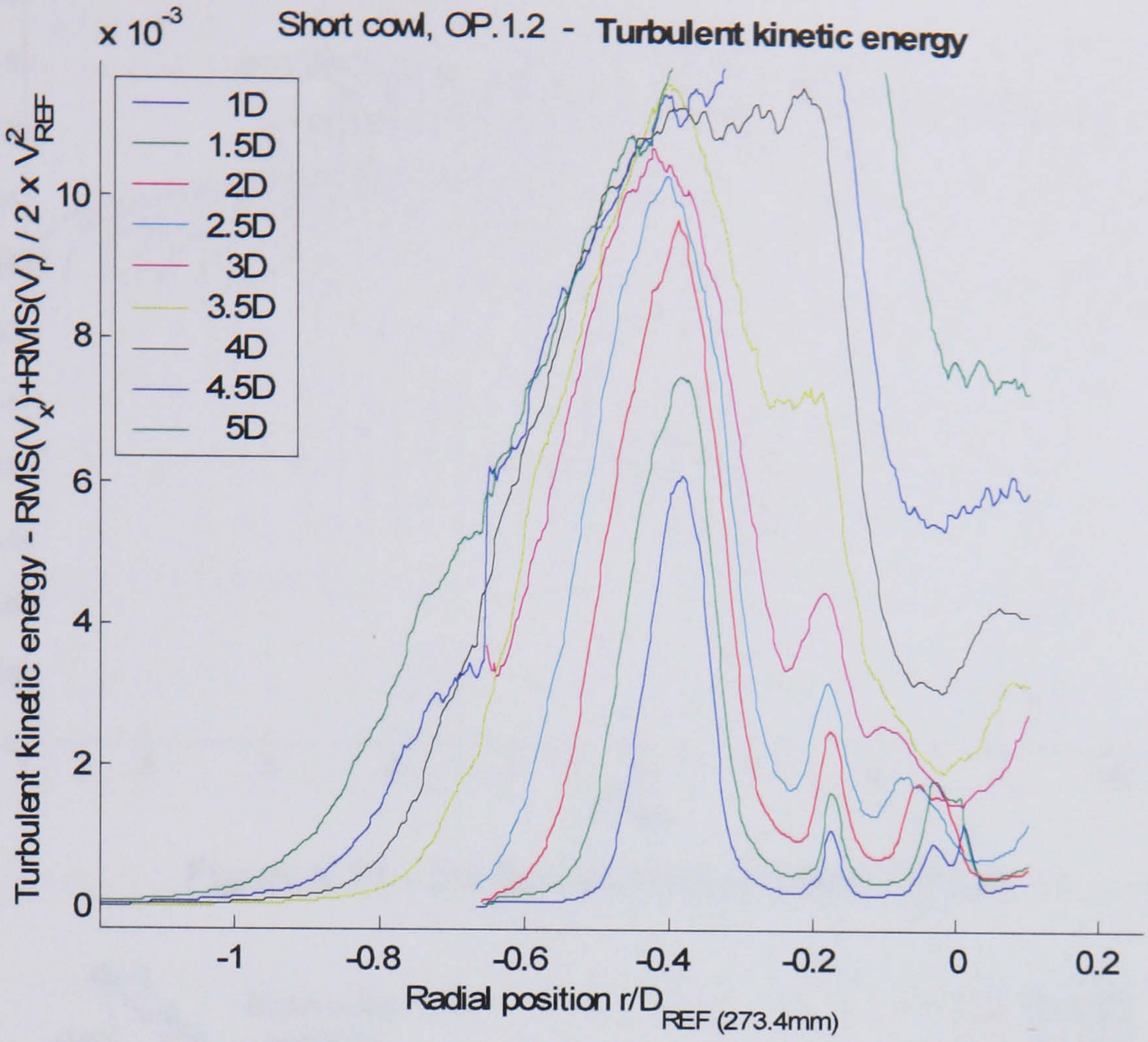

Figure 6.58 – Radial profiles of turbulent kinetic energy (short cowl; OP. 1.2).

6.5.4.2. Jet Deviation

One of the more notable features of the maps shown on pages 288 and 289 is the high downward bias of the mean radial component of velocity. There is also an associated deviation visible in the wake produced behind the short cowl nozzle's bullet. In order to quantify these effects, radial profiles were extracted every $D_{REF}/4$, and a central section thereof fitted with a 7^{th} order polynomial (which was found to fit the profiles almost perfectly). The maximum and minimum positions of the polynomial function (represented by squares and circles in Figure 6.59) are plotted against their axial position in Figure 6.60.

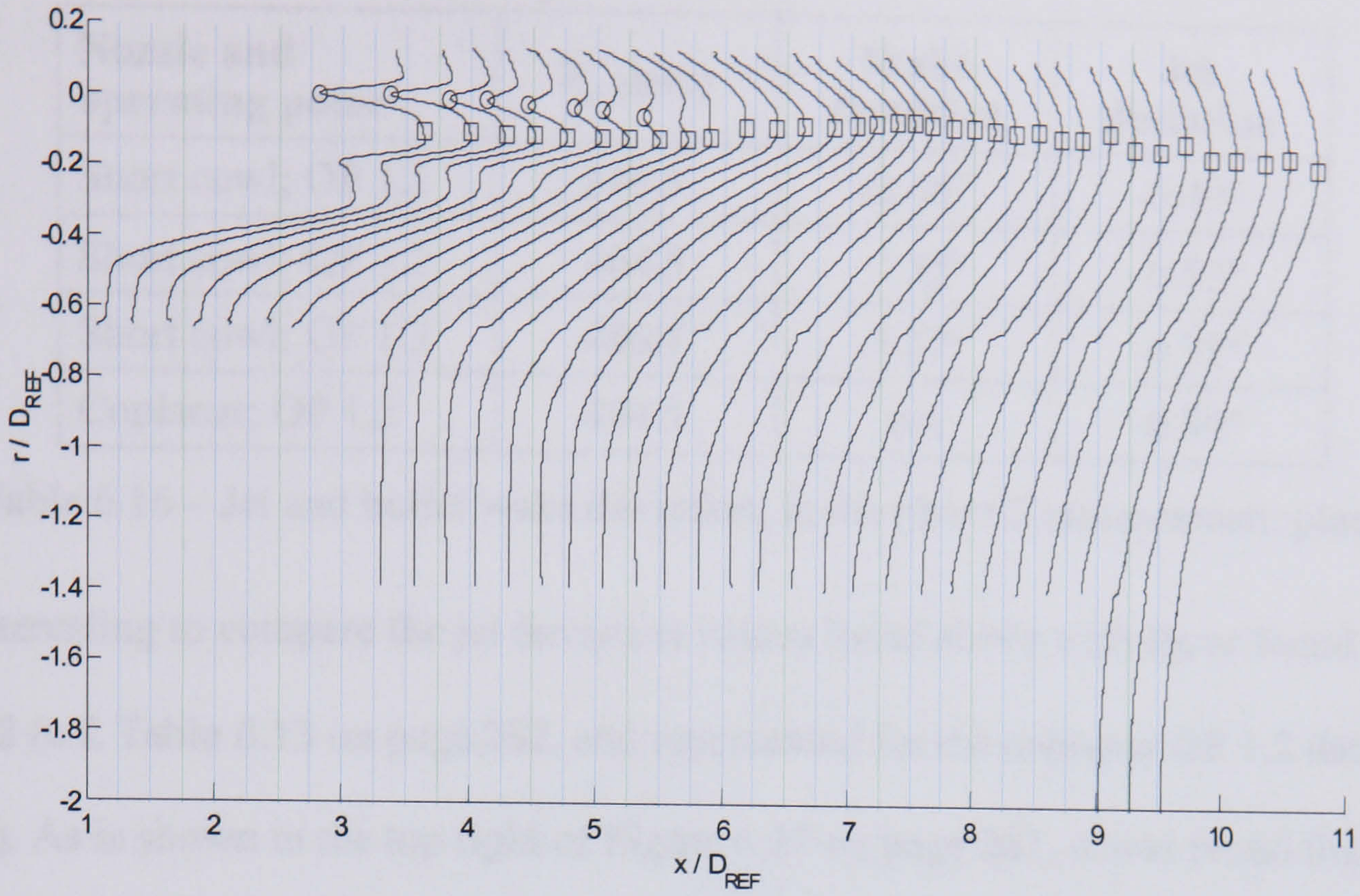

Figure 6.59 – Jet deviation (short cowl, OP1.2).

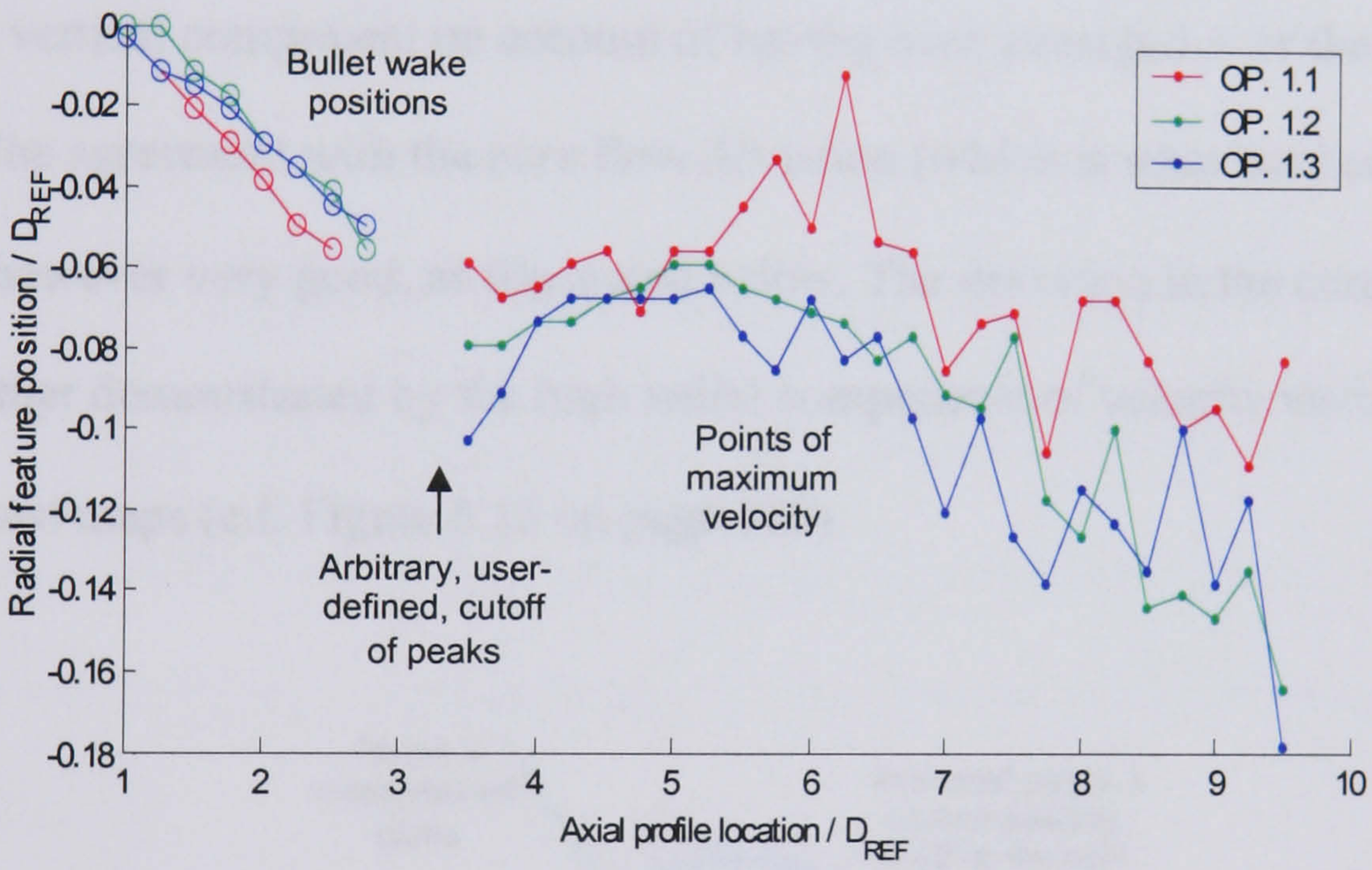

Figure 6.60 – Bullet wake position and jet centre vs. axial position.

The angles of the jet and wake – listed in Table 6.16 on page 294 – were calculated by means of a linear fit, applied to the data shown above. The lack of a distinguished peak in the mean axial velocity profiles leads to a certain degree of uncertainty in the measurement of the jet deviation, but it can be seen that there is a clear, almost proportional, relationship between the bullet wake angle, and the core jet speed V_p.

Nozzle and operating point	V_p **(m/s)**	**Wake deviation**	**Jet deviation**
Short cowl; OP 1.1	340.3	-2.06°	-0.40°
Short cowl; OP 1.2	404.5	-1.85°	-0.83°
Short cowl; OP 1.3	480.7	-1.52°	-0.72°
Coplanar; OP 1.2	404.5	n/a	-0.80°

Table 6.16 – Jet and bullet wake deviation, in the phase 3 measurement plane.

It is interesting to compare the jet deviation values listed above with those found during phase 2 (c.f. Table 6.13 on page 262, and represented for the coplanar OP 1.2 dataset below). As is shown in the top right of Figure 6.27 on page 261, it was found that the jet centre position changes with speed, with the *overall* phase 2 deviations only having a negligible vertical component on account of having been averaged over the whole of the exhaust. The agreement with the *core* flow deviation (which is what has been measured above) is however very good, as illustrated below. The deviation in the core flow is of course further demonstrated by the high radial components of velocity visible in the large exhaust maps (c.f. Figure 6.55 on page 289).

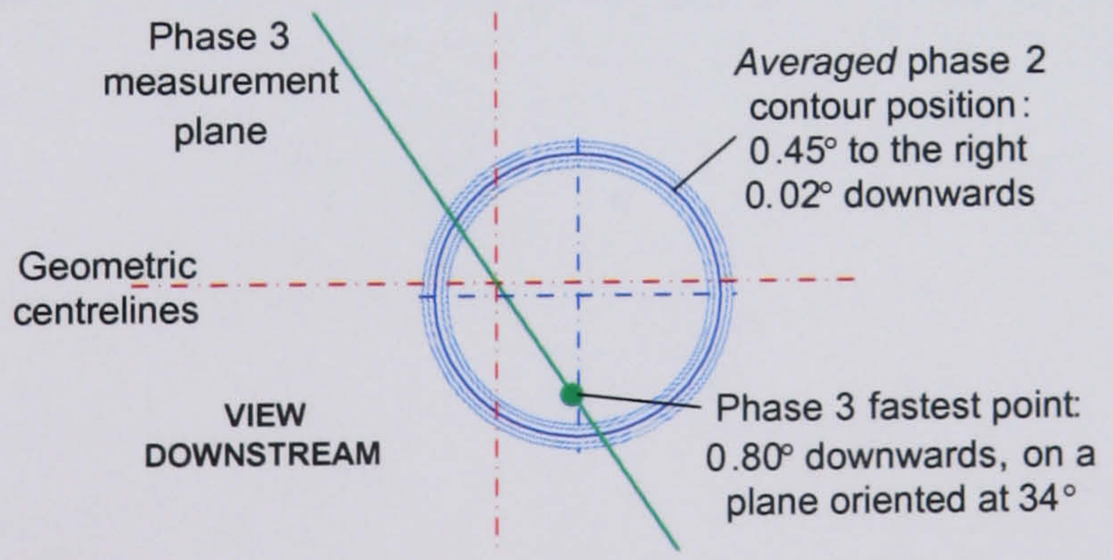

Figure 6.61 – Phase 2 and 3 jet deviation measurements (coplanar; OP 1.2).

6.5.4.3. Comparison with LDA

As stated in the previous chapter, LDA measurements were made during phases 3 and 4; both within the PIV measurement volume, and along a horizontal radial profile, as shown below:

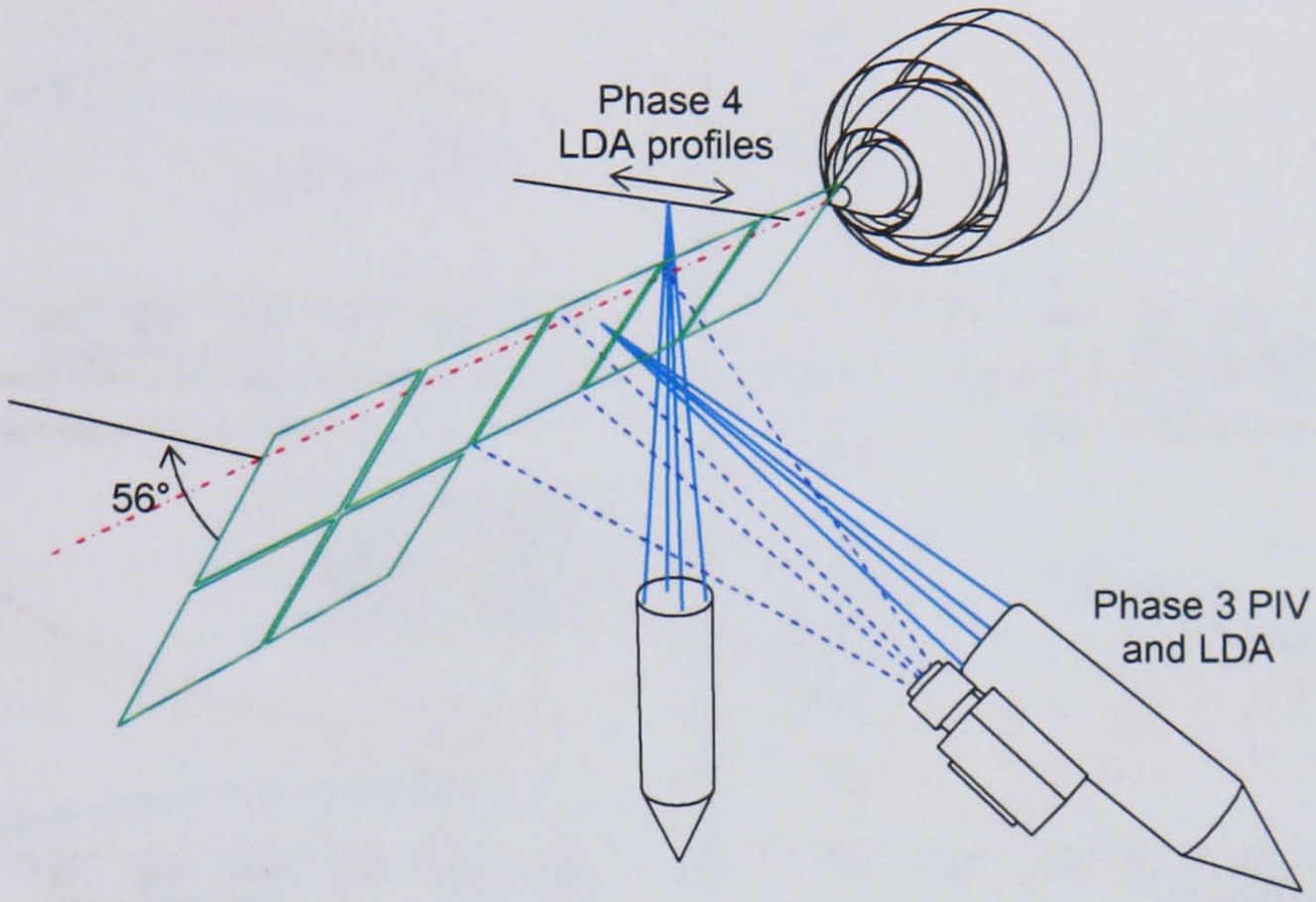

Figure 6.62 – Phase 3 and 4 LDA measurements.

The LDA data (where available) and phase 3 PIV measurements are plotted side by side on page 296, with the axial component of velocity shown on the left, and the radial component on the right. A number of observations, stemming from Figure 6.63, are listed on page 297.

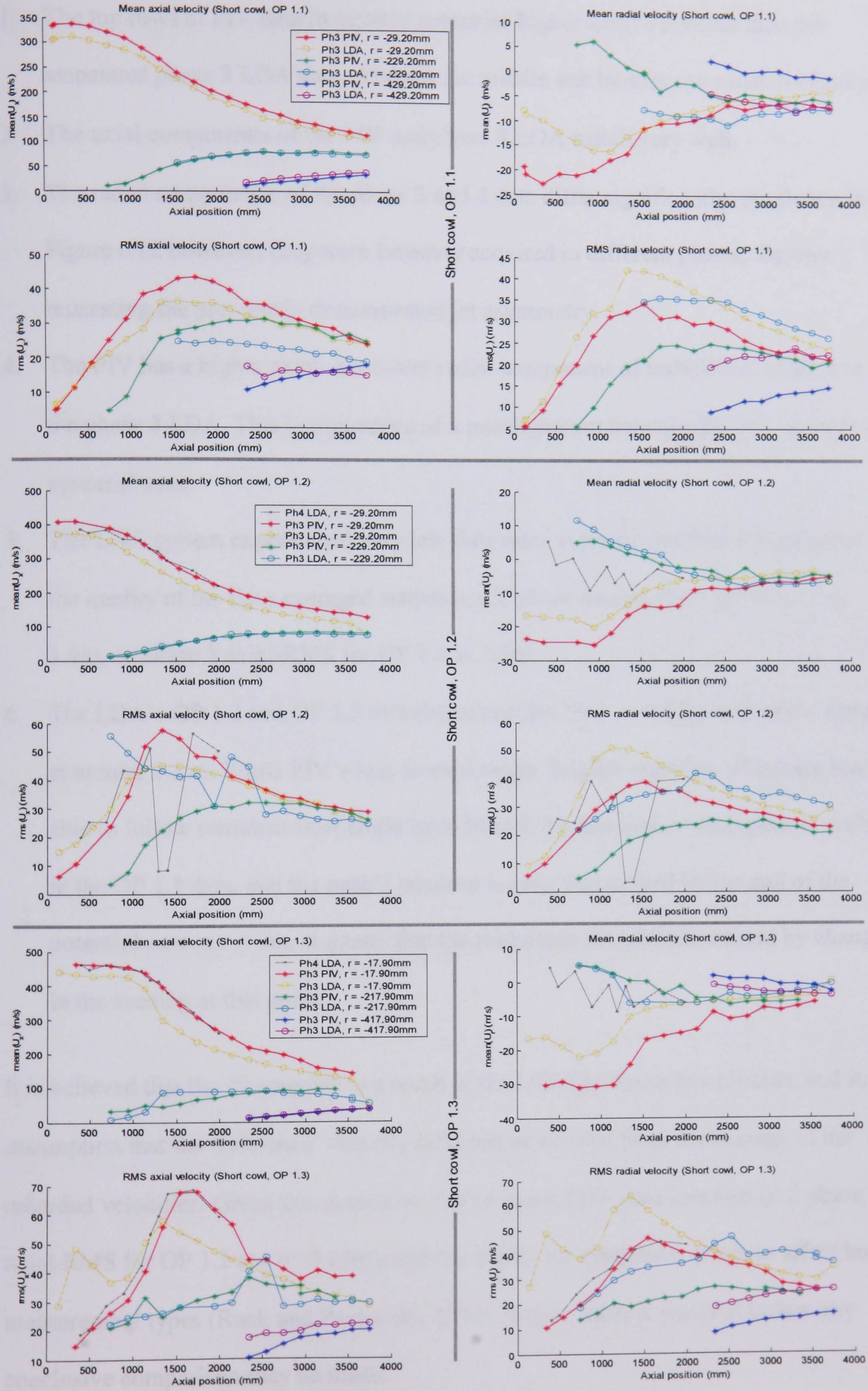

Figure 6.63 – Comparison of PIV and LDA data.

1. The top rows of PIV data invariably comprise higher axial velocities than the associated phase 3 LDA data, whereas the middle and bottom rows match closely.
2. The axial components of the PIV and phase 4 LDA match very well.
3. The radial components of the phase 3 and 4 data differ significantly. As shown in Figure 6.62 however, they were however acquired in different planes, thereby reiterating the previously demonstrated jet asymmetry.
4. The PIV has a higher axial- but lower radial-component of turbulence, relative to the phase 3 LDA. This is suggestive of a misalignment between the PIV and LDA systems' axes.
5. The LDA system experienced very low data rates at times, and this has impacted the quality of the time-averaged statistics, c.f. phase 4 axial-RMS for OP 1.2 at 1.4m, or phase 3 axial-RMS for OP 1.3 at 2.5m.
6. The LDA's OP 1.2 and OP 1.3 turbulence profiles for r = -0.22m both show a peak at around 2.2 m. While PIV's bias toward larger, brighter particles which are less able to follow turbulent flow could be to blame, the fact that no such peak is visible in the OP 1.1 data, and the peak's position *beyond* that caused by the end of the potential core at r = 0m, suggests that the peaks may be artefacts caused by changes in the seeding at that point.

It is believed that the 1st anomaly is a result of the left/right correction process, and its assumption that the 'reference' velocity field can be derived from the average of the recorded velocities. Given the anomalies visible in the LDA data however (c.f. phase 3 axial-RMS for OP 1.2 at r = -0.23m), and the ability for systematic errors to affect both measurement types (Ruck and Pavlovski, 1993), further work is required before any conclusive comparison may be made.

6.6. Phase 4 Processing & Results

As described in Section 6.3.1, the initial stage of phase 4 data processing comprised identification of the images belonging to each set of 6 time-series exposures (c.f. Figure 6.4 on page 226). Once this had been done, the images could be processed in exactly the same way as was described in Chapter 3, and as illustrated below:

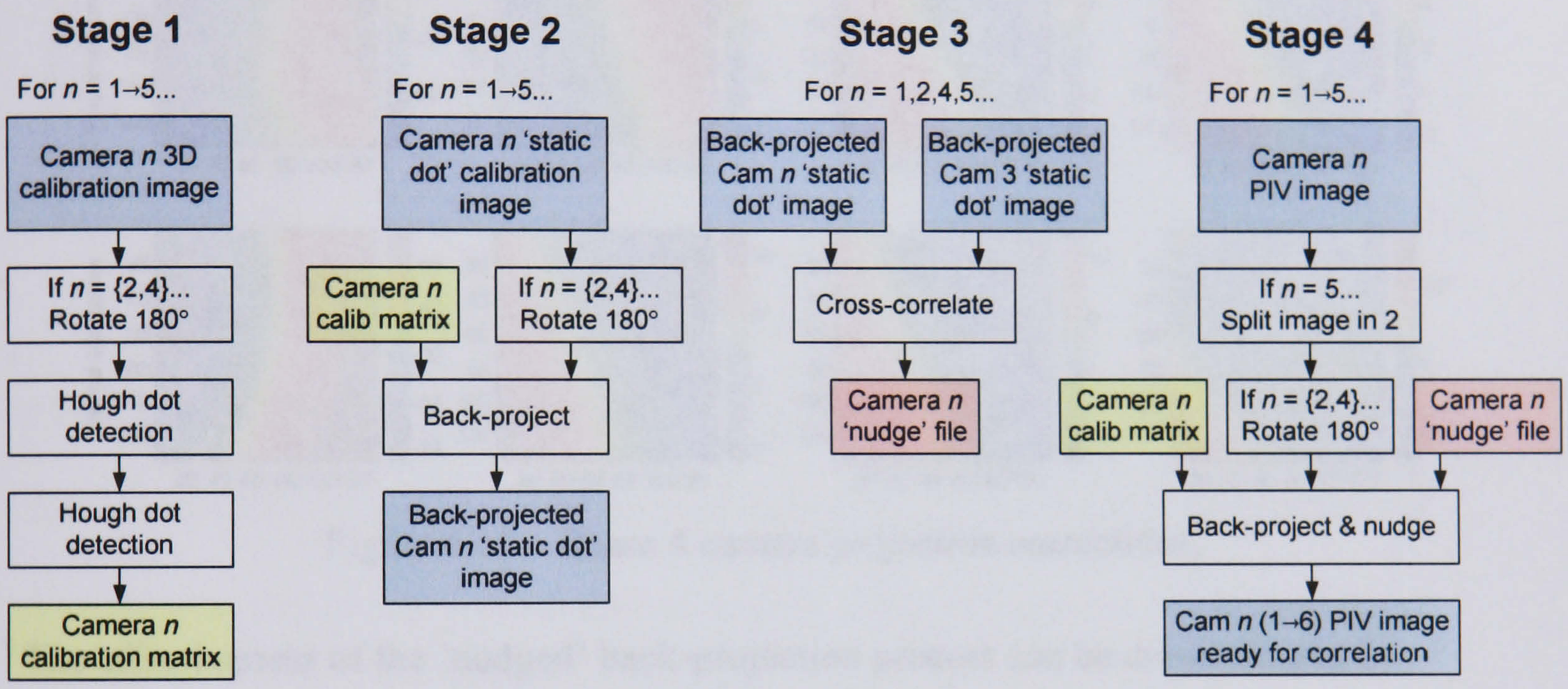

Figure 6.64 – Phase 4 processing.

6.6.1. High-Resolution Back-Projection

In order to be able to quantify the errors introduced by the back-projection process, and therefore calculate the amount by which to 'nudge' correct the images, 20 simultaneous exposures of 'Magican' spray smoke were captured by each of the cameras every morning. The ensuing images from cameras 1, 2, 4 and 5 were cross-correlated against that from camera 3, and the resulting vector maps averaged. The details of the cross-correlation and subsequent vector filtering operations are given in Table 6.17 on the next page, with the resulting corrections shown in Figure 6.65.

Correlation:	Multi-pass second-order correlation (c.f. p.[fig2.48]) with Whittaker image reconstruction between passes. 128px (50%) × 1 → 32px (50%) × 2
Vector filtering:	Median(1.2,1); Fill once
Averaging:	Only vectors within 1 × time-history RMS were included.
Post-processing:	Median(0.5,1); Remove(15); Fill all; Smooth(1 × 3×3)

Table 6.17 – Phase 4 projection correction correlation settings.

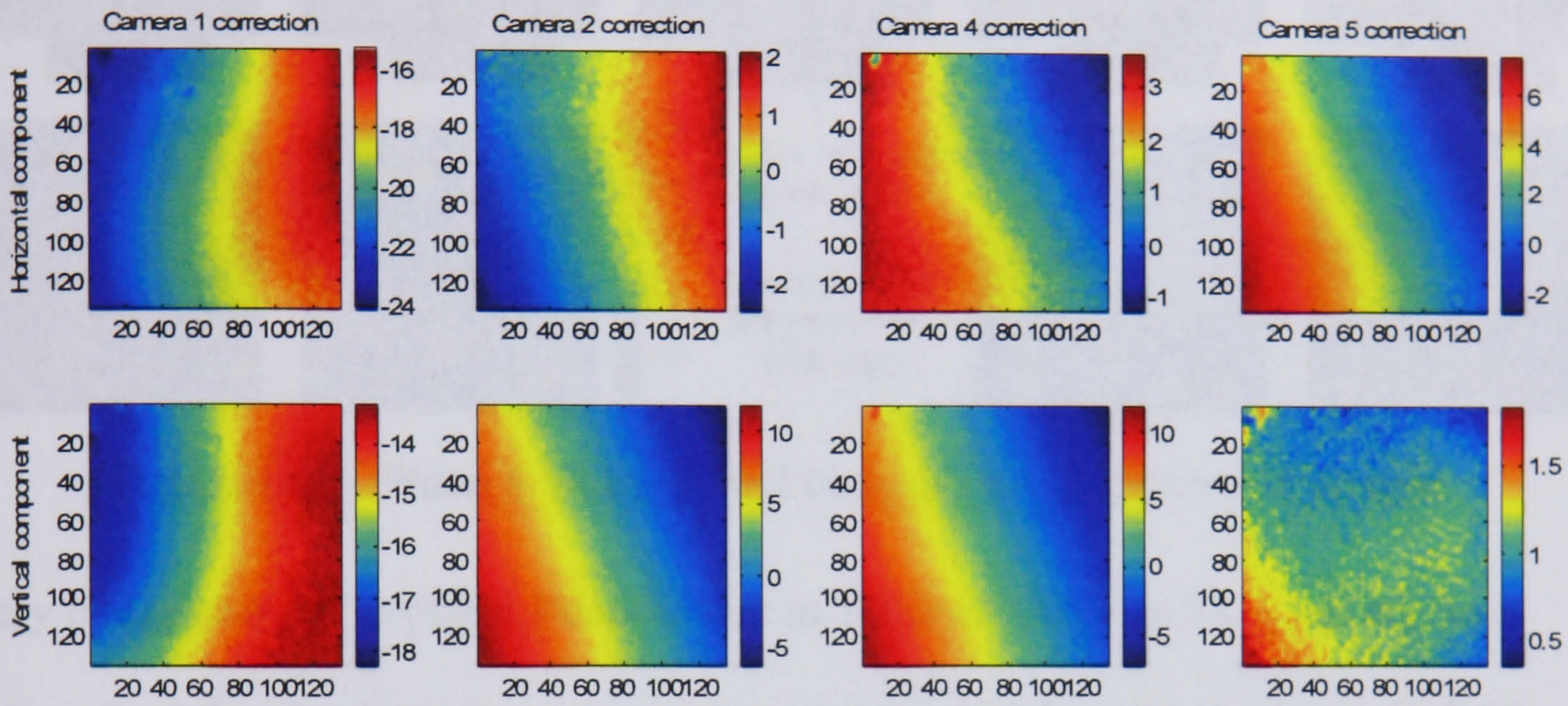

Figure 6.65 – Phase 4 camera projection corrections.

The effectiveness of the 'nudged' back-projection process can be demonstrated by cross-correlating thus corrected Magican images against each other, as shown in Figure 6.66 on page 300. It can be seen that the maximum difference in position relative to camera 3 is typically no greater than 0.1 px, or ~1% of the average moving particle displacement.

It is interesting to note the slight difference in particle brightness between those cameras in slight forward-scatter, and those in slight back-scatter (cameras 2 and 4). It can also be seen that the most accurately back-projected images result from camera 5, whose correction map contained the lowest gradients. Similarly the small areas of high value in Figure 6.66 correspond to those areas of the Figure 6.65 maps that are insufficiently

smoothed or, in the case of the top left corner, averaged from too few vector maps (as can be seen below, the Magican seeding rarely filled the entire FOV).

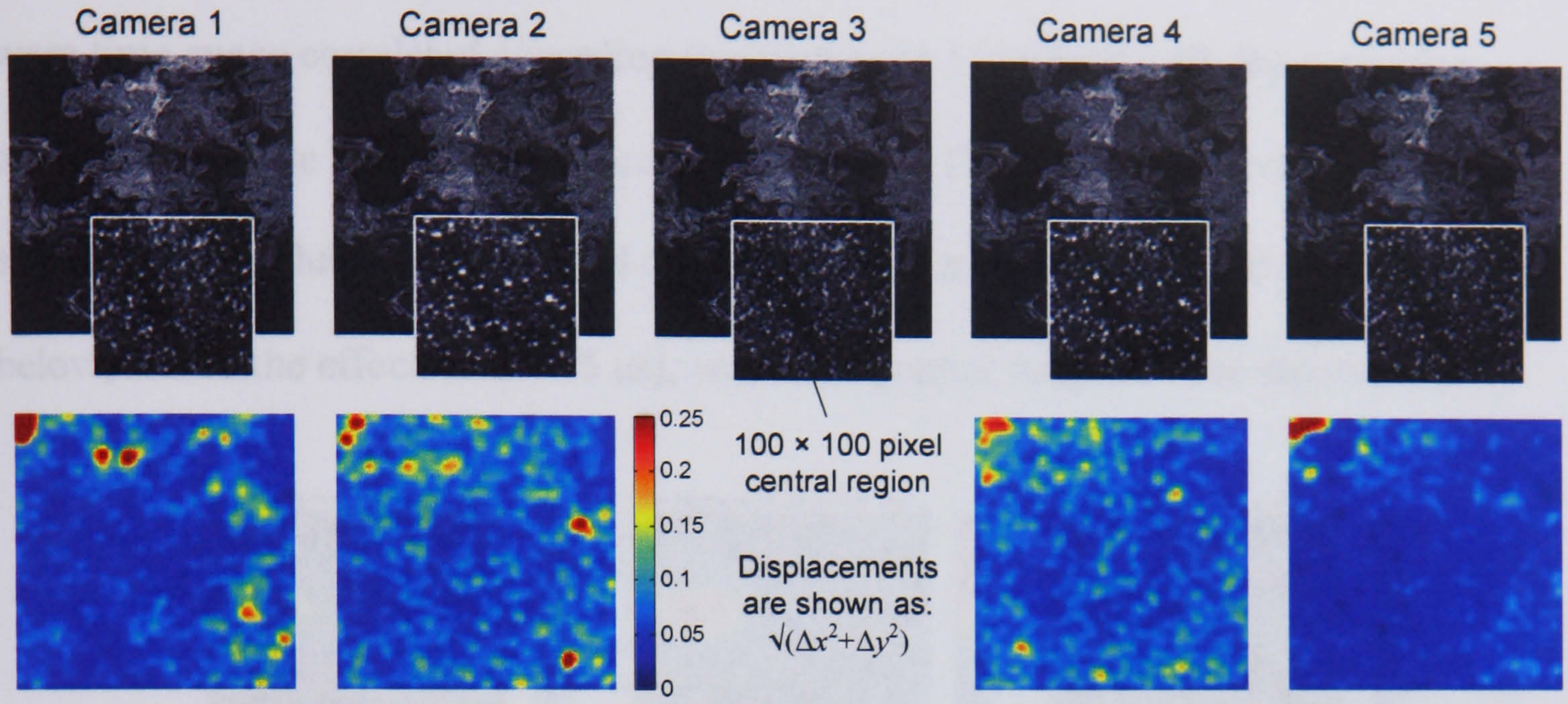

Figure 6.66 – Phase 4 'nudged' and back-projected calibration images.

Every image pair of the phase 4 data (listed in Table 6.3 on page 227), having been back-projected and 'nudged', was cross-correlated using the settings shown in Table 6.10 on page 252. Shown below are just 2 of the ~26,000 'movies' thus produced.

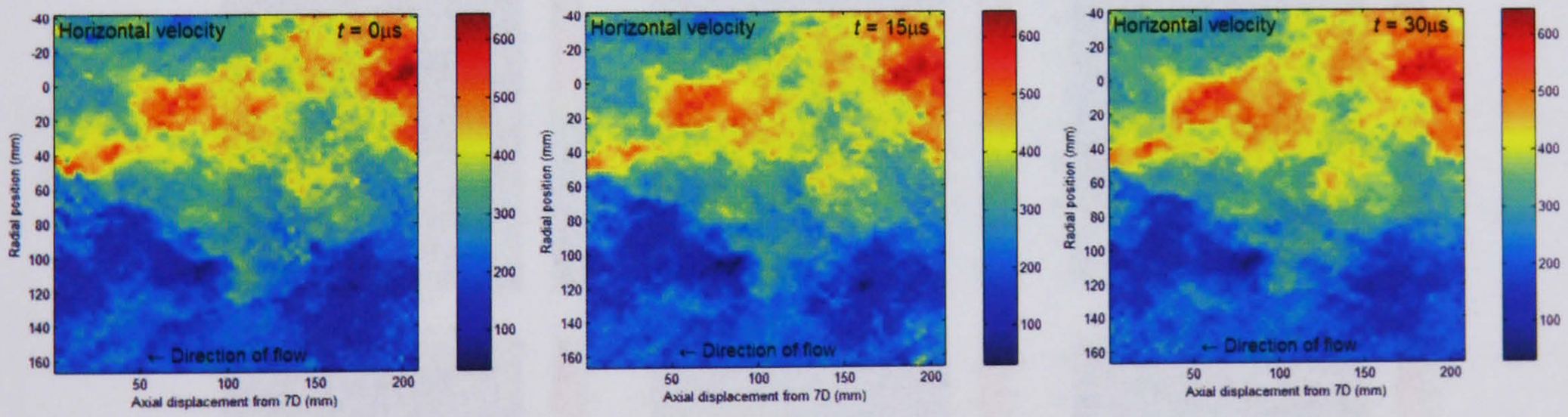

Figure 6.67 – 67 kHz 'movie' of axial flow velocity (2m from short-cowl nozzle).

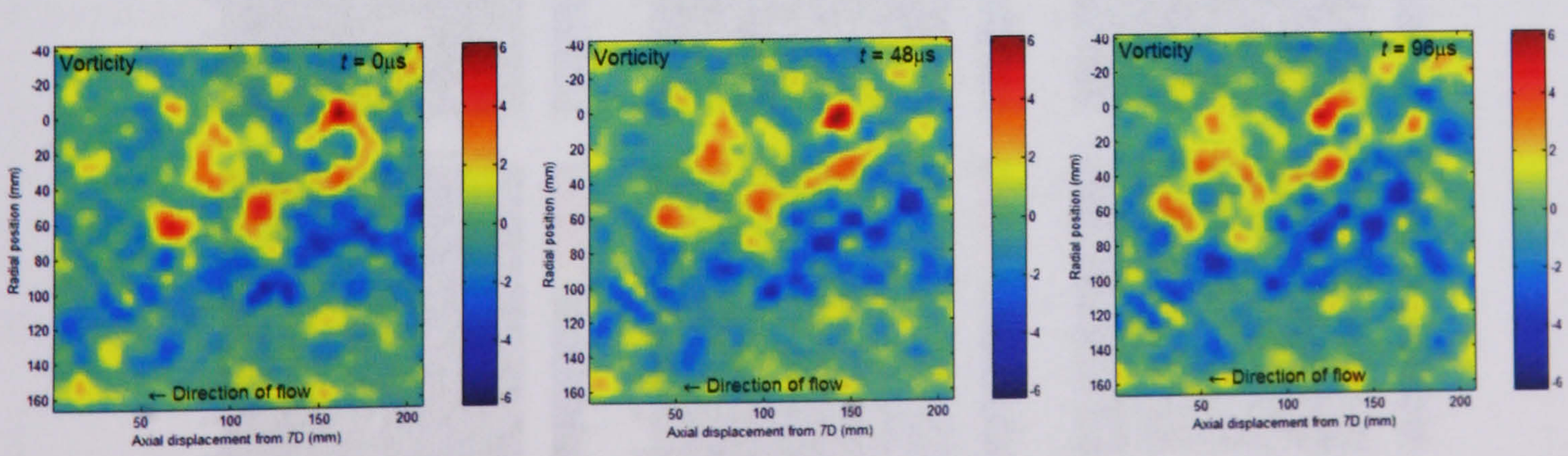

Figure 6.68 – 21 kHz 'movie' of large-scale vorticity (2m from short-cowl nozzle).

6.6.2. Time-Space Correlation

Consecutive axial velocity vector maps, as shown in Figure 6.67 on the previous page, were time-space correlated according to equation (4.1) on page 142. By averaging correlations made between exposures AB→CD and CD→EF, the effective number of samples per τ values was increased to 400, while correlations from AB→EF (as shown below, where the effective $\Delta t = 6$ μs), enabled a greater range of time separations.

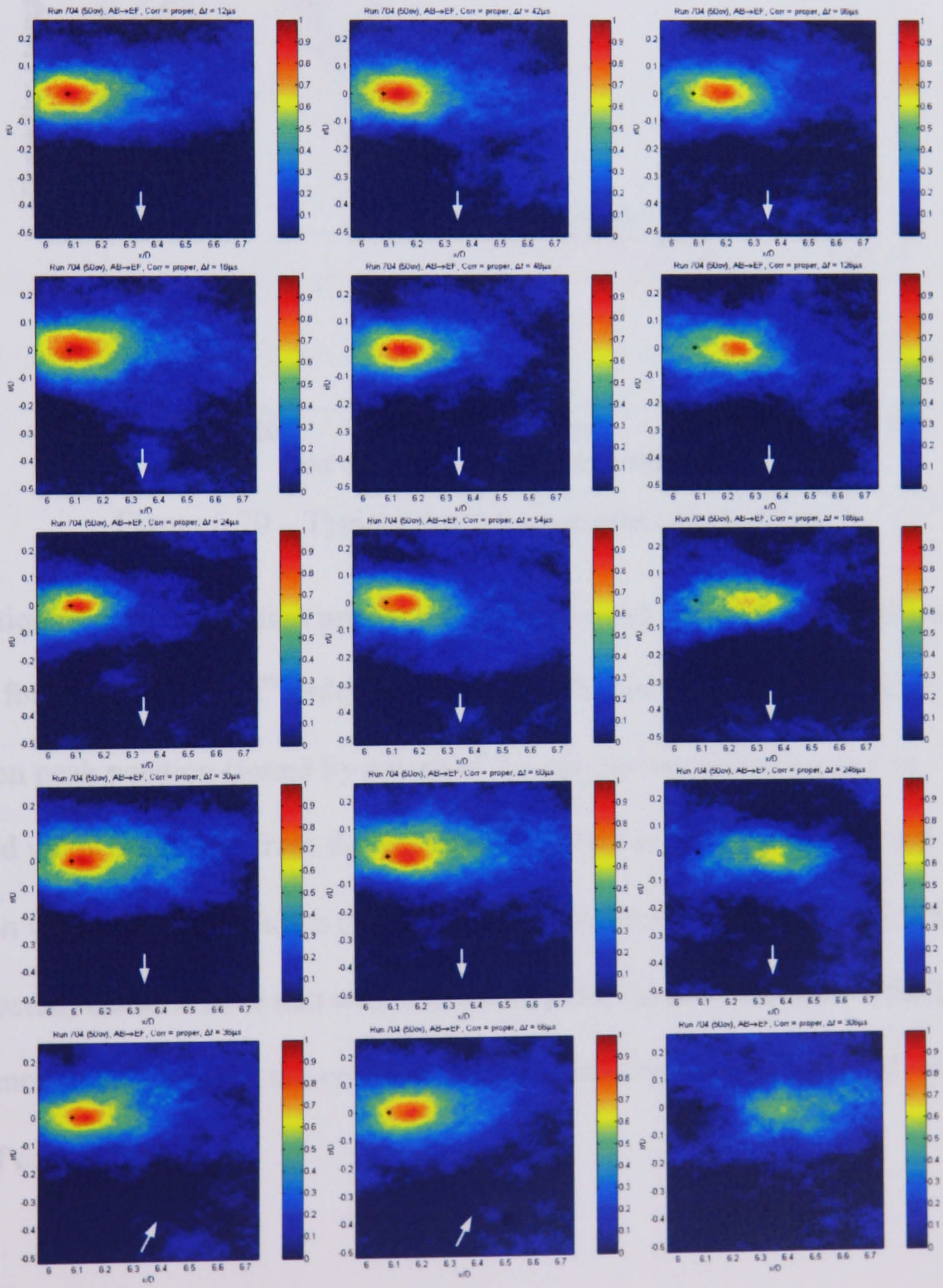

Figure 6.69 – Space-time correlation maps for 15 τ values; $\mathbf{x} = (0, 6.3)D$.

A typical set of axial profiles, extracted from a set of (400 sample) correlation maps at $\mathbf{x}_{radial} = 0$, are shown below. It can be seen that despite the relatively large number of samples, the correlation has yet to reach convergence.

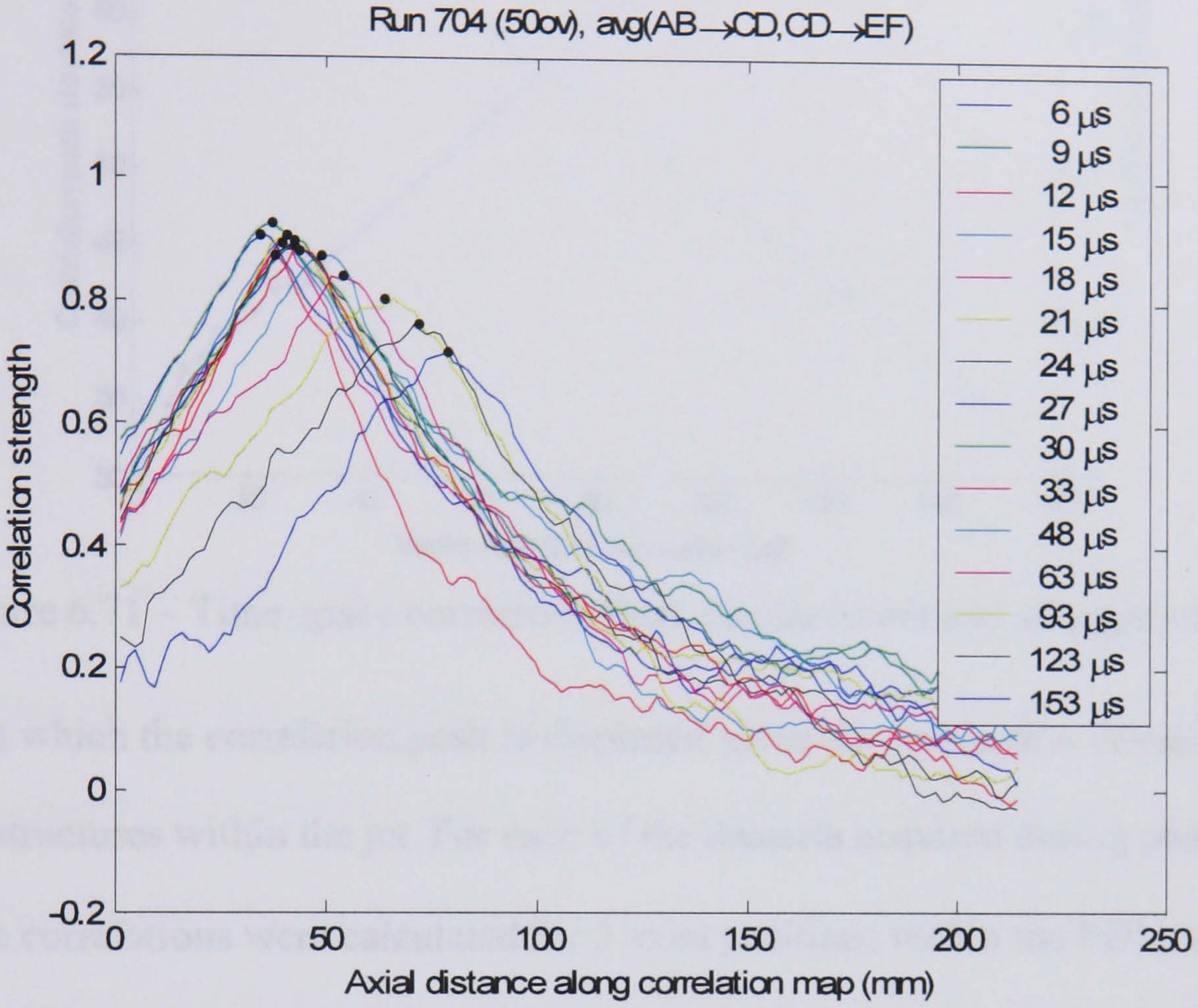

Figure 6.70 – Typical time-space correlation profiles.

The position of each correlation profile's maximum point (marked above with a black dot) was found by fitting a 4th order polynomial to the curve. Figure 6.71 shows the correlation peak position (found by means of the polynomial function) and its associated value (extracted from the data itself), plotted against the vector map time separation τ. The example shown (which is representative of nearly all of the phase 4 data collected) demonstrates that while the correlation value is affected by the lack of convergence in the samples, the correlation peak displacement can be found with a high degree of certainty.

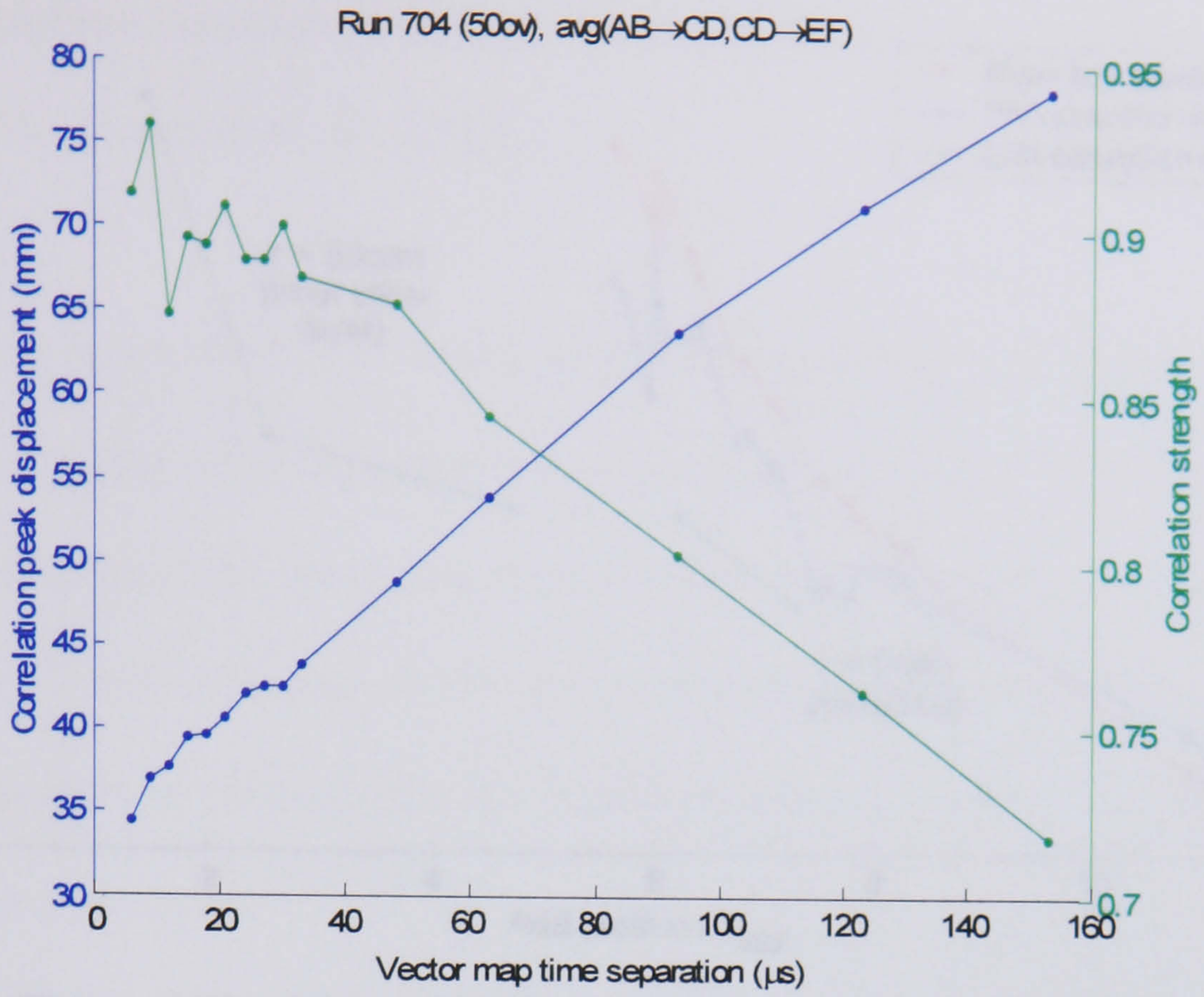

Figure 6.71 – Time-space correlation peak displacement and strength vs. τ.

The rate at which the correlation peak is displaced gives the convection velocity of turbulent structures within the jet. For each of the datasets acquired during phase 4, time-space correlations were calculated for 3 axial positions within the FOV, and the associated convection velocities found for each by line-fitting to the peak displacement values, as shown above.

Figure 6.72 on page 304 plots all of the convection velocities thus calculated against the correlation point's axial position. The axial component of velocity at the correlation point is also shown, as are the convection velocities calculated by means of the 2-point LDA. As can be seen, only 2 LDA surveys were performed beyond 5D (both of which were along the jet centreline), with 6 further surveys having been performed upstream at radial positions of 50 and 100 mm.

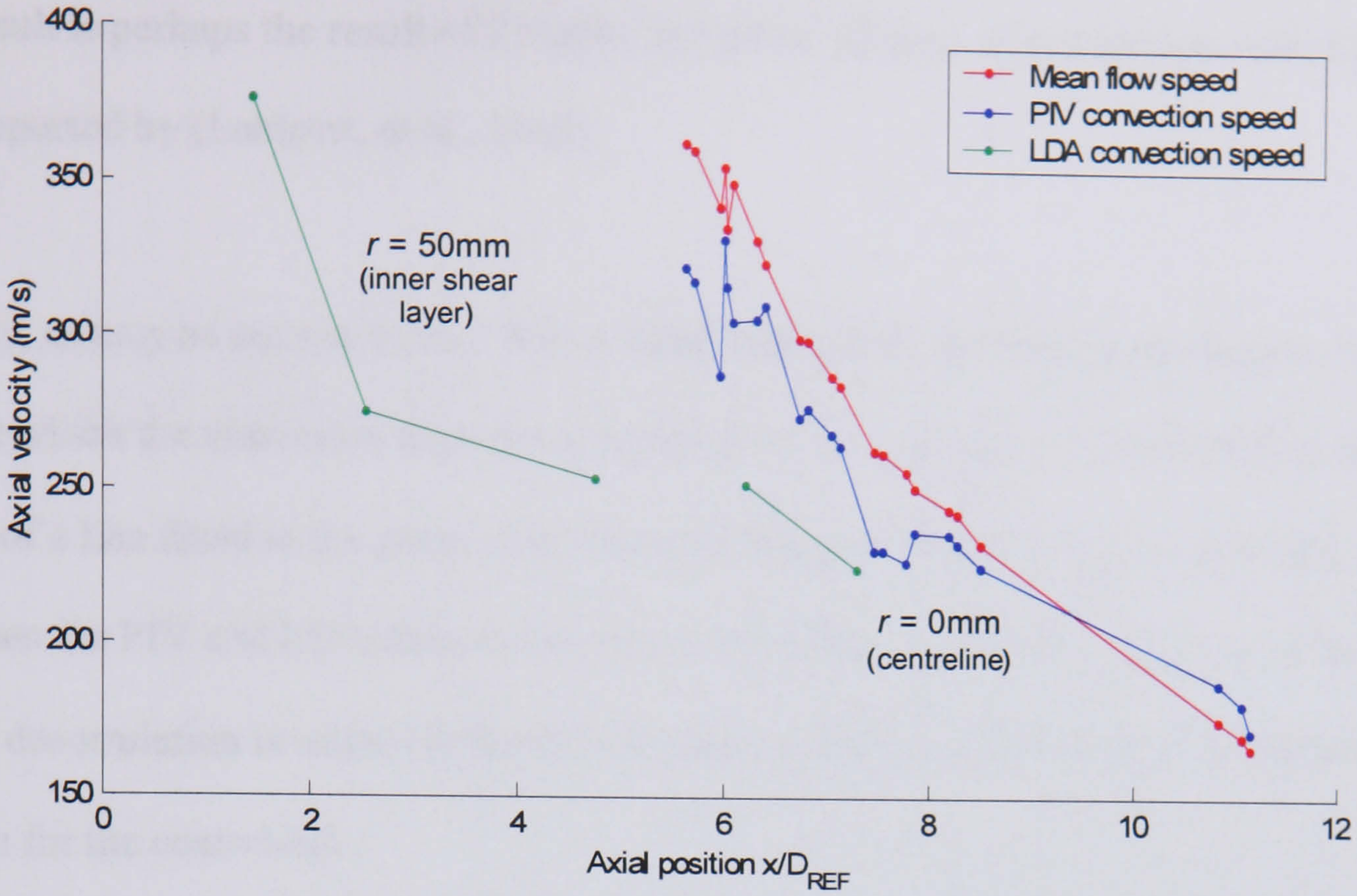

Figure 6.72 – LDA and PIV convection speed measurements.

It can be seen that the PIV convection speed is, on average, 114% higher than that measured using the 2-point LDA. In a comparison of 7 subsonic studies of shear-layer convection speed, (Blohm, et al., 2006) found that planar flow visualisation techniques almost invariably produced values either higher (by 120 – 150%) or lower (~70%) than theoretical calculations, due to uneven seeding between flow layers resulting in the convection speed of seeding patterns, rather than aerodynamic structures, being measured.

The fact that the areas in which phase 4 PIV and LDA can be compared are beyond the end of the primary potential core, means that the seeding should be fairly well mixed, and as a result, the difference in measured velocities is lower than that reported by Blohm. It is interesting to note however that the convection velocities at 11D are found to *exceed* the mean flow speed in that region. The correlation peak positions from these samples follow just as linear a progression as that shown in Figure 6.72, meaning that

the result is perhaps the result of 2 highly separated 'phases' of convection velocity, as was reported by (Lempert, et al., 2002).

Finally, as may be seen in **Error! Not a valid bookmark self-reference.** below, the rate at which the maximum time-space correlation value decreases over time (i.e. the slope of a line fitted to the green data shown in Figure 6.71), matches exceedingly well between the PIV and LDA data. It can also be seen that, as expected, the rate of time-space decorrelation is related to the flow's axial turbulence intensity (whose values are shown for the centreline).

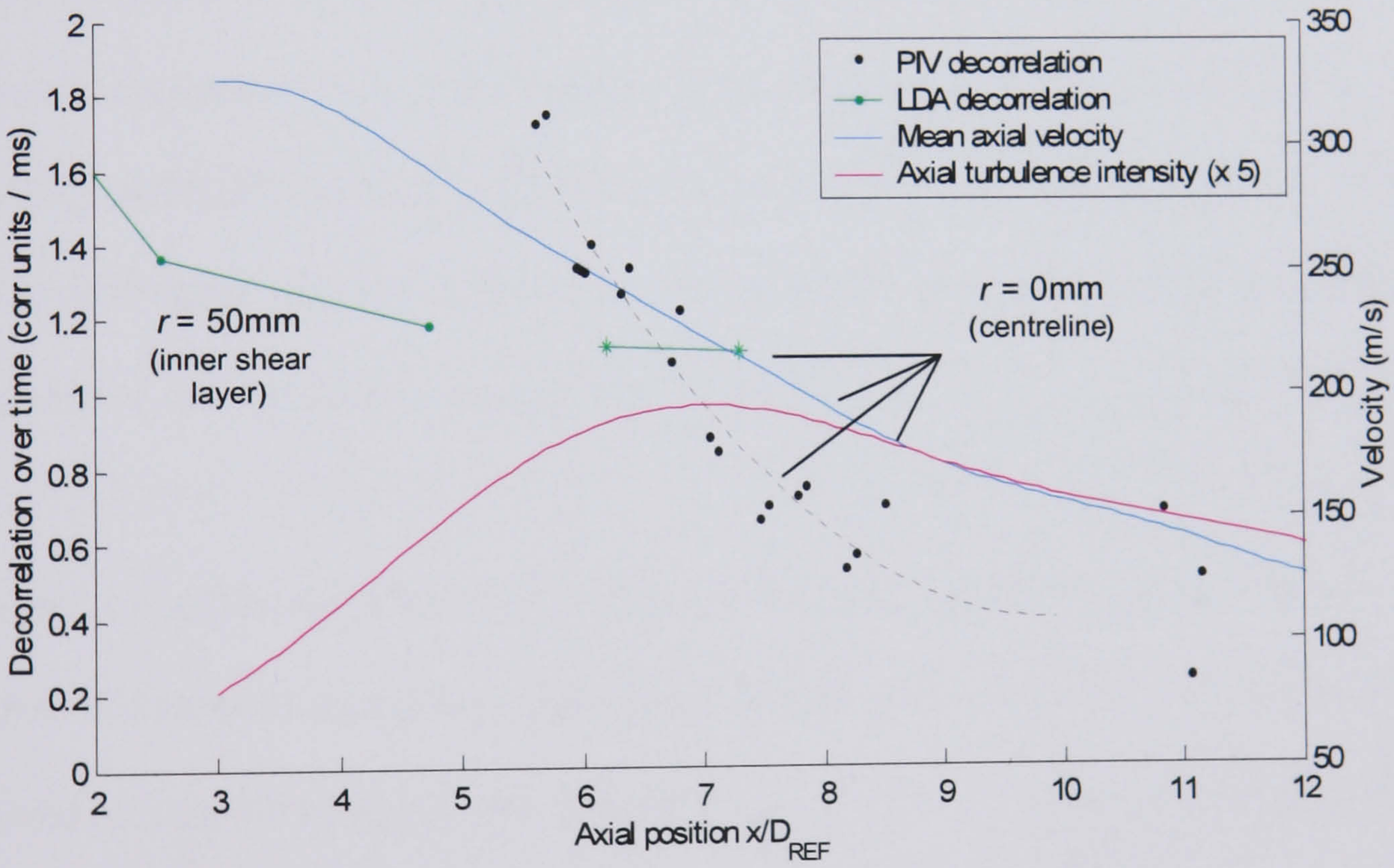

Figure 6.73 – Time-space 'decorrelation' rate vs. axial sample

7. Conclusions and Further Work

7.1. Conclusions

This thesis has detailed the design and construction of an industrialised jet exhaust measurement system, and its successful application to the CoJeN jet noise research project. The PIV system was assembled by the author from scratch, using cameras and lasers explicitly specified for the experiment, and custom-designed hardware, software and electronics, intended to fulfil the complex control requirements of the CoJeN tests.

The combination of bespoke control software and multiple RAID disk storage arrays enabled statistically converged PIV data to be collected from a 3.8 × 0.6 m area of exhaust in little over an hour. Additionally, the rig was used to assemble 3-dimensional, volumetric reconstructions of the exhaust flow, and these proved key to revealing a previously underestimated level of jet asymmetry. The system was also used to acquire the first time-space correlation measurements in a hot, coaxial $^{1}_{10}$ scale engine plume, using a novel and extensible multiple camera technique.

As described in Chapter 6, methodologies have been developed for the systematic removal of erroneous data points (resulting from the concurrent use of LDA and PIV) by means of innovative space- and time-domain statistical filtering. Thorough vector post-processing has been similarly employed to remove the effects of camera malfunction, caused by the extreme environment of the Noise Test Facility. As a result of these measures, independent comparison of the data with that obtained using LDA has shown good agreement, and the system will now be used by QinetiQ for future engine tests in the NTF.

7.2. Further Work

Based on its successful deployment during CoJeN, the Warwick PIV rig will be used for 2 further NTF jet exhaust tests, in early 2007. Unlike CoJeN, the German government funded LEXMOS, and UK funded ANDANTE programmes will test the noise-reduction efficacy of specific engine design geometries, instead of providing data from 'generic' nozzles for CFD validation purposes. LEXMOS will investigate the effects of vortex-inducing castellated nozzles, while ANDANTE will attempt to introduce turbulence into the bypass stream by means of variably permeable gauzes, fitted inside the nozzle. In both cases, the Warwick PIV rig will provide the only non-acoustic measurements.

The most significant rig alternation required by these tests results from the intention to acquire 3-component 'cross plane' data, in addition to 2-component 'in plane' maps, as per CoJeN. This is motivated by the need to measure the (highly 3-dimensional) vortices produced around the LEXMOS castellated nozzles; the realisation that the jet axis may not be aligned with the gantry; and the potentially non-radially symmetric nature of the ANDANTE flows, as a result of certain engine tests being performed in combination with a support pylon (to simulate the effect of real-world engine installation).

In order to support the stereoscopic camera arrangement, a removable welded steel frame will be added to the top of the rig (c.f. Figure 7.1 on page 309) and this will also support the single 'in plane' measurement camera which – as in CoJeN – will traverse vertically to cover the full jet exhaust radius.

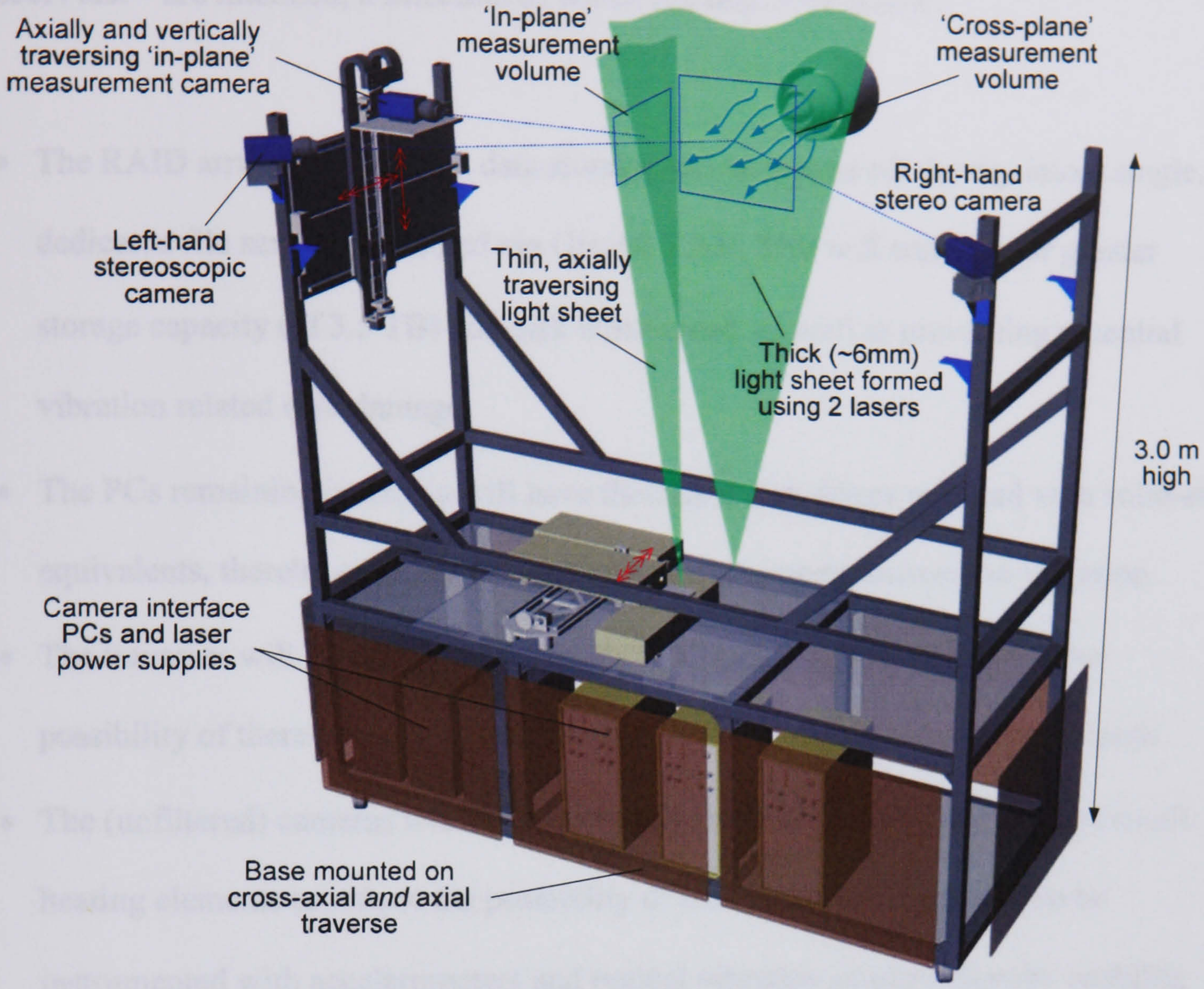

Figure 7.1 – The modified jet measurement rig.

While the use of single pco.2000 cameras in each position will limit acquisition rates to 7 Hz, the ability to simultaneously acquire data from the 2 – essentially independent – camera and laser systems will result in a high overall information bandwidth. Furthermore, by introducing a variable time delay between the 3D and 2D measurements, it will be possible to perform time-space correlation measurements at the same time as collecting time-averaged statistics. The addition of axial traverses for the 'in plane' camera and laser will allow the measurements' maximum phase delay, τ, to exceed the 300 μs possible during CoJeN.

A number of further improvements to the system – based on lessons learnt during the CoJeN test – are intended, a selection of which are described below:

- The RAID arrays used for fast data storage will be moved off the rig, into a single, dedicated file server, connected via Gigabit LAN. This will enable a far greater storage capacity (of 3.5 TB) and disk write speed, as well as preventing potential vibration related disk damage.
- The PCs remaining in the rig will have their hard disk drives replaced with solid-state equivalents, thereby ensuring the control system's imperviousness to vibration.
- The traverses will be refitted with encoded DC motor drives, to remove the possibility of there being insufficient torque to drive the camera and laser loads.
- The (unfiltered) cameras will be fitted with light-sensitive $f/2.0$ lenses, and small heating elements to reduce the possibility of malfunction. They will also be instrumented with accelerometers and optical vibration sensors, thereby enabling the calculation of spatial error margins, as well as offering early warning of potential damage resulting from 100 m/s flightstream flow.

By continuing to evolve in this way, the Warwick PIV system should prove capable of fulfilling ever more challenging measurement requirements in the years to come.